SANDSTONE PORE STRUCTURE: A QUANTITATIVE ANALYSIS OF DIGITAL SEM IMAGES

Vol 1

by

Thomas Martin Wissler
B.S., University of California, Riverside
(1979)

Submitted to the Department of
Earth, Atmospheric, and Planetary Sciences
in Partial Fulfillment of the
Requirements of the Degree of

DOCTOR OF PHILOSOPHY

at the

MASSACHUSETTS INSTITUTE OF TECHNOLOGY

18 March 1987

Signature of Author_____
Department of Earth, Atmospheric, and Planetary Sciences
18 March 1987

Certified by_____
M. Gene Simmons
Thesis Supervisor

Accepted by_____
W.F. Brace
Chairman, Departmental Committee on Graduate Students

Vol 1

SANDSTONE PORE STRUCTURE: A QUANTITATIVE ANALYSIS OF DIGITAL SEM IMAGES

by
Thomas Martin Wissler

Submitted to the Department of Earth, Atmospheric, and Planetary Sciences on 18 March 1987, in partial fulfillment of the requirements for the degree of Doctor of Philosophy

Abstract

Digital backscattered electron SEM images of polished epoxy impregnated sections were used to study quantitatively the pore structure in sandstones. Software implemented methods of image analysis were used to quantify geometric properties of the pore structure.

In previous studies of pore structure quantification by direct analysis, stereological parameters such as porosity and specific surface, S_V, have received the most application. Despite the existence of these and numerous other direct methods for studying pore structure, few substantive conclusions about the structure have been drawn previously.

For this study, the backscattered electron signal was digitized directly from the detector with the beam scan under digital control to acquire high quality images. Operating conditions which produce high signal-to-noise ratios and minimal geometric distortions were determined. Dichotomization of the full intensity image into a binary (pore–grain) image was based on a non-subjective threshold determination from intensity histogram peak locations.

Methods of quantitative stereology were applied to the binary images of 14 sandstones with bulk porosities of 10.5 to 30.5%. Porosity determined by areal fractions agrees well with bulk measurements. Individual feature parameters were used to estimate the theoretical variance in porosity. Larger sample variance indicates sample inhomogeneity or insufficient sampling. S_V and mean pore volume were estimated from line-sampled intercept distributions. The mean pore volume provides a good mean measure of pore size. Point-sampled intercept lengths were inverted by least squares methods for size–shape volume distributions of spheroids approximating the pore space. Oblate ellipsoids with aspect ratios near 0.3 are the best fitting shapes. In addition to numerical criteria, best fits were determined by the match to model independent bulk porosity, S_V, and mean pore volume. Volume distributions are nearly uniform for most samples. Deviation from the uniform distributions

correlates with petrographic descriptions of the samples.

Individual analysis of pore cross sections (*features*) in the image was performed using a line-by-line analysis algorithm. Subtractive mask segmentation (SMS) was developed to divide complex pore features into simpler shapes amenable to description. Bulk stereological parameters and mean feature parameters were measured by feature analysis and the effects of segmentation and resolution on these parameters were examined. S_V from feature analysis of unsegmented features agrees with S_V from lineal analysis. The *dynamic*-equivalent ellipse, defined as the ellipse with central principal moments identical to those of the feature, is a good representation of the simpler features, yielding location, orientation, and anisometry information. Expected aspect ratios of the pores computed from ellipse data agree with those from the size–shape inversion. Ellipsoid aspect ratios determined with the Fischmeister shape factor also agree with the size–shape aspect ratios. Global feature analysis by openings (granulometry curves) was performed using a symmetric structuring element. The information in granulometry curves is similar to that in area weighted distributions of feature area after SMS.

The non-centered covariance of pore features, NCC, was measured by both Fourier and binary methods. S_V from the NCC agrees with S_V from lineal analysis. The diameter of the sphere with volume equal to the mean pore volume correlates with the range of the NCC and with the maximum diameter of the granulometry curves.

Stochastic models of pore structure were examined to show what geometric information they contain. The transition and marginal probabilities of the first-order Markov model are shown to be completely specified by the porosity and specific surface of the material.

Previous empirical correlations and models of physical properties using directly measurable pore structure parameters were reviewed. Few truly quantitative empirical relations exist, but models are available which use well-defined geometric parameters. One such model is the equivalent conduit model of permeability. The conceptual difference between the classical Kozeny–Carman equivalent conduit model and the geometric equivalent conduit model was clarified. The available data from the literature and the data in this study support the classical Kozeny–Carman model as the better model. Permeability was predicted from this model for 11 samples, using porosity and S_V from image analysis and measured formation resistivity factor. The predicted permeability is within the range of measured permeabilities for 6 samples, 3 samples are within a factor of one, and 2 are within a factor of two.

Thesis Supervisor: M. Gene Simmons
Title: Professor of Geophysics

Acknowledgements

I am most grateful to Prof. Gene Simmons for the friendship and guidance he has given me during my stay at MIT. I thank him for the freedom he has permitted in my research. I am also indebted to Prof. Nafi Toksöz for his interest in my work and an introduction to the oil industry. Profs. Ted Madden and Brian Evans gave new perspectives on several aspects of this work.

I thank my cohorts for making life a little better on the third floor. Harvey Haines sparked my interest in computers and Lou Caruso always had mineral names to go with EDX spectra. Jeff Mann led me to serious (?) volleyball and Roy Wilkens revealed a lighter side of research. Frank Miller taught me the patience and thoroughness of an engineer and kept many pieces of equipment alive.

Graduate students certainly do make the school, and MIT has some of the best. Dave Olgaard, Scott Phillips, and Marty Godly are great friends. Karl Coyner offered encouraging words toward the end. I appreciate the friendship and help of these and the many others who remain unmentioned.

A special thanks to José Rosa for proofreading this thesis and to João Rosa for keeping José in line. I'll miss chimichunga night at the Black Table Restaurant. Roger Turpening kept me sane with talk of carbs and camshafts. He and Tien-when Lo also eased the chore of manuscript preparation.

I also thank my family for their support and faith in me. This thesis is dedicated to my wife Marlene: a remarkable person with unlimited talents. She kept me well fed, proofread the complete thesis several times, performed much of the SMS processing, drafted figures, and added innumerable hyphens. Her devotion, encouragement, and help are the reasons I was able to finish.

This research was supported in part by grants from the Schlumberger–Doll Research Center.

Contents

List of Figures

List of Tables

Notation†

a	major axis of ellipse, area of feature
a_1	range estimator of Serra (1982)
a_α	area of α-phase feature
$a^\star$	range estimate
b	minor axis of ellipse
d	pixel dimension
d_b	electron beam diameter
e	electron charge
$f_0(l), f_1(l)$	point-sampled (line-sampled) intercept length density
$f_p(x)$	pore indicator function
$g_V(z)$	volume fraction of object with size z
$g(0)$	DC component of power spectrum
$h, \mathbf{h}$	scalar spatial lag (or shift), vector lag
i_b, i_s	beam current, signal current
k	permeability, spatial lag index
$\overline{k}$	average line curvature
$\acute{k}$	"Kozeny constant", $(\acute{k} = k_0(L_e/L)^2)$
$k_{\text{calc}}, k_{\text{meas}}$	calculated permeability, measured permeability
k_0	shape constant in Kozeny–Carman models
$k_{\text{BK-C}}$	Berryman's (1985a) Kozeny–Carman permeability for penetrable spheres
$k_{\text{CK-C}}$	permeability from classical Kozeny–Carman model
k_{GEC}	permeability from geometric equivalent conduit model
$k_{\text{TK-C}}, k_{\text{SK-C}}$	tortuous (simple) Kozeny–Carman permeability for penetrable spheres
$k_{\text{W-P}}$	Weissberg–Prager (1962) upper bound on permeability
l	intercept (chord) length
$m, \overline{m}$	hydraulic radius, mean hydraulic radius from individual features
$mes(\cdot)$	Lebesgue measure, (e.g., area in 2-D)

$\bar{n}$	mean number of electrons per unit time
$n_0(l), n_1(l)$	number of point-sampled (line-sampled) intercepts
p	perimeter of feature
p_p	probability of pore phase occurrence (i.e., ϕ)
$p_p{}^*$	estimate of p_p
q	aspect ratio of spheroid
q^*	estimated aspect ratio of spheroid
q_F	estimated oblate spheroid aspect ratio from F
r	radius of circle
a^*	estimated range
$s(z)$	surface area of object of size z
$v(z)$	volume of object of size z
w	weighting in least squares inversion
x, y	distance, location
y_e	$\sqrt{1-(b/a)^2}$
$y(D_j, q_j)$	size–shape classes
z	size of object
A	average atomic number, cross-sectional area of material
A_l	flow area normal to flow streamlines
A_x	flow area normal to macroscopic flow direction
A_A	areal fraction
A_b, B_b, C_b	intensity baseline parabola coefficients
A_G, I_G, σ_G	Gaussian curve parameters for intensity histogram peaks
$ACOV(\mathbf{h})$	non-centered covariance computed by Fourier methods
$ACF(h)$	autocorrelation function
$AR(k\Delta x)$	autorun function
B	structuring element
$\check{B}$	transpose of B
C	intensity contrast
C_c, C_s	chromatic (spherical) aberration coefficient
C_F	Freeman direction codes
$CV(\cdot)$	coefficient of variation

D, D_i	major axis of spheroid, major axis of spheroid of class i
D_1, D_2, D_3	major, intermediate, and minor axes of spheroid
D_f	fractal dimension
$D_{\overline{V}_p}$	diameter of the sphere with volume equal to the mean pore volume
$E_0, \Delta E$	beam energy, uncertainty in beam energy
E_{bend}	bending energy in feature boundary
$E[\cdot]$	mathematical expectation
F	Fischmeister (1974a) three-dimensional shape factor
$\overline{F_{3S}}$	mean perimeter ratio (2-D shape factor)
F_R	formation resistivity factor
$G(\lambda)$	granulometry, (i.e., pore feature size distribution)
$\overline{H}$	mean projected height of object
I	pixel intensity
$\overline{K}_m$	average mean curvature
L	macroscopic path length (Kozeny–Carman models)
L_e	effective path length (Kozeny–Carman models)
L_V	length per unit volume
$\overline{L}$	mean intercept length
$\overline{L}_{3g}, \overline{L}_{3p}$	mean grain (pore) intercept length
$\overline{L}_p$	mean perimeter length
M	number of chord length classes, maximum intercept length index
N	noise level, number of occurrences, objects, classes
$N_{\text{even}}, N_{\text{odd}}$	number of even (odd) Freeman direction codes for a feature
N_A	number of features per unit area
N_{Ah}	number of holes per unit area (i.e., grains surrounded by pore)
N_G, N_P, N_T	number of grain pixels, number of pore pixels, total number of pixels
N_I, N_{Ip}	total number of intercepts, number of pore intercepts
N_L	number of feature interceptions per unit length

N_α	number of α-phase features
$NCC(h)$	non-centered geometric covariance
$P_b(I)$	parabolic baseline of intensity distribution
P_L	points of intersection per unit length
P_P	point fraction
P_α	points falling on α-phase
$P2A$	shape factor, $(p^2/4\pi a)$
$Pr(\cdot)$	probability of an event
R	sphere radius
R_{KO}	Kanaya–Okayama electron range
$S, S_{\max}, S_{\min}$	signal level, maximum signal, minimum signal
$S_2(h)$	two-point spatial correlation function for penetrable spheres
S_V	surface area per unit bulk volume
S_{Vg}	surface area per unit grain volume
S_{Vp}	surface area per unit pore volume
S_W	surface area per unit weight
$\overline{S}$	mean surface area of objects
$SD(\cdot)$	sample standard deviation
T_{A+}, T_{A-}	positive (negative) tangent counts per unit area
T_+, T_-	number of positive (negative) tangent counts
$\overline{V}_p$	mean pore volume
V_V	volume fraction
$\overline{V}$	mean volume of objects
$\gamma(\mathrm{h})$	variogram
W	width of test region
X, Y	digital sets (e.g., pore pixels)
Y_i	objects
Z	analysis mask (e.g., image area), atomic number
Δx	simulation increment in stochastic models
θ	orientation of feature
α	beam aperture angle
β_0, β_1	zero-th Betti number, first Betti number

ϵ	eccentricity of spheroid
ϵ_d	damping in least squares inversion
ϵ_c	electron collection efficiency
η	backscatter coefficient
$\lambda_{\max}$	maximum granulometry diameter
λ	electron wavelength
λ_M	Markov model parameter
ρ	density of Poisson process
ρ_b, ρ_g	bulk rock density, grain density
ϕ, ϕ_i, ϕ_b	porosity, porosity from image analysis, porosity from bulk measurement
$\sigma(\cdot)$	standard deviation
τ	tortuosity in Kozeny–Carman models, dwell time
$\mathcal{E}$	number of edges in network
$\mathcal{V}$	number of vertices in network
X^c	complement of X
$X \cup Y$	union of sets X and Y
$X \cap Y$	intersection of sets X and Y
$X \oplus B$	dilation of X by B
$X \ominus B$	erosion of X by B
X_B	opening of X by B, i.e.,$(X \ominus \check{B}) \oplus B = ((X \ominus \check{B})^c \ominus B)^c$
X^B	closing of X by B, i.e.,$(X \oplus \check{B}) \ominus B$
$X \setminus Y$	set subtraction, i.e., $X \cap Y^c$
X BIC Y	bit clear operator $\equiv X \setminus Y$
X XOR Y	eXclusive OR $\equiv (X \cup Y) \setminus (X \cap Y)$

† Additional definitions are given in Tables 5.1, 5.2, and 5.3.

Chapter 1

Introduction

The pore structure in sedimentary rocks is a primary factor controlling the physical response of the rock. This response may be, for example, the velocity of compressional waves, the permeability to fluids, or the electrical conductivity. Thus, to gain a better understanding of physical properties, it is important to characterize and to quantify the pore structure. In this thesis I use techniques of image analysis to extract quantitative measures of pore structure from digital scanning electron microscope (SEM) images of sandstones. Emphasis is placed on measures which describe the three-dimensional geometric structure of the pore space.

Investigators have often made appeals to pore structure to explain measured rock behavior. In his classic paper, which introduced the term *petrophysics*, Archie (1950) stressed the influence of the pore structure on physical properties of rocks. In Archie's study, as in others, pore structure was determined primarily by indirect measurement. The indirect approach uses a physical model which relates the response of the material to some measure of the pore structure. Mercury porosimetry (mercury capillary pressure response) is a good example of the indirect approach. With mercury porosimetry, the physical model is the intrusion of mercury into a cylindrical capillary. The

response is the volume of mercury injected as a function of injection pressure, and the measure of the pore structure is a distribution of equivalent pore diameters.

Direct analysis of pore structure in rocks is less common than indirect analysis. The direct analysis is so named because it is based on a direct image of the pore structure. The image is obtained with an optical or electron microscope. Direct methods of analysis have not been developed as fully as indirect methods, perhaps because of the relative youth of image analysis and the success of indirect analysis.

The block diagram in Figure 1.1 illustrates the basic steps in direct analysis of pore structure. These steps are followed to derive quantitative measures of pore geometry and to relate these measures to physical properties. In this thesis I contribute to the advancement of each step. Step one is the imaging of the pore structure. In this investigation, the image has been obtained by digitizing directly the signal of a backscattered electron (BSE) detector. The digital images so obtained are segmented into grain and pore phases. These two phase (binary) images are the principal subject of further analysis. In step two, measures are obtained from the binary images. Step three consists of the conversion of these image measures into structural measures using methods of quantitative stereology. These structural measures can then be related to physical response (Step 4) through empirical, phenomenological, or mechanistic models. Structural measures are closely tied to familiar concepts of rock texture (e.g., porosity, pore size distribution, grain size distribution). More generally then, these structural measures could be related to depositional environment or post-depositional alteration. In this thesis, emphasis is on the geometric structure, and said structure will be related only to physical response.

Also illustrated in Figure 1.1 is an alternate path whereby the measures

obtained from images are related directly to physical response. This alternate path typically results in an empirical relationship. Two important points arise in considering this alternative path. First, the application or goal of a direct analysis will guide the analysis. If one wants a relationship between image measures and some physical property (e.g., for the purpose of reservoir evaluation) then this type of empirical relationship may be ideal. If, on the other hand, a better physical understanding of the effect of pore structure on permeability is desired, then the full set of steps outlined is preferable. The full set of steps is used in this study. The second important point is that a clear distinction *must* be maintained between image measures and structural measures. The image measures are undeniably determined by the underlying pore structure. However, it is incorrect and misleading to equate, for example, the size distribution of pore cross sections on an image with the distribution of pore sizes.

Even a cursory examination of a scanning electron microscope (SEM) image (Figure 1.2) will reveal the complexity of the pore structure in sedimentary rocks. To describe this complexity requires some form of statistical treatment. It is not feasible or necessarily desirable to describe the structure in a deterministic sense. For example, given a complete map of the structure, a mechanistic model for determining any physical response does not exist. Structural measures will be statistically representative of the structure.

This study began with the primary goal of predicting physical properties of sandstones from quantitative pore structure measurements. However, the basic understanding of geometric aspects of the pore structure was found to be minimal. Methods of characterization were available, but there had been almost no application of these methods. Thus, the emphasis of this study shifted toward providing additional basic information on pore structure geometry, largely using available methods.

We use the general porosity terms of Choquette and Pray (1970) to describe the continuous "pore system" or "pore space" in sandstones. The term *pore* is used to designate local swellings, enlargements, or bulges within the pore system. The terms *pore throats* and *connective pores* are used to describe the more constricted openings which serve as connections between pores. The relatively large pores between grains are termed *intergranular pores*. Pores with nominal dimensions of a few microns, or less, are termed *micropores*.

1.1 Overview of Contents

Chapter 2 is a critical review of the previous direct analyses of the pore structure of sedimentary rocks. The review is confined primarily to quantitative studies. However, select qualitative studies are included to provide guidelines as to what measures of the pore structure will be the most useful, descriptive, and discriminatory. Chapter 2 attempts to fill a significant gap in the current literature. Previously, there did not exist a comprehensive, critical review of quantitative analysis methods which have been applied to sandstones.

Chapter 3 addresses the first step of direct analysis: imaging the pore structure. Optical imaging is first reviewed. Next, BSE imaging is considered to arrive at the conditions required for obtaining optimal digital SEM images. These conditions differ from those best suited for analog SEM images (photomicrographs) intended for visual interpretation. The best possible digital images are acquired so that they are not a limiting factor of the structural analysis. At the onset of this study it was not clear which methods of direct analysis would be used, so considerable effort was put into imaging. Information content of the digital image is considered and a dichotomization criterion is established.

In Chapter 4, methods of quantitative stereology are used to characterize

sandstone pore structure. These methods include the well-known measures of volume fractions (point, lineal, and areal measures) and specific surface. Mean pore intercept length and mean pore volume are estimated from linear intercept data. An advanced stereological method for approximating the pore structure with simple spheroidal shapes is applied in the second half of this chapter. This method involves inverting an intercept length distribution, which has been measured on the image, for the volume distribution of pore size and shape.

Feature analysis methods are applied in Chapter 5. *Features* in sandstone images are the intersections of the pore space with the plane of the image (i.e., pore cross sections). A new method is developed to segment the original features into relatively simpler shapes. Parameters of the simpler features, such as maximum and minimum dimensions, area, perimeter, and ellipticity, are measured. Both a line-by-line method and a boundary mapping method have been used. The results from feature analysis are used to evaluate the statistics of some stereological measures and to improve the stereological size-shape inversion (Chapter 4). Dynamic shape factors of features are also computed and are found to be very good indicators of feature anisometry and feature orientation.

In Chapter 6, measures of spatial correlation are computed from sandstone images. Both Fourier and binary methods are used. The spatial correlation functions must be computed correctly to preserve the geometric information contained therein. Spatial correlations provide measures of porosity, specific surface, and the range of correlation in the structure. Correlation measures are typically used in random media models of physical properties (Chapter 7).

In Chapter 7, the application of structural measures from image analysis is examined. First, the quantitative measures of structure, which were obtained in Chapters 4, 5, and 6, are compared to determine internal consis-

tency and relationships between them. Stochastic models of pore structure are also investigated because of the insight they give on the importance of various measures of pore structure. The equivalent conduit model is next used to predict permeability using specific surface measured by image analysis. Lastly, additional physical properties are discussed to indicate promising directions for work relating directly measured pore structure to those properties.

Chapter 8 is a summary of results of this thesis and a statement of the conclusions and directions for further research.

Details of imaging hardware, samples, sample preparation, and image analysis software are given in appendices.

Figure Captions

Figure 1.1. Schematic diagram of the steps used for the direct quantitative analysis of pore structure.

Figure 1.2. (*a*) Analog photomicrograph of Morrison formation sandstone (sample 2710). Backscattered electron (BSE) image of polished impregnated stub at 20° tilt. Scale bar is 100 μm. Black areas are epoxy filled pores. Note clay in upper left quadrant. White spots are zircons. Majority of grey grains are quartz. Lighter grains are feldspar. (*b*) Secondary electron (SE) analog photomicrograph of pore cast from Berea sandstone (sample 2124). Scale bar is 100 μm. Large flat regions are intergranular pores.

Figure 1.1 Steps in the Direct Quantitative Analysis of Pore Structure

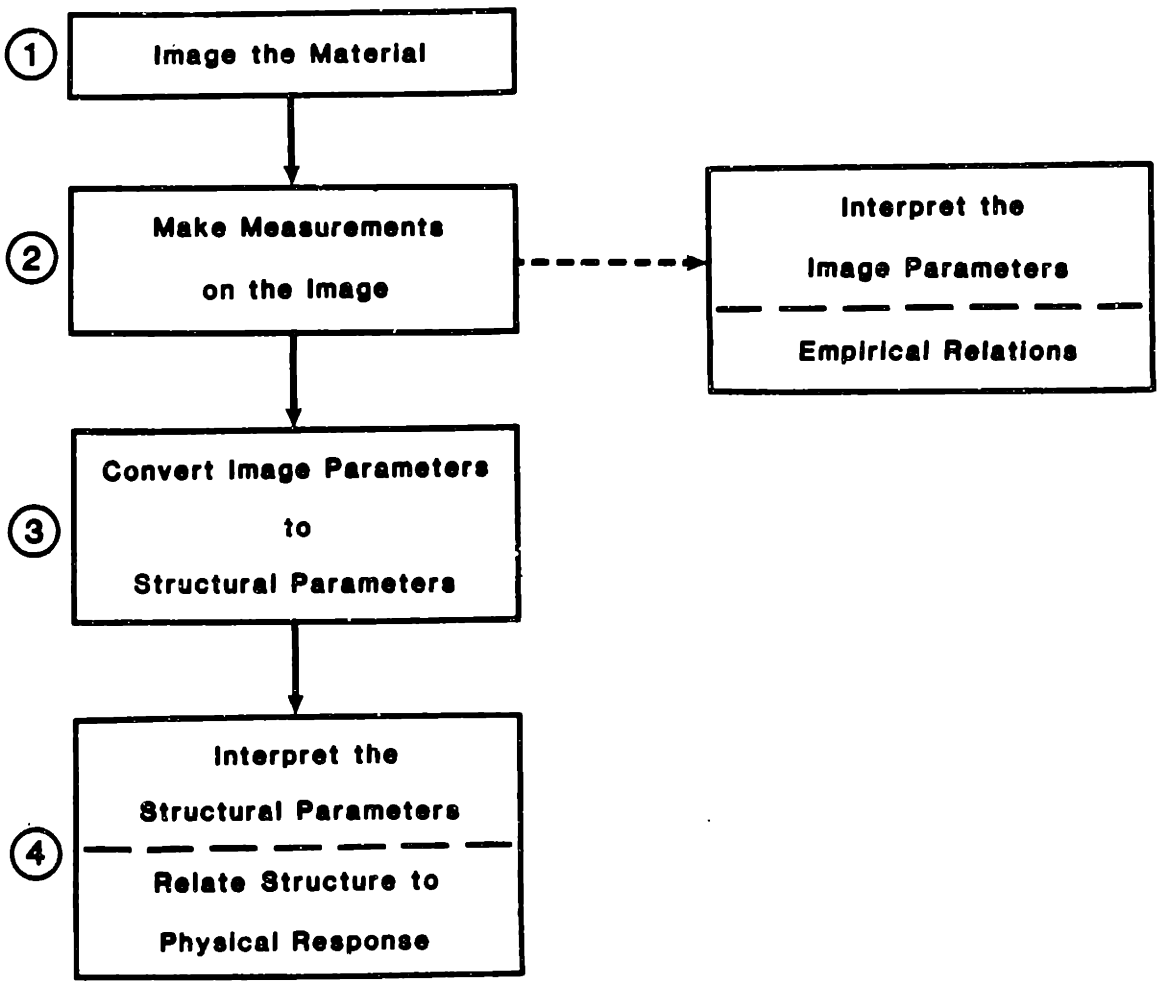

Figure 1.2

(a)

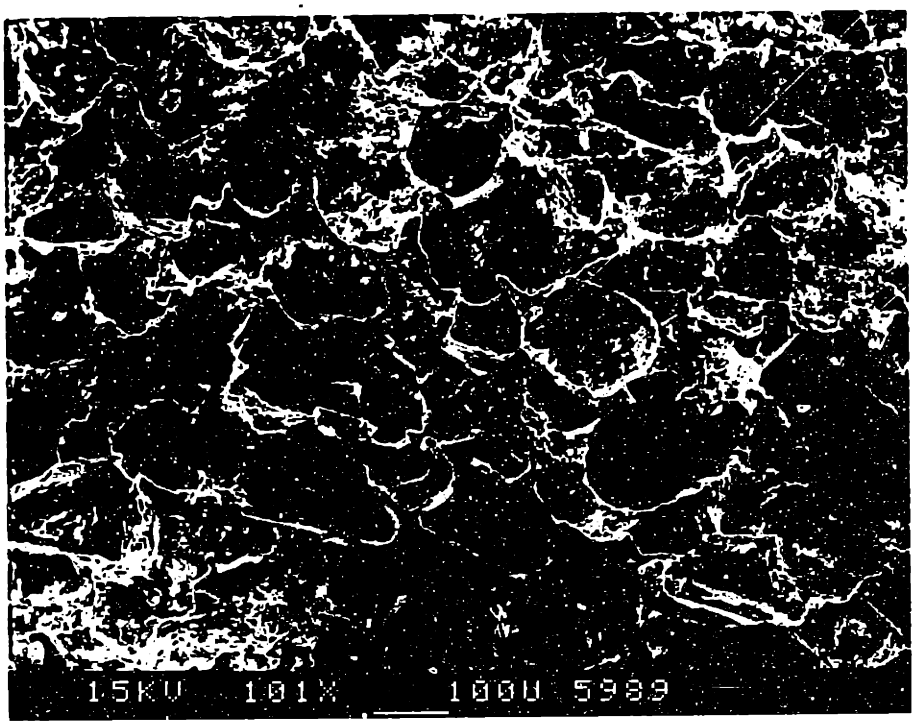

(b)

Chapter 2

Critical Review of Direct Quantitative Analysis Studies

2.1 Introduction

A large body of literature addresses the problem of quantitative characterization of the pore structure of sandstones by direct analysis. The previous work, performed in various disciplines, is distributed throughout many journals. In this chapter the methods and results of previous work are grouped into logical categories and discussed critically. Methods of direct analysis which have been applied to sedimentary rocks are emphasized in this review. Additionally, other methods with potential for application to sedimentary rocks are discussed.

The primary aim of this review is to describe the current state of pore structure characterization in sandstones and to indicate the most promising directions for additional research. We focus on results substantiated by data rather than repeat details of the measurement techniques. For many of the analysis methods, details of the measurement techniques are presented in later chapters where we apply the methods to digital SEM images of sandstones. A

critical review of previous results does not exist in the current literature. The only previous review (Fabbri, 1984, p. 173) briefly mentions a few studies but does not discuss the results. Fabbri (1984, p. 174) states that "A systematic study of rock texture in thin section or polished section has not yet started, although it is certainly overdue."

In the quantitative study of pore structure of sedimentary rocks, the conclusions of any one group of investigators have not been confirmed or verified by another group. To our knowledge, the only exception to this statement is the agreement between porosity measured by stereological methods and porosity measured by bulk methods (e.g., Wyllie and Spangler, 1952; Rink and Schopper, 1978; Ruzyla, 1984). Of course, the basis for this agreement is well-known in geology as the "point counting" method of measuring volume fraction (Chayes, 1949, 1956). The reason for the general lack of confirmation is more likely due to the unique approaches taken by each group, rather than the validity of individual results. Consequently, few facts or relations have been firmly established by image analysis of sandstones. Indeed, the literature contains very little data and almost no interpretation of the data that are presented.

In a general sense, all direct analysis methods could be categorized as image texture analysis (Haralick, 1979). For the present review, a different grouping is preferable to emphasize the study of pore structure. Methods of direct analysis have been grouped into the categories of stereology, feature analysis, image texture, fractals, and topology. The categories overlap to some degree, but these divisions aid in the discussion of the methods.

2.1.1 Binary or Full Intensity Images

An important distinction between methods of direct analysis is whether they operate on a binary or full intensity (grey scale) image. Most methods quan-

tify the structure from binary images. The few methods which operate on full intensity images are those which measure "texture" from grey scale variation statistics, power spectra, and spatial correlation. These methods do not assume that the image represents a geometric structure, but are better termed *classifiers* of images. It is notable that a binary image is required for a structural interpretation of spatial correlation.

Stereological and feature analysis methods assume that the image is a zero thickness slice through a composite material. A point on the image is either in pore space or in grain space. Some stereological methods are available which treat finite thickness sections and projected images (Underwood, 1970, Ch. 6). The segmentation of a full intensity image into a binary image has a direct influence on the subsequent structural interpretation. The dichotomization of full intensity images is treated in Chapter 3.

2.2 Qualitative Studies of Pore Structure

Prior to reviewing quantitative studies, we briefly review some previous qualitative studies. The qualitative studies reveal which parameters are believed to be important for describing pore structure. It may be possible to quantify some of these important qualitative parameters by direct measurement. Studies which have used the scanning electron microscope (SEM) are emphasized, as are studies which have made semi-quantitative measurements of parameters (e.g., pore-to-throat size ratio). We use the term semi-quantitative for those studies which have made manual measurements and which have not used stereological relations to interpret the measurements.

Pore structure is often described in terms of the *mechanism* (e.g., dissolution, replacement, overgrowth) which produced the structure (Choquette and Pray, 1970; Wardlaw, 1976; Schmidt *et al.*, 1977; Wardlaw and Cassan, 1979).

This genetic classification offers concise descriptions of intricate and complex structures. It is also appropriate for describing the origin and modification of porosity. From a purely structural viewpoint, the inferred origin of the structure should be avoided in favor of describing the quantitative geometrical aspects of the current structure.

2.2.1 Thin Section Analyses

Thin section analysis of pore structure reveals information on the spatial distribution, shape, and surface texture of pores (Stout, 1964; Weinbrandt and Fatt, 1969; Choquette and Pray, 1970; Timur *et al.*, 1971; Schmidt, *et al.*, 1977; Schmidt and McDonald, 1979; Wardlaw and Cassan, 1979; Simmons, *et al.*, 1982, 1983; Sneider *et al.*, 1983; Lucia, 1983). Spatial distribution is often referred to simply as "distribution of pores." This practice should be avoided because of the potential confusion with size distribution. It is preferable to use explicitly the adjective "spatial." Spatial distribution is important, for example, when describing the intersection of mesopores and megapores in carbonates which leads to enhanced effective porosity and increased permeability (Lucia, 1983).

Microporosity is identified by the presence of clays, other fines, or altering grains (Pittman, 1979b, 1984).

2.2.2 Pore Cast Analyses

Pore casts reveal the degree of interconnection (connectivity or coordination number), size and shape of pore throats, and size, shape, and spatial distribution of pores (Pittman and Duschatko, 1970; Wardlaw, 1976; Wardlaw and Cassan, 1978, 1979; Pittman, 1979ab; Schrank and Hunt, 1980; Simmons, *et al.*, 1982, 1983; Pittman, 1984). Although the sizes of throats can be esti-

mated visually from pore casts, petrophysical measurements (e.g., mercury porosimetry) are typically used to obtain throat sizes for comparison with pore sizes (Stout, 1964; Choquette and Pray, 1970; Wardlaw, 1976; Pittman, 1979ab; Wardlaw and Cassan, 1979; Brower and Morrow, 1985). However, it is well-known that mercury porosimetry gives a distorted measure of the volume distribution of throat size (Doe and Haynes, 1979; Dullien, 1979, p. 97; Wardlaw and Taylor, 1976).

High or low, large or small, are typical qualitative terms for pore-to-throat size ratios, coordination number, and pore-to-throat abundances. Even approximate orders of magnitude are seldom provided. Examples of commonly used shape terms for the more regular pores are: thread-like, tabular, sheet-like, and tube-like. These examples indicate that a quantitative measure of pore elongation or flattening is likely to be useful.

Wardlaw and Cassan (1979) made a manual semi-quantitative study of pore sizes in pore casts. They measured the diameters of maximum inscribed circles in pore features on a section through the pore cast. These features were from the larger pore spaces or intergranular pores as opposed to the pore throats. Throat sizes were estimated from capillary pressure curves. The ratio of these two sizes was compared to the recovery efficiency (see Chapter 7). They state that the common form of throats in sandstones is sheet-like.

Pittman and Duschatko (1970) state that, in sandstones which have a few percent porosity or greater, a continuous pore network surrounds every grain. Thus, the size of the connective pores is likely to be more important than the number of connective pores or the coordination number for properties sensitive to connectivity.

Microporosity is often expressed in pore casts as surface texture on larger pores. However, large regions of microporosity can be preserved in casts, provided that suitable preparation techniques are used (Pittman, 1984).

2.2.3 Summary of Qualitative Studies

The qualitative studies indicate that pore size and spatial distribution, both of which can be estimated by image analysis, are important descriptors of the pore structure. It is more difficult, perhaps impractical, to determine throat size with image analysis techniques. The frequently mentioned pore-to-throat size ratio may be obtained by comparing pore size determined by image analysis to throat size determined by mercury porosimetry.

In summary, except for total porosity, qualitative studies have not produced well-defined parameters which describe pore structure and which can be obtained by image analysis. The general parameters of abundance, size distribution, shape distribution, and spatial distribution should guide pore structure quantification by digital image analysis.

2.3 Quantitative Stereology

The term *stereology* was coined about 20 years ago to describe "a collection of mathematical methods which relate parameters defining three-dimensional structures to measurements obtainable on two-dimensional sections" (Weibel, 1974). Weibel (1974) presents an illuminating history of stereology as well as guidelines for applying stereological methods. Other general introductions to stereology can be found in Dehoff and Rhines (1968) and Underwood (1970). Current developments in stereology are reported in the *Journal of Microscopy*.

Stereological methods were first applied to crystalline rocks as a means for determining the modal fractions of the various mineral phases in the rock (Delesse, 1848). Despite this early application, commonly taken as the origin of stereology, most of the development and application of stereology has been in the fields of metallurgy and biology (for references, see Hougardy, 1981; Bradbury, 1983).

A fundamental assumption of most stereological methods is randomness in the phase under study. The phase is randomly positioned and randomly oriented. The randomness is necessary to compute orientation- and spatial-averages of structural measures. Stereological relations have been developed for some special non-random structures (e.g., laminated structures), but none appear applicable to pore structure in sandstones. The plane of investigation, the image(s), must contain all statistically significant representations of the material (Picklesimer, 1968; Underwood, 1970, Ch. 1). Otherwise, more images on the same plane or on planes at different orientations must be examined. In practice, the structure can be random or the sampling probes can be positioned randomly, or both.

The assessment of whether the acquired images are representative is difficult given our current level of understanding. To make progress in the study of pore structure, we assume that the pore structure is sufficiently random to allow application of stereological methods. As a fuller understanding of the pore structure develops, we may be able to assess the quality of this assumption.

Stereological methods have been used, in relatively few cases, to study the pore structure of sedimentary rocks. Such studies have measured porosity, specific surface (surface area per unit volume), shape factors, and pore size distributions. In this section, the previous studies of sandstones are reviewed. Relevant studies of other materials are also discussed.

2.3.1 Volume Fraction—Porosity

Perhaps the most fundamental notion of stereology is the equivalence of point, line, area, and volume fractions. That is, the volume fraction of a phase (e.g., pore space) in a composite medium is equivalent to the area fraction of the phase exposed on a plane through the medium. Using standard stereological

nomenclature (Underwood, 1970), the porosity (ϕ) is given by

$$\phi = P_P = L_L = A_A = V_V \,, \tag{2.1}$$

where P_P is the fraction of test points falling on the pore phase, L_L is the fraction of test line falling on the pore phase, A_A is the fraction of the plane area occupied by the pore phase, and V_V is the volume fraction of pore space (e.g., measured by Boyle's law methods). Point counting is routinely used to determine the modal composition of rocks by examining thin sections (Chayes, 1949, 1956). This application is not discussed here.

Rose and Wyllie (1950) and Wyllie and Spangler (1952) used the method derived by Chalkley *et al.* (1949) to determine, simultaneously, porosity and specific surface area from photomicrographs. The Chalkley *et al.* (1949) method is equivalent to separate counts of porosity (e.g., point counting) and specific surface (e.g., from linear intercepts). Porosities of 7 sandstones determined by the stereological method showed good agreement with porosities determined from dry and saturated weights (Wyllie and Spangler, 1952). Stereologically determined porosities were always larger than bulk porosities, but generally within 1% porosity.

Perez-Rosales (1967, 1969) and Perez-Rosales and Martinez (1971) propose the use of stereological methods for the determination of porosity of granular porous media (i.e., sandstones). These papers state the stereological formula and the last gives the porosity of a sand pack (36.9%), determined by point counting.

Dhawan (1972) measured the porosity of 6 sandstones using areal analysis of optical photomicrographs and compared the values with values determined from brine saturation. Typically, the stereological values were 1 to 3% higher in porosity than the bulk measurements.

Rink (1974) gave the porosity of one sandstone measured by areal analysis of digitized optical photomicrographs. The value was 0.7% porosity lower

than a bulk measurement. Rink and Schopper (1978) gave porosity data for 4 sandstones measured by areal analysis. The values are at most 2% porosity lower than the bulk measurements; no value was significantly higher than the bulk measurements.

Lin and Cohen (1982) state that porosity determined by areal fraction analysis of binary digital SEM images of Berea sandstone agrees with bulk measurements "within 6%." It is unclear whether they mean 6% porosity or 6% of the porosity. They present no data and do not indicate which measurement is larger.

Duda and Pitman (1982ab) estimate porosity of 3 sandstones from the areal fraction occupied by features in optical photomicrographs. Their manual digitizing of feature boundaries and feature classification was highly subjective. The image derived porosity of one sample was 4% higher than the bulk measurement. For another sample, the image porosity was 3.5% lower than the bulk measurement. The image porosity of the third sample agrees with the bulk measurement at 10× magnification, but is 3.9% lower at 40×. They attribute the disagreement to non-representative or inhomogeneous samples and non-random selection of areas in photomicrographs. The *ad hoc* exclusion of "clay-filled" pores brought the image and bulk measured porosities in closer agreement. Their study illustrates some of the uncertainties introduced by subjective procedures.

Bisdom *et al.* (1983a) measured the porosity of 2 sandstones using a Quantimet image analyzer (Metals Research Ltd., England) and backscattered electron (BSE) photomicrographs. Automatic discrimination between clay and pore was not possible, and manual image editing was required. Apparent porosity was the total areal fraction of pore and clay areas. The clay areas were manually identified and subtracted from the apparent porosity to yield the true porosity. Bisdom *et al.* (1983a) do not report bulk porosity values

but claim that they were "similar" to or larger than the stereologically determined porosities. Difficulties in discrimination using photomicrography are also discussed by Schoonderbeek *et al.* (1983). These difficulties and others are eliminated by digitizing directly the BSE signal (see Chapter 3).

Ruzyla (1984) presents porosity data, determined by areal analysis, for 12 carbonates, 2 sandstones, and a beach sand. These data were acquired using an image analyzer and optical or SEM photomicrographs. Mean values from the images are in good agreement with bulk measurement. Most image values are less than the bulk values. Image values for two samples of Berea sandstone are 2% and 5% porosity less than bulk measurements. Ruzyla used a significant number of photographs (10 to 25 at one or two magnifications) and found large standard deviations in image determined porosity. He does not state what averaging method was used for combining the data from different magnifications. Because an areal measure is used, the images should be weighted with respect to the physical area which they represent. Otherwise, a non-representative high magnification image could unjustifiably increase the standard deviation. Additional uncertainty may be due to the *ad hoc* threshold selection process used. The threshold was chosen to match *visually* a binary video image with the pore structure seen in the photomicrograph. Moore (1970) describes how visual interaction tends to introduce bias in stereological measurements.

In summary, porosity measured by image analysis has agreed well with bulk measurements. One reason for disagreement could be sample heterogeneity. Disparate values can occur if spatially distant samples are used for the two measurements. For example, there may be insufficient image analysis area for the scale of heterogeneity present in the rock. A second reason for disagreement is the subjective nature by which images are divided into pore and grain phases. Dichotomization is treated further in Chapter 3.

2.3.2 Surface Area per Unit Volume

Surface area per unit volume (S_V) of bulk material is essentially measured by counting elements of surface area which intersect the test plane through the material and normalizing for the test volume. Underwood (1970) reviews methods for obtaining S_V. The appropriate formula for determining pore–grain interface area, per unit bulk volume, in sandstone is

$$S_V = 2P_L = 4N_L \,, \tag{2.2}$$

where P_L is the number of intersections of a test line with traces of the pore–grain surfaces per unit length of test line, and N_L is the number of pore features intersected per unit length of test line. Surface area per unit pore volume, S_{Vp}, is given by

$$S_{Vp} = S_V/\phi \,, \tag{2.3}$$

and surface area per unit grain volume, S_{Vg}, is given by

$$S_{Vg} = \frac{S_V}{1-\phi} \,. \tag{2.4}$$

S_{Vp} can also be found from pore feature measurements using

$$S_{Vp} = \frac{4}{\pi}\frac{\sum p}{\sum a} \,, \tag{2.5}$$

where $\sum p$ is the sum of perimeter lengths of *all* pore features and $\sum a$ is the sum of the area of all pore features. The dimensions of S_V, S_{Vp}, and S_{Vg} are 1/length.

Wyllie and Spangler (1952) present S_{Vg} for 7 sandstones. They used the method of Chalkley *et al.* (1949) which is equivalent to Eqn. (2.2). Their values, re-expressed as S_{Vp}, lie in the range 0.155 to 0.198 μm^{-1}. They used their results in a model of fluid permeability which is discussed in Chapter 7. Wyllie and Spangler (1952) incorrectly stated that the stereological method

is invalid for anisotropic media. Provided that sections through the media are chosen randomly, and provided that these sections are representative of the material, the method is valid for such media (Hilliard, 1968a; Underwood, 1970).

Perez-Rosales (1967, 1969) and Perez-Rosales and Martinez (1971) suggest measuring specific surface area of porous media using a standard stereological technique. Perez-Rosales and Martinez (1971) found S_V to be 0.00245 μm^{-1} for a sand pack; a reasonable value for the grain size of 0.2cm.

Rink (1974) gives S_V (0.0247 μm^{-1}), S_{Vp} (0.0852 μm^{-1}), and ϕ (23.96%) measured by feature analysis (Eqn. (2.5)) for a single sandstone. However, the data are not consistent with Eqn. (2.3). Rink and Schopper (1978) give values of S_V, also measured by feature analysis, for 4 sandstones. The values range between 0.0228 to 0.0266 μm^{-1}.

Duda and Pitman (1982ab) measured feature parameters from manually digitized feature boundaries on photomicrographs. The photomicrographs of epoxy impregnated thin-sections were taken through an optical microscope. Manual tracing is a subjective process. Several significant errors were made by Duda and Pitman (1982b) because they confused the notions of bulk stereological parameters and individual feature parameters. They incorrectly computed S_{Vp} from the mean of the p/a ratios of individual features. The mean of these individual values is *not* equal to S_{Vp} obtained using Eqn. (2.5).

For a monodispersed (i.e., constant radius) assemblage of spheres it can be shown that the S_{Vp} computed from the mean of the feature values is a factor of (4/3) too large. The proof is constructed by comparing the ratio of the integrals of the weighted values

$$\frac{\int_0^R p(r)Pr(r)dr}{\int_0^R a(r)Pr(r)dr},$$

which would give Eqn. (2.5), with the integral of the weighted ratio

$$\int_0^R \frac{p(r)}{a(r)} Pr(r) \mathrm{d}r \ ,$$

where R is the radius of the spheres. $Pr(r)$ is the probability (i.e., weighting) that the intersection of the plane and a sphere gives a circle of radius r, $p(r)$ is the perimeter of the circle, and $a(r)$ is the area of the circle. S_{Vp} computed by averaging feature parameter ratios for shapes other than spheres and for mixtures of several shapes will also be biased.

Correct values for S_{Vp} can be computed from the $\sum p$ and $\sum a$ data given by Duda and Pitman (1982b). The correct S_{Vp} lie in the range 0.089 to 0.198 $\mu\mathrm{m}^{-1}$. The mean of the ratio $\sum p / \sum a$ obtained by individual feature analysis may have some utility for describing pore structure. However, such a use does not conform to the stereological meaning of the bulk parameters, and interpretation of the results cannot rely on the original stereological concepts.

Ruzyla (1984) has presented data on specific surface measured by image analysis. He measured 12 carbonates, 2 sandstones, and a beach sand. The notation and equation for S_{Vp}, given by Ruzyla (1984), are ambiguous. It is possible that he computed S_{Vp} incorrectly in the same manner as Duda and Pitman (1982b). The "mean specific surface" he gives (actually S_{Vp}), may have been obtained by averaging p/a of individual features. However, Ruzyla's S_{Vp} for Berea sandstone (0.52 and 0.32 $\mu\mathrm{m}^{-1}$) are close to the mean value (0.29 $\mu\mathrm{m}^{-1}$) obtained in this study. This agreement suggests that Ruzyla's value is an average from several images. We have no values with which to compare the S_{Vp} data (0.18 to 3.14 $\mu\mathrm{m}^{-1}$) given by Ruzyla for the carbonates. He notes that rocks with relatively large pores exhibit low specific surface values, and that those rocks with smaller pores have high specific surface values. Further, Ruzyla shows that measured permeability tends to increase as specific surface decreases.

Hilliard (1962, 1968a) proposed using specific surface estimates, made as a function of orientation, to quantify anisotropy in a structure. Simmons *et al.* (1975) have used a form of this analysis to study preferred orientation of cracks in low porosity (igneous) rocks. We know of no applications to sedimentary rocks. However, the technique has merit because the measurements are easy and *a priori* shape assumptions are not required. Note that the S_V measurement must be made by lineal methods (Eqn. (2.2)).

2.3.3 Mean Intercept Length

Intercepts or equivalently *chords* are the line segments of a test line which intersect the phase under study. An intercept length distribution is obtained when a series of test lines is positioned on a plane (i.e., image) and a tally is kept of the intercept lengths. Mean intercept lengths can be used as a measure of size. For a two phase image of grains and pores, the mean intercept lengths have been taken by others to be the mean grain "size" and the mean pore "width." It must be remembered that the representation on the image plane is a biased view of the three-dimensional structure and that inversions must be applied to the length distributions to obtain realistic three-dimensional measures of size.

Perez-Rosales (1967, 1969) and Perez-Rosales and Martinez (1971) suggest the use of mean grain size and mean pore width as useful measures of porous media. However, as for porosity and S_V, they present only a single example of a packed sand in the last paper.

Rink and Schopper (1978) reported mean pore intercept lengths between 34 and 40 μm for four sandstones. Mean grain intercepts were between 127 and 153 μm. They did not discuss the values.

Lin (1982b) measured mean grain intercept length on images of 4 adjacent samples from a cube of Berea sandstone. Sixteen images were recorded

for each sample. Magnification was 90× and each image covered about 2.9 mm^2. Results were used to determine the "homogeneity of the cube." Statistical tests were applied to the mean intercept lengths. Based on these tests, she concluded that the cube was homogeneous, but no physical significance was assigned to the mean intercept lengths. Lin (1982b) noted that the intercept length histogram for the grain intercepts behaved roughly with a $1/l$ dependence. The pore intercepts behaved roughly with a $1/l^2$ dependence.

Lin and Cohen (1982) measured mean grain intercept lengths for six samples of Berea sandstone (an unstated number of images) with different permeabilities. They compared the result with a size analysis of disaggregated grains. Four or eight diameters of 500 individual grains from each sample were measured using a LeMont Image Analyzer. The mean intercept lengths were between the mean (and median) of the maximum and minimum grain diameters for all six samples. There is no apparent correlation between the permeability values and the grain intercept lengths. Pore intercepts were not treated.

2.3.4 Three-Dimensional Shape Factors

In this section, three-dimensional shape factors, which can be obtained from stereological measurements, are examined. These shape factors differ from two-dimensional shape factors which describe the shapes of *features* on a plane. Two-dimensional shape factors are discussed separately (section 2.4.4).

Shape factors in quantitative stereology are combinations of parameters which yield shape-sensitive measures of a structure. To be useful, the shape factor must be independent of size, orientation, and spatial distribution of the structure of interest. The shape factor should also be free of *a priori* assumptions about the shape. Underwood (1970, Ch. 7) discusses shape factors (which he terms shape indices) and their measurement. Fischmeister (1974)

critically analyzed the shape factors listed by Underwood, and found a particular combination of stereological parameters which gives an optimal shape factor. This "Fischmeister shape factor," F, is given by

$$F = \frac{2}{3\pi}\frac{{P_L}^2}{V_V N_A}, \tag{2.6a}$$

$$F = \frac{1}{3}\frac{S_{Vp}}{\overline{K}_m}, \text{ or} \tag{2.6b}$$

$$F = \frac{1}{6}\frac{\overline{S}^2}{\overline{V}\,\overline{H}}, \tag{2.6c}$$

where N_A is the number of pore features (i.e., cross sections) per unit area of the test plane and $\overline{K}_m$ is the average mean curvature of the pore-grain interface. Equation (2.6c) is used to determine the shape factors of individual objects (e.g., oblate spheroids). $\overline{S}$ is the mean surface area of the object, $\overline{V}$ is the mean volume of the object, and $\overline{H}$ is the mean projected height of the object. The values of F measured on real materials can be compared with the F which has been computed for ideal shapes using Eqn. (2.6c).

2.3.4.1 3-D Shape Factors and Sandstones

Because the measurement of N_A is required to compute F, this shape factor is often associated with individual feature analysis, despite the stereological foundation. Consequently, in some previous studies, F has been incorrectly computed. Care must be taken to preserve the 3-D stereological information in F.

Rink (1974, 1976a) measured the necessary parameters for the calculation of F (i.e., S_{Vp} and $\overline{K}_m$), but he does not consider their combination. Rink and Schopper (1978) computed F by feature analysis, for four sandstones, giving values in the range of 1.6 ± 0.2. They offer no interpretation of the values.

Duda and Pitman (1982b) computed F for three tight gas sandstones. Unfortunately, their values are incorrect due to the same type of error they

made in the calculation of S_{Vp}. They manipulated Eqn. (2.6) into an incorrect equation to obtain a value of "F" for each pore feature (F is placed in quotes to indicate invalid calculation). Further, they lost a factor of $1/\pi$. The correct form of Eqn. (2.6) using bulk values of S_{Vp} and $\overline{L}_p$ is

$$F = \frac{2}{3\pi^2} S_{Vp} \overline{L}_p \,, \tag{2.7}$$

where $\overline{L}_p$ is the mean perimeter length of the pore features. Their data for S_{Vp} and $\overline{L}_p$ can be used in Eqn. (2.7) to yield correct values of F. The correct values of F range from 1.4 to 2.0, roughly a factor of 8 smaller than their incorrect values.

As with the mean of the ratio p/a, the values of "F" obtained by individual feature analysis may have some utility for describing pore structure. An interpretation of such individual feature averages will require computer simulations to determine the expected values for various structures of interest. Feature descriptors are discussed further in section 2.4.

Duda and Pitman (1982b) presented correct formulae for the shape factor F of oblate and prolate spheroids (using Eqn. 2.6c). For oblate ellipsoids with aspect ratio q

$$F_{\text{obl}}(q) = \frac{1}{2q} \frac{\left[1 + \frac{q^2}{2\epsilon} \ln\left(\frac{1+\epsilon}{1-\epsilon}\right)\right]^2}{q + \frac{\sin^{-1}\epsilon}{\epsilon}} \,, \tag{2.8}$$

and for prolate ellipsoids

$$F_{\text{pro}}(q) = \frac{\left[q + \frac{\sin^{-1}\epsilon}{\epsilon}\right]^2}{2\left[1 + \frac{q^2}{\epsilon} \ln\left(\frac{1+\epsilon}{q}\right)\right]} \,, \tag{2.9}$$

where $q = D_3/D_1$ and $\epsilon = \sqrt{1 - q^2}$.

Using Eqns. (2.8) and (2.9), Duda and Pitman (1982b) concluded that their values of "F" suggest that the pores are more tabular than tubular. Their values for "F" indicated aspect ratios near 0.02, which are unlikely, judging from the equant appearance of the features in their images. The correct values

of F cannot be produced by a tubular shape (i.e., prolate spheroid), whereas an oblate shape with aspect ratio near 0.2 does produce similar F values.

Ruzyla (1984) computed the Fischmeister shape factors for 12 of his carbonate samples. The resulting values were in the range of 2.26 to 4.95. From a plot of F versus S_{Vp}, he concluded that none of the samples has pores approaching spherical shape. However, in Chapter 7, it is shown that his values can be readily interpreted as oblate spheroids with various aspect ratios. Specifically, lines of constant spheroid major axis, which show S_{Vp} as a function of F (both are a function of aspect ratio), pass neatly through the points of his plot (see Figure 7.4). Further, the size associated with the spheroid correlates very well with the mean maximum Feret diameters (see section 2.4.3) of the pore features. The Feret diameter is the perpendicular distance between two parallel lines which are tangent to and on opposite sides of the feature. The maximum Feret diameter is the longest such distance for a feature.

Ruzyla's equation for F is ambiguous, similar to his equation for S_{Vp}. There is the possibility that he computed F from the mean of individual feature values of "F." His values of F are somewhat high, but may be reasonable for carbonates. Our interpretation of the S_{Vp} and F relationship holds even if there are errors in these values because the errors are proportional; only the equivalent aspect ratios will differ. Additional discussion of F will be found in Chapter 5 together with the results from images studied in this investigation.

In summary, care must be taken when computing three-dimensional stereological shape factors so that the assumptions of stereology are not violated. Two-dimensional (feature) shape factors are also important, but they contain different information. The Fischmeister shape factor F is well-suited to the characterization of pore space in sandstones, but only if properly computed.

2.3.5 Pore Size Distribution

Underwood (1968, 1970, Ch. 5) reviews stereological methods for the determination of the size distribution of objects from measurements made on a plane through a collection of those objects. The methods are straightforward inverse problems. Starting with a forward model, the expression on a plane through a collection of objects of known size is derived. Measurements of the expression in real materials are inverted to obtain the unknown size distributions. Dullien and collegues have applied pore size inversion methods to sandstones (Dhawan, 1972; Batra, 1973; Dullien and Dhawan, 1973, 1974, 1975).

Dhawan (1972) determined the pore size distributions of sandstones using both spherical and "general" shape models. This research is also presented in Dullien and Dhawan (1973, 1974, 1975). Dhawan used the Cahn and Fullman (1956) method to invert intercept length distributions for the number fraction size distributions of spheres. The number fraction size distributions were converted to volume fraction size distributions using the equation for the volume of a sphere. Photomicrographs were taken in reflected light from polished Wood's metal impregnated specimens. Cumulative chord length distributions were measured with a Quantimet image analyzer. Three photomicrographs, each analyzed at seven orientations, were required to obtain consistent chord length distributions. Each photograph represents about 0.16 mm^2 of physical area on the sample.

Eleven sandstones were studied with the sphere model. Generally, the size distributions were broad and symmetric with a range from 10 to 120 μm (Figure 2.1a). Distributions for four of the samples were sharper with a "peak" centered near 30 μm (Figure 2.1b). The sphere size distributions were compared with mercury porosimetry curves. The sphere model distributions were "expected to be more realistic than the mercury porosimetry curves" (Dullien and Dhawan, 1974).

The general pore shape model (Dhawan, 1972; Dullien and Dhawan, 1974) uses an experimentally determined pore shape. This general pore model was apparently motivated, in part, by the statistical grain shape studies of Scheil and Wurst (1936). Dhawan (1972) applied the general pore shape model to two sandstones. The general pore model size distributions agreed with the sphere models for sizes above 30 μm. Below 30 μm, the general pore models predict less pore volume. This behavior is due to the larger sizes in the general pore shape models accounting for more of the small pore features (on the image). The general shape is "sharper" and the edges of this shape account for small features (short chords).

Although some evidence indicates that the general pore shape model is an improvement over the spherical model for bead packs, none indicates that the general pore shape model is better for sandstones. Dullien and Dhawan (1974) believe that the sandstones have sufficiently isometric pore shapes so that the general pore shape model does not offer any advantage over the spherical model.

Because of simplifying assumptions and several stages of averaging, the "shape" of the general shape model appears to be lost in the inversion. Chang and Dullien (1976) state that the errors introduced by the simplifying assumptions are intractable. A rough geometric interpretation of the normalized shape function is that of opposing right circular cones with a common base, a reasonable approximation for the pores in a granular medium. The ratio of the base diameter to the height of the cones is lost because of the normalization used. The ratio can apparently vary in the inversion because of the normalizing even though only one shape is allowed in the formulation.

The results from both the Cahn-Fullman and the general pore shape models are *number* distributions of size. Inversions for the number distribution of size are inherently less stable than volume distribution inversion (Roethlis-

berger, 1955; Gundersen and Jensen, 1983). Dhawan (1972) apparently avoids stability problems because of smoothing applied to the intercept length distributions. The results are converted from a number distribution of size to a volume fraction distribution using the equation for the volume of a sphere (Dullien and Dhawan, 1973). For the general pore shape, an "average diameter" is computed as the product of a shape factor times the maximum section diameter for the shape. The shape factor is the normalized cube root of the mean of the cube of the section diameters. It is unclear what effect this averaging shape factor has on the volume-to-size relation.

Batra (1973) used the Cahn and Fullman (1956) method to invert intercept length distributions for the equivalent sphere size distribution in 12 sandstones. The resulting size distributions were similar to those of Dhawan (1972). Five of the samples had symmetric distributions, and 7 had the sharper distributions with peaks near 30 μm. Maximum sizes were 120 to 200 μm.

Chang and Dullien (1976) rederived the general shape model while maintaining mathematical rigor. Their model is further removed from practical application to pore sizing. The reason for this limitation is a more realistic shape function which uses fewer approximations. This shape function is difficult to measure because it requires serial sectioning of the objects. Additional simplifying assumptions would be required to model pores in sandstones. Such assumptions would negate the rigorous derivation and would yield essentially the formulation of Dhawan (1972).

2.3.6 Image Analyzers

Commercially available image analyzers are often used to obtain the data for microstructural analyses. These analyzers typically use a video camera to image a photomicrograph or to view directly through a microscope. The video signal is passed to analog or digital electronics which, based on the signal

level, compute metric measures of the features in the image. The first step in the analysis is the selection of the signal level produced by the phase of interest. After the phase is "detected," the area, perimeter lengths, intercept lengths, and other parameters may be measured. Current instruments contain advanced detection and feature classification algorithms. In a very good review, Bradbury (1983) discusses the application of image analyzers to the characterization of microscopical images. General functions and capabilities of image analyzers have been reviewed by many authors (e.g., Fisher, 1971; Cole and Bond, 1972; Klein and Serra, 1972; Terrell, 1974).

The Quantimet (Fisher, 1971) measures such feature parameters as area, number, perimeter, convex perimeter, vertical and horizontal projection, and Feret diameters. These parameters can be tabulated for only those features which meet some pre-specified parameter values such as minimum area. Newer versions of the Quantimet have advanced capabilities which include image preprocessing, grey level statistics compilation, and operations from mathematical morphology (Bradbury, 1983).

The Leitz Texture Analyzer implements the mathematical morphology approach developed by Matheron, Serra, and collegues (Klein and Serra, 1972; Serra, 1982).

Image analyzers are well-suited for routine studies and the newest image analyzers offer fully programmable analysis. Direct digitization of SEM detector signals is also possible with some machines and is preferable to video imaging of photographs to obtain a better signal (see Chapter 3). However, the high cost of image analyzers can be prohibitive for small research groups. The cost factor and the flexibility of general purpose computer systems have led to specialized software-based systems such as those developed by others (Rink, 1976abc; Fabbri, 1980, 1984; Young *et al.*, 1981) and the one developed in this study.

2.3.6.1 Studies Using Image Analyzers

Although most applications of image analyzers involve biological or metallurgical images (for references, see Hougardy, 1981; Bradbury, 1983), they have also been used with rock and soil samples. Image analyzers have provided at least half of the data published to date on microstructure of rocks. The applications studying sandstones are discussed below.

Dhawan (1972) used a Quantimet to obtain intercept length distributions, section diameter distributions, projected intercept distributions, and area fraction. Batra (1973) also used a Quantimet to obtain intercept length distributions. Results of Dhawan (1972) and Batra (1973) were described above.

Bisdom *et al.* (1983a) used a Quantimet to interpret BSE photomicrographs of thin sections of two sandstones. For the pores, they measured the distributions of feature perimeters and feature areas together with the total area. Their measurements suffer from a lack of intensity contrast in the SEM images (see section 2.3.1).

Ruzyla (1984) used a "Quantimet type" image analyzer to obtain the data for his investigation, which was described above. Ruzyla's measurements included total area, perimeter length, and "pore diameter" distribution. The pore diameters are, in fact, the maximum Feret diameters of pore *features*, a distinction which *must* be maintained. The diameters of pore features do not represent directly the three-dimensional sizes of the pores in the rock.

Pye (1984) used an IMAS image analyzer hardwired to the backscattered electron (BSE) signal of an SEM to measure volume fractions of phases. He was able to resolve the minerals plagioclase, microcline, and quartz from the BSE signal after using EDX spectra to associate individual minerals to BSE signal levels. The stated BSE resolution is 0.1 Z, with 0.1 μm spatial resolution.

Dilks and Graham (1985) analyzed backscattered electron (BSE) images

of sandstones with an image analyzer connected directly to an SEM. They determined mineral fractions through segmentation of the BSE intensities. Dilks and Graham (1985) used discrete thresholds to partition the intensities (mineralogical phases). A more accurate method would have been to fit the histogram peaks with curves and use the areas under the peaks as the volume fractions (see Chapter 3). Morphological data were obtained using the feature analysis operation of opening (discussed in Chapter 5).

The Quantimet has been used also in the quantitative characterization of soil fabrics and structure (Bullock and Murphy, 1980; Gillott, 1980; Bisdom and Schoonderbeek, 1983; Chretien and Bisdom, 1983; Jager *et al.*, 1983). Bullock and Murphy (1980) measured area, perimeter, Feret's diameter, and projection of features in image of soils. Basically, they tabulated histograms of feature area and a perimeter/area shape factor.

Bisdom and Schoonderbeek (1983) used the Quantimet to study BSE photomicrographs of thin sections of soils. They characterized mineral grains with measures of area, perimeter, and Feret diameters. They also characterized voids with these measures and divided the results into shape categories.

We are aware of only one published study which has used the Leitz Texture Analyzer. Sergeyev *et al.* (1980) describes the classification of clay soils using openings and projected lengths of pores. The openings are used to quantify pore "sizes" and the projected lengths are used to quantify anisotropy.

2.3.7 Good Attributes of Quantitative Stereology

Quantitative stereology has several attributes which make it well suited to quantifying the pore structure in sandstones. These include the probabilistic foundation, the direct geometric interpretation, and the small number of assumptions typically required. Because pore structure is very complex, a statistical characterization rather than a deterministic one is both appropriate

and practical. It is impractical to map the complete boundary surface between pore and grain phases.

Stereological methods are based on statistical concepts which have geometric interpretations. With the exception of size inversion methods, stereological techniques generally require only that the structure be random, or require the sampling (i.e., data acquisition) to be random or a combination of both. For the case of anisotropic materials, there are methods available to characterize the anisotropy (e.g., Hilliard, 1968a).

Stereological methods have been applied extensively in the fields of metallurgy and biology. The application of these methods to rocks may benefit from previous developments in those fields. Some of the least addressed aspects of stereology are the statistical validity of the measurements and the associated errors (Nicholson, 1978). Good measurement practices must be followed to get valid stereological results (Moore, 1970). In particular, systematic investigations should not use subjective (e.g., visually guided) decisions. The previous applications of stereology to sandstones are few, so accomplishing a measurement has been considered as important as the accuracy of the measure. On the basis of the experience in other disciplines, the applications to sandstones should develop rapidly.

Shape independent parameters, such as volume fraction, specific surface, and mean pore volume, are excellent measures of the pore structure. Also, for metals, the shape independent measures typically yield the best correlations between structure and physical properties (Rhines, 1980). Further, the shape independent properties are easy to measure. Easily measured properties tend to get the most application (Rhines, 1980).

A possible limitation of stereology is that average properties can be misleading, and measures of the variation of properties may have strong significance in describing the pore structure (see, Nicholson, 1978). Variation can

be addressed through individual feature analysis (see Chapter 5).

2.4 Feature Analysis

An image *feature* is a closed region on the image with specific textural characteristics. For sedimentary rock images, features are the cross sections of the pores or the grains in the image plane. The specific textural characteristic is simply that the area consists entirely of either grain or pore. We consider only pore features. Pore features which arise from the sectioning of a continuous phase can be very complex. We use the term "complex" for non-convex features with a large convex deficiency (i.e., deviation from the convex hull of the feature). Complex features have re-entrant and irregular boundaries (i.e., positive and negative curvature) with overall constrictions and bulges. The term "simple" is used to refer to features which are nearly convex.

Feature analysis methods can be divided into the categories of *individual feature analysis* and *global feature analysis*. For individual feature analysis, the spatial extent of individual features is delimited and *primary* parameters such as area, perimeter, horizontal and vertical dimensions are measured. *Secondary* parameters, such as perimeter/area ratio and feature centroid, are computed from primary parameters to describe further the features. Features with complex shapes may be simplified by segmentation prior to measurement. Statistics from the primary and secondary parameters are used to describe the material. Some parameters may also be converted by stereological relations to yield three-dimensional structural parameters.

For global feature analysis, individual features are *not* delimited. Only the phase (i.e., pore or grain) at each point (pixel in practice) is important. Measurements are made to characterize the spatial arrangement of the set of pore pixels in the image. Some of these measurements are *analogous* with

measurements which can be made on individual features, but the method of measurement is different.

2.4.1 Individual Feature Analysis

Moore and Wyman (1963), Moore (1964, 1968), Moore *et al.* (1968) and collegues at the National Bureau of Standards (NBS) pioneered early work on computer based analysis of microstructure. They developed software to characterize binary images of metallographic specimens. Their work was the foundation from which Rink (1973, 1974, 1976abc) developed a feature analysis system for sandstone images. Much of the software developed in this study is based on the work of both Moore and Rink.

We describe briefly the principal analysis operations of Moore's system. Two of the more significant analysis tools are the bit operations (BITOP) and the feature extraction and characterization (DISECT). BITOP performs a logical combination of a 3×3 pixel window which is translated over the image. Considerable flexibility is available because of the logical combinations which may be specified. The BITOP process could in principal perform most of the operations of the structuring element of mathematical morphology. This capability was developed before the theoretical formulation of mathematical morphology by Matheron (1967). The DISECT process locates features in the image, copies the features individually to a work area, and measures the primary feature parameters such as area, perimeter, height, and width. Combinations of the primary parameters, such as two-dimensional shape factors, area- and perimeter-equivalent ellipse axes, and "compactness factors" were computed.

Rink (1973, 1974) applied feature analysis to sedimentary rock images. He developed a software system for feature analysis which produces the same types of data as the DISECT process. The primary difference in Rink's ap-

proach is that only two lines of an image need to be stored in memory during the analysis instead of the entire image as needed by DISECT. The primary feature parameters are compiled simultaneously for all features which intersect a given line of the image. All features are characterized with one line-by-line pass through the image. Rink (1976ac) also developed a feature segmentation process which simplifies complex features. Segmentation is discussed further in section 2.4.3 and in Chapter 5.

Rink (1976a) incorrectly states that the rejection of features which touch the image boundary gives an "absolutely correct" statistical representation. Each feature will be measured correctly using this criterion. However, the relative proportions of features with specific characteristics will be distorted. Rejection of features will be more probable for the larger features. Thus, the fractions of features, or feature area per unit area of image, will be biased such that the smaller features appear to be more probable than they are. A heuristic proof of this bias can be seen in Figure 2.2. To be counted, the centroids of smaller features (Figure 2.2a) can lie within a larger area than the centroids of the larger features (Figure 2.2b). If the centroid lies outside the inner frame, the feature will touch the boundary and will be rejected. A related example for proper counting of linear intercept lengths is given by Serra (1972). The rigorous mathematical constraints are discussed in Serra (1982, Ch. 2). Briefly, accurate knowledge of the pore structure is available only within a reduced area of the image. This reduced area is produced by decreasing the image frame by the size of the measuring element. For individual feature analysis, the image frame should be reduced on all boundaries by half the maximum Feret diameter of the features being studied. Feature centroids are then required to lie within the reduced area (the mask). Alternatively, the anti-coincidence point (i.e., lowermost right point) could be used to identify counted features (Grant and Reid, 1981).

Rink (1973, 1974) and Rink and Schopper (1978) have used feature parameters to compute the stereological parameters of porosity, specific surface, mean pore intercept length, mean grain intercept length, average mean curvature, and the Fischmeister shape factor; all except average mean curvature were discussed in section 2.3. The stereological parameters calculated from feature parameters are theoretically identical to measures obtained by other stereological methods (e.g., from lineal analysis). The average mean curvature and, consequently, F deserve some additional scrutiny. The pore features are closed curves on the image plane and the average line curvature of any closed loop is $\pm 2\pi/p$; the sign is plus for an outer boundary and minus for an inner boundary. Rink and Schopper (1978) compute the average line curvature, $\overline{k}$, of the pore features as

$$\overline{k} = \frac{2\pi(N_{\text{outer}} - N_{\text{inner}})}{\sum p}, \tag{2.10}$$

where N_{outer} is the number of outer loops (i.e., the number of features) and N_{inner} is the number of inner loops. Inner loops represent holes ("floating grains") in pore features. In practice, the number of inner loops is small. DeHoff (1977) restricts the use of Eqn. (2.10) to convex features, that is, with positive curvature only. Cahn (1972) states that as long as there are differences in curvature (e.g., positive and negative), the stereologically obtained average curvature is of no use. Figure 2.3 shows two features which have the same average curvature because they both have the same boundary length. In essence then, the average curvature is just an alternative representation of the perimeter length of the pore features. As such, the average curvature does not offer additional independent information.

The average mean curvature of a surface in space, $\overline{K}_m$, is given by

$$\overline{K}_m = \frac{\pi}{4}\overline{k}. \tag{2.11}$$

The average mean curvature can be used in the evaluation of the Fischmeister (1974a) shape factor F (Eqn. (2.6b)). Considering the equivalence between average mean curvature and pore feature perimeter length, it is more appropriate, for sandstones, to formulate F in terms of $\overline{L}_p$ (i.e., Eqn. (2.7)).

About 40 primary and secondary feature parameters are described by Rink (1976a). The utility of all of these parameters for sandstone pore structure characterization is not fully known. Rink (1973) presents frequency histograms of feature area, Feret diameter, Krumbein diameter (maximum intercept length), and mean intercept length in the line scan direction for a single sandstone.

Rink and Schopper (1976) again describe the feature analysis method but present no data or interpretation. Rink (1976a) reports frequency distributions of area and hydraulic radius of pore features for a single sandstone, again, without discussion of the values. Rink and Schopper (1978) applied feature analysis to 4 sandstones. Representative values of primary and secondary feature parameters were listed as well as frequency histograms of feature area and hydraulic radii. Reproduction of their values would serve no purpose here.

Ruzyla (1984) measured Feret diameters as a function of orientation for pore features in 12 carbonates. The maximum Feret diameter of each feature was *"arbitrarily"* taken by Ruzyla to be the pore diameter. In order to show that the two are not equivalent, consider the case of a random packing of spheres, all with the same radius. The features produced by the spheres, on a plane through the aggregate, will have a wide distribution of diameters yet the spheres all have the *same* diameter. It is very misleading to equate feature diameter to pore diameter.

In summary, the significance of individual feature parameters, other than those used to compute stereological parameters, is poorly understood. Very little work has been done to relate feature parameters to sandstone pore struc-

ture. The measurement and interpretation of feature parameters is treated in Chapter 5 of this study.

2.4.2 Global Feature Analysis

In global feature analysis methods, the feature parameters are not measured on individual features. Rather, parameters are measured for all of the pore phase and normalized, by number or measure (e.g., area), to give average feature values. We use the term *global* to indicate the entire extent of the image(s), and *not* the entire extent of the material of which an image is a single sample. Mathematicians often use the term global to refer to the entire extent of the material and the term local to refer to its representation in an image (Serra, 1982). (Although, Serra occasionally uses global in the sense of our definition.) Global feature parameters are typically measured for use in *ad hoc* applications, such as regression analysis to physical properties. That is, the global feature parameters are not inverted to yield three-dimensional geometric parameters, although some parameters could be so inverted.

2.4.2.1 Feature Sizing by Erosions and Openings

The operations of erosion and opening, of mathematical morphology, can be used to measure the size distribution of features. Complete discussion of the theory can be found in Watson (1975) and Serra (1982). Only brief descriptions of the mathematical morphology operations are given here. Mathematical morphology is a collection of methods which have been rigorously derived mathematically and which describe aspects of the morphology of sets. The sets can represent the phases of a composite material such as the pores in a sandstone.

Erosion of the set X by the structuring element $\check{B}$ is defined as

$$X \ominus \check{B} = \{x : B_x \subset X\} , \tag{2.12}$$

which reads, all points x where the structuring element B translated to x is included in X. Opening of the set X by the structuring element $\check{B}$ is defined as

$$X_B = ((X \ominus \check{B})^c \ominus B)^c , \tag{2.13}$$

where X^c is the complement of X. The set X represents the pore pixels in the image and the set B is a ***structuring element*** which, for sizing features, is a convex set that approximates a disk.

Serra (1972) briefly described the use of structuring elements to measure the size distribution of image features by openings. Delfiner (1972) presents a more thorough description of the use of both erosion and openings to measure feature size. These methods do not require the identification of the extent of individual features (hence the term global). The sizing can be thought of as finding all points in X where the structuring element is completely included in the pore phase. Different sized structuring elements (produced by a scaling of the basic shape) are used to measure the distribution of sizes. This sizing is ***strongly*** dependent on the shape of the structuring element. Conceptually, the sizing performs a template matching with the pore area. If the template (e.g., a circle, square, or hexagon) fits within the pore phase, the *area* (not the feature) is attributed to that template size.

Feature sizing by openings is popular because the effects can be visualized. An image which is opened with successively larger structuring elements shows the progressive loss of pores which are smaller than the structuring element (see Figure 5.2). The simplification of feature shapes and the tendency for features to become similar to the shape of the structuring element are also apparent. The result of sizing by opening is an areal fraction distribution

of sizes. This distribution must then be interpreted or correlated with some other property.

Delfiner (1972) states that opening was applied to images of "reservoir rocks" by Delfiner (1971). He states further that, "provided that there are no (or few) bottlenecks to prevent communication between pores, the saturated volume (from mercury porosimetry) coincides with the opening of the pores with respect to a sphere of radius equal to the radius of curvature of the interface at that pressure." It is unlikely that he actually used a "sphere" in a three-dimensional opening operation. Realistically, most rocks contain many "bottlenecks" (i.e., constrictions or throats) between pores and the granulometry curves will not resemble the mercury porosimetry curves.

Recently, Dilks and Graham (1985) used the opening operation of a Kontron image analyzer to study pore feature sizes in one sandstone. The images were digitized directly from the BSE signal of an SEM and a square structuring element was used. They suggest that the histogram of sizes is a "fingerprint" of the pore structure. In essence then, they consider the histogram to be a *classifier* of the pore structure rather than a structural *quantification* of the pore structure. Dilks and Graham (1985) also suggest the comparison of the measured histogram with a simulated histogram from a structural model. This latter approach would presumably yield a more quantitative interpretation of the result. It may be possible to formulate an inverse problem using stereological concepts.

Ehrlich *et al.* (1984) have also applied sizing by opening to sandstone pore structure evaluation. They derive feature parameters globally from the image but also monitor the number of features so that the parameters may be cast as average results for the individual features. Alternatively, they may be performing the erosions on individual features as described by Young *et al.* (1981). The exact operations used by Ehrlich *et al.* (1984) to obtain "smooth" and

"rough" porosity fractions are not clearly described and they do not present a rigorous formulation. In fact, their description of the opening process appears to violate the established mathematical definitions (see Delfiner, 1972; Serra, 1982), particularly with regard to the treatment of boundary intersecting features. They do not erode the pore space from the sides of features which are defined by the image boundary. The effect of this convention on sizing is discussed in Chapter 5.

To aid in understanding the significance and implications of the method of Ehrlich *et al.* (1984), I postulate the following equations to describe their analysis. These equations are speculative but they are consistent with the descriptions given in their paper, with the exception that erosion also takes place at the image boundary. They have essentially accounted for the shape difference between the structuring element and the actual features by assigning that difference to "roughness on the pore" instead of assigning it as smaller pores.

The notation of Delfiner (1972) is used below. The mask erosion (for normalizing) is omitted to simplify the expressions. The size distribution of Delfiner (1972), $G(\lambda)$, is given by,

$$G(\lambda) = 1 - \frac{mes(X_{\lambda B} \cap Z)}{mes(X \cap Z)} . \tag{2.14}$$

The total, smooth, and rough porosity of Ehrlich *et al.* (1984) appear to be given by,

$$\begin{aligned} TP(\lambda) &= G(\lambda) - G(\lambda + \mathrm{d}\lambda) , \\ SP(\lambda) &= (N(X_{(\lambda-1)B} \cap Z) - N(X_{\lambda B} \cap Z))mes(\lambda B) , \text{and} \\ RP(\lambda) &= TP(\lambda) - SP(\lambda) , \end{aligned}$$

where $N(\cdot)$ is the number of features in the argument, X is the pore phase of interest, λ is the size scaling factor, B is the primary structuring element, $X_{\lambda B}$

is the opening of X by λB, Z is the frame of measurement (image), $mes(\cdot)$ is the area (Lebesgue measure) of the argument, $SP(\lambda)$ is the smooth (or size) porosity, $RP(\lambda)$ is the rough porosity, $TP(\lambda)$ is the total porosity, and $\cap$ denotes set intersection.

The critical aspect of this formulation is the sensitivity to and dependence on the *number* of features after each opening. The number of features will vary due to the opening process. Consider the case when the throat between two larger intergranular pores is lost during the opening process. The number of features *increases*, partially or completely offsetting the decrease due to small features which are lost (and attributed to the smooth porosity). It is for this reason that distributions dependent on number should be avoided with preference given to volume (area in 2-D) distributions which are more stable (Delfiner, 1972).

The "rough" porosity indicates the size and amount of the roughness, but it does not indicate the size of the smooth pores on which the roughness is located. In the study by Ehrlich *et al.* (1984), the emphasis is again more on the classification of pore structure rather than the geometric characterization of that structure. It remains to be demonstrated how splitting the porosity into the rough and smooth categories will aid characterization of the structure. Indeed, after the development, Ehrlich *et al.* (1984) abandoned the divisions when the opening results are decomposed by an "unmixing" algorithm (a factor analysis).

2.4.3 Feature Segmentation

The features in sandstone images are often very complex. A complex feature may represent, for example, two intergranular pores with a narrow connecting throat. For individual feature analysis, the complex features can be segmented into simpler features. Segmentation allows quantification by the rel-

atively simple individual feature parameters. Segmentation is different from dichotomization. We use the term dichotomization for the identification of the pore phase from the full intensity image. More generally, dichotomization is the selection of any phase for analysis; the image is divided into (1) the phase of interest and (2) all the rest. If the hardware facilities are available, manual editing of an image can be used to segment the features. However, manual editing is subjective, tedious, and slow. A simple, non-subjective, automatic segmentation is preferable.

The erosion and opening operations can be used for segmentation. These operations simplify features by removing irregularities of shape (i.e., deviations from the shape of the structuring elements) and small areas (i.e., smaller than the structuring element). With erosion alone, the size of features is reduced. Opening is less effective at segmenting features, but it roughly maintains the original sizes. As larger structuring elements are used for opening, the smaller features are lost and the larger features tend toward the shape of the structuring element. Rink (1976ac) has overcome several of the disadvantages of the opening process used for segmentation. He developed a "cutting" process which uses erosion, opening, and logical binary combinations to simplify features. Cutting "trims away" the parts of features which differ from the shape of a structuring element but does not eliminate the parts as does opening. The cutting process also has several disadvantages. Cutting produces excessive numbers of small pore features (the trimmed off parts) and also results in the loss of pore feature area from the image. A new method of segmentation which overcomes some disadvantages of cutting is presented in Chapter 5.

2.4.4 Feature Shape—Two-Dimensional Parameters

Many methods have been developed and used previously to characterize shapes of grain profiles or more generally, closed two-dimensional curves in a plane.

The parameters obtained with such methods can be used to describe the shapes of pore features in an image.

Barrett (1980) presents a thorough and critical review of 2-D shape descriptors used for geologic studies. He considers the shape of a particle to be expressed in terms of three independent properties: form (overall shape), roundness (large-scale smoothness), and surface texture. The form descriptors are mainly various ratios of principal axes. The roundness descriptors are mainly related to maximum or average curvature of the grain boundary. Barrett suggests specific shape measures for specific geologic applications. However, because pore features are representations on a plane and are *not* projections of particle outlines, none of his shape measures appear to be particularly well-suited for describing pore structure. A stereological inversion would be required to provide more geometric information from the shape measures. The general concept of several scales of shape description is noteworthy.

A review of shape descriptors of sedimentary particles has also been given by Clark (1981). Clark emphasizes Fourier methods of shape description and presents nine desirable attributes of shape descriptors, which include as a subset, uniqueness, parsimony, rotation invariance, scale invariance, and reflection invariance. He does not suggest a "best" descriptor, but rather, he states that the application will dictate the best descriptor.

Fourier methods of describing particle shape were first developed for sedimentology by Schwarcz and Shane (1969) and Ehrlich and Weinberg (1970). Fourier coefficients are used to parameterize the profile curve of the particles. Theoretically, any desired degree of accuracy is attainable, depending on the number of coefficients used. In practice, only the first few coefficients are used. Fourier methods have been used in a number of studies of sand grains (for a summary, see Boon *et al.*, 1982) and fossils (Anstey and Delmet, 1973; Lohmann, 1983). I am not aware of any application of Fourier methods to

pore feature characterization.

Beddow (1984) reviewed methods of characterizing particle shapes and sizes. His "morphic descriptors" are based on Fourier analysis of particle boundaries. Again, no specific descriptors appear well-suited for characterizing pore structure.

Rink (1976c) lists a number of 2-D shape descriptors for pore features (see Table 5.2). Although presented in the context of quantifying pore structure in sandstones, no data are given. Rink and Schopper (1978) give data for several 2-D shape factors of two sandstones but offer no interpretation of the data.

One interesting method of shape characterization involves the approximation of individual features with a *dynamically-equivalent* ellipse (Medalia, 1967, 1970; Medalia and Heckman, 1969). This method represents the feature as an ellipse with equivalent radii of gyration about the central principal axes. Every point (pixel) of the feature is considered when computing the radii of gyration. Two "dynamic" shape factors, the location (centroid) and the orientation of the feature, result from the analysis. With the dynamic shape factors there is no restriction on the complexity of the shape of the feature. By contrast, certain Fourier methods cannot represent re-entrant or highly complex contours (Clark, 1981). A significant point is that Medalia's factors can be found using Rink's line-by-line analysis method. Indeed, Rink (1976a) describes moments of inertia and inertia axes of features, and states, without exposition, that these quantities are very informative.

Panozzo (1983) describes the use of the projected length of features on the x-axis (of the image) as a method of shape-fabric analysis. Projected lengths are also available from Rink's line-by-line analysis method.

In summary, many methods are available for characterizing the 2-D shape of pore features in a sandstone image. The utility of these methods has not been explored. Rink's very powerful feature analysis method allows the cal-

culation of many 2-D and 3-D (stereological) parameters. It appears to be particularly well-suited for the analysis of pores in sedimentary rocks. We believe it will prove more valuable as a greater understanding of feature analysis develops. This method has been implemented in this study and is discussed further in Chapter 5 where it is applied to sandstone images.

2.4.5 Orientation of Features

Preferred orientation of pore features in an image should indicate anisotropy in the pore structure.

The dynamic feature analysis of Medalia (1970) gives the orientation of the principal axes of inertia of the feature. The method treats every pixel of the feature as an element of mass in a thin sheet and uses elementary mechanics to compute the moments of inertia. Rink (1976a) included the primary parameters necessary for computing the moments in his line-by-line analysis. He also gives the equations from computing principal moments and the orientation of the principal moments, but he presents no data.

Duda and Pitman (1982ab) used the orientation of the "largest dimension" (probably the maximum Feret diameter) of pore features to study the anisotropy of pore structure in 3 sandstone samples from the Uinta Basin of Utah. Pore feature boundaries were defined by manual digitizing. Results were presented as polar plots of the pore axis angles. They also counted pore intercepts as a function of test line orientation, which is similar to the method of estimating anisotropy in S_V described by Hilliard (1968a). Based on visual inspection of the plots, Duda and Pitman (1982ab) concluded, and we concur, that the images showed little if any anisotropy of pore structure.

A weighting of the orientation by the anisometry of the feature (i.e., the axial ratio) and the area of the feature would probably give a more realistic view of the anisotropy. Otherwise, nearly isometric features with random

orientation would mask highly anisometric oriented features. Further, it would be good to apply statistical tests for orientation (e.g., Mardia, 1972; Dudley *et al.*, 1975).

2.4.6 Summary of Feature Analysis

Feature analysis is an important part of a comprehensive study of pore structure because it gives a measure of the variation in the structure. Stereological parameters determined from average feature parameters should agree with the values obtained by other stereological methods (e.g., point counting, lineal analysis, tangent counts). Care must be taken to insure that the feature parameters are averaged correctly to get valid stereological parameters. However, conventional stereological methods, other than size inversions, give only average properties and do not quantify the variability as can be obtained from feature analysis.

Previous studies using feature analysis have developed methods of analysis and have demonstrated the measurement of parameters, but little interpretation has been presented. The full potential of feature analysis has yet to be realized.

2.5 Image Texture Analysis

Image texture is related to the more familiar concepts of rock texture (e.g., size, shape, sorting, orientation, and packing of grains, Blatt *et al.*, 1972). However, the relations between the "texture" measured in images and the physical microstructural features in the rock exist only for special cases. For example, the slope of the autocorrelation function at zero lag is proportional to S_V. In this section, the image texture measures which have been applied to sedimentary rocks are reviewed. Unlike quantitative stereology and feature

analysis, image texture analysis can use the full intensity grey scale image (e.g., for intensity co-occurance matrices). Image texture analysis is a global measure which is frequently applied to a low magnification image on which the individual phases are not resolvable.

2.5.1 General Comments on Image Texture

Haralick (1979) reviewed various approaches to the measurement of image texture. He defines texture as "an organized area phenomena which is constructed from tonal primitives with certain spatial organization." Methods which characterize image texture specify the tonal primitive properties (e.g., average tone, or maximum and minimum tone) and the spatial interrelations (e.g., structural, probabilistic, or functional dependence). Common measures of texture include autocorrelation functions, optical transforms, digital transforms, textural edgeness, structural elements (i.e., mathematical morphology), grey tone co-occurrence, run length, and autoregressive models (Haralick, 1979). Most of these techniques have been applied to rocks. An important aspect, yet to be understood, is the relation between tonal primitives (i.e., the descriptors of texture) and the microstructure of the rock.

2.5.2 Autocorrelation Functions

Fara and Scheidegger (1961) were the first to characterize the "image texture" of a sandstone. They proposed a one-dimensional autocorrelation function and three types of spectral analysis (digital transforms, harmonic function analysis, and orthogonal function analysis) to characterize the image. They did not estimate an autocorrelation function from their thin section photomicrograph.

Preston and Davis (1972) computed the autocorrelation function of digitized traces across photomicrographs, but only as a means of computing the

power spectra, which are discussed below.

Lin (1982a) computed autocorrelation functions of digital SEM images by discrete Fourier methods. She has examined digital micrographs of Berea sandstone and Whitestone limestone. Her calculations appear to be inconsistent with those required for geometric interpretation of the autocorrelation (for formulations, see Chapter 6). Briefly, it appears that she computed a "circular" autocorrelation from a full intensity image. The geometric interpretation of zero lag autocorrelation as porosity *requires* dichotomization of the image. Similarly, a "transient" autocorrelation is *required* for computing S_V. Lin's porosity value from the zero lag correlation does not agree with the porosity measured stereologically by areal fractions, which it should. Further, the S_V computed from the slope of the autocorrelation function at zero lag did not agree with stereological values, which it should. Lin (1982a) notes that the autocorrelation functions appear more similar than the images from which they were computed. No agreement was found among the *ad hoc* "3dB lag point" of the autocorrelation, mean grain size, and mean grain intercept lengths. It is perplexing how Lin can state that the autocorrelation function is not suitable for "their" study of pore structure, yet in a companion paper, can state that the autocorrelation shows that various samples are homogeneous (Lin, 1982a,b). If the measurement is unsuitable, in what sense are the samples homogeneous?

The importance of spatial correlation functions in models of two phase media is described in more detail in Chapters 6 and 7. Indeed, spatial correlation functions have some potential for describing pore structure. The autocorrelation is known to contain information on porosity, specific surface, and correlation length. However, this interpretation assumes that the image is a slice through a medium and, as such, is more similar to stereological methods than to image texture methods.

2.5.3 Digital Transforms

Fara and Scheidegger (1961) applied two techniques of spectral analysis to a single sampling of a single photomicrograph of a sandstone. Considering the limited statistical significance of their data, the predicted porosity of 26.8% was very close to the measured bulk porosity of 26.3%. They concluded that the spectral coefficients characterize the porous medium, however, they used the technique on only one sample. Their results are inconclusive because they did not show that the method could discriminate between two different samples. However, their pioneering work was an important contribution.

2.5.4 Optical Transforms

The power spectra of an image can be measured by optical processing. Optical processing has been applied to photomicrographs of rocks by several investigators (Pincus, 1966; Pincus and Ali, 1968; Pincus, 1969a,b,c; Preston and Green, 1969; Preston *et al.*, 1970). Davis and Preston (1972) provide a thorough review of work prior to 1970.

Power spectra are claimed to contain information on pore size distribution, pore spacing, and sedimentary structures (Pincus and Ali, 1968; Davis and Preston, 1972). However, relations have *not* been established between features of the power spectrum and conventional measures of rock texture (e.g., size, shape, packing, and orientation of grains). Nor have relations been established between physical properties (e.g., permeability) and power spectra, although some authors (e.g., Davis and Preston, 1972) assert that such correlations should exist.

Serra (1982, Ch. 9) states that the autocovariance is preferable to power spectra for describing structure in images because the geometric information, such as porosity and specific surface, are more easily computed from the au-

tocovariance than from the power spectra.

In summary, spectral results do show some character of the *image*, but it is uncertain how to relate the data to geometrical aspects of the structure. Further, the spectra have not been shown to relate quantitatively to *any* physical properties.

2.5.5 Grey Tone Co-occurrence

Haralick and Shanmugam (1973) characterized image texture of sandstones from the spatial grey tone (intensity) arrangement. Spatial grey tone arrangement is described in terms of (1) the linear dependency of grey tones, (2) the degree of "homogeneity" of the image, and (3) the angular variations of the image grey tone dependencies. These parameters are used to categorize digitized transmitted light photomicrographs. An identification rule (linear discriminant function) was obtained with training photomicrographs and was subsequently tested by identifying (categorizing) test photomicrographs. A high identification accuracy (89 to 93%) was obtained and the authors conjectured that image textural features may be used in a regression model for predicting physical properties (e.g., porosity, permeability, and formation factor). However, they have missed an indication that the prediction potential is low. The assignment errors in a contingency table of true category versus assigned category show *no* correlation to similarities in porosity or permeability of the categories (rock type). Thus, the textural features do not appear to be a function of either porosity or permeability.

Newbury and Joy (1973) measured grey level transition probabilities in digitized SEM photomicrographs in an effort to improve the signal-to-noise ratio of the SEM signal. They concluded that the transition probabilities are not useful when the signal has a high signal-to-noise ratio, as do the digital images from this study. No structural interpretation of the transition

probabilities was proposed nor is any apparent to us.

One application of grey level statistics (transitions and co-occurrence) may be that of identifying regions in an image which have structure *within* the pixels. These cases exist when the structure scale is smaller than the resolution of the image. An example is low magnification images of clay in pores. The physical pixel in this case will be composed of clay and pore space (epoxy). Clay regions may have specific textural characteristics which can be identified on the basis of grey level statistics. Alternatively, a higher magnification image can be used to measure the structure.

2.5.6 Summary of Image Texture

Examination of full grey scale images by texture analysis has not produced useful information on pore structure. Intuitively, one would expect that since the full grey scale image produces a complete visual description of the material, there should exist a wealth of structural information in the image. The full intensity digital image, particularly when digitized from photomicrographs, may not contain as much useful information as previously believed. The intensities in such an image are a function of the imaging process, the photographic process, and the digitization process. The accurate dichotomization (identification of the pore phase) of the image is the most important operation applied to full intensity images. The full intensity image must contain significant information for this operation. But, the local spatial relations of intensity variations probably carry no more useful information than the location of pore–grain and grain–grain boundaries.

2.6 Fractal Description of Pore Structure

The concepts of fractal behavior and fractal dimension (Mandelbrot, 1977, 1982) have been applied previously to the characterization of granular and porous media. The fractal dimension, D_f, is a measure of the area filling ability of a curve or the space filling ability of a surface. This dimension is a useful descriptor of the complexity of a boundary or surface. The measured boundary length or surface area will depend on the resolution of the measurement. The fractal dimension ranges between 1 and 2 for curves in a plane, and between 2 and 3 for surfaces in space. Curves and surfaces which differ from straight lines and planes, respectively, have larger values of fractal dimension. A curve or surface which can be described by a fractal dimension is said to express fractal behavior.

2.6.1 Fractal Description of Particle Boundaries

Kaye (1984) discussed the use of fractal dimension for characterizing "fineparticles." Of particular interest is the dependence of fractal dimension on the resolution of the measurement. Kaye (1984) found two distinct regions of behavior: a low resolution "structural fractal" and a high resolution "textural fractal". Kaye (1984) proposes that the physical significance of these two regions is that different mechanisms of particle formation are dominant at these two different scales. Rigaut (1984) has formulated a theory of non-ideal fractal behavior discussed below, which may offer a better interpretation.

Kennedy and Lin (1986) present methods of measuring fractal dimensions of closed curves. They also discuss the use of fractal dimension for the description of sedimentary particles.

Although the fractal dimension may contain some structural information, it is not a complete measure of gross morphology (Kaye, 1984). The fractal

dimension, for example, gives no information about the macroscopic aspect ratio of an object, thus it must be used in conjunction with other descriptors. Nonetheless, fractal dimension may be a useful descriptor of pore feature roughness.

2.6.2 Fractal Description of Pore–Grain Interface

Recently, Katz and Thompson (1985) measured the number of "edges" in secondary electron (SE) photomicrographs of sandstone fracture sections as a function of magnification. They identified edges as "secondary-electron-intensity extrema" (due probably to charging phenomena at edges). Somehow the number of features counted at a particular magnification is converted to a count of the number of features "of size L" (implying size measurement) per unit length. They claim that the pore spaces in these sandstones are "fractal geometries". Specifically, the "log-log plot of the number of geometric features of size L per unit length versus the size L" is linear with slope $2 - D_f$. Supporting evidence is the agreement between measured bulk porosity and porosity estimated from the fractal dimension. Also, the "pore-pore density autocorrelation function" is proportional to the parameter L^{D_f-3}. They do not provide derivations for any of these relations.

My primary criticism of Katz and Thompson (1985) is the vagueness with which they describe their measurements on SEM photomicrographs. They do not illustrate the measurement with either a photomicrograph or a schematic. Their description is unclear about what geometric quantity is actually measured (counted?). Further, because fracture surfaces produce strong topographic contrast in SE images and because of the inability to locate structures spatially without stereoscopic reconstruction, the length measurements are questionable. Lastly, Katz and Thompson (1985) assume that the fractal dimension, which they obtained for a limited range of measurement scales, is

valid outside of that range.

The remaining concepts discussed by Katz and Thompson (1985) are interesting. In particular, the relation between the autocorrelation function and D_f may be an alternative (and more rigorous?) way to measure fractal dimension.

2.6.3 Other Fractal Studies

Wright and Karlsson (1983) critically examine the application of fractal concepts to the study of microstructure. They conclude that the resolution used for a particular geometric measurement should depend on the detail required for the intended application or model of that geometric parameter. Only under special circumstances can the measurements at one scale be transformed to another scale. Typically, D_f is a function of the measurement resolution (i.e., non-ideal fractal behavior). This dependence emphasizes that the value of D_f obtained from one range of measurement scales must not be used to characterize behavior outside of that range. Wright and Karlsson (1983) also demonstrate that feature shapes cannot be adequately characterized or differentiated by fractal analysis.

Rigaut (1984) developed an interesting generalization of the fractal dimension concept. Ideal fractal behavior (i.e., constant D_f over some range) is a special case of the more general formulation by Rigaut. For the many applications when the usual log-log fractal plot is not linear, or is only piecewise linear, the general formulation appears most suitable for describing experimental results. The general formulation eliminates the need for subjective choice of linear segments. Note that the two regions of behavior found by Kaye (1984) might be better described by the non-ideal fractal formulation than the piecewise linear description.

2.6.4 Summary of Fractal Studies

The following statements summarize important points of the application of fractal concepts to the description of microstructure.

1. The resolution of a measurement should be determined by the intended application of the results (Wright and Karlsson, 1983).

2. A fractal dimension is valid only within the range of scales at which it was measured.

3. Fractal analysis does not adequately characterize feature shape, but may describe some scale of roughness of the feature boundary.

4. In practice, a large proportion of boundaries does not show ideal fractal behavior. The non-ideal fractal formulation is appropriate for those cases.

2.7 Serial Sections and Topology

It is generally accepted that the connectivity of a phase in three dimensions, among other parameters, cannot be measured on a single two-dimensional section (DeHoff, 1983). Exceptions exist for trivial unrealistic cases. Serial sectioning provides a means whereby the continuity of arbitrary objects or a continuous phase can be traced through three-dimensional space. The material is sliced into wafers which are thin enough for single objects (e.g., grains) or a short segment of the continuous phase (e.g., pores) to extend from the top face to the bottom face. Phases can be mapped in three dimensions and connectivity can be measured. In this section, topological properties of microstructures, and other properties which cannot be measured in two

dimensions, are reviewed. The methods for making the measurements and their application to sandstones are outlined.

2.7.1 Topological Properties

Barrett and Yust (1970) reviewed the essential notions of topology in the context of using topological measures to characterize metallurgical samples. Here I list, with brief definitions, the parameters which have been applied.

The zeroth Betti number, β_0 of a phase, X, is the number of separate components comprising X. For the pore phase, β_0 may be considered as a measures of the number of *separate* pore networks which are not connected to one another (Lin and Cohen, 1982). The first Betti number, β_1 is a measure of the number of "circuits" in the network. Thus, β_1 gives an estimate of the redundancy of path in a connected network. For a regular network, β_1 is related to the coordination number of the network. However, Dullien (1979, p. 91) points out that, in general, β_1 is not the same as the coordination number. β_1 is given by

$$\beta_1 = \mathcal{E} - \mathcal{V} + 1 \,, \tag{2.15}$$

where $\mathcal{E}$ is the number of edges (connecting paths) and $\mathcal{V}$ is the number of vertices (nodes where edges meet) in the network. The first Betti number is equitable to the genus of the network (Barrett and Yust, 1970). The second Betti number, β_2 is the number of internal surfaces in a two phase composite (e.g., pores and grains).

Note that the topological parameters given above describe a network, without regard to the size of the network or the volume occupied by the network. The parameters "genus per unit volume" (DeHoff *et al.*, 1972) and "genus per vertex" (Lin and Cohen, 1982) have been used to allow comparison of topological parameters with other properties. Fischmeister (1974b) also suggests

that connectivity be referenced to a specific volume.

Gray (1971) has discussed the topology of phases in two-dimensional space. The topology in two dimensions is not representative of three-dimensional structure and is useless for describing the three-dimensional pore network of sandstones.

2.7.2 Serial Sectioning

Serial sectioning and the determination of topological parameters were pioneered by Rhines, DeHoff, and collegues in the 1960's for the study of the sintering process (Rhines *et al.*, 1969; DeHoff *et al.*, 1972; Aigeltinger and DeHoff, 1975; Patterson and Rhines, 1979).

DeHoff *et al.* (1972) described in detail the procedures for estimating topological properties. Because the analysis is tedious, they suggested that application will be limited to very select problems. The data are taken from closely spaced sections produced by an ultra-microtome, or from a thick section which is repeatedly ground and polished.

Recently, Dehoff (1983) suggested that serial sectioning should be applied to more problems. He stated that the use of serial sectioning is "prohibitively expensive and tedious." Yet, serial sectioning is the only way to estimate certain properties such as number of objects, connectivity, and real object shape. These properties have a place in describing the pore structure of sandstones, but it is unclear whether they are worth the effort required for their measurement.

2.7.3 Serial Sectioning, Topology, and Sandstones

Both Lin and Cohen (1982) and Yanuka *et al.* (1984) have applied serial sectioning analysis to sandstones. Yanuka *et al.* (1984) present their sectioning

method (repeated grinding-polishing), optical imaging technique, photomicrograph digitization, and redisplay ("reconstruction"). They do not offer any further analysis.

Lin and Cohen (1982) measured the zeroth and first Betti numbers for an 0.2 mm^3 volume of Berea sandstone. They manually traced the pore features in analog SEM photomicrographs of a sequence of 15 serial sections (14–17 μm separation) and subjectively "connected" the features on successive sections. They concluded that the volume was inadequately sampled because the sections were too widely spaced. They obtained a large variation in β_1 per unit volume (5.4×10^{-7} to 1.68×10^{-6} μm^{-3}). They concluded that the sandstone sample is less connected than the *spheres* in a regular sphere pack of comparable porosity and grain diameter.

There is doubt that the topological parameters of a sandstone can be accurately measured by serial sectioning. For an accurate measurement, the number of paths leaving a volume must be a small fraction of the number of branches within the volume (Dullien, 1979, p. 91).

2.7.4 Discussion of Topology and Sandstones

It is unclear whether measurements of the topological parameters are worth the effort required for their measurement. Measuring the conduits themselves and the size range of the conduits appears to be more significant. Once connectivity is established, as it appears to be in most sandstones (Pittman and Duschatko, 1970), the size of the connections, a metric property, appears to be more important than connectivity. For example, the smaller constrictions in the larger paths through a material will control fluid flow. It is necessary to carry along metric information with the topological information. Network models of flow may offer insight into how topological parameters control fluid flow, however, suitable treatments of topology have apparently not been de-

veloped (Chatzis and Dullien, 1977).

In summary, topological results for sandstones are not substantive. Complete topological mapping of the pore structure is not necessarily desirable. Because of the variability of the structure and the difficulty of measurement, approachs such as stereological methods and metric measurements appear to be more promising.

2.8 Current State of Direct Analysis

The preceding review shows that many promising methods exist for characterizing sandstone pore structure. Lack of data and its systematic analysis are the primary shortcomings to date. The tools for describing structure are abundant but they have been used very little.

Stereological parameters such as porosity, specific surface, and the Fischmeister shape factor have been established as useful parameters for describing pore structure. Other parameters with strong significance for describing pore structure have not been identified and their nature will depend on the structural information required for specific applications. It is important to maintain rigor in the discussion of pore structure; particularly with regard to what is measured, how it is measured, and how the measurement relates geometrically to the structure.

Figure Captions

Figure 2.1. Sphere model pore size distribution, $\frac{dV(\delta)}{d\delta V(\delta)}$, as a function of

sphere diameter, δ, from Dhawan (1972). The area under the distribution is one. (*a*) Berea sandstone (E-2). (*b*) Reservoir sandstone (11-101). Note the strong peak at 30 μm.

Figure 2.2. Schematic illustration of the dependence of effective sampling area on feature size. The center of the circular features must lie within the inner box to be counted (shaded features). The smaller circles in (*a*) can lie within a larger area, without touching the outer frame, than the larger circles in (*b*). Thus, the smaller circles are sampled over a larger effective area. For simple features such as these, an analytic relation can be found to correct the sampling bias.

Figure 2.3. Schematic illustration of the ambiguity of average line curvature for a closed feature boundary. Both the irregular blob and the enclosing circle have the same average line curvature because they have the same perimeter length. The average line curvature does not distinguish between these two shapes which have greatly differing ranges of curvature along their boundaries.

Figure 2.1a Sphere Model Pore Size Distribution

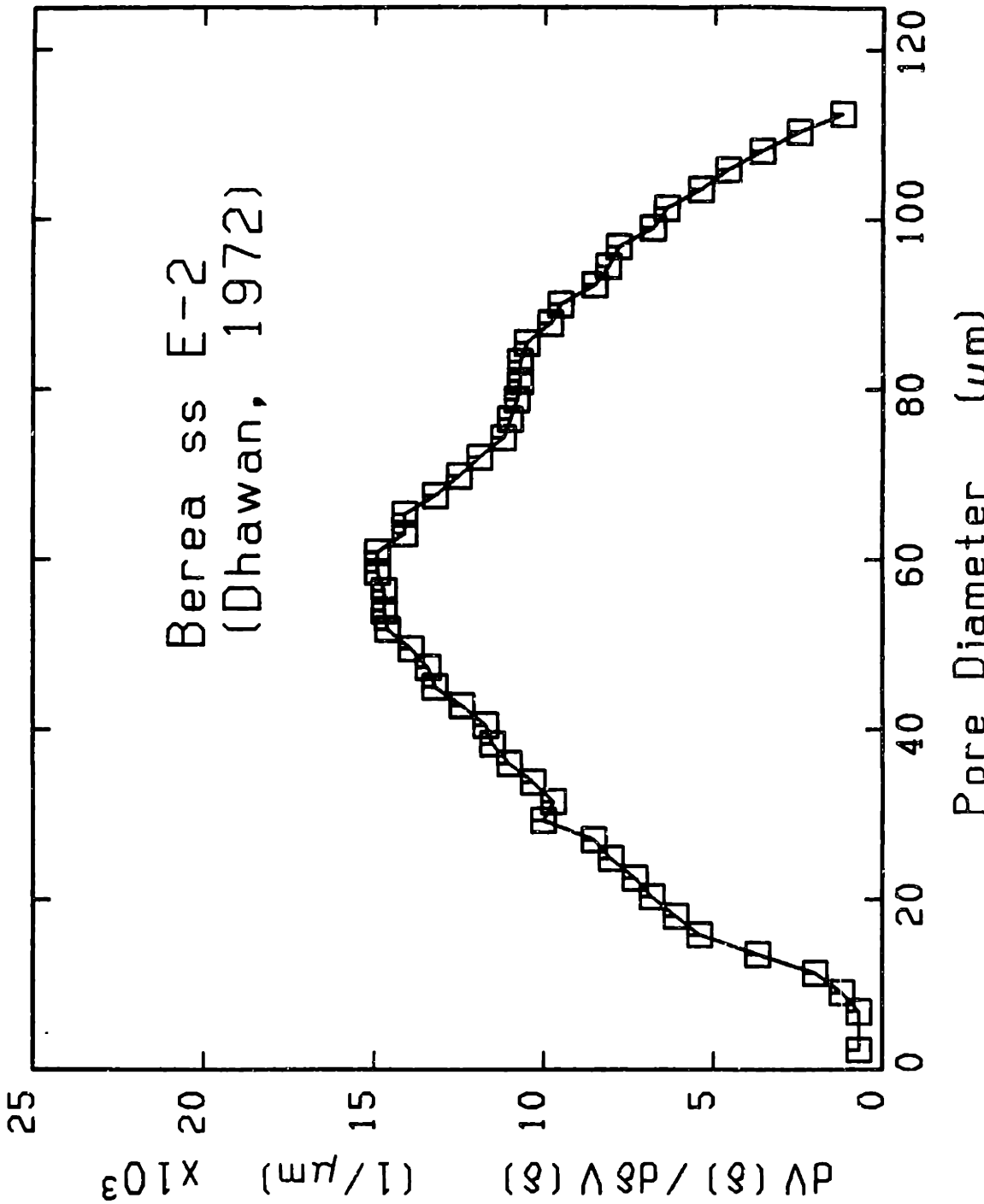

Figure 2.1b Sphere Model Pore Size Distribution

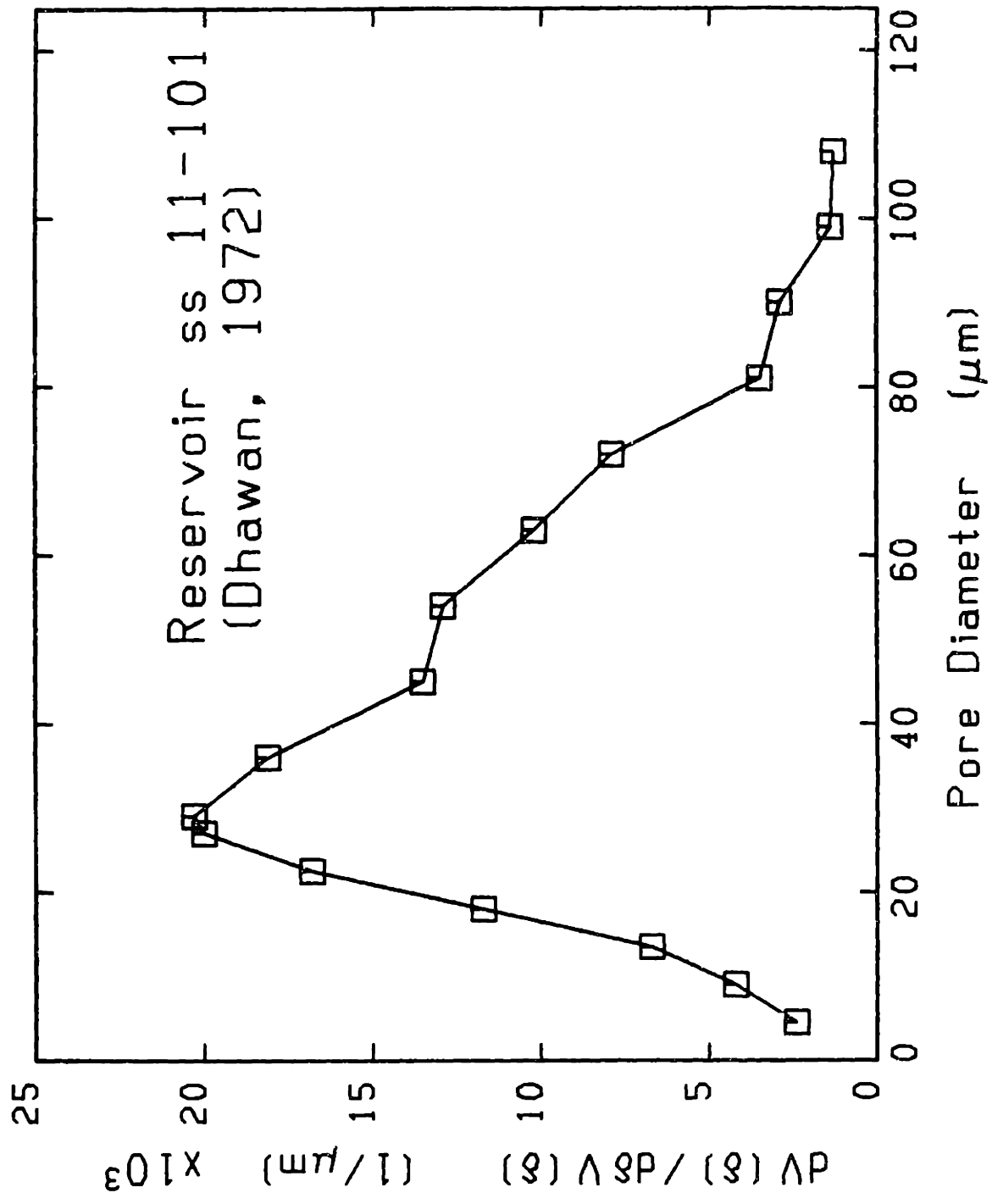

Figure 2.2

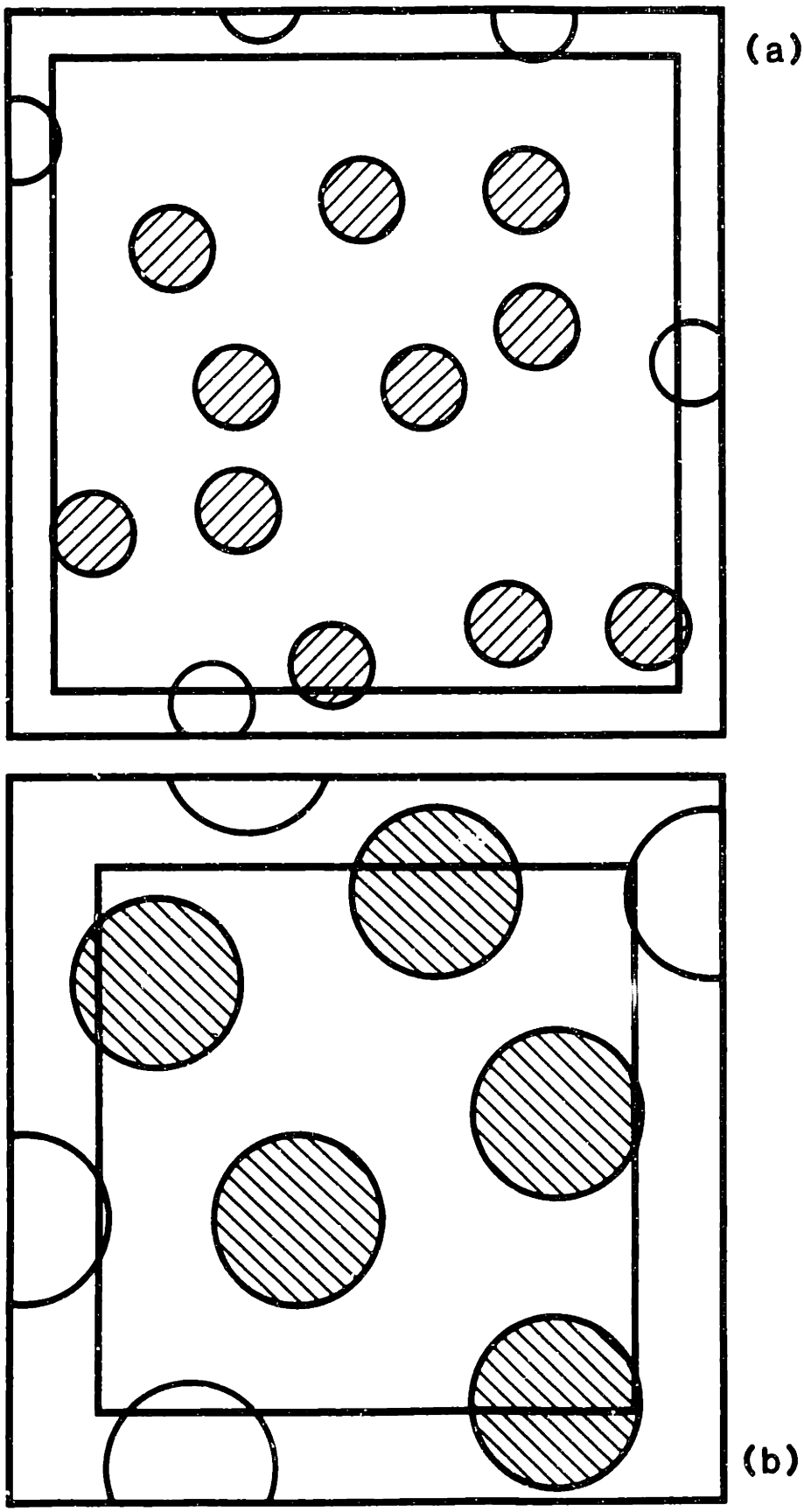

Figure 2.3

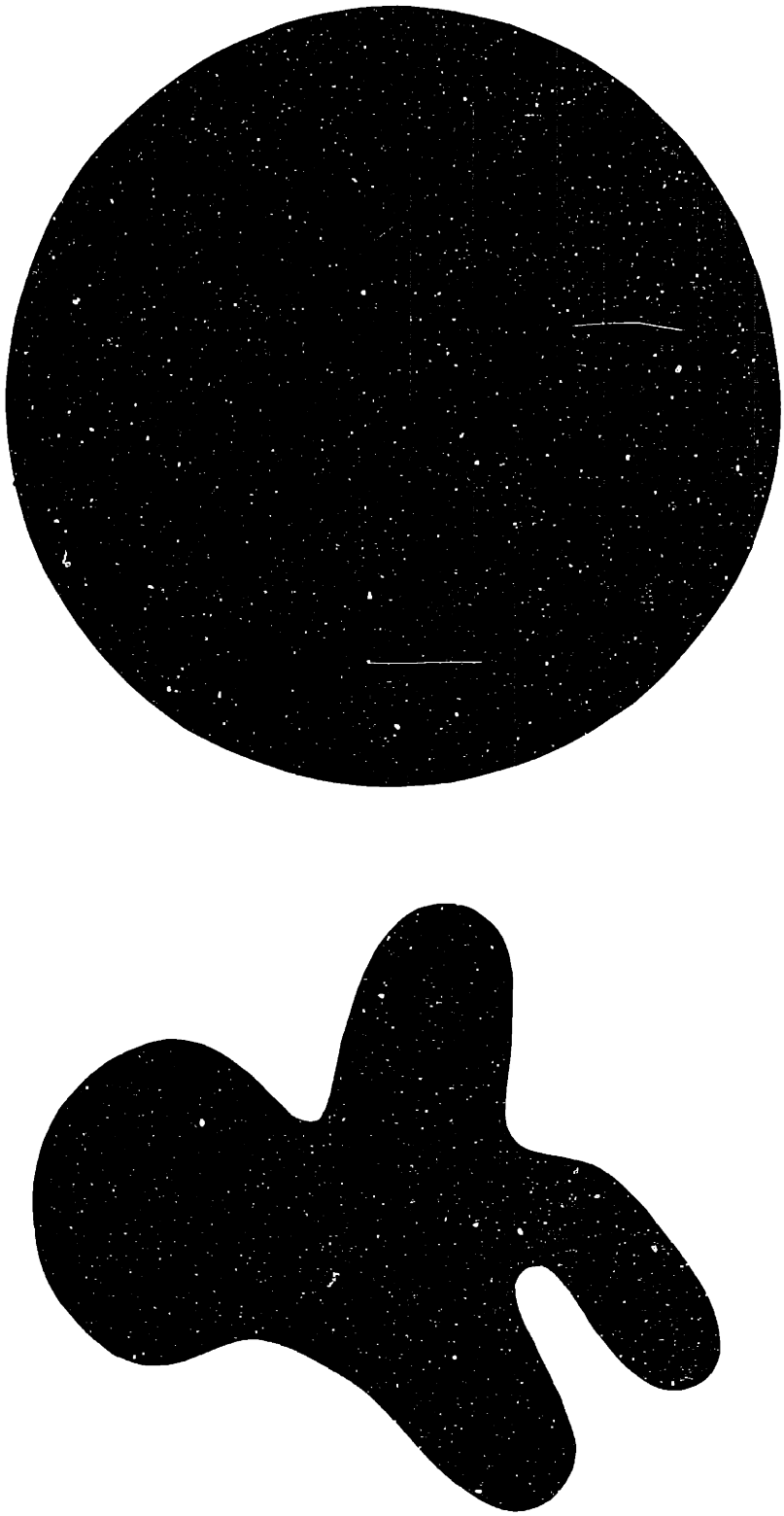

Chapter 3

Imaging the Pore Structure

3.1 Introduction

An accurate representation of the pore structure is required to facilitate the quantitative analysis and to insure an accurate analysis. In this chapter, conditions are established for obtaining optimal digital scanning electron microscope (SEM) images for quantitative analysis. The precision of the analysis depends, in part, on the precision of the data. We strive to collect high quality images because the information content of a digital image cannot be increased after acquisition. Optimal imaging conditions for photomicrographs intended for visual interpretation are *not* the same as the optimal imaging conditions for digital micrographs intended for quantitative analysis. Shading and contrasts which are pleasing to the eye do not improve the quantitative analysis and may degrade the analysis.

The general requirements for digital images used in quantitative analysis are the following. First, because the image is treated as a slice through the material, contrast due to topography should be minimized. Second, the images should allow accurate dichotomization to yield the binary image which is used in most quantitative analyses. Digital image quality may be judged as the

information content (e.g., signal strength, spatial resolution) versus defect content, where defects include geometric distortions, aliasing, ringing, moiré effects, and more generally, noise. Despite the widespread use of the SEM for qualitative examination of sedimentary rocks, the majority of previous quantitative image analysis has used the optical microscope.

This chapter begins with a brief review of techniques used in optical microscopy to obtain images suitable for quantitative analysis. Such a review allows comparison of the relative merits of optical and SEM imaging. Next, backscattered electron (BSE) image formation is considered with regard to digital image quality. Lastly, practical aspects of digital SEM image acquisition are presented.

3.2 Optical Microscopy for Quantitative Analysis

We discuss only those aspects of optical microscopy pertinent to obtaining images intended for quantitative analysis. An essential function of the imaging process is to produce an image which can be segmented into pore and grain phases. The image must have adequate intensity contrast between areas of pores and areas of grains. Both reflected light and transmitted light have been used to obtain this contrast.

3.2.1 Reflected Light

Samples prepared for reflected light imaging are first impregnated with Wood's metal (an alloy of Bismuth and Tin which has a melting point of 138°C(281°F)). The sample is polished until the Wood's metal is highly reflective. Dhawan (1972) details the extremely laborious polishing treatment. Because Wood's

metal is soft, it is difficult to polish the section without smearing the metal over adjacent grains. Also, because Wood's metal oxidizes rapidly, it remains highly and uniformly reflective for only a short time. A photomicrograph of the sample is made using high contrast film. In a print made from this film, the areas of high reflectivity (pores filled with Wood's metal) appear bright with respect to the dark areas of grains. Dhawan (1972) found that complete dissolution of the grains and replacement with epoxy produced a sample which was easier to prepare and had greater contrast. Still, the polishing procedures required with Wood's metal are tedious. Batra (1973) and Rink and Schopper (1978) also used Wood's metal and reflected light imaging. Swanson (1979) injected Wood's metal at various pressures to examine qualitatively the pore structure in sandstones.

3.2.2 Transmitted Light

When using transmitted light, the required contrast between pores and grains is obtained by impregnating the sample with dyed epoxy. A standard thin section is prepared for the impregnated rock. Low-viscosity epoxy is widely used to impregnate rocks prior to microscopic examination to aid in identifying porosity and describing pore structure (Pittman and Duschatko, 1970; Minoura and Conley, 1971; Gardner, 1980; Straley and Minnis, 1983; Yanguas and Dravis, 1985). The dye in the epoxy causes the light transmitted through the pores to have a unique wavelength (i.e., color). A film which is insensitive to this wavelength is then used to photograph the image. On a print, pores filled with the dyed epoxy appear dark. Alternatively, a photograph may be taken with high-contrast film through a filter. Pores which are the same color as the filter will transmit more light and the relative intensity will be greater.

Ehrlich *et al.* (1984) use transmitted light but eliminate the photographic process and digitize the intensity directly from the microscope using a video

scanner. A questionable consequence of their imaging process is the pore phase identification. In one example, they assigned a 10 μm square pixel to the pore phase when it contained "a pore as small as approximately 2 μm." The pore represents only 4% of the pixel area, whereas 96% is grain. The pixel assignment should be representative of the areal content of the pixel. Because thin sections are typically 30 μm thick, it makes little sense to use smaller pixels for transmitted light.

3.2.3 Limitations of Optical Imaging

There are several limitations associated with optical imaging for quantitative analysis. First, the sample preparation for reflected light imaging (i.e., Wood's metal impregnated) is very difficult and tedious (Dullien, 1972; Rink and Schopper, 1978). When using transmitted light, the finite thickness of the specimen distorts the image. The quantitative analysis assumes that the image represents a planar sampling of the structure, *not* a projection through a finite thickness. Some stereological techniques have been developed to treat projection errors (see Underwood, 1970, Ch. 6), but these techniques have not been used in previous studies of sandstones and they are generally less accurate than techniques used on a plane.

One drawback of optical imaging is that the recorded intensities have little intrinsic meaning. The intensities result from the convolution of the light source with the lenses of the microscope, the sample, the recording medium (film or video scanner), and the display medium (photographic paper or CRT). Provided that sufficient intensity contrast is present between the pore and grain phases, the intrinsic meaning may not be important. However, without an understanding of the factors which control the intensities, the dichotomization is likely to be subjective. For example, a threshold may be selected to produce a visual match between the resulting binary image and the original

full intensity image.

The lack of intrinsic meaning in the intensities is another reason why "image texture analysis" (see Chapter 2) on optical images is unlikely to reveal useful information about pore structure.

3.3 Limitations of Photographic Recording

Photographic recording is commonly used as an intermediate step in quantitative analysis. Photomicrographs can be taken on both optical and SEM imaging systems and later digitized with a video camera or optical scanner for subsequent analysis. There are limitations inherent in the photographic recording system and recording medium (i.e., film).

The photographic record is subjected to "hidden" image processing. For the SEM, this processing includes convolution with the recording CRT spot, optical transforms, the photographic process, and film influences. Even high quality SEM photographic systems (e.g., 2048 line resolution 5 in. CRT and 4×5 Polaroid camera) introduce some geometric distortion and, more significantly, they constrict the grey scale resolution and apply a non-linear transform to this grey scale. These degradations are generally unimportant for visual interpretation, provided the geometric distortion is small, because the eye can only recognize 10 to 20 levels of intensity on a photograph or on a CRT (Newbury and Joy, 1973). For optical imaging, because of the lack of intrinsic meaning of the original intensities, the intensity transformations of the photographic process are probably negligible.

Photomicrographs have been digitized with an optical scanner, for quantitative interpretation, in many studies (Moore, 1968; Haralick and Shanmugan, 1973; Newbury and Joy, 1973; Rink and Schopper, 1978; Tovey, 1980; Berryman and Blair, 1986). The digital image produced in this manner is limited

to the grey scale resolution of the photograph, suffers a loss of spatial resolution (from both the photographic process and the scanner), and may contain geometric distortions due to the scanning system. Photographs are also used in conjunction with video scanning image analyzers (see Chapter 2).

The SEM signal is not inherently restricted to the intensity representation afforded by a CRT or photomicrograph. This restriction is forced upon the image by displaying or storing the image on such a medium. Interpretation of an image *after* such a display is constrained by the limitations of the medium.

3.4 General Aspects of SEM Imaging

The scanning electron microscope (SEM) produces an image by sweeping a finely focused electron beam over a specimen in a raster pattern and monitoring the signal produced. A visual image is produced when the detected signal is used to modulate the intensity of an electron beam which is sweeped in a matching raster pattern on a CRT. The signals of interest in quantitative structural analysis are the secondary electron and backscattered signals. General information on the SEM can be found in Goldstein *et al.* (1981).

The backscattered electron (BSE) imaging mode of the SEM is recognized as a powerful petrographic tool (Robinson and Nickel, 1979; Hall and Lloyd, 1981; Caruso and Simmons, 1981; Pye and Krinsley, 1984; Pye, 1984; White *et al.*, 1984). For quantitative analysis, a principal strength of the BSE mode is the atomic number contrast of the image. With polished impregnated rock samples at near normal beam incidence, the atomic number contrast dominates the topographic contrast. Of course, if the area investigated does not contain spatial variations in atomic number, then the contrast will be due to topography. Other significant attributes of the BSE signal are the high signal-to-noise ratio of large solid angle detectors and the small charging ef-

fects relative to SE imaging.

3.4.1 The SEM at Low Magnification

Meakin and Fallon (1973) discussed the advantages of using the SEM at low magnifications (2 to 50×) instead of the optical microscope. These advantages include flexible brightness and contrast control, avoidance of image degradation by multiple scattering (such as occurs with visible light), and the ease of correlation of low magnification and high magnification data. Their considerations are equally valid from 50 to 500×, the range commonly used in this study for image analysis.

3.4.2 BSE Contrast and Signal

Wells (1977) reviews BSE imaging with the SEM and provides an extensive bibliography. Goldstein *et al.* (1981, Ch. 3, Ch. 4) also discuss general aspects of BSE imaging. Robinson (1975) describes the use of a large solid angle unbiased scintillator-light guide-photomultiplier BSE detector. This type of detector is good for imaging specimen topography at non-normal angles of beam incidence: the signal due to topography is due primarily to BSE's scattered at low angles. At normal incidence, for flat specimens, the contrast in the signal is primarily due to average atomic number differences in the sample, provided that an atomic number difference is present. The character of the specimen largely determines the dominant contrast mechanism. If an atomic number difference does not exist, then, of course, any image contrast will be due to topography.

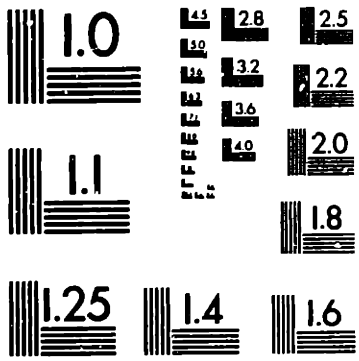

MICROCOPY RESOLUTION TEST CHART
NATIONAL BUREAU OF STANDARDS
STANDARD REFERENCE MATERIAL 1010a
(ANSI and ISO TEST CHART No. 2)

3.4.3 BSE Imaging of Rocks

Robinson and Nickel (1979) were among the first to describe the use of the BSE signal for imaging rocks. They illustrate principally that the BSE signal can be used at soft vacuums with moisture present. Hall and Lloyd (1981) presented several examples of the power of BSE imaging together with a plot of backscatter coefficient versus average atomic number.

Several more recent studies have also reviewed BSE imaging of rocks and presented examples of the good attributes (Caruso and Simmons, 1981; Bisdom *et al.*, 1983a, 1983b; White *et al.*, 1984; Pye and Krinsley, 1984). Basically, these studies point out the advantages of BSE imaging and give a few applications. The applications frequently illustrate the discrimination between phases based on atomic number intensity contrast.

3.5 SEM Imaging Theory

The SEM is a complicated imaging system. There are many parameters which affect the information content of the final image. Most of them can be adjusted either directly or indirectly to optimize the information content of the image (Hearle *et al.*, 1970; Pfefferkorn *et al.*, 1978). Because of this complexity, it is unreasonable to determine empirically the "best" operating conditions for digital imaging. Also, visual discrimination of the best conditions for digital imaging is not valid and there is no well-established measure of the digital image which indicates quality. Therefore, theoretical considerations of BSE imaging theory have been used to determine the best operating conditions. In this section I discuss the conditions which are best for acquiring BSE digital micrographs. In particular, signal strength, spatial resolution, and geometric integrity are considered. Some of the discussion uses values specific to the SEM imaging system used in this study (e.g., beam currents dwell times).

However, these values are generally applicable to modern SEMs.

For general discussions of scanning electron microscopy and the use of digital computers with the SEM, see Goldstein *et al.* (1981), Jones and Unitt (1980), Jones and Smith (1978), and Jones and Unitt (1982).

3.5.1 BSE Signal

The information content of the digitized BSE signal will be considered with respect to two characteristics: the signal-to-noise (S/N) ratio and the spatial resolution. Both parameters depend on the same imaging conditions (e.g., beam energy, beam current, probe size, dwell time, interaction volume-atomic number of specimen) and each is improved at the expense of the degradation of the other.

3.5.1.1 S/N Ratio and Contrast Detection

The S/N ratio can be used to express the maximum number of levels required to represent a signal (Newbury and Joy, 1973). This number of levels can alternatively be expressed as a minimum detectable contrast (Goldstein *et al.*, 1981). Below, we determine the S/N ratio required to obtain 8 bit resolution using reasonable signal currents and dwell times. Previous treatments have dealt with analog scans, analog detector signals, and CRT display. We consider the digital imaging case and use an approach similar to that used by Goldstein *et al.* (1981, p. 172).

A detectable intensity difference exists between two points (pixels) when the "visibility" criterion

$$S_{\text{max}} - S_{\text{min}} = \Delta S > N \tag{3.1}$$

is satisfied; where S_{max} is the maximum signal level, S_{min} is the minimum signal level, and N is the noise level. The signal strength is determined by a

temporal stochastic process where the average number of electrons, $\bar{n}$, arriving at the detector in a given time interval follows a Poisson distribution to first approximation (Newbury and Joy, 1973). Due to the Poisson nature of this process, the signal has a mean value of $\bar{n}$ with a standard deviation of $\sqrt{\bar{n}}$ (Newbury and Joy, 1973; Goldstein *et al.*, 1981, p. 173). Assuming a constant backscatter coefficient throughout the interaction volume, the noise is given as

$$N = \sqrt{\bar{n}} \,. \tag{3.2}$$

Combining Eqns. (3.1) and (3.2), the visibility criterion is

$$\Delta S > \sqrt{\bar{n}} \,. \tag{3.3}$$

The contrast, C, is obtained by normalizing Eqn. (3.3) with respect to S

$$C = \Delta S/S > \sqrt{\bar{n}}/S = \sqrt{\bar{n}}/\bar{n} \,. \tag{3.4}$$

Equation (3.4) can be rearranged to find the mean number of electrons required to obtain a given contrast C

$$\bar{n} > C^{-2} \,. \tag{3.5}$$

The signal current relation is given as

$$i_s = \bar{n}e/\tau \,, \tag{3.6}$$

where i_s is the signal current which arises from $\bar{n}$ electrons of charge e (1.6×10^{-19} coul) impinging on the detector during dwell time τ. Combining Eqns. (3.6) and (3.5) we obtain a relationship which defines the minimum signal current required, over dwell time τ, to produce the "visible" contrast C

$$i_s > \frac{e}{C^2\tau} \,. \tag{3.7}$$

Contrast is defined as

$$C = (S_{\max} - S_{\min})/S_{\max} , \tag{3.8}$$

where C ranges from 0 to 1. Contrast increments can be expressed by the number of bits (N_{bits}) over which this range is divided, or by the number of intervals into which $S_{\max}$ is divided. Table 3.1 lists N_{bits} values from 1 to 8, the number of intervals which these values represent, and the corresponding contrast increments.

3.5.1.2 Signal Current Requirements

Equation (3.7) defines the dwell times and signal currents required to use the full resolution afforded by 256 level (8 bit) digitization. Figure 3.1 is a plot of Eqn. (3.7) with contours of constant signal current i_s. Signal current is related to beam current, i_b, by the relation

$$i_s = \epsilon_c i_b , \tag{3.9}$$

where ϵ_c is the collection efficiency which depends on the specimen (e.g., atomic number and topography), the detector efficiency, and the geometric relation among the beam, sample, and detector. A reasonable assumption of the minimum collection efficiency of a Robinson BSE detector imaging quartz at zero tilt is 0.001 (Wells, 1977; Goldstein *et al.*, 1981, Ch. 4).

Figure 3.2 is an alternative presentation of Eqn. (3.7) in which it is easier to identify the signal current requirements for a given dwell time and contrast resolution.

3.5.1.3 Dwell Times

A dwell time of 4096 μsec has been used in this study. This dwell time is a practical maximum for two reasons. First, the specimen will be damaged by

heat buildup during longer dwell times. If the target area (pixel) has a low coefficient of thermal conductivity (as does the epoxy), then a relatively short dwell will damage the target. Although some mineral grains can withstand constant irradiation without significant damage, the pore filling epoxy is damaged for dwell times longer than about 7 msec. Damage to the epoxy has not been observed with a dwell of 4096 μsec. The second factor limiting dwell times is beam scan stability. An undistorted scan is required over the entire image field. Longer dwell times than those specified could potentially produce unacceptable frame times, leading to drift (Jones and Unitt, 1980). The SEM used in this study has a very stable and accurate digital scan (see section 3.5.3 on geometric integrity). Scan stability is not considered a limitation with our system and imaging procedures.

3.5.1.4 Photomicrograph Dwell Time

It is instructive to compare the dwell time for a photomicrograph with the dwell used during digital image acquisition. The photographic CRT image is 127×127 mm (photo area is about 88×114 mm and has a 2048 line resolution. The analog photo CRT pixel size is thus about 62×62 μm and the total number of pixels is 2048×2048. The shortest frame time for an analog photo is 40 seconds or about 9.5 sec/pixel. Each photo CRT pixel of a 256×256 digital image (80×80 mm) is 312.5×312.5 μm, thus, the digital image photo pixel covers an area equivalent to 25.4 analog photo pixels. The digital pixel dwell time which would provide equivalent irradiation per unit area is 241 μsec. This dwell would justify about 5 or 6 bits contrast resolution at a reasonable signal current of 10^{-12} amps and is more than adequate for the photograph, considering that a photograph has 4 or 5 bit contrast representation. Longer analog frame times can be used when the signal current is lower.

3.5.2 Spatial Resolution

In this section, the factors controlling spatial resolution are addressed. These factors include the scanning raster type and size, and the sampling aperture (i.e., probe size and specimen interaction volume). Most factors yield an upper limit on the resolution (i.e., the smallest resolvable feature).

3.5.2.1 Digital Image Size

The desired magnification determines the size of the area which is physically sampled on the specimen. This area is divided into picture elements (pixels), whose size is determined by the scanning raster type (e.g., square or hexagonal) and the scanning raster size (i.e., number of pixels). The scanning raster size is commonly referred to as the digital image size.

An image size of 256×256 has been used exclusively in this study for several reasons. This size is convenient for storage and transfer and an image of this size can be contained entirely within core memory of the processing computer (see Appendix A). Further, Jones and Unitt (1980) suggest that this size is adequate for general image analysis. A maximum practical image size of 512×512 is available with our imaging system. This maximum size is determined by the storage capacity of the diskette used during image acquisition.

3.5.2.2 Scanning Raster Type

Three possible scanning rasters were considered because the digital scan generator has a resolution of 4096×4096, yet the maximum desired image size is 512×512. The possible rasters are shown in Figure 3.3.

The 45 degree grid, or so-called "staggered" grid, provides a better rendition of *nearly* vertical and horizontal lines than does the square raster. This attribute is of no particular value for quantitative structural analysis of sand-

stones and there is no other advantage of the staggered grid over a conventional square grid.

Hexagonal grids have been used successfully in hardwired image analyzers (Klein and Serra, 1972; Golden and Hunn, 1980). These grids are commonly used with three primary vectors which combine to form isotropic sizing elements (i.e., homothetic hexagons). Thus, the hexagonal grid provides circular symmetry and also has a higher degree of spatial resolution for a given number of pixels per unit area than the square grid. Consequently, the hexagonal grid yields less spatial aliasing and is more appropriate than a square grid for a circular sampling aperture (Schreiber, 1982). Mersereau (1979) showed that hexagonal scanning offers savings in machine storage and arithmetic computations for many signal processing operations. Deutsch (1972) found that thinning algorithms for hexagonal arrays performed better than those for rectangular arrays. Given all of the above features, the hexagonal array appeared to be a good choice. However, the square grid was ultimately chosen for the following reasons.

Because isotropic pore features are rarely observed in sedimentary rocks (e.g., Pittman and Duschatko, 1970; Timur *et al.*, 1971; Pittman, 1979ab, 1984; Simmons *et al.*, 1982, 1983), it's not necessary to represent such shapes to a high degree of accuracy. The hexagonal grid is also more difficult to display than a square grid and the appropriate processing algorithms are more complicated. A hexagonal grid can only be approximated using the square raster of the digital beam control. Assuming exact positioning by the digital beam control on the square raster, the approximate hexagonal grid would have line-to-line spatial positioning errors of 5% and overall frame errors of 0.01%. In conclusion, the square grid was deemed best-suited to this study. The square grid provides sufficient flexibility for shape representation and is commonly used for digital image analysis (Pratt, 1978).

3.5.2.3 Pixel Size

Having selected a square raster and a maximum image size, the pixel size can be determined. Three types of pixels are recognized: the "physical pixel" on the specimen, the photo CRT pixel, and less importantly, the display CRT pixel. The physical pixel is the area on the specimen corresponding to the area of the pixel in the digital image.

The photo CRT pixel is important in calibrating the magnification of the digital image. The digital image acquisition area is 80×80 mm on the photo CRT. Table 3.2 lists the pixel sizes and total specimen area for four image sizes at five magnifications.

The physical pixel size is the upper limit of spatial resolution (i.e., the best resolution possible). A theoretical lower limit on probe size (beam size) is set by the beam brightness and lens aberrations (Goldstein, *et al.*, 1981). The actual sampled volume from which the signal arises is larger than the probe size and depends on the beam parameters (e.g., beam current, accelerating voltage), specimen composition, and the configuration of the beam, sample, and detector. The objective is to match the probe size to the physical pixel size.

3.5.2.4 Electron Probe Size

The diameter of an electron beam (probe) carrying current i_b is given by

$$d_b^2 = \frac{i_b}{B\alpha^2} + \left(\frac{1.22\lambda}{\alpha}\right)^2 + \frac{C_s^2\alpha^6}{4} + \left(\frac{\Delta E}{E_0}C_c\alpha\right)^2 \qquad (3.10)$$

from Goldstein *et al.* (1981, p. 44, Eqn. 2.17). The terms represent, in order, contributions due to beam current, diffraction, spherical aberration, and chromatic aberration.

Probe diameter has been computed, with Eqn. (3.10), as a function of working distance and accelerating voltage and is plotted as contours of con-

stant beam diameter in Figure 3.4. Values of the parameters used are given in Table 3.3. A beam current of 6×10^{-8} amps was used in accordance with the signal-to-noise requirements of the previous section. This beam current is the maximum produced by the ISI DS-130 SEM used in this study (see Table 3.4). The aberration coefficients were taken from the ISI technical documentation. Gun brightness was taken from Goldstein *et al.* (1981, p. 45) for a tungsten filament at 2820°K. At this high current, the beam diameter is dominated by the current contribution which is 2 to 3 orders of magnitude larger than the other contributions. The probe current diameter used here is defined as the diameter which contains 85% of the total current.

Comparison of the probe sizes of Figure 3.4 with the pixel sizes in Table 3.2 shows that the probe size is not always smaller than the pixel sizes, particularly for combinations of higher magnifications, small accelerating voltages, and large working distances. At the high current of 6×10^{-8} amps, the probe sizes are much larger than the 10 nanometer maximum resolution which is typically quoted for the SEM. Figure 3.4 illustrates that, at low magnifications, the working distance and accelerating voltage can be chosen such that the probe size is approximately the same size as the physical pixel, which is desirable to prevent spatial aliasing. If the specified high current is used, then the probe cannot be made as small as the physical pixel at higher magnifications. Consequently, spatial resolution will be larger than the pixel size. If the current can be reduced to 5×10^{-9} amps, the probe can be made smaller than the pixel size with an attendant loss of intensity resolution (Figure 3.5). The loss of intensity resolution may not be significant because the detection efficiency estimate used earlier was a minimum estimate (see Wells, 1977).

Several authors have suggested that the probe should be defocused so that it more closely matches the physical pixel size for both analog and digital imaging (Jones and Unitt, 1980; Yew and Pease, 1974). Meakin and Fallon

(1973) are opposed to defocusing and suggest that accurate edge detection is more important than prevention of aliasing. Aliasing is discussed in greater detail in section 3.5.2.6. We believe that selection of the appropriate current, working distance, and accelerating voltage, to obtain the desired probe size, is preferable to defocusing. Defocusing is inherently imprecise.

3.5.2.5 Interaction Volume

The sampling aperture from which the signal arises depends on both the probe size and the interaction volume. The interaction volume size is a function of the average atomic number of the target (i.e., sample) and the electron beam energy (i.e., accelerating voltage). This size is an increasing function of accelerating voltage and is a limiting factor in the choice of voltages. Two concepts are helpful to understand the interaction volume. The first is the range of a primary beam electron in the sample and the second is the spatial distribution of emerging backscattered electrons.

Electron Range—The range is defined as the distance which the incident primary electron travels in the specimen before it is elastically scattered out of the sample or converted to other forms of energy. Kanaya and Okayama (1972) derived an empirical relationship for the range. The Kanaya–Okayama range, R_{KO} is given by (Goldstein *et al.*, 1981, p. 72)

$$R_{\mathrm{KO}} = \frac{0.0276 A {E_0}^{1.67}}{Z^{0.889}\rho_g}\,, \tag{3.11}$$

where the range is given in μm when the beam energy, E_0, is given in keV, the average atomic weight, A, is given in g/mol, the density, ρ_g, is given in g/cc, and Z is the atomic number. Table 3.5 is a compilation of R_{KO} for common rock forming minerals. This table is, in part, derived from the table of mean atomic numbers and backscattering coefficients given by White *et al.* (1984), together with densities from Deer *et al.* (1966), and average atomic weights.

R_{KO} is the maximum distance an electron is expected to travel within the sample. Table 3.5 demonstrates that the range is comparable to the physical pixel size at lower magnifications. At higher magnifications the range is larger than the physical pixels.

Spatial Distribution—The *majority* of signal carriers (BSEs) arises from an area which is smaller than R_{KO} (Murata, 1973; Goldstein *et al.*, 1981). Thus, details much smaller than R_{KO} are typically resolved. White *et al.* (1984) present several examples of analog BSE imaging with resolution better than 1μm in typical sandstones and shales. Similar resolution has been observed with our SEM using analog scans at high magnifications. Kiss and Brinkies (1976) note that the resolution capability of BSE imaging is not yet fully understood. Features smaller than the probe size (sampling aperture) are typically resolved.

The "depth of information" of backscattered electrons is approximately 0.3 of the R_{KO} (Goldstein *et al.*, 1981, p. 121). It is important for this sampling depth to be small so that the image represents a plane through the material, not a thick slice.

In summary, the operator can control the interaction volume only to a limited extent through the choice of an appropriate accelerating voltage. At higher magnifications (above 100×) it is desirable to use higher voltages to reduce beam size. Unfortunately, the interaction volume increases with increasing voltage. The reasonable approach is to use lower accelerating voltages to minimize the interaction volume and shorter working distances to reduce the probe size if it is large compared to the physical pixel. In this study, accelerating voltages of 20 to 30 kV (i.e., beam energies of 20 to 30 keV) have been used in conjunction with working distances of 20 to 35 mm.

3.5.2.6 Spatial Frequency

Using the information on pixel size, beam size, and interaction volume, the constraints imposed by the sampling theorem are now considered. Selection of an aperture size for digitizing is not a well-defined process and is commonly guided by empirical rules (Schreiber, 1982). The sampling theorem states that an image can be reconstructed exactly for all spatial frequencies less than B cycles per unit length provided that the original image is sampled $2B$ times per unit length (Pratt, 1978, p. 104; Duda and Hart, 1973, p. 302). The maximum spatial frequency is analogous to the well-known Nyquist frequency in time series analysis (Kanasewich, 1975). Spatial frequencies greater than B will be aliased back into the data. To provide an accurate image, aliased energy must be eliminated or at least reduced.

In the line scan direction, aliasing can be eliminated by the installation of an analog low pass filter on the detector output (Jones and Unitt, 1980); a technique identical to that employed in temporal signal analysis. The cutoff frequency for such a filter must be adjusted to correspond to the image size, the magnification, and the scan rate: an onerous task. There is no analogous filtering method applicable to the frame scan direction. Indeed, the low pass filtering technique is *not* applicable when a *digital* scan is used as opposed to an analog scan. The solution for both line and frame scan directions when using a digital scan is an increase in the size of the sampling aperture. High frequencies are smoothed when the sampling aperture matches the physical pixel size, whereby the pixel value represents a spatial average of the signal over the entire pixel area. It was shown above that the sampling aperture can be matched approximately to the pixel size at low magnifications through the choice of accelerating voltage and working distance. The sampling aperture can always be made as large or larger than the physical pixel. It is never constrained to be smaller than the physical pixel.

Meakin and Fallon (1973) suggested that accurate edge detection is more important than the prevention of aliasing. Localization of edges in the images requires a small sampling aperture. We note that they considered an *analog* scan and line-to-line aliasing. With a digital scan, as used in this study, resolution is limited to the physical pixel size and there is no advantage in using a sampling aperture smaller than the physical pixel size. The pixel value should accurately represent the entire physical pixel area.

Despite the exact relationship which determines the spatial resolution at a given sampling increment (i.e., sampling theorem), the choice of a sampling aperture size is not rigorous. The sampling aperture varies with compositional variation of the specimen, and may be sensitive to the energy selectivity of the detector. All "diameters" and "ranges" given here as guidelines are approximate. These guidelines do assist in the choice of appropriate operating conditions. The practical operating conditions are given in section 3.6.

3.5.3 Geometric Integrity of the Image

Geometric integrity is a measure of how well spatial relations and metric properties of the specimen are represented by the image. Distortions of the imaging system must be identified and compensated prior to obtaining accurate metric properties from the image. Distortion can arise due to nonlinearity of the scan, distortion in the CRT display, and lens aberrations. Distortion in the image is also produced by tilting the specimen to optimize signal levels. At the magnifications used in this study, the distortions due to lens aberrations are negligible. Distortion is most commonly due to the CRT display device. In this section, distortion due to specimen tilt and scan nonlinearity are discussed. Distortion due to the CRT is illustrated in section 3.6.4, but is not important in this study because the BSE signal is digitized directly from the detector.

3.5.3.1 Sample Tilt

Samples are typically tilted with respect to the incident electron beam to produce a stronger BSE signal. Non-normal incidence creates an electron path and interaction volume which are closer to the surface of the sample. The probability of BSEs escaping from the sample and hitting the detector is increased by tilting. Additionally, due to the angular dependence of the trajectories, when using directional detectors, tilting directs more BSEs toward the detector. Tilting is *not* required to produce a strong BSE signal with our SEM imaging system. In fact, tilting creates undesirable side effects.

The difficulty of accurately correcting for tilt is a primary reason why it is undesirable. Correction of the obvious cosine distortion due to the tilt was rigorously treated by Lane (1969). Hilliard (1972) presented an approximate analysis based on a parallel projection geometry which is claimed to be valid above 500×. Ghosh (1979), in treating scan distortions, presented stronger evidence that 2000× is a more appropriate lower bound for the parallel projection approximation. Tilt correction requires an accurate determination of the tilt angle and the scan distortions. These two parameters can be found only through calibration with well-known samples (e.g., grids, diffraction gratings, latex spheres) under the desired operating conditions.

Modern SEMs commonly have tilt correction circuits. The tilt of the specimen is dialed into the console and the scan (beam or CRT) is altered to provide the cosine compensation. The correction is valid only for flat samples. With our SEM and presumably with others, the correction is calibrated only for a fixed working distance because it alters the *angular* sweep of the beam. Further, the correction axis is *not* tied to the tilt axis of the stage. The image must be electronically rotated to align the correction axis with the tilt axis. Otherwise, the "correction" introduces *additional* distortion instead of compensating the distortion due to tilt.

Artifacts Due to Tilting—Tilting enhances the visual appearance of a photomicrograph because directional illumination provides additional information about a scene (Schreiber, 1982). Shadowing and edge effects improve perception of spatial relations and "textures." However, the vision process is not simulated when quantifying pore structure and directional illumination causes undesirable artifacts. Bright edges due to charging, topography of the sample, and uneven coatings are enhanced by tilting. These edge effects create uncertainty in phase boundary locations. Threshold dichotomization (see section 3.7) of the image, from a tilted specimen, yields distorted boundary representations.

Visual Interpretation and Tilting—Because observers are used to directional top lighting, Goldstein *et al.* (1981, p. 168) stress that top (directional) illumination must be used when presenting SEM photomicrographs in order to preserve the sense of topography in the image. If the apparent illumination comes from some other direction, the sense of topography may become inverted. Howell (1975) states that top illumination is also important when viewing stereo pair images. Topographic contrast is not desired in digital images intended for quantitative interpretation.

In summary, there is no benefit to using non-normal incidence for images intended for quantitative analysis and there are several ways in which tilting degrades the image.

3.5.3.2 Geometric Distortions

Geometric scan distortions can be divided into four types: differential scale, radial, tangential, and spiral (Ghosh, 1979). These distortions must be corrected prior to quantitative analysis. Much of the work treating scan distortions has been done to produce accurate photogrammetric measurements with the SEM (Boyde, 1974; Howell, 1975; Maune, 1975; Ghosh, 1979). Ghosh

(1979) summarized general matrix formulations which can be used to correct for scan distortions. Hilliard (1972) described measurements relative to scales which have been superimposed on the photomicrograph to eliminate projection prospective errors (i.e., using a calibration standard). Boyde (1970) and Boyde *et al.* (1974) demonstrated that most distortion in photomicrographs is due to distortion in the recording CRT. This source of distortion is not present in our digital imaging system because the BSE signal is digitized directly from the detector signal.

One particular source of distortion at low magnification is the variation of magnification from edge to center of the image, due to the angular sweep of the beam. Meakin and Fallon (1973) showed that magnification variation is less than 2% for magnifications above 25× at 20 mm working distance (15× at 40 mm). Thus, when low magnifications are used, it is desirable to use longer working distances.

Geometric and magnification calibrations used in this study are described in section 3.6.

3.6 Practical Aspects of Digital SEM Imaging

In previous sections, the best theoretical conditions for digital SEM imaging were discussed. In this section the conditions used in practice are discussed, together with the general procedure for digital image acquisition. The digital SEM image acquisition hardware and image analysis hardware are described in Appendix A.

3.6.1 Specimen Considerations

Sample preparation is described in Appendix B. Polished thin sections, crack sections, and polished stubs have been used in this study. Polished stubs

are preferred because they are relatively easy to prepare and they are least susceptible to preparation induced damage. Although the sample should be flat, some topographic relief is always present because the pore filling epoxy is softer than the mineral grains and is, thus, preferentially removed during polishing.

The sample surface is oriented normal to the electron beam with the aid of high precision bubble levels. One level is placed on a machined surface on top of the electron column, the second level is placed on the specimen stage with the specimen chamber door ajar. The stage is tilted until the levels read the same. The level on the stage does not vary noticeably when the door is pivoted. Presumably then, the reading when the door is ajar agrees with the reading when the door is closed and the specimen is in position. Positioning errors of the stage are estimated to be $\pm 0.5°$. Additional error is present because the specimen surface may be tilted with respect to the specimen holder (which rests on the specimen stage). The additional error is negligible for thin sections and crack sections. However, polished stubs may be tilted by $\pm 0.5°$ due to the nature of the specimen holder. Combining the two sources of error yields an estimate of tilt accuracy of $\pm 1.0°$.

3.6.2 Reduction of Topographic Contrast

A simple modification was made to the Robinson backscattered electron detector to reduce topographic contrast in the BSE image. The modification consisted of shielding the detector with lead (0.8 mm thick) to produce a symmetric detector area above the specimen. Before modification, topographic contrast on certain edges was apparent in the image. The contrast was due to the linear configuration of the detector. Although the beam passes through the detector and the detector subtends a large solid angle around the beam, there is more detector surface area to one side of the sample. This surface area

extends from the final aperture to the side of the specimen chamber where the detector is mounted. With the lead shielding in place, the bright edges were eliminated. The resulting detector configuration is similar to a semiconductor detector mounted on the pole piece. However, the higher efficiency and faster frequency response of the Robinson detector are retained.

Conventional analog scan BSE photomicrographs taken at normal incidence with the detector shield in place look "odd." A distinct "difference" is detected by experienced but uninformed SEM operators, but the absence of directional illumination is not usually identified.

3.6.3 Operating Conditions

Table 3.6 is a list of typical operating conditions used in this study for digital SEM imaging. These conditions are the result of the theoretical considerations given earlier and are also derived from practical experience.

The scanning raster of the SEM rotates with respect to the stage axis as a function of working distance. The scan must be electronically rotated such that the scan axes are aligned with the stage axis so that orientation information is preserved. The ISI DS-130 is equipped with such an electronic beam rotation control which functions under both analog and digital scanning. The scan rotation is adjusted such that a mechanical translation of the stage along one axis produces pure translation of the image along the corresponding axis of the display CRT.

Electronic scan shift controls function by shifting the beam off axis. Therefore, they are zeroed (centered) to prevent distortion due to this source.

3.6.4 Scan Calibration

Two components of scan calibrations are treated in this section. The first is the rectilinearity of the scan and the second is the magnification calibration. Scan calibration is complicated by the need to use some form of display during the calibration. Often, the display is a primary source of distortion (Boyde, 1970).

3.6.4.1 Scan Rectilinearity

The following procedure has been used in this study to calibrate scan rectilinearity. Scan rectilinearity is a measure of how well the scan corresponds to a square raster. First, a symmetric square test raster is generated with the digital beam control. This test raster sweeps both the electron beam and the recording CRT spot. A photo is taken of the raster on the recording CRT. The size of the test raster is measured in X and Y directions on the photograph between several points, including a cross through the center of the pattern. If the size differs from an *a priori* selected size, the gain of the digital scan generator is adjusted, with particular attention to setting the X and Y gains equal. Error in the test raster size determination is less than ± 0.5 mm over the 80.0 mm length on the photomicrograph.

The above adjustment establishes reference settings for the digital scan generator, thereby giving a reference scale for the scan (which is the same in both scan directions). The magnification between the electron beam scan and the photo CRT scan must be calibrated separately. Also, any distortions in the beam scan must be identified. Corrections for magnification and beam scan distortions are done by software processing (coordinate transformation) of the digital image.

A 400 mesh calibration grid (obtained from Ernest F. Fullam, Inc., New

York) was used to determine the scan distortions of the SEM under digital beam control. The results indicate that software corrections for scan distortions are *not* necessary at the magnifications used in this study. Figure 3.6 is a photomicrograph of the calibration grid taken with the standard analog scan of the SEM. There is a slight pincushion distortion apparent on the vertical lines of the grid (i.e., the midpoints of the vertical lines are pulled toward the center of the image). The horizontal lines of the grid appear to be undistorted. Figure 3.7 is an analog photomicrograph of the same area taken under digital scan control. The pincushion distortion is still apparent. Contrast in these secondary electron (SE) images is primarily due to topography, with high edges of the grid appearing bright.

Three digital images of the calibration grid were collected under digital scan control. Figure 3.8 is a Versatec (electrostatic dot matrix printer-plotter) display of the images after dichotomization by thresholding the intensities. The threshold was chosen subjectively such that only the brighter pixels were assigned to the grid phase. The threshold value is not critical to the following discussion. It is readily apparent that the the scan lines of the digital images follow the ridge edges of the grid. Distortion associated with the Versatec display is limited to scale distortions in the paper feed direction due to irregularities in the feed rate. The regularity of the Versatec image is verification of the colinearity of the digital beam control scan. We conclude that the distortion in the analog scan and digital scan photomicrographs resulted primarily from the photo CRT display.

3.6.4.2 Magnification Calibration

At a fixed working distance, magnification in the SEM is due to the ratio between the angle through which the electron beam is swept and the angle through which the display and recording CRT beams are swept. The digital

beam control produces a sequence of discrete analog values which drive the SEM analog scanning circuits. Electronics in the SEM control the ratio of the electron beam-to-CRT beam angular displacement. Magnification calibration consists of determining the accuracy of the indicated ratio with respect to the true ratio.

Both the calibration grid and latex spheres were used for magnification calibration. Because of the topography of the spheres (dispersed on a glass slide) they are not useful for geometric scan calibration. The spheres do not appear spherical in SE micrographs because of the shadowing due to the configuration of the SE detector. The SE detector is not symmetric with respect to the SEM beam axis.

Two size classes of latex spheres with nominal diameters of 90.7 μm and 25.7 μm (obtained from Ernest F. Fullam, Inc., New York) were used for magnification calibration. Analog scan photomicrographs were taken at four magnifications for each size class. The magnifications used were 58×, 115×, 296×, and 583× for the 90.7 μm class and 115×, 297×, 584×, and 1150× for the 25.7 μm class. Ten spheres, which were visible at all magnifications, were selected from each class. Two orthogonal diameters were measured on each sphere at each magnification. The diameters were averaged and the results are plotted in Figure 3.9. Because of the large standard deviation in the sphere diameters from each class, the spheres are not suitable (without extensive sampling) for absolute magnification calibration. However, they do serve to verify the linearity of the magnification. Correlation coefficients for regression lines through the points on Figure 3.9 are 0.999 for both classes. Therefore, an absolute magnification calibration need only be established at one magnification. This absolute calibration is made with the calibration grid.

For the absolute calibration, the calibration grid spacing was measured with an optical microscope. The grid and a micrometer scale were viewed

simultaneously. The measured spacing was compared to the spacing measured on digital micrographs. The magnification indicated on the console of the SEM was determined to be a factor of 1.07 ± 0.02 too high at 30 kV and beam current of 6×10^{-8} amps. Thus, true magnification is 0.93 times the indicated magnification. This factor is used to adjust the computed pixel size.

3.6.5 Digital Image Acquisition

A computer program (**IAP**—Image Acquisition Program) was written to control the digital image acquisition. This program is used to (1) record all pertinent image and SEM parameters, (2) adjust the signal intensity, (3) generate and sample a digital raster, and (4) store the digital image on diskette. A digital photomicrograph is typically taken during digital image acquisition for documentation purposes. This photomicrograph is not suitable for other than gross visual interpretation because the recording CRT spot size is too small to create a spatially continuous image at the 256×256 resolution of the digital image scan.

3.6.5.1 Intensity Adjustment

An important adjustment made prior to acquiring a digital image is the setting of the SEM brightness and contrast controls. These controls are located, electronically, before the analog-to-digital (A-D) converter which digitizes the detector signal. Thus, these controls can be adjusted such that the detector signal spans the entire 8-bit resolution of the A-D converter. Care is taken to use the entire range without saturating the converter at the lowest or highest intensities. A real-time digitized line-scan display is generated by **IAP** and used for coarse adjustment. Next, a histogram of the intensities in the current digital image area is acquired and displayed. Final adjustments are based on

the character of this histogram. If the entire intensity range is not being used, the SEM contrast is increased. If both ends of the histogram are saturated, the SEM contrast is reduced. If one end is saturated, the SEM brightness is changed. Typically, the histogram decreases to small values at each limit. For all images, the number of counts in the end bins is limited to less than half the height of the nearest primary intensity peak.

A second set of brightness and contrast controls is located after the digital-to-analog converter (D-A) which converts the digitized signal into an analog signal for visual display. These controls are set in a conventional manner to produce a good visual image on the display CRT.

3.7 Dichotomization

The digital BSE image, acquired according to the criteria given in earlier sections, has a strong bimodal intensity distribution (Figure 3.10a). The bimodal distribution reflects the essentially bimodal nature of impregnated sandstones; high average atomic number grains and low average atomic number epoxy filling the pores. Secondary peaks due to less abundant phases may also be present. Clays appear to the left of the quartz peak. Carbonates, potassium feldspar, and heavy oxides, for example, appear to the right of the clay peak (see the η values in Table 3.5). Most methods of quantitative pore structure analysis of sandstones are performed on binary images. The full intensity digital image must be dichotomized to produce a binary image.

The simplest method of dichotomization is to choose a range of intensities which correspond to the phase of interest. Two threshold intensities are selected to delimit the range. A digital band pass filter is then applied which assigns pixels with intensities between the thresholds to the phase of interest and the remaining pixels to the "other" phase.

Dichotomization by thresholding is independent of the spatial position of the pixels. Provided that this method of dichotomization is successful, it is preferable to a spatial operation because it is simpler to perform. A spatial operation would consist of some form of line or edge recognition (e.g., Abdou and Pratt, 1979; Canny, 1983). The current state of pore structure characterization does not warrant such a pattern recognition process. Further, the dichotomization by thresholding is successful.

In this study, binary images are stored in a "packed byte" format in which each bit in the byte represents one pixel (see Appendix D). A bit can be in one of two states. The set state is signified by a value of 1 and is used to represent a pixel assigned to the pore phase. The clear state is signified by a value of 0 and is used to represent a pixel assigned to the grain phase.

3.7.1 Threshold Selection

Weszka (1978) reviews threshold selection methods applicable to general image analysis. For BSE images of impregnated sandstones, the lower threshold of the pass band is zero. The upper threshold selection is the topic of this section. The threshold selection has been *ad hoc* in previous studies. Lin and Cohen (1982) stated that a threshold is chosen between the two principal intensity peaks. Ruzyla (1984) illustrated the choice of a threshold immediately beyond the pore peak. He further stated that "the threshold setting can be checked interactively;" presumably, for his imaging system, by visual comparison of the binary image with the SEM photomicrograph. Berryman and Blair (1986) also determined an "appropriate threshold" interactively by visual comparison. One ad hoc threshold commonly used is the point of inflection of the cumulative intensity distribution (Figure 3.10b). Note the linear segment which contains the point of inflection. This linear segment is typical of sandstone BSE images, thus, the location of the inflection point is visually

ambiguous. Any point along this linear segment would qualify as an "inflection point," yet the estimated porosity (from areal fractions) would vary by several percent depending on the threshold chosen. The objective of this section is to find a reliable and nonsubjective method for threshold selection.

Castleman (1979, p. 305) observed that choosing a local minimum in the intensity histogram minimizes the sensitivity to feature area variation in the dichotomized image. However, unless the minimum has steep sides, the location is unreliable. Peak locations in the intensity histogram are more stable than the location of the local minimum, and a threshold chosen at a fixed position relative to the peaks is better than one based on a local minimum. The local minimum in the intensity histogram is equivalent to the inflection point of the cumulative distribution.

3.7.2 Pixel Classes

Because of the exceptionally good intensity resolution of our digital images, it is reasonable to consider threshold selection in greater detail. In particular, the intensities maintain a direct relation to the atomic number of the specimen and this relation has not been degraded by photographic or other nonlinear processes. Three primary classes of physical pixels are identified; pixels entirely within pores, pixels entirely within grains, and pixels containing both pore and grain phases. Intensity peaks of the pore and grain pixels appear to have a Gaussian shape on the histogram, whereas multiphase pixel intensities appear to be uniformly distributed between the two peaks. Figure 3.11 is a display of the pixels of image #1048 which have intensities between the principal peaks. The pixels are aligned with pore-grain boundaries and are also located in regions of clays and altering feldspars.

Based on the observed distributions, the fractions of the three pixel classes can be found by fitting appropriate curves to the histograms. Two possible

segmentation thresholds then appear reasonable. The threshold may be taken as the intensity between the peaks at which the pixel has equal probability of belonging to each peak. Alternatively, the interpeak pixels may be divided equally between the two phase classes by selecting a threshold which lies at the midpoint between the two peaks. Pixels with intensities greater than the principal grain peak plus one or two standard deviation units are ignored in the curve fitting. In a more complex treatment, the interpeak pixels could be considered to be due, in part, to combinations of these higher intensity phases and the low intensity pore phase. The objective of using a curve fit is to produce a nonsubjective threshold selection.

3.7.3 Curve Fitting the Intensity Histogram

A computer program (**HISFIT**) was written to fit Gaussian curves and a parabolic baseline to the intensity histograms. Each peak is parameterized by a center intensity, I_G, an area, A_G, and a width, σ_G. The nonlinear Gaussian curves and the baseline parabola are linearized and solved in an iterative, least-squares, manner following Menke (1984, p. 198). The baseline parabola, P_b, is parameterized in a unique manner to provide greater numerical stability. The parameterization is

$$P_b(I) = A_b \left(\frac{B_b (I - C_b)^2}{C_b{}^2} + 1 \right) , \tag{3.12}$$

where I is the intensity, C_b is the location of the vertex, A_b is the baseline level at the vertex, and $A_b B_b / C_b{}^2$ is the parabolic distortion.

Initial estimates of the curve parameters are derived automatically. Initial peak locations are found with a simple peak maximum locator algorithm. Initial standard deviations, σ, are estimated from the histogram intensities at which the histogram counts correspond to the amplitude reduction expected for a Gaussian curve (e.g., 0.33 times the peak height at 1.5σ or 0.88 times the

peak height at 0.5σ). Area estimates are computed from the measured area within the estimated σ limits, normalized by the expected area fraction within the σ limits for a Gaussian curve (e.g., 87% contained within $\pm 1.5\sigma$ or 38% contained within $\pm 0.5\sigma$). The initial baseline focus is taken as the midpoint between the estimated peak locations, and the baseline level is taken as the number of counts in the midpoint histogram bin. The parabolic distortion is given a small positive value. The inversion is damped by limiting the size of the perturbations in each iteration.

A second computer program (**HISINF**) was written to fit a cubic spline to the cumulative intensity distribution. The spline curve is analytically differentiated to compute the slope of the distribution and to locate the inflection point. The location of the local minimum in slope gives the location of the inflection point. Additionally, the value of the slope indicates the sensitivity of the porosity to the threshold. The fit is applied between the locations of the principal peaks and uses 9 to 11 knots. Typically, there are 110 to 160 points between the peaks.

3.7.4 Results from Curve Fit of Intensity Histograms

Both curve fitting techniques work well. For the Gaussian curves, the peaks are accurately located and the peak widths are visually reasonable. The cubic spline fit deviates at most by 0.1% from the cumulative histogram. The fitted curve is visually indistinguishable from the data at normal plotting scales. Notably, a *unique* point of inflection is found for each curve. Visually selected inflection points typically lie within 5 intensity bins of the analytic inflection points. The visually selected inflection point is taken as the center of the "linear segments" of the cumulative distribution.

Minimum sensitivity to threshold intensity ranged from 0.001 to 0.005 in units of fractional porosity per intensity step. Sensitivity increases in both

directions away from the inflection point. The magnitude of this sensitivity indicates that a wide range of "porosities" can be produced, depending on the choice of the threshold. Thus, it is important to use a reliable and consistent threshold selection method. Images collected at lower S/N ratios (e.g., those which use photographic process) will have *higher* sensitivities to threshold selection.

Out of more than 75 images, the Gaussian curve fitting failed to locate the pore peaks for only two. These two images (#1101 and #1103 of sample #2687) do not satisfy a basic assumption for the curve fit. Both images lack distinct pore peaks, due to low porosity represented in these images ($\approx 10\%$) and relatively high clay content ($\approx 15\%$). Thresholds were estimated from the grain peaks, which were always located by the curve fitting, and from the thresholds of other images of the same sample acquired with the same SEM settings.

To measure the relative quality of the two threshold methods, we can compare the standard deviations in porosity for sets of images from individual rocks. The threshold is used to produce a binary image and the porosity is estimated from the areal fraction of pore space (see Chapter 4). Statistics from the estimated porosities are given in Table 3.7. Nine images were used for each rock. The coefficients of variation are always smaller for the midpoint thresholds and the standard deviations are usually smaller for the midpoint threshold values. The midpoint threshold produces more consistent values of porosity.

3.7.5 Discussion of Curve Fit Results

The threshold placed midway between the peak locations is the better threshold. The equal-probability point is not a good choice for the threshold. Almost always, the equal-probability point occurs at some probability which is on the

order of the roundoff errors in the calculations. This behavior indicates that an interval exists between the peaks for which the probability of a pixel belonging to either peak is essentially zero. The intensities within this interval must result from physical pixels which contain significant fractions of both pore and grain phases.

Standard deviations for the fitted grain peaks are typically too large. This is illustrated in Figure 3.12 which shows the difference between the histogram and the fitted curves. The bins on the sides of the peaks have fewer counts than the amount predicted from the fitted curves. The large standard deviations are probably due to pixels which belong to higher intensity grain peaks. These peaks are *not* included in the model used to fit the histogram. Thus, the standard deviation of the main peak is increased as the inversion tries to account for these pixels. Alternatively, the peaks may not be true Gaussian curves and, thus, the model will not be able to account for them entirely.

Attempts to use additional peaks to model the higher intensity grain peaks have not been successful. Because the peak locations are very close, the solution oscillates. Damping the perturbations does not prevent the oscillations. Perhaps an additional constraint on the minimum separation of the peaks would help.

The physical mechanisms which control peak width are not well-known. Contributing causes are (1) the variation of atomic number of the phase, (2) the variation due to sampling a stochastic process, and (3) topographic contributions to the intensity. The contribution due to variation in average atomic number is expected to be negligible for quartz grains, but may be larger for more variable minerals such as feldpar and clay. The epoxy may also have a large variation in average atomic number.

The measured intensity of a pixel is a result of sampling a stochastic process. Natural variation in this process will broaden the intensity peak. How-

ever, the signal-to-noise considerations above indicate that, for a target with a constant backscattering coefficient, the signal should have a resolution of one intensity level. The pore peak may be expected to be wider than the grain peak because of the longer range of the electrons in the epoxy. This longer range allows electrons more opportunities to be scattered deeper into the sample or to be scattered out of the sample. Thereby, the intensities are expected to be more variable. The widths of the peaks are probably also related to the proximity (or interfacial area) of the various phases. Phases which are more frequently close to phases with different backscatter coefficients can expect contributions to intensities from the adjacent phases.

Topography of the specimen will contribute to broadening the intensity peak. When the lead detector shield, described above, is *not* used, the topographic influence can be seen. Figure 3.13a is a display of the pixels with intensities corresponding to the left half of the grain peak and Figure 3.13b is for the right half. In Figure 3.13b, features represent the bright halves of the quartz grains. The detector is oriented at about 1 o'clock and extends to the chamber wall in that direction. The lower intensity areas of the quartz grains can be seen in Figure 3.13a. Features of both images are uniformly distributed, normal to the detector axis, over the entire image area. Thus, the peak broadening is not due to spatial variation in the illumination of the sample. That is, the beam intensity and the detector configuration are uniform (homogeneous) over the whole image area. With the lead detector shield in place, the detector configuration is also nearly isotropic.

The peaks in the intensity histograms resemble Gaussian curves. The tails of these peaks can contain a significant percentage of the pixels which belong to the compositional class defined by the peak. Because of the direct correspondence between BSE intensity and mean atomic number, the intensities of the grain peak(s) can be partitioned to estimate the modal composition of the

sample. Dilks and Graham (1985) used a simple threshold cutoff to partition the intensities. Because of the nature of the peaks, a curve fitting method will produce a more accurate segmentation.

The peak locations identified by the inversion could probably be identified with a simple maximum amplitude algorithm. Such a simple algorithm would not have indicated the low probability of intrapeak pixels belonging to the major peaks. The objective of curve fitting was to find a method for nonsubjective threshold selection. This objective has been attained. Further attempts to segment and quantify the various mineral fractions from the histogram will require additional development of the histogram curve fit.

Figure Captions

Figure 3.1. Signal current requirements as a function of dwell time and contrast increments. Contours are constant signal current. Contrast increments are represented on the righthand abscissa as the number of bits, N, used to express the intensity values. N bits correspond to 2^N intensity levels. To obtain beam current requirements, divide signal current by the collection efficiency.

Figure 3.2. Number of bits used to represent intensity values as a function of dwell time and signal current. Contours are constant number of bits. For a given dwell, the signal current requirements to afford N bit resolution of the intensities can be found.

Figure 3.3. Available raster patterns for digital images. (*a*) Square grid (used in this study). (*b*) Staggered or 45° grid. (*c*) Hexagonal grid.

Figure 3.4. Electron beam (probe) diameters as a function of working distance and accelerating voltage for beam current of 6×10^{-8} amps. Contours are of constant probe diameter. Assumes that contributions to the probe diameter are due solely to the current contribution in Eqn. 3.10, that the distance from the aperture (100 μm diameter) to the specimen is equal to the working distance, and that the filament has a typical tungsten brightness.

Figure 3.5. Electron beam (probe) diameters as a function of working distance and accelerating voltage for beam current of 5×10^{-9} amps. Contours of constant probe diameter. Assumes that contributions to the probe diameter are due solely to the current contribution in Eqn. 3.10, that the distance from the aperture (100 μm diameter) to the specimen is equal to the working distance, and that the filament has a typical tungsten brightness.

Figure 3.6. Analog scan photomicrograph of the calibration grid. Secondary electron image. Scale bar is 100 μm. Note the pincushion distortion.

Figure 3.7. Digital scan photomicrograph of the calibration grid. Secondary electron image. Approximately the same scale as Figure 3.6. Note the pincushion distortion.

Figure 3.8. Binary (Versatec) images of digital micrographs of the calibration grid. Thresholds of full intensity secondary electron image were selected to display only the high intensity ridges of calibration grid. Note that the scan lines of the digital image follow the ridge lines of the calibration grid. (*a*) Scale bar is 500 μm. 50× original magnification.

(*b*) Scale bar is 100 μm. 100× original magnification. (*c*) Scale bar is 50 μm. 500× original magnification.

Figure 3.9. Mean sphere diameter as a function of the magnification displayed on the SEM console. Standard deviations at each point are large because of the large standard deviation in sphere sizes. Strong linearity verifies that the displayed magnification is linear with respect to true magnification. Correlation coefficient of both lines is 0.99. Circles are for 90.7 μm sphere class. Pluses are for 25.7 μm sphere class.

Figure 3.10. Pixel intensity histograms of backscattered electron digital image of Morrison formation sandstone (sample 2710, image #1048). (*a*) Conventional histogram of intensities. Note strong bimodal character. Low intensity peak represents pore pixels. High intensity peak represents grain pixels. (*b*) Cummulative distribution of intensities. Note linear segment which contains point of inflection of curve.

Figure 3.11. Binary image of pixels with intensities between the principal pore and grain peaks of the intensity histogram. Note that pixels are located near grain perimeters and in regions of clays. Apart from the local arrangement, note that the pixels are distributed uniformly over the entire image area.

Figure 3.12. Difference between histogram of Figure 3.10 and peaks fitted to the histogram.

Figure 3.13. Binary images of pixels with intensities within 3σ of the location of the grain peak (image #1048). (*a*) Intensities between intensity at peak and -3σ from peak. (*b*) Intensities between intensity at peak and $+3\sigma$ from peak. Note the uniform spatial distribution of features normal to the detector axis at 1 o'clock.

Table 3.1

Contrast Increments for Various Digitization Intervals

Number of Bits	Number of Intervals	Contrast Increment (%)
1	2	50.00
2	4	25.00
3	8	12.50
4	16	6.25
5	32	3.12
6	64	1.56
7	128	0.78
8	256	0.39

Table 3.2a

Pixel Sizes for Various Magnifications and Image Sizes

Image Size	CRT Pixel (μm)	Physical Pixel Size (μm) Magnification 10	50	100	500	1000
128	6250	62.50	12.50	6.25	1.250	0.625
256	3125	31.25	6.25	3.12	0.625	0.312
512	1562	15.62	3.12	1.56	0.312	0.156
1024	781	7.81	1.56	0.78	0.156	0.078

CRT digital image length = 80.0 mm

Table 3.2b

Physical Image Areas at Various Magnifications

Magnification	Physical Image Length (μm)	Physical Image Area (μm^2)
10	8000.0	64.0×10^6
50	1600.0	2.56×10^6
100	800.0	640000.0
500	160.0	25600.0
1000	80.0	6400.0

CRT digital image length = 80.0mm

CRT digital image area = 6400.0mm^2

Table 3.3

Parameters Used in Eqn. 3.10 to Compute Probe Sizes

Parameter	Description	Value	Units
i_b	Beam current	6×10^{-8} (Fig. 3.4) 5×10^{-9} (Fig. 3.5)	(amps)
B	Gun factor	1.53β	(amps/cm^2 sr)
β	Gun brightness	$53.0E_0$	(amps/cm^2 sr)
α	Beam divergence	$D_a/2WD$	–
D_a	Aperture diameter	0.1	(mm)
WD	Working distance		(mm)
λ	Wavelength	$1.24/\sqrt{E_0}$	(nm)
ΔE	Energy range	2.0	(eV)
E_0	Energy		(keV)
C_s	Spherical aberr. coefficient	$-19.5 + 5.91WD$	(mm)
C_c	Chromatic aberr. coefficient	$6.78 + 1.15WD$	(mm)

Table 3.4

Probe Sizes and Currents of ISI DS-130 SEM

Console Settings*		Probe	Probe
Function	Spot Size	Diameter (μm)	Current (amps)
HR	S	0.007	8×10^{-12}
	L	0.012	2×10^{-11}
STD	S	0.025	8×10^{-11}
	L	0.045	3×10^{-10}
LM	S	0.090	1×10^{-9}
	L	0.180	5×10^{-9}
LCT	S	0.330	2×10^{-8}
	L	0.500	6×10^{-8}

All values taken from ISI DS-130 technical documentation. Conditions: 40keV, 15mm working distance.

* HR – high resolution

STD – standard operation

LM – low magnification

LCT – large current

L – large spot

S – small spot

Table 3.5a

Mean Atomic Number, Bulk Density, Average Atomic Weight and Backscattering Coefficients for Minerals of Ideal Formula Commonly Found in Rocks

Mineral Name Formula	Z	ρ (g/cc)	A (g/mol)	η
Mg chlorite $Mg_5Al_2Si_3O_{10}(OH)_8$	10.17	2.64	15.44	0.124
Kaolinite $Al_4Si_4O_{10}(OH)_8$	10.24	2.63	15.18	0.125
NaMontmorillonite $Na_{0.33}(Al_{1.67}Mg_{0.33})Si_4O_{10}(OH)_2 \cdot H_2O$	10.40	2.35	16.50	0.127
CaMontmorillonite $Ca_{0.17}(Al_{1.67}Mg_{0.33})Si_4O_{10}(OH)_2 \cdot 2H_2O$	10.41	2.35	15.37	0.127
Albite $NaAlSi_3O_8$	10.71	2.63	20.17	0.132
Quartz SiO_2	10.80	2.65	20.03	0.132
Dolomite $CaMg(CO_3)_2$	10.87	2.86	18.44	0.133
Illite $K_{1.5}Al_{5.5}Si_{6.5}O_{20}(OH)_4$	11.16	2.85	18.74	0.136
Muscovite $K_2Al_6Si_6O_{20}(OH)_4$	11.33	2.83	18.97	0.138
Orthoclase $KAlSi_3O_8$	11.85	2.60	21.41	0.145
Calcite $CaCO_3$	12.57	2.75	20.02	0.150

Table 3.5a (cont.)

Mean Atomic Number, Bulk Density, Average Atomic Weight and Backscattering Coefficients for Minerals of Ideal Formula Commonly Found in Rocks

Mineral Name Formula	Z	ρ (g/cc)	A (g/mol)	η
Biotite $K_2(Mg_2Fe_4)Al_2Si_6O_{20}(OH)_4$	14.59	3.00	21.83	0.174
Fe chlorite $Fe_5Al_2Si_3O_{10}(OH)_8$	16.05	3.30	19.82	0.188
Siderite $FeCO_3$	16.47	3.96	23.17	0.190
Rutile TiO_2	16.93	4.90	78.79	0.195
Goethite $FeO \cdot OH$	19.23	4.30	22.21	0.222
Hematite Fe_2O_3	20.59	5.25	31.94	0.238
Pyrite FeS_2	20.65	4.95	39.99	0.247

In part from White *et al.*(1984).

η is at 20 keV.

Table 3.5b

Kanaya-Okayama Ranges (μm)
as a Function of Accelerating Voltage
for Minerals in Sedimentary Rocks

Mineral	Accelerating Voltage (kV)			
Name	10	20	30	40
Mg chlorite	0.96	3.06	6.01	9.72
Kaolinite	0.94	3.00	5.90	9.54
NaMontmorillonite	1.13	3.60	7.08	11.45
CaMontmorillonite	1.05	3.35	6.59	10.65
Albite	1.20	3.83	7.53	12.18
Quartz	1.18	3.74	7.37	11.91
Dolomite	1.00	3.18	6.25	10.10
Illite	1.00	3.16	6.23	10.06
Muscovite	1.00	3.18	6.26	10.12
Orthoclase	1.18	3.76	7.39	11.95
Calcite	0.99	3.15	6.20	10.03
Biotite	0.87	2.76	5.43	8.78
Fe chlorite	0.66	2.09	4.12	6.66
Siderite	0.62	1.99	3.92	6.34
Rutile	1.68	5.34	10.51	17.00
Goethite	0.48	1.53	3.02	4.88
Hematite	0.54	1.70	3.34	5.40
Pyrite	0.71	2.25	4.43	7.16

NOTES: Computed from Eqn. (3.11). Ranges are in μm. Mineral formulae are given in Table 3.5a.

Table 3.6

Operating Conditions For Acquiring
Digital BSE Images of Sandstones

Parameter	Setting
Accelerating voltage (kV)	20–30
Beam current (amps)	6×10^{-8}
Working distance (mm)	30 at 50×
	20 at 100×
	20 at 500×
Sample tilt (degrees)	0.0
Tilt correction	0.0
Dynamic focus	0.0
Electron gun and column alignment	Adjust by procedure in manual. Should be no image shift when beam current is changed.
Astigmatism	Adjust for the sharpest image. Image should go through focus without tearing.
Electronic Image Shift	Controls centered.

NOTE: Some settings may be specific for the ISI DS-130 used in this study. All settings were listed to provide guidelines for other SEMs.

Table 3.7

Statistics on Porosity Determined by the
Inflection Point and Midpoint Intensity Thresholds

Sample	Threshold	Porosity					
Number	Method	Mean	$SD(\phi)$	$CV(\phi)$	Min.	Max.	Range
2523	Mid	18.39	2.49	0.136	14.23	22.13	7.90
	Inf	14.86	2.62	0.176	10.42	19.34	8.92
2687†	Mid	21.25	9.64	0.454	11.60	41.29	29.70
	Inf	16.85	9.55	0.567	7.55	36.46	28.91
2700	Mid	23.55	2.69	0.114	18.33	27.52	9.19
	Inf	20.11	2.80	0.139	14.21	24.42	10.21
2704	Mid	19.28	4.79	0.249	8.51	22.93	14.42
	Inf	16.00	4.82	0.301	6.40	19.89	13.50
2710	Mid	28.87	4.51	0.156	21.17	37.70	16.53
	Inf	26.59	5.21	0.196	16.86	36.52	19.66
2842	Mid	14.36	2.50	0.174	9.88	18.55	8.67
	Inf	12.93	2.45	0.190	8.52	16.79	8.27

†Not all images used due to curve fit failures.

Figure 3.1

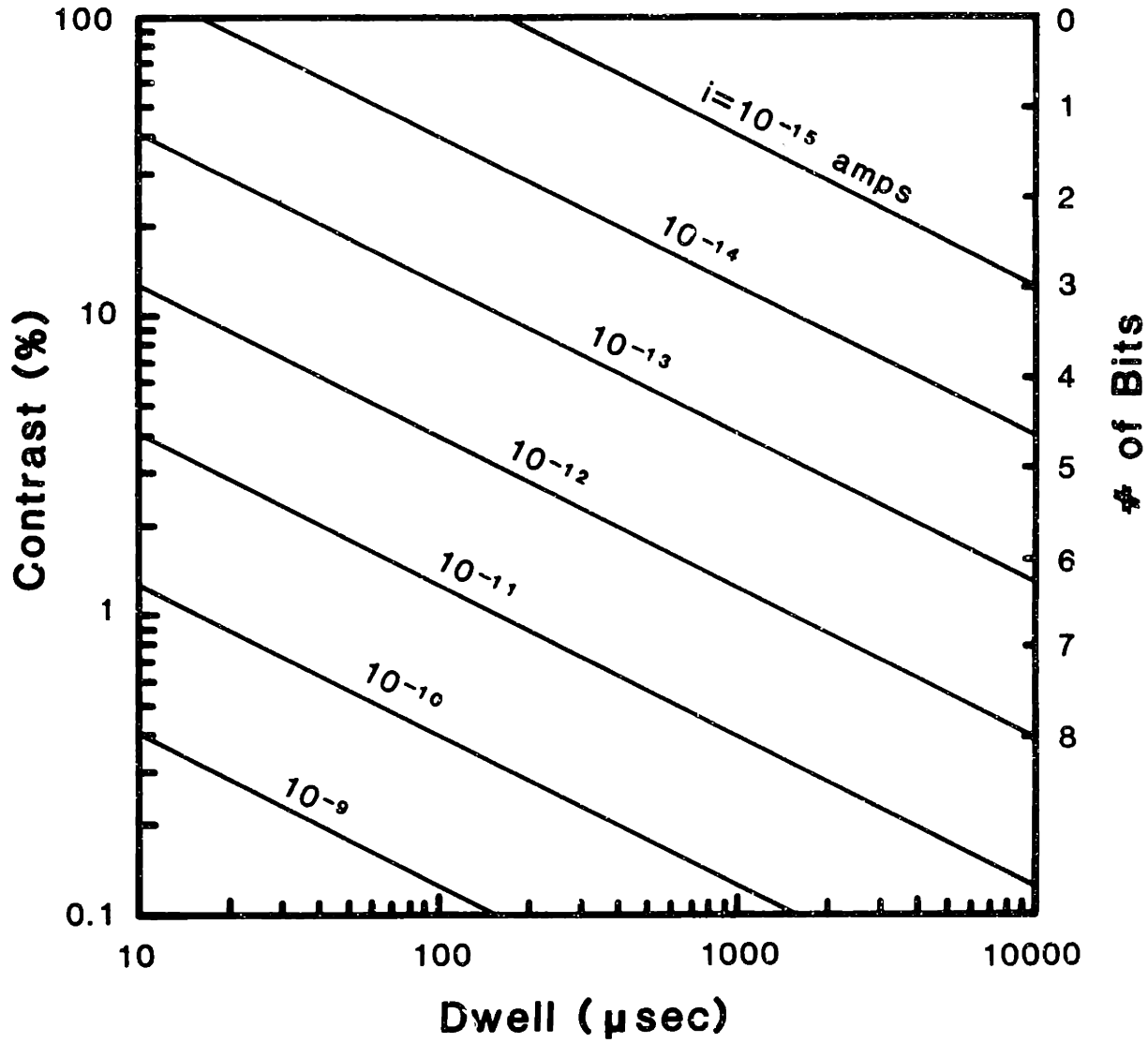
100
10
1
0.1
Contrast (%)
10
100
1000
10000
Dwell (μsec)
0
1
2
3
4
5
6
7
8
# of Bits
i=10-15 amps
10-14
10-13
10-12
10-11
10-10
10-9

Figure 3.2

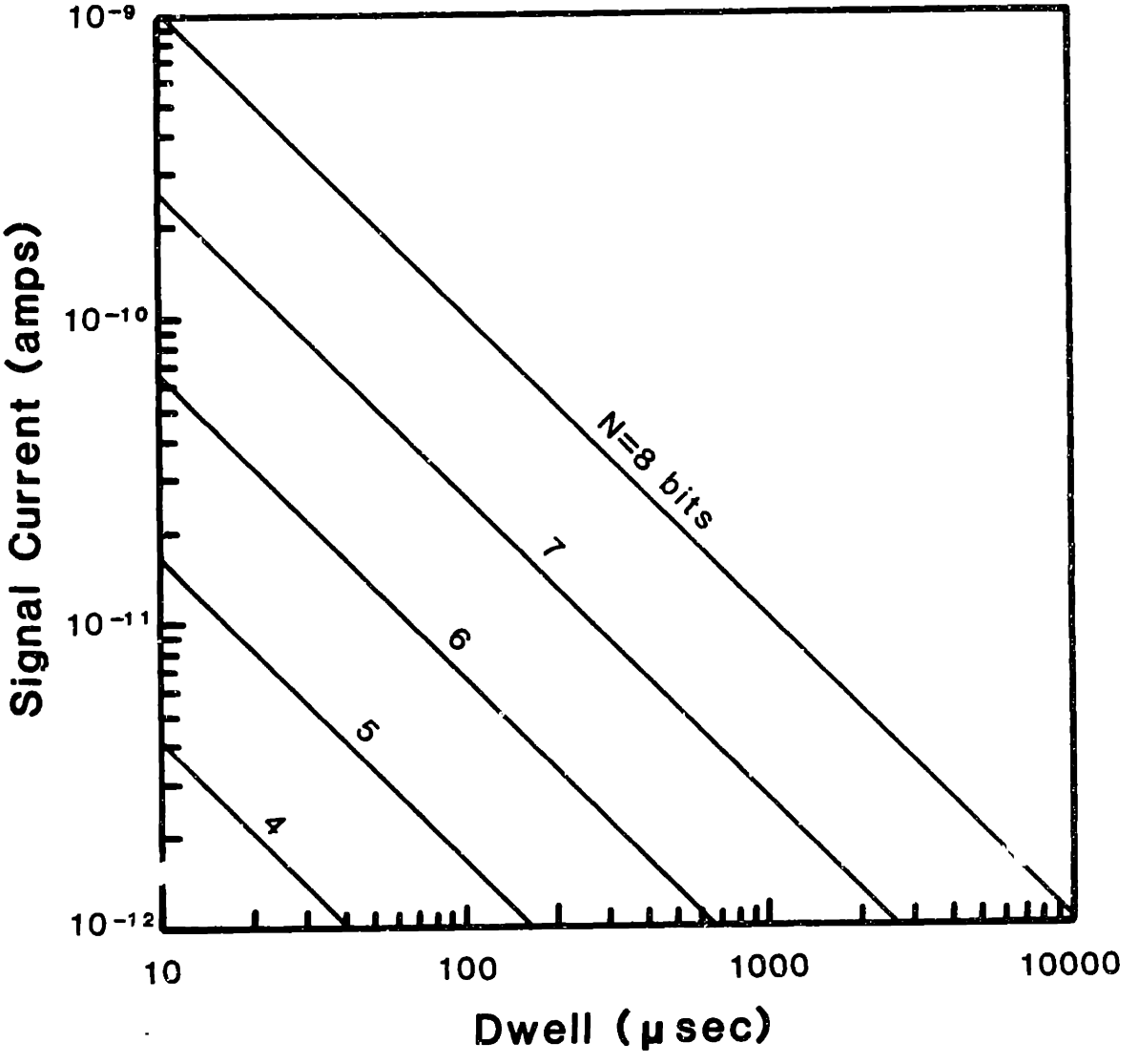
Signal Current (amps)
10⁻⁹
10⁻¹⁰
10⁻¹¹
10⁻¹²
N=8 bits
7
6
5
4
10
100
1000
10000
Dwell (μsec)

Figure 3.3

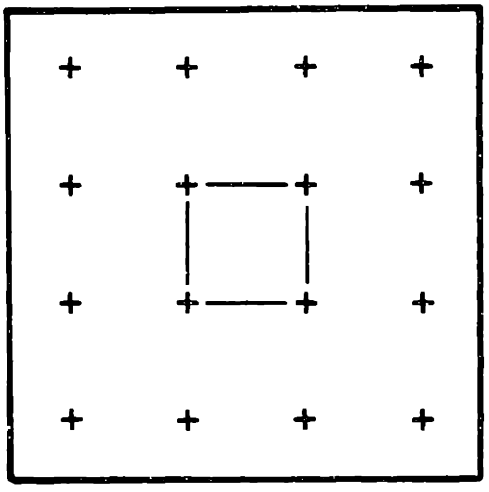

(a)

Square Grid

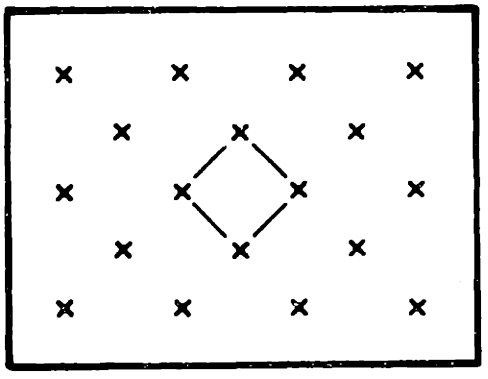

(b)

Staggered (45°) Grid

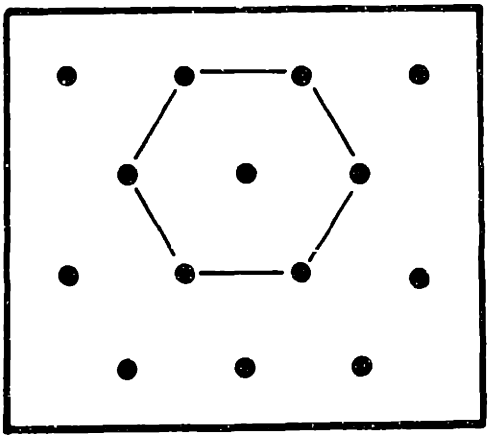

(c)

Hexagonal Grid

Figure 3.4

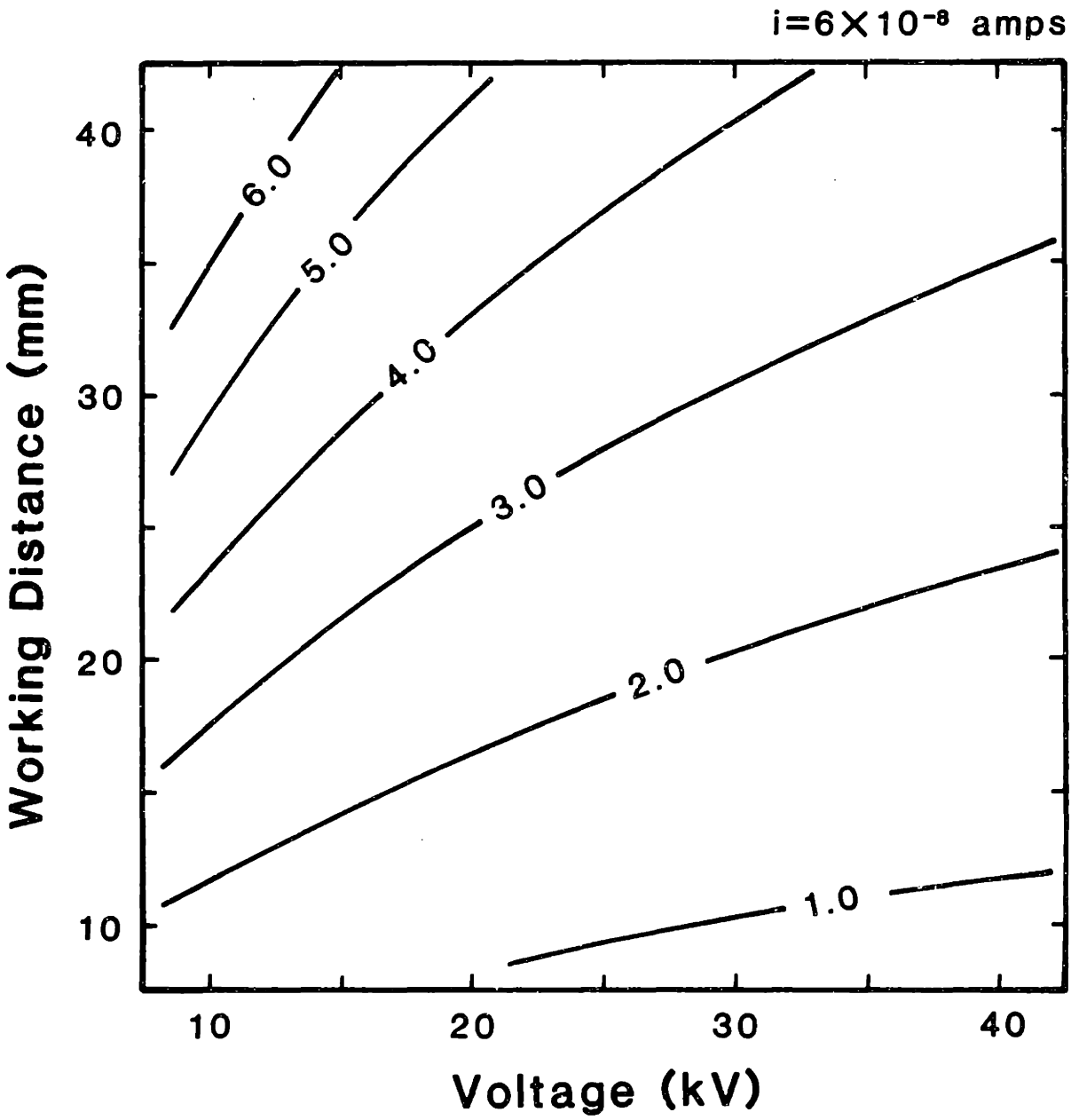
i=6X10⁻⁸ amps
Working Distance (mm)
40
30
20
10
6.0
5.0
4.0
3.0
2.0
1.0
10
20
30
40
Voltage (kV)

Figure 3.5

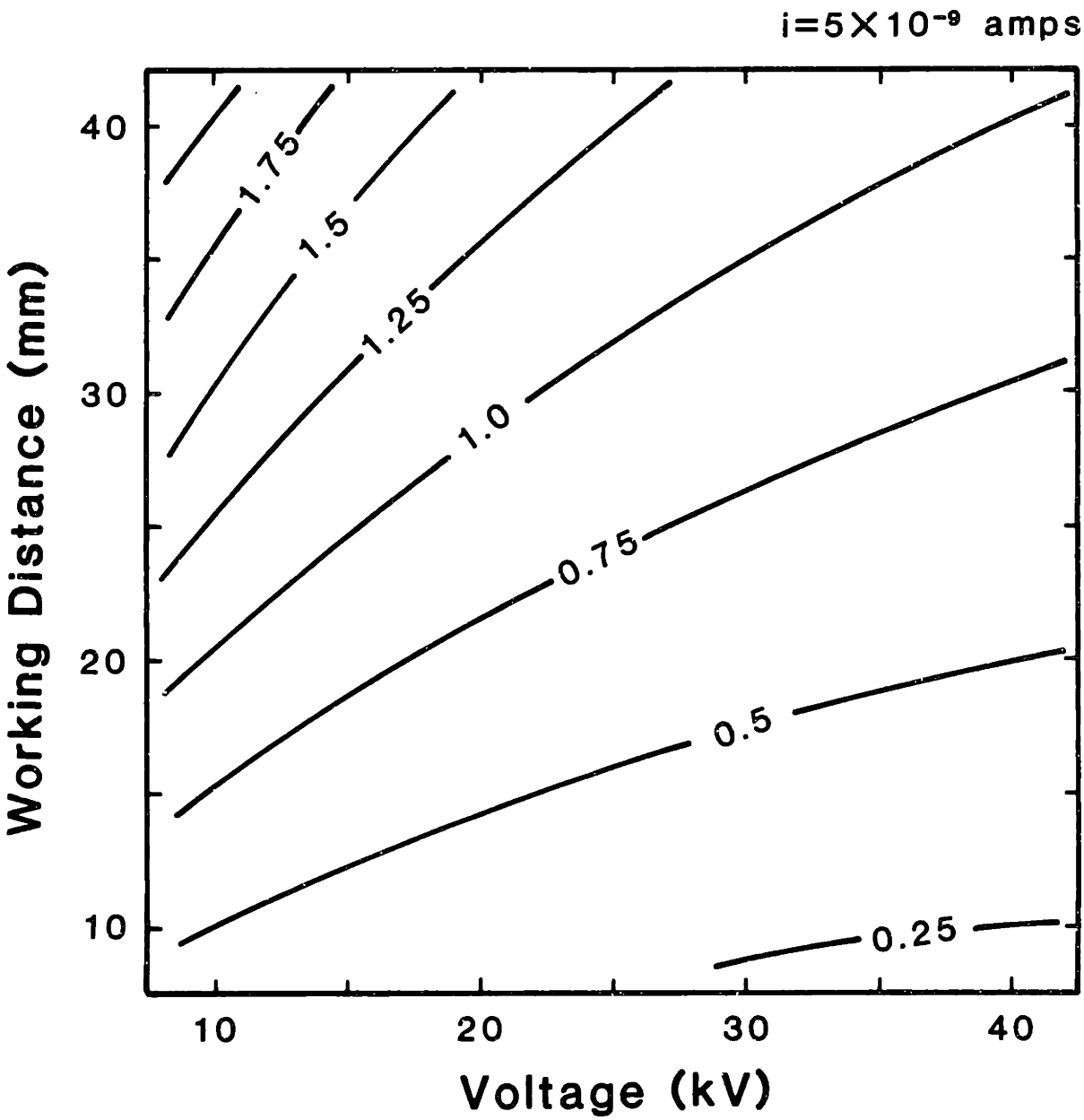
i=5X10⁻⁹ amps
Working Distance (mm)
40
30
20
10
1.75
1.5
1.25
1.0
0.75
0.5
0.25
10
20
30
40
Voltage (kV)

Figure 3.6

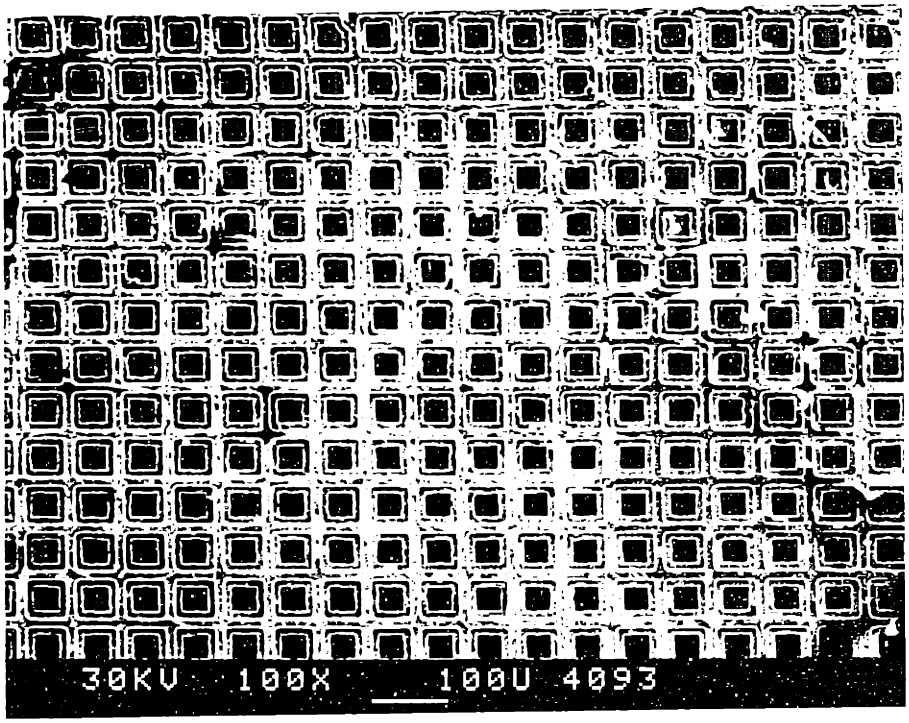

Figure 3.7

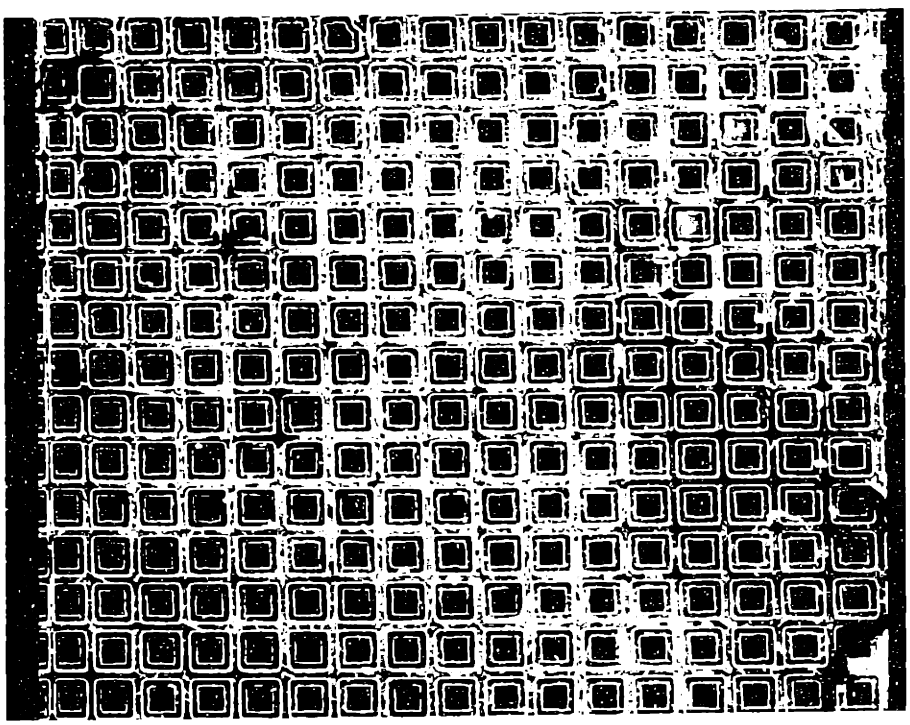

Figure 3.8

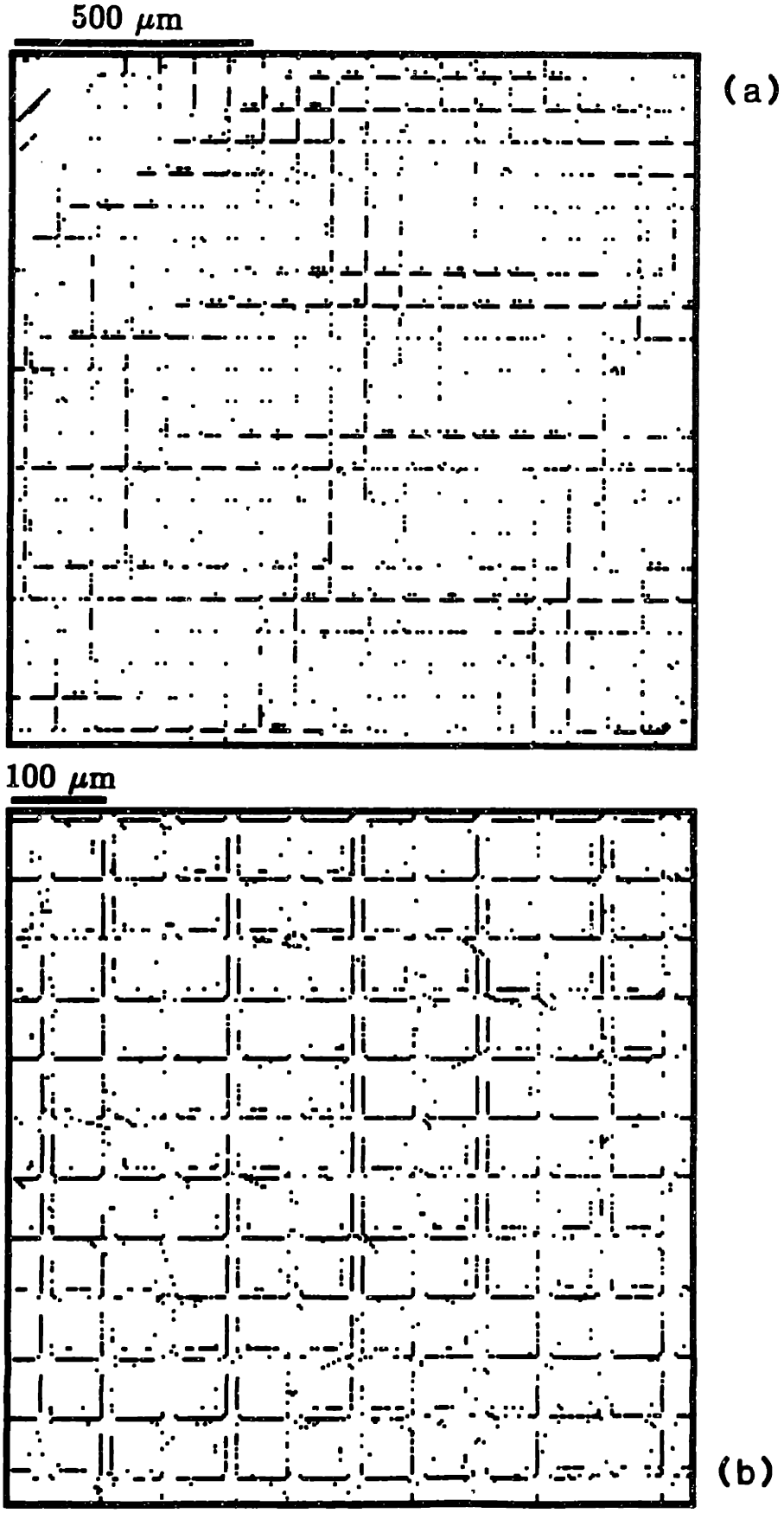

Figure 3.8

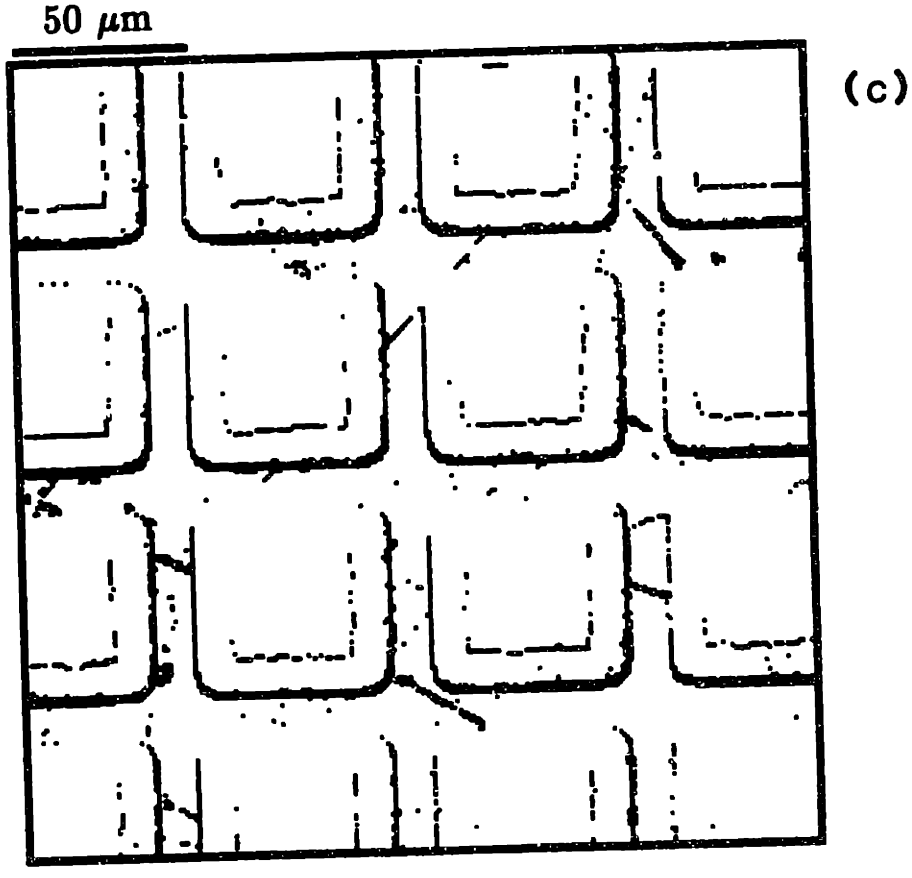

Figure 3.9 Sphere Diameter versus Magnification

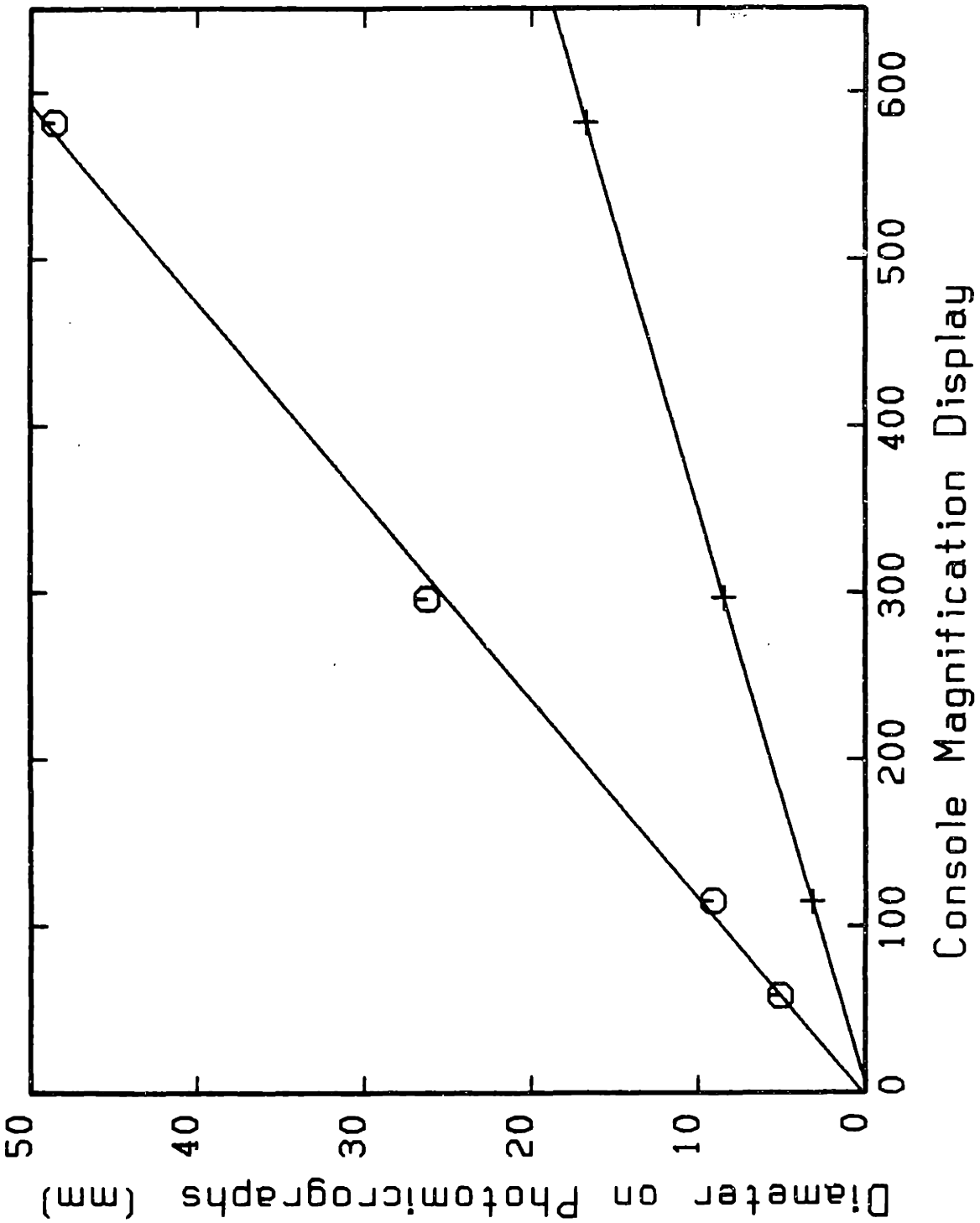

Figure 3.10 Intensity Histograms

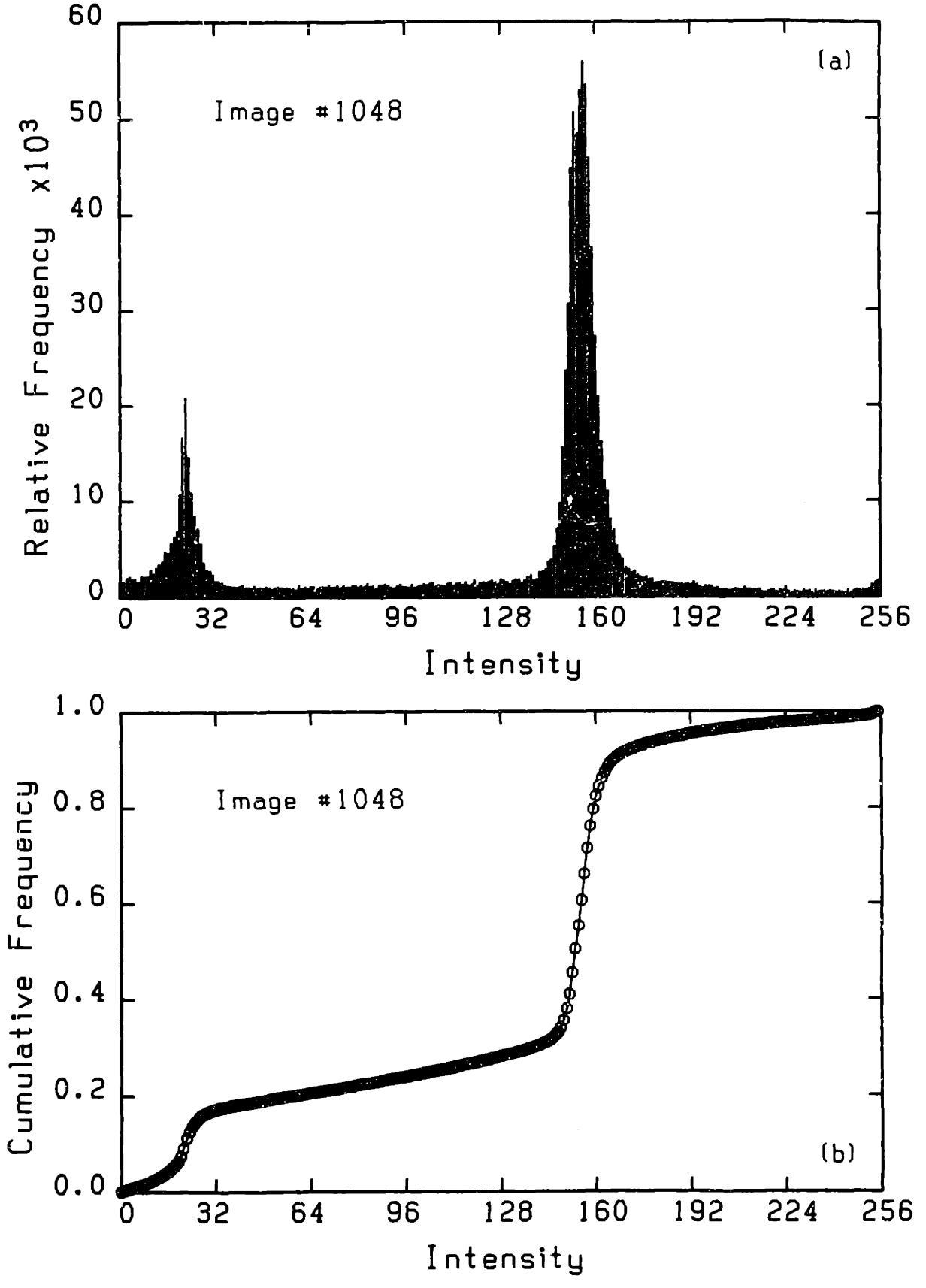

Figure 3.11

Figure 3.12 Intensity Histogram Difference

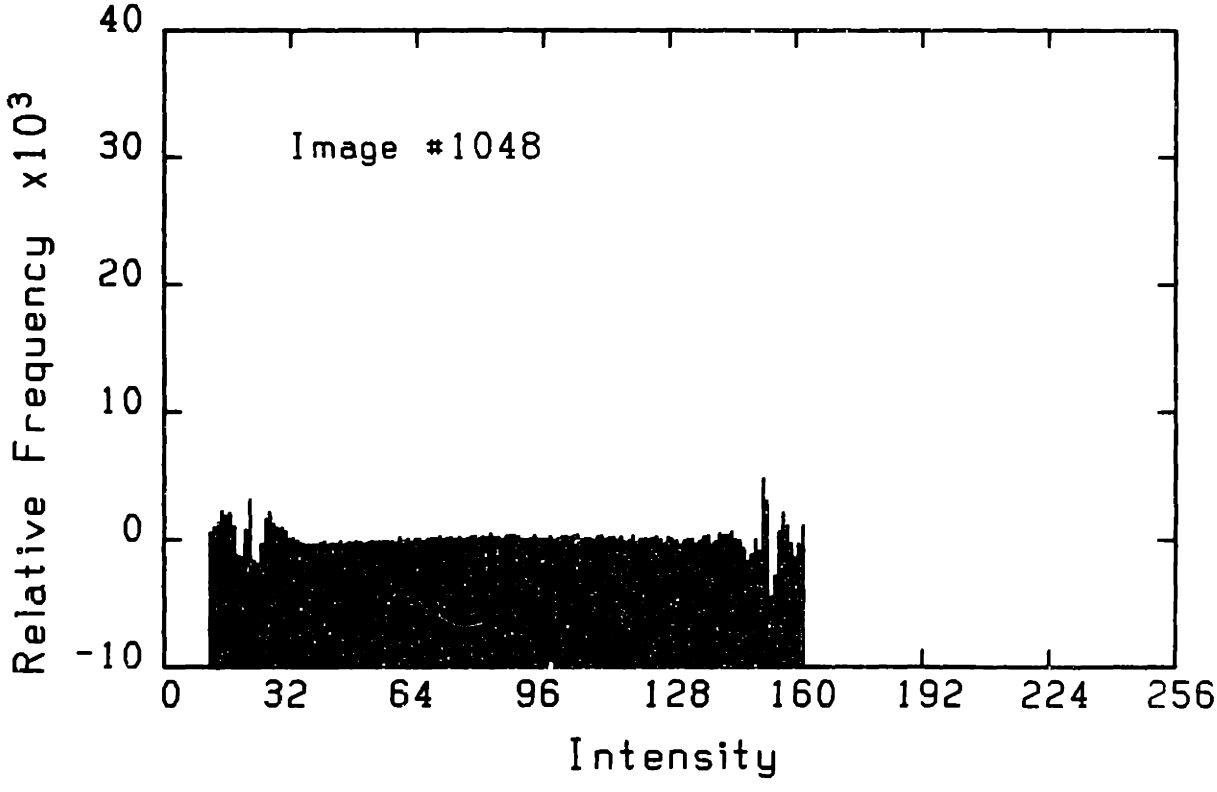

Figure 3.13

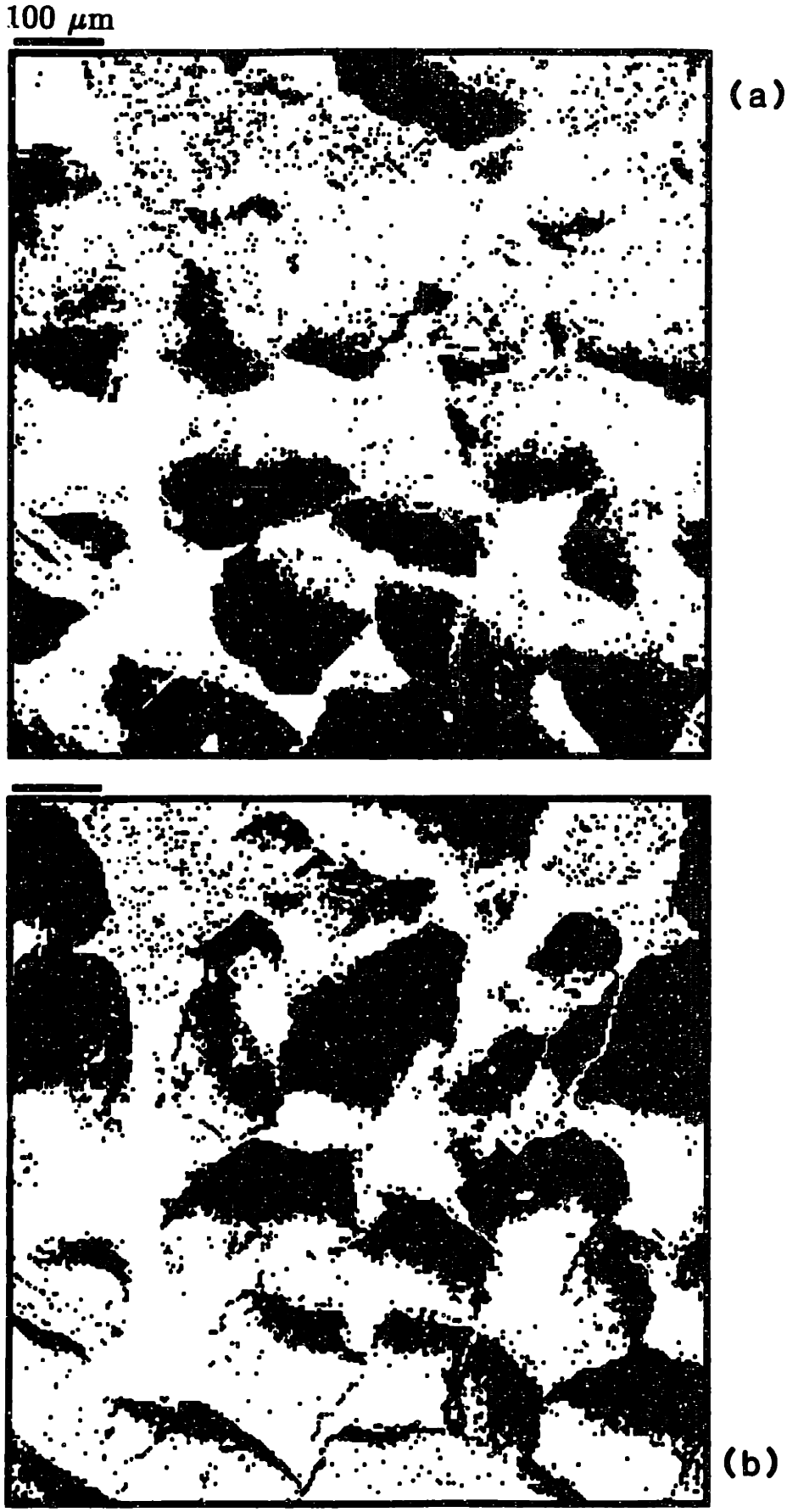

Chapter 4

Quantitative Stereology Applied to Sandstones

4.1 Introduction

The methods of quantitative stereology yield geometric measures of the pore space. These measures include, for example, the volume fraction of the pore space and the specific surface of the pore-grain interface. In this chapter, the methods of quantitative stereology are applied to digital SEM micrographs of sandstones. In stereology, the phases of interest are first identified and then measured. Here, the phase of interest is the pore phase, which has been identified by the dichotomization process described in Chapter 3. Measurements are subsequently made on the binary images. All of the information required for stereological analysis is carried in the geometric properties of the phases (or features) in the image plane. The image is treated as a distortion-free, zero thickness slice through the material.

Some differences exist between historically practiced manual methods of stereological analysis and those methods which are best suited for automatic analysis of digital SEM micrographs. The primary difference is that "efficiency

of analysis" arguments are not valid for automatic methods. These differences are addressed in this chapter. The notation of Underwood (1970) is used with a few exceptions.

Weibel (1974) divides the methods of stereology into two broad classes; those which estimate bulk properties, and those which estimate size distributions. The bulk properties are also referred to in the literature as additive, global, volumetric, linear, or Gestalt properties. Both bulk properties and size distributions are treated here. This chapter begins with the estimation of porosity using areal fraction measurement. Point and lineal fraction estimates are also considered. Next, specific surface area is estimated from intercept chord counts. Mean pore intercept length is computed from line-sampled intercept length distributions. The point-sampled intercept length distribution is used to estimate mean pore volume. Lastly, an advanced method of approximating the pore phase with spheroidal shapes is developed and applied. The approximation assumes the presence of discrete size–shape classes of pores and inverts the measured point-sampled intercept length distribution to obtain the volume distribution of pore space between these classes. From a mathematical viewpoint, the inversion is inherently non-unique. However, by specifying additional geometric constraints, a best-fitting distribution is found.

Stereological concepts are also used in Chapters 5 and 6. The distinction between the treatment in Chapter 4 and that in the later chapters is related primarily to the method of measurement. Here, and in Chapter 6, we need only identify whether a pixel belongs to the pore phase or grain phase in order to make the measurement. In Chapter 5, we must identify individual pore features (spatially contiguous pore pixels) and then make measurements on these features. Also, because we can extract additional information from the individual feature analysis, it warrants the separate treatment.

4.2 Porosity Estimation

The equivalence between volume fraction of a phase, in a composite material, and the surface representation of that phase on a section through the material is well-established (for reviews, see Chayes (1956), Hilliard and Cahn (1961) and Underwood (1970, Ch. 2)). The surface representation may be measured by the fraction of a test probe which lies on the phase of interest. Depending on the probe, these measures are the point fraction of an array of test points, the linear fraction of a test line lying on the phase of interest, or the area fraction of the phase in the section. Hilliard and Cahn (1961) derived and compared the variance for these three methods. They found the two-dimensional systematic point count to be the "most efficient," particularly when a coarse sampling grid is used. A coarse grid is one in which the majority of features do not occupy more than one grid point. Hilliard and Cahn (1961) also found that the variance is determined primarily by the number of observations, not the type of observation. This supports their conclusion that for greatest efficiency, the easiest method (i.e., point counting) is preferred. Stroeven (1976) compared experimental scatter from the areal and lineal methods applied to volume fraction analysis of concrete with artificial aggregates. He found that both methods were more accurate than predicted. In addition, both had similar scatter, as expected from the Hilliard and Cahn (1961) study.

Areal fraction measurement is preferred for analysis of digital images because it uses all available information, as opposed to the point count method which discards the information between points. Note that both point and lineal methods are essentially means for estimating the areal fraction present on the plane (Chayes, 1956). The efficiency arguments of Hilliard and Cahn (1961) are not appropriate for digital image analysis because the "effort" required by the computer is essentially the same for all methods. However,

their analysis of variance for the point and areal measurements are valuable for determining the precision of the volume fraction estimate. The theoretical precision (coefficient of variation) can be compared with the experimental precision to determine if adequate sampling has been accomplished.

4.2.1 Systematic Point Count

A two-dimensional systematic point count is one in which the test points are arranged in a regular (typically square) grid. The phase of interest is termed the alpha phase. Here, the alpha phase is the pore phase. The coefficient of variation of number fraction for a 2-D systematic point count on a coarse grid is

$$CV(P_P) = \frac{\sigma(P_P)}{P_P} = \frac{1}{\sqrt{P_\alpha}}, \tag{4.1}$$

where, $\sigma(P_P)$ is the standard deviation of the fraction of points falling on the alpha phase, P_P is the expected fraction of points falling on the alpha phase, and P_α is the expected number of points falling on the alpha phase.

Prior to point counting, the spacing for the sub-sampling grid must be determined according to the coarse grid criterion specified above. Rigorously, this spacing will depend on each image (i.e., the character of the sample and the magnification of the image). The maximum chord lengths or Feret diameters in the X and Y directions can be measured, and a grid spacing can be chosen which is equal to or greater than the maximum length. These are overly strict criteria, since the requirement is that *most* of the features should occupy only one grid point. A more reasonable criterion would be related to the mean chord length plus 1 standard deviation or perhaps the geometric mean chord length. With either of these criteria, the typical image will be sampled approximately every 1/10 of the image width. With a 256×256 image, this sampling results in a decimation of the data by a factor of almost

1000. For every point of the image which is tested, about 1000 points are discarded. We cannot use the efficiency argument to say that point counting is better than areal analysis, because there is negligible difference in the time required for the two analyses.

4.2.2 Lineal Analysis

The image must be sampled along linear traverses to obtain a measure of lineal fraction. With digital images, the most convenient lineal analysis is parallel to either the X or Y scan directions. There is no boundary constraint when performing a linear sampling for volume fraction. The estimate will not be biased by linear traverses which begin or end on the phase of interest. Therefore, the entire image width (or height) can be sampled. If the test lines are too close (e.g., every image scan line), then the variational coefficients given by Hilliard and Cahn (1961) are inappropriate. Below, it is shown that certain boundary constraints are appropriate when performing lineal analysis for specific surface estimates or chord length distribution measurement. There is no particular benefit of lineal analysis for porosity estimation from digital images.

4.2.3 Areal Analysis

The statistical accuracy of an areal analysis is related to the number of features within the analysis area and the character of the features. A *feature* is a discrete area of intersection of the image plane with the alpha phase. In the case of a digital image, a feature is a region of spatially contiguous pore pixels. Hilliard and Cahn (1961) give the following equation for the coefficient

of variation of the areal fraction

$$CV(A_A) = \frac{\sigma(A_A)}{A_A} = \sqrt{\frac{(\sigma(a_\alpha)/\bar{a}_\alpha)^2 + 1}{N_\alpha}}, \qquad (4.2)$$

where, $\sigma(A_A)$ is the standard deviation of areal fraction, A_A is the expected areal fraction, $\sigma(a_\alpha)$ is the standard deviation of feature areas, $\bar{a}_\alpha$ is the expected feature area, and N_α is the number of features observed. The assumptions used in the derivation of Eqn. (4.2) are (1) that the alpha phase is randomly distributed spatially, (2) that the phase occurs as discrete areas, and (3) that the only contribution to variance is the selection of a sub-area for analysis (i.e., no experimental error). A small volume fraction for alpha is implicit in the derivation, but experimental evidence suggests that this is not a limitation. Further, variance is reduced with increasing volume fraction of alpha (Hilliard and Cahn, 1961).

The quantity $(\sigma(a_\alpha)/\bar{a}_\alpha)$ can be calculated for a given size and shape distribution of objects. For spheres of a constant size, the value is 0.45. For a complex structure like the pore space in sandstones, it is appropriate to use experimental estimates, provided that a sufficiently large number of features are measured. Here, the individual feature analysis described in Chapter 5, was used to estimate the average feature area and the standard deviation of feature area. These estimates will depend on the pre-processing and feature segmentation applied to the image (see Chapter 5). They also depend on whether the smallest features are included. For example, the image areas of clay regions or altering feldspars are likely to contribute many small features.

A computer program (**SETBIT**) was written to count the number of pore pixels (set bits) in a user-specified sub-area of a binary image. The areal fraction is simply the number of pore pixels divided by the number of pixels in the sub-area. Feature analysis of the raw (non-segmented) binary image also yields the area fraction occupied by features (pores) together with the

size distribution of feature areas (see Chapter 5).

4.2.4 Results of Areal Analysis

Results of areal analysis of binary images from 14 sandstones are given in Table 4.1. Mean values, experimental coefficients of variation, and standard deviations were computed from the areal fraction of all images of each rock. Note that the experimental mean areal fraction is weighted by the area of each image, which was constant for most rocks in this study. This weighting is equivalent to dividing total area of pores in all images by the total area of all images. It is stereologically invalid to average areal fractions of individual images if the images differ in the amount of area covered. When more than one magnification was used, the standard deviations and CV were computed using only the high magnification images. Average bulk porosity from air pycnometer measurements on 3 orthogonal plugs is given in Table 4.1 for comparison with image derived porosity. Minimum porosity, maximum porosity, and range in porosity for the high magnification images are given in Table 4.1b.

Theoretical coefficients of variation were computed (Eqn. 4.2) using the mean feature area and standard deviation from all high magnification images of each rock (Table 4.1). Feature analysis results from the raw images were used here. Feature analysis of segmented images (i.e., features split into simpler, nearly convex shapes) gives smaller coefficients of variation due to increased numbers of features and reduced standard deviation of the feature area. Mean feature area is also reduced, but the reduction in standard deviation is proportionally greater. For the purpose of estimating the standard deviation in porosity, there is no justification for using the segmented feature statistics. Therefore, the raw image feature parameters have been used. See Chapter 5 for additional discussion of individual feature analysis.

4.2.5 Discussion of Areal Analysis

Figure 4.1 is a plot of image derived porosity versus bulk porosity. The agreement is quite good, with a slight positive bias in image values. Three exceptions are samples 2687, 2704, and 2710. These three rocks have large intergranular pores and inhomogeneous pore structure at the scale of investigation and are discussed below. The images do not sufficiently represent the large intergranular pores which, although few in number, contribute greatly to the porosity.

The slight positive bias in samples 2124, 2509, 2519, 2843, and 2841 is due to the subjective selection of the image location on the sample. Only two to four images were acquired for these rocks, with the intention of obtaining "representative images of the pore structure." Anisometry in the detector area also may have contributed to the bias (see Section 4.3.3). Still, the subjective selection of image location is the most probable source of the positive bias for these samples. No rock, for which only 2–3 images were collected, has negative bias in the image derived porosity.

Sandstones can be inhomogeneous at the scale of direct analysis (i.e., 100× images) and, thus, large variations in the porosity estimated from each individual image can occur. The practical utility of the theoretical coefficient of variation is to determine if sufficient images of a particular specimen (polished section) have been collected to be statistically representative. Alternatively, it can be used to determine if a particular sample is homogeneous at the scale of sampling. If the experimental coefficient of variation is less than or equal to the theoretical coefficient of variation, then it can be assumed that sufficient sampling has been completed for this particular specimen at this scale of sampling. That is, the variations are within the range expected upon sampling a homogeneous specimen. If the experimental coefficient of variation is larger than the theoretical value, then additional sampling, perhaps at other magni-

fications, must be done because the sample is inhomogeneous at the current sampling scale.

Table 4.1 shows that most of the rocks have been sampled sufficiently, with some exceptions. Samples 2523 and 2842 have low theoretical standard deviations, with experimental values about double the theoretical values. Samples 2519, 2687, and 2704 have intermediate theoretical standard deviations, with experimental values more than 2 times the theoretical values. The relatively high theoretical values for samples 2686, 2841, and 2843 are probably the result of only two images being used for each sample. They have moderate experimental variation partly because the image areas were selected subjectively. The results for samples 2687 and 2704 indicate that these rocks are inhomogeneous at the scale of sampling. Indeed, one of the images for sample 2687 had a 300 μm wide moldic pore extending entirely across the image (Figure 4.2b). Inspection of a hand specimen confirms the presence of a large volume of large pores, probably due to dissolution of primary grains. Sample 2704 also contains some intergranular pores which are larger than the framework grains. These appear to be secondary porosity resulting from the dissolution of feldspar grains. Samples 2704 and 2710 both show significant volume fractions of large pores in their pore size–shape distributions (see section 4.6).

The high experimental standard deviation of sample 2519 is a result of only two images being used, their subjective selection, and the inhomogeneity in pore structure due to the extremely poor sorting of the sample. Intergranular pores in 2519 are typically a factor of 10 smaller than the largest grains.

The criterion for sufficient sampling for porosity estimation may be useful to determine if sufficient images have been collected to give representative values for structural parameters other than porosity. Few theoretical results are available to determine when sufficient sampling has been accomplished for estimating other parameters (e.g., Hilliard and Cahn, 1961; Nicholson, 1978).

Typically, a parameter is monitored as more measurements are added until the additional measurements do not change an average value (or distribution of values) by more than some specified level of tolerance.

Use of the above criterion does not ensure that sufficient sampling has been done, but it does indicate a potential source of error if the sampling is apparently insufficient. Due to the nature of this research (i.e., development of analysis methods as opposed to exhaustive analysis of individual rocks), all rocks have not necessarily been sampled sufficiently, as judged by the above criterion.

From the theoretical coefficients of variation from areal analysis, we can estimate the sample area which would need to be covered by point counting to provide an equivalent precision. The expense of the "easier" point counting is the need to examine a larger area. Thus, for a fixed area (i.e., the digital image), areal analysis is more precise.

In summary, the relations between image derived porosity and bulk porosity demonstrate several important points. First, the image derived porosity is in good agreement with bulk measurements of porosity. The subjective selection of image location can, however, introduce bias in the image porosity. A similar bias can be expected if the dichotomization criteria used for identifying pore and grain pixels is subjective. Second, statistics derived from the image can indicate the sufficiency of sampling. Thus, the number of additional images required for a given accuracy can be determined from the information in the images already acquired. Lastly, the threshold selection criteria developed in Chapter 3 appear to yield an unbiased estimate of porosity.

4.3 Specific Surface Area

The amount of surface area between two phases is recognized as a fundamental parameter for describing composite media (Underwood, 1970; Moore, 1972). Here, the surface area of interest is the pore-grain interface in sandstones. Specific surface, S_V, is defined as the surface area per unit *bulk* volume of a material. Many studies of pore structure in sandstones have touched on the specific surface (see Chapter 2), but few give it sufficient emphasis. Later chapters show that specific surface is a common link among the various approaches to pore structure analysis (viz., stereology, feature analysis, and autocovariance). Specific surface is also a central component of the most successful model for predicting permeability from direct pore structure measurements (see Chapter 7). What attribute of specific surface makes it important? On the theoretical side, specific surface is independent of assumptions about the size and shape of the pore structure. Measurements of specific surface are even valid for non-random structures, provided that appropriate sampling methods are used (Hilliard, 1968a). From a practical viewpoint, this research indicates that the specific surface in sandstones, measured by direct analysis, is more strongly dependent on pore size than on pore shape. Thus, specific surface yields information on the pore sizes in sandstones. In general, specific surface merits greater emphasis and further study in the description of pore structure.

In this section, specific surface is determined from digital SEM images by counting linear intercepts. This method, as well as other image based methods, yields a value of specific surface which differs greatly from the values obtained by bulk methods such as gas adsorption (Rink and Schopper, 1978). The difference arises from the limited resolution of the digital images. This limitation has proven to be advantageous in the case of modeling fluid permeability. Presumably, only the surface area which is important for determining

flow is measured (see Chapter 7). For other applications, the adsoption derived value may be appropriate.

For describing pore structure, it can be more appropriate to use the surface area normalized by the pore volume, S_{Vp} (the surface area per unit pore volume). Such a normalization will reduce the influence of unrepresentative porosity of a single image in a set of images. The importance of the size of the test area is also reduced by such a normalization (Underwood, 1970, p. 38). Specific surface is given by

$$S_V = 2P_L \,, \tag{4.3}$$

and surface area per unit pore volume is given by

$$S_{Vp} = \frac{S_V}{\phi_i} = \frac{2P_L}{\phi_i} \,, \tag{4.4}$$

where P_L is the number of points of intersection of a test line with the pore surface (i.e., boundary of the feature) per unit length of test line and ϕ_i is the porosity determined by areal or lineal analysis. We have used line-sampled intercepts to count the intersections. Each intercept has two points of intersection, one at each end.

Stereological relations for the determination of S_{Vp} from feature parameters are discussed in Chapter 5 (for review see also, Chapter 2).

4.3.1 Line-Sampled Intercepts for Specific Surface

Line-sampled intercepts are obtained by placing a test line on the area of investigation (i.e., digital image) and measuring all intersections of the test line with the phase of interest. Line-sampled intercepts used to estimate surface area must satisfy certain boundary criteria. These criteria are weaker than those which apply when measuring the distribution of intercept lengths. First, the assumption is made that the test line begins and ends on the pore phase with equal probability. This assumption is reasonable because the digital

image is positioned randomly on the section. Further, the probability of ending on the pore phase is assumed to be independent of the phase on which the test line began. Independence is a reasonable assumption because the correlation range of the pore structure is much less than the width of the image (see Chapter 6). The following criteria are specified so that an unbiased count of the number of intersections per unit test line length is obtained. Chords which lie in the pore phase at the beginning of the test line are counted. If the test line ends in the pore phase, the last chord is *not* counted. Equivalently, chords which begin in the pore phase could be discarded and those which end in the pore phase counted.

A program (**CHORDX**) was written to measure and tabulate chord lengths in a binary image in the X image direction. Intercepts in the Y direction are obtained by rotating the image 90 degrees with **IMGROT** and using **CHORDX**. Accurate intercept length measurement is not important when determining specific surface, and a guard region (described below) is not required. However, the criteria used for accurate length measurement also produce accurate specific surface determination. Thus, these criteria, which are described in section 4.4.1, were actually used for chord sampling.

4.3.2 Specific Surface Results

The program **CRDSTA** is used to compute stereological parameters from the line-sampled intercept distribution. Specific surface and the surface area per unit pore volume are given in Tables 4.2 and 4.3, respectively. In each table are average values and standard deviations for the X and Y image directions as well as a combined value for both directions. The average values were determined by combining the intercept counts and test line lengths from all images of each rock. Averaging S_V values from individual images is valid only if the test line lengths are the same for all images. Here, the combined S_V

data are equal to the average S_V because the test line lengths were equal for all images. However, the combined S_{Vp} is not equal to the average S_{Vp} from individual images because of the difference between the averages $\langle S_V \rangle_{\text{avg}} / \langle \phi \rangle_{\text{avg}}$ and $\langle S_V / \phi \rangle_{\text{avg}}$. Errors generated by incorrect averaging are not uncommon in the computation of stereological measures and must be avoided. Henceforth, when we speak of average values, they are from properly combined data, not just averages of the individual image values. Porosity for S_{Vp} was found from the lineal analysis and may differ slightly from the areal analysis, due to the chord sampling criteria and different images being used. The difference was always less than the experimental standard deviation of porosity and was usually less than half that value. Standard deviations in S_V and S_{Vp} were computed using the values from individual images and the mean value from the combined intercept data.

4.3.3 Discussion of Specific Surface

The specific surface estimates from line-sampled intercepts are compared with other direct measures of specific surface in Chapter 7. Here, magnitudes, standard deviations, and anisotropy are discussed. The most striking characteristic of the data is the larger value of S_V and S_{Vp} in the Y direction for all rocks. The difference is smaller for all images acquired after the detector modification which was described in Chapter 3. The modification produces a more nearly isotropic detector sensitivity. For these images, the range *between* (not of) the average S_V in the X and Y directions is less than the standard deviation for the individual directions. The difference between X and Y values in individual images is, at most, 50% of the standard deviation between images, and usually it is about 30% of the standard deviation. Most of these rocks had one or more images for which the X direction S_V was *larger* than the Y direction S_V. For the images collected prior to the installation of the detec-

tor shield, the differences between X and Y values in individual images were usually less than or equal to the standard deviation of S_V between images.

The differences in S_{V_p} for X and Y directions follow the same proportional relationships with their inter-image standard deviations as those just described for S_V.

The difference between X and Y values is most likely due to the nature of the SEM imaging configuration. Two contributing sources are the anisometry of the detector area and the raster scan pattern. The detector area is still slightly anisometric, despite the improvement provided by the lead shield described in Chapter 3. The bright edges which were oriented normal to the detector axis are no longer visible in the image, but apparently, there is still a slight non-visible bias. The binary images do *not* show visual characteristics which indicate a more "broken" character in the Y direction sampling.

The detector is oriented about 20° clockwise from the Y image axis and "catches" more BSE's which have trajectories parallel to the detector axis (and electrons scattered through slightly lower angles). Edges oriented normal to the vertical plane containing the detector axis are likely to be enhanced. As more edges are detected, the estimate of S_V increases. Because of the large reduction in anisotropy in S_V due to the addition of the detector shield, the majority of the remaining anisotropy is believed to be due to the remaining anisometry in the detector.

The raster scan pattern probably does not contribute to the anisotropy in S_V. The image scan is more or less continuous in X and discrete in Y. The beam is actually stopped at each pixel location during sampling, but the beam is always on, even during the move from one pixel to another. Thus, we might expect more continuity in the X direction because adjacent pixels of a line scan are occupied consecutively. Alternatively, the Y direction "scan" is composed of pixels with a constant X coordinate, selected from the X scan

lines. The interpixel irradiation may smooth the signal variations in the X direction because of the spatially continuous sampling volume of the beam. However, the time for the interpixel move ($\approx$ 1 μsec) is negligible compared to the dwell time at the pixel. Further, the spatial positioning between line scans has been shown to be accurate (see Chapter 3).

The character of S_V may indicate the need for additional shielding of the detector. Alternatively, a spatial dichotomization operator (i.e., an edge detector) may produce a binary image without the edge enhancement in one direction.

The anisotropy due to the imaging method precludes the detection of minor structural anisotropy from chord data. Prominent anisotropy in S_V can be clearly identified for individual images (see for example, Figure 4.2b). The absence of prominent anisotropy in the average values suggests that the rocks do not have strong anisotropy. We note that the slight anisotropy in all rocks is due not only to an excess of short chords. If the shorter chords are eliminated from the S_V calculations, the bias is reduced, but still exists. This observation reinforces the conclusion that the anisotropy is due to the anisometric detector area rather than alignment errors in the raster scan.

The range of S_V in the rocks studied is from 0.027 to 0.063 μm^{-1}. The range of S_{Vp} is from 0.14 to 0.36 μm^{-1}. The coefficients of variation are typically smaller for S_V than for S_{Vp} for all rocks except samples 2686 and 2843. We expected the S_{Vp} values to be somewhat "self-normalizing" for the variation in porosity from image to image which leads to variation in S_V but not in S_{Vp}. Apparently, variations in size and shape of the pores, which control the S_{Vp} values, are more significant. There may also be a relationship between the variation in porosity and the size and shape of the pores. The range in values of both S_V and S_{Vp} from different images of the same rock can be quite large as is shown by sample 2687. The standard deviations are smaller for the

rocks where the image locations were selected subjectively (i.e., rocks with 2 to 4 images).

For some rocks in this study, the dependence of S_V on porosity makes it desirable to use ϕ_i from areal analysis and S_{Vp} to compute S_V. For these rocks, the porosity estimate from chord data is not good because only a few high magnification images are used and the chord sampling criteria reduce the sampled area. Sample numbers 2519, 2686, 2687 (due to the omission of image #1106), and 2841 are in this category.

Our results compare favorably with the few values in the literature. The S_V values of Wyllie and Spangler (1952) for seven clean isotropic sandstones fall in the middle of the range of values reported here. The S_{Vp} values given by Rink and Schopper (1978) for four sandstones fall at the low end of the range of our values. Their images do not show significant detail at the small pore sizes, which may explain their generally lower values. Ruzyla (1984) gives two different S_{Vp} results for Berea sandstone, one of which is very close to the value for Berea (sample 2124) reported here. The other value is 50% larger. No information on the petrologic difference between the two samples was given. The standard deviations of his results are a factor of 3 greater than those reported here. Correspondingly, his range is a factor of 4 greater. Lin *et al.* (1986) report values of specific surface for Masillon sandstone and a tight gas sand from Cotton Valley. Their value for Masillon (our sample 2686) is a factor of 10 or 50 greater than the value reported here, depending on whether they are giving S_V or S_{Vp} , an unclear point from their ambiguous notation. In either case, their values are much too high. Berryman and Blair (1986) report a value of S_V for Berea sandstone measured by spatial correlation methods (see Chapter 6), using 100× images, which is about 1/2 the value reported here for our Berea sandstone.

4.4 Mean Pore Intercept Length

The mean pore intercept length is a measure of the mean distance between grains in the sandstone. To allow more detailed treatment of the continuous pore space, we will usually consider it to be made up of approximately convex, discrete regions. This follows the well-established convention, in the qualitative study of pore space, whereby the space is said to be composed of enlargements (or bulges or intergranular pores) termed *pores* and constrictions (or throats or necks or connective pores) termed *throats*. The mean pore intercept length can now be interpreted as some mean dimension of the regions. It is not appropriate to term this measure the mean "size" of the regions because of the stereological relationships involved (see section 4.6). The mean pore intercept length is also closely related to specific surface.

Intercept *length* measurement is not required to compute mean pore intercept length. The mean pore intercept is related to the specific surface by (Underwood, 1970, Ch. 4)

$$\overline{L}_{3p} = \frac{4\phi}{S_V} = \frac{\phi}{N_L} = \frac{4}{S_{Vp}} . \tag{4.5}$$

Equation (4.5) requires only the volume fraction (e.g., from areal analysis) of the pore phase and the *number* of chords per unit length of test line. In practice, the intercept lengths are required here for the size–shape inversion, so it is logical to use them directly to compute mean intercept lengths. Because the combined pore and grain phases are space filling, we have the following relation for mean grain intercept length

$$\overline{L}_{3g} = \overline{L}_{3p} \frac{1-\phi}{\phi} . \tag{4.6}$$

Theoretical development of the mean intercept length relation considers, rigorously, isolated discrete particles within a continuous matrix (e.g., Underwood, 1970, Ch. 4). In such a case, the mean intercept length of the continuous

phase is termed the mean free distance, or mean edge-to-edge distance. The pore phase is continuous in our samples, but we will use the mean intercept length terminology to correspond to our conceptual treatment of pore regions.

4.4.1 Line-Sampled Intercepts

Appropriate sampling criteria must be followed to obtain unbiased line-sampled intercept lengths. The sampling criteria consist of a fixed width guard region at the end of the test line and an exclusion rule for intercepts which start at the left border of the image (Figure 4.3a). These constraints are the same as those outlined by Gundersen and Jensen (1983, Figure 2). The left border constraint is simple. If a chord touches the left border, it is rejected. All chords which begin before the start of the guard region are counted.

The guard region is used to provide an unbiased measurement of length. The effect of the exclusion and guard criteria is that each chord length is sampled over the same effective test line length. Consider a chord of length l. The center of this chord cannot lie closer than $l/2$ to the left boundary, otherwise it will touch the left boundary and will be rejected. The center of this chord cannot lie farther than $l/2$ to the right of the start of the guard region, otherwise it would not extend onto the test line (within the valid counting region). The effective test line length is then the width, W, of the test region, minus $l/2$ at the start, plus $l/2$ at the end, giving an effective test line length of W for all chord lengths.

In theory, the guard region must be wider than the longest chord to be measured. In practice, this constraint eliminates a significant fraction (up to 20%) of the image from measurement. The guard region width is thus chosen smaller than the longest chord. The bias introduced by this convention is sufficiently small for the guard regions used in this study. An additional counting criterion must then be specified to treat the chords which start to

the left of the guard region and continue to the right border of the image. If these spanning chords are rejected, a significant amount of information is lost because there are few long chords. If the chord is assumed to end at the right border, the assigned length is smaller than or equal to the true length. To retain the most information, spanning chords are counted as if they end at the right border. The reasoning for this decision follows. First, the guard region is chosen to be wider than the length of most of the chords. Second, because there are so few long chords, the probability of one spanning the guard region is small. Third, for a chord which spans the guard region, the fraction of length which extends past the right boundary will usually be small, so the bias introduced by clipping the length should be small. Fourth, the criteria yield unbiased S_V values, whereas, the rejection of spanning chords would underestimate S_V. Presently, the guard length is taken as the mean value plus one standard deviation of the maximum chord length in each pore feature as determined from feature analysis on the unsegmented image. Porosities determined from chords sampled with these criteria agree well with those determined from areal analysis. The agreement indicates that the length of the excluded chords is approximately equal to the chord length included from the guard region.

Serra (1972) discusses the use of a guard region when measuring feature sizes. For the guard region he proposed, a bias toward larger feature sizes is expected. However, the simpler guard criteria described above, yield an unbiased chord length distribution for a sufficiently wide guard region. If the guard criteria described here are combined with the local knowledge (mask) criterion of Serra (1972), then a maximum area of the image can be used for sampling chords. The mask criterion simply allows for a guard region which varies with the size of the chord being measured. The guard is short for short chords and long for long chords. This form of variable mask requires

a subsequent normalization of the chord length histogram to account for the variable guard length. The variable guard introduces additional bookkeeping operations. Note that the mathematical morphology method of measuring chord lengths is computationaly inefficient in our system because it requires a large number of erosions. It is preferable to use simple chord detection and length measurement.

Hilliard (1968) derived correction factors which could be applied to the intercept distribution obtained by rejection of all boundary touching chords (e.g., automatic image analyzers with no guard region capabilities). The correction has the same effect as the one-sided guard region used here. Other discussions of edge effects in lineal sampling can be found in Bockstiegel (1972ab) and Exner (1972).

4.4.2 Mean Pore Intercept Results

The computer program **CHORDX** has been used with the above criteria to measure intercept lengths in the X direction of a binary image according to the sampling criteria described above. Chords in the Y direction are measured by first rotating the image 90 degrees and then using **CHORDX**. The mean pore intercept lengths, computed by averaging the measured intercept lengths, are given in Table 4.4. The mean grain intercept lengths, computed with Eqn. (4.6), are given in Table 4.5. Porosity in Eqn. (4.6) is obtained from the linear fraction of the test line in the pore space.

4.4.3 Discussion of Mean Pore Intercept Lengths

Mean pore intercept lengths are compared with correlation distances and pore size distribution results in Chapter 7. In general, the mean pore intercept lengths are very short and they do not reflect the mean size of the pores

expected from observations of pore casts and thin sections.

The comments made about S_{Vp} in section 4.3 apply to $\overline{L}_{3p}$ because of their inverse relationship (Eqn. (4.5)). The anisotropy observed in S_{Vp} manifests itself as shorter $\overline{L}_{3p}$ in the Y direction than in the X direction.

4.5 Mean Pore Volume

In this section, an estimator of mean pore volume, which is size and shape independent, is applied to data from digital SEM images of sandstones. The mean pore volume estimator has been rigorously derived for convex isolated particles (Matheron, 1967; Gundersen and Jensen, 1983). Recently, Gundersen and Jensen (1985) derived a mean volume estimator which is valid for arbitrary non-convex, but still closed, shapes (also see Jensen and Gundersen, 1985). The general non-convex estimator is difficult to apply and requires an identification of which linear intercepts on the image belong to which objects. The concept of a "mean volume" of the pores in a sandstone is not rigorous because the pore space is continuous. Again we use the conceptual model of continuous pore space being approximated by a collection of discrete, nearly convex regions. The mean volume estimate then represents the mean volume of the regions. This same approach is also used with the pore size–shape inversion described in section 4.6. Thus, the mean volume estimator for convex objects appears suitable for our conceptual model of the pore space. Further, we avoid the identification problem. The mean pore volume is interpreted as follows. If we select a "pore" at random with respect to volume abundance, then, on the average, it will have a volume equal to the mean pore volume. This is quite different from the expected mean volume obtained from a number distribution of pore sizes.

The mean pore volume estimator is given by

$$\overline{V}_p = \frac{\pi}{3} E_0[l^3] \,, \tag{4.7}$$

where the 0 subscript on the expectation, E, indicates that the point-sampled intercept distribution is used. The only assumption used in the derivation of Eqn. (4.7) is that the objects are convex. This mean volume estimator is also applicable for estimating mean grain volume from the point-sampled intercept distribution of grain intercepts.

The mean volume estimate is equivalent to the three-dimensional "star" in the nomenclature of mathematical morphology (Haas *et al.*, 1967ab; Serra, 1972; Serra, 1982, p. 325, p. 332, p. 346). The star has a stereological interpretation of measure weighted moments (i.e., volume weighted expected volume). The star has a physical interpretation as the average volume which can be "seen" in all directions from points in the pore space. For this interpretation, the notion of isolated convex regions is not required.

4.5.1 Point-Sampled Intercepts

The distribution of point-sampled intercept lengths is used to estimate the mean pore volume. This sampling method yields a measure weighted intercept length distribution, much the same as would a linear erosion operator (see Serra, 1982, Ch. 10). When counting chords for specific surface area and measuring intercepts for the mean pore intercept length, all intercepts along a test line (probe) placed on the sample (image) were counted provided that they satisfied the appropriate boundary constraints. Such intercepts are termed line-sampled and they yield a number weighted distribution of lengths. With point-sampled intercepts, the test probe is a set of points (Figure 4.3b). All intercepts, with a pre-defined orientation, which intersect the points are counted. The effect of point sampling is to apply a volume weighting to the

intercept length distribution.

Intercept length sampling for both mean volume determination and inversion for size–shape volume distribution requires accurate measures of the relative frequencies of chord lengths. The absolute number of chords is not important because porosity is determined by areal analysis. It is most important to measure chords accurately and to treat the boundary intersecting chords properly. Two rules are used for counting. (1) If a chord hits the first test point of a line and touches the left boundary, it is rejected. (2) All chords which touch the right side are also rejected. Gundersen and Jensen (1983) suggest the use of "guard areas" on the sides of the image. These areas must be wide enough to contain the longest expected chord. Chords which hit the leftmost and rightmost test points and which end before the edge of the image are counted. Chords which hit these test points and touch the image boundary are rejected. With true point-sampled intercepts, these simple criteria are sufficient to produce an unbiased intercept length distribution.

The spacing of test points for point-sampled intercepts merits some attention. For statistically independent chord sampling, a rigorous condition may be the same as that applied to the spacing of points for point counting. Such a condition would allow, at most, one chord per feature. Roethlisberger (1955) shows four points hitting the largest feature in a schematic illustration of point sampled intercepts. The intercept is counted once for *each* test point it intersects. That is, the histogram bin for that particular chord length is incremented for each test point hitting the chord. In the limit of very small point spacing, the number of test points is equal to the number of pixels in the chord. Indeed, this limit is the basis for the relationship between the the point-sampled intercept length distribution and the line-sampled intercept length distribution. A point to recognize is that, for the same number of intercepts, the intercept length distribution obtained from dense point-sampling

is not as robust as the distribution obtained from sparse sampling. This is similar to the situation when point-counting is too dense, the samples are not independent. Still, the line-sampled intercepts are measured for specific surface and mean intercept length estimates. It is easier to convert the line-sampled intercepts to the equivalent point-sampled distribution than it is to perform true point-sampling.

4.5.2 Point-Sampled Intercepts From Line-Sampled Intercepts

The point-sampled intercept length distribution is related to the line-sampled intercept length distribution by (Serra, 1980, Ch. 10; Gundersen and Jensen, 1983)

$$f_0(l) = \frac{l f_1(l)}{E_1[l]} . \tag{4.8}$$

The 0 subscript indicates point-sampling and the 1 subscript indicates line-sampling. $E_1[l]$ is the expectation of the intercept length from the line-sampled intercept distribution. When line-sampled intercepts are used to obtain the point-sampled distribution, the relative frequencies of the line-sampled intercepts must also be unbiased. The sampling criteria required are those described above for the mean pore intercept length. The program **CVTCRD** is used to convert line-sampled intercept distributions to point-sampled distributions.

4.5.3 Mean Pore Volume Results

The mean pore volume results are given in Table 4.6. These values were computed from the converted line-sampled intercept length distribtions. To aid interpretation, the diameters of the spheres with equivalent volume, $D_{\overline{V}_p}$, are also given. The major axis of the oblate ellipsoid with equivalent volume

and with aspect ratio determined from the size–shape inversion (see section 4.6) is also given. The mean pore volume ranges from about 74000 μm^3 to 2015000 μm^3 which corresponds to sphere diameters of 52 μm to 157 μm.

The longest point-sampled intercept observed is not necessarily the longest intercept used in the mean pore volume estimation. Commonly, a couple of very long chords are measured which fall in bins well above the end of the "continuous" distribution (i.e., chord lengths shorter than the length at the first bin with no chords). The very long chords usually pass through and join "separate" nearly convex pore features. They mark the relatively rare circumstances when the largest "separate" features are joined in the image plane. The longest intercept allowed (Table 4.6) is determined from the size of the largest class used in the size–shape inversion of section 4.6. This size is the best one as determined by the measures of goodness of fit of the inversion. The size typically corresponds to the length of the chord at the end of the "continuous" distribution.

The true point-sampled intercept distribution was measured for Berea sandstone (2124), using both a sparse point spacing, and a dense point spacing of 1 pixel. The distribution from the dense point-sampling is identical to the converted line-sampled intercept distribution. This agreement illustrates internal consistency of the sampling and conversion programs. The distribution from the sparse point-sampling also agrees well with the converted line-sampled intercept distribution. No statistical test was applied, but the distributions look the same, with only slight variation in "random" detail. The true point-sampled intercept distribution appears to have fewer long chords, an expected difference because the probability of these chords is low in general. The converted line-sampled intercept distribution gives a somewhat smoother curve as expected because of the greater number of chords which were sampled. The mean pore volumes estimated from the true point-sampled distributions

were within 5% of the value from the converted line-sampled distribution.

4.5.4 Discussion of Mean Pore Volume

The diameters of the mean pore volume equivalent sphere, $D_{\overline{V}_p}$, appear reasonable when compared to a qualitative assessment of pore casts and polished sections. Also, the $D_{\overline{V}_p}$ correlate very well with the range of the non-centered covariance (see Chapters 6 and 7). The mean pore volume is used in section 4.6 to check the goodness of fit of the size–shape inversion.

The mean pore volume has not been reported previously for sandstones. Haas *et al.* (1967) report the value of 66.5×10^6 μm^3 for the "star" in a crystalline rock.

The interpretation of the mean pore volume in the sense of the star has strong appeal. The "mean volume seen from each point in the pore space" contains no assumptions about the size or shape of the pore space. This interpretation should merit the same significance as porosity and specific surface in line with their independence of restrictive assumptions.

4.6 Size–Shape Volume Distribution

The stereological methods of previous sections gave information on the average bulk properties of the pore space. To gain information about the variability of the pore space, we look at the distribution of pore sizes. The size distribution of an aggregate of objects can be determined from data taken on a plane through the aggregate. An exact solution is available for objects with simple shapes, such as spheres. Objects with complex shapes and continuous phases (e.g., sandstone pore space) can be approximated by simple discrete shapes and the distribution, in number or volume, can be estimated. In this section we approximate the pore space in sandstones with spheroidal shapes (oblate

and prolate ellipsoids) and invert intercept length distributions for volume distributions of size and shape. In particular, a new method of inversion by numerical least squares techniques is developed and applied. Additional measures of the goodness of fit of the inversion come from porosity, specific surface area, and mean pore volume determined by the shape independent methods of the previous sections. The inversion approach allows more than one shape, and size and shape can be independently specified. In practice, we have restricted the application to a single shape for all size classes.

The "objects" referred to in this section (ellipsoids in practice) are also referred to in the literature as particles, inclusions, and grains. These latter terms are closely associated with the grain phase. The term objects is preferred here because it is the pore phase that is modeled. However, the model is general and could be applied to the grain phase. Below, the necessary stereological theory is reviewed, the inverse problem is formulated, constraints for the inversion are developed, and results are discussed.

4.6.1 Review and Development of Theory

Underwood (1968; 1970, Ch. 5) presents a thorough and illuminating introduction to the determination of object size distributions from planar measurements. He classifies the analytical methods according to the quantity which is measured on the section plane. The quantities are (1) diameters of features, (2) areas of features, and (3) intercept (chord) lengths. Here, only the category which uses the distribution of intercept lengths will be used.

Several authors have considered the determination of the size distribution of a collection of ellipsoidal objects (Wicksell, 1926; DeHoff, 1962, 1965; DeHoff and Bousquet, 1970; Cruz Orive, 1976, 1978; Gundersen and Jensen, 1983). These studies have used diameters (major and minor axes of elliptical features, DeHoff, 1962; Cruz Orive, 1976, 1978) and linear intercepts (DeHoff

and Bosquet, 1970; Gundersen and Jensen, 1983) as the observed data. A common approach among these theoretical studies has been to derive the forward and inverse relations for a collection of objects with a single shape. Cruz Orive (1976) proved that statistical independence between size and shape was not required, provided that only prolate *or* oblate ellipsoids are used. Thus, it is valid to combine several sizes and several shapes from the same class. The problem is indeterminant (although solvable numerically) when mixtures of oblate and prolate shapes are used. However, Cruz Orive (1976) uses feature semiaxes as the quantity measured on the plane and his results cannot be extended directly to the inversion of intercept lengths. We suspect, but have not proven, that the problem is indeterminant when more than one shape (i.e., aspect ratio) is used in the inversion of intercept lengths.

Below, the assumptions and the essential equations for the size–shape inversion problem are presented. Following Gundersen and Jensen (1983), the single-shape multiple-size object case is first presented. The single-shape case is shown to be extensible to the case with a mixture of object shapes and sizes. However, in practice, only a single shape has been used.

4.6.1.1 Intercept Length Distribution

The frequency distribution of point-sampled intercept lengths sampling a reference space which contains a collection of objects is given by

$$n_0(l_i) = \frac{P(l_i)}{P(\text{obj})}\,, \tag{4.9}$$

where l_i is the i^{th} length interval, $P(l_i)$ is the number of test points hitting intercepts of length l_i, and $P(\text{obj})$ is the total number of test points hitting the object space. The subscript 0 denotes point-sampling (zero-dimensional) and the subscript 1 denotes line-sampling (one-dimensional). Note that this frequency distribution is independent of the total porosity and, as such, does

not yield information on porosity. The term volume fraction therefore refers to a fraction of the pore volume. If the probability density of point-sampled intercepts is given by $f_0(l)$, then the expectation of the frequency distribution is given by

$$E[n_0(l_i)] = \frac{E[P(l_i)]}{E[P(\text{obj})]} = \int_{c_{i-1}}^{c_i} f_0(l)\mathrm{d}l \,, \tag{4.10}$$

where the i^{th} length interval is (c_{i-1}, c_i).

4.6.1.2 Probability Density of Intercept Lengths

Consider the discrete case of a collection of N isolated objects $Y_1, \ldots, Y_j, \ldots, Y_N$ of arbitrary shape. The probability density of point-sampled intercepts is given by

$$f_0(l) = \sum_{j=1}^{N} f_0(l|Y_j) \frac{v(Y_j)}{\sum_k v(Y_k)} \,, \tag{4.11}$$

where $f_0(l|Y_j)$ is the probability density of the length of a point-sampled intercept through the object Y_j and $v(Y_j)$ is the volume of the j^{th} object. From Eqn. (4.11) it is apparent that the intercepts have a probability of originating from a given object in direct proportion to the volume fraction of the object.

Gundersen and Jensen (1983) extend Eqn. (4.11) to the case of a collection of objects that are of the same shape with size parameter z_j. For the discrete case we have

$$f_0(l) = \sum_{j=1}^{N} f_0(l|z_j) \frac{v(z_j)}{\sum_k v(z_k)} \,. \tag{4.12}$$

For a continuous distribution of size we have

$$f_0(l) = \int_0^{z_{\max}} f_0(l|z) g_V(z)\mathrm{d}z \,, \tag{4.13}$$

where $z_{\max}$ is the largest object size and $g_V(z)$ is the probability that a random volume element, $\mathrm{d}v$, chosen from the total object volume belongs to an object of size z. Equivalently, $g_V(z)$ is the volume distribution of object size. Thus, Eqn. (4.13) gives a relation between the point-sampled intercept distribution

and the volume distribution of object size. The size parameter z has been unspecified to this point because it may take several different forms (Gundersen and Jensen, 1983).

It is important to emphasize that a volume distribution of size is being considered as opposed to the more commonly treated number distribution of size. The volume distribution, also referred to as a measure weighted distribution, is more robust than a number distribution. Grain size distributions from sieve analysis are the classic geological example of a measure weighted distribution. Number distributions overemphasize the smaller individual units, thereby preventing a good overall description of the material. For additional discussions of volume weighted distributions, see Delfiner (1972), Kellerhals *et al.* (1975), Serra (1982, Ch. 10), and Gundersen and Jensen (1983).

4.6.1.3 Relation Between Line-Sampled and Point-Sampled Probability Density

The point-sampled intercept density is related to the line-sampled intercept density through

$$f_0(l|z) = \frac{l f_1(l|z)}{E_1[l|z]}, \tag{4.14}$$

where,

$$E_1[l|z] = \frac{4v(z)}{s(z)}, \tag{4.15}$$

and $s(z)$ is the surface area of the object of size z. Equations (4.14) and (4.15) are valid for both convex and non-convex objects. Equations (4.13) and (4.14) are combined to give a relation between the volume distribution of size and the point-sampled intercept distribution. The primary requirement for the use of these equations is knowledge of the conditional line-sampled intercept distribution for the single object shape. We can extend the development of Gundersen and Jensen (1983) to the case of multiple sizes and multiple shapes.

4.6.1.4 Multiple Size–Shape Relations

It is convenient to consider the individual objects in Eqn. (4.11) to be *object classes* which are a function of both size and shape. Let

$$Y_j = y(D_j, q_j) \,, \tag{4.16}$$

where D_j is the size of the object class (to be taken later as the length of the major axis of the ellipsoid) and q_j is the shape of the object class (to be taken later as the length ratio of the minor to major axis of the ellipsoid). Now, N represents the number of size–shape classes, instead of the number of objects. Combining Eqns. (4.11), (4.14), and (4.16) we have

$$f_0(l) = \sum_{j=1}^{N} \frac{l f_1(l|D_j, q_j)}{E_1[l|D_j, q_j]} g_V(D_j, q_j) \,. \tag{4.17}$$

Equation (4.17) provides a relation between the parameters measured on a plane (i.e., digital image) and the volume distribution of the size–shape classes of the objects which make up the phase of interest. In the next section this relation is formulated into an inverse problem.

We note that Gundersen and Jensen have incorrectly moved E_1 out of the integral in their equation 3.13, which is comparable to Eqn. (4.17) above. E_1 depends on object size, thus it must remain within the integral (within the summation in Eqn. (4.17)).

4.6.2 Inverse Problem Formulation

Historically, the inversion for size distributions has been done by analytic solutions, tables, or graphical constructions. Cruz-Orive (1983) recently summarized the various methods of solution for number distributions of sphere size. We consider only the "distribution free" methods which do not impose a specific parametric form for the size distribution. Further, we restrict the

term "unfolding" to those finite difference methods which use tables or graphical constructions. Before presenting our formulation, a few comments on the analytical solutions and "unfolding" procedures are in order. In particular, statements on the theoretical behavior of inversions are put in perspective.

The statistical properties of the the inversion of diameter and intercept data for the number distribution of spheres have been well studied (Tallis, 1970; Watson, 1971). It is known that with ungrouped data of unlimited resolution, the "method of moments" estimator of the distribution has infinite variance. This estimator is based on the direct substitution of measured diameters into a summation which approximates the analytic integral solution. Watson (1971) also suggests that the inversion of intercept lengths leads to an "arbitrary" solution because it involves the estimation of the density function, $f_1(l)$. These undesirable properties are a problem mainly for the theoreticians. Nicholson (1976) points out that the observational thresholds of real data and the grouping of data into cells, give finite known variance, thereby removing the infinite variance stigma. Grouping of data is a feature common to all practical inversion methods. Parameterization of the data can also yield estimators which are better behaved statistically (Tallis, 1970; Nicholson, 1976).

A thorough description of unfolding methods can be found in Underwood (1968, 1970, Ch. 5). However, Underwood does not consider the statistical aspects of the methods. Briefly, the unfolding procedure begins with the binning of measured chord lengths into the same length categories chosen to represent the size distribution of spheres. In general, the formulation is a set of linear equations, with a triangular coefficient matrix, which is solved by back-substitution. Back-substitution has been used directly by Nicholson and Merckx (1967, 1969) and Dhawan (1972). Various graphical methods and tables have also been developed for performing the back-substitution (see Underwood, 1970, Ch. 5). The major flaw in these methods is the propagation

of data errors through the calculations. Typically, the errors are larger for the smaller sizes, which are computed last. Negative amounts for these smaller sizes are common (DeHoff, 1983).

Cruz-Orive (1983) selects a finite difference method because the alternative solutions are not tractable for the complex model he treats (i.e., with a resolution threshold, capping, and overprojection).

The statistical properties of unfolding point-sampled intercept data for the volume distribution have not been investigated. We may expect some of the same undesirable theoretical behavior as with number distributions. We should also expect that the results in practice will not be as bad as theory predicts. Our guide will be the statistical behavior of the numerical inversion. In addition, note that the number of objects per unit bulk volume, N_V, is not estimated in the volume distribution inversion. The classical estimator of N_V is often criticized because it has infinite variance (Tallis, 1970; Watson, 1971).

Nicholson and Merckx (1969) suggest using least squares techniques in a general formulation of the inversion for number distributions of sizes of spheres. They state that the least squares estimate is unbiased. Further, they consider a weighted least squares approach using an estimate of the data covariance as the weight matrix. This latter approach is similar to the method of maximum likelihood, MLE (for example, Menke, 1984, Ch. 5). However, since the data covariance is a function of the model parameters, the MLE approach is not strictly valid. Still, the weighted least squares approach gives a theoretically well-behaved estimator. Nicholson and Merckx (1969) did not actually use least squares and no other study using least squares is known.

The weighted (i.e., damped) least squares method used below is identical in form to the stochastic inverse where model and noise are each assumed to be independent with identical variance for all respective components (see Aki and Richards, 1980, Ch. 12). Because of covariance in the problem, as formulated,

we cannot use the strict interpretation of the stochastic inverse. Instead, we simply consider the damped least squares as a numerical technique.

4.6.2.1 Relation Between Chord Length Histogram and Volume Fractions

To obtain a relation between the measured chord length histogram and the desired volume fraction distribution of size–shape, Eqn. (4.10) is first discretized by taking $f_0(l)$ to be constant within each length interval. The expectation of the number of intercepts in this interval is then given by

$$E[n_0(l_i)] = f_0(l_i)\Delta l \; . \tag{4.18}$$

Combining Eqns. (4.15), (4.17), and (4.18) we have

$$E[n_0(l_i)] = \Delta l \sum_{j=1}^{N} \frac{l_i f_1(l_i|D_j, q_j)}{4v(D_j, q_j)/s(D_j, q_j)} g_V(D_j, q_j) \; . \tag{4.19}$$

Equation (4.19) can be expressed in matrix notation as

$$\mathbf{n} = \mathbf{F}\mathbf{g}_V \; , \tag{4.20}$$

where $\mathbf{n}$ is a vector of length M containing the normalized chord length distribution. M is the number of chord length classes. $\mathbf{F}$ is the $M \times N$ coefficient matrix with coefficients given by

$$F_{i,j} = \Delta l \frac{l_i f_1(l_i|D_j, q_j) s(D_j, q_j)}{4v(D_j, q_j)} \tag{4.21}$$

and $\mathbf{g}_V$ is a vector of length N with values equal to the volume fractions in the N size–shape classes.

The number of chord classes will always be greater than the number of size–shape classes giving $M > N$. The chord length classes, l_i, are an integer multiple of the pixel size, d, of the image or images from which the chords have been sampled. The parameter Δl then takes on the value of d. Equation (4.20) is an overdetermined system of linear equations which can be inverted by standard least squares techniques.

4.6.2.2 Least Squares Inversion

Menke (1984) describes the various techniques which may be used to solve equations similar to Eqn. (4.20). The techniques of least squares, which minimize the L_2 norm, have been used here. The damped and undamped solutions both with and without additional constraints have been applied. The damped least squares solution is given by

$$\mathbf{g}_V{}^* = [\mathbf{F}^T\mathbf{F} + \epsilon^2\mathbf{I}]^{-1}\mathbf{F}^T\mathbf{n}\,, \tag{4.22}$$

where ^{T} is the transpose, $^{-1}$ is the inverse, $\mathbf{I}$ is the identity matrix, and ϵ^2 is the damping parameter. Equation (4.22) gives the undamped solution when ϵ^2 is zero.

4.6.2.3 Additional Constraints for the Inversion

Two additional constraints are readily identified and can be included in the inversion. First, all volume fractions must be positive (non-negative). Second, the sum of the volume fractions must equal one to account for all of the porosity. Recall that the volume fraction refers to the fraction of the pore volume, not to the fraction of bulk volume. Both constraints arise from the need to satisfy physical reality.

The summation constraint can be imposed by decreasing the number of size–shape classes by one and computing the volume fraction of this class directly as 1.0 minus the volume fractions of the other classes. We have no *a priori* knowledge of which class to remove and feel that it is unreasonable to remove any one class arbitrarily. The constraint is imposed in an alternative way by adding an additional equation to the system in Eqn. (4.20). The components of this equation are given by

$$n_{N+1} = w \quad \text{and} \tag{4.23}$$

$$F_{N+1,j} = w^{-1}\,, \tag{4.24}$$

where w is a weight applied to this constraint. This method of implementation forces the prediction error of the constraint to be small at the expense of increasing the prediction error of the other equations (Menke, 1984, p. 55).

The positivity constrained problem is solved using Householder transformations in the manner described by Menke (1984, Sec. 7.9 and 12.4). Basically, if the fit to the data cannot be improved with a *positive* volume fraction of a particular size–shape class, that class is dropped from the inversion. Householder transformations simplify the adding and dropping of classes.

The FORTRAN subroutine PLS (Menke, 1984, p. 231) has been used to solve the undamped case with a positivity constraint. There are several errors in Menke's listing of subroutine PLS. In the calls to both ADD and SUB, the argument pairs *mst,nst* and *mpst,npst* must be transposed to read *nst,mst* and *npst,mpst*. Also, in the subroutine SUB, the upper limit of the "do 6" loop must be *mcur*, not *ncur*.

4.6.2.4 Resolution and Covariance

Model resolution and covariance matrices for the solution are computed from standard formulae (Menke, 1984, Ch. 3).

4.6.2.5 Intercept Length Probability Density Functions

The intercept length probability density functions for oblate and prolate ellipsoids can be given in closed form. Gundersen and Jensen (1983) correct an error in the derivation of DeHoff and Bousquet (1970) and give the density functions in an appendix. The density of line-sampled intercept length for oblate ellipsoids is

$$\begin{aligned} f_{\text{obl}}(l|D,q) &= \frac{q^2}{\epsilon\gamma} t_{\text{obl}}\left(\frac{1}{q^2}-1\right) l\,, \qquad 0 \le l \le qD \\ &= \frac{q^2}{\epsilon\gamma} t_{\text{obl}}\left[\left(\frac{D}{l}\right)^2 - l\right] l\,, \qquad qD < l \le D \\ &= 0\,, \qquad \text{otherwise.} \end{aligned} \tag{4.25}$$

with

$$t_{\text{obl}}(x) = (1+x)^{3/2}\sqrt{x} + \frac{3}{2}(1+x)^{1/2}\sqrt{x} + \frac{3}{2}\ln(\sqrt{x}+\sqrt{1+x})\,, \tag{4.26}$$

$$\gamma = D^2 + \frac{1}{2}\frac{q^2D^2}{\epsilon}\ln\left(\frac{1+\epsilon}{1-\epsilon}\right)\,, \tag{4.27}$$

$$\epsilon = \sqrt{1-q^2}\,, \tag{4.28}$$

where l is the length of the intercept, D is the length of the major axis, q is the ratio of major and intermediate axes to the minor axis, ϵ is the eccentricity, and $\pi\gamma/2$ is the surface area of the oblate ellipsoid.

The probability density of line-sampled intercept length for prolate ellipsoids is

$$\begin{aligned} f_{\text{pro}}(l|D,q) &= \frac{1}{q\epsilon\delta} t_{\text{pro}}(1-q^2) l\,, \qquad 0 \le l \le qD \\ &= \frac{1}{q\epsilon\delta}\left\{t_{\text{pro}}(1-q^2) - t_{\text{pro}}\left[1-\left(\frac{qD}{l}\right)^2\right]\right\} l\,, \qquad qD < l \le D \\ &= 0\,, \qquad \text{otherwise.} \end{aligned} \tag{4.29}$$

with

$$t_{\text{pro}}(x) = (1-x)^{3/2}\sqrt{x} + \frac{3}{2}(1-x)^{1/2}\sqrt{x} + \frac{3}{2}\sin^{-1}\sqrt{x}\,, \tag{4.30}$$

$$\delta = q^2D^2 + \frac{qD^2}{\epsilon}\sin^{-1}\epsilon\,, \tag{4.31}$$

$$\epsilon = \sqrt{1-q^2}\,, \tag{4.32}$$

where l is the length of the intercept, D is the length of the major axis, q is the ratio of major to the intermediate and minor axes, ϵ is the eccentricity, and $\pi\delta/2$ is the surface area of the prolate ellipsoid.

Figures 4.4a and 4.4b illustrate the probability density functions for line-sampled intercepts through oblate and prolate ellipsoids, respectively. Note that for a given aspect ratio, longer intercepts are more numerous for oblate ellipsoids than for prolate ellipsoids. At smaller aspect ratios, the prolate ellipsoids show a strong peak which is centered at the length of the intermediate and minor axes.

4.6.3 *A priori* Parameter Estimates

It is desirable to use *a priori* information to select values for some parameters used in the size–shape inversion. Specifically, we require initial estimates of the aspect ratios and the sizes of the spheroidal classes.

4.6.3.1 Visual Examination of Pore Cast

A visual examination of a pore cast from a sample can indicate whether the pores are more nearly tube-like (prolate) or sheet-like (oblate). Further, approximate aspect ratios can be determined from rough estimates of dimensions. These observations can then be used to determine approximate shape classes to use in the inversion. For our samples, sheet-like pores are much more predominant than tube-like pores.

4.6.3.2 Aspect Ratio from the Fischmeister Shape Factor

The Fischmeister shape factor, F, is a stereological measure of the shape of objects in a matrix. This shape factor is independent of assumptions about the shape of the objects and is independent of the size of the objects. We

postpone a full discussion of the F until Chapter 5, because estimation requires the identification and counting of individual features in the image (for review, see also, section 2.3.4). Here, we will make use of the one-to-one relationship between the F and the aspect ratio, q, of oblate or prolate ellipsoids. The equations for F in terms of q were given in Chapter 2 (Eqns. (2.8) and (2.9)). We have not attempted to derive closed forms which express q in terms of F. Instead, a simple iterative scheme is used which perturbs a guess for q and computes F based on the perturbed value. If the computed F is sufficiently close to the measured F, then the iterations are terminated. Otherwise, q is again perturbed and a new F is computed. Note that we must choose the shape category (oblate or prolate), because the same F values are common to the two categories for nearly equant shapes. Our images yield F values which are consistent for oblate shapes only (see Chapter 5).

One difficulty encountered with using F to guess the aspect ratio is the need for segmentation of the features on the image. The segmentation tends to produce more equant features, thus the low aspect ratio features are reduced in number. Consequently, the F values from these segmented images predict high aspect ratios (nearly equant ellipsoids). Without segmentation, the features do not usually appear as nearly convex shapes which could have arisen from ellipsoids. Thus, the relation between the F values and aspect ratio for ellipsoids can be a poor approximation to the data. We note that chord sampling provides an inherent degree of segmentation which preserves both the long chords and the high aspect ratio features.

4.6.3.3 Aspect Ratio From Feature Shape

Estimates of object aspect ratio can be obtained from measures of the aspect ratios of features on the image. Underwood (1970, p. 136) describes how the class of objects, prolate or oblate, and the aspect ratio can be determined,

provided that all objects have the same aspect ratio. For prolate objects, the *minor* axis of the most unequiaxed ellipse is equal to the diameter of the largest circular section. For oblate objects, the *major* axis is equal to the diameter of the largest circular section. The aspect ratio of the objects is taken as the aspect ratio of the most unequiaxed ellipse. Our images agree with the oblate case. Further, the oblate shape class best satisfies all other indicators of object shape and yields the best fitting volume distributions. Below, we consider only the oblate shape class.

Kellerhals *et al.* (1975) have also suggested a means for estimating the aspect ratio of ellipsoids based on the semiaxes lengths measured on sections. They used computer simulations to obtain distributions of major and minor axes of ellipses produced by random cuts through individual ellipsoids of various aspect ratios. They found that the sample mean of the major axis of the elliptic features, a, is within 10% of the true intermediate axis,D_2, of the generating ellipsoid. Similarly, the sample mean of the minor axis of the elliptic features, b, is within 10% of the true minor axis, D_3 of the generating ellipsoid. Therefore, for a *single* size–shape class, an estimate of D_2/D_3 can be found from the a and b data (for oblate ellipsoids, D_2/D_3 is the aspect ratio). An important focus of the study by Kellerhals *et al.* (1975) is their emphasis on volume weighted sampling methods. This emphasis eliminates many biases which can occur. Their extension to the case of several sizes and shapes is ad hoc. We disagree with their "intuitive" argument that the distribution of a will resemble the true distribution of D_2 (similarly for b and D_3). A single size–shape class (defined by D_1 and D_2) produces a distribution of a and b values. With several size–shape classes, complex distributions of values are produced. This complexity motivates the entire process of the stereological inversion. Kellerhals *et al.* (1975) claim only that their method produces rough estimates. A more complete mathematical formulation of the

object aspect ratio estimation from feature measurements is available.

Cruz Orive (1976, 1978) developed a theoretically rigorous estimator of the mean aspect ratio of ellipsoidal objects (oblate or prolate) from feature axes data. Input to the estimator is the major and minor axes of the elliptical features. The objects under consideration can be any combination of sizes and aspect ratio (provided that they are either oblate or prolate). In the notation above, we define D_1 to be the major axis of the objects and D_3 to be the minor axis. The major axis of the ellipse on the section is denoted by a, the minor axis of the ellipse by b, and $y_e^2 = 1 - (b/a)^2$. The estimator for mean aspect ratio of oblate ellipsoids is given by

$$E[D_3/D_1] = \frac{\sum_{i=1}^{n}(1/a_i)\sqrt{1-y_{ei}^2}}{\sum_{i=1}^{n}(1/a_i)Q(y_{ei})}\,, \tag{4.33}$$

where

$$Q(y) = \frac{2}{\pi}(1-y^2)^2\int_0^{\pi/2}\frac{1+2y^2\sin^2\theta)}{(1-y^2\sin^2)^{5/2}}\mathrm{d}\theta\,, \tag{4.34}$$

using i as the index of features on the image and n as the number of features. By numerical investigation, we have found that Eqn. (4.34) is approximated quite accurately by

$$Q(y) = 1.002 - 0.022y + 0.288y^2\,. \tag{4.35}$$

Equation (4.33) represents a summation over measured feature parameters to yield an estimate of the mean aspect ratio. We note that this is the mean of the number distribution of ellipsoids and the formulation assumes a dilute Poisson distribution of object centers. Cruz Orive (1976) states that Eqn. (4.33) is a consistent (not necessarily unbiased) estimator, but that it can have infinite variance and may be unreliable in practice. If size and shape are assumed to be independent, then Eqn. (4.33) reduces to the simpler consistent estimator

$$q^* = \frac{\sum_{i=1}^{n}\sqrt{1-y_{ei}^2}}{\sum_{i=1}^{n}Q(y_{ei})}\,, \tag{4.36}$$

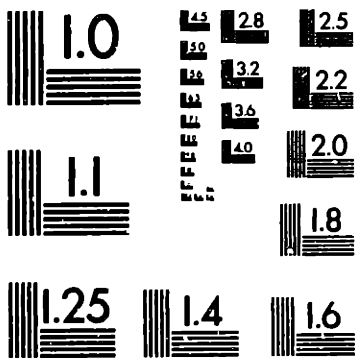

MICROCOPY RESOLUTION TEST CHART
NATIONAL BUREAU OF STANDARDS
STANDARD REFERENCE MATERIAL 1010a
(ANSI and ISO TEST CHART No. 2)

which has finite variance. It is also likely that the estimator of Eqn. (4.33) will have finite variance if the data are grouped. If we use a single shape model for the pore space, then Eqn. (4.36) can be used to estimate the aspect ratio of the objects. Further, with the assumption of a single shape, the estimated aspect ratio will be the same for both the number distribution and the volume distribution. We have used major and minor axes from dynamically equivalent ellipses, fit to the feature data (see Chapter 5), to estimate the aspect ratio for single shape objects. Note that these axes lengths always appear as y in Eqn. (4.36), so only their ratio is important.

Lower limits on aspect ratios can be obtained from the maximum chord length measured on the image. Taking the longest chord length as the longest ellipsoid dimension and the pixel size as the shortest dimension, a limiting aspect ratio is the pixel size over the longest chord. This limitation is imposed by the finite resolution and the discrete nature of the digital image. In practice, we have not used aspect ratios approaching this limit.

4.6.3.4 Size Estimates

An estimate of the largest object size comprising the phase of interest can be obtained from the measured chord length distribution. The longest chord is due presumably to the largest object. An exception occurs when a chord passes through two "separate" convex pore regions which share a common, although imaginary, boundary. In this study, the initial maximum ellipsoid size is usually chosen as the maximum of the continuous portion of the chord length distribution. This maximum size is adjusted to give the best overall fit in the inversion, but it primarily influences the model predicted mean pore volume.

It is not unreasonable to choose ellipsoid sizes which are larger than the maximum measured chord length. For example, the longest feature dimension

(see Chapter 5) can be taken as the largest feature size if the pore features have been segmented before measurement. The ellipsoid model accepts sizes which are larger than the longest chord and the absence of longer chords does *not* contribute to the error of the fit. This contribution is small for most cases because of the low probability density of the longest chords.

The minimum size of an ellipsoid is the physical pixel size of the digital image. This is not a practical minimum because this smallest size cannot be adequately resolved by the inversion. In practice, the minimum size is taken as 3 to 5 times the pixel size. The range from the minimum to maximum sizes is initially divided into 7 to 12 classes.

4.6.4 Goodness of Fit of the Inversion

The solution of the size–shape volume distribution inverse problem is non-unique. Different combinations of size–shape classes exist which will fit the observed chord length distribution equally well from a numerical viewpoint. Therefore, we require additional measures of the goodness of fit of the inversion. These additional measures come from model independent stereological parameters. The measures include total porosity, surface area, and mean object volume.

4.6.4.1 Non-uniqueness of the Inversion

Cruz Orive (1976) has presented analytic proofs that the inversion of feature semiaxes for a combination of shape classes (i.e., prolate and oblate) is non-unique. Conceptually, the proof shows how a single distribution of feature semiaxes can arise from infinitely many pairs of prolate and oblate ellipsoid distributions. From an alternative viewpoint, we can think of the mixture of prolate and oblate ellipsoids (or a collection of triaxial ellipsoids) as be-

ing defined by a three-dimensional distribution function, whereas, the distribution of feature semiaxes is only two-dimensional. The two-dimensional distribution contains insufficient information to determine uniquely the three-dimensional distribution. If we extend this concept, the one-dimensional intercept length distribution is expected to contain insufficient information to determine uniquely a two-dimensional distribution (i.e., a collection of oblate ellipsoids with size and shape variations). DeHoff and Bousquet (1970) restrict their inversion of intercept lengths to a single shape class. For the case of randomly oriented triaxial ellipsoids, they present a novel method of determining the axial ratios of the ellipsoid from the most unequiaxed feature and the intercept length distribution. Gundersen and Jensen (1983) only consider the single shape case of their model in detail. Perhaps they recognized that the variable size and shape model would prove indeterminant. In practice, we have restricted models to a single oblate shape for all size classes. Additional constraints and measures of goodness of fit are then used to determine the best fitting volume distributions of size–shape. The single shape models provide a very good fit for all rocks studied.

4.6.4.2 Total Porosity

Recall that the total porosity was not constrained rigorously by the elimination of a size–shape class from the inversion. Instead, an additional weighted constraint was applied. One measure of how well the size–shape model fits the pore structure is how well the model accounts for the total porosity. Provided that the weighting is zero or held constant, a better fit is indicated when the sum of the volume fractions is closer to one.

4.6.4.3 Surface Area

A second measure of how well the size–shape model approximates the pore space is the agreement between the surface area per unit pore volume, S_{Vp}, measured by a shape independent stereological method (see section 4.3) and the S_{Vp} predicted by the model. The model predicted value is affected by both the aspect ratio of the ellipsoids and the size distribution.

4.6.4.4 Mean Pore Volume

The mean pore volume determined in section 4.5 is compared with the model predicted mean pore volume as a third measure of the goodness of fit. The deviation of the model mean volume from the model independent mean volume is used as a measure of agreement. The deviation is given by

$$\Delta\overline{V}_p = \frac{\overline{V}_{p\text{model}} - \overline{V}_{p\text{chords}}}{\overline{V}_{p\text{chords}}} . \tag{4.37}$$

4.6.4.5 Numerical Measures of the Fit Quality

Standard numerical measures of the inversion quality are also used to measure the overall quality of the fit. These measures include standard deviations (coefficients of variation), resolution, and variance reduction. A better fitting model is indicated when coefficients of variation are small and resolution is high. These two conditions are oppositional and both depend on damping.

The variance reduction is computed from the original data variance and the residual variance. This is different from those cases where perturbations on a starting model (e.g., non-linear inversion) are determined. In these later cases, the starting variance is computed from the residuals of the starting model. When this investigation began, we did not know what would be a good starting model. However, after the analysis, it appears that a uniform distribution would make a good starting model. For some rocks, the best

model was uniform within the tolerance of the results. Use of a starting model would also allow a more rigorous interpretation of the inversion in terms of a stochastic inverse problem. In particular, the residuals would more nearly resemble realizations of a random variable with zero mean.

4.6.4.6 Adjustments for a Better Fit

Using the above criteria for the goodness of fit, the sizes and shape of the size–shape classes are adjusted to yield the best fitting model of the pore space. Damping in the inversion is also adjusted.

Size classes are shifted and damping is adjusted such that no class has a volume very close to zero. Classes which require excessive damping to produce a positive volume fraction and classes which have very poor resolution or a high CV are removed. We probably don't choose the best size classes, so the addition of damping "smooths" the distribution to yield a better fit. A smooth distribution is expected because the mechanisms which form the pore space do not operate in a discrete manner. Instead, they produce pores which vary in size, perhaps about some most likely size.

If the deviation in the mean volume estimator is positive, then the largest size class may be too large, and vice versa.

We chose a minimal amount of damping consistent with the conditions of all positive volume fractions and all CV smaller than one. This choice tends to favor higher resolution at the expense of higher standard deviations. It is artificial to reduce further the standard deviations with additional damping. Standard deviations are usually scrutinized more closely than resolution. Thus, increased damping would make the result appear better, but the resolution would be worse.

Here we summarize the criteria which constitute a good fit. The distribution should be smooth. The volume sum should be within 5% of 1.00. The

model S_{Vp} should be within 10% of the stereologically determined value. Mean volume deviation should be less than ±30%, which corresponds to less than a 10% diameter difference for a volume equivalent sphere. Variance reduction (raw data to model residuals) should be larger than 95%. Coefficients of variation of the volume fractions should be less than 1.0. Diagonal elements of the resolution matrix should be larger than 0.5. The best fitting model may violate one or more of these criteria, but, for most rocks, all are satisfied.

4.6.5 Results of the Size–Shape Inversion

The results of the size–shape inversions for 14 sandstones are presented in this section. Tables 4.7a to 4.7n contain the volume distributions of pore sizes and measures of the goodness of fit for the inversions. The cumulative volume distributions are plotted in Figures 4.4a to 4.4n. As with other geologic data, the results are best displayed as cumulative distributions because they are not sensitive to the choice of size intervals (Griffiths, 1952).

4.6.5.1 General Character of the Results

The damped least squares solution without a volume sum constraint and without a positivity constraint was used for all of the final fits. Volume sums were very close to 1.0 for all rocks without imposing the volume sum constraint and damping alone was able to prevent negative volume fractions.

The best fitting volume distributions, by all measures of the goodness of fit, were the smoothest distributions. These distributions have from 6 to 11 size classes. The range of aspect ratios for oblate shapes was from 0.27 to 0.36. Damping ranged from none (0.0) to a maximum of 3.0×10^{-5}. Less than 10 inversion trials per rock (i.e., with different size classes, aspect ratio, and damping) were required to find the best fitting distributions. Further

refinement of the fits appears unwarranted at present.

Overall, the volume distribution curves most closely resemble a uniform distribution of sizes. This means that the volume of the pore space is divided equally among all pore sizes. Numerically, this translates to a large number of smaller pores and relatively fewer large pores. A true uniform distribution is expressed as a straight line on the cumulative distribution plot and the distributions of some rocks differ strongly from uniform. None of the volume distributions resemble a normal distribution; particularly with regard to the behavior at small sizes.

Individual character of the distributions for different rocks is expressed most strongly in the large size range. Three different classes of behavior are seen in the large size range. The distribution can approach the largest size in a straight line, in an asymptotic manner, or with a large jump in cumulative fraction at or near the largest size. Distributions for samples 2519, 2523, and 2700 showed the asymptotic approach to the maximum size. Distributions for samples 2521, 2686, and 2710 showed a large jump at the largest size. The remainder of the samples approached the maximum size in a straight line.

4.6.5.2 Covariance Matrices

The diagonal terms of the model covariance matrices are given in Tables 4.7a to 4.7n as the standard deviation. Tables 4.8a and 4.8b contain representative covariance matrices for the samples.

The first sub-diagonal terms of the covariance matrix show negative correlation between adjacent size classes. The magnitude of the correlation is usually less than half of the diagonal element for the next smaller size class and is about equal to the next larger class diagonal element. At larger size classes, the correlation for the smaller class can approach the value of the diagonal term. This correlation decreases rapidly away from the diagonal. These

relations are not surprising since adjacent size classes have intercept density distributions which are similar. The larger of two adjacent classes spans all the chord lengths produced by the smaller class.

4.6.5.3 Resolution Matrices

The diagonal elements of the model resolution matrices are given in Tables 4.7a through 4.7n. Tables 4.8a and 4.8b contain representative resolution matrices for the samples. The diagonal elements are larger than 0.5 for all size classes of all rocks. The first off-diagonal elements (first sub-diagonal) show positive relations between adjacent model classes. The size of these relations is typically less than 20% of the diagonal elements. Elements of the second sub-diagonal are typically less than 5% of the diagonal elements and are usually negative. Negative values are physically unrealistic in the sense that the "true" size class is an average of the model size classes, where the resolution elements represent the coefficients of the average. Nonetheless, the size of the second sub-diagonal elements indicates an insignificant contribution when compared to the sum of the diagonal and first sub-diagonal elements.

4.6.5.4 Effect of Shape Variation

Aspect ratio was varied primarily to satisfy the stereologically determined S_{Vp}. However, the narrow range of aspect ratios used indicates that the size distribution of the pores, not the shape of the pores, accounts for the majority of the differences in specific surface for different rocks.

4.6.5.5 Effect of Damping

The effect of damping was very important for the successful inversion of the size distributions. In the application of a damped least squares inverse method, a point is usually made about how the damping parameter allows an optimum

tradeoff between model resolution and covariance. More important here is the fact that the damping parameter adds the criterion of minimum solution length to the minimization criteria. Minimizing the solution length gives a smoother distribution by reducing the volume fractions in classes with large fractions and, thereby, promoting increases in the volume fractions of other, typically adjacent, classes. For all rocks in this study, a small amount of damping was adequate to yield all positive volume fractions. Although damping does not strictly impose a smoothness constraint, it appears preferable here to other methods of imposing a smoothness or flatness constraint.

Some partitionings of the size range give classes which are so poorly resolved (underdetermined) that damping does not improve the solution. Typically, this condition occurs when the classes are too close together. If too much damping is used, the volume fractions all tend toward a uniform distribution with a greatly reduced volume sum. The overall fit, in this case, is poor.

Although the solution here has not been cast in terms of a stochastic inverse, the damping values agree with the formulation for uncorrelated data and uncorrelated model parameters. With the noise (considered the residual here) variance given as ${\sigma_n}^2$ and the model variance given as ${\sigma_m}^2$, the damping is related by (Aki and Richards, 1980, p. 697)

$$\epsilon_d{}^2 = \frac{{\sigma_n}^2}{{\sigma_m}^2} \,. \tag{4.38}$$

The damping, residual (noise) variance, and model variances of the inversions are consistent with Eqn. (4.38), even though our model parameters are correlated and have non-zero mean.

4.6.5.6 Sensitivity to the Chord Length Distribution

Figures 4.5a and 4.5b show two representative point-sampled chord length histograms. Rocks with 9 images generally have smoother histograms (e.g.,

Figure 4.5b) and better overall quality of fit in the inversion than those rocks with fewer images (e.g., Figure 4.5a). With equal amounts of damping, the rocks with more images have higher resolutions. Still, the results from the rocks with only two images indicate that two images contain adequate information to yield a size–shape distribution with reasonable error limits.

Checks on the numerical inversion were made using synthetic chord length distributions. These tests gave very good results. Observed differences in volume fractions were less than one percent and could be attributed to the effect of discretization of the intercept data. If the "wrong" size classes or shape class were used for the inversion, then the fit was not as good. If "extra" classes were included with the correct classes, the extra classes were assigned zero volume fractions.

Inversion results from true point-sampled intercept length distributions are equivalent to results from converted line-sampled intercept length distributions.

4.6.6 Discussion of the Size–Shape Inversion

Overall, the size–shape inversion by least squares methods works well. The resulting size distributions and uncertainties are both reasonable. Most significant is that the ellipsoidal model satisfies the model independent properties of total porosity, specific surface, and mean pore volume.

4.6.6.1 Agreement with Qualitative Descriptions

The pore size–shape distributions agree very well with qualitative descriptions of the pore space based on observations of pore casts and thin sections. In particular, the relative abundance of large intergranular pores is well-quantified by the distributions. For example, sample 2521 (Tensleep Fm.) has a high

abundance of intergranular pores which are larger than the framework grains (Simmons *et al.*, 1982). These pores are represented by the more than 20% of the pore volume in the 325 μm class (Figure 4.5e). Similarly, the pore structure of sample 2710 (Morrison fm.) is "dominated by large intergranular pores which comprise more than 2/3 of the total porosity" (Simmons *et al.*, 1983). Figure 4.5k shows about 25% of the pore volume in the largest pore class; in good agreement with the visual estimate. The samples which have more nearly uniform volume distributions are typically described as having a "moderate" abundance of intergranular pores.

4.6.6.2 Validity of Ellipsoidal Shape

Oblate ellipsoids have been used here as the basic shape element of the pore size–shape inversion. These shapes are reasonable for the following reasons. The ellipsoidal shape is a tractable shape which has a closed form representation for the intercept density function. Many models of physical properties use ellipsoidal shapes, again primarily because it is tractable yet offers a good approximation to reality.

The better fit of the oblate shapes versus prolate ellipsoids is consistent with observation of the pore structure in pore casts. It is easy to visualize oblate shapes arising from the random packing of adjacent grains of a granular material. To obtain tubular prolate shapes requires more esoteric packings. Indeed, when tubular structures exist, they are usually short and represent a tiny volume fraction. We don't discount the importance of throats in the pore structure, but the majority of the pore volume in the sandstones studied here is best described by oblate shapes.

The various measures of goodness of fit indicate that oblate ellipsoids can model the pore space and satisfy several of the geometric properties of the pore phase. These geometric properties include, total porosity, specific surface, and

mean pore volume.

The Fischmeister shape factors determined by feature analysis (Chapter 5) indicate that the underlying objects can be considered ellipsoidal. Segmentation of images in Chapter 5 shows that the general non-convex pore features can be broken down into nearly convex shapes that are approximated quite well by ellipses.

Dhawan (1972) found an empirical shape for sandstone pores by measuring the intercepts of individual features, combining the results from several features, and fitting an analytical curve. The empirical shape is very close to that obtained by joining together two right circular cones at their bases. The averaging which enters this estimation prevents a confident statement of the shape. His method of shape presentation yields the same shape function for *all* possible aspect ratios of triaxial ellipsoids.

Shapes other than ellipsoids can be used in the model presented here. The only requirement is that the probability density of intercept lengths must be known for the shape. For the ellipsoids, we have a closed form representation of this function. However, the function for other shapes could be found from computer modeling. Very few shapes have sufficient symmetry to allow a closed form solution. Shapes with sharp edges are particularly difficult to treat. Therefore, computer simulation appears to be a reasonable approach for shapes more complex than ellipsoids.

4.6.6.3 Good Attributes of the Model

Several good attributes of the model presented here are readily notable. The model is flexible in the choice of shape. Use of ellipsoid shapes is well-defined and other shapes can be used if the intercept probability density functions are known. No assumption is made about the spatial distribution of the objects. Clustering is acceptable, provided that orientations are random (or sampling is

sufficiently random). The inversion is numerically straightforward and yields an estimate of the error in the solution. Intercepts are easier to measure than feature semiaxes and are unambiguously identified. Inversions based on intercept lengths are said to be more stable than those based on semiaxes (DeHoff and Bousquet, 1970). Further, chords provide an intrinsic segmentation of the pore space. Chords must lie entirely within the pore space, thus they only sample "convex" regions. The probability of a chord passing through two or more nearly convex regions is small.

4.6.6.4 Alternative Methods of Solution

This section considers the inverse problem in the context of other methods of solution proposed in the stereological literature. In particular, we consider whether an alternate form of solution may be preferable. Some additional theoretical considerations are addressed.

Two possible modifications to the present formulation may improve the model. Instead of using a delta function for each size class, the classes could be considered to have a finite width with a uniform volume fraction contribution over the width. Because the volume distributions are nearly uniform, it may be beneficial to subtract this initial model from the data and operate on the residual intercept length distribution. This procedure could lead to a formulation as a stochastic inverse problem.

Cruz-Orive (1983) reviews the alternative approaches of inversion for size distributions. In all cases, he considers a spherical shape and the number distribution of size. Still, we can gain some insight for the volume distribution of ellipsoids from his considerations. Because of the nature of our images, we are not concerned with overprojection errors (as occur when viewing a thin section through transmitted light). Capping, which is the loss of features above the resolution threshold, is also not a problem. The resolution threshold

deserves further attention. We have been concerned mainly with the analysis of the larger pores of the rock. However, there is no restriction on the sizes to which the model can be applied. Provided that sufficient data of a suitable resolution are available, smaller pores could be modeled.

The product-integration scheme developed in recent years (Tallis, 1970; Anderssen and Jakeman, 1975ab, 1976) may be applicable to the ellipsoid problem by using the "shape factor" formulation of DeHoff and Bousquet (1970) (after correcting their orientation averaging error; Gundersen and Jensen, 1983). Parametric approaches appear to be out of the question because neither the chord length data nor the volume distribution can be easily parameterized.

Recall that Nicholson and Merckx (1969) suggested using a weighted least squares solution where the inverse of the data variance matrix is the weight matrix. This approach is quite similar to the method of maximum likelihood and it raises an interesting point. In a maximum likelihood approach, the most certain data are weighted most heavily, thus the information content is presumably maximized. This procedure is equivalent to weighting the data by the expected variance, where the data points with highest variance are weighted least. Unfortunately, the longest chords in the inversion are the least probable and they have the highest variance. Yet these chords carry important information about object size. A very small number of long chords can represent a large volume fraction. We have seen that the point-sampled intercept distribution is "weighted" by the length of the chords, thus, the long chords carry information proportional to their length. The importance of the long chords, and their high variance are at odds. The dichotomy may be best served by just giving the data equal weight as we have done.

Lastly, we pose a more basic question. Given the fundamental approximation of the continuous pore space with ellipsoidal shapes, is it justifiable to consider a more complex formulation and solution of the problem? This

question can only be answered by considering the objective of the analysis. A point often raised in the stereological literature is that the size distribution may *not* be required for a particular application. Here, we investigated the inversion purely for the geometric description of the pore space, so the size distribution was required. Further refinements of the numerical inversion itself are probably not justifiable for descriptive purposes. Refinements which incorporate more information (e.g., feature semiaxes length distributions) are certainly worthwhile.

4.7 Summary of Stereological Results

Stereological parameters provide fundamental geometric information about the pore structure. The bulk properties of porosity, specific surface, and mean pore volume (interpreted as the "star") require no assumptions about the size and shape of the pore space. The size–shape volume distribution requires assumptions about the nature of the pore space. In turn, the volume distribution satisfies the fundamental bulk properties and yields additional information.

It is important to adhere to the established stereological formulations and understand their probabilistic foundation. Stereological parameters cannot always be manipulated in simple algebraic ways. The underlying principles of geometric probability must be maintained.

4.7.1 Porosity

Provided that no subjective bias was introduced, the image derived porosity was found to be in very good agreement with bulk measurements. Inhomogeneity at the scale of sampling of the digital images could be detected from the experimental and theoretical statistics derived from the images.

If a sufficiently large sample is available, it may be preferable to measure

porosity by bulk methods. In this way, a better average may be obtained. Image derived parameters, such as S_{Vp}, can then be related to the bulk porosity. However, if only small samples (e.g., cuttings) are available, the stereological methods can be applied and they yield accurate values.

4.7.2 Specific Surface

Specific surface measured by lineal analysis does not indicate strong anisotropy of pore structure in our samples. The observed directional bias in S_V, due probably to imaging artifacts, is smaller than the standard deviations in S_V, but it precludes detection of slight anisotropy. The measured S_{Vp} will be used in Chapter 7 in an equivalent conduit model of fluid permeability.

Even for the rocks with biased porosity estimates from a few images chosen subjectively, the S_{Vp} will be valid because it is measured with respect to the observed pores. Indeed, for the explicit purpose of measuring S_{Vp} it may be more efficient to consider only images with higher percentages of porosity.

4.7.3 Mean Pore Volume

The mean pore volume computed from point-sampled intercepts appears to be a good single size parameter for the pore space. Mean intercept length computed from line-sampled intercepts greatly underestimates the "average size" of the pores.

4.7.4 Size–Shape Volume Distribution

Size–shape volume distributions, using oblate ellipsoids as the object shape, are nearly uniform for the samples studied. Best fitting aspect ratios were between 0.27 and 0.36. The character of the distributions at large sizes corresponds with qualitative descriptions of the pore space. The distributions also

satisfy the bulk geometric properties of the pore space.

By accounting for the larger pores, we have described most of the pore volume. With the information on the intergranular pores we may be able to put limits on the character of the connective pores (pore throats), which are not well-characterized by the size–shape distribution.

We envision using feature data, obtained by the methods of Chapter 5, to augment the stereological inversion process. In particular, it may be possible to incorporate semiaxes of segmented features using the formulations of Cruz Orive (1976, 1978).

Figure Captions

Figure 4.1. Image Porosity versus Bulk Porosity.

Figure 4.2. Binary images of sample 2687. (*a*) Image #1100. This image has the highest S_{Vp} of the nine images of the sample. The values are the same for X and Y directions (see Max. values in Table 4.3). (*b*) Image #1106. This image has the lowest S_{Vp} for this sample. The X and Y values differ by a factor of 2 (see Min. values in Table 4.3).

Figure 4.3. Schematic of the methods of sampling intercepts. (*a*) Line-sampled intercepts. The dashed line indicates the start of the guard region. Emphasized intercepts are sampled. Intercepts beginning at or before filled arrows are ignored. Note that one intercept which spans the guard region is sampled. The bias introduced by this convention is suffi-

ciently small for the guard regions used in this study. (*b*) Point-sampled intercepts. Intercepts which hit test points (+) are sampled.

Figure 4.4. Line-sampled intercept density distributions for ellipsoids of revolution. (*a*) Oblate ellipsoids with aspect ratios of 0.2, 0.3, 0.5, and 1.0 (sphere). (*b*) Prolate ellipsoids with aspect ratios of 0.2, 0.3, 0.5, and 1.0 (sphere).

Figure 4.5. Volume Distribution of Pore Size–Shape.

(*a*) 2124.	(*e*) 2521.	(*i*) 2700.	(*m*) 2842.
(*b*) 2509.	(*f*) 2523.	(*j*) 2704.	(*n*) 2843.
(*c*) 2513.	(*g*) 2686.	(*k*) 2710.	
(*d*) 2519.	(*h*) 2687.	(*l*) 2841.	

Figure 4.6. Point-sampled Intercept Distributions. (*a*) Sample 2513. Distribution from two images. (*b*) Sample 2710. Distribution from nine images.

Table 4.1a

Porosity from Areal Analysis

Sample Number	ϕ		$SD(\phi_i)$		$CV(\phi_i)$	
	Bulk (%)	Image (%)	Exper. (%)	Theor. (%)	Exper.	Theor.
2124	17.8	20.44	1.58	2.32	0.077	0.113
2509	18.1	21.45	2.06	2.19	0.096	0.102
2513	21.7	21.82†	1.29	2.49	0.059	0.118
2519	10.6	12.06†	5.53	2.48	0.458	0.141
2521	24.1	23.64†	0.83	2.94	0.035	0.120
2523	16.8	18.39	2.49	1.10	0.136	0.060
2686	26.0	26.78†	4.12	6.20	0.154	0.245
2687	24.1	18.57	10.04	2.92	0.540	0.157
2700	23.4	23.55	2.69	2.54	0.114	0.108
2704	23.8	19.28	4.79	1.97	0.249	0.102
2710	30.5	28.87	4.51	4.38	0.156	0.152
2841	26.7	28.95†	3.79	6.07	0.131	0.335
2842	13.8	14.36	2.50	1.35	0.174	0.094
2843	23.1	26.58	2.97	6.17	0.106	0.232

† Image porosity, ϕ_i, is an area weighted average of all images of the rock. Standard deviations and coefficients of variation are from high magnification images only, using the all image mean value and n weighting. For each rock, the high magnification images are all at the same magnification, typically 100×.

Table 4.1b

Porosity from Areal Analysis—Additional Data

Sample Number	Individual Image ϕ_i			Feature Parameters			#Images
	Min. (%)	Max. (%)	Range (%)	$\bar{a}_\alpha$ (μm)	$SD(a_\alpha)$ (μm)	N_α	
2124	18.76	22.04	3.28	159.1	1021.0	3290	4
2509	19.99	22.90	2.91	528.7	2360.8	2012	2
2513	20.17	22.56	2.39	189.7	1083.9	2414	3
2519	17.47	17.71	0.24	1072.0	3827.0	2381	2
2521	24.25	24.64	0.39	565.4	3064.2	2095	2
2523	14.23	22.13	7.90	114.9	652.3	9214	9
2686	22.33	30.55	8.22	629.6	5985.1	1705	2
2687	5.80	41.24	35.44	88.0	1522.0	12195	9
2700	18.33	27.52	9.19	122.0	1380.0	11154	9
2704	8.51	22.93	14.42	133.7	1237.4	8305	9
2710	21.17	37.70	16.53	185.7	2660.0	8955	9
2841	32.04	33.33	1.29	421.3	4728.2	2882	2
2842	9.88	18.55	8.67	156.3	1054.1	5291	9
2843	24.58	28.58	4.00	184.6	1812.6	1807	2

NOTES: $\bar{a}_\alpha$ - mean feature area. $SD(a_\alpha)$ - standard deviation of feature area. N_α - number of features. The number of images is the number of high magnification images used in the statistics calculations.

Table 4.2

S_V from Lineal Analysis

Sample Number	S_V (μm^{-1})	Individual Image Statistics				
		$SD(S_V)$ (μm^{-1})	$CV(S_V)$	Min. (μm^{-1})	Max. (μm^{-1})	Range (μm^{-1})
2124 X	0.0565	0.0045	0.080	0.0502	0.0606	0.0104
Y	0.0620	0.0045	0.073	0.0560	0.0668	0.0108
Avg	0.0592	0.0044	0.074	0.0531	0.0637	0.0106
2509 X	0.0333	0.0006	0.017	0.0329	0.0337	0.0008
Y	0.0365	0.0013	0.035	0.0356	0.0374	0.0018
Avg	0.0349	0.0009	0.026	0.0342	0.0355	0.0013
2513 X	0.0500	0.0020	0.040	0.0479	0.0518	0.0039
Y	0.0540	0.0010	0.019	0.0533	0.0552	0.0019
Avg	0.0520	0.0015	0.028	0.0506	0.0535	0.0029
2519 X	0.0267	0.0031	0.116	0.0245	0.0289	0.0044
Y	0.0279	0.0037	0.132	0.0253	0.0305	0.0052
Avg	0.0273	0.0034	0.124	0.0249	0.0297	0.0048
2521 X	0.0343	0.0012	0.035	0.0335	0.0352	0.0017
Y	0.0362	0.0005	0.014	0.0359	0.0366	0.0007
Avg	0.0353	0.0008	0.024	0.0347	0.0359	0.0012
2523 X	0.0628	0.0064	0.102	0.0546	0.0755	0.0209
Y	0.0633	0.0066	0.105	0.0562	0.0766	0.0204
Avg	0.0630	0.0065	0.103	0.0554	0.0760	0.0206
2686 X	0.0438	0.0085	0.194	0.0378	0.0498	0.0120
Y	0.0497	0.0088	0.178	0.0435	0.0560	0.0125
Avg	0.0468	0.0087	0.185	0.0406	0.0529	0.0122

Table 4.2 (cont)

S_V from Lineal Analysis

Sample Number	S_V (μm^{-1})	Individual Image Statistics				
		$SD(S_V)$ (μm^{-1})	$CV(S_V)$	Min. (μm^{-1})	Max. (μm^{-1})	Range (μm^{-1})
2687 X	0.0610	0.0124	0.204	0.0386	0.0795	0.0409
Y	0.0634	0.0132	0.208	0.0391	0.0842	0.0451
Avg	0.0622	0.0127	0.205	0.0388	0.0819	0.0430
2700 X	0.0602	0.0081	0.135	0.0509	0.0736	0.0227
Y	0.0616	0.0080	0.130	0.0517	0.0749	0.0232
Avg	0.0609	0.0080	0.132	0.0516	0.0742	0.0226
2704 X	0.0494	0.0108	0.219	0.0272	0.0638	0.0366
Y	0.0518	0.0119	0.229	0.0273	0.0666	0.0393
Avg	0.0506	0.0113	0.224	0.0272	0.0652	0.0379
2710 X	0.0594	0.0083	0.140	0.0499	0.0775	0.0276
Y	0.0615	0.0078	0.127	0.0508	0.0784	0.0276
Avg	0.0604	0.0080	0.132	0.0504	0.0779	0.0276
2841 X	0.0477	0.0041	0.086	0.0448	0.0506	0.0058
Y	0.0556	0.0055	0.099	0.0517	0.0595	0.0078
Avg	0.0516	0.0048	0.093	0.0482	0.0550	0.0068
2842 X	0.0320	0.0040	0.124	0.0255	0.0363	0.0108
Y	0.0328	0.0038	0.115	0.0262	0.0363	0.0101
Avg	0.0324	0.0039	0.119	0.0258	0.0361	0.0103
2843 X	0.0563	0.0062	0.109	0.0520	0.0607	0.0087
Y	0.0642	0.0047	0.074	0.0609	0.0676	0.0067
Avg	0.0603	0.0054	0.090	0.0564	0.0641	0.0077

NOTES: The locations of images from rocks with fewer than 9 images were selected subjectively. Thus, the porosity values may not be representative and more accurate estimates of S_V may be found using Eqn. (4.4) and Tables 4.3 and 4.1. Average porosities in Table 4.1 include lower magnification images which were not included in the above data. The number of images used for each rock is the same as that listed in Table 4.1b.

Table 4.3

S_{Vp} from Lineal Analysis

Sample Number	S_{Vp} (μm^{-1})	Individual Image Statistics					
		$\langle S_{Vp} \rangle$ (μm^{-1})	$SD(S_{Vp})$ (μm^{-1})	$CV(S_{Vp})$	Min. (μm^{-1})	Max. (μm^{-1})	Range (μm^{-1})
2124 X	0.279	0.279	0.030	0.108	0.260	0.324	0.065
Y	0.316	0.316	0.037	0.118	0.291	0.372	0.081
Avg	0.297	0.299	0.034	0.113	0.275	0.348	0.073
2509 X	0.156	0.156	0.013	0.080	0.148	0.165	0.018
Y	0.173	0.173	0.011	0.062	0.166	0.181	0.015
Avg	0.164	0.165	0.012	0.070	0.157	0.173	0.016
2513 X	0.238	0.238	0.018	0.073	0.223	0.258	0.034
Y	0.256	0.256	0.017	0.066	0.239	0.273	0.034
Avg	0.247	0.247	0.017	0.069	0.231	0.265	0.034
2519 X	0.152	0.152	0.019	0.127	0.138	0.166	0.027
Y	0.160	0.160	0.025	0.156	0.142	0.178	0.035
Avg	0.156	0.156	0.022	0.142	0.140	0.172	0.031
2521 X	0.142	0.142	0.007	0.052	0.137	0.148	0.010
Y	0.147	0.147	0.004	0.026	0.145	0.150	0.005
Avg	0.145	0.145	0.006	0.039	0.141	0.149	0.008
2523 X	0.350	0.354	0.046	0.129	0.287	0.416	0.128
Y	0.351	0.354	0.039	0.110	0.292	0.411	0.119
Avg	0.350	0.354	0.042	0.119	0.290	0.414	0.124
2686 X	0.170	0.171	0.007	0.041	0.166	0.176	0.010
Y	0.197	0.198	0.010	0.051	0.191	0.205	0.014
Avg	0.183	0.184	0.008	0.046	0.178	0.190	0.012
2687 X	0.378	0.421	0.155	0.369	0.243	0.704	0.461
Y	0.347	0.422	0.177	0.418	0.145	0.709	0.564
Avg	0.361	0.422	0.165	0.392	0.194	0.707	0.512

Table 4.3 (cont)

S_{Vp} from Lineal Analysis

Sample Number	S_{Vp} (μm^{-1})	Individual Image Statistics					
		$\langle S_{Vp} \rangle$ (μm^{-1})	$SD(S_{Vp})$ (μm^{-1})	$CV(S_{Vp})$	Min. (μm^{-1})	Max. (μm^{-1})	Range (μm^{-1})
2700 X	0.269	0.270	0.038	0.139	0.232	0.358	0.126
Y	0.274	0.276	0.043	0.156	0.241	0.378	0.138
Avg	0.271	0.273	0.040	0.146	0.237	0.368	0.131
2704 X	0.263	0.273	0.073	0.266	0.199	0.432	0.233
Y	0.279	0.300	0.099	0.328	0.207	0.486	0.279
Avg	0.271	0.287	0.084	0.294	0.203	0.459	0.256
2710 X	0.218	0.223	0.045	0.202	0.161	0.291	0.130
Y	0.226	0.232	0.048	0.210	0.170	0.308	0.138
Avg	0.222	0.227	0.047	0.206	0.166	0.299	0.134
2841 X	0.145	0.145	0.010	0.073	0.138	0.152	0.015
Y	0.175	0.175	0.010	0.057	0.168	0.182	0.014
Avg	0.160	0.160	0.010	0.064	0.153	0.167	0.015
2842 X	0.231	0.235	0.029	0.124	0.196	0.283	0.087
Y	0.243	0.245	0.026	0.106	0.207	0.285	0.078
Avg	0.237	0.240	0.027	0.113	0.202	0.284	0.082
2843 X	0.212	0.212	0.001	0.003	0.211	0.212	0.001
Y	0.241	0.242	0.011	0.046	0.234	0.250	0.016
Avg	0.226	0.227	0.006	0.026	0.223	0.231	0.008

NOTES: Porosity values used to determine S_{Vp} are from lineal analysis and may not be identical to areal values in Table 4.1 because of the chord sampling criteria. The closeness of these two values is a measure of goodness of the sampling criteria (i.e., the exclusion region length), provided that the same images are used for both methods. The average S_{Vp} from the images may differ from the combined S_{Vp} due to the different effective averaging (i.e., $\langle S_{Vp}/\phi \rangle$ versus $\langle S_{Vp} \rangle / \langle \phi \rangle$). The number of images used for each rock is the same as that listed in Table 4.1b.

Table 4.4

Mean Pore Intercept Lengths

Sample Number	$\overline{L}_{3p}$ (μm)	Individual Image Statistics					
		$SD(\overline{L}_{3p})$ (μm)	$CV(\overline{L}_{3p})$ (μm)	Min. (μm)	Max. (μm)	Range (μm)	#Images
2124 X	14.4	1.42	0.099	12.3	15.4	3.1	4
Y	12.7	1.36	0.107	10.7	13.7	3.0	4
Avg	13.5	1.39	0.103	11.5	14.6	3.0	4
2509 X	25.6	2.06	0.080	24.2	27.1	2.9	2
Y	23.1	1.43	0.062	22.1	24.1	2.0	2
Avg	24.4	1.74	0.072	23.2	25.6	2.5	2
2513 X	16.8	1.21	0.072	15.5	17.9	2.4	3
Y	15.6	1.05	0.067	14.6	16.7	2.1	3
Avg	16.2	1.12	0.069	15.1	17.3	2.2	3
2519 X	26.5	3.37	0.127	24.1	28.9	4.8	2
Y	25.3	3.97	0.157	22.5	28.1	5.6	2
Avg	25.9	3.67	0.142	23.3	28.5	5.2	2
2521 X	28.1	1.47	0.052	27.1	29.2	2.1	2
Y	27.2	0.69	0.025	26.7	27.7	1.0	2
Avg	27.6	1.08	0.039	26.9	28.4	1.5	2
2523 X	11.5	1.57	0.137	9.6	13.9	4.3	9
Y	11.4	1.30	0.114	9.7	13.7	4.0	9
Avg	11.4	1.42	0.124	9.7	13.8	4.1	9
2686 X	23.4	0.95	0.040	22.8	24.1	1.3	2
Y	20.2	1.03	0.051	19.5	20.9	1.4	2
Avg	21.8	0.99	0.045	21.1	22.5	1.4	2

Table 4.4 (cont)

Mean Pore Intercept Lengths

Sample Number	$\overline{L}_{3p}$ (μm)	Individual Image Statistics					
		$SD(\overline{L}_{3p})$ (μm)	$CV(\overline{L}_{3p})$ (μm)	Min. (μm)	Max. (μm)	Range (μm)	#Images
2687 X	10.6	3.50	0.331	5.7	16.4	10.8	9†
Y	11.6	6.56	0.568	5.6	27.5	21.9	9
Avg	11.1	4.90	0.443	5.7	22.0	16.3	9
2700 X	15.0	1.81	0.120	11.2	17.3	6.1	9
Y	14.7	1.90	0.129	10.6	16.6	6.0	9
Avg	14.9	1.82	0.122	10.9	16.9	6.0	9
2704 X	15.4	3.34	0.217	9.2	20.0	10.8	9
Y	14.4	3.90	0.270	8.2	19.4	11.1	9
Avg	14.9	3.58	0.240	8.7	19.7	11.0	9
2710 X	18.6	3.70	0.199	13.7	24.8	11.0	9
Y	18.0	3.72	0.207	13.0	23.6	10.6	9
Avg	18.3	3.69	0.202	13.4	24.2	10.8	9
2841 X	27.7	2.01	0.073	26.2	29.1	2.8	2
Y	22.9	1.31	0.057	21.9	23.8	1.8	2
Avg	25.3	1.66	0.066	24.1	26.4	2.3	2
2842 X	17.3	2.13	0.124	14.1	20.4	6.2	9
Y	16.5	1.71	0.104	14.0	19.3	5.3	9
Avg	16.9	1.89	0.112	14.1	19.8	5.8	9
2843 X	18.9	0.06	0.003	18.8	18.9	0.1	2
Y	16.6	0.76	0.046	16.0	17.1	1.1	2
Avg	17.7	0.41	0.023	17.4	18.0	0.6	2

† Sample 2687 results include image #1106 which is not in chord length distribution used for inversion and mean pore volume.

Table 4.5

Mean Grain Intercept Lengths

Sample Number	$\overline{L}_{3g}$ (μm)	Individual Image Statistics					
		$SD(\overline{L}_{3g})$ (μm)	$CV(\overline{L}_{3g})$ (μm)	Min. (μm)	Max. (μm)	Range (μm)	#Images
2124 X	56.7	5.05	0.089	53.7	64.3	10.6	4
Y	52.0	3.92	0.075	49.2	57.6	8.5	4
Avg	54.4	4.43	0.081	51.4	61.0	9.5	4
2509 X	94.3	4.06	0.043	91.5	97.2	5.7	2
Y	86.4	5.32	0.062	82.7	90.2	7.5	2
Avg	90.4	4.69	0.052	87.1	93.7	6.6	2
2513 X	63.2	2.79	0.044	61.5	66.4	4.9	3
Y	58.4	0.99	0.017	57.7	59.6	1.8	3
Avg	60.8	1.89	0.031	59.7	63.0	3.3	3
2519 X	124.4	14.54	0.117	114.1	134.7	20.6	2
Y	119.3	15.10	0.127	108.6	130.0	21.4	2
Avg	121.9	14.82	0.122	111.4	132.3	21.0	2
2521 X	88.3	2.60	0.029	86.5	90.2	3.7	2
Y	83.2	0.84	0.010	82.6	83.8	1.2	2
Avg	85.8	1.72	0.020	84.6	87.0	2.4	2
2523 X	52.8	6.10	0.116	42.4	61.2	18.8	9
Y	52.4	6.24	0.119	41.4	59.6	18.2	9
Avg	52.6	6.14	0.117	41.9	60.4	18.5	9
2686 X	69.6	18.86	0.271	52.3	83.0	26.7	2
Y	61.5	15.61	0.254	50.5	72.6	22.1	2
Avg	65.6	17.24	0.263	53.4	77.8	24.4	2

Table 4.5 (cont)
Mean Grain Intercept Lengths

Sample Number	$\overline{L}_{3g}$ (μm)	Individual Image Statistics $SD(\overline{L}_{3g})$ (μm)	$CV(\overline{L}_{3g})$ (μm)	Min. (μm)	Max. (μm)	Range (μm)	#Images
2687 X	57.8	17.16	0.297	44.0	97.8	53.8	9†
Y	54.4	18.32	0.337	39.6	96.8	57.1	9
Avg	56.1	17.38	0.310	42.8	97.3	54.5	9
2700 X	52.4	7.72	0.147	40.7	61.8	21.1	9
Y	51.1	7.18	0.140	40.3	60.8	20.5	9
Avg	51.8	7.42	0.143	40.5	61.2	20.7	9
2704 X	70.3	25.16	0.358	53.4	134.3	80.9	9
Y	67.9	27.00	0.398	50.3	137.4	87.1	9
Avg	69.1	26.06	0.377	52.5	135.8	83.3	9
2710 X	49.8	7.20	0.145	37.8	59.1	21.2	9
Y	48.0	6.39	0.133	38.0	58.4	20.3	9
Avg	48.9	6.76	0.138	37.9	58.7	20.8	9
2841 X	56.4	5.21	0.092	52.7	60.1	7.4	2
Y	49.5	5.86	0.118	45.3	53.6	8.3	2
Avg	53.0	5.54	0.105	49.0	56.9	7.8	2
2842 X	109.6	17.45	0.159	90.2	141.4	51.3	9
Y	107.0	15.66	0.146	93.5	138.3	44.8	9
Avg	108.3	16.50	0.152	91.9	139.9	48.0	9
2843 X	52.5	7.90	0.150	47.0	58.1	11.2	2
Y	45.9	5.37	0.117	42.1	49.7	7.6	2
Avg	49.2	6.63	0.135	44.5	53.9	9.4	2

† Sample 2687 results include image #1106 which is not in chord length distribution used for inversion and mean pore volume.

Table 4.6

Mean Pore Volume

Sample Number	Mean Pore Volume (μm^3)	Equivalent Sphere Diameter (μm)	Equivalent Ellipsoid Major Axis (μm)	Maximum Chord Length (μm)
2124	202182	72.8	108.8	180
2509	422657	93.1	140.7	225
2513	256555	78.8	116.5	175
2519	821820	116.2	175.6	300
2521	1445590	140.3	217.0	325
2523	112212	59.8	92.6	175
2686	1257620	133.9	195.8	275
2687	74248	52.1	77.9	150
2700	827409	116.5	178.0	300
2704	827778	116.5	174.0	275
2710	1502770	142.1	212.3	320
2841	2014910	156.7	218.3	350
2842	370679	89.1	134.6	210
2843	871007	118.5	166.6	240

NOTES: The equivalent sphere diameter, D_{V_p}, is the diameter of a sphere with the same volume as the mean pore volume. The equivalent spheroid major axis is the major axis of an oblate ellipsoid with the same volume as the mean pore volume and aspect ratio found from the size–shape inversion. The maximum chord length allowed corresponds to the maximum size class used in the size–shape inversion.

Table 4.7a

Pore Size Distribution Inversion Results for Sample #2124

Class Number	Major Axis (μm)	Normalized g_V	Cumulative g_V	$SD(g_V)$	Resolution
1	10	0.090	0.090	0.002	1.000
2	20	0.110	0.200	0.006	0.999
3	40	0.141	0.341	0.013	0.995
4	60	0.124	0.466	0.025	0.982
5	80	0.176	0.642	0.039	0.953
6	100	0.075	0.717	0.052	0.907
7	120	0.056	0.773	0.063	0.848
8	140	0.083	0.856	0.059	0.872
9	180	0.144	1.000	0.032	0.967

Aspect ratio: 0.30

Damping: 1×10^{-5}

Goodness of Fit Measures

Volume Sum	S_{Vp}		Mean Pore Volume			Sum Resol.
	Chords (μm^{-1})	Model (μm^{-1})	Chords (μm^3)	Model (μm^3)	Dev.	
0.975	0.30	0.29	202182	214511	0.061	8.52

Data variance: 9.62×10^{-5}

Residual variance: 3.57×10^{-7}

Variance reduction: 99.6 %

Table 4.7b

Pore Size Distribution Inversion Results for Sample #2509

Class Number	Major Axis (μm)	Normalized g_V	Cumulative g_V	$SD(g_V)$	Resolution
1	20	0.109	0.109	0.004	0.999
2	50	0.083	0.192	0.016	0.976
3	75	0.102	0.294	0.029	0.901
4	100	0.166	0.460	0.036	0.818
5	125	0.120	0.580	0.039	0.750
6	150	0.048	0.628	0.040	0.671
7	175	0.210	0.838	0.041	0.673
8	225	0.162	1.000	0.030	0.881

Aspect ratio: 0.29

Damping: 2×10^{-5}

Goodness of Fit Measures

Volume Sum	S_{Vp}		Mean Pore Volume			Sum Resol.
	Chords (μm^{-1})	Model (μm^{-1})	Chords (μm^3)	Model (μm^3)	Dev.	
1.001	0.16	0.16	422657	544527	0.288	6.67

Data variance: 5.20×10^{-5}

Residual variance: 2.20×10^{-7}

Variance reduction: 99.6%

Table 4.7c

Pore Size Distribution Inversion Results for Sample #2513

Class Number	Major Axis (μm)	Normalized g_V	Cumulative g_V	$SD(g_V)$	Resolution
1	10	0.092	0.092	0.003	1.000
2	30	0.153	0.246	0.010	0.998
3	50	0.068	0.314	0.020	0.991
4	75	0.093	0.407	0.029	0.979
5	100	0.220	0.627	0.046	0.944
6	125	0.143	0.769	0.062	0.890
7	150	0.190	0.959	0.071	0.845
8	175	0.041	1.000	0.049	0.933

Aspect ratio: 0.31

Damping: $\times 10^{-5}$

Goodness of Fit Measures

Volume Sum	S_{Vp}		Mean Pore Volume			Sum Resol.
	Chords (μm^{-1})	Model (μm^{-1})	Chords (μm^3)	Model (μm^3)	Dev.	
0.981	0.25	0.25	256555	228892	−0.11	7.58

Data variance: 8.05×10^{-5}

Residual variance: 4.44×10^{-7}

Variance reduction: 99.4%

Table 4.7d

Pore Size Distribution Inversion Results for Sample #2519

Class Number	Major Axis (μm)	Normalized g_V	Cumulative g_V	$SD(g_V)$	Resolution
1	20	0.091	0.091	0.003	1.000
2	40	0.066	0.157	0.008	0.997
3	60	0.107	0.264	0.013	0.992
4	100	0.180	0.444	0.020	0.981
5	140	0.088	0.532	0.033	0.944
6	180	0.174	0.706	0.046	0.879
7	220	0.123	0.829	0.054	0.797
8	260	0.121	0.951	0.059	0.735
9	300	0.049	1.000	0.043	0.885

Aspect ratio: 0.29

Damping: 5×10^{-6}

Goodness of Fit Measures

Volume Sum	S_{Vp}		Mean Pore Volume			Sum Resol.
	Chords (μm^{-1})	Model (μm^{-1})	Chords (μm^3)	Model (μm^3)	Dev.	
0.997	0.16	0.15	821820	948086	0.154	8.21

Data variance: 3.39×10^{-5}

Residual variance: 1.16×10^{-7}

Variance reduction: 99.6%

Table 4.7e

Pore Size Distribution Inversion Results for Sample #2521

Class Number	Major Axis (μm)	Normalized g_V	Cumulative g_V	$SD(g_V)$	Resolution
1	20	0.102	0.102	0.003	0.998
2	50	0.063	0.165	0.011	0.980
3	75	0.122	0.287	0.022	0.911
4	100	0.078	0.365	0.029	0.797
5	125	0.081	0.446	0.031	0.686
6	150	0.047	0.494	0.031	0.610
7	175	0.059	0.553	0.031	0.558
8	200	0.130	0.683	0.030	0.518
9	225	0.070	0.753	0.032	0.577
10	275	0.045	0.798	0.032	0.587
11	325	0.202	1.000	0.029	0.770

Aspect ratio: 0.27

Damping: 2×10^{-5}

Goodness of Fit Measures

Volume Sum	S_{Vp}		Mean Pore Volume			Sum Resol.
	Chords (μm^{-1})	Model (μm^{-1})	Chords (μm^3)	Model (μm^3)	Dev.	
0.980	0.14	0.15	1445590	1481580	0.025	7.99

Data variance: 2.76×10^{-5}

Residual variance: 1.42×10^{-7}

Variance reduction: 99.5%

Table 4.7f

Pore Size Distribution Inversion Results for Sample #2523

Class Number	Major Axis (μm)	Normalized g_V	Cumulative g_V	$SD(g_V)$	Resolution
1	10	0.136	0.136	0.002	1.000
2	25	0.136	0.272	0.006	1.000
3	50	0.274	0.546	0.014	0.997
4	75	0.062	0.608	0.025	0.989
5	100	0.226	0.835	0.039	0.972
6	125	0.055	0.890	0.039	0.972
7	175	0.110	1.000	0.023	0.990

Aspect ratio: 0.27

Damping: 5×10^{-6}

Goodness of Fit Measures

Volume Sum	S_{Vp}		Mean Pore Volume			Sum Resol.
	Chords (μm^{-1})	Model (μm^{-1})	Chords (μm^3)	Model (μm^3)	Dev.	
1.003	0.35	0.37	112212	139658	0.244	6.92

Data variance: 1.20×10^{-4}

Residual variance: 2.95×10^{-7}

Variance reduction: 99.8%

Table 4.7g

Pore Size Distribution Inversion Results for Sample #2686

Class Number	Major Axis (μm)	Normalized g_V	Cumulative g_V	$SD(g_V)$	Resolution
1	10	0.047	0.047	0.003	1.000
2	25	0.142	0.189	0.009	0.997
3	50	0.083	0.272	0.020	0.984
4	75	0.059	0.332	0.033	0.956
5	100	0.093	0.425	0.037	0.943
6	150	0.104	0.529	0.054	0.843
7	175	0.104	0.633	0.062	0.762
8	225	0.085	0.718	0.061	0.783
9	275	0.282	1.000	0.048	0.884

Aspect ratio: 0.32

Damping: 2×10^{-5}

Goodness of Fit Measures

Volume Sum	S_{Vp}		Mean Pore Volume			Sum Resol.
	Chords (μm^{-1})	Model (μm^{-1})	Chords (μm^3)	Model (μm^3)	Dev.	
0.978	0.18	0.18	1257620	1317890	0.048	8.15

Data variance: 2.87×10^{-5}

Residual variance: 5.50×10^{-7}

Variance reduction: 98.1%

Table 4.7h

Pore Size Distribution Inversion Results for Sample #2687

Class Number	Major Axis (μm)	Normalized g_V	Cumulative g_V	$SD(g_V)$	Resolution
1	10	0.182	0.182	0.003	1.000
2	25	0.203	0.385	0.009	1.000
3	50	0.158	0.543	0.019	1.000
4	75	0.130	0.674	0.035	1.000
5	100	0.240	0.913	0.053	1.000
6	125	0.087	1.000	0.039	1.000

Aspect ratio: 0.30

Damping: (none)

Goodness of Fit Measures

Volume Sum	S_{V_p}		Mean Pore Volume			Sum Resol.
	Chords (μm^{-1})	Model (μm^{-1})	Chords (μm^3)	Model (μm^3)	Dev.	
0.966	0.36	0.40	74248	76535	0.031	6.00

Data variance: 2.06×10^{-4}

Residual variance: 5.58×10^{-7}

Variance reduction: 99.7%

Table 4.7i

Pore Size Distribution Inversion Results for Sample #2700

Class Number	Major Axis (μm)	Normalized g_V	Cumulative g_V	$SD(g_V)$	Resolution
1	10	0.127	0.127	0.001	1.000
2	25	0.075	0.203	0.004	0.999
3	50	0.130	0.332	0.009	0.992
4	75	0.043	0.376	0.014	0.979
5	100	0.128	0.503	0.016	0.974
6	150	0.177	0.681	0.019	0.961
7	200	0.174	0.855	0.022	0.948
8	300	0.145	1.000	0.016	0.976

Aspect ratio: 0.28

Damping: 1×10^{-5}

Goodness of Fit Measures

Volume Sum	S_{Vp}		Mean Pore Volume			Sum Resol.
	Chords (μm^{-1})	Model (μm^{-1})	Chords (μm^3)	Model (μm^3)	Dev.	
0.985	0.27	0.28	827409	889964	0.076	7.83

Data variance: 3.85×10^{-5}

Residual variance: 1.06×10^{-7}

Variance reduction: 99.7%

Table 4.7j

Pore Size Distribution Inversion Results for Sample #2704

Class Number	Major Axis (μm)	Normalized g_V	Cumulative g_V	$SD(g_V)$	Resolution
1	10	0.110	0.110	0.002	1.000
2	25	0.133	0.242	0.005	0.996
3	50	0.072	0.315	0.010	0.984
4	85	0.210	0.525	0.016	0.953
5	120	0.093	0.618	0.023	0.871
6	150	0.065	0.683	0.029	0.719
7	175	0.056	0.739	0.029	0.712
8	225	0.149	0.888	0.029	0.737
9	275	0.112	1.000	0.024	0.850

Aspect ratio: 0.30

Damping: 3×10^{-5}

Goodness of Fit Measures

Volume Sum	S_{V_p}		Mean Pore Volume			Sum Resol.
	Chords (μm^{-1})	Model (μm^{-1})	Chords (μm^3)	Model (μm^3)	Dev.	
0.969	0.27	0.27	827778	760630	−0.081	7.82

Data variance: 4.30×10^{-5}

Residual variance: 1.75×10^{-7}

Variance reduction: 99.6%

Table 4.7k

Pore Size Distribution Inversion Results for Sample #2710

Class Number	Major Axis (μm)	Normalized g_V	Cumulative g_V	$SD(g_V)$	Resolution
1	10	0.083	0.083	0.002	0.999
2	20	0.061	0.144	0.004	0.997
3	40	0.095	0.239	0.009	0.985
4	60	0.035	0.274	0.016	0.947
5	80	0.049	0.323	0.022	0.878
6	100	0.066	0.390	0.024	0.844
7	130	0.079	0.469	0.024	0.845
8	170	0.184	0.653	0.027	0.785
9	210	0.115	0.768	0.028	0.707
10	260	0.022	0.790	0.029	0.682
11	320	0.210	1.000	0.024	0.841

Aspect ratio: 0.30

Damping: 3×10^{-5}

Goodness of Fit Measures

Volume Sum	S_{Vp}		Mean Pore Volume			Sum Resol.
	Chords (μm^{-1})	Model (μm^{-1})	Chords (μm^3)	Model (μm^3)	Dev.	
0.969	0.22	0.22	1502770	1495820	−0.005	9.51

Data variance: 2.76×10^{-5}

Residual variance: 1.64×10^{-7}

Variance reduction: 99.4%

Table 4.71

Pore Size Distribution Inversion Results for Sample #2841

Class Number	Major Axis (μm)	Normalized g_V	Cumulative g_V	$SD(g_V)$	Resolution
1	10	0.059	0.059	0.002	1.000
2	25	0.111	0.170	0.006	0.998
3	75	0.135	0.305	0.020	0.973
4	100	0.095	0.401	0.028	0.945
5	175	0.168	0.569	0.043	0.816
6	200	0.075	0.644	0.050	0.589
7	225	0.085	0.729	0.047	0.526
8	250	0.056	0.785	0.049	0.583
9	300	0.088	0.873	0.051	0.618
10	350	0.127	1.000	0.043	0.804

Aspect ratio: 0.37

Damping: 2×10^{-5}

Goodness of Fit Measures

Volume Sum	S_{Vp}		Mean Pore Volume			Sum Resol.
	Chords (μm^{-1})	Model (μm^{-1})	Chords (μm^3)	Model (μm^3)	Dev.	
0.988	0.16	0.16	2014910	2194170	0.089	7.85

Data variance: 1.95×10^{-5}

Residual variance: 3.28×10^{-7}

Variance reduction: 98.3%

Table 4.7m

Pore Size Distribution Inversion Results for Sample #2842

Class Number	Major Axis (μm)	Normalized g_V	Cumulative g_V	$SD(g_V)$	Resolution
1	10	0.089	0.089	0.003	1.000
2	20	0.026	0.114	0.008	0.999
3	40	0.108	0.223	0.018	0.994
4	60	0.071	0.294	0.026	0.987
5	90	0.190	0.484	0.032	0.981
6	130	0.124	0.609	0.045	0.959
7	170	0.234	0.842	0.064	0.912
8	210	0.158	1.000	0.048	0.952

Aspect ratio: 0.29

Damping: 1×10^{-5}

Goodness of Fit Measures

Volume Sum	S_{Vp}		Mean Pore Volume			Sum Resol.
	Chords (μm^{-1})	Model (μm^{-1})	Chords (μm^3)	Model (μm^3)	Dev.	
1.014	0.24	0.23	370679	461990	0.246	7.78

Data variance: 5.76×10^{-5}

Residual variance: 5.40×10^{-7}

Variance reduction: 99.1%

Table 4.7n

Pore Size Distribution Inversion Results for Sample #2843

Class Number	Major Axis (μm)	Normalized g_V	Cumulative g_V	$SD(g_V)$	Resolution
1	10	0.135	0.135	0.007	0.999
2	30	0.096	0.230	0.012	0.997
3	50	0.071	0.302	0.024	0.988
4	70	0.082	0.384	0.031	0.980
5	100	0.068	0.452	0.041	0.963
6	130	0.096	0.548	0.055	0.928
7	160	0.216	0.765	0.066	0.891
8	200	0.082	0.846	0.073	0.861
9	240	0.154	1.000	0.052	0.935

Aspect ratio: 0.36

Damping: 1×10^{-5}

Goodness of Fit Measures

Volume Sum	S_{V_p}		Mean Pore Volume			Sum Resol.
	Chords (μm^{-1})	Model (μm^{-1})	Chords (μm^3)	Model (μm^3)	Dev.	
1.072	0.23	0.24	871007	750642	−0.138	8.54

Data variance: 3.86×10^{-5}

Residual variance: 5.00×10^{-7}

Variance reduction: 98.7%

Table 4.8a

Covariance and Resolution Matrices for Sample 2513

Model Covariance Matrix ($\times 10^3$)

0.007	−0.007	0.008	0.000	−0.003	−0.003	0.000	0.004
	0.094	−0.138	0.041	0.037	0.042	−0.013	−0.054
		0.388	−0.336	0.064	−0.104	0.069	0.094
			0.862	−0.873	0.384	−0.118	0.022
				2.155	−1.908	0.512	0.028
					3.808	−2.816	0.572
						5.093	−2.823
							2.439

Model Resolution Matrix

1.000	0.000	0.000	0.000	0.000	0.000	0.000	0.000
	0.998	0.003	−0.001	−0.001	−0.001	0.000	0.001
		991	0.008	−0.002	0.003	−0.002	−0.002
			0.979	0.022	−0.012	0.005	−0.001
				0.944	0.054	−0.021	0.003
					0.890	0.091	−0.025
						0.845	0.085
							0.933

Table 4.8b
Covariance and Resolution Matrices for Sample 2710

Model Covariance Matrix ($\times 10^3$)

0.003	−0.004	0.003	0.000	−0.002	−0.001	0.001	0.001	0.000	0.000	−0.001
	0.015	−0.020	0.008	0.008	0.004	−0.007	−0.007	0.001	0.004	0.002
		0.079	−0.089	0.019	−0.011	0.031	0.025	−0.025	−0.018	0.008
			0.248	−0.222	0.064	−0.035	−0.020	0.080	0.016	−0.049
				0.497	−0.357	0.070	−0.003	−0.062	0.043	0.026
					0.589	−0.343	0.047	0.015	−0.047	0.049
						0.590	−0.337	−0.003	0.036	−0.007
							0.712	−0.403	−0.079	0.064
								0.795	−0.329	−0.086
									0.832	−0.457
										0.564

Model Resolution Matrix

0.999	0.001	−0.001	0.000	0.000	0.000	0.000	0.000	0.000	0.000	0.000
	0.997	0.004	−0.002	−0.001	−0.001	0.001	0.001	0.000	−0.001	0.000
		0.985	0.018	−0.006	0.004	−0.007	−0.007	0.009	0.002	−0.002
			0.947	0.054	−0.023	0.011	0.010	−0.030	0.007	0.008
				0.878	0.100	−0.032	−0.001	0.036	−0.036	0.006
					0.844	0.100	−0.025	−0.016	0.040	−0.026
						0.845	0.106	−0.019	−0.014	0.010
							0.785	0.162	−0.023	−0.009
								0.707	0.180	−0.025
									0.682	0.170
										0.841

Figure 4.1 Image Porosity versus Bulk Porosity

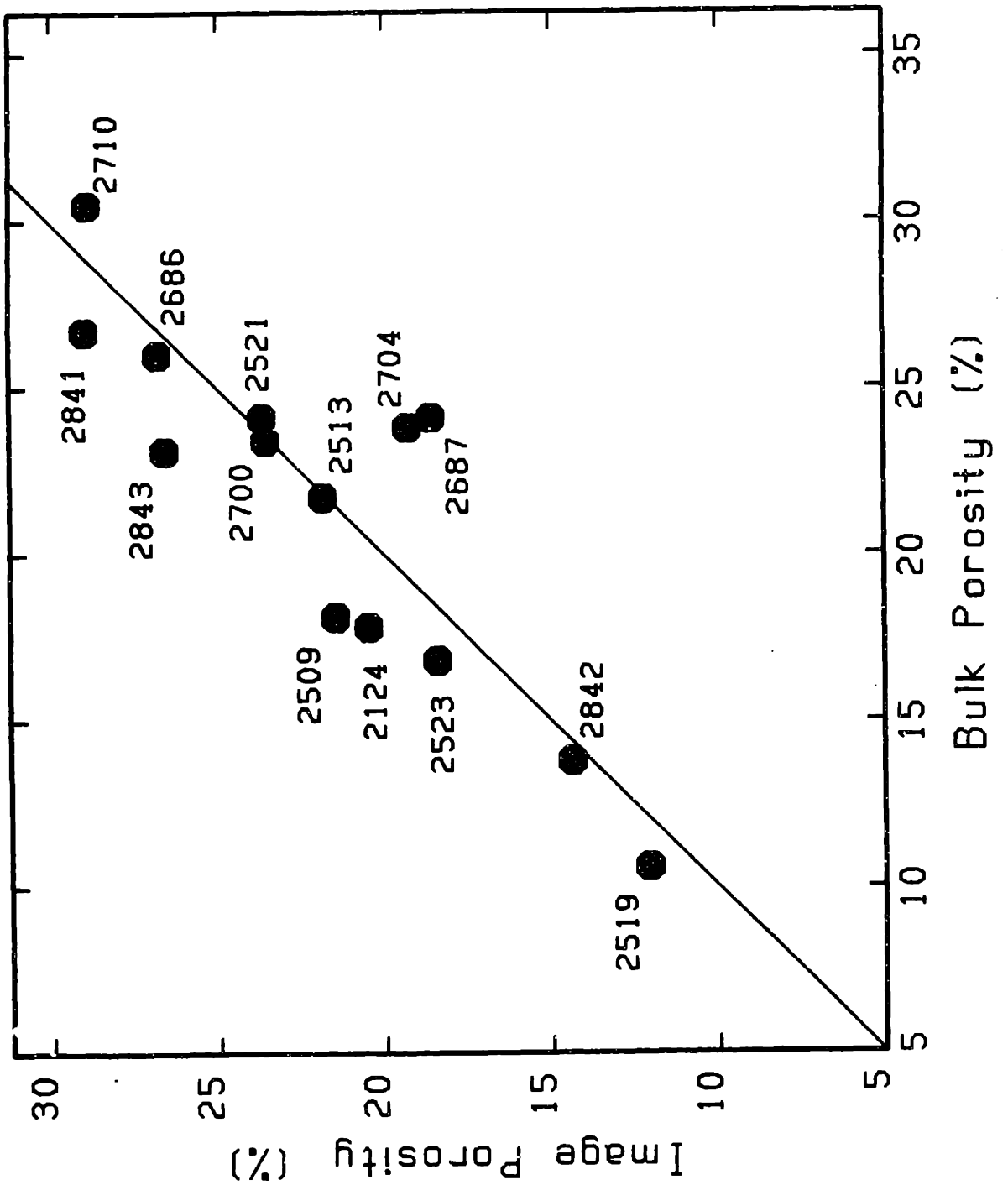

Figure 4.2

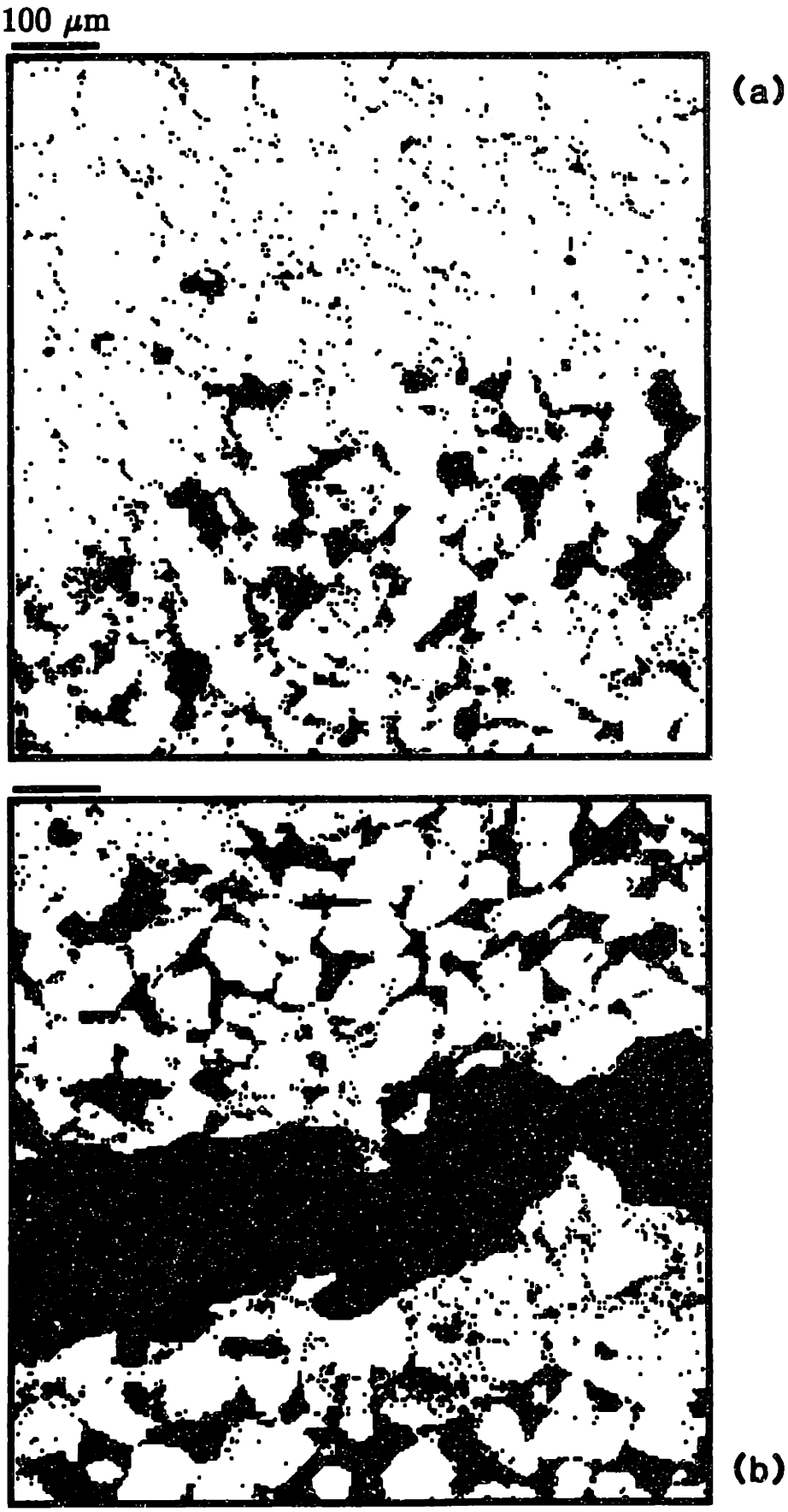

Figure 4.3 Intercept Sampling Schematic

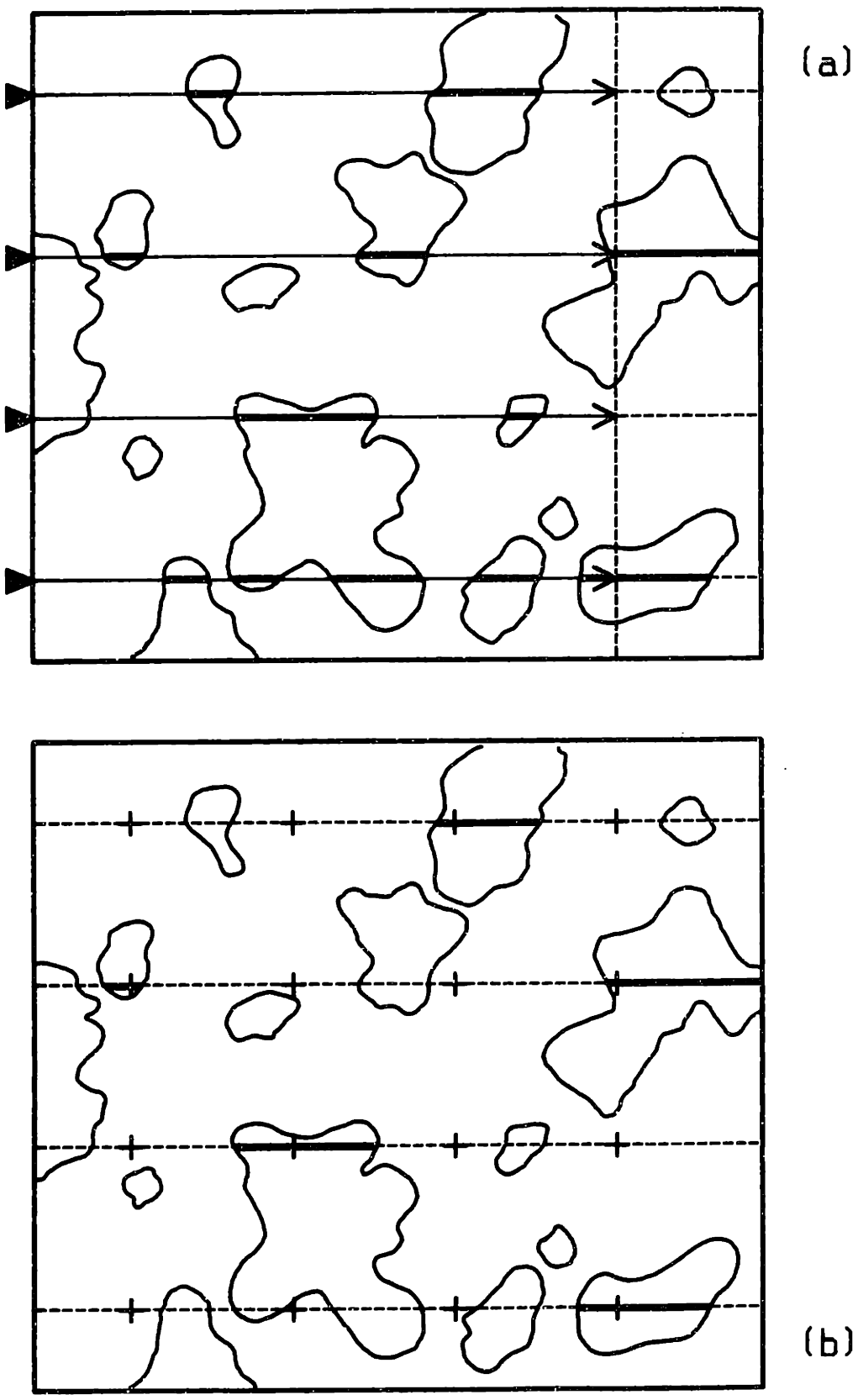

Figure 4.4 Intercept Length Density

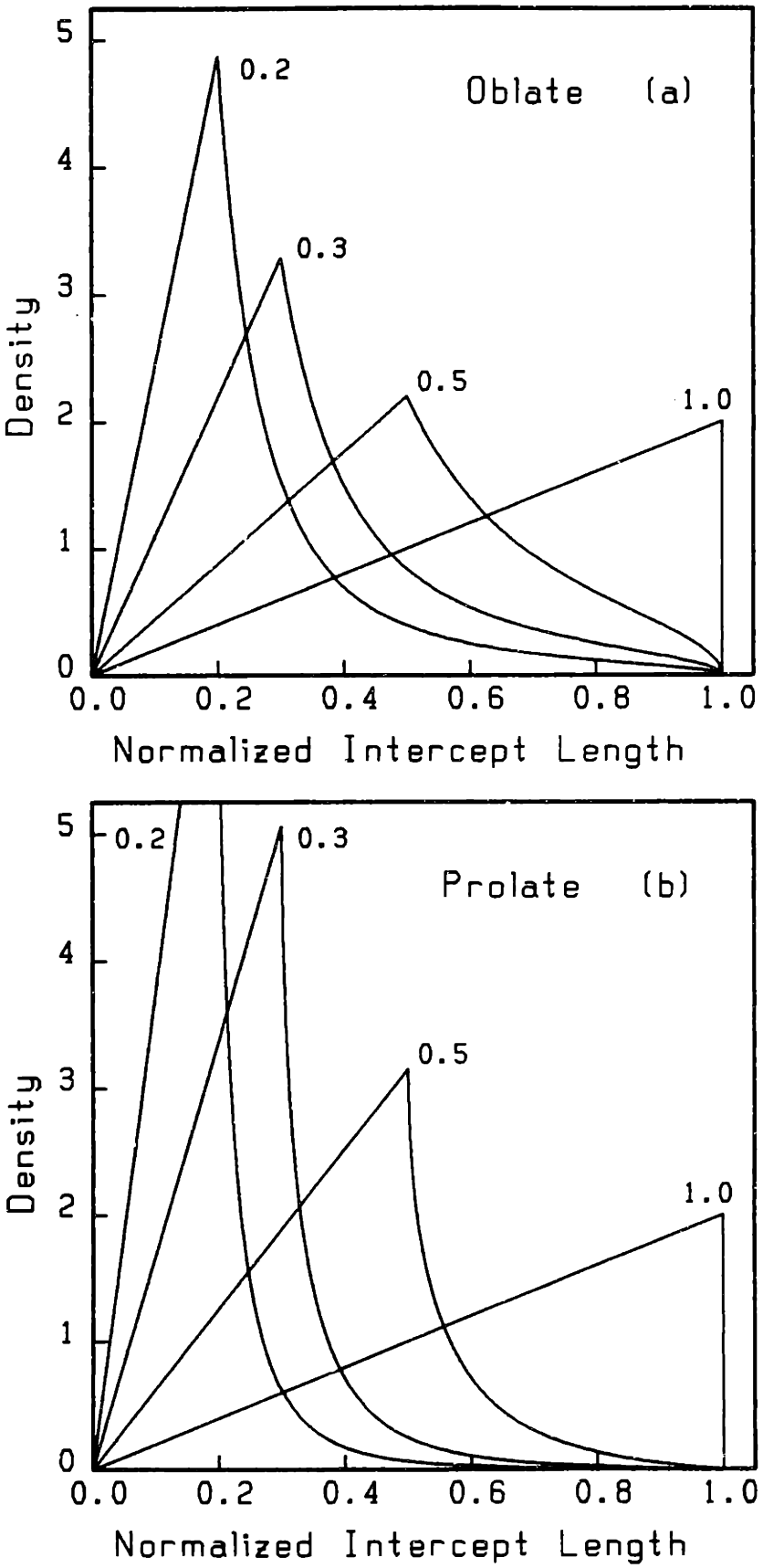

Figure 4.5a Volume Distribution of Pore Size (2124)

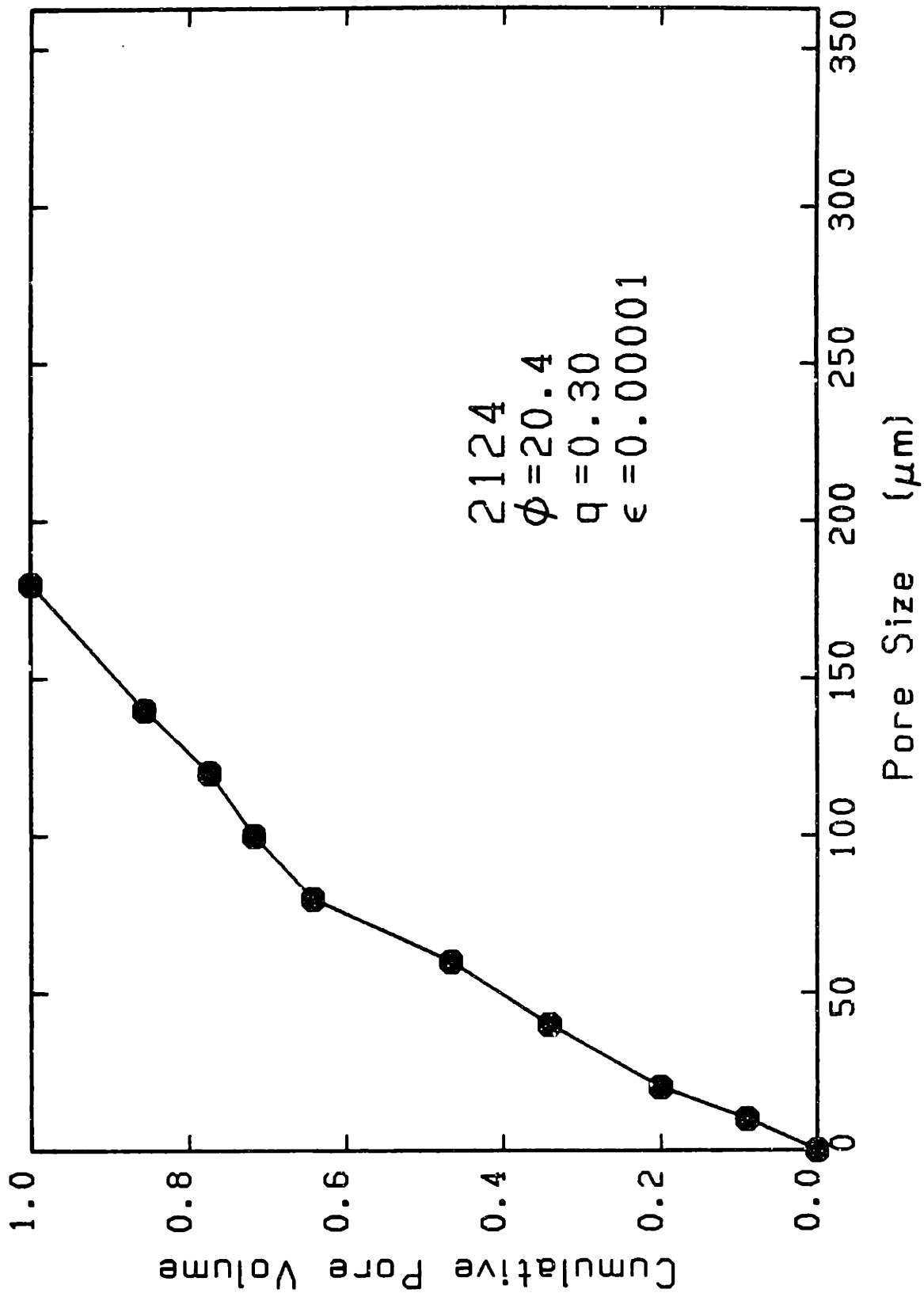

Figure 4.5b Volume Distribution of Pore Size (2509)

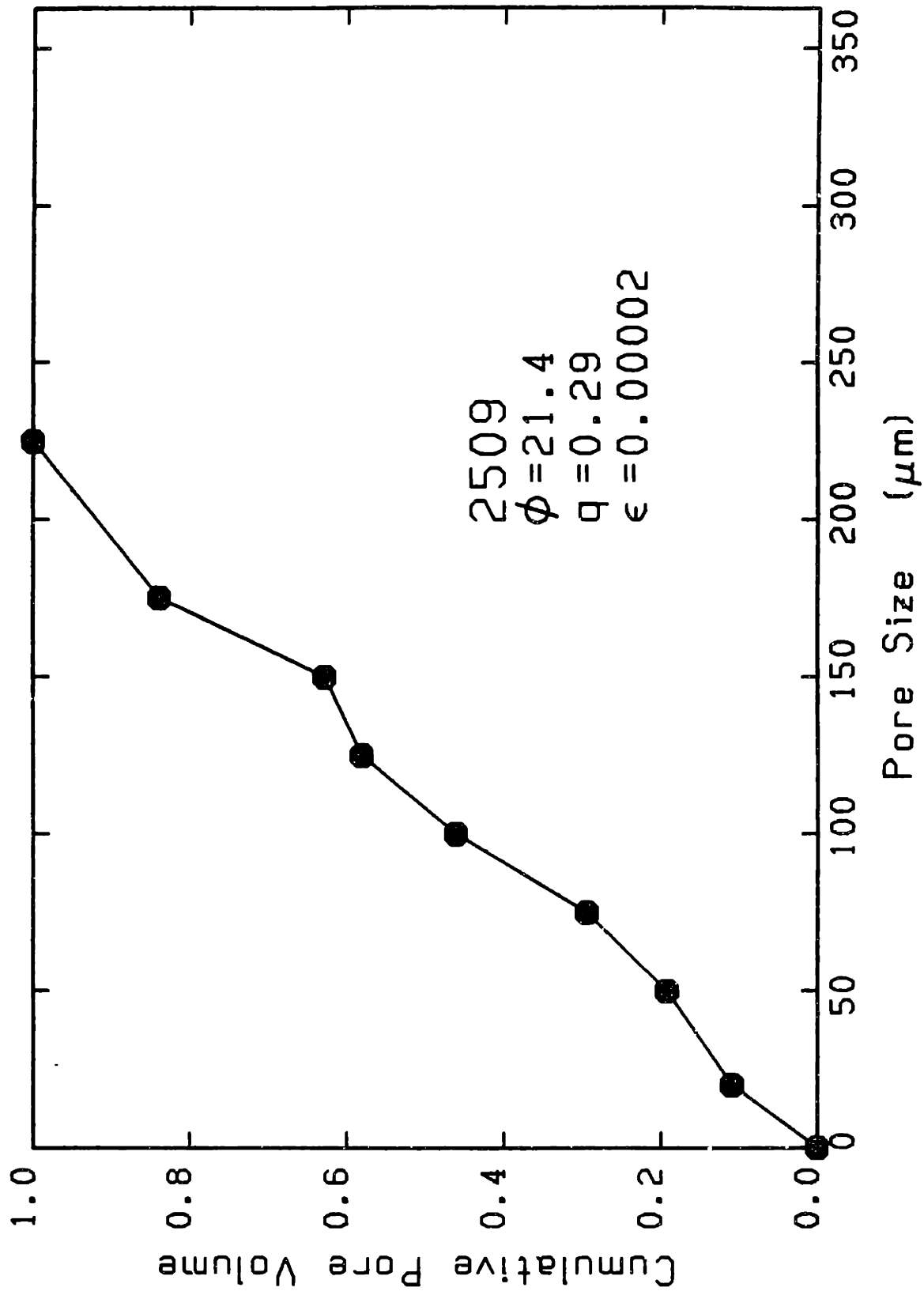

Figure 4.5c Volume Distribution of Pore Size (2513)

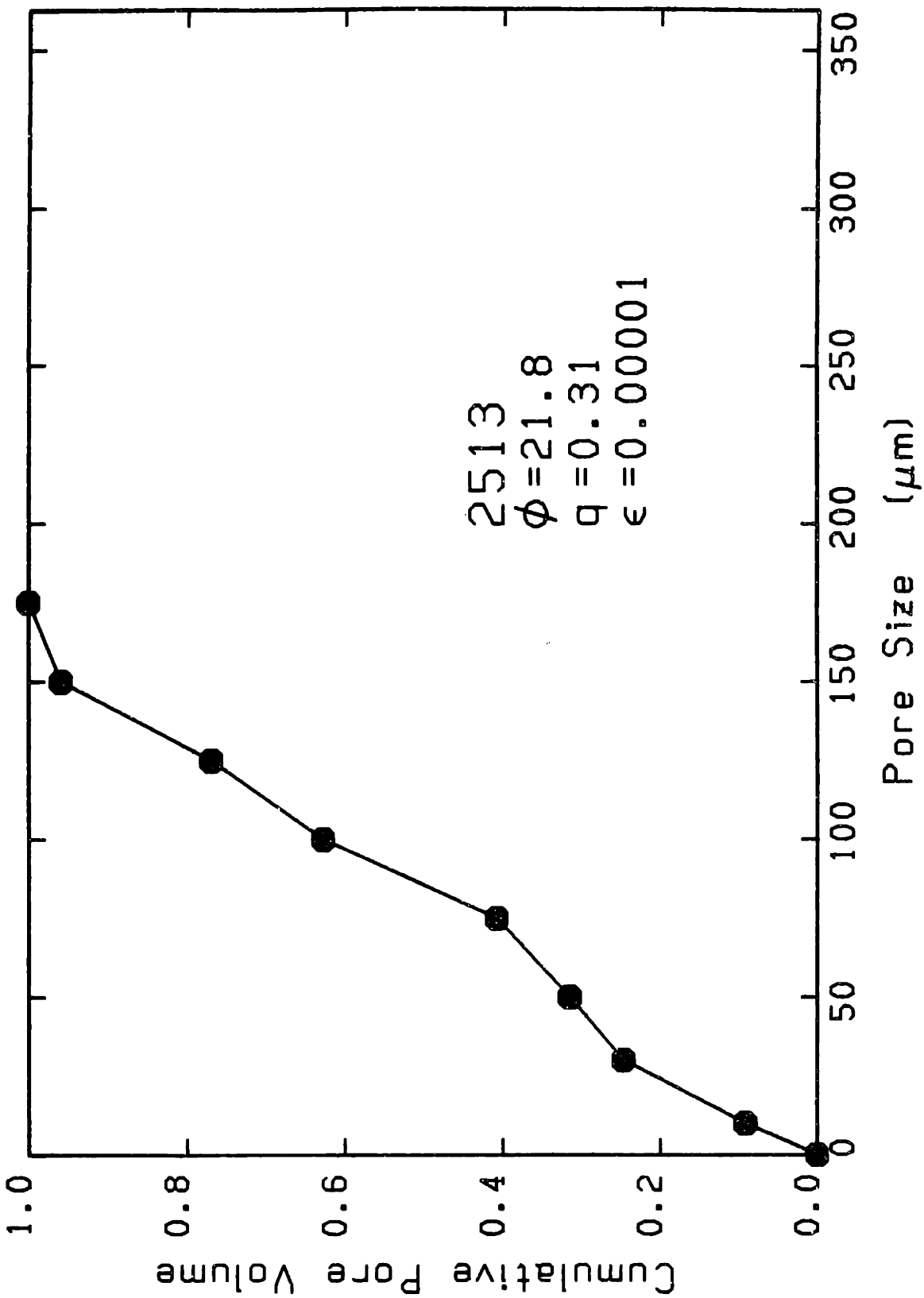

Figure 4.5d Volume Distribution of Pore Size (2519)

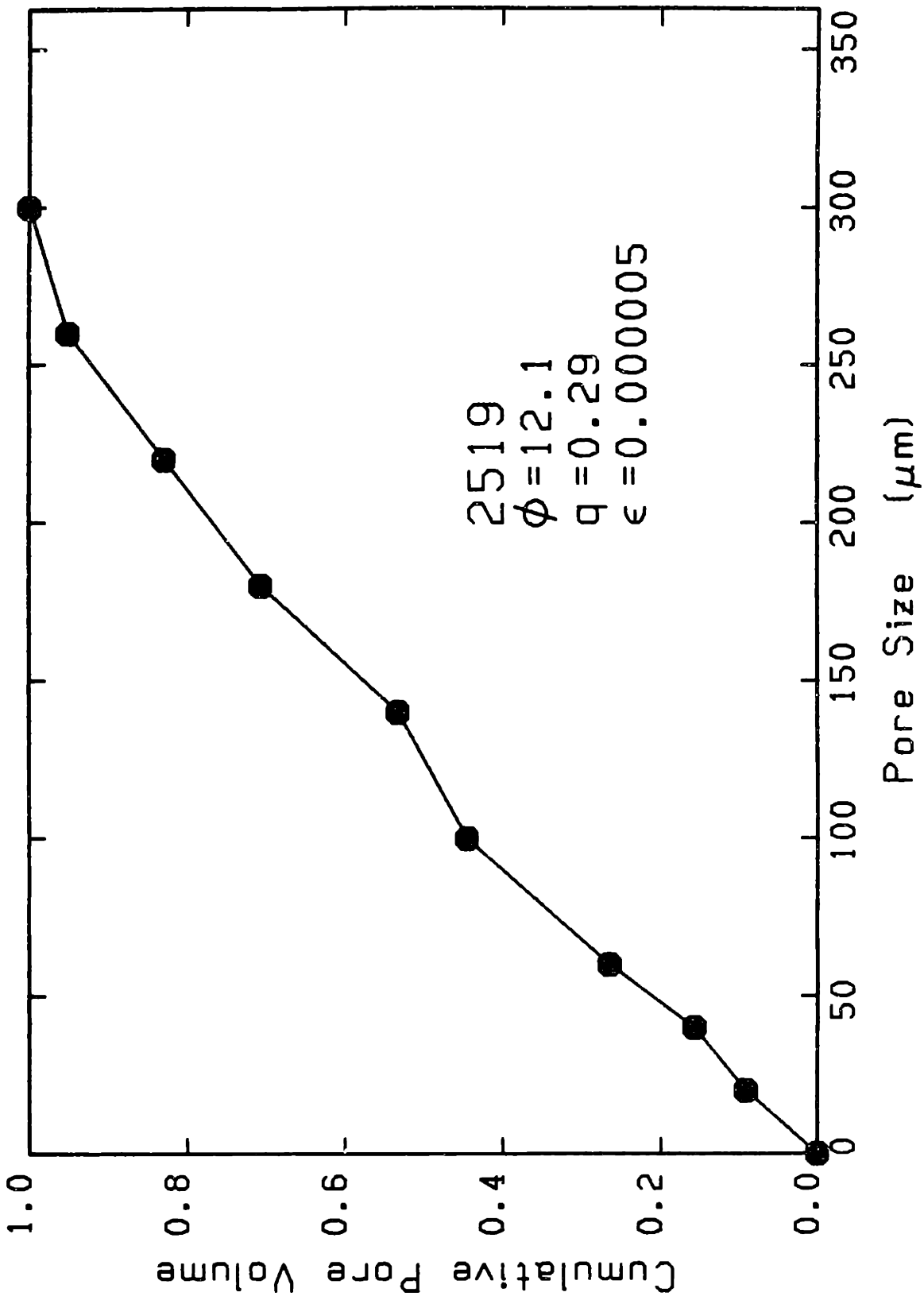

Figure 4.5e Volume Distribution of Pore Size (2521)

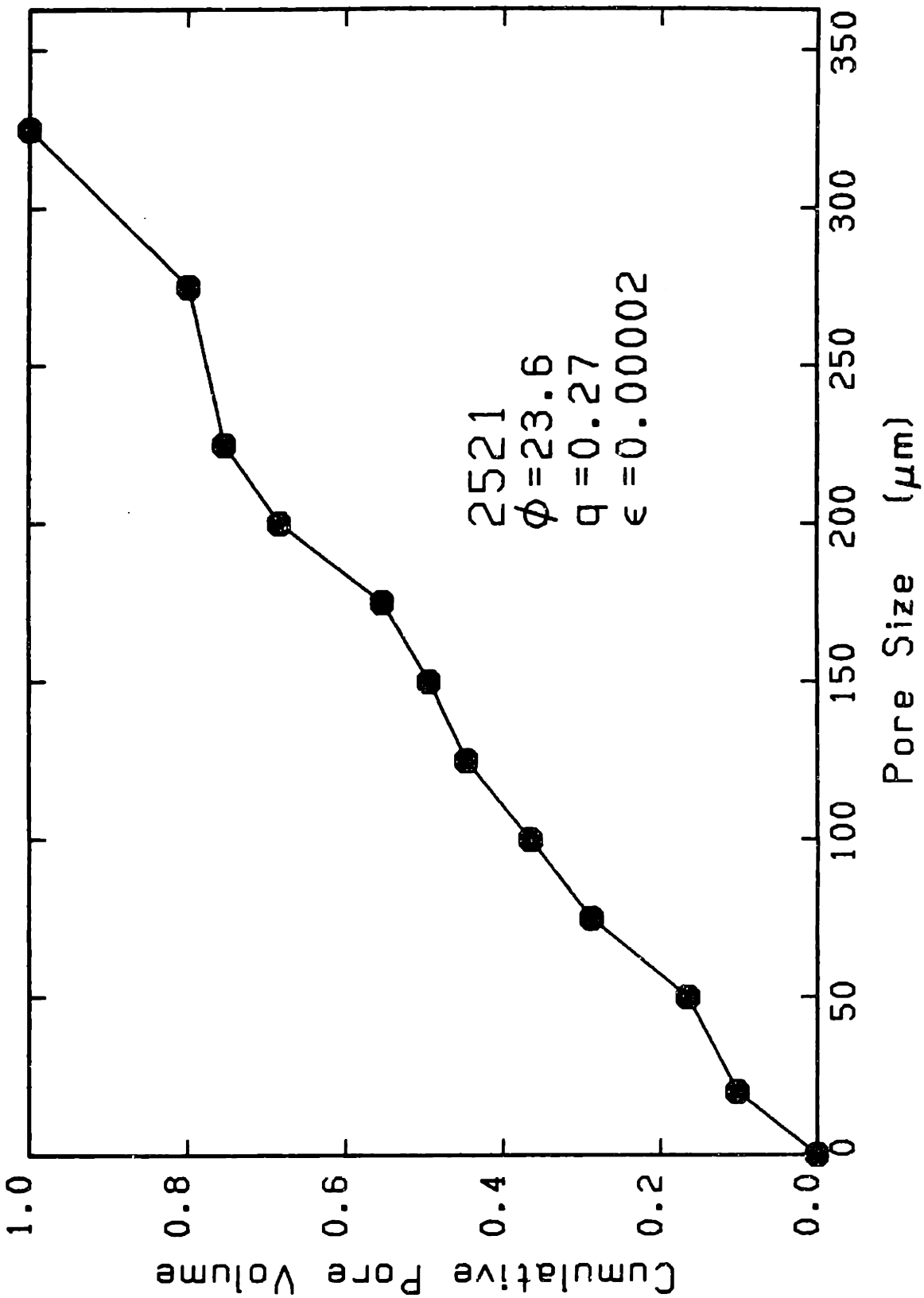

Figure 4.5f Volume Distribution of Pore Size (2523)

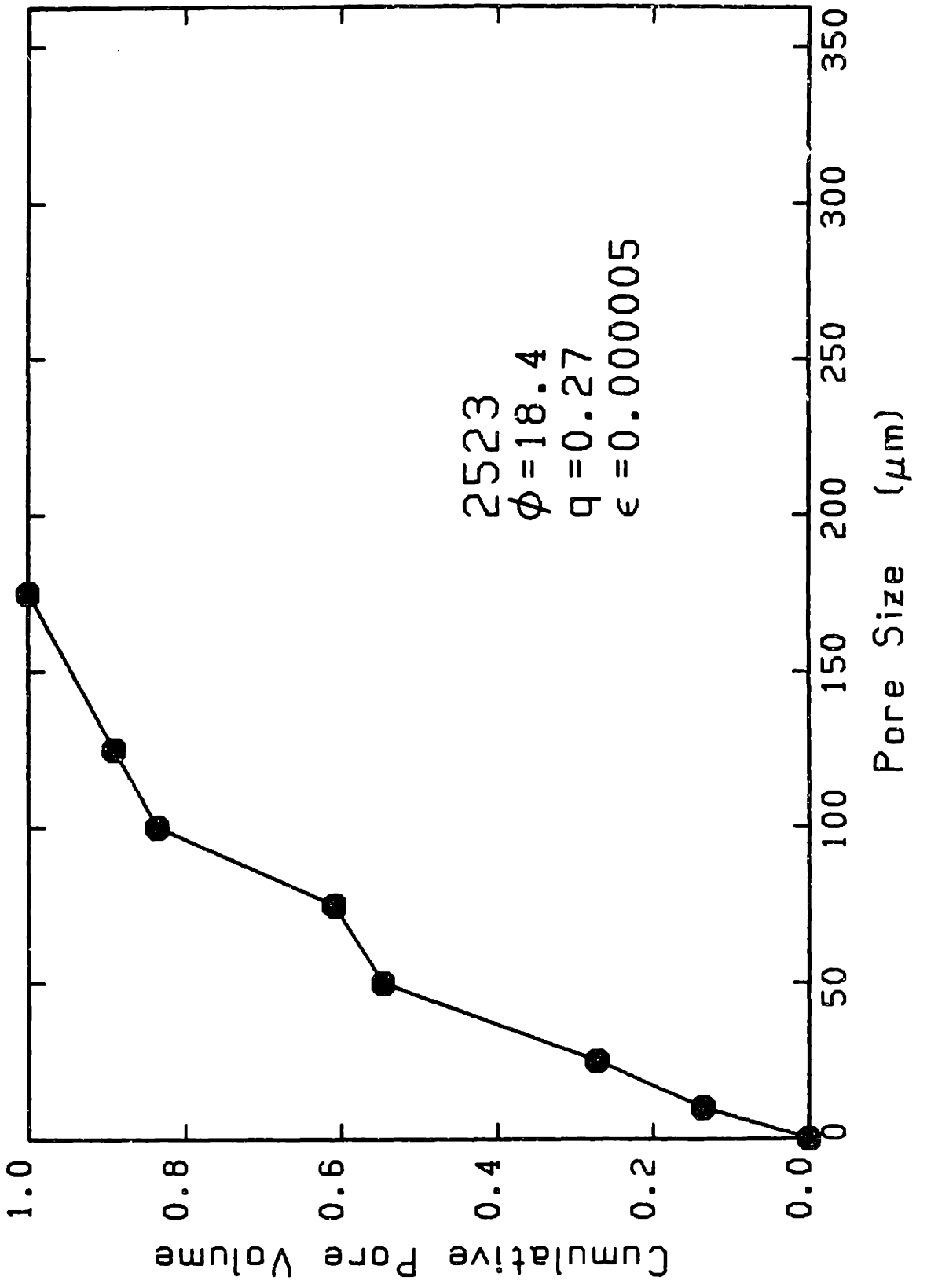

Figure 4.5g Volume Distribution of Pore Size (2686)

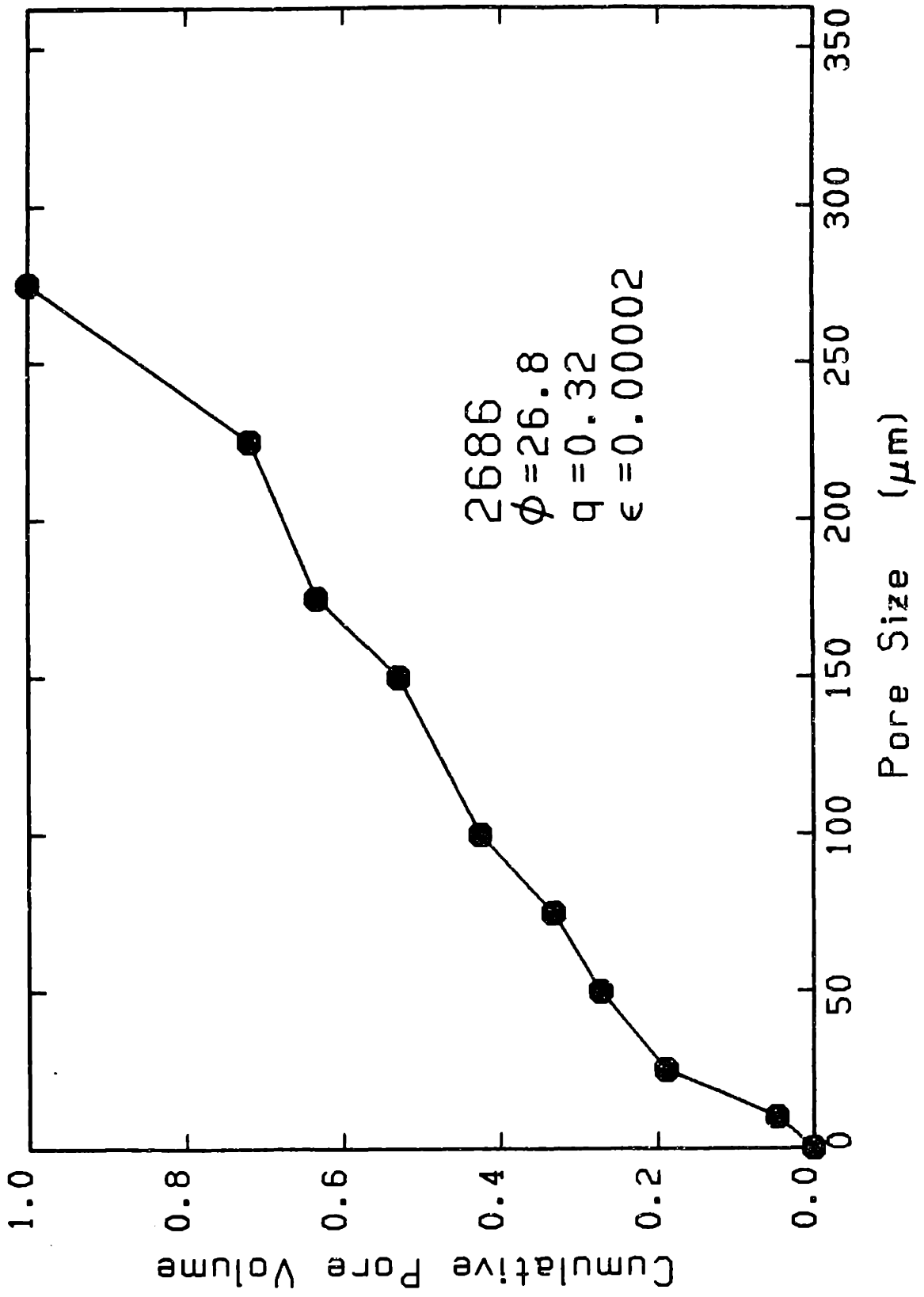

Figure 4.5h Volume Distribution of Pore Size (2687)

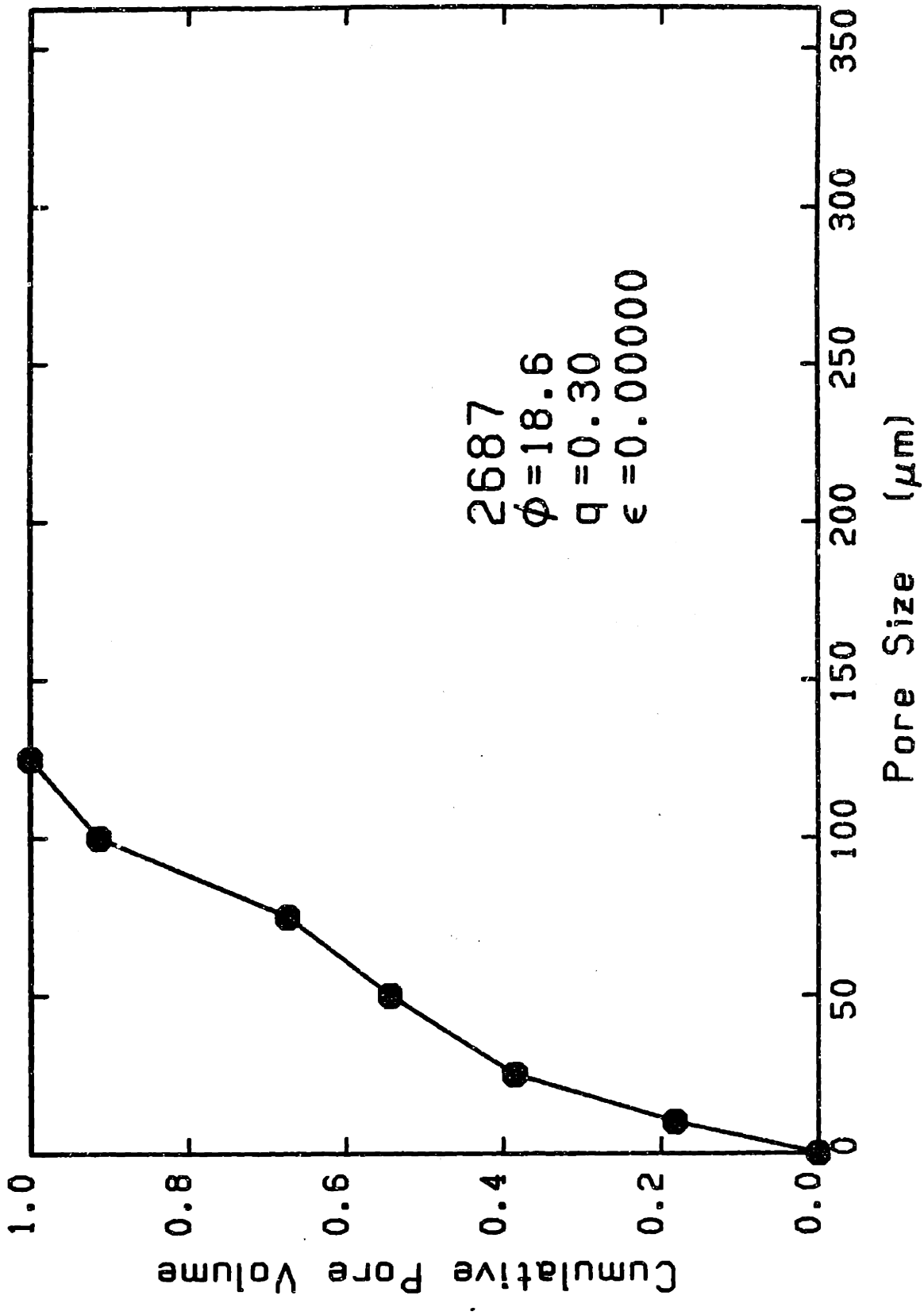

Figure 4.51 Volume Distribution of Pore Size (2700)

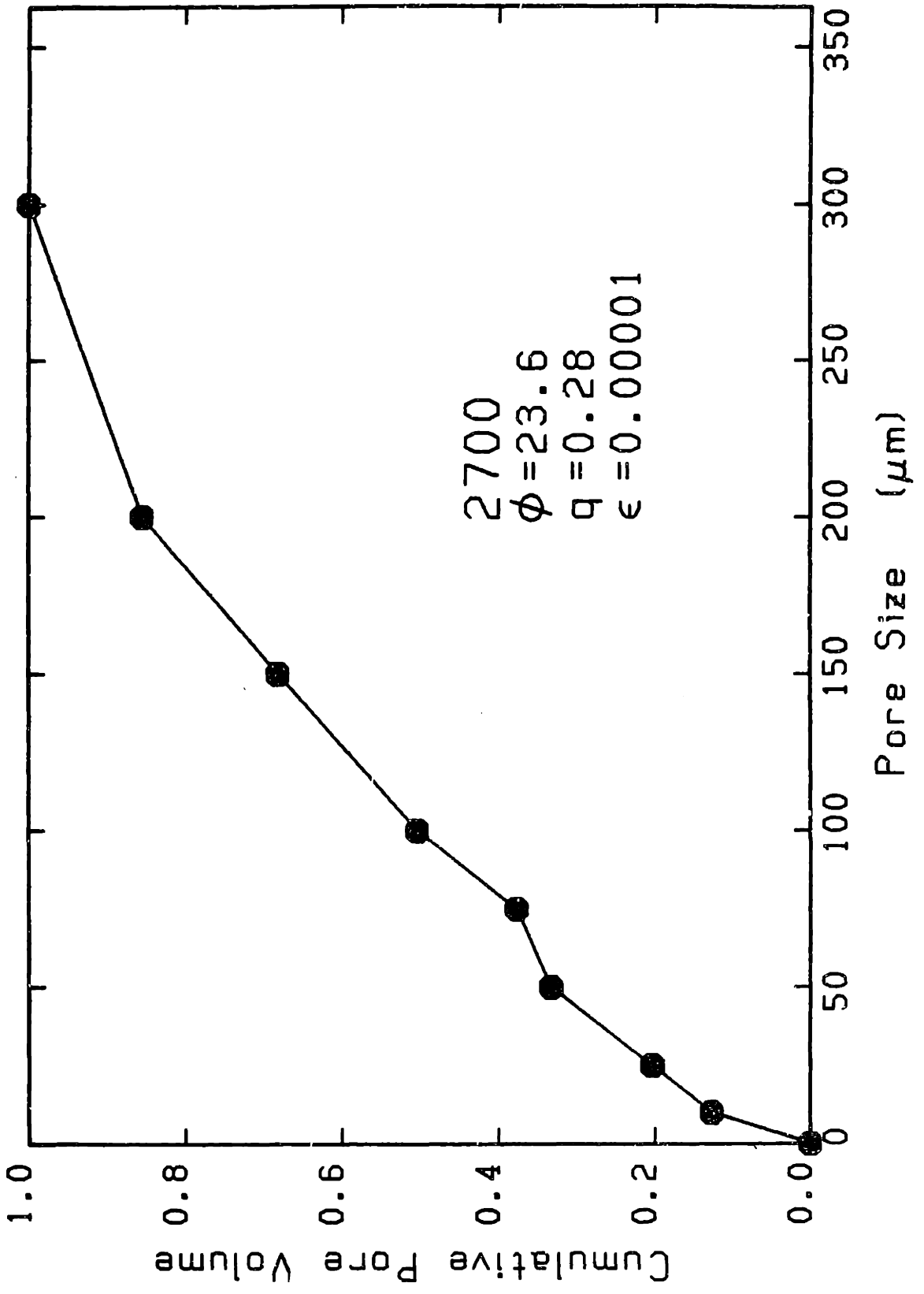

Figure 4.5j Volume Distribution of Pore Size (2704)

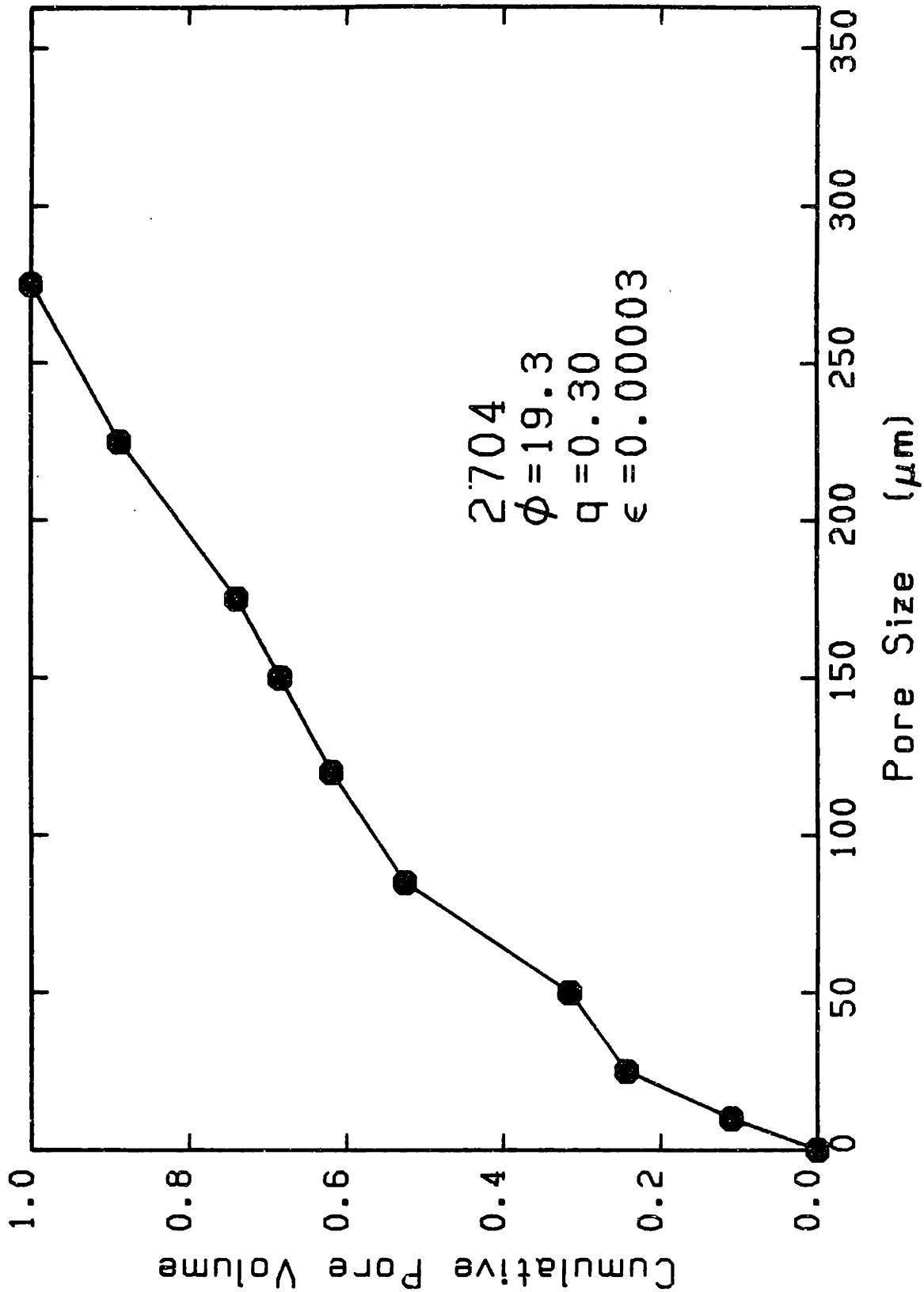

Figure 4.5k Volume Distribution of Pore Size (2710)

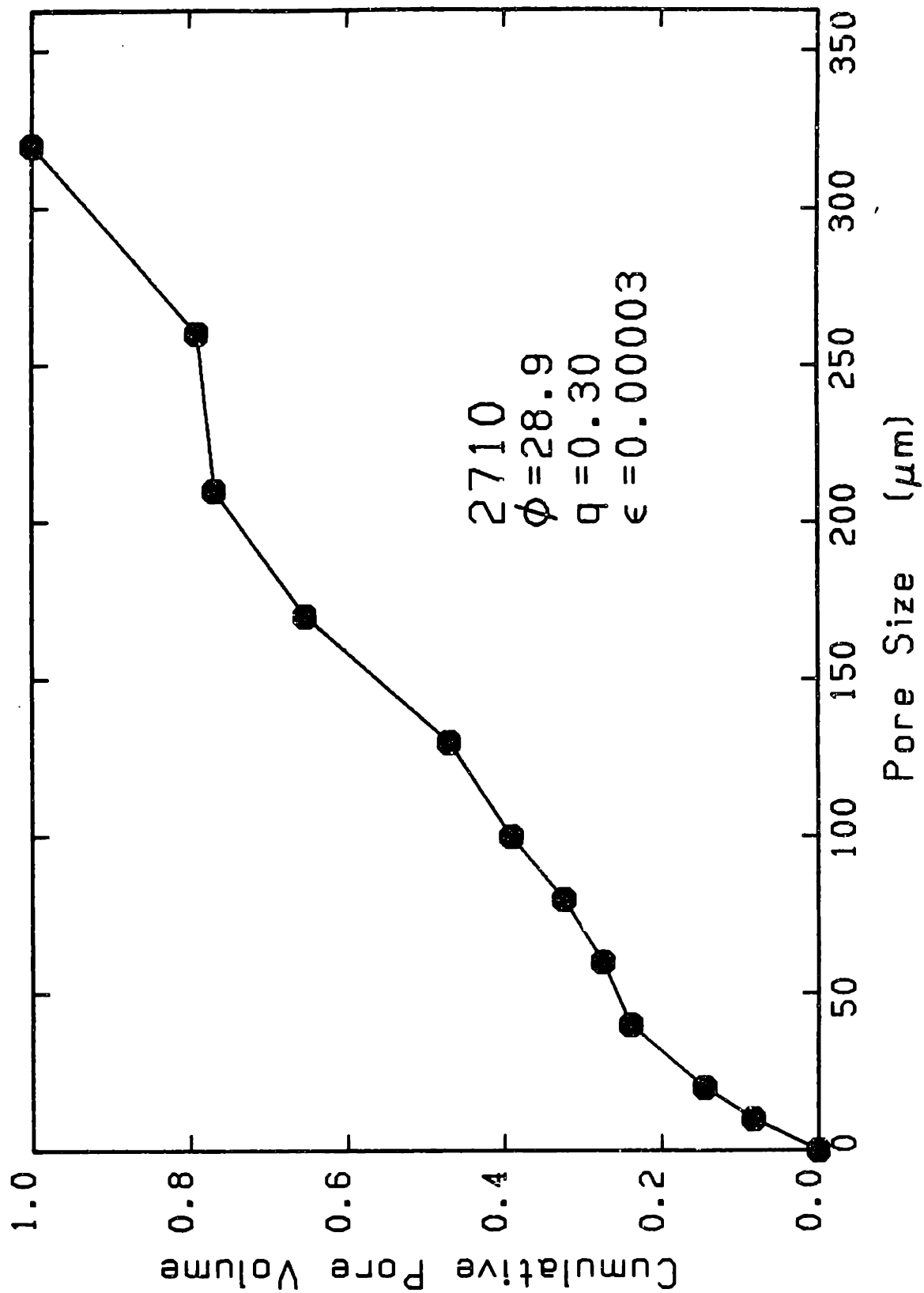

Figure 4.51 Volume Distribution of Pore Size (2841)

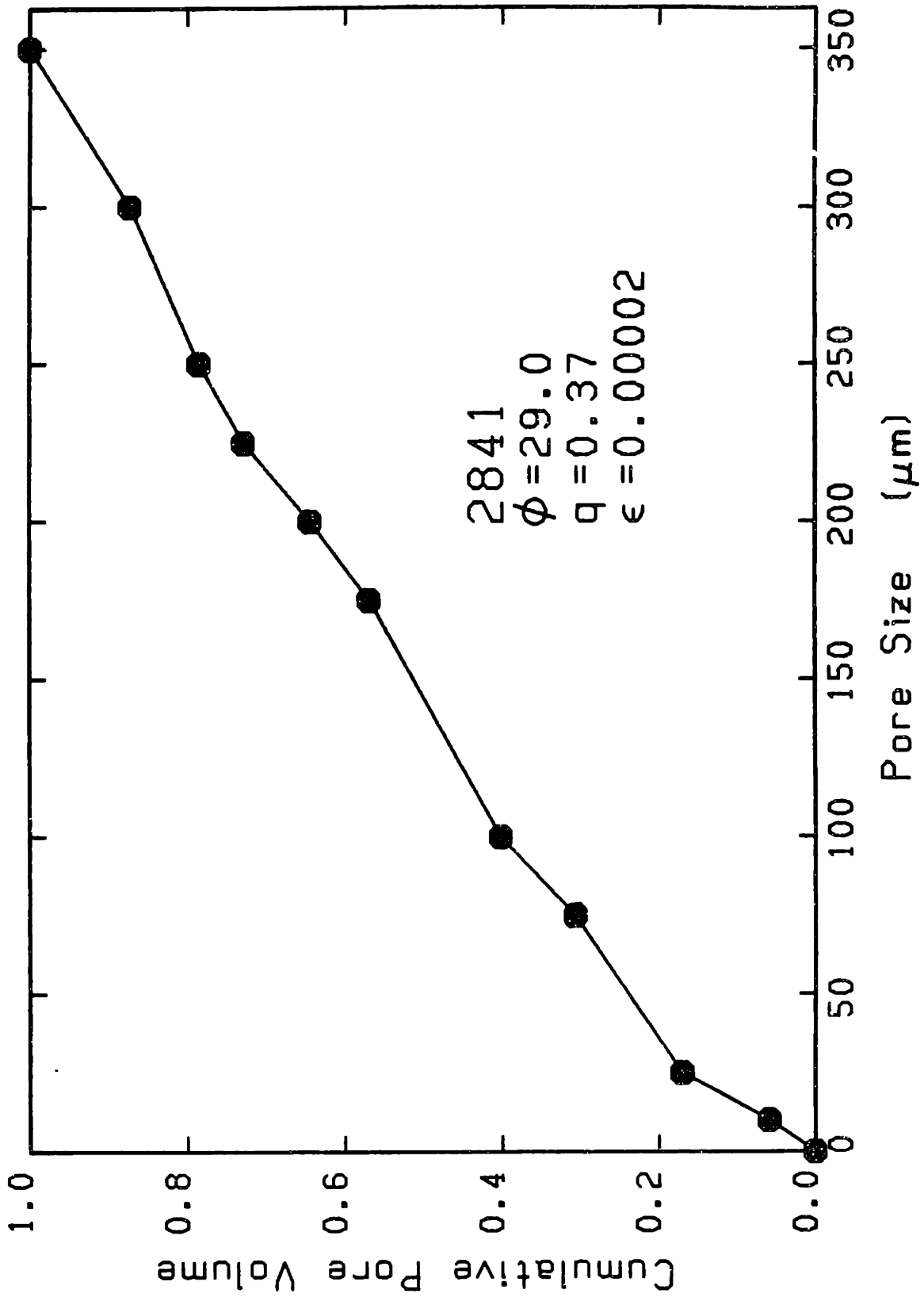

Figure 4.5m Volume Distribution of Pore Size (2842)

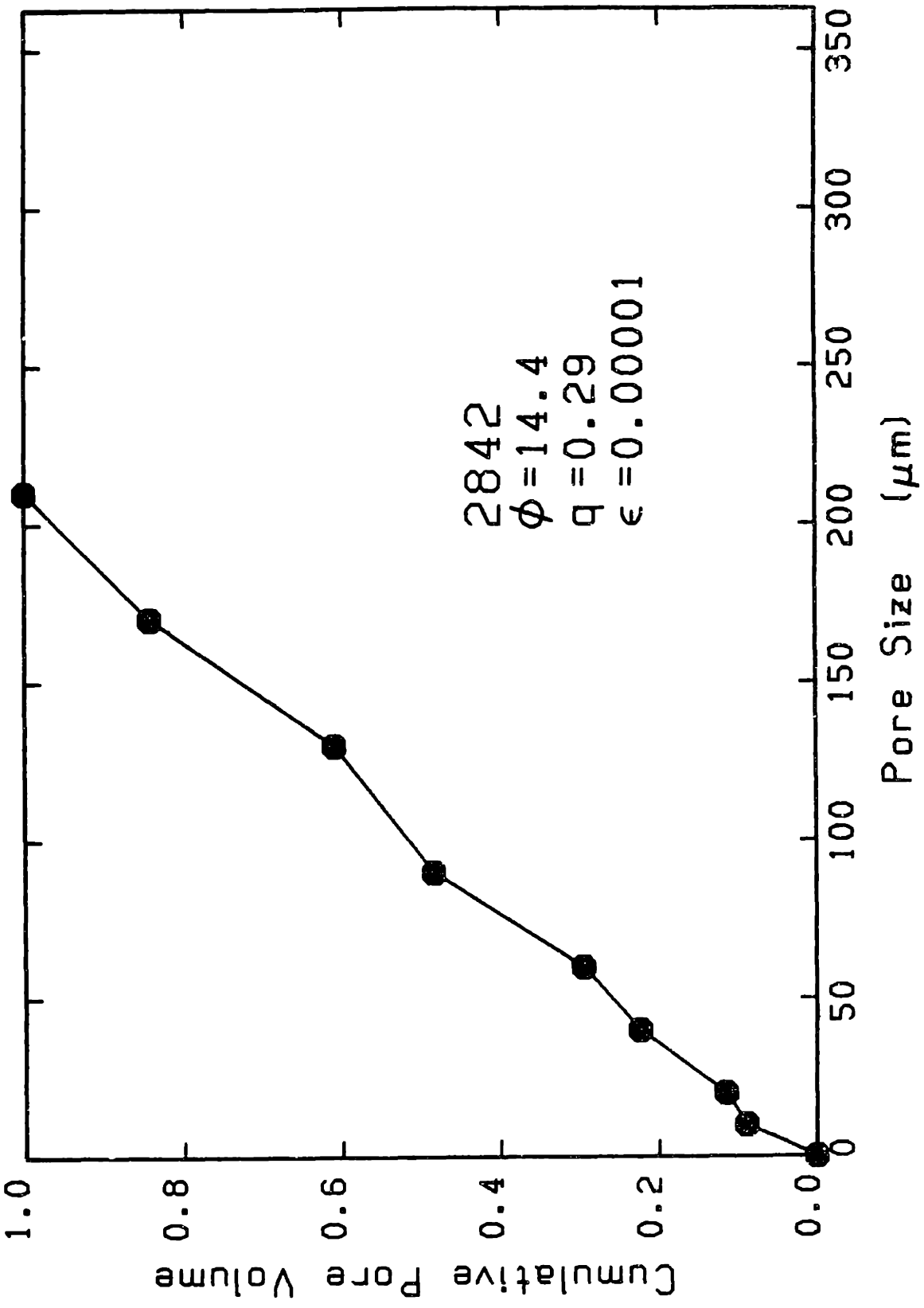

Figure 4.5n Volume Distribution of Pore Size (2843)

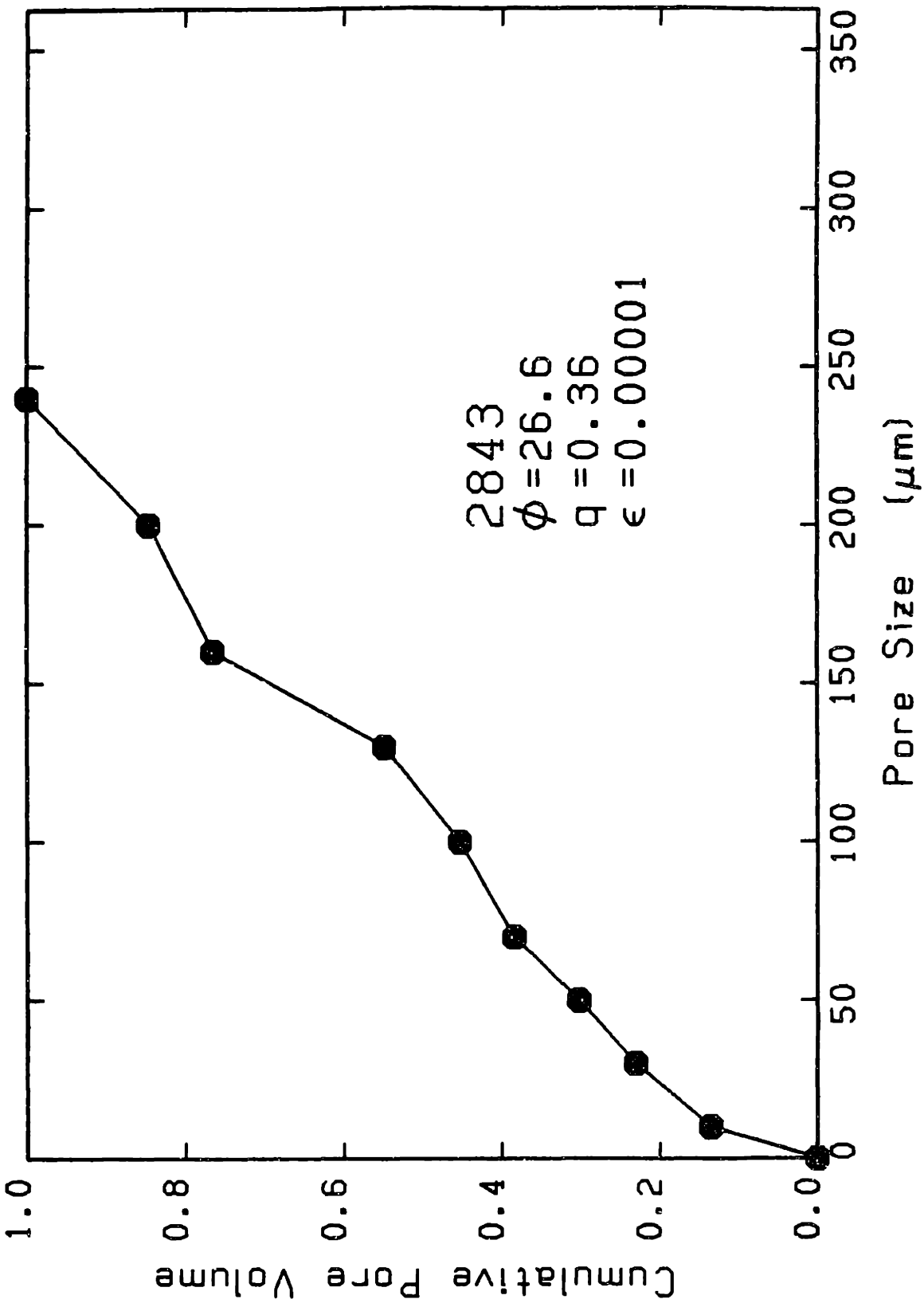

Figure 4.6 Point-sampled Intercept Length Distribution

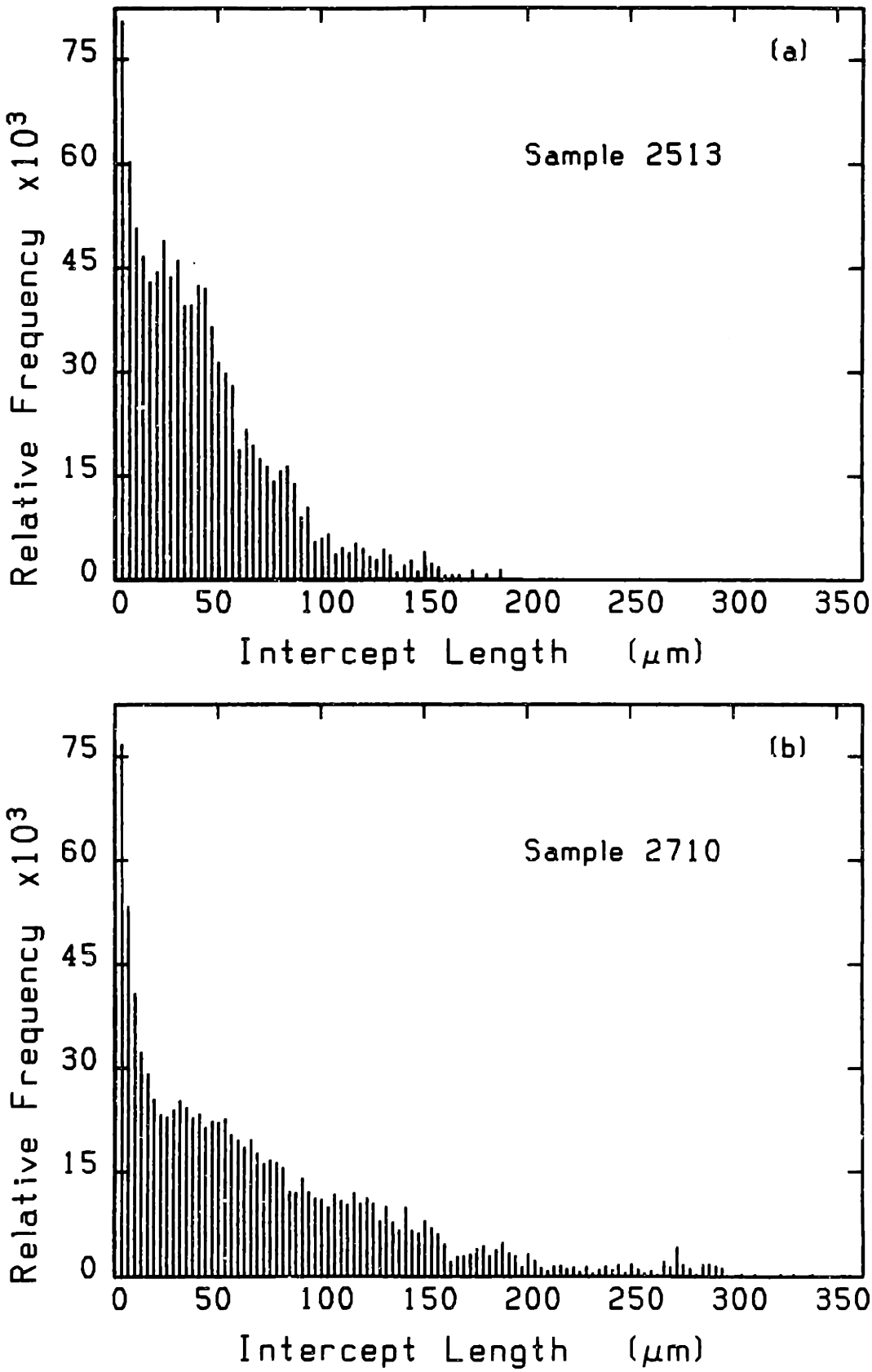

Chapter 5

Feature Analysis of Sandstone Images

5.1 Introduction

In this chapter, methods of feature analysis are applied to binary digital SEM images of sandstones. The results of feature analysis are measures of the character of the *features* (i.e., pore cross sections) in the image. Some feature parameters can be inverted by stereological methods to provide geometrical information about the three-dimensional structure. Other feature parameters can be related empirically or via models to the physical properties of the material. We will examine both classes of parameters. The stereological parameters are important because they contain direct geometric information. The other parameters are important because they give information on structural variability (i.e., the range of characteristics which the pore space may assume). To date, little is known about empirical relations between feature parameters and physical properties. Feature analysis has been used commonly to measure bulk stereological parameters (e.g., porosity, specific surface, Fischmeister's shape factor).

Our use of feature analysis is an application within the more general category of "shape analysis" in image processing. Pavlidis (1978) reviewed the

algorithms for shape analysis and divided the methods according to several significant differences among them. He distinguished the algorithms based on whether they operate on the whole feature area or just on the feature boundary. A second distinction was made on the basis of whether the output of the algorithm was an image (space domain technique) or a scalar (scalar transform). A third distinction was made between algorithms which preserve information (allow reconstruction of the image) and those which don't preserve information. Generally, for the quantitative description of pore space, we prefer those algorithms which operate on the whole feature area, those algorithms which produce a scalar result, and those algorithms which preserve information. These attributes are addressed in this chapter. Briefly, our reasons for the preferences are: 1) the whole feature area methods are more robust than feature boundary methods, 2) scalar results can be used in subsequent modeling and correlation studies, and 3) a quantitative description of the pore space is desired, not a classification.

Below, we address feature segmentation, individual feature analysis by local methods, and one method of feature analysis by a global method. The decomposition of complex features into simpler components is termed *segmentation*. Strictly, segmentation should not be required when feature analysis is used to measure bulk stereological parameters. For other applications of feature analysis, segmentation is essential for a tractable analysis. A new method of segmentation is presented and applied to sandstone images. We also investigate the effect of segmentation on the bulk stereological parameters.

Two methods of individual (local) feature analysis have been considered in this study. The first method consists of mapping the boundaries of the features and using these boundary contours to measure the desired feature parameters. This method was found to be inferior to the second method for our purposes. Results from the application of the boundary method to sandstone images are

not presented.

The second method of individual feature analysis is a modified form of the line-by-line comparison method of Rink (1976ab). A major improvement to the line-by-line method is our separation of the measurement of primary parameters from the computation of secondary parameters and the compilation of statistics. We present the results of individual feature analysis of sandstone images.

Global feature analysis has been done by applying the opening operation (erosion-dilation sequence) of mathematical morphology to digital images. The feature sizing accomplished in this manner is termed *granulometry* by Delfiner (1972). Granulometry results in a distribution of feature area as a function of the size of the largest structuring element which "fits" within the features. Granulometry is distinct from individual feature analysis in that it does not require segmentation of the binary image. Results of granulometry of sandstone images are presented.

5.2 Feature Segmentation

The features of the pore phase usually appear on the binary image as complex, convoluted shapes which defy simple description. For example, the feature may result from the image plane cutting through several "distinct" pores and connecting pore throats (Figure 5.1). For individual feature analysis of a continuous phase (i.e., the pore network), the connected complex features must be divided into simpler features which can then be analyzed. Typically, these simpler features are nearly convex, whereas the original features may have re-entrant angles. Segmentation is required to simplify the arbitrarily complex true features into features which satisfy the assumptions inherent in the shape descriptors and which then present a tractable problem. However,

we must strive to preserve the essential aspects of the structure for the intended application of the feature analysis results.

Rink and Schopper (1978) advocate and employ a feature segmentation process in their analysis of sandstone images. They state that the data from the simplified features better represent the hydrodynamic behavior of the rock than the data from the original features. That is, the hydraulic radii of the simple features are closer to the effective hydraulic radii that fluids respond to in the rock. Their study is an example of segmentation justified by the application. However, one should be wary of the use of segmentation to alter the results of an analysis so that they support the model under investigation. We will demonstrate that segmentation has a significant effect on structural parameters.

A new method of feature segmentation has been developed for application to sandstone images. Before the new method is presented, we review previous methods of segmentation.

5.2.1 Segmentation by Opening

The opening operation of mathematical morphology is one of the simpler methods of segmentation. The opening of X by $\check{B}$ is defined in terms of erosion and dilation as

$$X_B = (X \ominus \check{B}) \oplus B \,, \tag{5.1}$$

where erosion is defined as

$$X \ominus \check{B} = \{x : B_x \subset X\} \,, \tag{5.2}$$

and dilation is defined as

$$X \oplus B = \{x : \check{B}_x \cap X \neq \emptyset\} \,. \tag{5.3}$$

The set X represents all of the pore pixels of the image, and a set with a lower case subscript (vector) indicates translation of the set by the vector (e.g., X_b is X translated by b). The set B is the *structuring element* used in the opening. For segmentation and sizing, B is typically an approximation, on the discrete grid, of a disk. The "check" indicates the reflection of the structuring element (or set) through the center (or origin). This reflection is also referred to as the transpose of the set (Serra, 1982). The erosion operation identifies the points (i.e., pore pixels) at the origin (i.e., center) of B where B can be positioned and is fully contained in X. The dilation operation identifies the points at the origin of B where B can be positioned and it intersects X. The opening operation identifies *all* points of B where B is fully contained in X. For additional background on these operations, see Watson (1975), Serra (1982, Ch. 2), and Fabbri (1984, Ch. 3).

Opening segments features by removing smaller connective pieces between features. Opening also eliminates small features and removes small details of larger features. The small features are lost and the accuracy of the larger features is reduced. Segmentation by opening imposes the shape of the structuring element on the segmented image. These disadvantages may not be detrimental depending on the subsequent image analysis to be performed and the intended use of the results. The loss of features which are smaller than the structuring element is the primary disadvantage of segmentation by opening. Figure 5.2a through 5.2d are examples of segmentation by opening of Figure 5.1 with structuring elements of different sizes. Note the smoothing of the larger features and the absence of the smaller features. Pseudo-octagonal structuring elements have been used for the opening and are described in more detail in section 5.6. Note that the features tend toward the convex shape of the structuring element for larger openings. In this example, we used the *ad hoc* assumption that the border touching features extend indefinitely beyond

the image border. Such an assumption is valid for segmentation purposes, but is questionable for granulometry (see sections 5.2.5 and 5.6).

5.2.2 Segmentation by Cutting—Rink's Method

Rink (1976a,c) recognized the limitations of segmentation by opening and developed the "cutting" process. Although he described the process verbally, he did not provide an algorithm. Basically, he combined opened and dilated images with the original image such that the features were "cut" into simpler shapes. Figure 5.3 is a schematic of the cutting process used here which produces results like those described by Rink (1976ac). The original image, A, is opened to produce image B_i, where i represents the size (or step) of the opening element. This opened image is dilated by one step to produce image C_i. The opened and dilated image contains features which were larger than the opening step, and these features are larger, by one dilation step, than the original features. Images B_i and C_i are combined by eXclusive OR (XOR) to produce the cutting image D_i. This cutting image contains the perimeter pixels which were just outside the features on the opened image. The cutting image is used as a template to erase pixels (E_i BIC D_i) in the original image. The bit clear operator, BIC, or equivalently, the set difference, is used to clear set bits (i.e., remove pore pixels) in the original image if the corresponding bit (pixel) was part of the cutting template in the cutting image. The BIC operator is equivalent to (D_i^c AND E_i), where the ^{c} indicates complementation. Rink (1976a) suggested that cutting be repeated until no further segmentation takes place.

Subsequent to cutting the original image with several cutting images, the cut image can be opened by one step to remove "relics" of the cutting operations and produce the "clear cut" image, H. The smallest features of the original image (i.e., those lost by the final one step opening) can be restored to

the clear cut image by filtering them out of the original image, G, and adding them to the clear cut image to produce the "clear cut+" image, !. From the reasoning of Rink and Schopper (1978), it is not necessary to add back the smallest features for hydrodynamic applications because they contribute little to the hydrodynamic response.

Figures 5.4a through 5.4d illustrate 4 stages of the cutting of Figure 5.1, and Figures 5.5a through 5.5d illustrate the corresponding clear cut images. Figures 5.4 and 5.5 correspond to the F and H images, respectively, on Figure 5.3 for different n. The symmetric structuring elements described in section 5.6 were used during opening and erosion operations. Again, we used the *ad hoc* assumption that the boundary touching features extend indefinitely beyond the image border. Comparison of Figures 5.4 or 5.5 with Figure 5.2 shows that cutting imposes the same smoothing effect on the features as does opening. In fact, the features which remain at each opening step are *identical* to the corresponding features at the equivalent cutting step. Details of the features have been lost and there is a tendency in feature shape toward the structuring element shape. The porosity lost during each cutting operation is given in the figure caption. Figure 5.4 also shows that intermediate sized features, cut from the larger features, are chopped into many small pieces. These are the "relics" mentioned by Rink (1976a). The final opening of cut images, used to remove these relics, actually removes many of the intermediate sized features along with the smallest features (compare Figures 5.2c and 5.4c). Thus, cutting suffers the same drawbacks as opening but to a lesser degree. With cutting, not all features smaller than the largest opening are lost. Cutting also has the advantage that it produces a single output image. This single image was desired by Rink (1976a) so that his analysis could be completed "in just one computer run."

Both cutting and opening have a "cookie cutter" effect, whereby a dispro-

portionally large number of features are produced which have the same shape and area as the structuring element used.

5.2.3 Segmentation and the Boundary Image

A method of feature analysis which was tried and rejected in this study was based on the measurement of feature boundaries. We tried the method primarily to measure feature boundary curvature and bending energy (see section 5.3.1). The segmentation process for this analysis method consists of the sequence of steps which produce the boundary image. Two different methods have been used to produce feature boundary images. The first is from Moore (1968) and is termed the "CUSTER" operation after the well-known general. In Moore's words, "In this operation the image points originally located at the perimeter of a particle (feature) are preserved, while all those in the interior are eliminated." This operation is based on the logical combination of the 9 elements in a matrix (3×3) operator and is one special case of the BITOP command (see Chapter 2). The CUSTER operator could also be cast as a Hit or Miss transform of mathematical morphology (see Serra, 1982, Ch. 2). A pixel is assigned to the boundary image if that pixel (center element) lies on a pore pixel and one of the four corner pixels lies on the grain phase. A wider boundary can be generated by weakening the condition and requiring any one of the eight neighboring elements to lie on the grain phase. Figures 5.6a through 5.6d are examples of the CUSTER operation applied to the opened images of Figure 5.2.

A boundary image can also be derived by a combination of erosions and logical operations. The starting image is first eroded by one step. This eroded image is combined with the starting image using the eXclusive OR (XOR) operator to remove pixels from the interior of the features. The results are identical to those in Figure 5.6 provided that the starting image has been

"cleaned" or opened prior to making the boundary images.

Cleaning consists of an opening of the pores followed by an opening of the grains. These two steps eliminate the smallest pore features and the smallest grain features (i.e., "floating grains" in pores). Opening or cleaning the image is required because a simple boundary tracing algorithm was used. Otherwise, the boundary tracing is likely to fail. Indeed, some of the boundaries in Figure 5.6a would not be mapped correctly. A more sophisticated boundary tracer may not require such cleaning The segmentation of features in the boundary image is largely dependent on the element size used in cleaning or opening. If the CUSTER operation is applied to the images produced by SMS segmentation (see section 5.2.5), tractable boundaries are produced and only a small amount of detail is lost. The smallest features cannot be mapped and may not be negligible for some applications.

The loss of resolution on the larger features and the inability to map the smallest features are the primary drawbacks of the boundary analysis method. Duda and Hart (1973, p. 290) discuss additional difficulties with boundary mapping methods.

Boundary images are similar to cutting images. The boundary image consists of the perimeter pore pixels of the features, whereas, the cutting image contains the layer of grain pixels surrounding the feature. The similarity is reflected in the analogous processes used to create the images.

The structuring elements and cleaning methods used to create the boundary image determine the connectivity of the boundary contour. Specifically, erosion by plus "+" structuring elements eliminates right angle "L" connections. Rather, the connection will be along a diagonal.

5.2.4 Segmentation by Connected Criterion

For the line-by-line feature analysis method, a limited degree of feature segmentation can be effected by requiring that the chords of a feature be 4-connected. A chord in the investigation line is 4-connected to a chord in the previous (comparison) line if both chords have pixels in a common column. The simplicity of this criterion allows it to be easily included in the line-by-line feature extraction program. This simplicity is reflected in the limited degree of segmentation produced.

This criterion is effective for images which have not been opened by more than a single step, and it is desirable in this case. The criterion has no effect on images which have been opened by more than one step. Images which have been opened two or more times contain only 4-connected features. That is, the structuring elements used here do not preserve any single-pixel diagonal connections for two steps or more. Thus, if opening is used for pre-processing the binary image, then the connectivity criterion will be useful only for the one step opening. If cutting is used for pre-processing segmentation, the connectivity criterion can be applied to all stages of cut images, provided that only one opening has been applied to the original or cut image.

We use the 4-connected criterion when analyzing the images produced by SMS segmentation. This is particularly important for the final SUB image which contains the smaller features.

5.2.5 Subtractive Mask Segmentation—SMS

One motivation for Rink's segmentation by cutting was that the final result was a single image. Thereby, he could perform a full analysis, including statistical analysis, "in just one computer run." Because several images are generally required to produce statistically valid results we have taken a different

approach for segmentation, feature extraction, and statistical analysis. Our segmentation of a single image produces several images which contain parts of the original pore features.

This new method of segmentation, termed *Subtractive Mask Segmentation* (SMS), overcomes some of the limitations of segmentation by opening or cutting. SMS uses operations of mathematical morphology (i.e., erosion, dilation, and set combinations) to perform the segmentation. Aspects of both the opening and cutting segmentation are used by SMS. Segmentation by SMS is also similar to the method used by Moore (1968) to eliminate features smaller than some selected size, yet accurately represent the larger features.

Figure 5.7 is a flow chart of the SMS process and Figure 5.8 shows the result of SMS segmentation of Figure 5.1. The first operation of SMS is an opening of the original image which preserves only the features larger than some selected size. The opened image is then dilated by one step to produce a mask image. This mask image is then combined with the starting image (original) via an intersection operation. All pixels which represent pores in *both* the original and the mask image are included in the output. We term the resulting image an SMS image. It contains features which were equal to or larger than the selected size. The dilation of the mask image before combination restores some of the small detail on the large features which was lost during the opening. Next, the SMS image is subtracted from the starting image to produce a SUB image. The SUB image contains only features which are smaller than the size used to produce the SMS image.

The SMS sequence is repeated using the SUB image as the starting image. A second SMS image is produced which contains features which are smaller than those in the first SMS image. Another SUB image is produced, and the SMS sequence may be repeated. Typically, 3 or 4 iterations are required for adequate segmentation. The resulting 3 or 4 SMS images and the final SUB

image together contain all of the pore pixels of the original image. Figures 5.8a through 5.8d show the results of SMS segmentation applied to Figure 5.1.

5.2.5.1 Selection of Opening Sizes

The opening size used to produce each SMS image is determined subjectively at present. We select the opening which breaks the largest connection in the image and gives nearly convex features. The sizes used for the SMS segmentation of Figure 5.1 dictated the opening and cutting images displayed in Figures 5.2 and 5.4.

To automate the segmentation and remove subjectivity, the size of the opening could be conditional on the character of the resulting features. We could require that the resulting features have a convex deficiency less than some prespecified value. Convex deficiency is the difference in area between the feature and its convex hull (Duda and Hart, 1973, p. 352). Alternatively, some other measure of convexity could be used, such as the bulkiness from the dynamic feature parameters.

5.2.5.2 Advantages of SMS

The features produced at each step by SMS are similar to the features in the opened or cut images except more detail is preserved by SMS (compare Figures 5.8 and 5.2). Also, the intermediate sized features (Figures 5.8b and 5.8c) are intact. In general, SMS produces an intuitively appealing segmentation. All of the porosity and the smallest features are retained. Small features can later be eliminated in the statistical analysis if desired. The "cookie cutter" effect is also reduced in the SMS process.

We investigated, but abandoned, the segmentation processes (i.e., fast segmentation and segmentation by watersheds) discussed by Serra (1982, Ch. 11). The reasons for not using those methods were: 1) the relative complexity of

the algorithms, 2) inconsistencies and errors in Serra's thickening and segmentation formulae, and 3) the development of the SMS segmentation which yields very good results.

A modification of the cutting segmentation yields a single segmented image which is quite similar to the SMS images. In this modification, only those cuttings corresponding to the opening steps of the SMS segmentation are applied to the original image (Figure 5.9). There is still some loss of porosity and feature details, so we prefer the SMS method.

Figure 5.10 shows the results of applying the CUSTER operation to the SMS and final SUB images. All boundaries of the SMS images, including the closed boundaries of the SUB images, are mapped properly. Details consisting of unclosed strings of more than one pixel are lost.

5.2.6 Segmentation Summary

The SMS segmentation method is better than opening or cutting because it preserves all of the porosity and does not fragment the intermediate sized features. Also, it yields an intuitively appealing segmentation. The method is easy to apply and is not computationally intensive.

There are applications for which segmentation may not be necessary (e.g., determining bulk stereological parameters) and the unsegmented image will yield a valid analysis. However, most models of physical properties consider simplified or highly idealized models of the pore structure. Thus, the motivation for segmentation is to reduce the complex pore features to the simpler shapes which can be used in models or compared with model results.

5.3 Parameter Measurement

After the binary digital image has been segmented, the primary feature parameters may be measured. These primary feature parameters are listed in Table 5.1. The line-by-line analysis method measures these primary parameters directly. The boundary mapping method stores a representation of the feature boundary from which the primary and secondary parameters can be computed.

5.3.1 Feature Parameters from Feature Boundaries

Moore's (1968) approach to feature analysis was to copy a feature into a work area then measure the parameters of the feature. Our method of creating a feature boundary image and mapping the boundaries is similar to Moore's approach in that features are identified and analyzed one at a time.

The procedure for mapping boundaries is straightforward. First, the boundary image is searched from the upper left corner, line-by-line, until a boundary pixel is detected. The coordinates of this pixel are stored together with an index for the boundary. The 8 neighboring pixels are then searched, in a clockwise direction from 12 o'clock, for the continuation of the boundary. The direction code for the next boundary pixel is stored with the starting coordinates. The location pointer is moved to this next boundary pixel and the neighboring pixels are again searched. By repeating the search, record, and move procedure, a direction code string is compiled which maps the location of the boundary pixels of the feature. The direction codes of Freeman (1961) are used to describe the direction of the boundary (Figure 5.11). Direction codes are used because they take less space than a table of boundary pixel coordinates. The coordinates of a boundary pixel are obtained by adjusting the starting coordinates according to the direction codes which point to the

pixel. As each boundary is mapped, it is erased from the boundary image. When the end of the boundary is reached, a termination code is appended to the direction codes. The termination code may indicate boundary closure, intersection with a side of the image, or an unclosed boundary due to failure of the boundary follower. If the termination code is other than the closed boundary code, the location pointer is repositioned to the starting pixel and the boundary is searched in the "other" direction. Direction codes for this second search are appended to the previous codes.

The boundary following algorithm used was very simple. The algorithm does not remember the last direction in which it moved and it moves to the first new neighbor it finds. Consequently, if the boundaries are not well-behaved, the boundary mapping does not work well. Specifically, if two closed contours are touching (4-fold or 8-fold), the algorithm may cross over from one to the other and conclude that the boundary for the active feature is not closed. For non-touching closed boundaries the boundary mapping works well.

With a complete map of the feature boundary, additional feature parameters can be obtained which are not obtainable through the line-by-line method. Specifically, more elaborate descriptors of boundary shape, such as Fourier methods (Schwarcz and Shane, 1969; Ehrlich and Weinberg, 1970) or fractal analysis (Kaye, 1984), may be applied. However, the value of such a specific characterization of pore feature shape has not been demonstrated to date. A good review of other two-dimensional shape descriptors is given by Clark (1981). Our motivation for boundary mapping was specifically the computation of the "bending energy" (Young *et al.*, 1974).

5.3.1.1 Parameters from Chain Codes

Three feature parameters can be readily computed from the boundary chain codes. These are area, perimeter, and bending energy stored in the boundary.

Secondary parameters which are based on these three are also readily computed (e.g., perimeter-to-area ratios). Area, a, is obtained from a boundary integral over the coordinates of the feature boundary. For a discrete approximation we use,

$$a = \sum_{i=1}^{n} \frac{y_{i+1} + y_i}{2(x_{i+1} - x_i)} , \tag{5.4}$$

where the point (x_{n+1}, y_{n+1}) is the same as the point (x_1, y_1). The sign of this summation can be changed, depending on the coordinate conventions used and depending on the direction of the boundary traverse. An adjustment is made to the value obtained with Eqn. (5.4) to yield the area which is truly occupied by the feature pixels, as opposed to the area within the polygon defined by the central coordinates of each pixel. The dichotomization process assigns a pixel to the pore phase if it contains more than 50% pore by area. Thus, the full area of all pixels of the feature is the best measure of pore area. Because boundary chain coordinates give the location of the center of the boundary pixels, the area estimate will miss a one-half pixel wide strip around the perimeter of the features. The adjustment consists of adding one-half of a pixel area for each boundary pixel and adding one more pixel area to account for the four extreme corners of the feature which are not accounted for by the original equation or the first adjustment.

Perimeter is computed with the equation,

$$p = d(N_{\text{even}} + \sqrt{2}N_{\text{odd}}) , \tag{5.5}$$

where d is the pixel size, N_{even} is the number of even direction codes, and N_{odd} is the number of odd direction codes (Castleman, 1979, p. 324). An adjustment is also made to the perimeter by adding two pixel widths to the value computed with Eqn. (5.5). In a manner analogous to the area adjustment, this adjustment moves the perimeter to the outside of the pixels which comprise the boundary.

Bending Energy—Bending energy is a two-dimensional shape descriptor of simply connected closed contours which was developed by Young *et al.* (1974). The bending energy, E_{bend}, represents the amount of work required to form the contour out of an initially straight linear medium. E_{bend} is a function of the contour length and is a minimum for any given length if the contour forms a circle. The "average bending energy per unit length" as formulated by Young *et al.* (1974) is essentially an integral, over the length of the boundary, p, of the line-curvature squared, $|k(p)|^2$. They give the equation,

$$E_{\text{bend}} = \frac{1}{p}\int_0^p |k(\acute{p})|^2 \mathrm{d}\acute{p} \,. \tag{5.6}$$

Note that although E_{bend} appears to be normalized by perimeter length in Eqn. (5.6), the E_{bend} is ***size dependent***, which violates a usual requirement for a shape descriptor (Fischmeister, 1974a; Underwood, 1975; Clark, 1981).

Young *et al.* (1974) also gave an algorithm for computing the bending energy from the Freeman chain codes, C_F, of a boundary. The algorithm approximates the curvature at each boundary point from the previous and next direction codes. The curvature is simply the change in direction of the boundary per unit boundary length. The angular change can be 0, $\pm\pi/4$, or $\pm\pi/2$ depending on the code sequence. The boundary length increment is taken as,

$$\Delta p = L(C_F(n)) + L(C_F(n-1)) \,, \tag{5.7}$$

where

$$\begin{aligned} L(m) &= d/2 \qquad \text{for } m \text{ even} \\ &= d\sqrt{2}/2 \quad \text{for } m \text{ odd} \,, \end{aligned}$$

and d is the pixel size. The maximum line curvature expressible on a digital grid is thus,

$$k_{\max} = \pi/d \,. \tag{5.8}$$

The maximum curvature in the boundary images produced by our methods is $\pi/2d$.

The simple algorithms presented by Young *et al.* (1974) are not correct. Specifically, the difference chain, used for determining the directional change from one point to another, does not give the correct angular change in direction for the following code combinations,

$C_F(n-1)$	$C_F(n)$	Difference Angle	Correct Angle
0	6	$6\pi/4$	$-\pi/2$
0	7	$7\pi/4$	$-\pi/4$
1	7	$6\pi/4$	$-\pi/2$
6	0	$-6\pi/4$	$\pi/2$
7	0	$-7\pi/4$	$\pi/4$
7	1	$-6\pi/4$	$\pi/2$

We have avoided the errors in angular change by using a lookup table accessed by the current and previous chain codes. Invalid chain code sequences (e.g., backtracking) are recognized by special codes in the lookup table.

Also, in their discrete formulation for estimating E_{bend} from boundary chains (their last unnumbered equation on p. 369) Young *et al.* (1974) have dropped the boundary length increments (Δp) over which the summation is computed. Without the additional Δp, the E_{bend} computed for a simple 4 code circular boundary does not agree with the expected value of $(2\pi/p)^2$. After correcting the two errors, accurate results were obtained for simple test figures.

We attempted to reproduce the $P2A$ and E_{bend} values presented by Young *et al.* (1974) for the curves in their Figure 6. The curves were photographically enlarged by 7×. A grid was superimposed over the enlarged contour and the boundary codes determined from the grid. The grid spacing was 2.54

mm; slightly greater than the line width of the enlarged figure. There is general disagreement, the source of which is not known. Errors in our coarse hand digitization cannot explain the large differences in the $P2A$ ratio. Our perimeter measurements are probably slight overestimates due to the grid size and thereby give estimates of the maximum $P2A$. However, Young's values are *larger* than ours. The E_{bend} values can be made to match by careful choice of pixel size, but *different* pixel sizes must be chosen for each of the six shapes. Recall that E_{bend} is dependent on size.

Bowie and Young (1977ab) used the bending energy to study biological shape and concluded that it was superior to mean absolute curvature and $P2A$. They used many simplifying assumptions and dropped several constant factors to the extent that even their perimeter measurements are not accurate. Their simplifications are suitable for their application because the original contours are noisy and they are not interested in the metric character of the shapes, just the *classification* of the shapes. Their approximations are not valid for quantitative characterization.

5.3.1.2 Computing Parameters from Chain Codes

A computer program (**BDYSTA**) was written to compute area, perimeter, line-curvature, and bending energy from boundary chain codes. The parameters of line curvature and bending energy are unique to this analysis method. The other parameters can also be found by the line-by-line feature analysis method.

Boundary mapping and analysis were applied to boundary images from the SMS segmentation. Preliminary results from the analysis showed that the line-curvature and average bending energy reflected, primarily, differences in feature boundary length in these images. Because of this relation and the availability of the other parameters from the line-by-line analysis, we have not applied the boundary analysis to enough images to justify the presentation of

results.

The strength of the E_{bend} lies in the analysis of feature shapes which are more complex than those in our segmented images. Such an analysis is not in line with our approach of segmentation and analysis of simpler features. Additional difficulties can be expected when producing boundary images from the non-segmented images. We decided not to persue this line of analysis.

As mentioned above, the E_{bend} is basically a measure of the mean squared line curvature of the contour. By casting the E_{bend} in this manner, the physical significance is apparent, as is the dependence on feature size.

5.3.2 Line-by-Line Parameter Measurement

A computer program (**FTREXT**) has been written to extract primary feature parameters (see Table 5.1) using the line-by-line comparison method of Rink (1976a). All parameters described by Rink as well as several additional parameters are compiled for the interpretation of digital SEM images. These primary parameters are essentially the same as those given by Moore (1968, p. 96). The "special cases" for feature extraction, which are apparently described in an earlier paper (Rink, 1970, as cited by Rink, 1976a), have been treated. These special cases include the merging of originally independent features, the splitting of a feature, and the rejoining of a split feature. Agrawala and Kulkarni (1977) also present a line-by-line method for extracting feature parameters.

Rink's method requires only 2 image lines in memory at any one time, and feature parameters are built up by intricate bookkeeping and indexing. In the line-by-line comparison method, the feature parameters for all features which cross the current test line are compiled simultaneously. Starting with the first line of the image, all chords on this line are assumed to be independent features and the parameters for the chords are recorded (e.g., end-point coordinates,

length, area). Each feature is assigned an active feature number. Line 2 then becomes the "test" line and line 1 the "comparison" line. All chords of the test line are checked for "connection" with chords of the comparison line. Connection is defined as both chords having a pixel in the same column of the image (four-connected), or less restrictively, having pixels in the same or adjacent columns (eight-connected). When a chord of the test line is connected to a chord of the comparison line, the feature parameters corresponding to the comparison chord are updated using the test line chord (e.g., add to the area, check for new minimum or maximum coordinates).

If a test chord is connected to more than one comparison chord, the feature parameters of all connecting chords are assigned to the lowest active feature number. Those chords which are not connected to active features are assumed to be the beginnings of new features and are compiled as such. After all chords in the test line have been accounted for, line 2 becomes the new comparison line and line 3 the new test line. The remainder of the image is processed in this manner.

A feature is complete when it is no longer increasing in size because of the addition of new chords. Following Rink (1976a), the area of each active feature is checked after each test line is processed. If the area does not increase, the feature is removed from the active list and the feature parameters are stored. Unlike Rink's "one run" approach, the primary parameters are stored for each feature. Secondary parameters and parameter statistics are subsequently computed from the stored primary parameters.

5.3.2.1 Secondary Parameters and Statistics

Secondary feature parameters are computed from primary parameters and consist mostly of two-dimensional shape factors (Table 5.2). These parameters are attempts to describe the feature by comparisons with simple shapes,

such as circles, rectangles and ellipses. The parameters which have been demonstrated to be useful for describing pore structure are area (for porosity), perimeter (for specific surface), a combination of these two (hydraulic radius), and Fischmeister's shape factor (for shape description). Note that these are all *stereological* parameters. Other stereological parameters available from feature analysis are the number of features per unit area, N_A, the mean intercept length, $\overline{L}$, and the positive tangent count, T_+. The utility of purely two-dimensional feature descriptors has not yet been demonstrated, but certainly they contain useful information about the structure. The representation of a feature by a "dynamically-equivalent" ellipse, in particular, yields very descriptive information. The dynamic parameters are discussed in section 5.3.3.

A computer program (**FTRSTA**) has been written to compute secondary parameters and compile frequency statistics for both primary and secondary parameters. Filters may be applied to any primary or secondary parameter to include or exclude particular features in the statistics. For example, an obvious filter is one which selects features with areas within a particular range. Our separation of feature extraction (primary parameter measurement) from the statistical analysis yields a very flexible analysis system. Each image is analyzed only once. Subsequently, all analyses are applied to the stored primary parameters. The features from one image can be selected with a set of filters and combined with the features from another image selected with different filters. Special consideration is required for the case of a single image which has been separated into several images (e.g., SMS segmentation). A flag is used to differentiate those images (i.e., primary parameter feature files) which represent additional analysis area from those containing feature data from the same area. The distinction is required mostly for computation of bulk stereological parameters.

The bulk stereological parameters of ϕ (Eqn. (2.1), area fraction), S_{V_p} (Eqn. (2.5)), mean pore intercept length (Eqn. (4.5)), and Fischmeister's shape factor, F (Eqn. (5.9)), are computed from all features which satisfy the filters. S_V and N_A are also computed. These parameters depend on the area of investigation and two different areas are used.

The first area is a listing mask specified by the user and the second is the area of the minimal mask which fully contains the counted features. The listing mask is used to provide a correction for sampling bias which depends on feature size. The listing mask is equal to or smaller than the image frame. To be counted, a feature must not touch the frame and the centroid of the feature must lie within the listing mask. Optionally, features which lie partially within the listing mask can be counted or rejected, depending on whether they touch the frame. Similarly, features which do not lie entirely within the listing mask can be rejected. Provided that the distance from the listing mask to the frame is greater than half the maximum Feret diameter of the features, the counted feature statistics will be unbiased. In practice, we have set the listing mask equal to the image frame and we have allowed frame contact. Some bias will be introduced by these choices, but it was deemed better to use the full image areas because we have only a few images for some rocks. In a routine analysis with a large number of images, the listing mask should be smaller than the frame.

The minimal mask is used only for the calculation of bulk stereological parameters. When computed using the area of the minimal mask, these parameters give maximum estimates for the porosity, the number of features per unit area, and the specific surface per unit bulk volume.

5.3.2.2 Rink's Inward Angle Correction

Rink (1976a) proposed the use of a right-angle inward corner count to adjust feature circumference and feature area measurements. An inward angle results whenever the end points of two connected chords are not in the same column. Rink states that the adjusted values represent, more accurately, the true feature values. His argument is valid for the perimeter adjustment, but unjustified for the area adjustment. The digitized representation of the perimeter undoubtedly gives an overestimate of the true perimeter, and the adjustment reduces the perimeter estimate. The maximum distance which the perimeter can travel through a pixel is the diagonal distance. The inward angle correction imposes this upper limit as opposed to using the sum of two sides of the pixel as the distance. Grant and Reid (1981) and Kulpa (1977) also use corrections for perimeter length.

The inward angle correction is *not* a valid adjustment of the area of the feature. In this case, the adjustment can only increase the area estimate of the feature. The pixels accurately indicate the phase which occupies more than 50% of the pixel area. Thus, the area estimate is unbiased and it cannot be improved. In Rink's schematic figure, the "corrected area" is seen to overestimate the feature area. Rink advocates the adjustment because the adjusted perimeter is still an overestimate of the true feature perimeter. However, neither the amount of bias remaining in the corrected perimeter measurement nor the amount of bias introduced by applying the correction to feature area is known. Without knowledge of the bias, the effect on the parameters or ratios of parameters cannot be known. It is unreasonable to apply a correction which produces an unknown effect.

5.3.3 Dynamic Description of Pore Features

A novel method of shape description, developed for particles, has a direct application to the description of pore structure. Medalia (1967, 1970) presented a "dynamic" method for describing objects by representation as an ellipsoid which has equivalent radii of gyration about the central principal axes. We are interested in the two-dimensional application in which a feature in a plane is represented by an ellipse which has equivalent radii of gyration about the central principal axes of the feature. Strictly speaking, both the feature and the equivalent ellipse are considered to be solid figures cut from thin sheets. The feature and the ellipse then have equivalent rigid body dynamic response (i.e., motion in space) when subjected to a force in proportion to the respective masses, which differ. The principal strengths of this method of representation are that 1) all points of the feature are used to compute the shape factors, 2) the shape factors are parsimonious, 3) feature orientation is obtained, and 4) the shape factors are robust (i.e., insensitive to minor variations in shape), yet easily computed.

Medalia (1970) principally treats two shape factors which are obtained from the dynamic analysis. Anisometry is the ratio of the axes of the equivalent ellipse, and bulkiness is the ratio of the area of the ellipse to the area of the feature. Our application to sandstones will emphasize the orientation of the equivalent ellipse, the location of the center of the ellipse (center of mass of the feature), and the anisometry.

Moments have also been used for pattern recognition, particularly with regard to character recognition (Hu, 1962; Alt, 1962; Castleman, 1979, Ch. 16). In these applications, the moments are often reduced to moment invariants which are independent of position, size, and orientation of the feature. Such properties are the essence of a geometric description of pore structure and must be preserved for our purposes. We are not trying to match pore features

with a pre-defined set of shapes (i.e., character recognition). Rather, we wish to describe, tersely, the infinite variety of feature shapes found in sedimentary rock images.

5.3.3.1 Calculation of Moments

Table 5.3 lists the equations for computing moments and dynamic shape factors. Moments of inertia for the feature are first calculated about the X and Y axes of the image (M_x, M_y, M_{xy}), using all pixel coordinates of the feature (see Table 5.1). These moments are combined to give the moments about the central principal axes of the feature (I_x, I_y, I_{xy}). The center of mass (centroid) of the feature (x_{cm}, y_{cm}) is also found from the pixel coordinates. The origin of the central principal axes frame is at the centroid of the feature, and the orientation of the feature (θ) is defined by the orientation of the major axis. Equations for computing moments of thin sheets can also be found in standard physics texts on mechanics.

The data used to compute the moments are obtained with the feature extraction program (**FTREXT**) and the calculations are performed in the feature statistics program (**FTRSTA**).

The ellipse used to represent the feature is defined by the central principal moments and the orientation of the central principal axes. The semiaxes of the ellipse are taken to be two times the radius of gyration of the feature. The radius of gyration, $K_{A,B}$, is a standard parameter used to represent the moment of inertia of a body. This radius is the distance from the axis of rotation at which a point mass, equal to the mass of the feature, would be placed to give an equivalent principal moment of inertia about that axis. The radii of gyration of an ellipse are equal to half of the semiaxes. Thus, a feature which is shaped like an ellipse will have a moment-equivalent ellipse which has identical semiaxes, identical principal moments of inertia, and identical

area (mass). Features which depart from the ideal elliptic shape have radius-equivalent ellipses which have a larger area (mass) and, correspondingly, larger principal moments of inertia.

5.3.3.2 Dynamic Shape Factor Calculation

The shape factors are anisometry and bulkiness. The anisometry, Q_{dyn}, is the ratio of the longer radius of gyration to the shorter radius. Bulkiness, B_{dyn}, is the ratio of the area of the radius-equivalent ellipse to the area of the feature and will always be equal to or greater than 1.0. The term bulkiness is used here in the sense of not compact as opposed the the sense of massive. A bulky feature gives a poor visual match to an elliptic shape. The departure of the feature from an ellipse is greater for larger values of bulkiness. Direct interpretation of the bulkiness factor is difficult. Generally, the bulkiness can be considered as a measure of the similarity between the feature and its convex hull. This similarity is in the sense of the ratio of the area of the convex hull to the area of the feature.

The orientation of the feature is taken as the orientation of the long axis of the ellipse with respect to the Y image axis and positive angles indicate a clockwise rotation. The image axes can be referenced to an absolute (i.e., rock) reference frame. The long axis of the ellipse is normal to the principal axis about which the feature has the largest moment of inertia. Note that the location of the centroid of the feature assigns an unambiguous location to the feature.

Medalia (1970) states that all of the dynamic factors, anisometry, bulkiness, and orientation are "unequivocal." He further illustrates that the dynamic factors are superior to parameters based on the convex hull of the feature such as the Hausner rectangle. The Hausner rectangle is defined by the two orthogonal Feret diameters of a feature which give the smallest area to

the rectangle enclosing the feature. Orientations determined by the dynamic method are also superior to those determined from the orientation of the maximum Feret diameter or from the orientation of the maximum intercept length. Both of the latter are boundary methods.

Boundary methods, based on convex hulls or intercept lengths, consider only a few extreme points of the feature, whereas the dynamic method considers all points of the feature. Thus, convex hull methods are overly sensitive to minor variations in shape. The dynamic method is reasonably sensitive to variations in shape. Further, the dynamic method is robust for re-entrant feature profiles, a situation which some shape descriptors (e.g., many Fourier series expansions) cannot treat.

Results from dynamic shape factor analysis of sandstone pore features are presented in section 5.5.

5.3.4 Curvature and Feature Analysis

The average mean curvature of a surface is a geometric property which can be measured without any assumption about the shape of the object (DeHoff, 1977). In this section, the descriptive limitations of average mean curvature are discussed. Simplistically, the average mean curvature measured for the pore features in sandstone images results in an alternative representation of the specific surface, but it gives no new information.

The average curvature of a closed curve on a plane is $+2\pi$ divided by the length of the curve, regardless of the complexity of the curve. Consequently, the average curvature does not distinguish between the two feature boundaries shown in Figure 2.3.

DeHoff (1977) developed the geometric interpretation of the integral mean curvature for the cases of convex particles, convex polyhedra, grain structures, and tubules. The integral mean curvature is the product of the average mean

curvature, $\overline{K}_m$, and the surface area. For convex particles, the integral mean curvature is related to the mean caliper diameter of the particles. Other than this relation, which is accessible by simpler methods, the integral mean curvature does not appear to offer any significant information for sandstone pore structure. DeHoff (1977) also states that the average mean curvature, as determined by feature counts, should only be used for convex particles.

Average mean curvature can be used as one component of the general shape factor of Fischmeister (1974a) (see Chapter 2). Both Rink and Schopper (1978) and Ruzyla (1984) used a stereological estimate of average mean curvature for this purpose. The interpretation of the shape factor in this manner is not appropriate. Fischmeister (1974a) intended the formulation employing curvature to be used for *open* features. For closed features, the appropriate formulation uses surface area per unit object volume (i.e., S_{V_p}).

Ultimately, the results will be the same, whether the tangent count (i.e., curvature) or the perimeter length (i.e., surface area) is used to compute the shape factor. We raise the objection here to emphasize that new independent information about curvature is *not* being obtained. Rather, the specific surface and N_A are being expressed in an alternative manner.

Following Rink (1976a), the number of holes in each feature is tabulated as a primary feature parameter. Most of the holes are but a few pixels in size. If segmentation is used to simplify the features, more than half of the holes are eliminated. The remaining holes contribute less than 1% to the average mean curvature estimate.

5.3.4.1 Variation in Curvature

Additional information for non-convex particles can be obtained from the variation in curvature determined by the tangent count. A tangent count is performed by sweeping a test line across the image and recording the number

of times that the line forms a tangent with the features. By convention, the tangents with convex arcs, where the line lies outside the feature, are positive. Tangents with concave arcs are negative.

A positive tangent count, T_+, has been added to the primary parameter measurement in **FTREXT** to determine the variations in curvature. The tangent count is one at the start of a new feature and is incremented for each bottom lobe on the feature. A negative tangent count is not necessary because for any closed curve on a plane (i.e., a feature boundary), the net tangent count will equal +2. Positive tangents within holes in the features are also counted. The net tangent count for a hole is −2. The hole count is used in the computation of T_-. The magnitude of the tangent count (sum of negative and positive counts) on a feature appears to have potential as a measure of feature complexity. Neither T_+ nor the magnitude of the tangent count has much significance for features which have been simplified by segmentation.

Some comments can be made about tangent counts in terms of the representation of a curve by parameterized cubic curves. Evans *et al.* (1985) describe the use of parametric cubic splines to study grain shapes. It appears that the tangent count indicates the number of knots required to describe adequately the feature shape. A good approximation for the number of knots is the sum of T_+ taken in two orthogonal directions.

5.3.5 Anisometry, Orientation, and Anisotropy

Stereological methods offer two ways to quantify anisotropy of structure. These are the variation of mean intercept length and specific surface with respect to the orientation of the test line. Feature analysis also offers tools to study anisotropy. These include the anisometry of feature shape and the orientation of anisometric features.

In a continuous structure, precise definition of structural anisotropy is dif-

ficult for concepts other than the orientation of surfaces. Our interpretation of anisotropy includes the orientation of surface area, out more generally includes the volume fractions of the pore space which are parts of oriented "objects." The description of anisotropy of pore structure can be broken down into several categories: 1) the anisometry of the "objects" which constitute the pore space, 2) the orientation of the "objects," and 3) the spatial distribution of the "objects."

The spatial distribution can be studied by measuring the clustering of features in individual images and the relative abundances of features in images from different areas of the rock. The locations of features are specified by the locations of the feature centroids which are available from the dynamic feature analysis. Schwarz and Exner (1983) discuss the characterization of feature arrangement and provide extensive references on cluster analysis. They use nearest neighbor distances and state that more sophisticated treatments are not necessarily desirable. A measure of spatial position is also important for Poisson and Boolean models of pore structure (see section 7.3.3). In our study, feature centroids were determined but the spatial distribution has not been studied. Anisometry of features and the orientation of features are considered in more detail.

5.3.5.1 Anisometry of Features

Anisometry of features is found from the two-dimensional shape factors which attempt to match some feature parameter to an equivalent simple anisometric shape. These shape factors include 1) the axial ratio of the ellipse based on the approximate maximum Feret dimension and mean intercept normal to this length, 2) the axial ratio of the ellipse with area and perimeter equivalent to those of the feature, and 3) the axial ratio of the dynamic ellipse with equivalent radii of gyration. The equivalent ellipse based on the maximum

Feret dimension is a convex hull method and is not robust. Here we consider only the area- and perimeter-equivalent ellipse and the dynamically-equivalent ellipse.

To afford a better representation of the anisometry, the size of the feature should be considered, not just the anisometric ratio. For example, a two-pixel feature has an aspect ratio of 0.5, yet contributes little to the anisotropy at the scale of the image. On the other hand, a large feature of the same aspect ratio contributes more to the anisotropy of the structure because it represents more volume (i.e., area). Thus, a weighting factor proportional to area is appropriate. The area weighting yields a porosity weighted measure of anisometry. As is true for many structural parameters, a volume weighted measure is preferred over the number weighted measure.

The axial lengths from the area- and perimeter-equivalent ellipse can be used directly because they already contain the area factor. The area of the dynamically-equivalent ellipse is rarely the same as that of the feature. Thus, it is preferable to use the measured area of the feature as a weighting factor, together with the axial ratio of the ellipse.

5.3.5.2 Orientation of Features

Orientation of features can be obtained by several measures. These include the orientation of the maximum Feret diameter or the orientation of the maximum intercept length. Both of these measures are available from the boundary contour method of feature analysis (see section 5.3.1; see also, Lin, 1983), but neither has been used in this study. Here, the orientation is found from the orientation of the dynamically-equivalent ellipse. The orientation from the dynamically-equivalent ellipse is more robust than the other methods which are based on the convex hull or on the boundary of the feature.

As with anisometry, the orientation measure should be weighted to give a

better representation of the anisotropy. Larger features should be given more weight than smaller features because the larger features represent more of the pore volume. Again, a weighting factor which is proportional to feature area is applied. Additional weighting with respect to the degree of anisometry is also reasonable but *ad hoc*. Those features with higher degrees of anisometry can be given more weight than nearly isometric features. A weighting factor which is proportional to feature anisometry is investigated below.

Orientation results can be presented for visual interpretation using rose diagrams. Quantitative interpretation is afforded by various statistical tests (Watson, 1966, 1970ab; Mardia, 1972; Dudley *et al.*, 1975). We have computed the vector mean and circular standard deviation using standard formulae (Mardia, 1972). Dudley *et al.*, (1975) discuss stereological corrections required for number based analysis of preferred orientation. They avoid the volume weighted analysis (i.e., weighting by area) because it is "inconvenient for statistical testing." The theoretical inconvenience is unfortunate because the volume weighted analysis is more significant physically for pore structure.

5.4 Two-Dimensional Shape Factors

One area of feature description which merits discussion and clarification is the difference between three-dimensional (3-D) and two-dimensional (2-D) shape factors. The 3-D shape factors are based on stereological relations, whereas 2-D shape descriptors are simply descriptors of planar features. The 3-D shape factors use measurements from the plane with the understanding that these measurements are a biased representation of the three-dimensional structure. The data from the plane are then converted, with appropriate stereological formulae, to obtain structural information. Alternatively, the 2-D shape descriptors are *not* converted to structural information through stereological

relations. The 2-D shape descriptors simply describe the appearance of the structure on a plane.

The only 3-D shape factor used in this study is the Fischmeister shape factor, F, discussed in Chapters 2 and 4. Results for F are presented below. Table 5.2 lists the 2-D shape factors computed by **FTRSTA** from primary feature parameters. Dynamic shape factors (Table 5.3) describe anisometry and compactness of features and are thus 2-D.

The interpretation of 2-D shape factors depends on computer modeling of the features produced by the sectioning of simple shapes (e.g., ellipsoids, opposed cones, tubes). The values of the 2-D shape factors produced by simple shapes are then compared with the values measured on the image. More complex shapes and structures can be modeled as understanding is advanced. Both the mean values and standard deviations of the shape factors are important for describing the structure.

Very little modeling of 2-D shape factors has been reported and none of this modeling pertains to interconnected structures (Fischmeister, 1974c). Still, with the increasing application of computers to the analysis of structure, additional modeling is expected. Thus, the results from some 2-D shape factors are included in this study. As an immediate application, these shape factors could be compared to physical properties through empirical analyses.

5.5 Results of Individual Feature Analysis

The results of individual feature analysis are presented in three categories. These are bulk stereological parameters, individual feature parameters, and dynamic feature parameters. We focus on the effects of segmentation and the influence of smaller features on the various parameters.

The smaller features are important. They have a very significant effect on

some stereological parameters because of their abundance. Below, we examine the effects of the smaller features by using a minimum area filter when compiling feature parameter statistics. The minimum area of the filter was arbitrarily restricted to the range of two to ten pixels, corresponding to areas of 20 to 380 μm^2 (depending on image magnification). This range was selected because the more significant effects, due to the smaller features, occur within it.

Examination of the effects of the smaller features is useful for several purposes. First, it will indicate the relative roles which various feature sizes play in determining the values of pore structure parameters. Second, it will provide a basis for determining the effect of elimination (perhaps unintentionally) of smaller features; the presence of the smaller features depends on the imaging resolution and on image preprocessing. For example, if the features are identified by hand-drawing of pore contours (as used for example by Lin and Cohen, 1982; Duda and Pitman, 1982ab), then many of the smaller features are likely to be missed. Similarly, if the imaging system has a low resolution, the smaller features may not be detected accurately. Finally, if an opening or other such cleaning (or smoothing) operation is routinely applied to the image before analysis, then the smaller features may be lost. Parameters measured on images which do not contain the smaller features will yield significantly different values than those obtained from an image containing the smaller features. To understand the differences in parameters (perhaps obtained in different studies), the differences in the images should be recognized, monitored, and reported.

5.5.1 Bulk Stereological Parameters

The stereological parameters are given in Table 5.4 for both the unsegmented (original) images and SMS segmented images. The stereological parameters

include porosity, specific surface per unit pore volume, mean intercept length, number of features per unit area, Fischmeister's shape factor, positive tangent count per unit area, and negative tangent count per unit area.

The porosity is the same for both unsegmented and segmented images because SMS segmentation preserves all of the pore space.

Specific surface is increased by segmentation. A remarkable linear relationship is observed between S_{Vp} from the original images and S_{Vp} of the segmented image (Figure 5.12). Coefficients of the best fit line are given in the caption of Figure 5.12. On average, SMS segmentation increases the original S_{Vp} by 0.04 μm^{-1}.

Predictably, the largest percentage increase (40%) occurs for a sample (2841) with an initially small S_{Vp} and the smallest percentage increase (12%) occurs for a sample (2687) with an initially large S_{Vp}. These extremes in percentage change in S_{Vp} also correlate with the number of iterations used in the SMS process. A representative image (#1099) from sample 2687 is shown in Figure 5.13a. This image required 2 iterations; other images from this rock required from 1 to 3 iterations. A representative image (#1052) from the rock (2841) with the largest increase in S_{Vp} is shown in Figure 5.13b. This image required 5 iteration steps, the most used in this study. It is the nature of the pore structure which dictates the number of SMS iterations required and, thereby, determines the increase in specific surface. Most samples required 3 iterations per image and have similar increases in S_{Vp}.

The increase in S_{Vp} reflects the amount of contact between the "separate" nearly convex pore features. If we consider the segmented S_{Vp} value as the "true" S_{Vp} of the objects comprising the pore space, then less than 20% of the surface area is lost after the objects have combined into the resulting pore space. This reasonably small value supports the use of the discrete object model of the pore space used in Chapter 4.

The mean intercept length reflects the behavior of S_{Vp} because of their inverse relationship (Eqn. (4.5)). Segmentation reduces the mean intercept length. As expected, the proportional decrease is greatest for sample 2841 and smallest for sample 2687.

Predictably, the number of features per unit area, N_A, increases with SMS segmentation. N_A of the segmented images is linearly related to N_A of the original image (Figure 5.14). Coefficients of the best fit line are given in the caption of Figure 5.14. If the lower 3 values of N_A are excluded, then the best fit line has a slope of 0.99, with an offset of 0.0005. This latter relation corresponds to a uniform increase in N_A due to segmentation and independent of the starting value.

Fischmeister's shape factor, F, changes with segmentation in a manner which reflects the changes of the stereological components which comprise F. For rocks with initial values of F less than about 0.83, F increases upon segmentation. For initial values greater than about 0.83, F decreases slightly upon segmentation. Several formulae for F were given in Eqn. (2.6). Additionally, F can be represented by

$$F = \frac{1}{6\pi}\frac{{S_{Vp}}^2 V_V}{N_A} . \tag{5.9}$$

The volume fraction of pore space, V_V, does not change with SMS segmentation, but both S_{Vp} and N_A increase with segmentation. Values of S_{Vp} and N_A show a rough positive correlation. Thus, the fractional increase in S_{Vp} is proportionally greater than the increase in N_A for small initial F so these values increase upon segmentation. At larger initial values of F, the increase in N_A exceeds the increase in ${S_{Vp}}^2$ causing F to decrease upon segmentation. The F values generally retain their relative positions with respect to each other, indicating that F from the segmented image distinguishes the same "shapes" as does F from the unsegmented image.

The positive tangent count per unit area, T_{A+}, increases with segmentation due to the increase in N_A. The negative tangent count per unit area, T_{A-}, gives a measure of the deviation of the features from the convex shape. T_{A-} is given by

$$T_{A-} = T_{A+} - 2(N_A - N_{Ah}) , \tag{5.10}$$

where N_{Ah} is the number of holes per unit area. We neglect N_{Ah} because it is typically less than 1% of N_A. For purely convex features, T_{A-} equals zero. On average, T_{A-} decreases by 40% upon segmentation because the features tend toward more nearly convex shapes.

5.5.1.1 Effects of Small Features on Stereological Parameters

Results for stereological parameters, obtained with minimum area filters on SMS features, are given in Table 5.5. The minimum values are inclusive. For example, the 2-pixel minimum area filter omits single-pixel features and includes features consisting of two pixels.

The features smaller than 10 pixels account for up to 28% *of* the porosity (5.1% porosity) of the sandstones. Generally, equal amounts of porosity are contained within the intervals delimited by the minimum area cutoffs. If not nearly equal, more porosity is usually contained in the two- to four-pixel interval. For example, sample 2710 (Morrison Fm.) has 1.1% porosity in one-pixel features (from the unfiltered and 2-pixel minimum filter results), 1.2% porosity in two- to four-pixel features (from the 2- and 5-pixel minimum filter results), and 1.0% porosity in five- to nine-pixel features (from the 5- and 10-pixel minimum filter results).

For all samples, S_{Vp} decreases with the omission of the smaller features. The decrease is greatest for omission of the smallest, one-pixel, features. The decrease is proportionally less as the next larger features are eliminated. The decreases reflect the high perimeter-to-area ratio of the smaller features. They

contribute proportionally more surface area than porosity. The original unsegmented image S_{Vp} values lie between or close to the values for filtered SMS images at 2- and 5-pixel minimum areas.

Mean intercept length is increased with the elimination of the smaller features. The increases are described via the changes in S_{Vp} and the inverse relationship between S_{Vp} and $\overline{L}_{3p}$.

The number of features per unit area, N_A decreases significantly with the omission of smaller features. More than 50% of the features, by number, are single-pixel features. Features between two and four pixels in area constitute approximately 25% of the features by number.

Fischmeister's shape factor increases with the omission of smaller features. The increase reflects the changes in the parameters which constitute F (Eqn. (5.9)). These changes are dominated by the reduction in N_A. The reductions in both S_{Vp} and porosity are subordinate. Here we see how strongly the smaller features contribute to the overall "shape" of the pore structure.

5.5.2 Feature Parameter Results

Results are presented here for individual feature parameters which provide useful information without stereological inversion. The distribution of feature area, the approximate maximum Feret diameter, the concavity factor, and the hydraulic radius are several such parameters (see Table 5.2 for definitions). Except for feature area, only the mean values of the parameters are considered. For feature area, the distribution is also considered. Again, the effects of SMS segmentation and minimum area filters are examined.

Some general statements can be made about feature parameters which are not otherwise addressed. The area- and perimeter-equivalent rectangle often does not exist because the area is too large for the perimeter. Wadell's diameter exists for all features, but it has little significance for features which

deviate from a circle.

5.5.2.1 Feature Area and Perimeter

The mean feature areas for the original and SMS segmented images are given in Table 5.6. Table 5.7 lists the mean feature areas of filtered SMS features. The mean feature area decreases with SMS segmentation and, logically, increases with the omission of the smaller features. The mean area typically increases by 50% with the omission of single-pixel features.

The feature areas typically span 4 or 5 orders of magnitude. The relative abundances also range over several orders of magnitude. Thus, it is convenient to present the distribution of areas in the form of a cumulative histogram with a logarithmic area scale. Figure 5.15 is representative of the number weighted and the area weighted cumulative fraction distributions for the rocks studied. Note the significant differences between these curves. The area fraction curve indicates that over 70% of the pore volume is represented by features larger than 1000 μm^2 whereas, numerically, fewer than 5% of the features are larger than 1000 μm^2.

Figure 5.16 is an alternate representation of the area weighted cumulative histogram. Here, the area has been converted to the diameter of an equivalent area circle. This curve is similar in appearance to the granulometry curves of section 5.8 and the similarity is discussed in section 5.9.

Mean perimeter is reduced by SMS segmentation (Table 5.6), but is increased by the omission of smaller features (Table 5.7).

5.5.2.2 Two-Dimensional Shape Factors

We have not done the modeling required for the interpretation of two-dimensional shape factors, nor has such modeling, appropriate for pore structure interpretation, been presented in the literature. Still, some results are worthy

of presentation to establish data for future work. In general, the data show very little variation and, as such, do not show strong shape differences. The concavity factor and $\overline{F_{33}}$ are two such two-dimensional shape factors.

The concavity factor, F_{cv}, gives an indication of the convex deficiency of features. Original images have F_{cv} values of 1.02 to 1.04. SMS segmentation reduces F_{cv} by 0.01 to 0.02, which indicates that the features in the SMS images are more nearly convex.

The mean hydraulic radius, $\overline{m}$, for original images ranges from 1.06 to 2.49 μm (Table 5.6). SMS segmentation increases the mean hydraulic radius. The increase is not reflected by the changes in the mean area and perimeter.

Fischmeister (1974a) suggested that the mean perimeter ratio, $\overline{F_{33}}$, would give a sensitive characterization of shape. $\overline{F_{33}}$ is given by

$$\overline{F_{33}} = \overline{\left(\frac{p}{\sqrt{2\pi a}}\right)} \tag{5.11}$$

and is the mean, over all features, of the ratio of the measured perimeter length, p, to the perimeter length of an equivalent area circle, $\sqrt{2\pi a}$. The measured $\overline{F_{33}}$ for both original and SMS images is very close to 1.2, with little variation from rock to rock (see Table 5.6). Therefore, either the pore features vary little in "mean shape," or $\overline{F_{33}}$ is not sensitive to the shape variation. Omission of smaller features increases $\overline{F_{33}}$.

The mean axial ratios of the area- and perimeter-equivalent ellipses are always greater than 2.0. The value reflects the large perimeter-to-area ratio of most features. Segmentation reduces the mean axial ratio, whereas omission of smaller features increases the ratio. The larger features are apparently more anisometric than the smaller features.

The mean approximate maximum Feret diameter, $d_{F\ max}$, is reduced by SMS segmentation (Table 5.6). Surprisingly, these values are usually less than the mean intercept lengths for both original and SMS segmented images.

Omission of the smaller features increases the mean approximate maximum Feret diameters (Table 5.7). Corresponding mean intercept lengths are always less than $d_{F\ max}$ when smaller features are omitted.

5.5.3 Dynamic Feature Parameter Results

Results are presented here for individual feature parameters which are computed from the dynamically-equivalent ellipse. These parameters include feature orientation, anisometry (or aspect ratio), and bulkiness (departure from elliptic shape). We also present the location (centroid), orientation, and anisometry parameters indirectly via a synthetic ellipse image. Further, the expected aspect ratio of the underlying ellipsoids is determined using the theoretical results of Cruz Orive (1976).

5.5.3.1 Orientation

Mean orientation and circular standard deviation are given in Table 5.8. The mean orientations are all close to $-80°$, which is subparallel to the Y image axis. Segmentation tends to shift the mean by a few degrees. The circular standard deviation is very large for original images and usually increases upon segmentation. The large standard deviations indicate only weak preferential orientation of the features.

Because their orientation is undefined, isometric features are not included in the compilation of orientation statistics. Thereby, all single-pixel features are already omitted. Omission of larger features causes the mean orientation to change by up to 20°, whereas the circular standard deviation fluctuates by a few degrees.

Orientations of the dynamically-equivalent ellipses are presented as rose diagrams to give visual indications of preferred orientation. Figure 5.17a is a

number weighted rose diagram of all anisometric features in 9 images of sample 2710. Note the modes at 45° intervals. This character is due to the discrete nature of the image and the strong influence of small features. This number weighted rose diagram does not give a good indication of pore space orientation because it does not reflect the volume fractions represented by the oriented features. Figure 5.17b is an area weighted rose diagram of the same features from sample 2710. Except for the ±90° mode, the modes at 45° intervals have been de-emphasized. Further, a new mode at −60° has emerged. Figures 5.18a and b are area weighted rose diagrams in which features smaller than three (29.3 μm^2) and five (48.8 μm^2) pixels, respectively, have been omitted. Both of the filtered rose diagrams show a decrease in the bins at 0 and 90° relative to the −60° mode. Further, Figure 5.18b shows a decrease in the bins at ±45°, reflecting the omission of three-pixel "L" shaped features. Omission of features smaller than 10 pixels yields a rose diagram almost identical to Figure 5.18b.

The preferential orientation between −90 and −55° is in good visual agreement with the features in the images from this rock. However, it is unlikely that this orientation would have been detected by visual inspection. The number weighted mean orientation from SMS images is also in good agreement with the preferential orientation.

Various statistical methods are available to determine preferred orientations (Watson, 1966, 1970ab; Mardia, 1972; Dudley *et al.*, 1975). We have not applied any statistical tests because they use number frequency of occurrence and the area weighted representation is preferred from a geometric point of view. Still, many aspects of feature orientation remain to be investigated and the statistical tools will be beneficial.

5.5.3.2 Anisometry and Bulkiness

Mean anisometry, Q_{dyn}, and bulkiness, B_{dyn}, for original and SMS segmented images are given in Table 5.8. The anisometry does not show much variation and is near 1.5 for both original and SMS images. Omission of smaller features increases the anisometry to near 2.0 for most rocks, again, with little variation (Table 5.9).

Table 5.8 also contains estimates of the underlying ellipsoid mean aspect ratio, q^*, based on the dynamic axes ratios (see section 4.6.3.3). The single-shape estimator of Cruz Orive (1976), given in Eqn. (4.36), was used to compute the mean object aspect ratio. The estimate was only computed for rocks with 9 images. When all features were used in the estimate, all rocks gave similar values near 0.74. Omission of the single-pixel features dropped all estimates to about 0.44 (see Table 5.9). Omission of larger features caused small increases in mean aspect ratios. The equant shape of the single-pixel features has a strong effect on the estimated aspect ratio because of their abundance.

The mean bulkiness of original and SMS image features is less than 1.0 (Table 5.8). This is due to the discrete nature of the calculations and the abundance of single-pixel features. These features are a degenerate case for which ellipse axes lengths equal to the pixel size are assigned. Thereby, the pixel has a larger area than the dynamic ellipse yielding a bulkiness less than one. When single-pixel features are omitted (see Table 5.9), the mean bulkiness of SMS features is very close to 1.0 for all rocks. Omission of the next larger features further increases the bulkiness. Omission of features from the original images yields bulkiness values (Table 5.9) which are larger than those from the SMS images. Exceptions exist for omission of single-pixel features, where both values are usually less than 1.0. Thus, the features in the SMS images are more nearly convex and more similar to an elliptic shape than those in the original images.

5.5.3.3 Synthetic Ellipse Image

In order to visualize the quality of the dynamic ellipse approximation, we use the ellipse parameters to generate a synthetic ellipse image. This image is then compared to the original image. The synthetic ellipse image is a re-representation of the SMS segmented image, not a simulated slice through a medium composed of ellipsoids.

Figure 5.19a is the synthetic ellipse image corresponding to image #1048 of sample 2710 shown in Figure 5.1. Figure 5.19b is the XOR (eXclusive OR) combination of Figure 5.1 and the synthetic ellipse image. The XOR image shows all of the differences between the two images and can be expressed as the set combination $(A \cup B) \setminus (A \cap B)$. Although the dynamic-equivalent ellipse was not formulated to match visually the SMS features, it does match quite well for all nearly convex features. One example of a poor visual match is given by the feature which has the highest bulkiness value (4.2) in the SMS image. This feature is indicated by an arrow on Figure 5.19a. It represents a hooked feature in the SUB image in Figure 5.8d. Clearly, the original feature has a very large convex deficiency. The mismatch is visually prominent in Figure 5.19b.

The semiaxes of the dynamically-equivalent ellipses agree in both magnitude and orientation with the visual appearance of the pore structure. This verifies the accuracy of the pore feature orientation parameter.

The porosity of an unscaled synthetic ellipse image will differ from the original image by an amount represented through the bulkiness parameter. The synthetic image in Figure 5.19 was generated with an axis scaling parameter (0.9), based on the mean bulkiness, to give an image with nearly the same porosity as the original image (#1048).

Synthetic ellipse images have been analyzed with SMS segmentation and the feature analysis programs (**FTREXT** and **FTRSTA**) in the same way as

original images are analyzed. All of the dynamic parameters (e.g., moments, centroid locations, axes ratios) of the synthetic ellipse image agree with those of the original image. Minor differences are attributed to the discrete representation. One predictable difference is that the bulkiness of the synthetic ellipse features equals 1.0 for all but the single-pixel features. Generally, after the porosity is matched by scaling, the synthetic images preserve the bulk stereological parameters of the pore structure.

5.6 Discussion of Individual Feature Analysis

For many bulk geometric properties, the smaller features contribute disproportionate influence on number averaged parameters and area weighted parameters appear to describe better the bulk of the pore structure. Of course, for some applications of the pore structure data, the small features may be very important (e.g., surface area dependent properties). For these applications, the impact of the small features can be observed from the data we have presented. If the smaller features are of central interest, it may be preferable to extract these features directly from the original image to prevent any changes by segmentation. Further, if appropriate for the application, the statistics of the small features from original images can be combined with the statistics of the larger features from the segmented images. The analysis system presented here allows such special combinations.

The influence of the smaller features also illustrates the importance of image resolution on the results. To allow comparisons of results, the effective resolution, whether due to subjective influence or hardware configuration, must be available.

5.6.1 SMS Segmentation

SMS segmentation is used to reduce complex pore features to simpler features which can be described by simple parameters. These parameters allow comparisons of different rocks and are tractable in models of physical properties. Methods exist for characterizing very complex features (e.g., Fourier methods). However, such characterizations are generally intractable in models and their physical significance is not clear.

SMS segmentation does not produce a large number of relics or single-pixel features. The changes in feature parameters due to segmentation are always much less than the changes due to the omission of smaller features. SMS segmentation preserves details of the pore structure which are lost by cutting segmentation. Also, no porosity is lost by SMS segmentation, in contrast to the significant amounts lost by cutting.

Some features with large convex deficiencies can remain after SMS segmentation (e.g., Figure 5.8d). Such features can be identified by high bulkiness values or high concavity indices. Instead of additional SMS iterations, it may be preferable to treat these features individually. The local extrema methods of feature segmentation described by Duda and Hart (1973, p. 353) appear to be well-suited for such individual segmentation.

5.6.2 Stereological Parameters

Significant changes in stereological parameters, particularly the number sensitive parameters, occurred when small features were omitted from the calculations. This points out the strong numerical impact of the small features. Area weighted parameters (e.g., porosity) are less sensitive to the small features and are often more representative of the pore space.

5.6.3 Mean Feature Parameters

The two-dimensional shape factors did not show strong variations for the suite of rocks investigated. The rocks were quite similar and may not have had much variation. Indeed, in Chapter 4, the aspect ratios of the ellipsoids used to model the pore space showed little variation. Our results indicate that methods of size characterization are more discriminative than methods of shape characterization.

The $\overline{F_{33}}$ shape factor suggested by Fischmeister (1974a) is the square-root of $P2A$, so it shows less variation than $P2A$. Fischmeister's shape factor, F, is proportional to the ratio of the mean perimeter squared over the mean area. The similarity of these shape factors to the classic $P2A$ indicates the limited scope of the descriptors of shape.

The hypersensitivity of many parameters to the omission of smaller features indicates that area weighting (i.e., porosity weighting) is often a more robust approach than number weighting.

5.6.4 Dynamic Feature Parameters

The dynamic-equivalent ellipse is a good representation of SMS segmented image features. The dynamic parameters provide location, anisometry, and orientation information. Even when the visual match is not good, the centroid location and orientation of the dynamic-equivalent ellipse are consistent with the visual appearance of the feature. The anisometry measure of a feature with a high convex deficiency is generally a good estimate of the anisometry of the convex hull of the feature. For all features, the dynamic-equivalent ellipse gives a robust representation of the feature with very few parameters. These dynamic parameters are "information preserving," in the sense of Pavlidis (1978), because they can be used to reconstruct the original image. The

reconstruction is not perfect, but it is very good for the number of parameters used.

It is not clear why the mean orientations were near $-80°$ for all rocks. The synthetic ellipse image clearly shows that the orientations are computed correctly and that they represent the pore structure. The area weighted rose diagram for 2710 was also in visual agreement with the images from that rock. The mean orientations agree with the consistently higher values of S_V measured in the Y direction by lineal analysis. Additional work must be done to understand whether the bias truely reflects rock structure or is an imaging artifact.

SMS tends to reduce features to more equant shapes due to the symmetric structuring elements used for opening and plating. Also, the 4-fold connectivity criterion splits diagonal chains of pixels into individual features, thereby increasing the aspect ratio of the features. Thus, the mean aspect ratio estimator will probably be biased toward more equant shapes.

Information given by the dynamically-equivalent ellipse has application in the Boolean model of pore structure (see Chapter 7). The ellipses give an estimation of the population from which the family of features (elements) is drawn. The locations of the ellipsoids give a spatial distribution function (e.g., areal density and nearest neighbor distances) for use in positioning the elements. Further, the population can be parameterized or expressed in a two-dimensional histogram as functions of semi-major axis and aspect ratio.

5.7 Feature Sizing by Opening

Opening is an operation of mathematical morphology which can be used to determine the size distribution of features on an image (Delfiner, 1972; Serra, 1982, p. 333). The operation can be applied to features of arbitrary complexity

and connectivity. Previous uses of openings for sizing pores in sandstones were discussed in Chapter 2. Briefly, Delfiner (1972) presented an excellent theoretical development of sizing by opening. He apparently applied the method to sandstone images but he presented no data or results. Ehrlich *et al.* (1984) have applied an *ad hoc* form of opening to optical images of sandstones to determine "pore-complex spectra". They presented no direct results, but show a ternary diagram of "inferred end member spectra" into which the "pore-complex spectra" can be decomposed. Dilks and Graham (1985) used opening to study SEM images of sandstone pores. They presented histograms for one sample and suggested that the histograms were good classifiers of pore structure.

Two important points about sizing by openings must be noted. First, the pore *features* are being sized, not the three-dimensional pores. Second, the sizing is strongly dependent on the shape of the structuring element used in the opening. Below, a symmetric structuring element is developed and applied to digital SEM images of sandstones.

5.7.1 Opening and the Structuring Element

The opening operation was defined in section 5.2.1. There we showed that opening was a combination of erosion and dilation operations using the structuring element B. The structuring element B must be convex and can be thought of as a small spatial array. The opening operation is a means of determining the areas in the pore features where the element B will lie completely in the pore phase.

Mathematically, the opening of X with respect to B can also be described as the set of points x such that there exists a translated B containing x and

included in X (Delfiner, 1972),

$$X_B = \{x; \exists y \in \Re^2 : x \in B_y \subset X\} . \tag{5.12}$$

The process described by Ehrlich *et al.* (1984) is not rigorously equivalent to opening. They did not give equations defining their operator, but verbally they use the "prairie fire" analogy described by Blum (1973) and Duda and Hart (1973, p. 356). They apparently remove (erode) or add (dilate) pixels directly from the boundaries of features. Further, they apparently monitor the splitting of individual features into two or more features during the operations, which suggests that they may use a feature-by-feature operator similar to that described by Young *et al.* (1981). Such an approach may also explain their propensity for number weighted parameters.

5.7.2 Size Distribution Function—Granulometry

The opening operation assigns a "size" to each point of the set X (i.e., each pore pixel). This size corresponds to the size of the structuring element. A set of increasingly larger structuring elements is used to determine the size of all of the pore pixels. Ideally, the structuring elements are homothetics of a primitive element, B, with the scaling given by the parameter λ. The results of openings are expressed as a size distribution by the relation,

$$G(\lambda) = 1 - E\left[\frac{mes(X_{\lambda B} \cap Z)}{mes(X \cap Z)}\right] , \tag{5.13}$$

where $E[\cdot]$ is the expectation, $mes(\cdot)$ is the areal measure of the argument, and Z is the mask (i.e., image area). Equation 5.13 is termed a "granulometry curve." The size λ at which $G(\lambda)$ first reaches 1.0 and beyond which further opening eliminates all features is termed "the ultimate opening." The size of the structuring element at the ultimate opening is called the "maximum

diameter", λ_{max}. Rigorously, the mask, Z, must also be eroded by the structuring element to reflect the smaller area over which complete knowledge of X is available. The local knowledge mask is given by

$$Z_{local} = Z \ominus (B_1 \oplus B_2 \oplus \ldots \oplus B_n) \,, \tag{5.14}$$

where the B_i are primary structuring elements used for eroding or dilating the set X (i.e., the pore phase).

Ehrlich *et al.* (1984) use an *ad hoc* mask treatment whereby the features are eroded (or dilated) from "external boundaries" and the features touching the image frame are assumed to extend to infinity and are not eroded (or dilated) from the boundary. Such a treatment gives a positive bias to the sizes determined. The boundary touching features will appear to be larger than their true size. The bias is obvious at larger sizes. We have observed a 40% increase in λ_{max} when using the *ad hoc* mask as compared to λ_{max} when using the local knowledge mask. Visually, the bias is observed by noting that the last features to be eliminated by opening frequently touch a boundary. The bias is not as apparent in the smaller sizes of the granulometry curve.

We coin the term "infinite feature" mask for the *ad hoc* mask of Ehrlich *et al.* (1984) and have used this mask in our SMS segmentation. The infinite feature mask makes the greatest use of the image area, instead of reducing the area in accordance with the local knowledge criterion. Because the segmentation is not used to measure the pore structure, there is no conflict or bias.

5.7.3 Symmetric Structuring Elements

The various size structuring elements are constructed by the successive application of primary elements. Such a procedure is based on the property of

iterativity (Serra, 1982, p. 46) which is given by

$$(X \ominus B_1) \ominus B_2 = X \ominus (B_1 \oplus B_2) , \quad (5.15)$$

$$(X \oplus B_1) \oplus B_2 = X \oplus (B_1 \oplus B_2) , \quad (5.16)$$

whereby the successive application of B_1 and B_2 is equivalent to the application of $B_1 \oplus B_2$. Use of iterativity simplifies erosion and dilation software and is the reason why we occasionally refer to erosion (or dilation) "steps" or "iterations" or "cycles".

The structuring elements used here are not homothetics of a single shape. We have developed a sequence of structuring elements, pseudo-octagons, which are constructed from two primary structuring elements. The composite element gives better area resolution and a more symmetric shape, on the square grid, than does a single element or other composite elements composed of different primary elements.

The first eight composite structuring elements are shown in Figure 5.20 together with the primary elements used at each step. The filled portions of the composite elements indicate the area added at each step. Table 5.10 lists the areas of the elements, and the diameters of the maximum inscribed circles, of the minimum circumscribed circles, and of the equal area circle.

Because an areal distribution of size is used here, there is no complication with the subtle shape differences between the structuring elements. More importantly, the Feret diameter of each sizing element is closely related to the diameter of a circle with area equal to the area of the element. This "equal area" diameter is slightly less than the Feret diameter, whereas the circumscribed circle diameter is larger than the Feret diameter (see Table 5.10). Consequently, the Feret diameter is used as the representative diameter of the sizing element.

Every even numbered composite structuring element has an even width,

but a unique origin is defined by the position of the starting primary element. We are not actually assigning a size to individual pore pixels, but rather, are interested in the area fraction of the various sizes. Still, there is no difficulty in assigning sizes at individual points, as suggested by Rink (1976a), for some other even width elements. If the square primary element is rotated by 90, 180, or 270°, the same granulometry curve results. Further, if the image is rotated by 90°, the same granulometry curve results.

One consequence of the "opening" process used by Ehrlich *et al.* (1984) is that the structuring element is not well-defined. Therefore, the reference shape on which the size is based is poorly defined. Although their schematic figures imply that the effective structuring element is a disk, the pore structure image (their Figure 5) reveals that the element is diamond shaped. Such a composite element is obtained if the primary elements are "+" shaped. Their measure of size is thus related to the horizontal (or vertical) Feret diameter of the diamond. Note that the infinite feature mask effects a spatially varying structuring element.

Circular symmetry is important for sizing by openings. A circularly symmetric structuring element is independent of image orientation and yields the most general sense of diameter or size. The effective structuring elements of Ehrlich *et al.* (1984) are diamonds, which have poor circular symmetry. The elements of Dilks and Graham (1985) are squares which also have poor circular symmetry.

5.7.4 Descriptive Granulometry Parameters

The granulometry curve can also be represented as a histogram of sizes. This histogram is found by differencing successive values of the cumulative size distribution function. Additional normalization is required because of the form of the sizing elements. The spacings of successive sizings are not constant

because the size increments of the sizing elements are not constant. The histogram bin widths alternate between one and two pixel units except for the first class which is three pixel units wide. The unequal bin widths are used because they represent the data best. If the data were averaged to provide a uniform bin width, some of the resolution and accuracy would be sacrificed.

The cummulative distribution is used for display, but the arithmetic mean feature diameter and standard deviation are calculated from the histogram representation. The median (50%) diameter, the 95% diameter, and the maximum (100%) diameter are read from the cummulative curve.

5.8 Results of Feature Granulometry

A computer program (**GRANUL**) was written to apply the opening operation to a binary image using a pair of user-specified primary structuring elements. The primary structuring elements described above were used. This program uses the rigorous local knowledge mask criterion and computes $mes(X \cap Z_{\text{local}})$ within the appropriately eroded mask, Z_{local}, at each opening step. A second program (**GRNHST**) converts the granulometry curve into a histogram and computes mean diameter and standard deviation. Note that the mean diameter is an area weighted mean.

The granulometry curves from the individual images of each rock are combined by averaging. This averaging is equivalent to applying the granulometry to a single image with the same total area. The average curves are given in Figures 5.21a through 5.21n. Diameters are given in Table 5.11.

Some general observations can be made about the granulometry curves. The granulometry curves from all of the rocks with 9 images are somewhat smoother than the curves from rocks with 2, 3, or 4 images. All curves have the highest slope near the origin and the slope decreases monotonically at

larger diameters. At or near the maximum diameter, the slope may increase. Typically, a large decrease in slope occurs between 80 and 100% area fraction. We refer to the transition region of the large slope decrease as a "knee" in the curve. The knees of some rocks with only 2 images are poorly defined (e.g., samples 2686, 2841), others are well-defined (e.g., sample 2509). The area fraction above the knee represents the largest pore features, which in some cases are significantly larger than the majority of the pore features (e.g, sample 2704).

Only the higher magnification images of each rock were used for the average granulometry curves. The lower magnification images yield quite similar granulometry curves. Figure 5.22 is the granulometry curve from a 50× image of samle 2513. Note the similarity of Figure 5.22 to 5.21c.

The initial slope of the granulometry curve can be estimated from the median diameter. Typically, this diameter lies within the initial linear segment of the curve. Thus, the median diameter is a convenient tool for comparing the relative abundances of small pore features. The difference between the 95% diameter and the maximum diameter can indicate the presence of a "tail" in the feature size distribution. This difference ranged from 10 to 50 μm. The maximum diameter is the largest symmetric dimension of the pore features although there will be longer linear dimensions due to anisometric features.

5.9 Discussion of Feature Granulometry

The symmetric structuring elements developed here together with the local knowledge mask provide an accurate implementation of sizing by opening. If different structuring elements are used, then a different granulometry curve is obtained. This emphasizes the interplay of size and shape.

There is a strong similarity between the granulometry curve and the fea-

ture area distribution with respect to equivalent area circle diameter. Both of these curves are area fraction distributions of feature size. The feature area distribution is shifted to larger sizes relative to the granulometry curve. The shift results because the granulometry curve assigns to smaller sizes the difference between the true feature and the largest structuring element which "fits" into the feature (i.e., the "rough" porosity). We discuss this further below.

There is a general similarity between the granulometry curves and the ellipsoid size-shape distributions (Figure 4.5). The sizes in the ellipsoid distribution are shifted to larger values with respect to the granulometry curve. This shift is expected because the granulometry represents an isotropic sizing of features not pores. The initial slope characteristics of the two curves are similar. If there is a large fraction of small pores, both initial slopes are large.

Serra (1982, p. 336) states that two-dimensional openings "(by disks) possess less of a stereological meaning than the linear (intercept) size distribution, and their moments have no three-dimensional interpretation similar to the star. Their major interest is to synthesize size and shape description (of individual features) in a single approach." That granulometry curves contain less stereological meaning does not infer that they contain less useful information. The information contained in the granulometry is just more difficult to relate directly to the geometric character of the pore space.

The previous treatments of feature granulometry have recognized this difficulty and have used or proposed various "classification" schemes for interpretation. Dilks and Graham (1985) suggest that the granulometry gives a fingerprint of the two-dimensional morphology. Further, they suggest that the measured granulometry could be compared to the granulometry generated from some model pore space, presumably to determine equivalent model parameters.

Factor analysis and end member analysis have been applied, by others, to

opening histograms to characterize the size distributions. For example, Serra (1980, 1982, p. 339) describes an investigation by Kolomenski and Serra (1976) in which openings and closings (opening of the grains) were used to study the pore feature sizes in dolerites. A factor analysis was applied to the size curves. It is difficult to ascertain from Serra's cryptic explanation, but the primary factors appear to reflect the total porosity, the proportion of fine porosity, and the overall (median? or maximum?) size of the pore features.

Ehrlich *et al.* (1984) decompose "pore-complex spectra" into end member components for classification. Judging from the number of class intervals, the ternary diagram of spectra in their Figure 10 appears to be for the smooth porosity spectra (see Chapter 2). The end members of their diagram correspond roughly to (1) the smaller pore features, (2) the intermediate sized pore features, and (3) the largest pore features. These three end members also correspond roughly to the descriptive parameters used here: (1) the initial slope of the granulometry curve, (2) the distance between the 50% and 95% diameters, and (3) the maximum diameter.

We have not attempted a factor analysis of the granulometry curves, although it appears to be a reasonable method for their characterization. The factors can then be used in correlations with physical properties as has been done by Kolomenski and Serra (1976). However, unless the geometric character of the factors or end members is understood, it is unlikely that their empirical correlation to physical properties will reveal the physics of the relationship. It is possible that the geometric character of interest can be better obtained by an alternative direct analysis. Presently, little is known about extracting geometric characteristics directly from granulometry curves.

5.9.1 Template Matching Analogy

The analogy of sizing by opening to template matching offers insight into the sizing process (see Delfiner, 1972). In effect, the opening process is identifying those areas of the pore features where the structuring element lies completely within the pore features. This area is recorded and then "removed" from further consideration. The area which "remains" is matched with larger elements and the process is repeated. Thus, the parts of larger features which do not lie within the matched area are assigned to smaller pore sizes. These parts may actually represent anisometry of the larger features. The approach of Ehrlich *et al.* (1984) is commendable in that they try to account for the fraction of the parts (their rough porosity) versus the area fraction due to isolated features of the same size (their smooth porosity). One uncertainty in such a classification scheme is the identification of the larger size to which the rough porosity is attributed. Apparently, the rough porosity may be attached to any of the smooth porosity which is larger than the roughness. If the opening is performed on an individual feature basis, then some indication is given of the smooth size to which the rough porosity is associated. Such an individual characterization is discussed by Serra (1982, p. 336).

The SMS segmentation and individual feature analysis approach is similar to the sizing by opening in that an area distribution of size can be obtained (Figure 5.16). Certainly, the feature area distribution curve contains information equivalent to the granulometry curve. To first order, the similarity of the curves (Figures 5.16 and 5.21k) reflects the equivalence. However, the individual analysis offers the additional information of feature anisometry, feature orientation, and feature location. Further, the individual feature analysis probably gives a more realistic average diameter of the features because anisometry is allowed. There is some splitting of "roughness" from features with the SMS segmentation process, but it is insignificant in comparison to that

which occurs with sizing by openings.

If the reader found the ellipse approximation of features questionable, he would probably abhor the idea of using a fixed orientation square element for approximation. The opening operations are effectively doing just that if a square element is used. A circularly symmetric element is better, but the anisometry data for the SMS features indicate that most features are anisometric. We have not observed many pore features, other than single-pixel features, for which a fixed orientation square gives a better approximation than an ellipse with variable aspect ratio and variable orientation.

Computationally, the SMS segmentation and individual feature analysis require only modest additional processing compared to openings alone. However, the individual feature analysis is not fully automated because the opening sizes for SMS segmentation are selected subjectively at present.

With this understanding of the opening process it is apparent that individual feature analysis offers an alternative means to obtain similar information. Individual feature analysis also offers additional information not contained in the opening. The intended application of the pore structure results will likely determine the best measurement method. Most importantly, the desired geometric information should be considered directly, to determine if it may be better obtained by individual feature analysis.

Figure Captions

Figure 5.1. Binary image (#1048) of Morrison Formation (sample 2710). This image is representative of the complex connected features which

are typically observed in this sample. Pore features are black. The scale bar is 100 μm. The image area is the same as the center of Figure 1.2a.

Figure 5.2. Four openings of Figure 5.1. Note the loss of small features and the simplification of larger features. The "infinite mask" criterion was used for illustrative purposes. (*a*) Opening index of 1. (*b*) Opening index of 2. (*c*) Opening index of 5. (*d*) Opening index of 11. The opening index corresponds to the size of the structuring element used (see Figure 5.20).

Figure 5.3. Schematic of Rink's "cutting" process for feature segmentation.

Figure 5.4. Cut images resulting from the application of Rink's cutting process to the binary image in Figure 5.1. Note the generation of many small relics at the higher cutting steps. (*a*) One cutting iteration. (*b*) Two cutting iterations. (*c*) Five cutting iterations. (*d*) Eleven cutting iterations.

Figure 5.5. Clear cut images produced by opening the images of Figure 5.4 with a + element (#1 of Figure 5.20). Note that many intermediate sized features have been cut into small features or lost altogether.

Figure 5.6. Results of the CUSTER operation applied to the images of Figure 5.2. These images are used as input to the feature boundary mapping program (MAPCNT).

Figure 5.7. Schematic of the SMS process for feature segmentation.

Figure 5.8. Segmented image produced by the application of the SMS process to Figure 5.1. At each iteration, the largest remaining features are extracted. (*a*) First iteration (SMS #1), opening index of 11. (*b*) Second iteration (SMS #2), opening index of 5. (*c*) Third iteration (SMS #3), opening index of 2. (*d*) Final SUB image. This SUB image contains all of the pore area not in the SMS images.

Figure 5.9. Modified cutting of Figure 5.1, using only the opening indices used in the SMS segmentation. The features in this image are quite similar to those in Figure 5.8.

Figure 5.10. Results of the CUSTER operation applied to the SMS segmentation in Figure 5.8.

Figure 5.11. Freeman direction codes. Current location is at "×." The direction of the next pixel of the boundary is indicated by the appropriate number. The next location then becomes the current position and the process is repeated.

Figure 5.12. S_{Vp}—Original versus SMS Image values. The equation of the best fit line is

$$S_{VpSMS} = 0.043 + 1.04 S_{VpOrig} .$$

Note the nearly uniform increase in S_{Vp} as a result of SMS segmentation. The dashed line shows a one-to-one relationship.

Figure 5.13. (*a*) Binary image (#1099) from the Dakota sandstone (sample 2687). This image required only 2 iterations for SMS segmentation. (*b*) Binary image (#1052) from the Boise sandstone (sample 2841). This image required 5 iterations for SMS segmentation.

Figure 5.14. N_A—Original versus SMS Image values. The dashed line shows a one-to-one relationship. The equation of the best fit line is

$$N_{ASMS} = 0.000256 + 1.15 N_{AOrig} .$$

Figure 5.15. Cumulative fractions of segmented features versus log area. Note the distinct difference between the number-weighted fraction and the area-weighted fraction.

Figure 5.16. Cumulative area fraction versus equivalent area diameter disk. This curve is a re-representation of the data in the area-weighted curve of Figure 5.15.

Figure 5.17. Rose diagram of feature orientation of sample #2710. (*a*) Number-weighted representation. (*b*) Area-weighted representation.

Figure 5.18. Minimum area filtered area-weighted rose diagram of feature orientations of sample #2710. (*a*) Minimum area of features is 3 pixels (29.3 μm^2). (*b*) Minimum area of features is 5 pixels (48.8 μm^2).

Figure 5.19. Synthetic ellipse image representations of Figure 5.1. (*a*) Synthetic ellipse image with an axis scaling factor of 0.9. (*b*) XOR of Figure 5.1 and 5.19a.

Figure 5.20. Symmetric structuring elements used for segmentation and granulometry. The pluses indicate the origin of the primary elements.

Figure 5.21. Granulometry results.

(*a*) 2124.	(*e*) 2521.	(*i*) 2700.	(*m*) 2842.
(*b*) 2509.	(*f*) 2523.	(*j*) 2704.	(*n*) 2843.
(*c*) 2513.	(*g*) 2686.	(*k*) 2710.	
(*d*) 2519.	(*h*) 2687.	(*l*) 2841.	

Figure 5.22. Granulometry result for low magnification image of sample 2513.

Table 5.1
Primary Feature Parameters

Symbol	Dim.	Description
n		Number of pixels in the feature.
$x_{\min}$	μm	Minimum x coordinate.
$x_{\max}$	μm	Maximum x coordinate.
$y_{\min}$	μm	Minimum y coordinate.
$y_{\max}$	μm	Maximum y coordinate.
x_{proj}	μm	Multiple projection length on the Y axis.
y_{proj}	μm	Multiple projection length on the X axis.
$l_{\max}$	μm	Maximum chord length in the X direction (Krumbein diameter).
v	μm	Number of right-angled inward corners on the feature boundary.
κ		Connectivity (# of holes in the feature).
f_c		Image frame contact flag (indicates side of first contact).
T_+		Positive tangent count.
M_x	μm^3	First moment of x coordinates.
M_y	μm^3	First moment of y coordinates.
M_{xx}	μm^4	Second moment of x coordinates.
M_{yy}	μm^4	Second moment of y coordinates.
M_{xy}	μm^4	Cross moment of x and y coordinates.

NOTES: Modified after Rink (1976a). The dimension of the parameters (Dim.) is arbitrarily reported in microns.

Table 5.2

Secondary Feature Parameters

Symbol and Definition	Dim.	Description
$d_{Fx} = x_{\max} - x_{\min}$	μm	Feret diameter in X direction.
$d_{Fy} = y_{\max} - y_{\min}$	μm	Feret diameter in Y direction.
$a = nd^2$	μm^2	Area.
$\bar{l}_x = a/x_{\text{proj}}$	μm	Mean chord length in X direction.
$\bar{l}_y = a/y_{\text{proj}}$	μm	Mean chord length in Y direction.
$d_W = 2\sqrt{a/\pi}$	μm	Diameter of equivalent area circle (Wadell diameter).
$d_{F\ \max} = (l_{\max}/d_{Fx})^2 \max(d_{Fx}, d_{Fy}) + \left(1 - (l_{\max}/d_{Fx})^2\right)\sqrt{{d_{Fx}}^2 + {d_{Fx}}^2}$	μm	Approximation of maximum Feret diameter.
$\bar{l}_{d_{F\ \max}} = a/d_{F\ \max}$	μm	Mean dimension normal to $d_{F\ \max}$.
$\bar{l}_{ed_{F\ \max}} = 4a/\pi d_{F\ \max}$	μm	Minor axis of ellipse of area a and major axis $d_{F\ \max}$.
$f_{\text{elong\#1}} = d_{F\ \max}/\bar{l}_{d_{F\ \max}} = {d_{F\ \max}}^2/a$		Elongation factor #1.
$f_{\text{elong\#2}} = d_{F\ \max}/\bar{l}_{ed_{F\ \max}} = \pi {d_{F\ \max}}^2/4a$		Elongation factor #2.
$f_{ct} = a/d_{Fx}d_{Fy}$		Compactness factor.
$f_{cv} = (x_{\text{proj}} + y_{\text{proj}})/(d_{Fx} + d_{Fx})$		Concavity factor.
$p = 2(x_{\text{proj}} + y_{\text{proj}})$	μm	Perimeter, length of the polygon limiting the feature.
$p_v = p - v(2 - \sqrt{2})d$	μm	Adjusted Perimeter, compensated for internal angles.
$a_v = a + vd^2/2$	μm^2	Adjusted Area, compensated for internal angles.

Table 5.2 (cont)
Secondary Feature Parameters

Symbol and Definition	Dim.	Description
$m = a/c_v$	μm	Feature hydraulic radius.
$\mathrm{PAR} = c_v/a$	$\mu\mathrm{m}^{-1}$	Perimeter to area ratio.
$P2A = {c_v}^2/4\pi a = {F_{33}}^2$		Perimeter squared over area.
$F_{33} = \sqrt{P2A} = c_v/2\sqrt{\pi a}$		Perimeter ratio (Circularity shape factor).
$f_{\mathrm{circ}\#2} = 4\pi a/{c_v}^2 = 1/P2A$		Circularity shape factor #2
$a_{ee}, b_{ee} = (2/3\pi)\left[c_v + \sqrt{\pi a} \pm \sqrt{(c_v + \sqrt{\pi a})^2 - 9\pi a}\right]$	μm	Axes of area- and circumference-equivalent ellipse.
$q_{ee} = a_{ee}/b_{ee}$		Ratio of axes of ellipse.
$l_{er1,2} = (1/4)\left[c_v \pm \sqrt{{c_v}^2 - 16a}\right]$	μm	Sides of area- and circumference-equivalent rectangle.
$q_{er} = l_{er1}/l_{er2}$		Ratio of sides of equivalent rectangle.

NOTES: Modified after Rink (1976a). Some notations have been changed to be more symbolic. The dimension of the parameters (Dim.) is arbitrarily reported in microns. d is the pixel size. Note the similarities between m, PAR, $P2A$, F_{33}, and $f_{\mathrm{circ}\#2}$. Each is computed because each provides a different averaging effect when the values are summed over all features.

Table 5.3

Dynamic Feature Parameters

Symbol and Definition	Dim.	Description
$x_{cm} = M_x/a$	μm	X center of mass of feature (X centroid coordinate).
$y_{cm} = M_y/a$	μm	Y center of mass of feature (Y centroid coordinate).
$I_X = M_{yy} - y_{cm}M_y$	μm^4	Central moment about X.
$I_Y = M_{xx} - x_{cm}M_x$	μm^4	Central moment about Y.
$I_{XY} = M_{xy} - x_{cm}M_y$	μm^4	Central cross moment of inertia.
$I_A, I_B = (I_x + I_y)/2 \pm \sqrt{[(I_x + I_y)/2]^2 - (I_x I_y - I_{xy}{}^2)}$	μm^4	Central principal moments about A and B.
$K_A = \sqrt{I_A/a}$	μm	A radii of gyration.
$K_B = \sqrt{I_B/a}$	μm	B radii of gyration.
$a_{\text{dyn}} = 4K_A$	μm	Equivalent ellipse major axis.
$b_{\text{dyn}} = 4K_B$	μm	Equivalent ellipse minor axis.
$\theta_{\text{dyn}} = \arctan[(I_X - I_A)/I_{XY}]$		Orientation angle of the principal inertial axes (A,B).
$Q_{\text{dyn}} = K_A/K_B$		Anisometry, ratio of radii of gyration.
$B_{\text{dyn}} = 4\pi K_A K_B/a$		Bulkiness.

NOTES: Notation after Medalia (1970). The dimension of the parameters (Dim.) is arbitrarily reported in microns. Primary parameters are listed in Table 5.1. a is the area of the feature (Table 5.2).

Table 5.4

Bulk Stereological Parameters from Feature Analysis

Sample Number		ϕ (%)	S_{Vp} (μm^{-1})	$\bar{L}_{3p}$ (μm)	N_A $\times 10^3$ (μm^{-2})	F	T_{A+} $\times 10^3$ (μm^{-2})	T_{A-} $\times 10^3$ (μm^{-2})
2124	Orig	20.44	0.325	12.3	1.28	0.89	2.99	0.423
	SMS	20.44	0.394	10.1	1.91	0.89	4.07	0.252
2509	Orig	21.45	0.183	21.8	0.41	0.94	0.94	0.133
	SMS	21.45	0.225	17.8	0.63	0.91	1.33	0.060
2513	Orig	21.08	0.277	14.4	1.11	0.77	2.55	0.328
	SMS	21.08	0.340	11.8	1.61	0.80	3.41	0.194
2519	Orig	17.59	0.170	23.6	0.27	0.98	0.67	0.127
	SMS	17.59	0.214	18.7	0.45	0.95	0.96	0.066
2521	Orig	24.45	0.163	24.6	0.43	0.80	0.99	0.124
	SMS	24.45	0.203	19.7	0.66	0.81	1.38	0.060
2523	Orig	18.39	0.386	10.3	1.60	0.91	3.64	0.440
	SMS	18.39	0.453	8.8	2.20	0.91	4.66	0.267
2686	Orig	26.44	0.198	20.2	0.72	0.76	1.83	0.382
	SMS	26.44	0.254	15.8	1.24	0.72	2.73	0.230
2687	Orig	18.57	0.390	10.2	2.12	0.71	4.51	0.272
	SMS	18.57	0.439	9.1	2.50	0.76	5.18	0.176
2700	Orig	23.55	0.300	13.3	1.94	0.58	4.26	0.384
	SMS	23.55	0.354	11.3	2.42	0.65	5.11	0.258
2704	Orig	19.28	0.301	13.3	1.44	0.64	3.22	0.339
	SMS	19.28	0.346	11.5	1.81	0.68	3.84	0.217
2710	Orig	28.87	0.240	16.7	1.56	0.57	3.60	0.486
	SMS	28.87	0.293	13.7	2.05	0.64	4.47	0.369

Table 5.4 (cont)

Bulk Stereological Parameters from Feature Analysis

Sample Number		ϕ (%)	S_{Vp} (μm^{-1})	$\overline{L}_{3p}$ (μm)	N_A $\times 10^3$ (μm^{-2})	F	T_{A+} $\times 10^3$ (μm^{-2})	T_{A-} $\times 10^3$ (μm^{-2})
2841	Orig	32.68	0.175	22.8	0.93	0.57	2.21	0.354
	SMS	32.68	0.245	16.3	1.47	0.71	3.15	0.210
2842	Orig	14.36	0.263	15.2	0.92	0.57	2.01	0.171
	SMS	14.36	0.312	12.8	1.21	0.61	2.53	0.104
2843	Orig	26.58	0.255	15.7	1.44	0.64	3.30	0.417
	SMS	26.58	0.316	12.6	2.06	0.68	4.38	0.259

NOTES: All values are from high magnification images only. For each rock, the high magnification images are all at the same magnification, typically 100×. Exponents in table heading modify headings not values. Orig stands for original unsegmented image values. SMS stands for SMS segmented image values.

Table 5.5
Area Filtered Bulk Stereological Parameters

Sample Number	Minimum Area† (μm^2)	ϕ (%)	S_{Vp} (μm^{-1})	$\overline{L}_{3p}$ (μm)	N_A $\times 10^3$ (μm^{-2})	F	q_F
2124	19.5	19.54	0.337	11.9	0.98	1.20	0.41
	48.8	18.34	0.289	13.8	0.52	1.57	0.26
	97.6	17.22	0.258	15.5	0.34	1.78	0.21
2509	75.7	20.12	0.185	21.6	0.28	1.29	0.36
	189.2	18.89	0.161	24.9	0.16	1.66	0.24
	378.4	17.78	0.147	27.3	0.11	1.82	0.21
2513	22.1	20.16	0.285	14.0	0.77	1.12	0.49
	55.3	19.10	0.244	16.4	0.40	1.49	0.28
	110.5	18.13	0.219	18.2	0.27	1.70	0.23
2519	73.9	16.76	0.183	21.9	0.22	1.33	0.34
	184.8	15.81	0.161	24.9	0.13	1.69	0.23
	369.7	14.83	0.146	27.5	0.09	1.91	0.19
2521	73.9	23.11	0.166	24.0	0.30	1.13	0.48
	184.8	21.88	0.144	27.7	0.17	1.40	0.31
	369.7	20.59	0.129	30.9	0.12	1.52	0.27
2523	19.5	17.20	0.371	10.8	0.98	1.28	0.36
	48.8	16.06	0.320	12.5	0.53	1.65	0.24
	97.6	14.88	0.286	14.0	0.34	1.87	0.20
2686	22.1	25.84	0.224	17.8	0.70	0.97	–
	55.2	24.99	0.197	20.3	0.41	1.26	0.37
	110.5	24.01	0.176	22.7	0.27	1.44	0.29
2687	19.5	16.40	0.396	10.1	1.17	1.16	0.45
	48.8	14.76	0.319	12.5	0.52	1.53	0.27
	97.6	13.42	0.275	14.5	0.31	1.74	0.22

Table 5.5 (cont)

Area Filtered Bulk Stereological Parameters

Sample Number	Minimum Area† (μm^2)	ϕ (%)	S_{Vp} (μm^{-1})	$\overline{L}_{3p}$ (μm)	N_A $\times 10^3$ (μm^{-2})	F	q_F
2700	19.5	22.09	0.270	14.8	0.93	0.92	–
	48.8	20.73	0.217	18.4	0.40	1.30	0.35
	97.6	19.78	0.190	21.0	0.25	1.54	0.26
2704	19.5	18.27	0.275	14.5	0.78	0.95	–
	48.8	17.20	0.224	17.8	0.35	1.32	0.34
	97.6	16.33	0.195	20.5	0.21	1.57	0.26
2710	19.5	27.73	0.238	16.8	0.88	0.94	–
	48.8	26.54	0.200	20.0	0.41	1.36	0.32
	97.6	25.53	0.177	22.6	0.25	1.68	0.23
2841	30.5	31.54	0.206	19.4	0.72	0.99	–
	76.3	30.14	0.176	22.7	0.38	1.31	0.34
	152.6	28.93	0.158	25.3	0.26	1.50	0.27
2842	19.5	13.63	0.242	16.5	0.46	0.91	–
	48.8	13.02	0.202	19.8	0.22	1.28	0.36
	97.6	12.57	0.182	22.0	0.15	1.47	0.28
2843	19.1	25.55	0.263	15.2	0.99	0.95	–
	47.9	24.32	0.221	18.1	0.49	1.27	0.37
	95.7	23.15	0.192	20.8	0.30	1.49	0.28

NOTES: All values are from high magnification images only. For each rock, the high magnification images are all at the same magnification, typically 100×. Exponents in table heading modify headings not values.

† Minimum areas for each sample correspond to 2-, 5-, and 10-pixel minimum area features.

Table 5.6

Mean Feature Parameters

Sample Number		a (μm^2)	p_v (μm)	$\overline{F_{33}}$	$\overline{m}$ (μm)	q_{ee}	$d_{F\ max}$ (μm)
2124	Orig	159.1	40.6	1.26	1.26	2.96	11.1
	SMS	107.1	33.2	1.24	1.51	2.73	10.4
2509	Orig	528.7	76.0	1.24	2.44	2.87	21.5
	SMS	338.7	59.7	1.21	2.86	2.58	18.8
2513	Orig	189.8	41.3	1.24	1.32	2.84	11.9
	SMS	131.2	35.0	1.23	1.62	2.68	11.1
2519	Orig	643.1	85.6	1.26	2.42	3.06	22.1
	SMS	393.2	65.9	1.24	3.00	2.73	20.5
2521	Orig	565.4	72.3	1.23	2.49	2.76	20.7
	SMS	369.3	58.9	1.21	2.91	2.54	18.6
2523	Orig	114.9	34.9	1.24	1.19	2.82	9.7
	SMS	83.8	29.8	1.22	1.37	2.64	9.2
2686	Orig	365.5	56.7	1.28	1.40	3.16	14.2
	SMS	211.9	42.2	1.26	1.85	2.86	13.4
2687	Orig	87.7	26.9	1.20	1.15	2.54	7.8
	SMS	74.3	25.6	1.20	1.27	2.48	7.8
2700	Orig	121.6	28.7	1.20	1.06	2.54	7.7
	SMS	97.1	27.0	1.20	1.28	2.52	8.2
2704	Orig	133.7	31.6	1.22	1.13	2.67	8.7
	SMS	106.4	28.9	1.22	1.33	2.61	8.9
2710	Orig	185.7	34.9	1.22	1.08	2.70	8.5
	SMS	140.9	32.4	1.23	1.38	2.70	9.9

Table 5.6 (cont)

Mean Feature Parameters

Sample Number		a (μm^2)	p_v (μm)	$\overline{F_{33}}$	$\overline{m}$ (μm)	q_{ee}	$d_{F\ max}$ (μm)
2841	Orig	352.0	48.4	1.22	1.39	2.72	11.2
	SMS	211.1	42.7	1.23	2.01	2.67	13.3
2842	Orig	156.3	32.3	1.20	1.20	2.54	9.4
	SMS	118.3	29.0	1.20	1.39	2.48	9.1
2843	Orig	184.6	37.0	1.24	1.16	2.80	10.0
	SMS	128.9	32.0	1.23	1.47	2.70	10.2

NOTES: All values are from high magnification images only. For each rock, the high magnification images are all at the same magnification, typically 100×. Orig stands for original unsegmented image values. SMS stands for SMS segmented image values.

Table 5.7

Area Filtered Mean Feature Parameters

Sample Number	Minimum Area† (μm^2)	a (μm^2)	p_v (μm)	$\overline{F_{33}}$	$\overline{m}$ (μm)	q_{ee}	$d_{F\ max}$ (μm)
2124	19.5	199.3	52.7	1.34	2.19	3.37	17.3
	48.8	355.5	80.6	1.45	3.13	4.07	26.6
	97.6	506.0	102.4	1.50	3.88	4.41	33.5
2509	75.7	709.9	103.1	1.32	4.49	3.22	34.4
	189.2	1207.6	152.5	1.40	6.31	3.74	51.1
	378.4	1594.3	183.7	1.42	7.53	3.89	61.2
2513	22.1	260.4	58.4	1.34	2.46	3.34	19.5
	55.3	471.6	90.5	1.44	3.59	4.01	30.4
	110.5	665.3	114.6	1.48	4.46	4.32	38.3
2519	73.9	750.5	107.7	1.34	4.48	3.40	34.9
	184.8	1233.8	155.8	1.43	6.12	4.00	50.5
	369.6	1698.6	194.2	1.48	7.46	4.32	62.3
2521	73.9	767.5	100.4	1.30	4.57	3.11	33.5
	184.8	1264.7	143.5	1.37	6.29	3.50	48.2
	369.6	1710.9	173.9	1.38	7.61	3.58	58.3
2523	19.5	176.0	51.3	1.34	2.10	3.36	16.8
	48.8	303.0	76.3	1.44	2.90	4.00	25.0
	97.6	431.7	96.9	1.49	3.56	4.37	31.4
2686	22.1	366.3	64.4	1.35	2.63	3.47	21.2
	55.6	612.5	94.6	1.45	3.65	4.10	31.2
	110.5	880.5	121.6	1.51	4.58	4.52	39.8
2687	19.5	140.4	43.6	1.30	1.95	3.08	14.4
	48.8	283.3	71.0	1.40	2.94	3.69	23.5
	97.6	434.2	93.9	1.44	3.81	4.00	31.0

Table 5.7 (cont)

Area Filtered Mean Feature Parameters

Sample Number	Minimum Area† (μm^2)	a (μm^2)	p_v (μm)	$\overline{F_{33}}$	$\overline{m}$ (μm)	q_{ee}	$d_{F\ max}$ (μm)
2700	19.5	236.5	50.2	1.32	2.08	3.25	16.4
	48.8	520.3	88.6	1.45	3.34	4.13	28.8
	97.6	797.8	119.4	1.52	4.37	4.58	38.4
2704	19.5	235.6	50.9	1.33	2.05	3.34	16.7
	48.8	493.8	87.0	1.47	3.17	4.24	28.6
	97.6	776.6	119.0	1.55	4.18	4.79	38.6
2710	19.5	315.0	58.8	1.36	2.18	3.56	18.8
	48.8	646.1	101.2	1.52	3.36	4.67	32.3
	97.6	1013.5	140.8	1.62	4.45	5.43	44.3
2841	30.5	438.9	71.0	1.33	3.09	3.30	23.1
	76.3	799.4	110.4	1.42	4.57	3.92	35.9
	152.6	1134.7	140.9	1.47	5.75	4.25	45.4
2842	19.5	292.8	55.6	1.31	2.36	3.15	18.7
	48.8	590.8	93.6	1.41	3.72	3.76	31.7
	97.6	838.1	119.9	1.44	4.68	3.98	40.4
2843	19.1	258.5	53.4	1.34	2.22	3.40	17.8
	47.9	492.2	85.3	1.46	3.30	4.19	28.7
	95.7	762.3	115.0	1.52	4.36	4.63	38.4

NOTES: All values are from high magnification images only. For each rock, the high magnification images are all at the same magnification, typically 100×.

† Minimum areas for each sample correspond to 2-, 5-, and 10-pixel minimum area features.

Table 5.8
Dynamic Feature Parameters

Sample Number		θ_{dyn} (degrees)	Q_{dyn}	B_{dyn}	q^*
2124	Orig	-89.4 ± 52.9	1.54	0.89	
	SMS	88.5 ± 55.4	1.58	0.90	
2509	Orig	-87.8 ± 46.9	1.41	0.88	
	SMS	-88.0 ± 51.4	1.49	0.88	
2513	Orig	-79.3 ± 48.4	1.55	0.87	
	SMS	-77.5 ± 53.2	1.57	0.89	
2519	Orig	-87.4 ± 55.7	1.46	0.88	
	SMS	-85.0 ± 62.4	1.53	0.89	
2521	Orig	-83.0 ± 57.9	1.42	0.87	
	SMS	-89.1 ± 59.0	1.47	0.88	
2523	Orig	-61.9 ± 77.7	1.46	0.87	
	SMS	-64.2 ± 82.6	1.50	0.88	0.73
2686	Orig	-76.7 ± 44.0	1.65	0.89	
	SMS	-74.5 ± 48.8	1.67	0.91	
2687	Orig	-78.9 ± 61.9	1.43	0.85	
	SMS	-78.7 ± 63.0	1.45	0.86	0.74
2700	Orig	-66.2 ± 65.9	1.39	0.84	
	SMS	-63.9 ± 65.6	1.44	0.86	0.76
2704	Orig	-87.4 ± 60.8	1.48	0.85	
	SMS	-83.4 ± 63.3	1.52	0.87	0.73
2710	Orig	-84.8 ± 72.1	1.44	0.85	
	SMS	-77.0 ± 70.4	1.51	0.88	0.73

Table 5.8 (cont)
Dynamic Feature Parameters

Sample Number		θ_{dyn} (degrees)	Q_{dyn}	B_{dyn}	q^*
2841	Orig	-80.0 ± 41.4	1.47	0.84	
	SMS	-78.0 ± 45.5	1.54	0.88	
2842	Orig	-83.3 ± 63.9	1.41	0.84	
	SMS	-85.8 ± 66.3	1.45	0.85	0.76
2843	Orig	-80.2 ± 48.8	1.55	0.87	
	SMS	-79.0 ± 52.3	1.61	0.89	

NOTES: All values are from high magnification images only. For each rock, the high magnification images are all at the same magnification, typically 100×. Orig stands for original unsegmented image values. SMS stands for SMS segmented image values. q^* is given by Eqn. (4.36).

Table 5.9

Area Filtered Dynamic Feature Parameters

Sample Number	Minimum Area† (μm^2)	θ_{dyn} (degrees)	Q_{dyn}	B_{dyn}		q^*
				SMS	Orig	
2124	19.5	88.5 ± 55.4	2.13	1.00	1.01	
	48.8	85.3 ± 58.6	2.15	1.18	1.30	
	97.6	83.5 ± 62.0	2.02	1.24	1.46	
2509	75.7	-88.0 ± 51.4	2.09	1.00	1.07	
	189.2	-88.1 ± 56.2	2.07	1.15	1.41	
	378.4	-87.3 ± 56.4	1.94	1.19	1.52	
2513	22.1	-77.5 ± 53.2	2.18	1.00	0.99	
	55.3	-69.5 ± 55.1	2.22	1.16	1.29	
	110.5	-61.4 ± 56.9	2.10	1.22	1.45	
2519	73.9	-85.0 ± 62.4	2.07	1.00	1.03	
	184.8	-88.7 ± 66.6	2.05	1.14	1.29	
	369.6	-73.0 ± 62.7	1.93	1.19	1.46	
2521	73.9	-89.1 ± 59.0	2.03	0.99	1.03	
	184.8	-86.7 ± 60.1	1.98	1.12	1.28	
	369.6	88.5 ± 61.1	1.84	1.16	1.38	
2523	19.5	-64.2 ± 82.6	2.12	1.00	1.02	0.44
	48.8	-47.2 ± 80.9	2.10	1.17	1.27	0.47
	97.6	-41.4 ± 77.5	2.00	1.23	1.42	0.50
2686	22.1	-74.5 ± 48.8	2.19	1.01	1.00	
	55.6	-64.8 ± 49.5	2.23	1.16	1.26	
	110.5	-60.6 ± 45.9	2.16	1.22	1.44	
2687	19.5	-78.7 ± 63.0	2.08	0.96	0.95	0.45
	48.8	-73.8 ± 61.4	2.07	1.14	1.19	0.48
	97.6	-71.2 ± 59.6	1.93	1.20	1.32	0.52

Table 5.9 (cont)
Area Filtered Dynamic Feature Parameters

Sample Number	Minimum Area† (μm^2)	θ_{dyn} (degrees)	Q_{dyn}	B_{dyn}		q^*
				SMS	Orig	
2700	19.5	-63.9 ± 65.6	2.13	0.97	0.94	0.43
	48.8	-53.5 ± 60.1	2.15	1.17	1.25	0.46
	97.6	-49.6 ± 57.4	2.03	1.24	1.41	0.49
2704	19.5	-83.4 ± 63.3	2.22	0.98	0.96	0.42
	48.8	-83.1 ± 62.0	2.33	1.18	1.26	0.44
	97.6	-74.9 ± 62.8	2.18	1.27	1.45	0.47
2710	19.5	-77.0 ± 70.4	2.19	1.00	0.96	0.43
	48.8	-74.3 ± 65.7	2.27	1.21	1.25	0.44
	97.6	-76.3 ± 68.3	2.18	1.30	1.47	0.46
2841	30.5	-78.0 ± 45.5	2.10	0.99	0.93	
	76.3	-72.5 ± 48.6	2.05	1.15	1.20	
	152.6	-72.8 ± 51.0	1.92	1.21	1.37	
2842	19.5	-85.8 ± 66.3	2.18	0.96	0.96	0.44
	48.8	-84.4 ± 66.1	2.21	1.14	1.24	0.46
	97.6	-89.5 ± 64.2	2.07	1.19	1.36	0.49
2843	19.1	-79.0 ± 52.3	2.27	1.00	0.98	
	47.9	-72.7 ± 52.3	2.37	1.18	1.27	
	95.7	-66.1 ± 57.3	2.22	1.27	1.54	

NOTES: All values are from high magnification images only. For each rock, the high magnification images are all at the same magnification, typically 100×. Orig stands for original unsegmented image values. SMS stands for SMS segmented image values. q^* is given by Eqn. (4.36).

† Minimum areas for each sample correspond to 2-, 5-, and 10-pixel minimum area features.

Table 5.10

Properties of Symmetric Structuring Elements

Index	Δ Area	Area	Diameters†			
			D_F	D_A	D_C	D_I
	(d^2)	(d^2)	(d)	(d)	(d)	(d)
1	5	5	3	2.52	3.16	1.41
2	7	12	4	3.91	4.47	2.83
3	12	24	6	5.53	6.32	4.47
4	13	37	7	6.86	7.62	5.83
5	20	57	9	8.52	9.49	7.07
6	19	76	10	9.84	10.77	8.48
7	28	104	12	11.51	12.65	10.00
8	25	129	13	12.82	13.93	11.40
9	36	165	15	14.49	15.81	12.73
10	31	196	16	15.80	17.09	14.14
11	44	240	18	17.48	18.97	15.62
12	37	277	19	18.78	20.25	17.03
13	52	329	21	20.47	22.14	18.38
14	43	372	22	21.76	23.41	19.80
15	60	432	24	23.45	25.30	21.26
16	49	481	25	24.75	26.57	22.67
17	68	549	27	26.44	28.46	24.04
18	55	604	28	27.73	29.73	25.46
19	76	680	30	29.42	31.62	26.91
20	61	741	31	30.71	32.89	28.32

NOTES: Diameters are given in units of pixel size d.

† D_F is the horizontal and vertical Feret diameter of the structuring element. D_A is the diameter of a circle with area equal to the area of the structuring element. D_C is the diameter of the smallest circle which can circumscribe the structuring element. D_I is the diameter of the largest circle which can be inscribed within the structuring element.

Table 5.11

Feature Granulometry Diameters

Sample Number	Diameters			
	Average (μm)	Median (μm)	95% (μm)	Maximum (μm)
2124	22.9 ± 22.1	19.6	55.3	84.4
2509	34.2 ± 31.6	33.1	67.1	92.3
2513	27.0 ± 25.9	25.3	59.2	79.8
2519	38.3 ± 36.4	33.7	85.8	127.7
2521	47.0 ± 45.3	40.2	107.5	164.1
2523	18.4 ± 17.5	15.8	42.4	65.6
2686	40.0 ± 38.6	36.5	82.6	93.1
2687†	17.2 ± 16.4	13.0	44.2	65.6
2700	35.1 ± 34.3	29.6	98.8	115.6
2704	35.5 ± 34.7	27.4	107.1	140.6
2710	43.3 ± 42.5	36.3	109.4	150.0
2841	46.9 ± 45.5	44.7	101.1	109.4
2842	30.1 ± 29.0	29.1	62.9	84.4
2843	37.9 ± 36.8	37.3	84.4	92.8

NOTES: All values are from high magnification images only. For each rock, the high magnification images are all at the same magnification, typically 100×.

† Image #1106 was omitted from the granulometry.

Figure 5.1

Figure 5.2

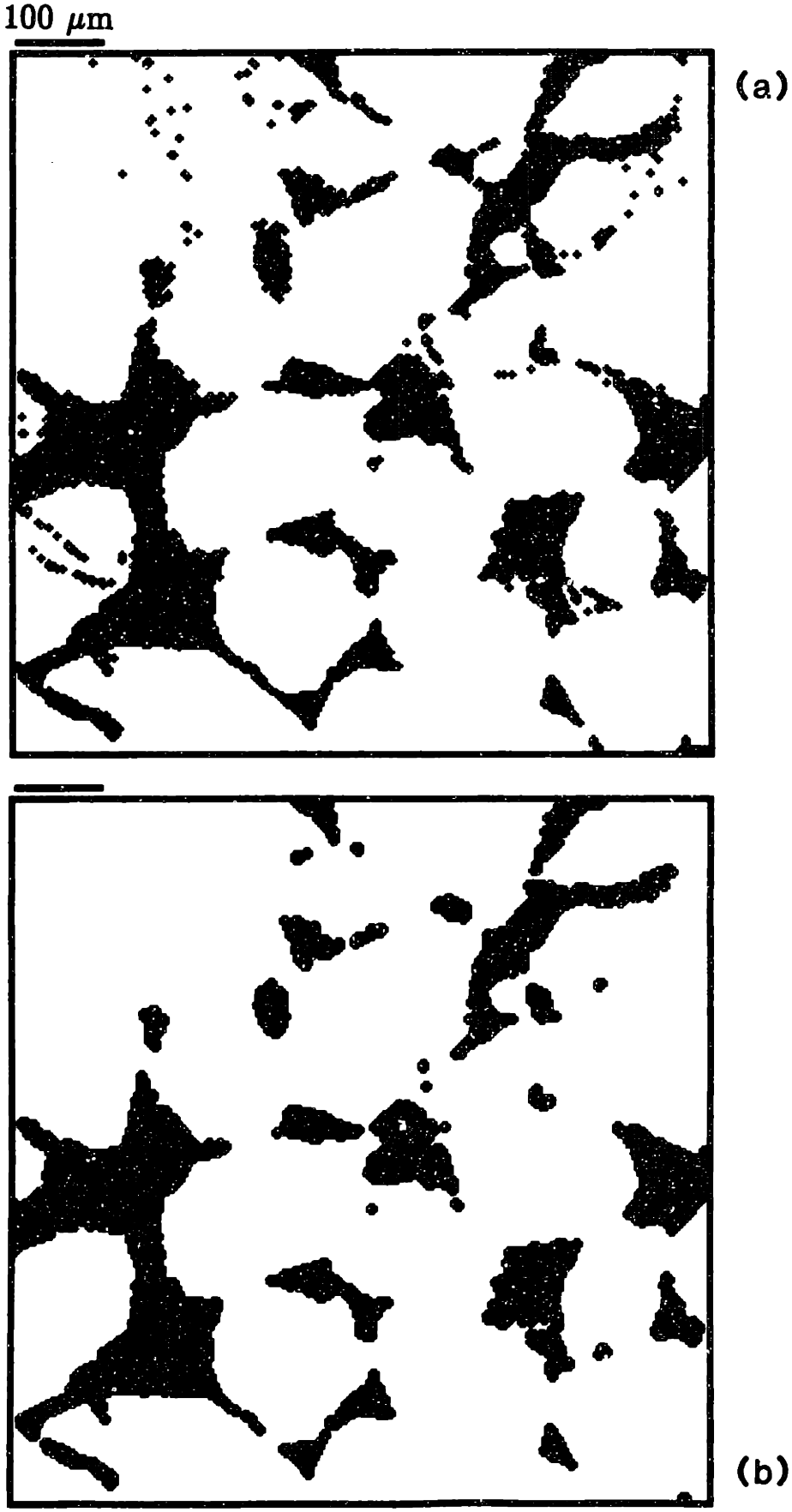

Figure 5.2

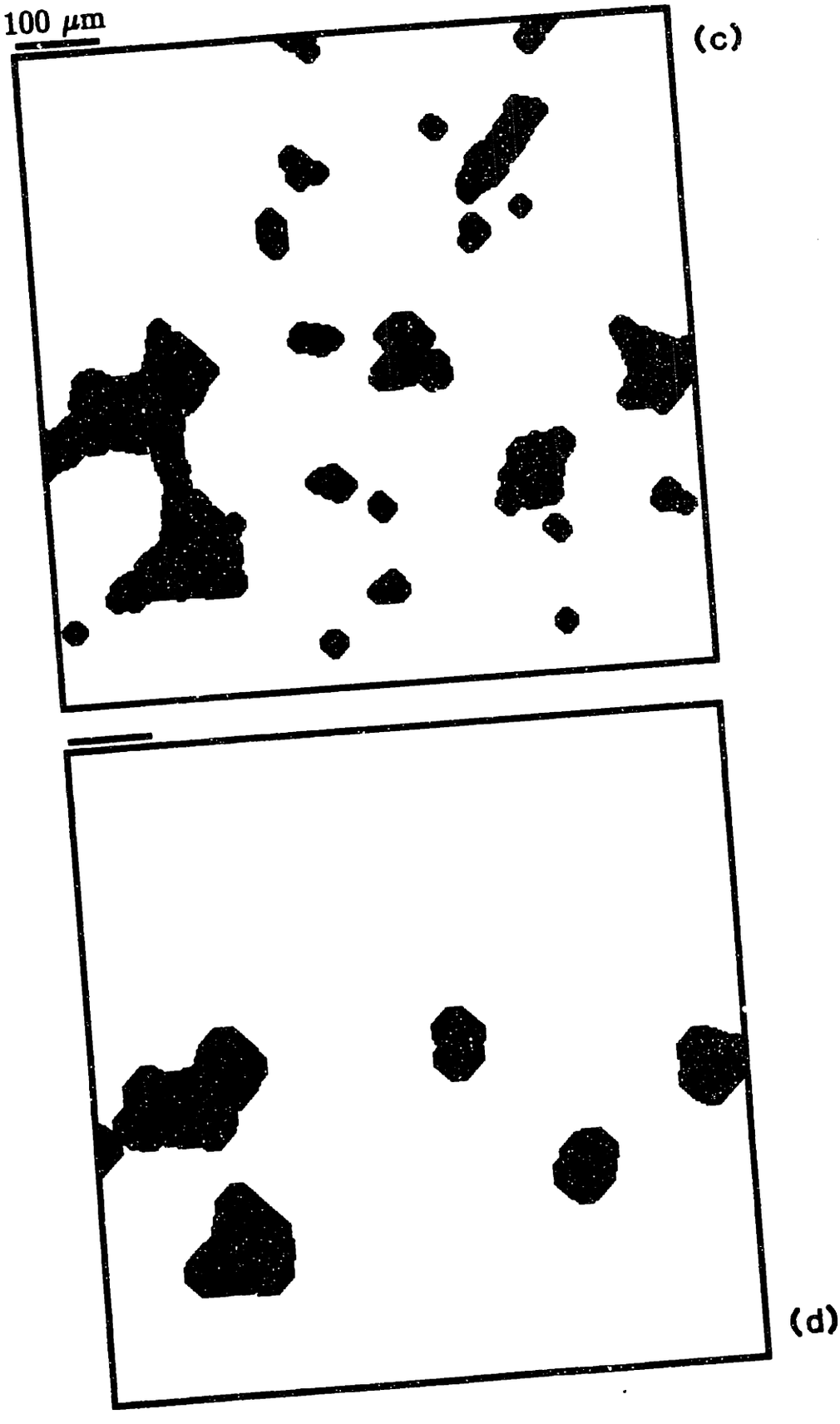

Figure 5.3 Image Cutting Process

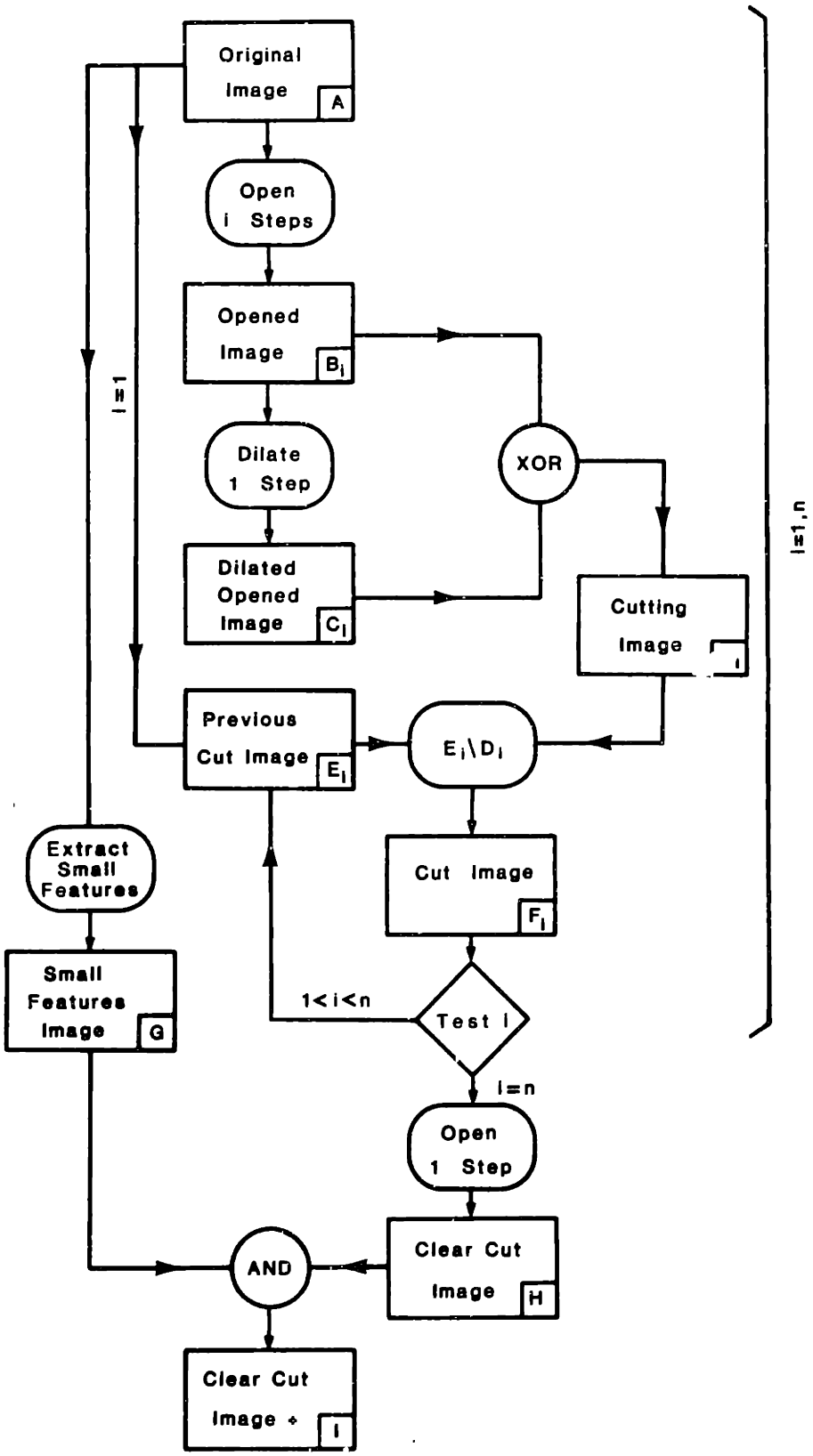

Figure 5.4

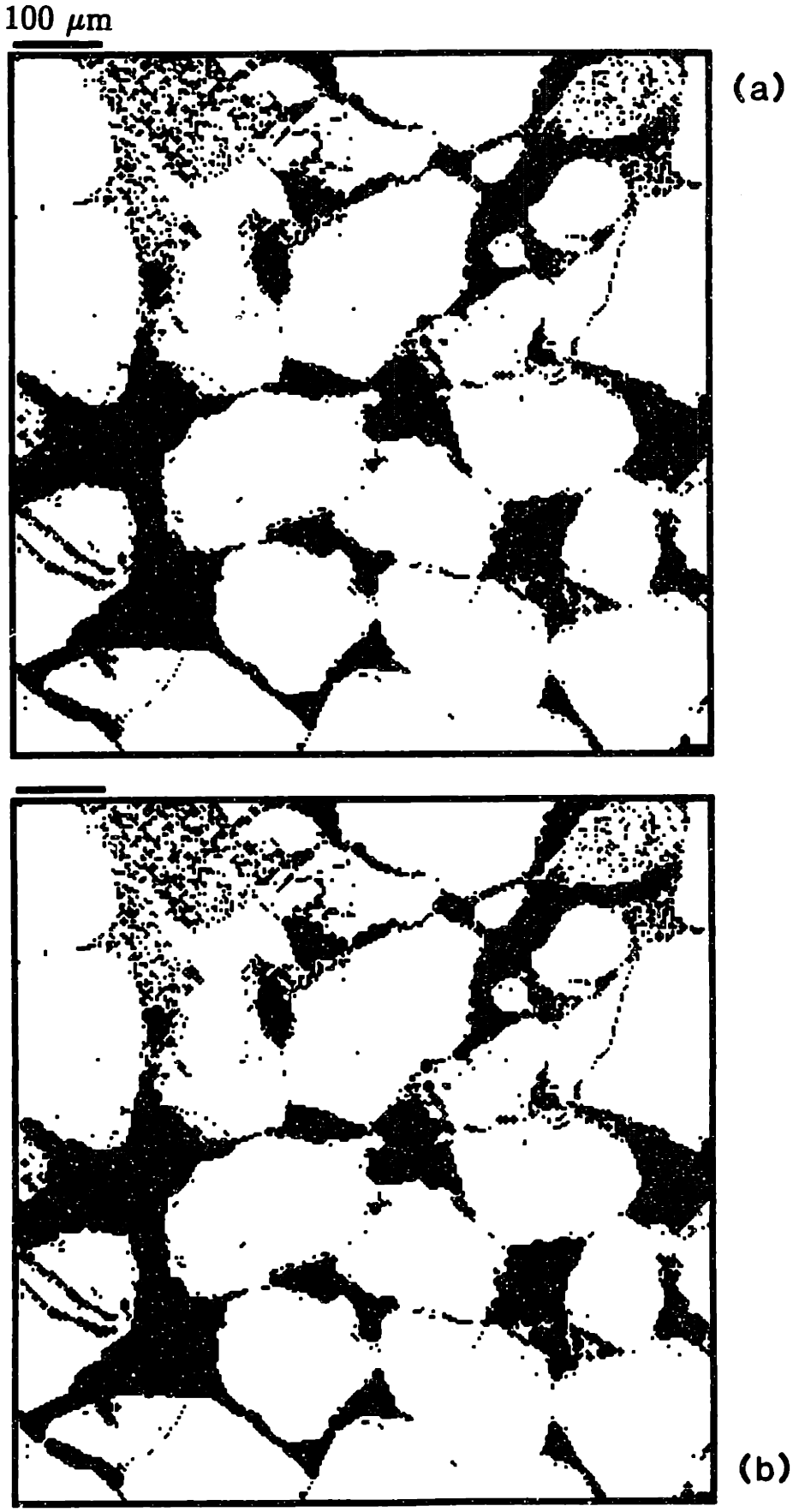

Figure 5.4

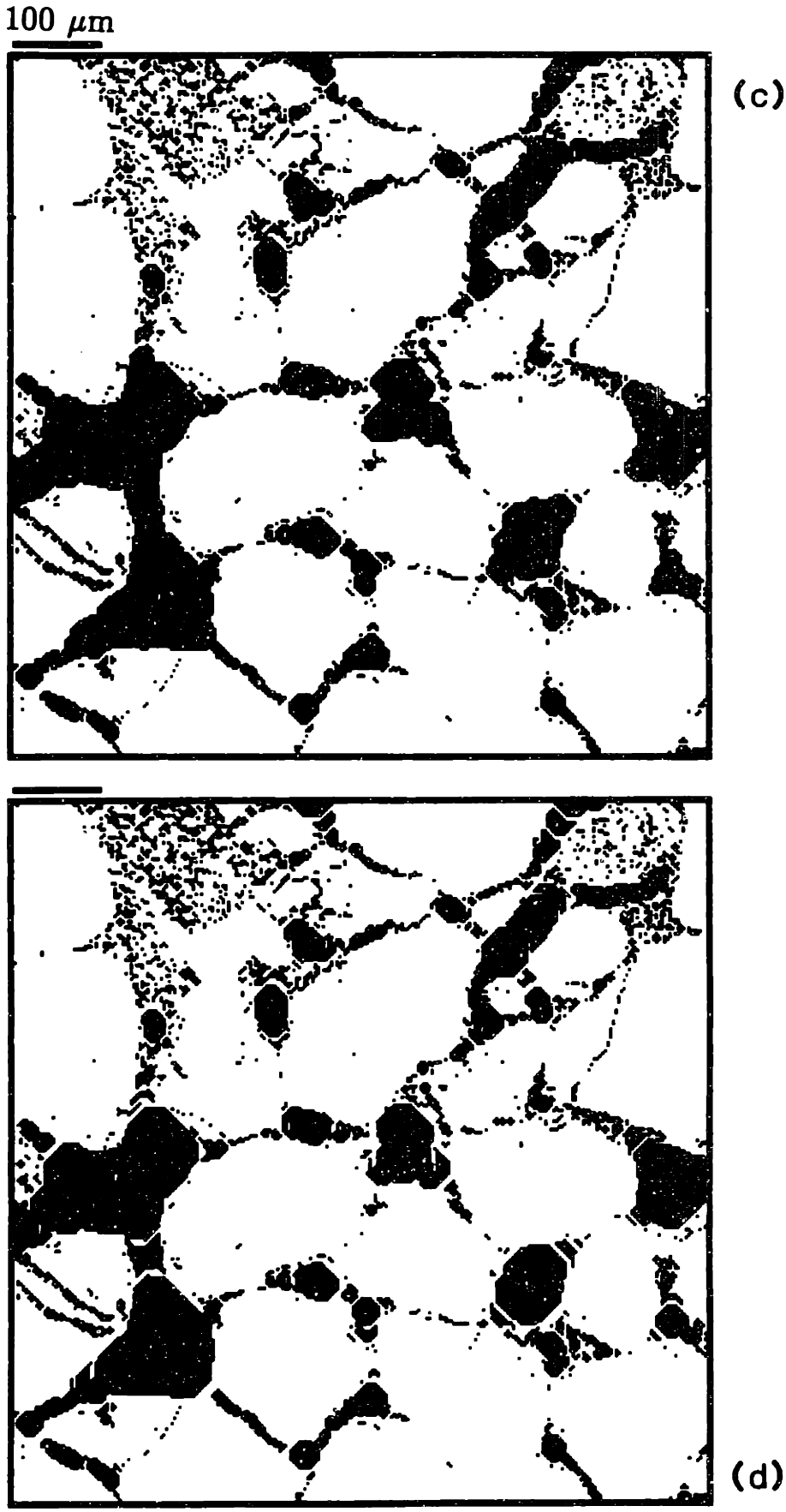

Figure 5.5

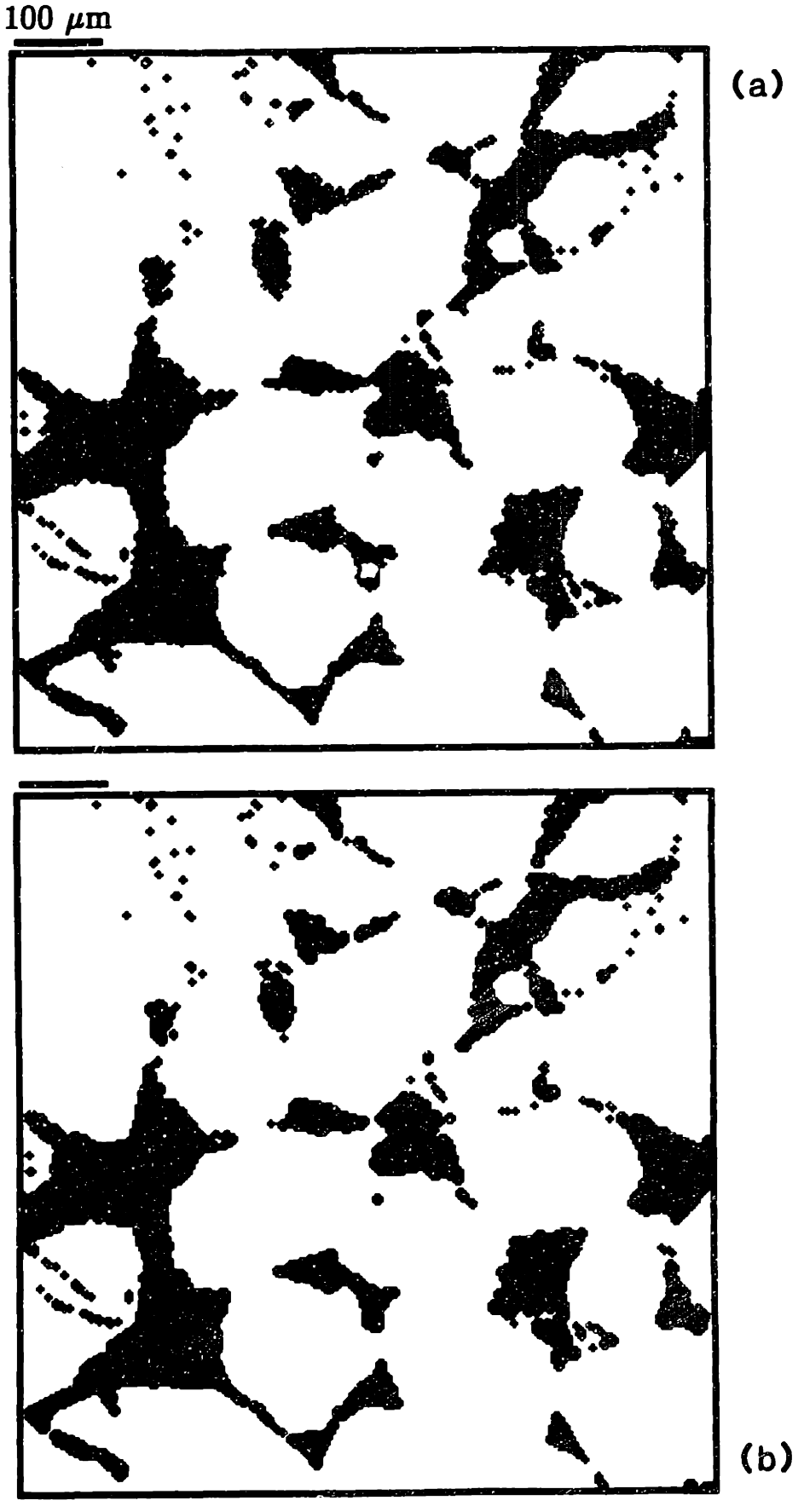

Figure 5.5

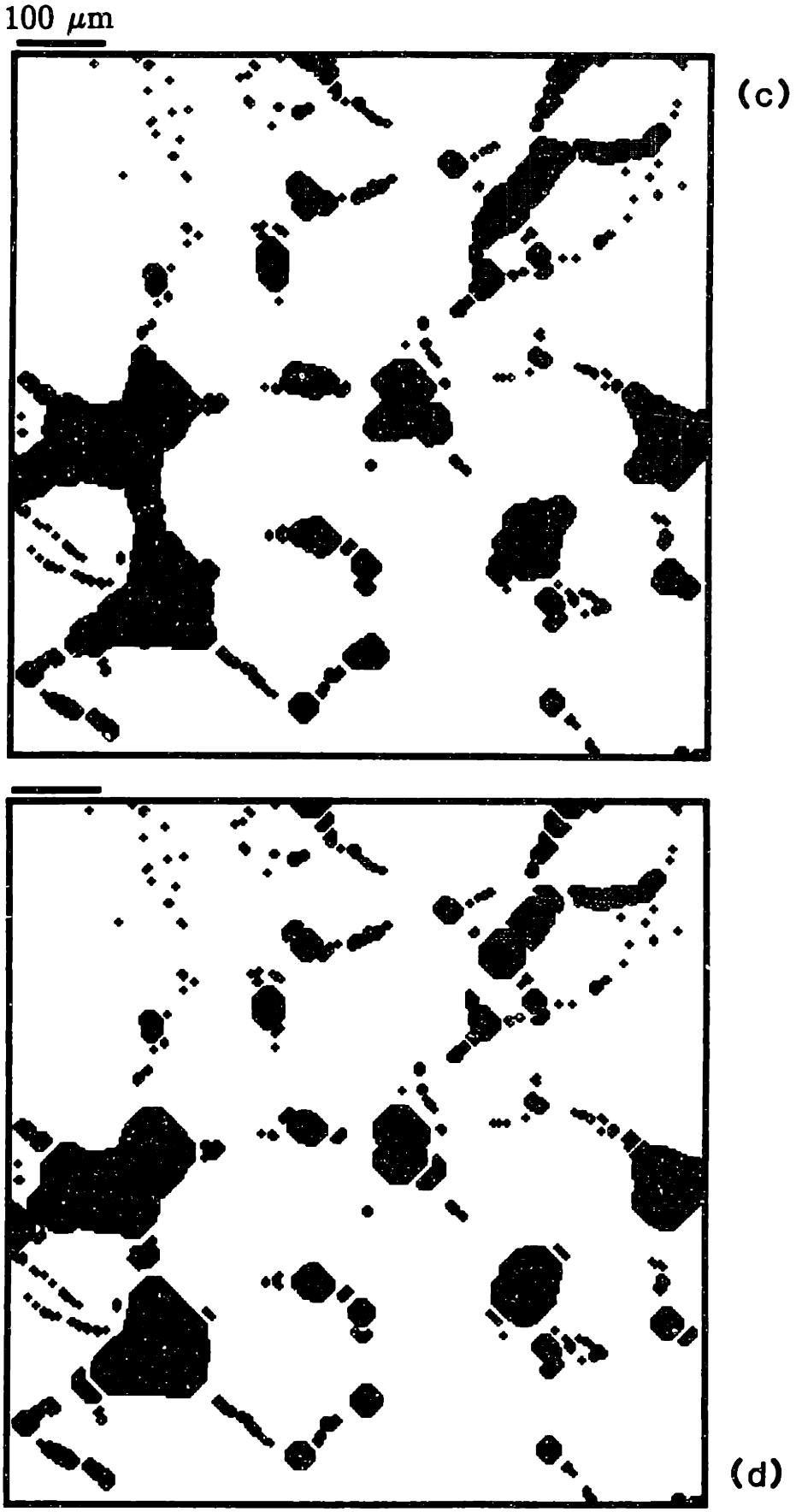

Figure 5.6

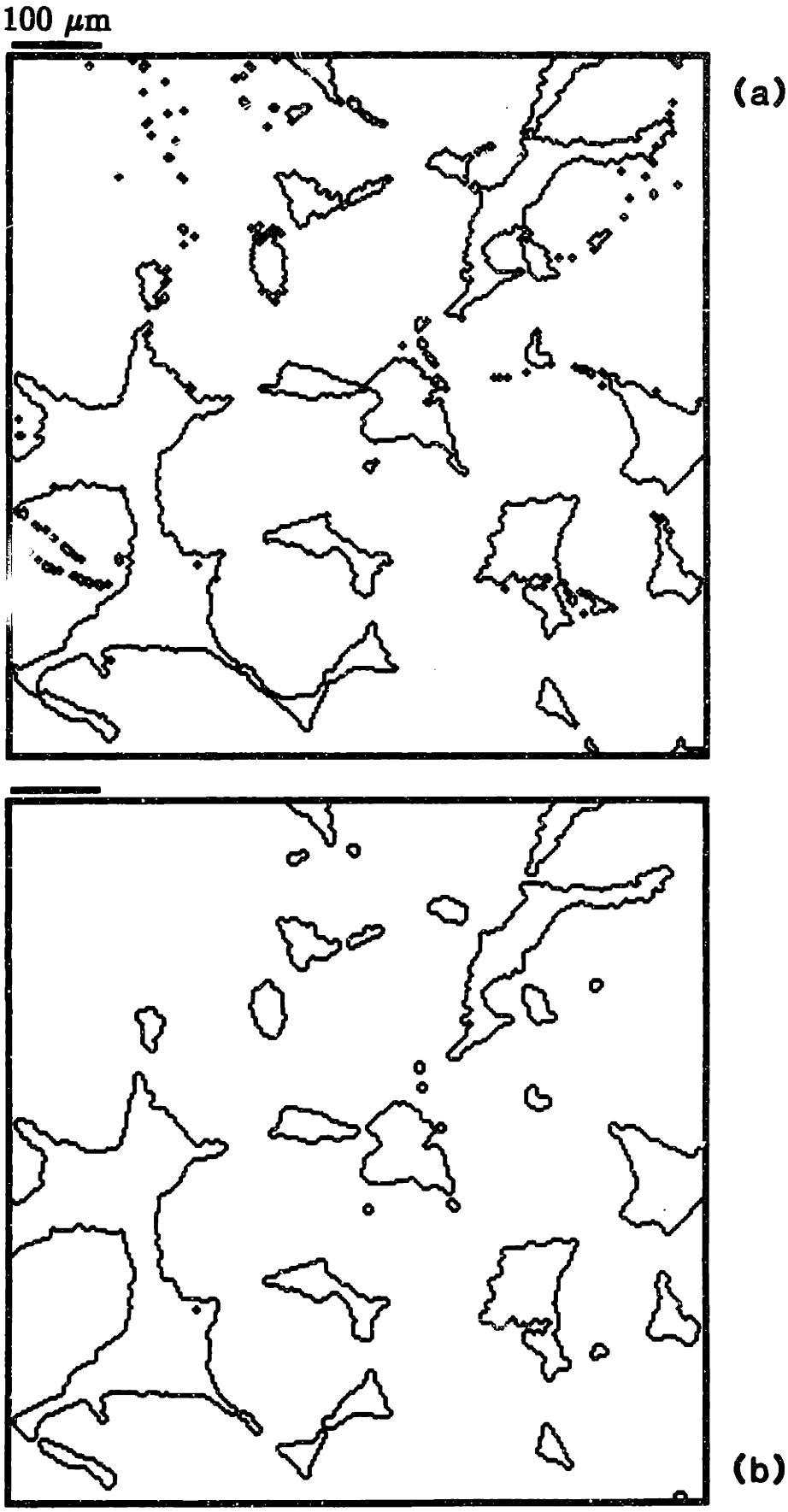

Figure 5.6

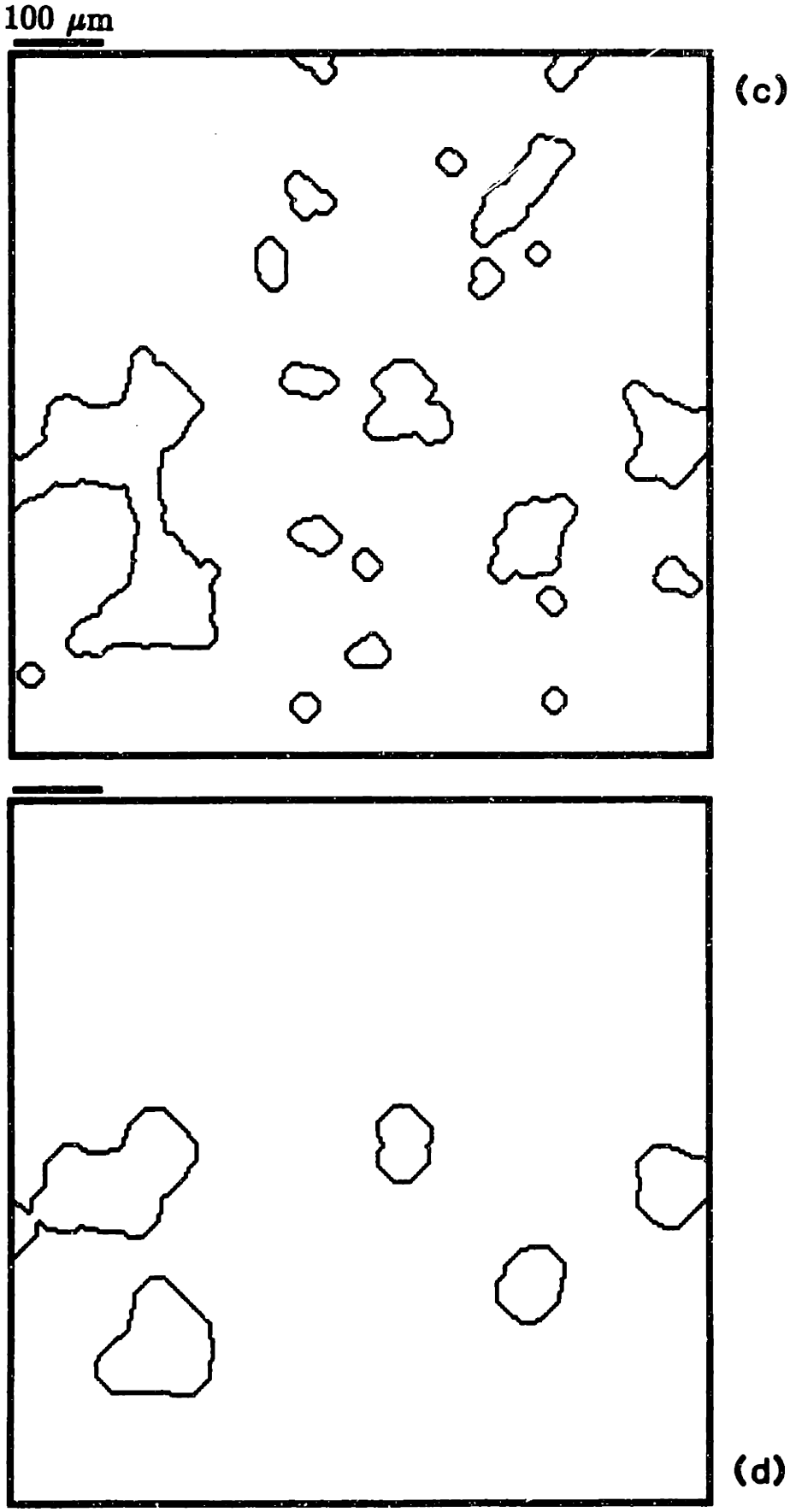

Figure 5.7

Subtractive Mask Segmentation

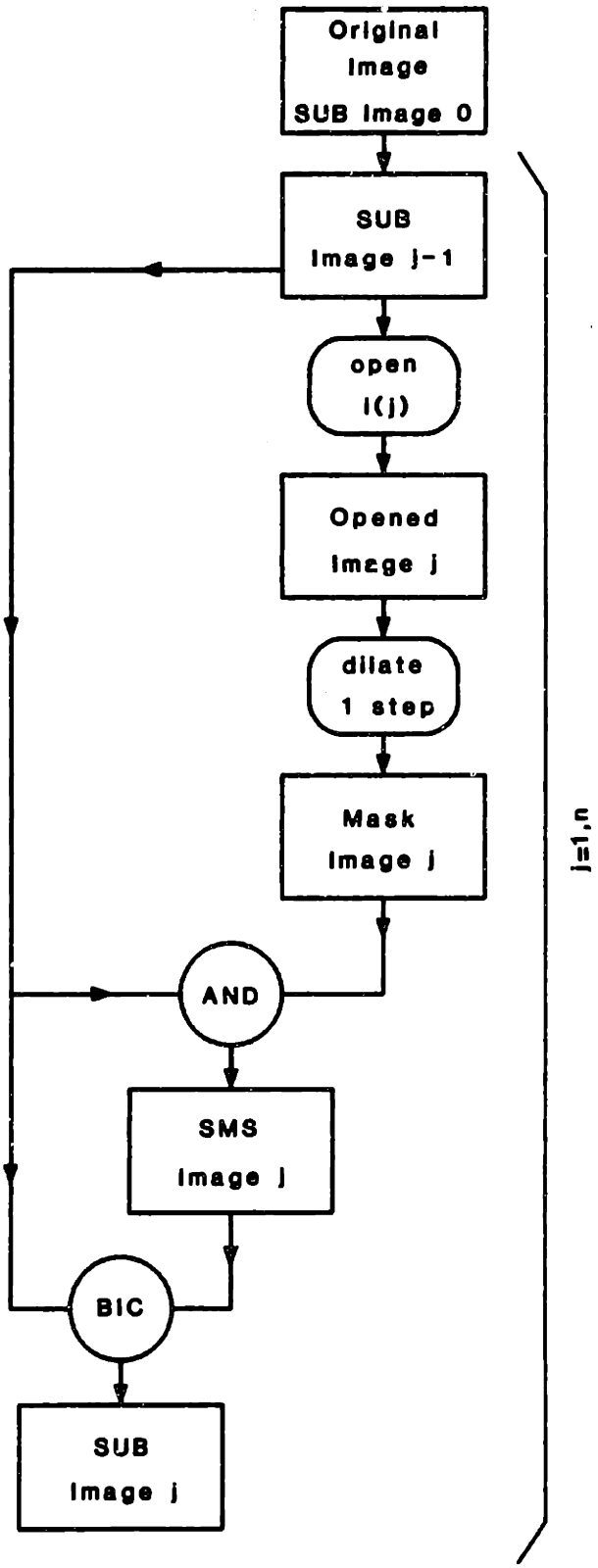

Figure 5.8

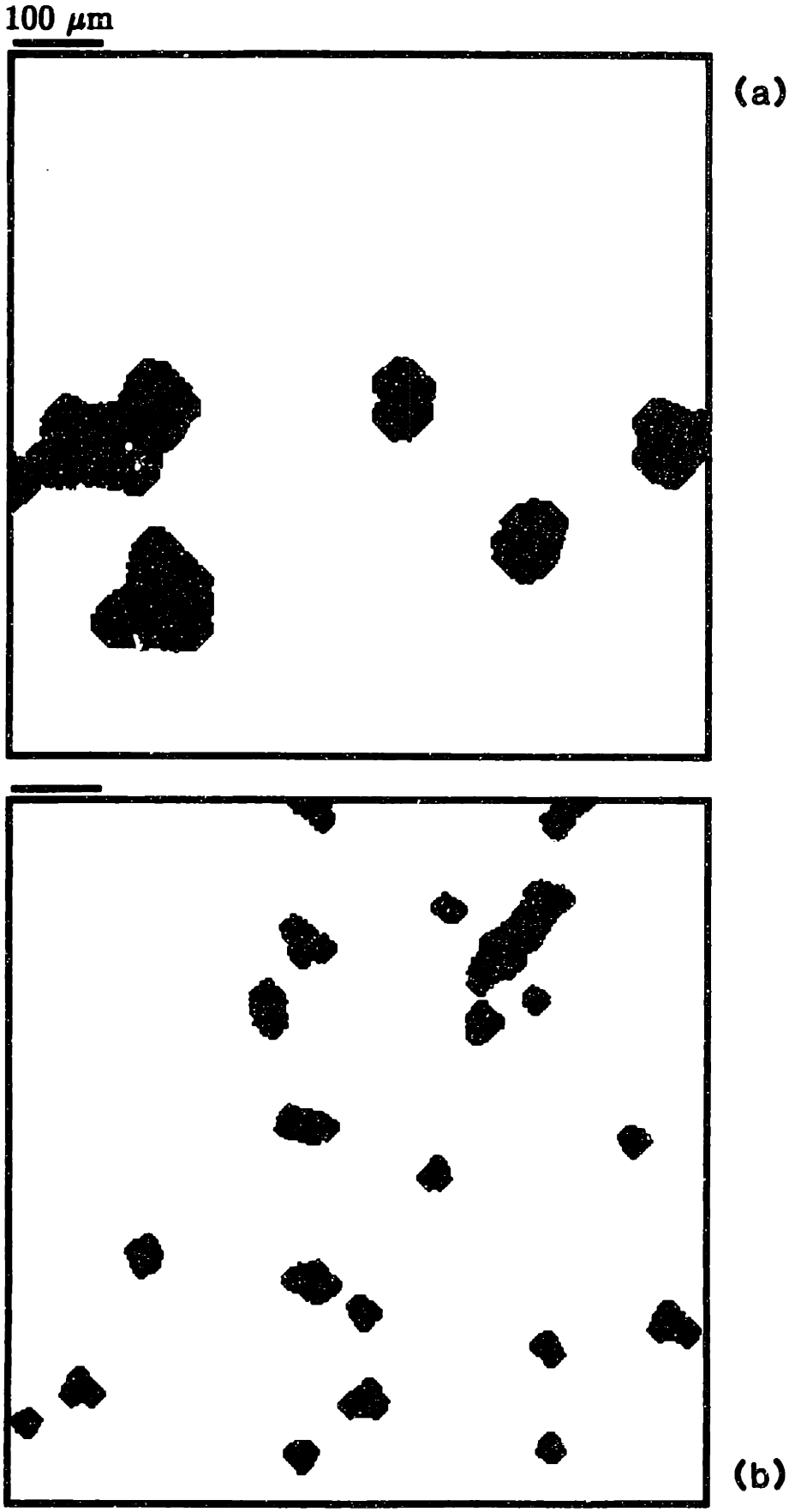

Figure 5.8

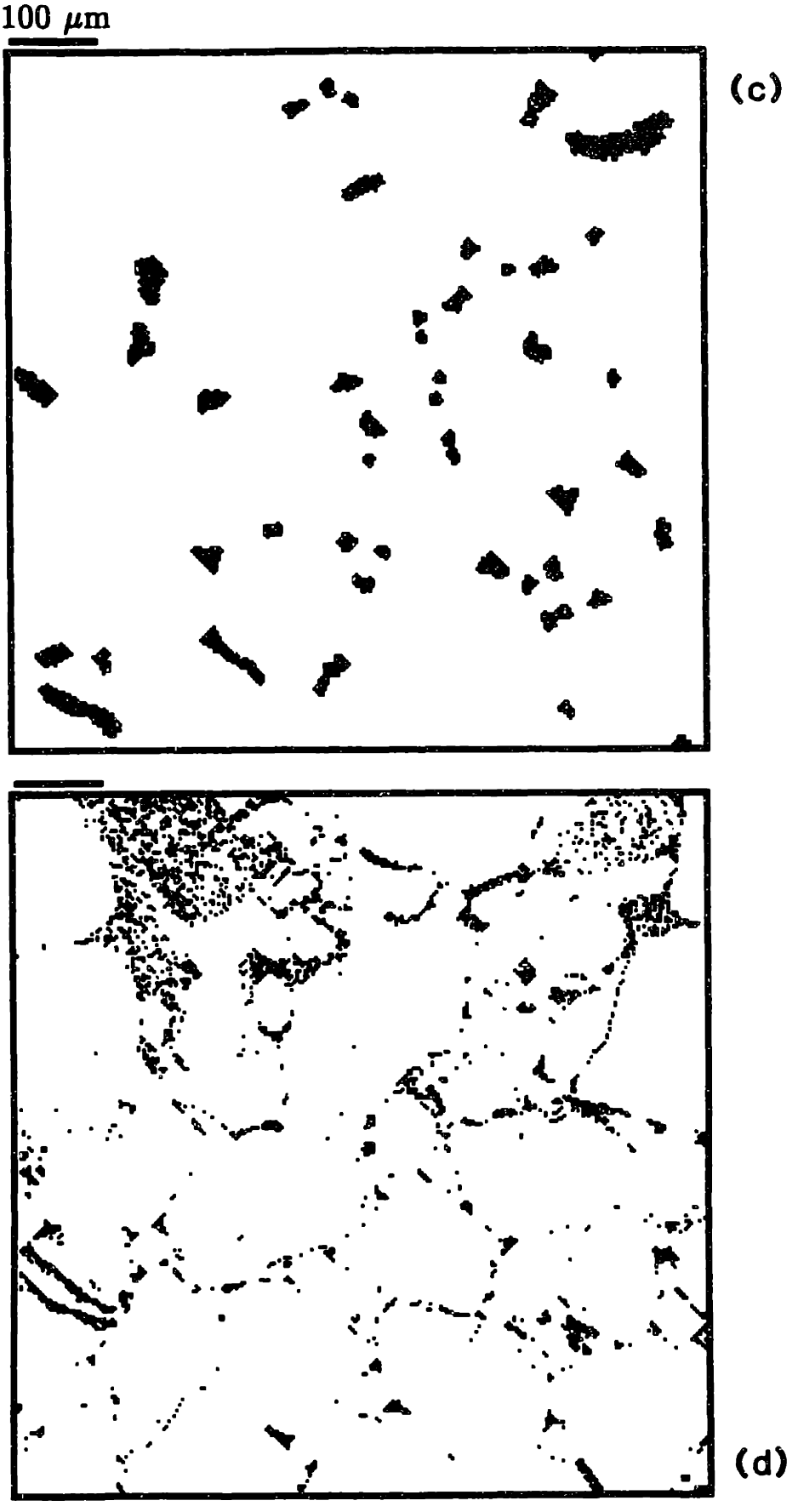

Figure 5.9

Figure 5.10

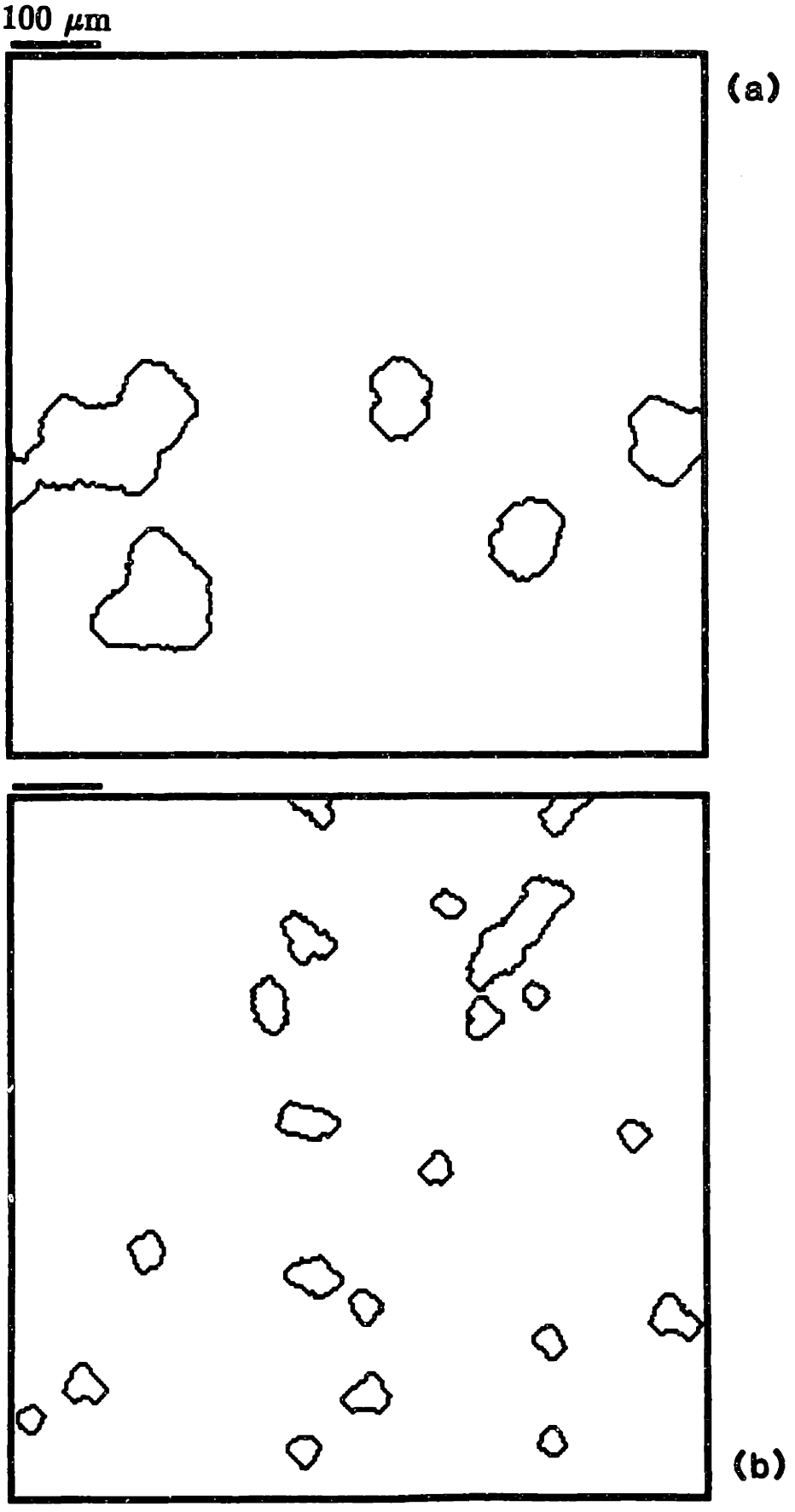

Figure 5.10

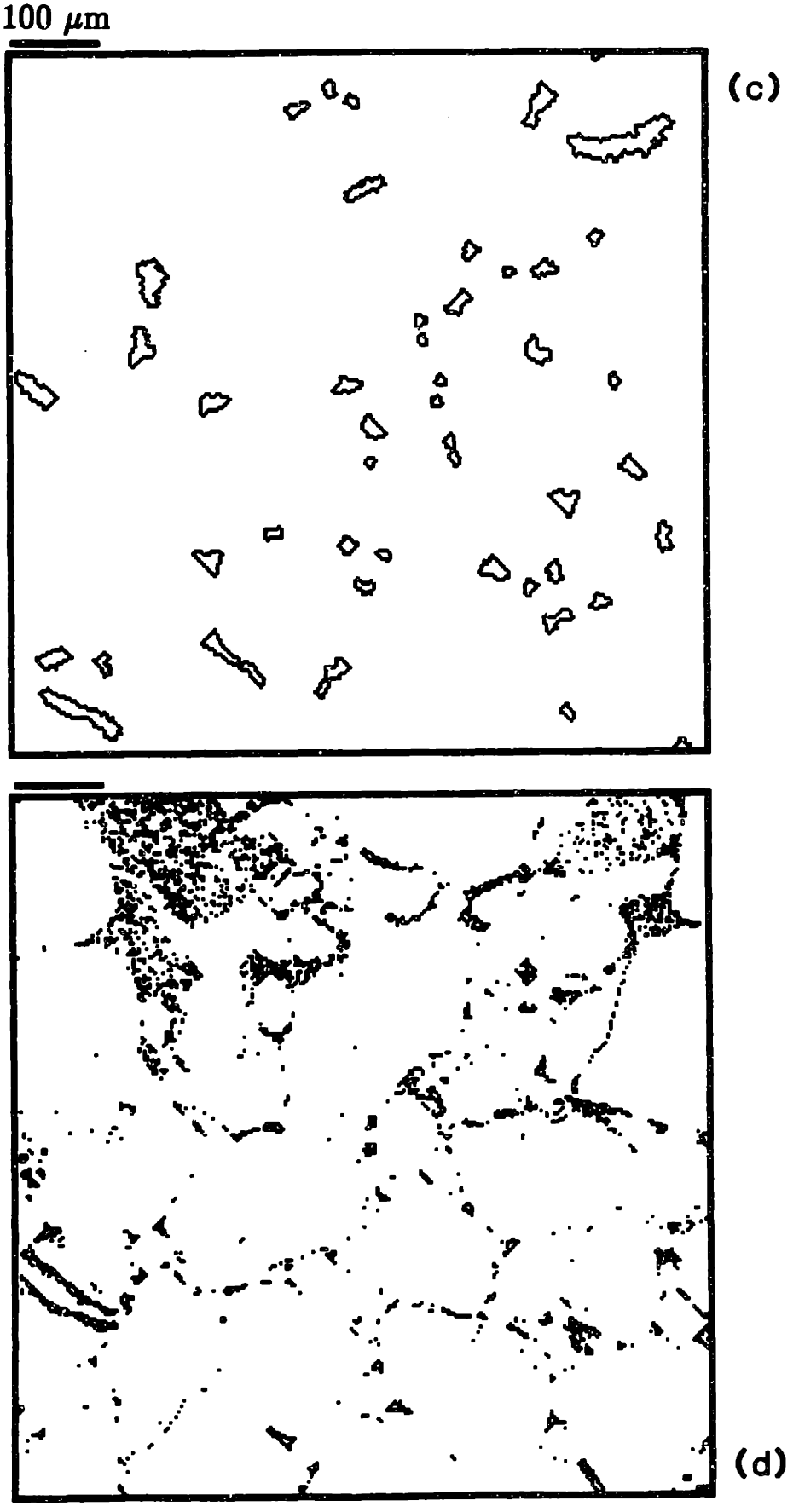

Figure 5.11 Freeman Direction Codes

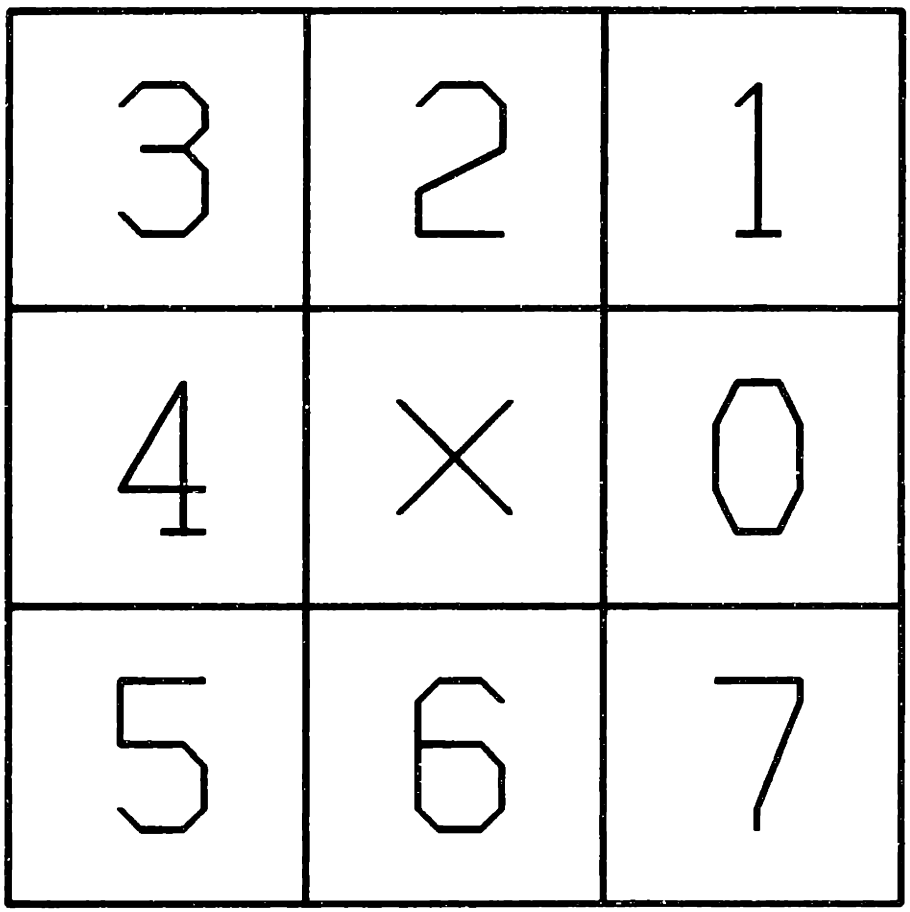

Figure 5.12 S_{Vp} Original versus SMS Image

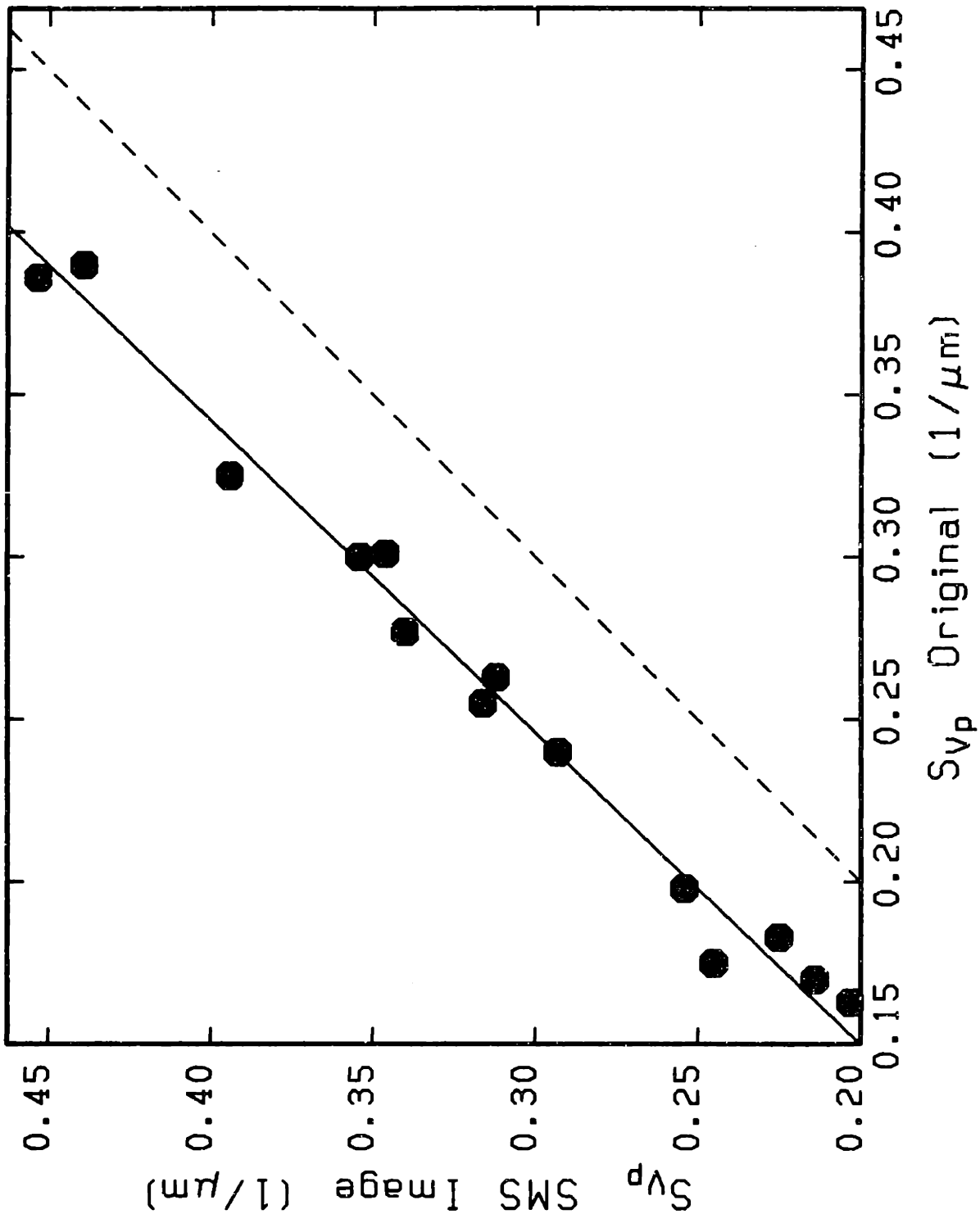

Figure 5.13

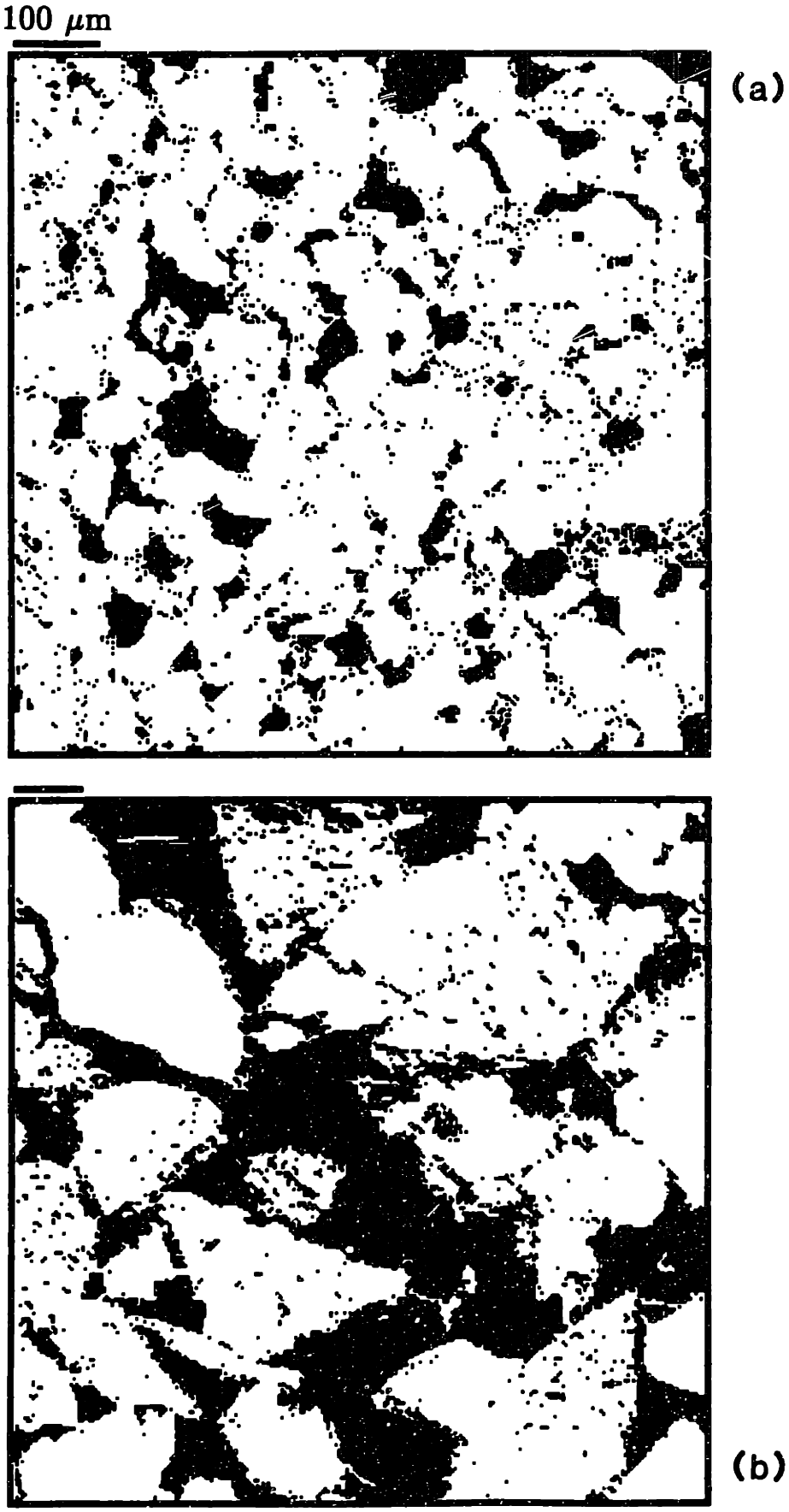

Figure 5.14 N_A Original versus SMS Image

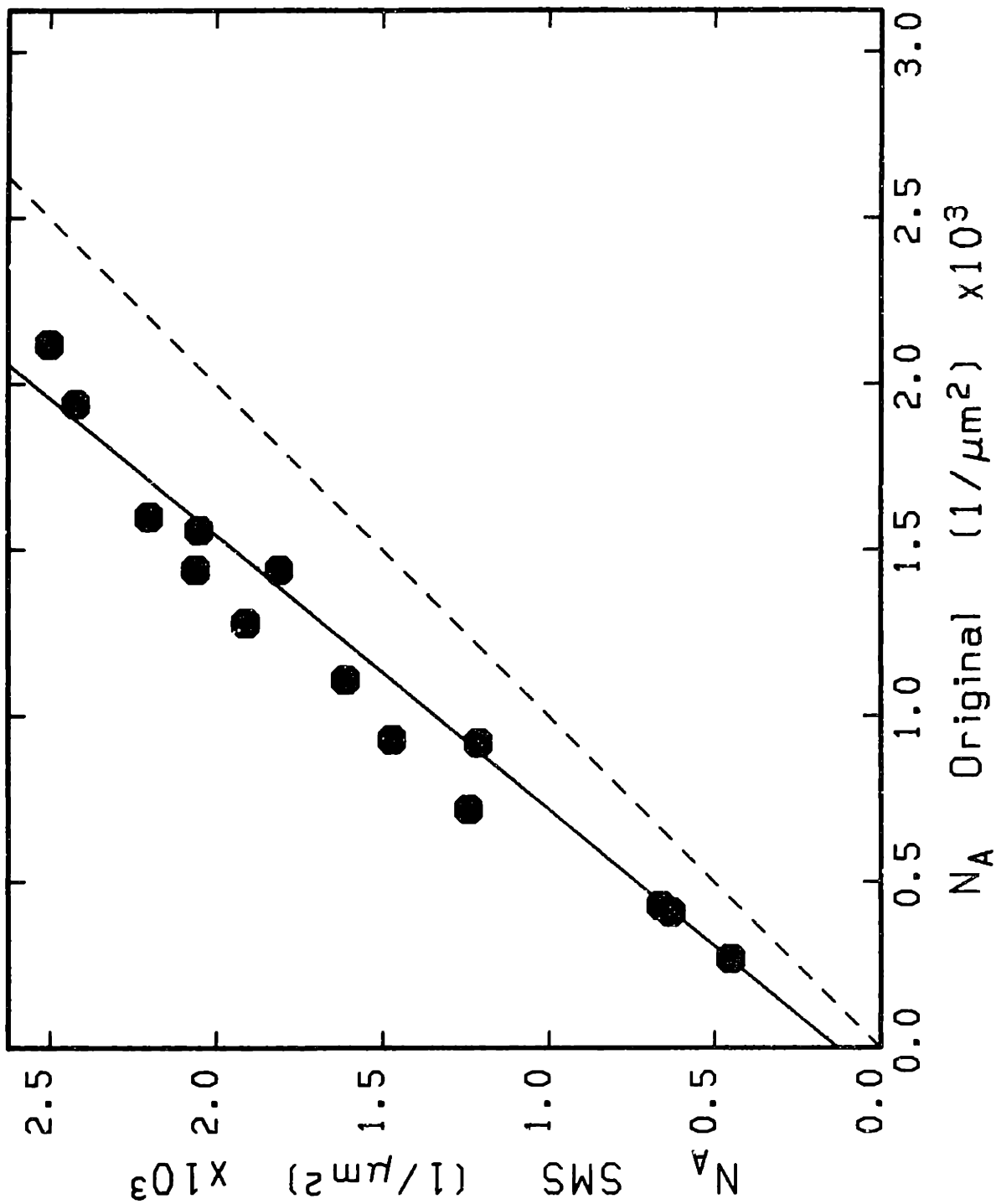

Figure 5.15 Cumulative Fraction versus log Area

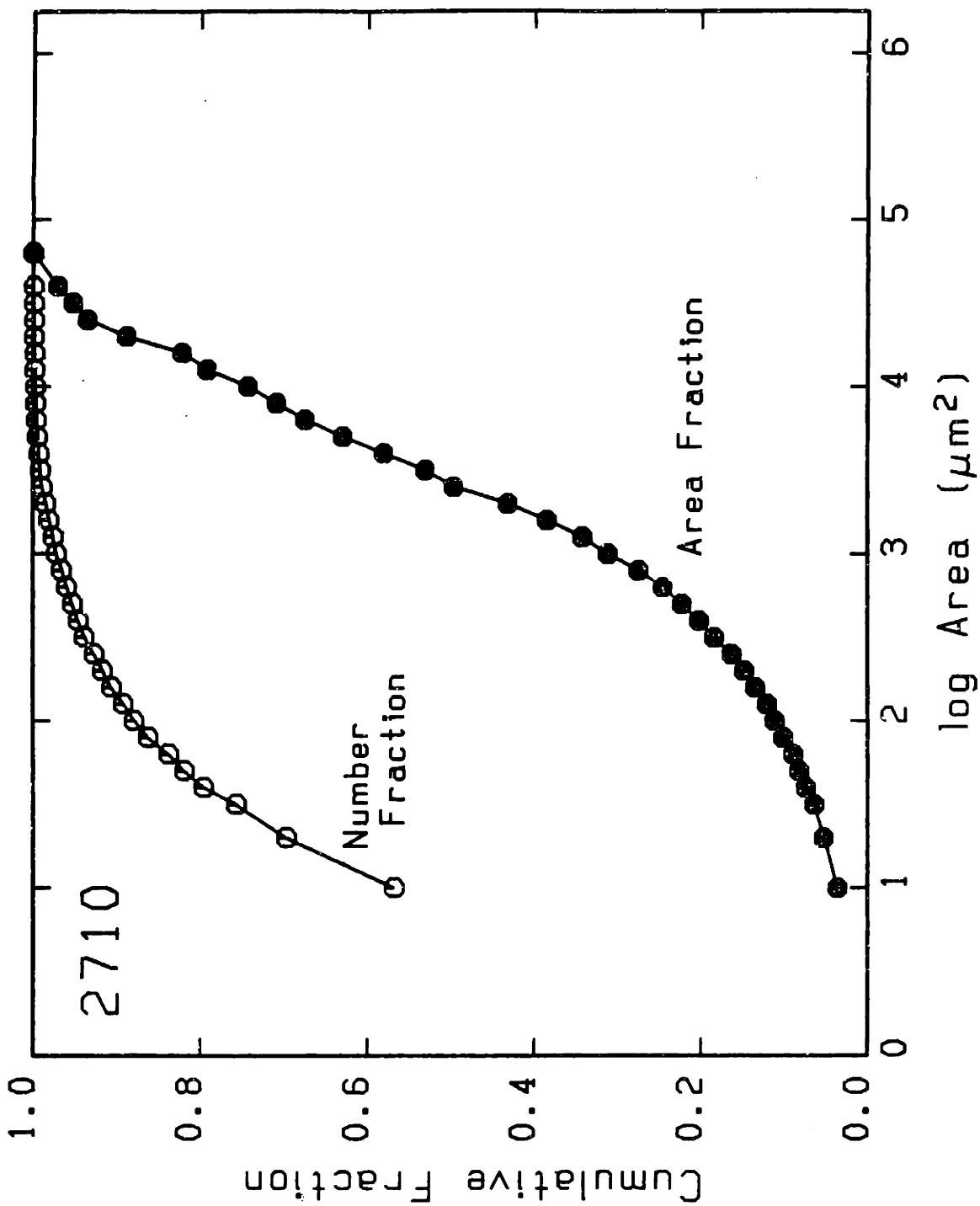

Figure 5.16 Cumulative Area Fraction versus Diameter

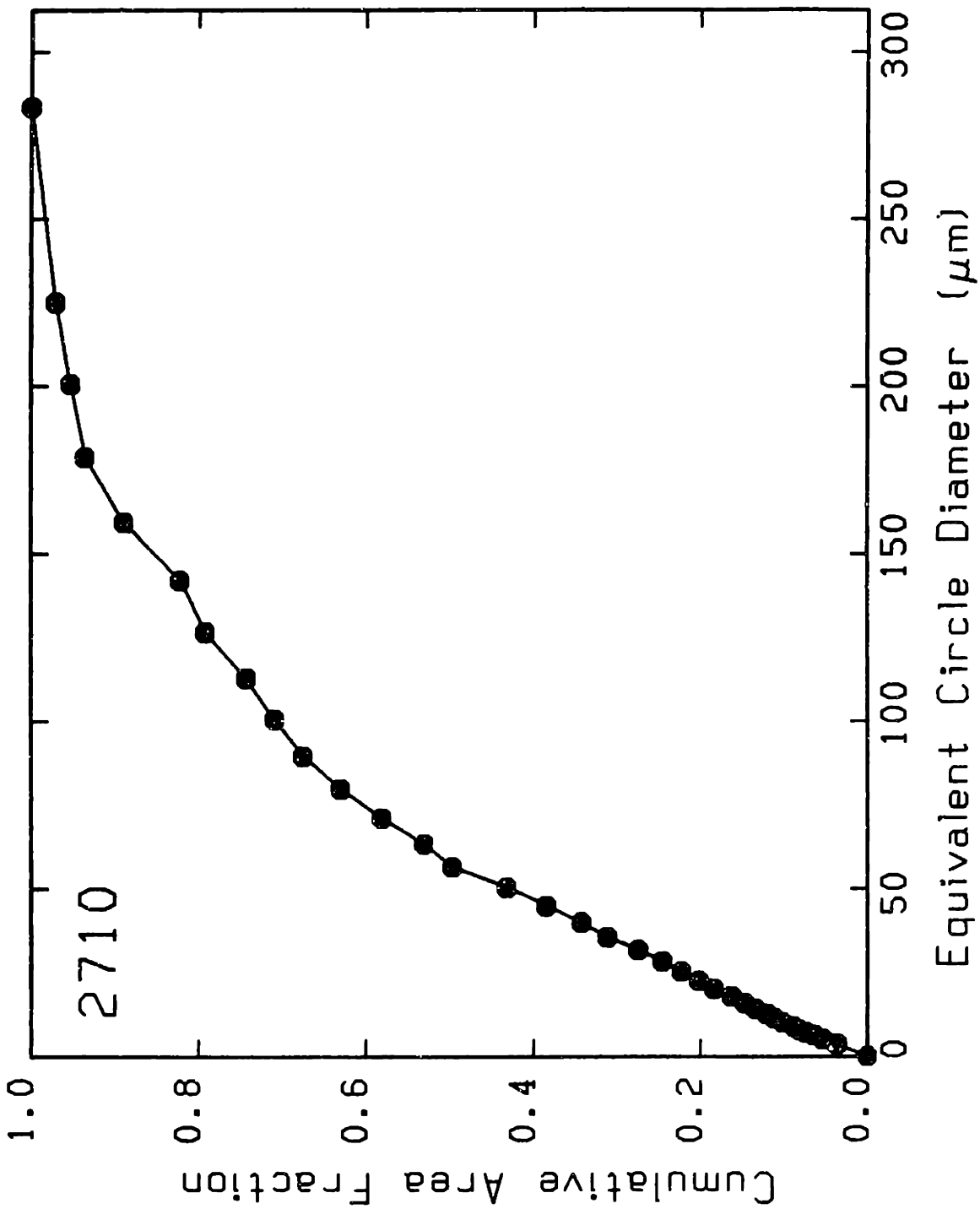

Figure 5.17 Feature Orientation for Sample 2710

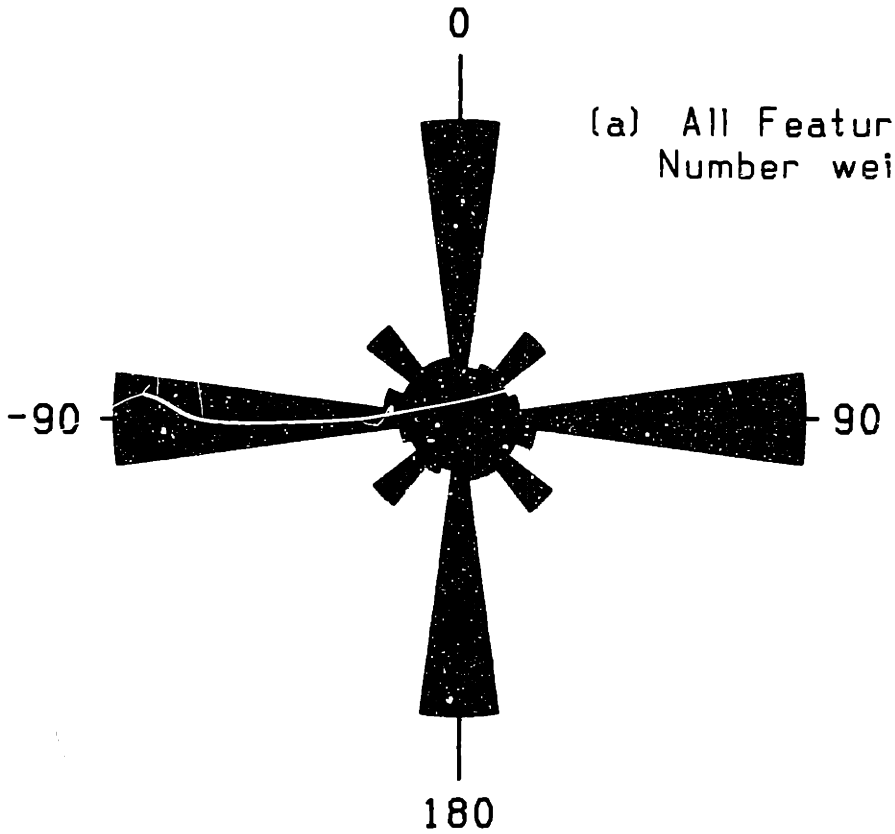

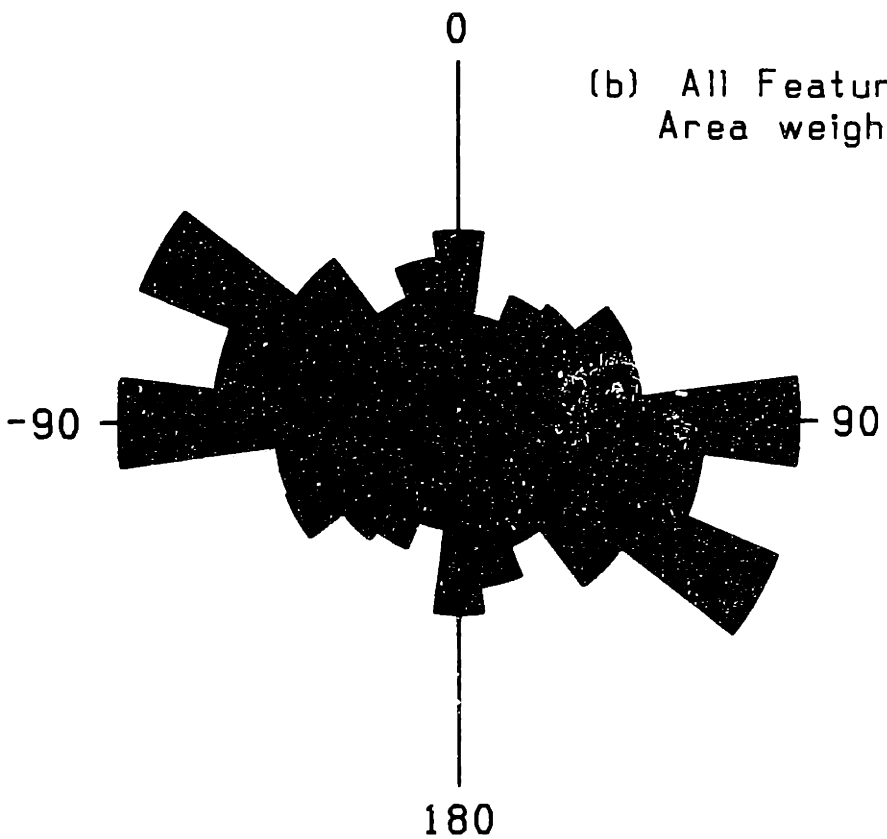

Figure 5.18 Feature Orientation for Sample 2710

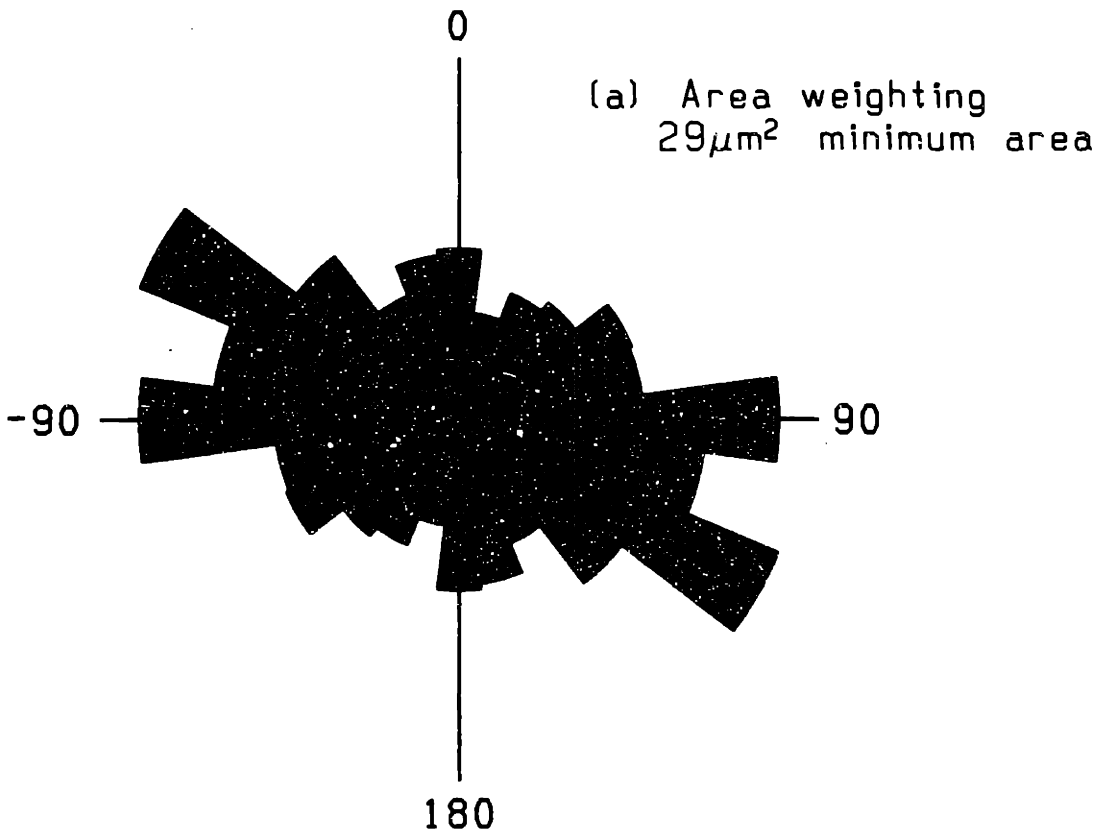

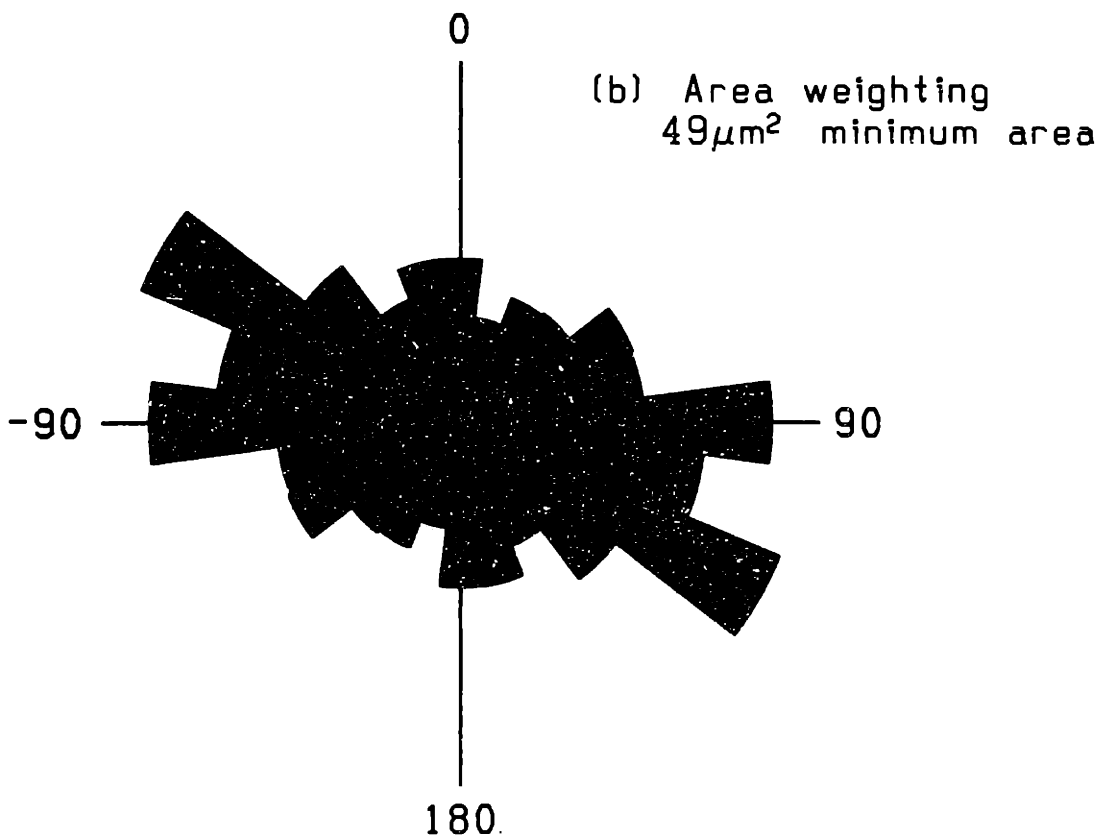

Figure 5.19

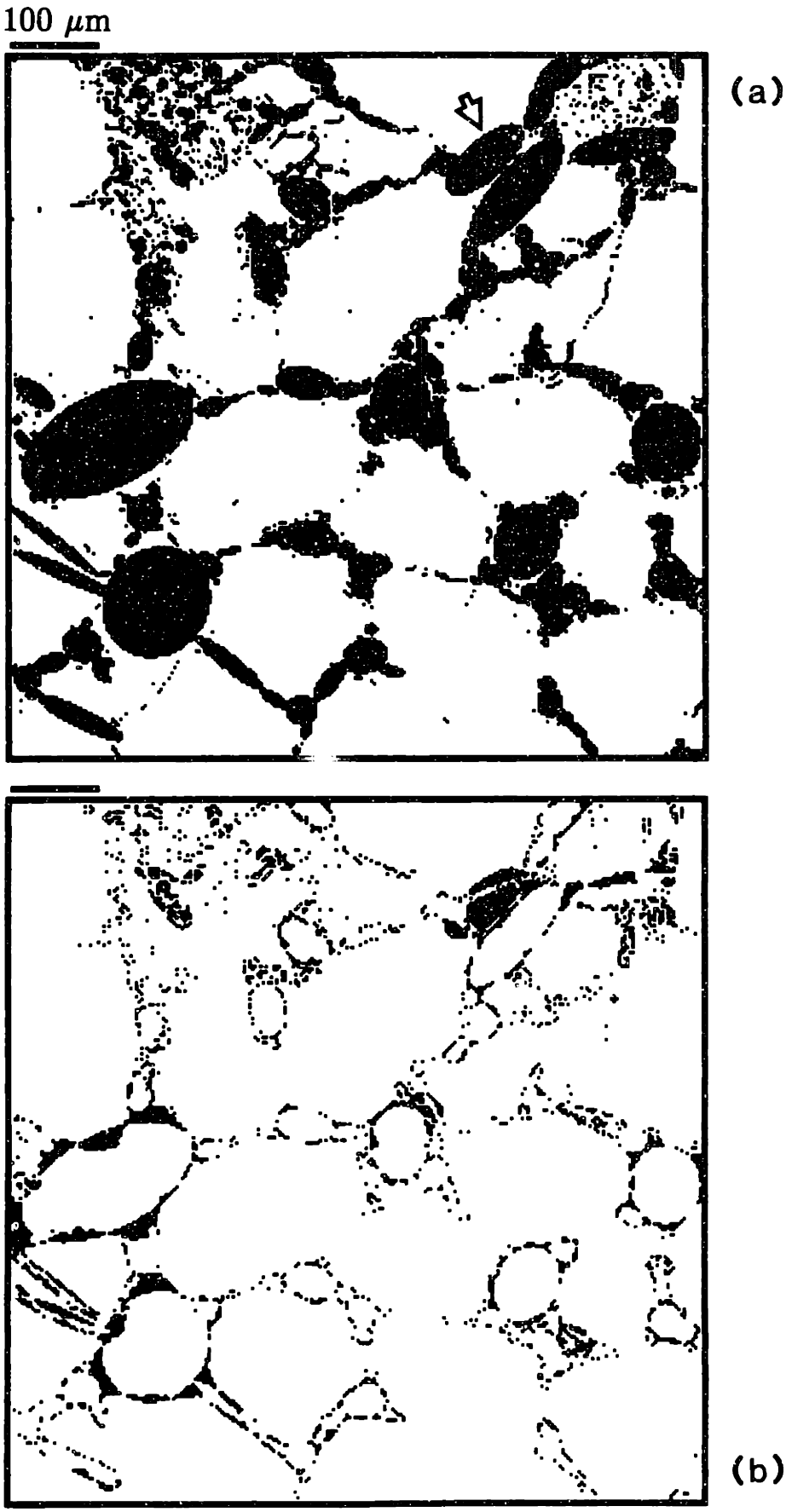

Figure 5.20

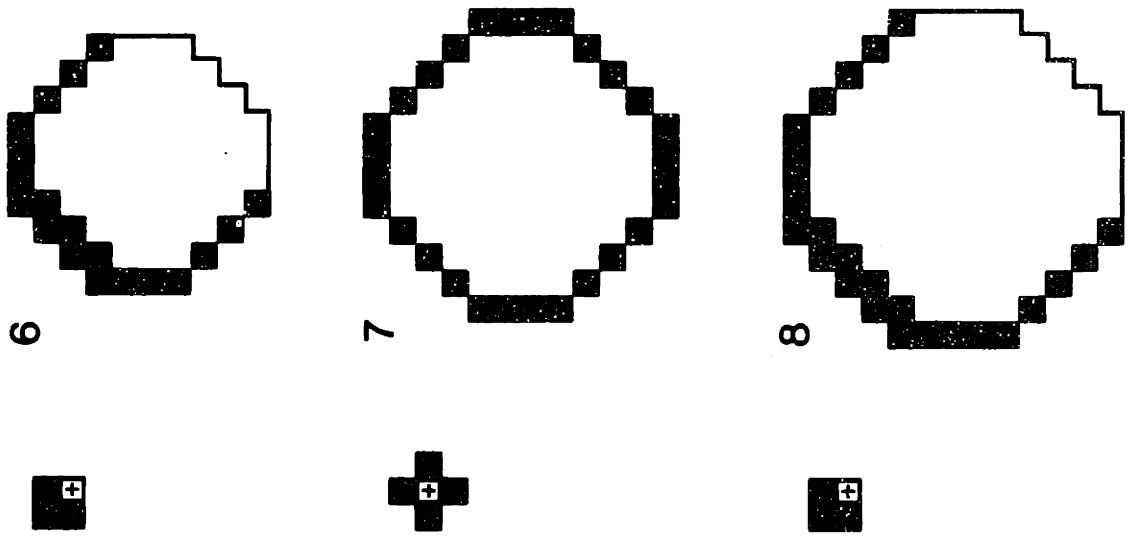

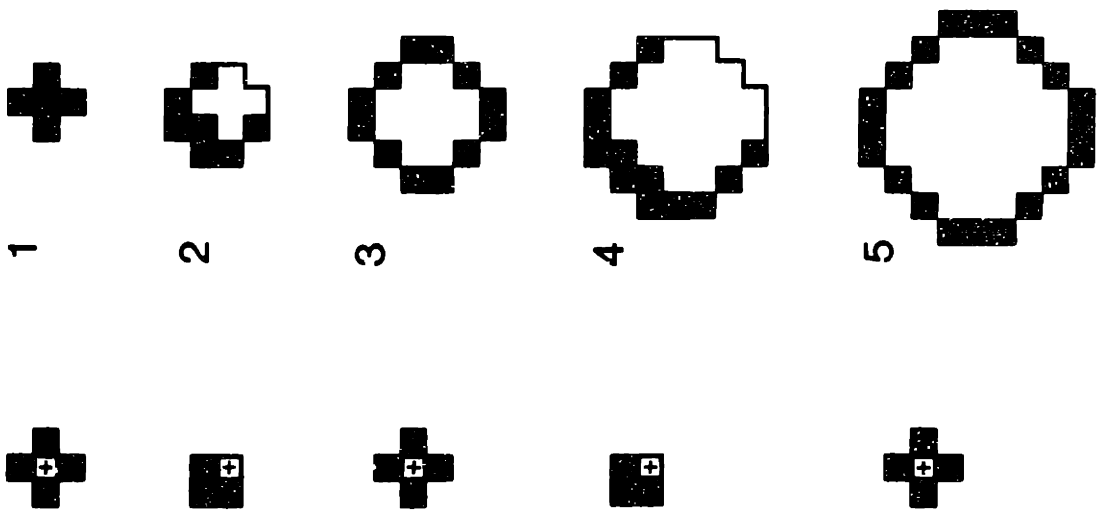

Figure 5.21a Feature Granulometry (2124)

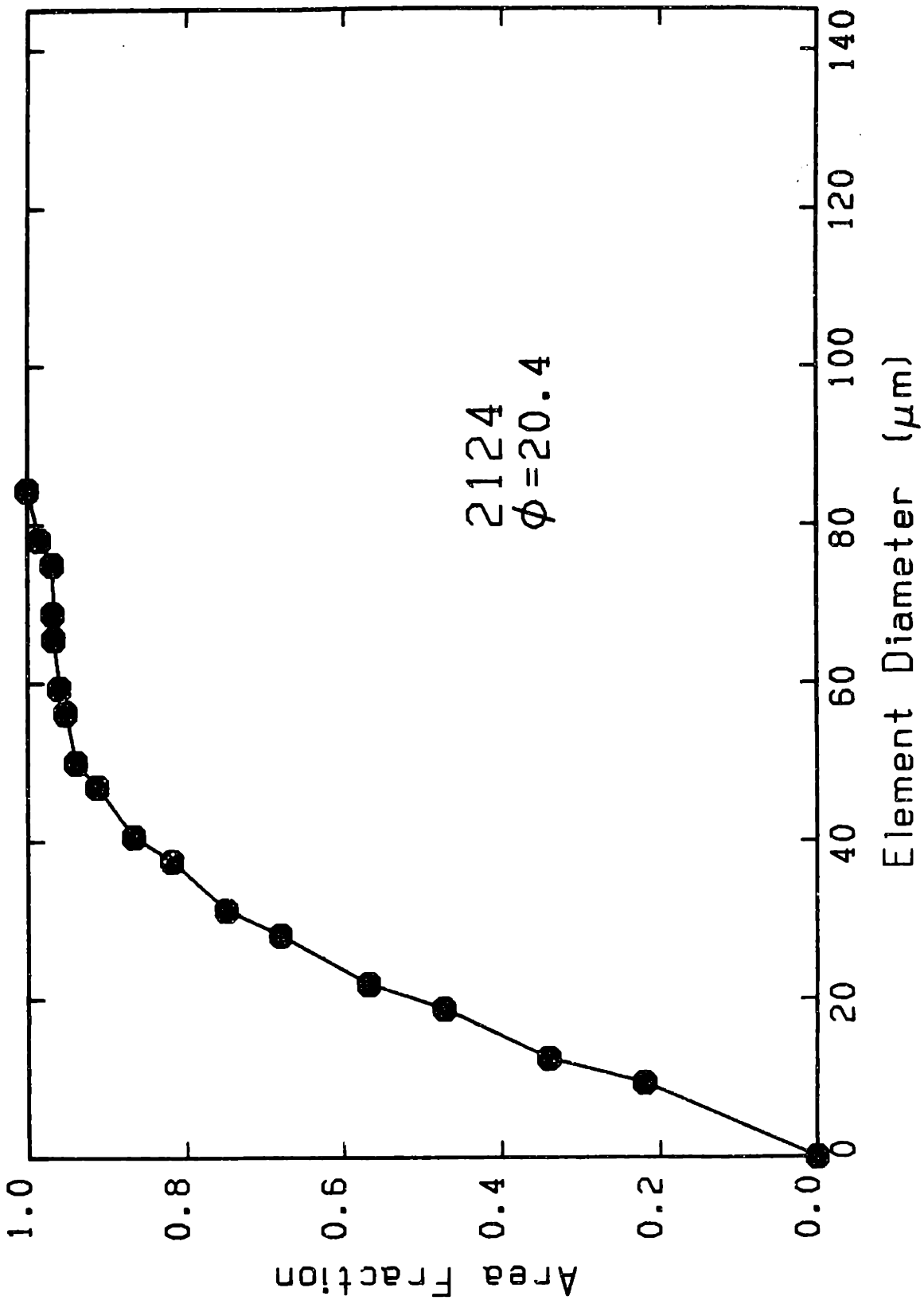

Figure 5.21b Feature Granulometry (2509)

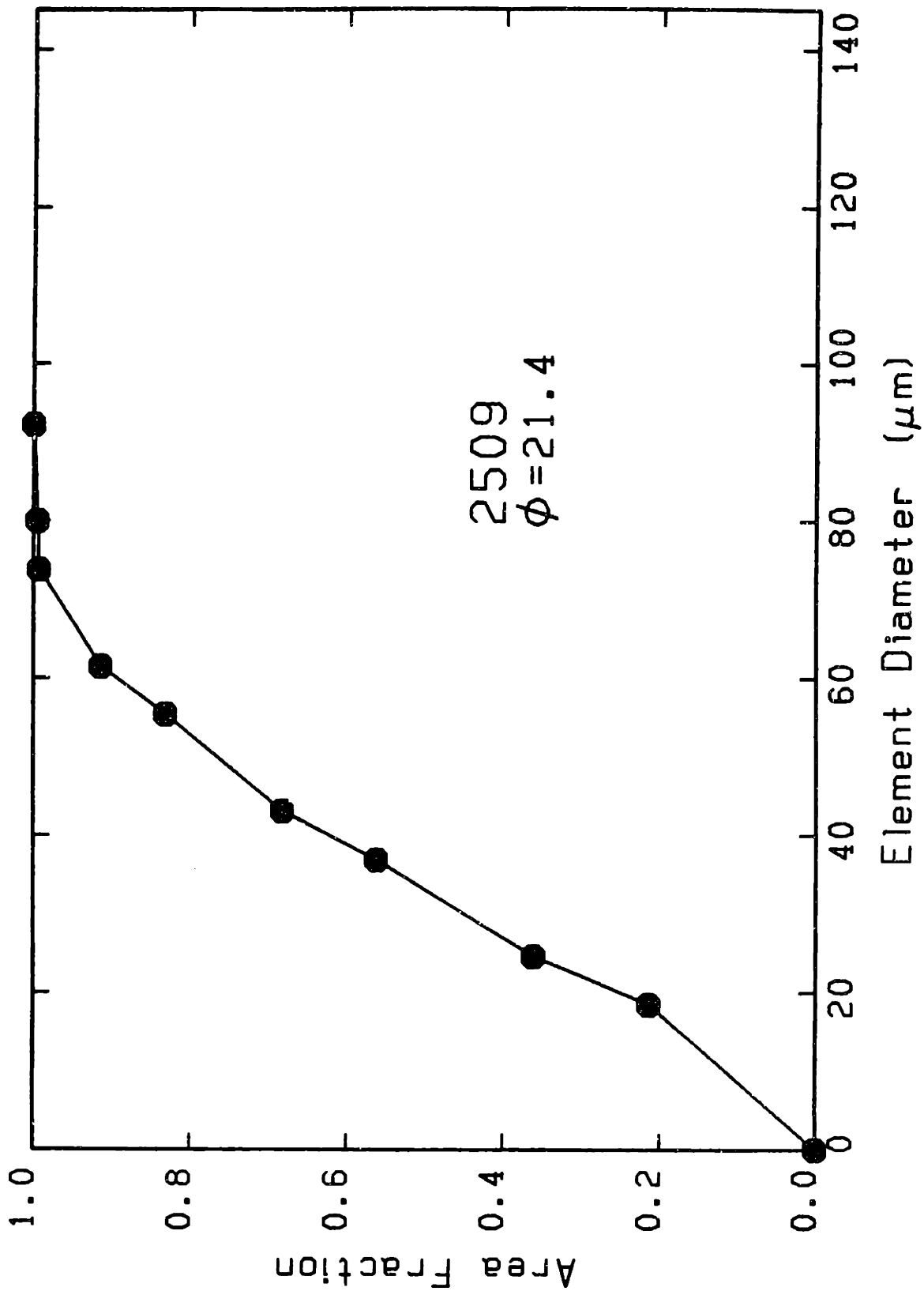

Figure 5.21c Feature Granulometry (2513)

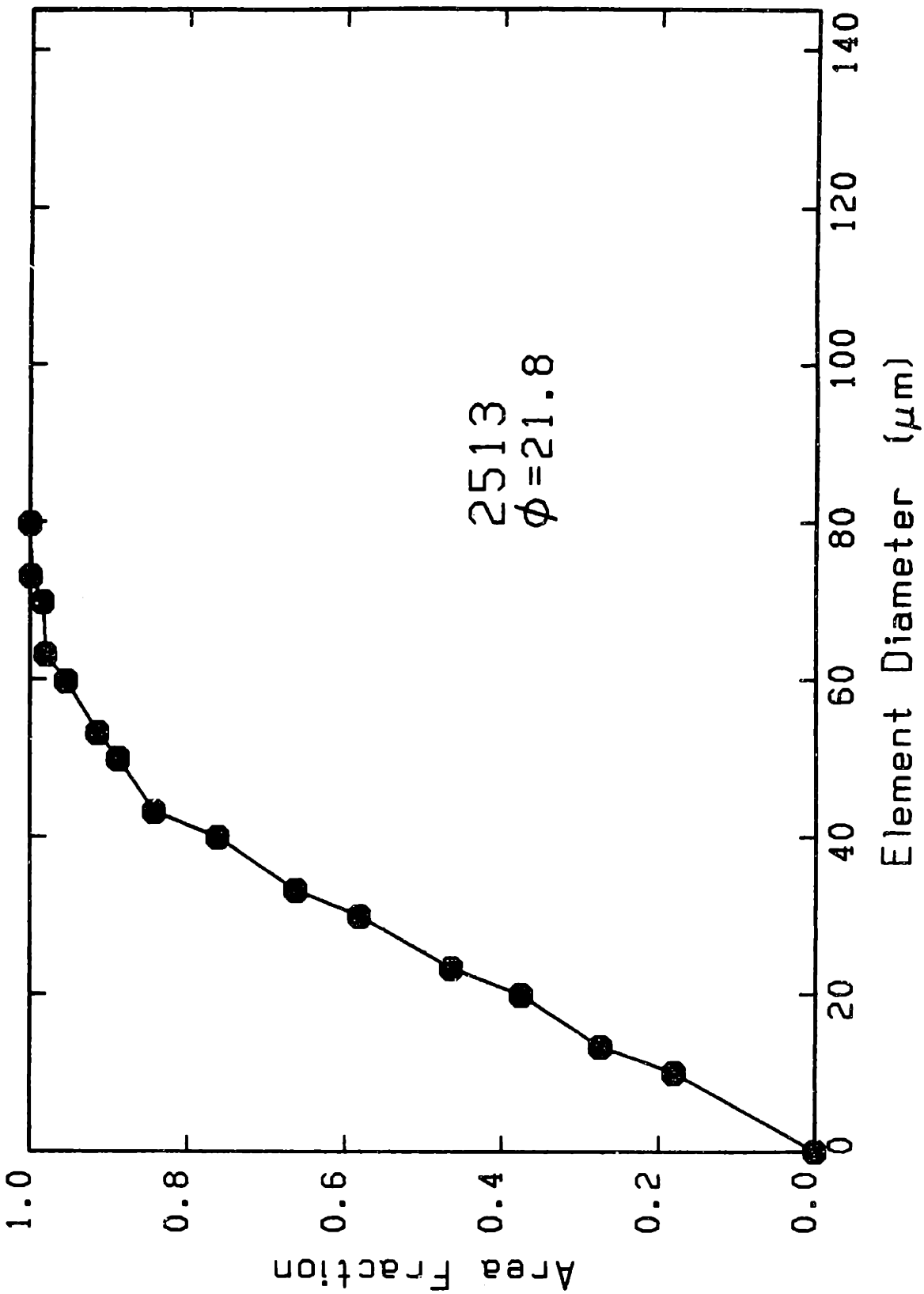

Figure 5.21d Feature Granulometry (2519)

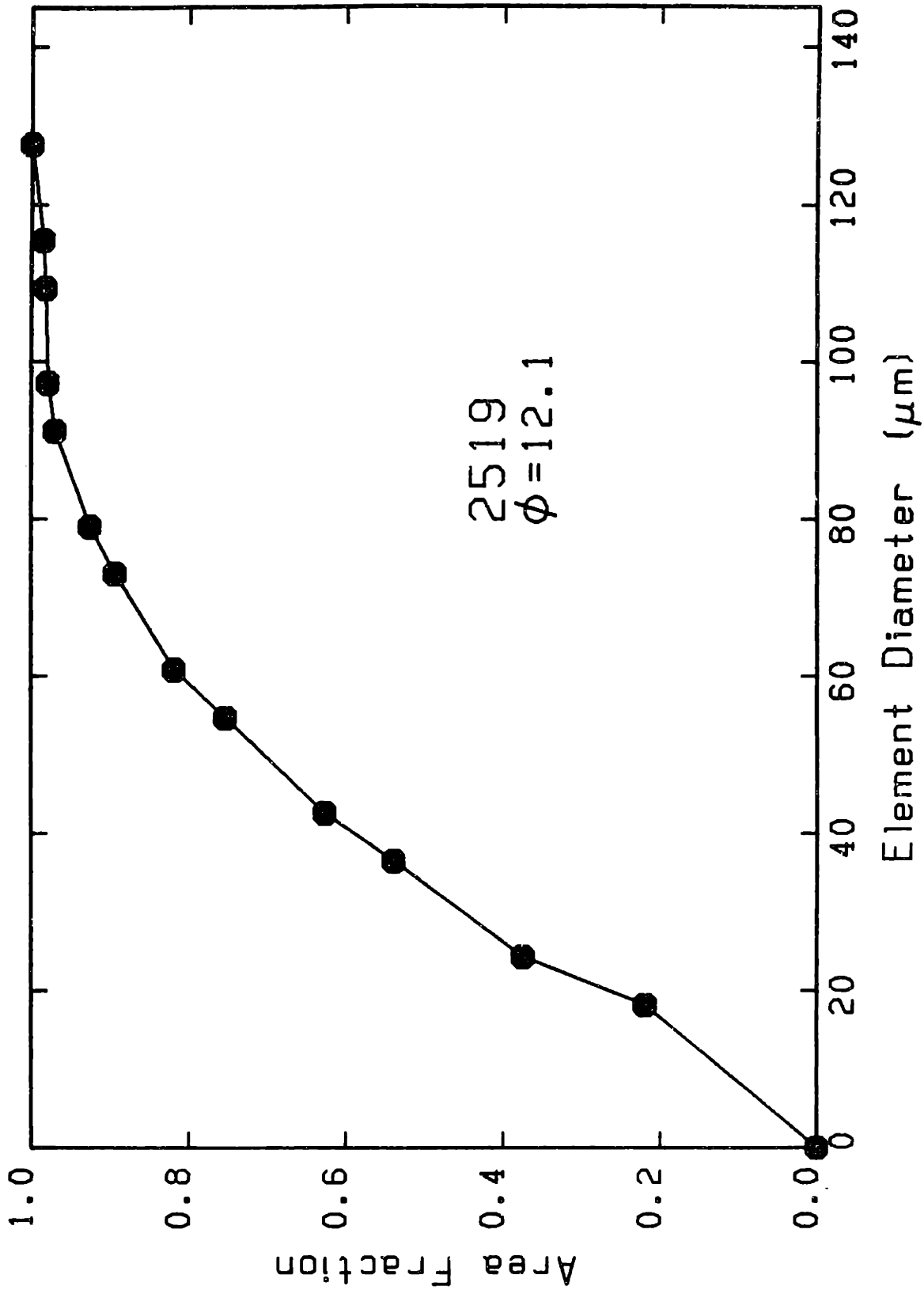

Figure 5.21e Feature Granulometry (2521)

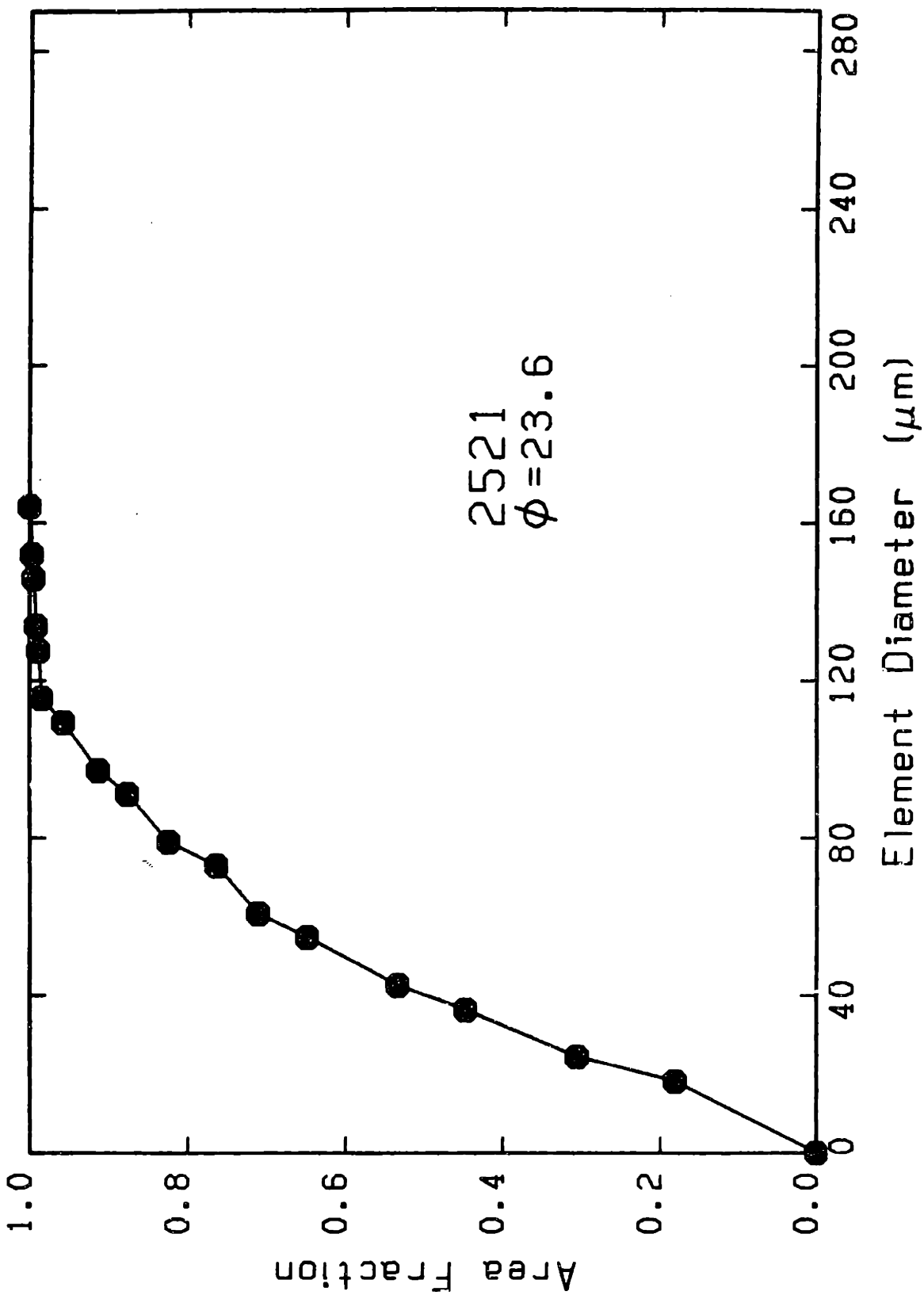

Figure 5.21f Feature Granulometry (2523)

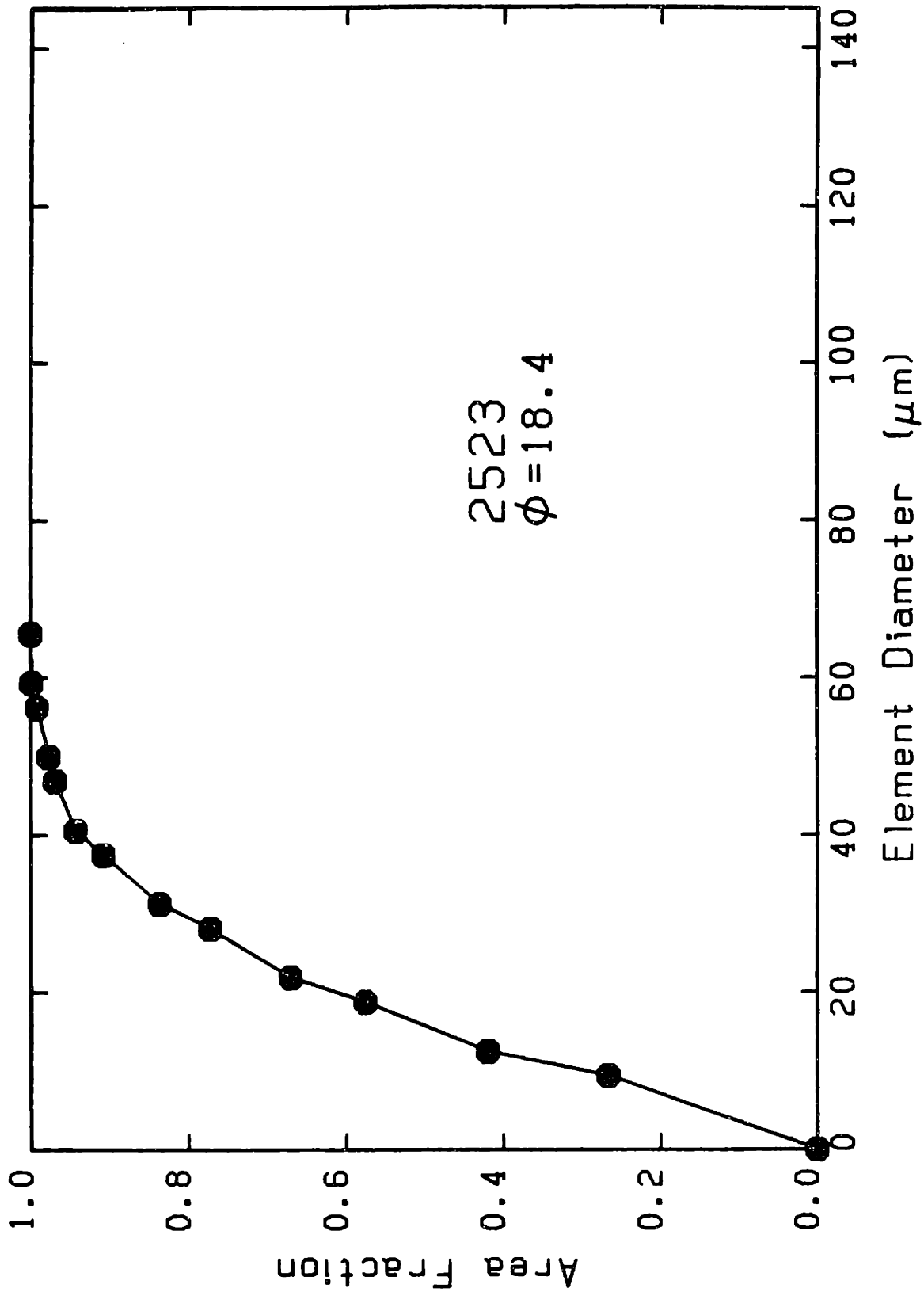

Figure 5.21g Feature Granulometry (2686)

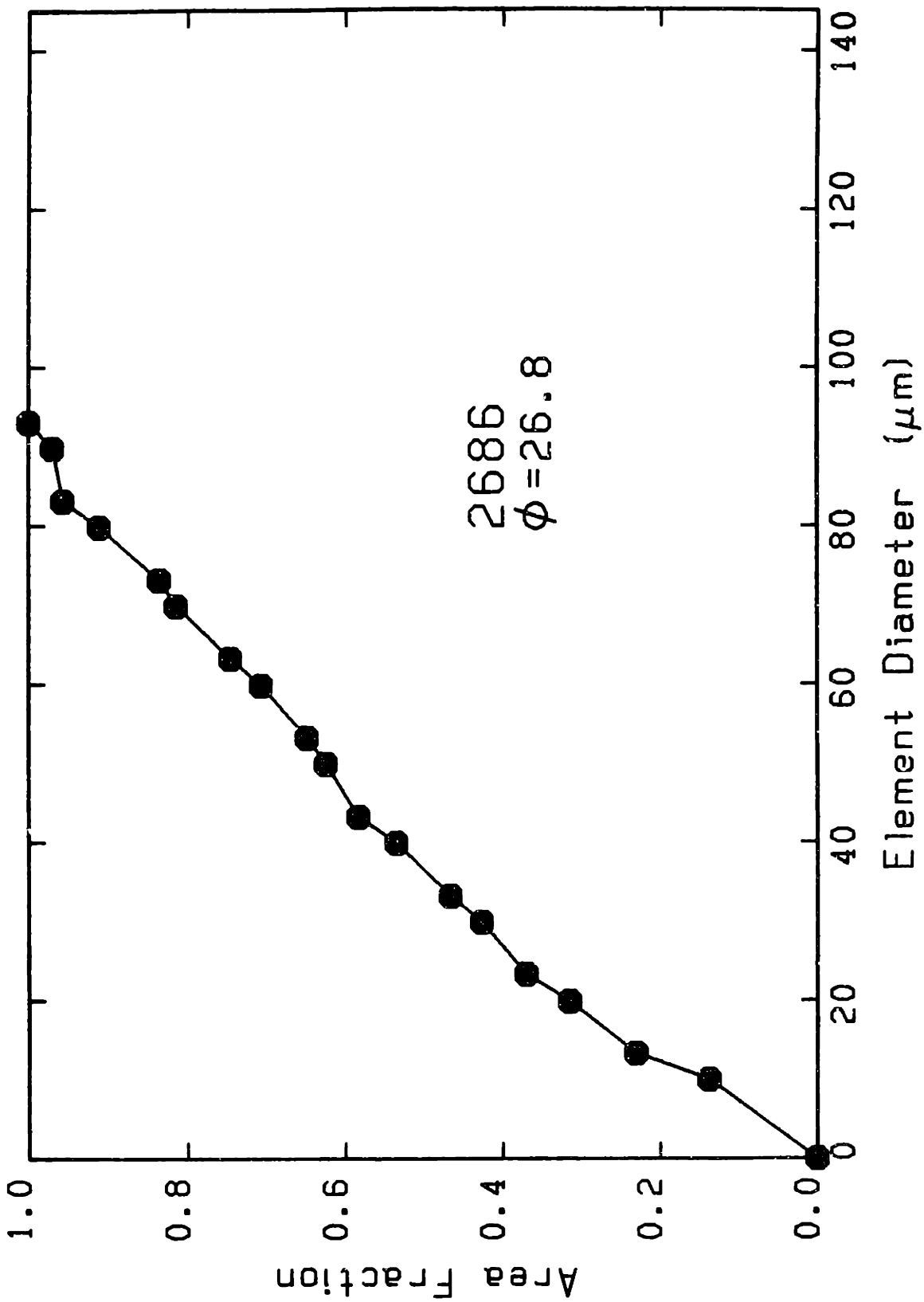

Figure 5.21h Feature Granulometry (2687)

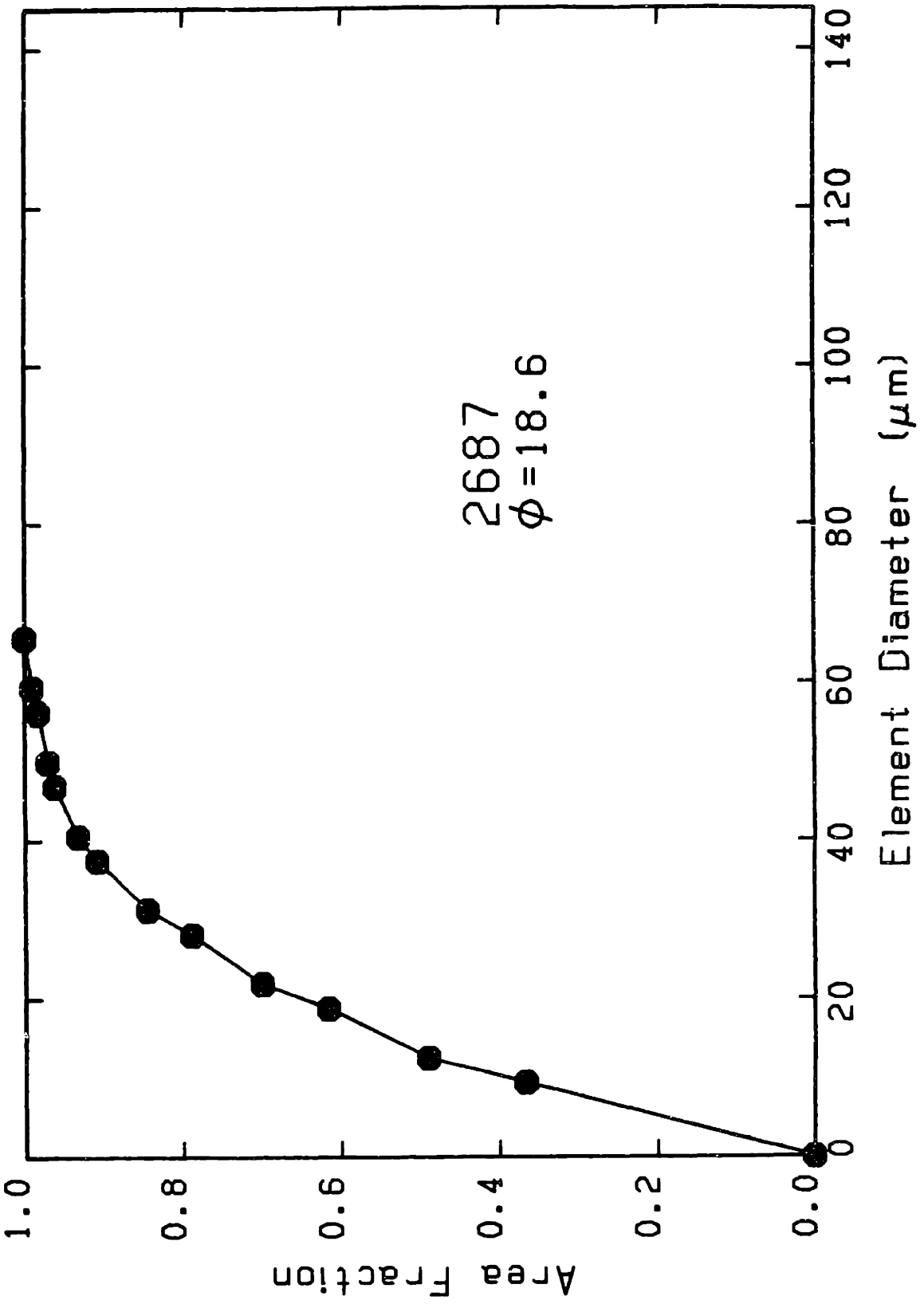

Figure 5.211 Feature Granulometry (2700)

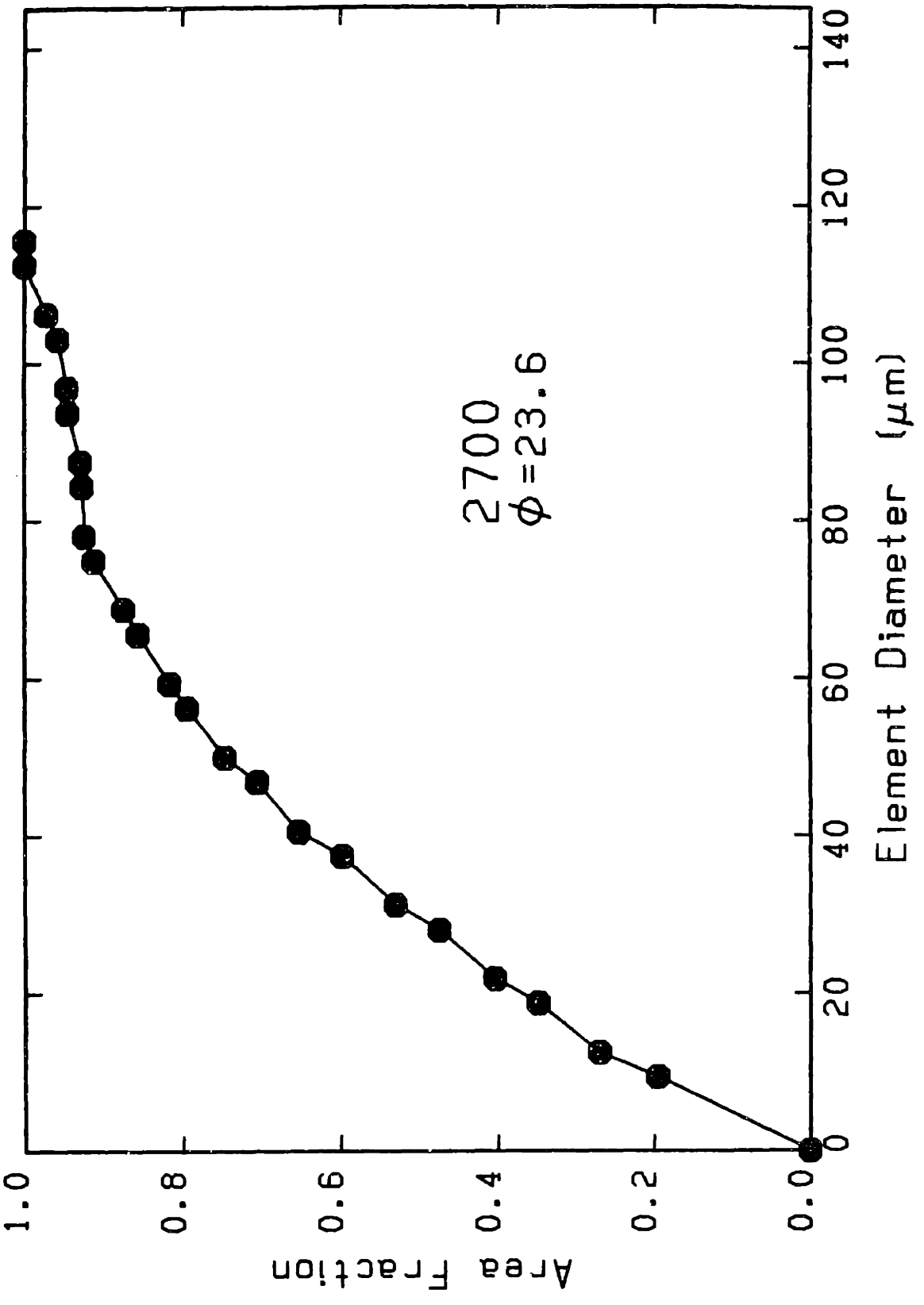

Figure 5.21j Feature Granulometry (2704)

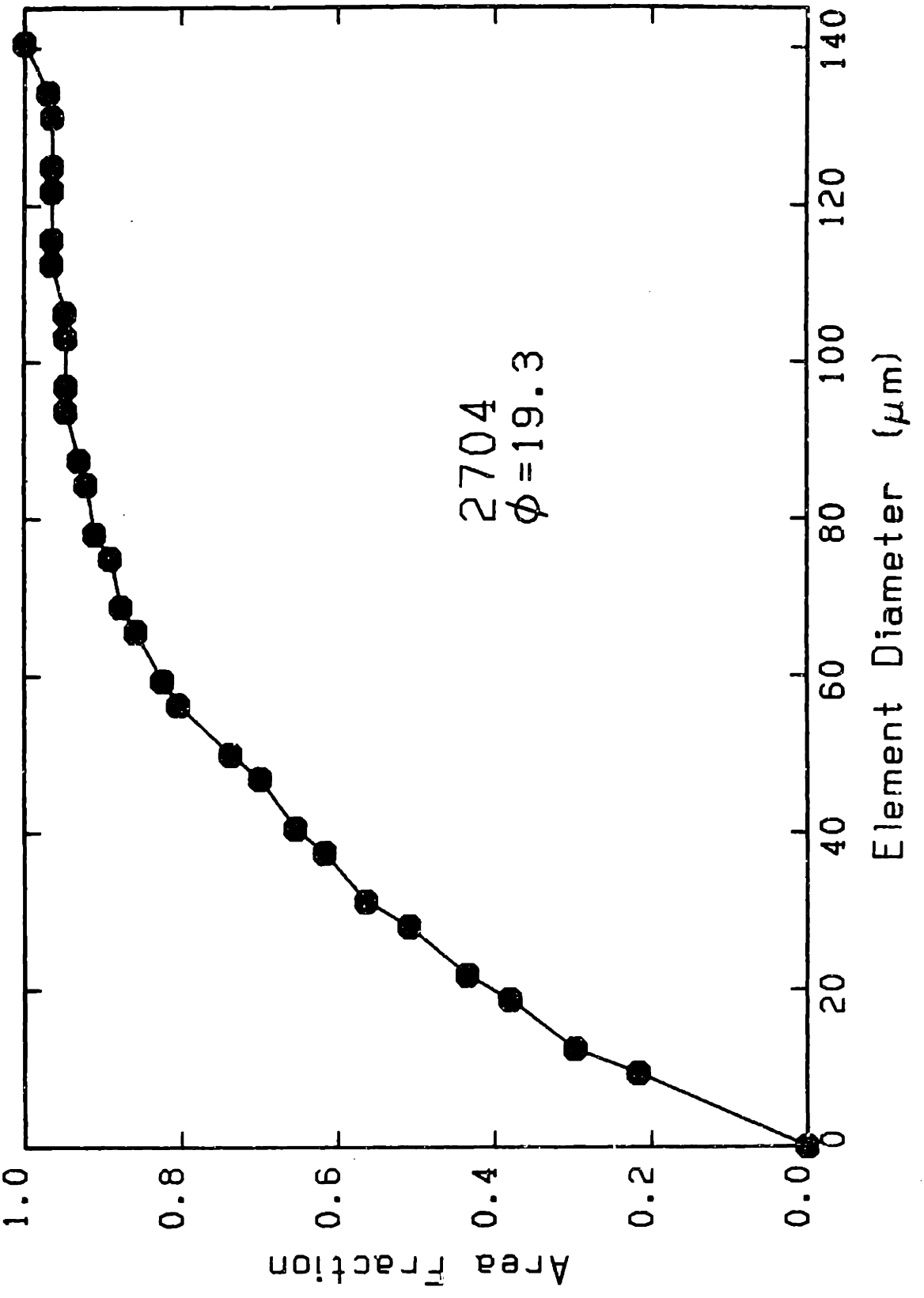

Figure 5.21k Feature Granulometry (2710)

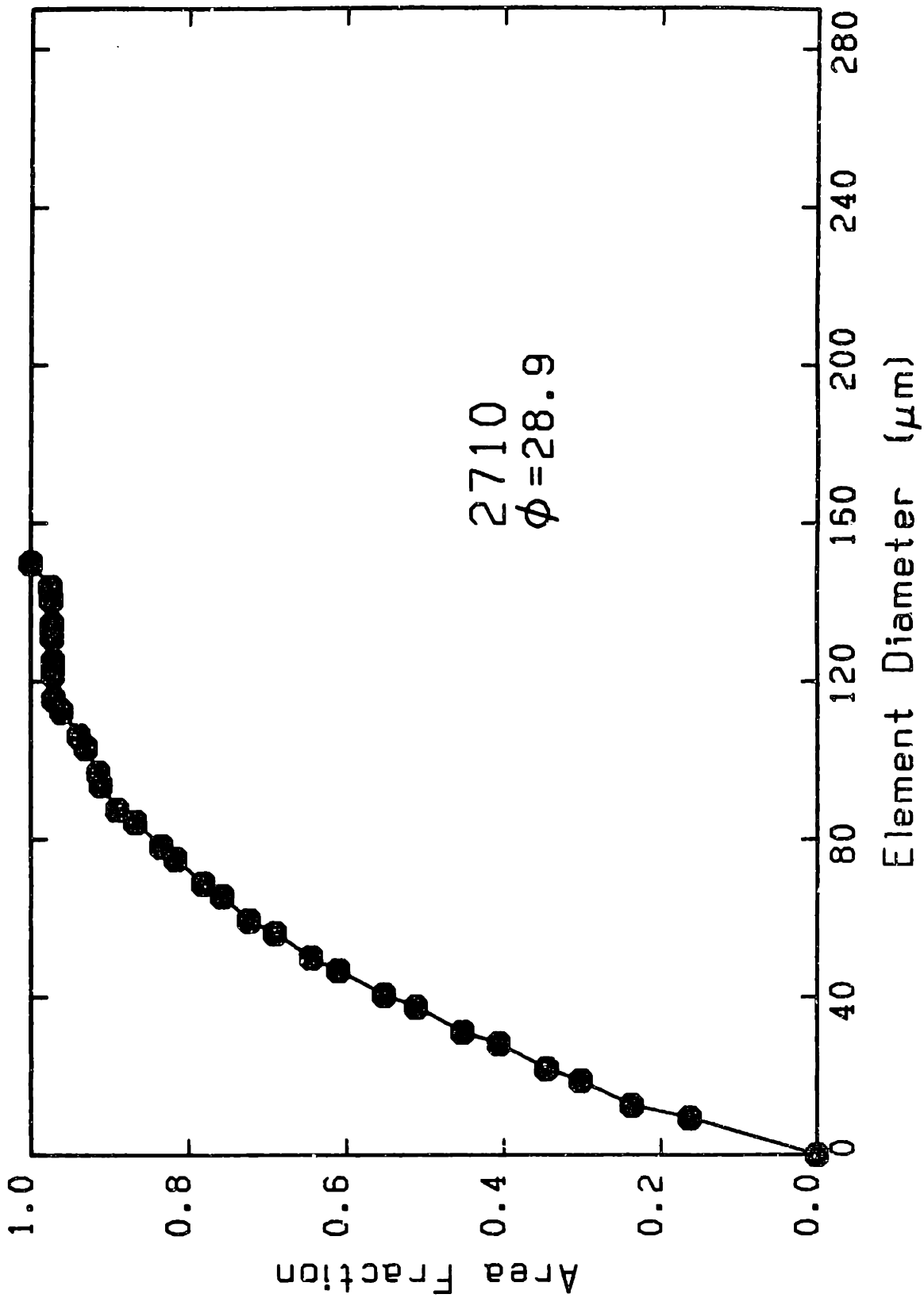

Figure 5.211 Feature Granulometry (2841)

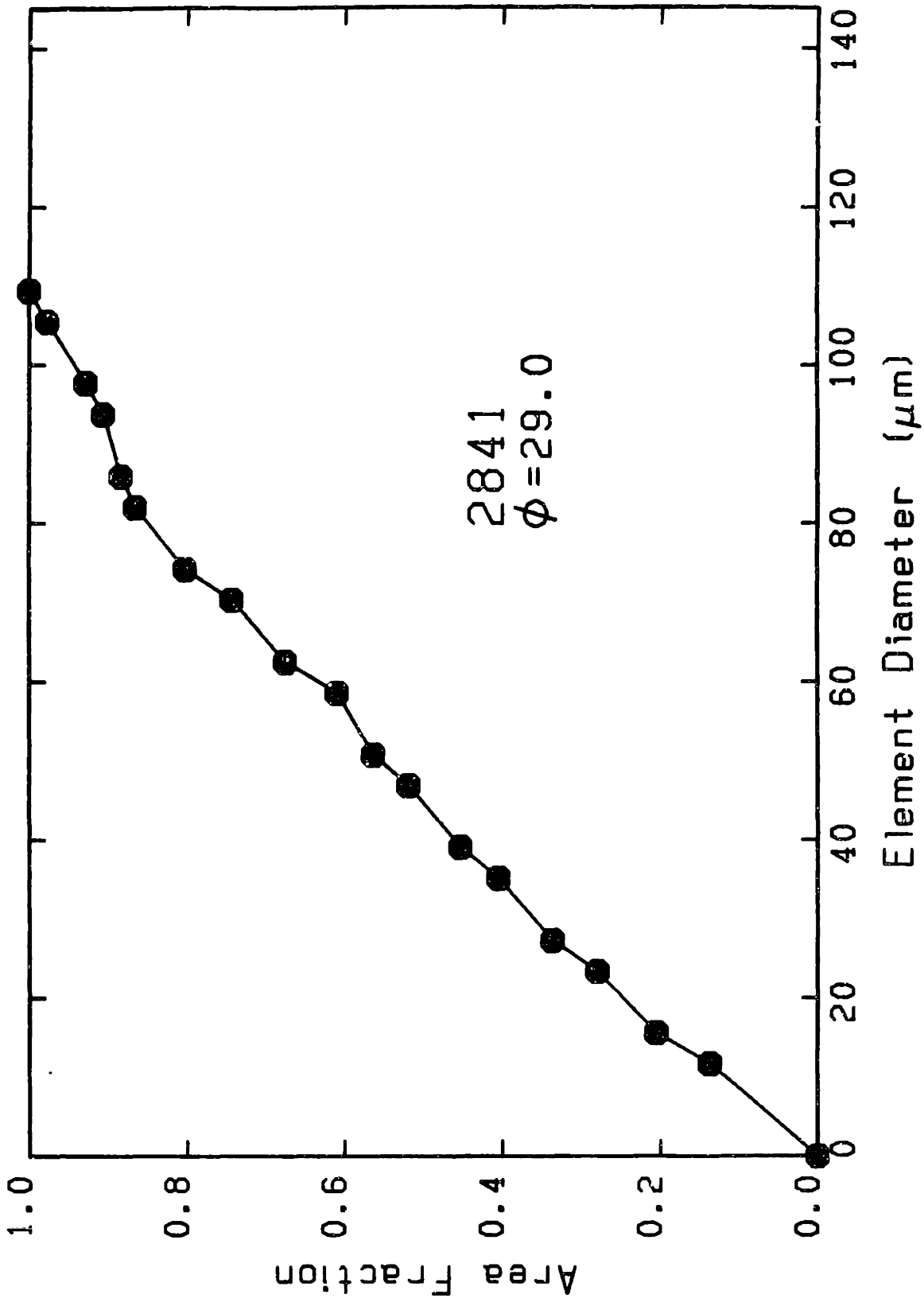

Figure 5.21m Feature Granulometry (2842)

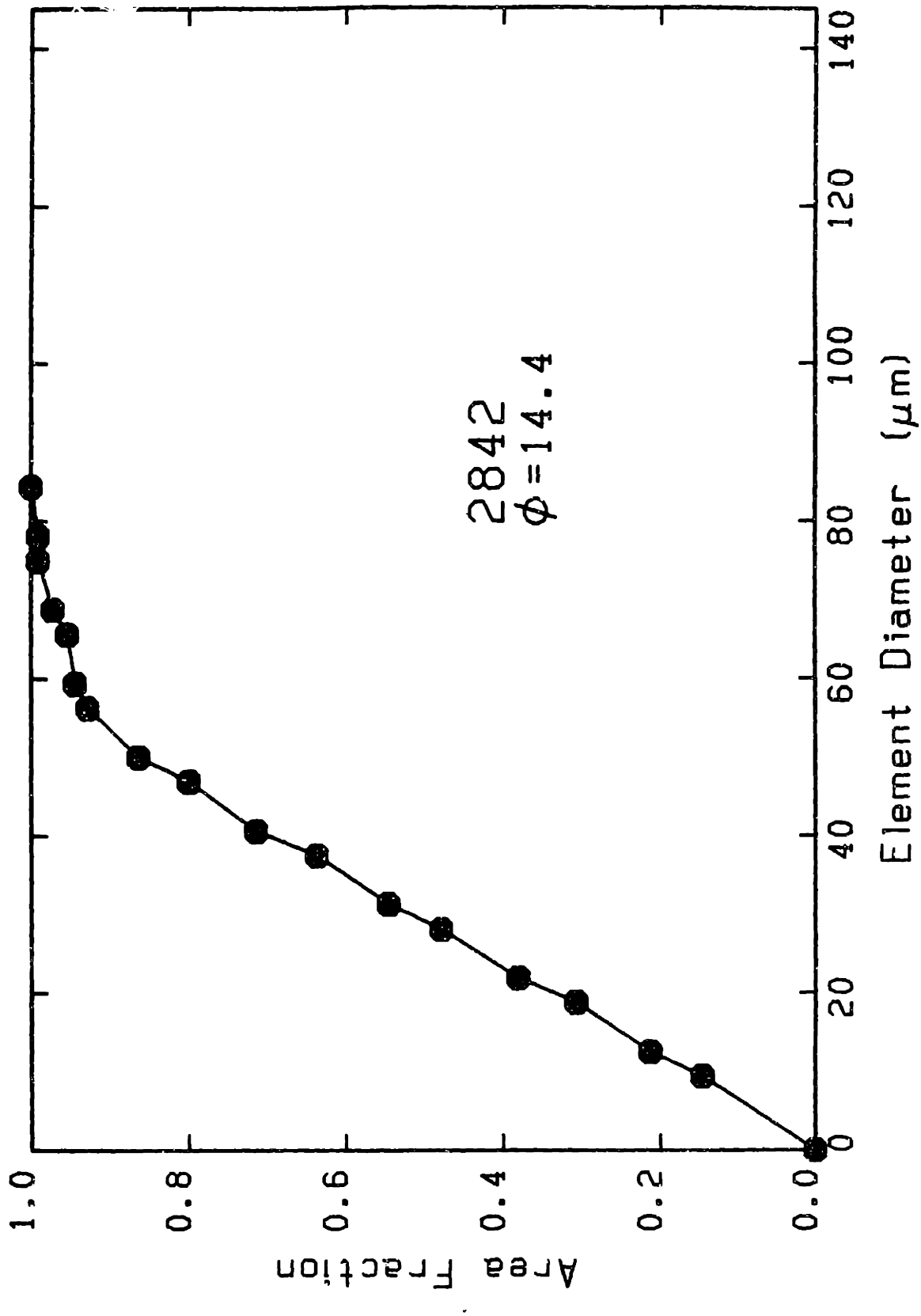

Figure 5.21n Feature Granulometry (2843)

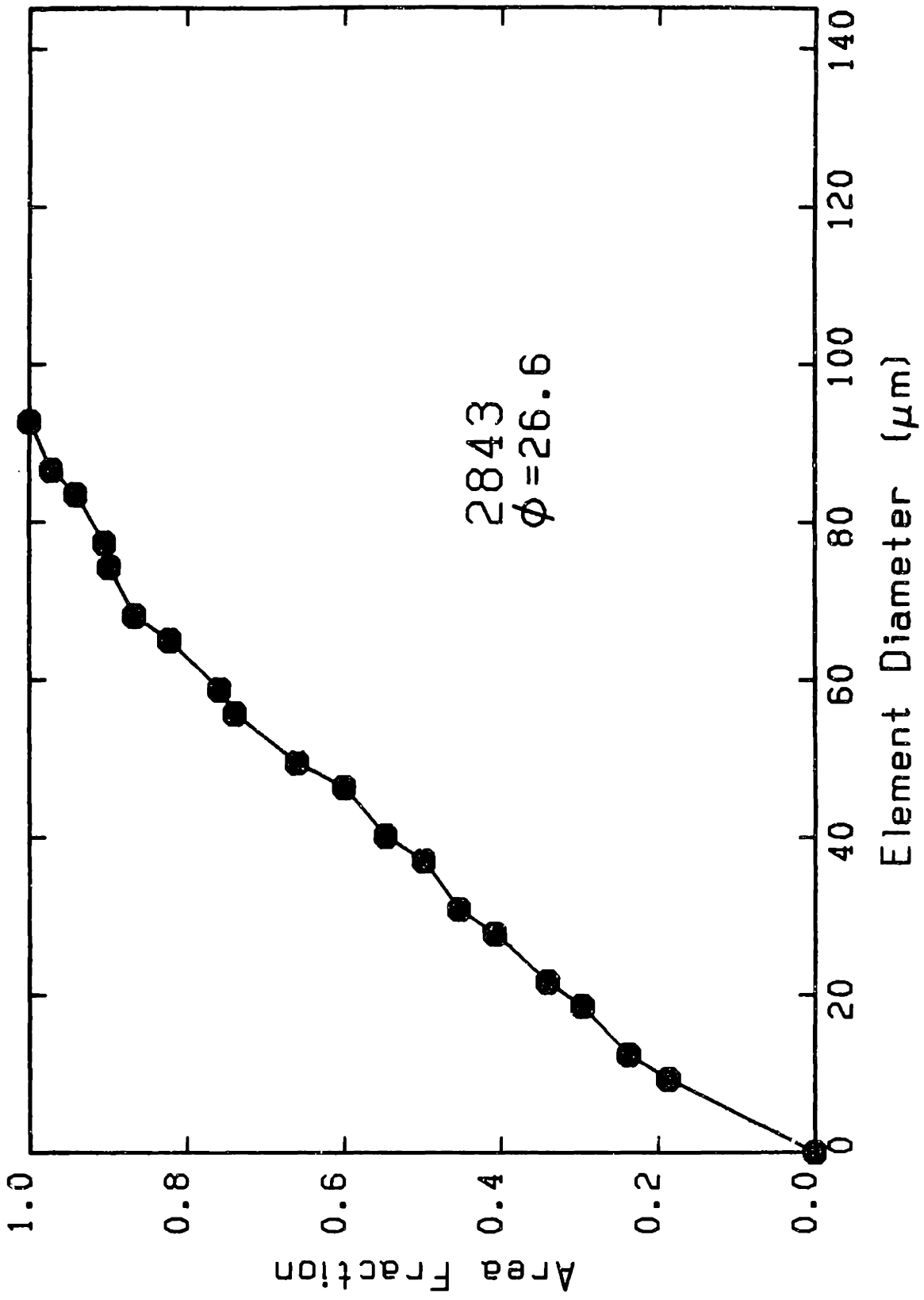

Figure 5.22 Feature Granulometry (2513)

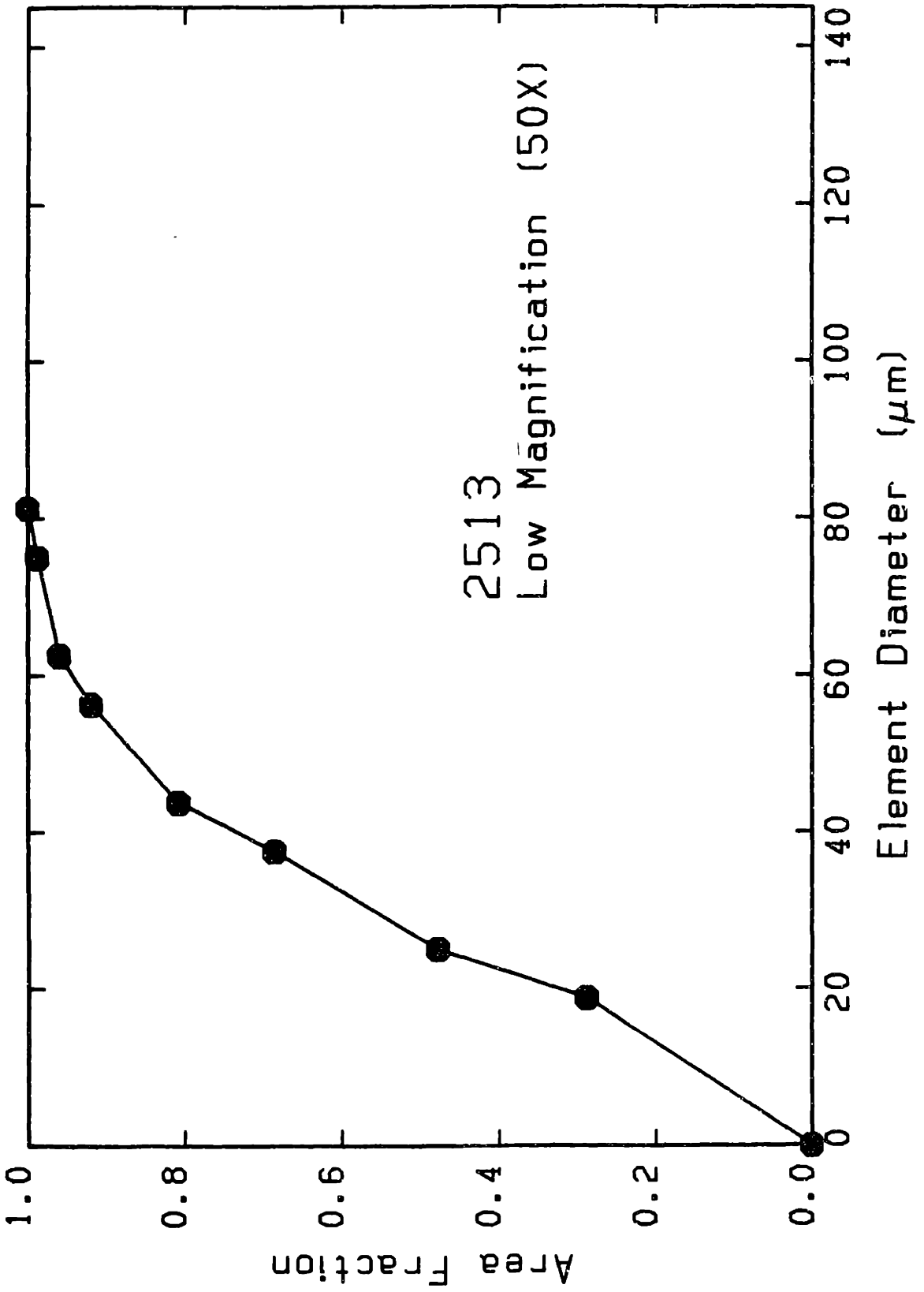

Chapter 6

Spatial Correlation in Sandstone Images

6.1 Introduction

Methods of direct analysis, such as quantitative stereology and feature analysis, do not readily yield information about the spatial correlation of pore space. Anisometry, orientation, and location of features are measured by feature analysis and could be used to extract spatial correlation. However, measures of covariance provide more direct access to spatial correlation parameters. Depending on the correlation tool used, the parameters can yield information about porosity, surface area, range of correlation, anisotropy, and the similarity between the pore structure and stochastic models of pore structure.

Previous applications of spatial correlation measures to sandstone images were discussed in Chapter 2. The optimistic claims of Preston and Davis (1976) (i.e., complete characterization) are somewhat balanced by the pessimistic statements of Lin (1982a) (i.e., no useful information). The true usefulness of spatial correlation measures lies somewhere between their two viewpoints. A spatial correlation function (SCF) contains specific geometric

information about the pore structure. Also, the SCF is essential for certain stochastic models of porous media. Higher order correlations (e.g., three-point) are sometimes used in stochastic models (Torquato and Stell, 1982, 1983ab). Here, only two-point correlation functions are treated. Higher order correlation functions have not been measured for our sandstone images.

In this chapter, the various measures of spatial correlation are investigated. Relations between the measures are discussed, as are their relation to geometric properties of the pore phase. The noncentered covariance of digital SEM images of sandstones is then estimated using Fourier and binary methods. The results are discussed in terms of the geometric information in the SCF.

6.2 Spatial Correlation Theory

Measures of spatial correlation will be discussed in the context of probabilistic models. The image is considered to be a realization of the stochastic indicator function for the pore structure (Watson, 1975; Serra, 1982, Ch. 9). The indicator function is assumed to be a stationary random function which is defined as

$$f_p(x) = \begin{cases} 1 & \text{if } x \in \text{pores} \\ 0 & \text{if } x \in \text{grains} . \end{cases} \tag{6.1}$$

The indicator function, f_p, assumes the value one when the point x falls on a pore feature in the image. A binary image is a realization of the indicator function.

Many measures of spatial correlation have been proposed and applied to the study of porous media, including covariance, autocorrelation, variogram, covariogram, autocorrelogram, and autorun analysis. Significant differences exist between these various measures which are due to the character of the formulation (i.e., discrete or continuous, global or local, bounded or unbounded

set) and the normalization applied or assumed for the indicator function (i.e., zero mean, normalized with respect to variance). Serra (1982, Ch. 9) discusses some of these different formulations.

When applying spatial correlation measures to binary digital images of sandstones, the discrete and local (within the image frame) formulations are appropriate. The prefix "auto" is explicitly stated for some measures and is implicit in all others when the spatial correlation of the function is with respect to itself. Only measures of auto-spatial correlation are considered here and the auto prefix is implicit if not explicitly stated. The principal measures of spatial correlation will now be defined and the relations between them discussed.

6.2.1 Noncentered Covariance

The noncentered covariance, $NCC(h)$, of the indicator function is given by Watson (1975) as

$$NCC(h) = E[f_p(x)f_p(x+h)] = Pr(x, x+h \in \text{pores}) , \tag{6.2}$$

where h is the lag or spatial shift, and both x and h can be vectors. The covariance is noncentered because the mean of the indicator function is not zero. The expectation of the pore indicator function is

$$E[f_p(x)] = p_p = \phi . \tag{6.3}$$

The NCC is a common measure of spatial correlation because it can be easily implemented for digital images. Quiblier (1984) states that the correlation output of the Quantimet 720 Texture Analyzer is the NCC, which he calls the "covariogram." Serra (1982, p. 273) uses the term "covariogram" to describe the form of Eqn (6.2) when it is applied to a deterministic, continuous, and summable function.

6.2.2 Autocorrelation Function

The autocorrelation function, $ACF(h)$, of f_p is given by Quiblier (1984) as

$$ACF(h) = \frac{E[(f_p(x) - p_p)(f_p(x+h) - p_p)]}{E[(f_p(x) - p_p)^2]} . \tag{6.4}$$

The autocorrelation function is shifted for the non-zero mean (p_p) of the indicator function and is normalized by the variance of the indicator function. Thus, this formulation for the ACF is dimensionless. Two pieces of information, the mean and variance of $f_p(x)$, have been removed in the ACF formulation. Both of these pieces contain significant geometric information and should be determined by an alternative method if the ACF formulation is used. A relation can be established between $NCC(h)$ and $ACF(h)$ by expanding the right side of Eqn. (6.4) (Quiblier, 1984) to obtain

$$ACF(h) = \frac{NCC(h) - {p_p}^2}{NCC(0) - {p_p}^2} . \tag{6.5}$$

When the spatial correlation is computed by Fourier methods it is commonly referred to as an autocorrelation function. However, unless the original data were adjusted for the non-zero mean and the results normalized, it is more appropriate to call the result the noncentered covariance. Computation of the noncentered covariance by Fourier methods is described in section 6.3.

6.2.3 Variogram

Huijbregts (1975) defines the variogram as

$$\mathcal{V}(h) = \frac{1}{2} E[(f_p(x+h) - f_p(x))^2] . \tag{6.6}$$

The variogram depends on a weaker hypothesis which requires only that the increments $(f_p(x+h) - f_p(x))$ be weakly stationary instead of the indicator function itself being weakly stationary. The weaker hypothesis allows the mean of the indicator function to vary spatially, which may represent a realistic variation in pore structure (i.e., inhomogeneity). The variogram is used typically for the estimation of regionalized variables where there is incomplete spatial sampling (Huijbregts, 1975). In practice, when the variogram is used to describe local structure, the indicator function is assumed to be weakly stationary and the so-called "point" or "punctual" variogram is then given by (Huijbregts, 1975; Serra, 1982, p. 280)

$$\mathcal{V}(h) = NCC(0) - NCC(h) \,. \tag{6.7}$$

When the variogram is estimated in this way, we see that it is simply an alternative representation of the noncentered covariance.

Serra (1982, p. 316) states that the variogram is a better representation of spatial correlation because it will always exist, whereas the covariance may not exist. In practice, the covariance will exist for all sandstone images. For local structure, there is no advantage to using the variogram.

6.2.4 Autorun Analysis

Şen (1984) has proposed using the one-dimensional "autorun" function as an alternative to the autocorrelation function. He claims that the autorun function is more flexible than the autocorrelation function and that the autorun function contains more information. These claims are true in terms of the classical autocorrelation function which has been normalized for mean and variance of the indicator function. However, the autorun analysis contains no more information than other measures of spatial correlation such as the noncentered covariance. Both the autorun function and the noncentered co-

variance contain information on the porosity of the medium and the surface area of the medium.

Şen (1984) defines the autorun function, AR, for discrete processes as a conditional probability,

$$AR(k\Delta x) = Pr(f(k\Delta x) > m | f(\Delta x) > m) \,, \tag{6.8}$$

where k is the lag factor, Δx is the point spacing, and m is the truncation level. Şen (1984) has assigned a value of -1 to the "grain state" of the indicator function (Eqn. (6.1)). The truncation level then takes on the values $-1 > m > +1$, exclusively.

The finite sample estimator of the AR is given by

$$AR(k\Delta x) = \frac{2n_k}{n-k} \,, \tag{6.9}$$

where n_k is the number of grain-grain *and* pore-pore pairs which are separated by the distance $k\Delta x$ and n is the number of points in the realization of the indicator function. The quantity $n - k$ is a normalizing factor for the finite sampled area. The autorun function is related simply to the autocorrelation coefficients (Şen, 1977).

6.2.5 Geometric Properties of Spatial Correlation Functions

There are several important relations between spatial correlation functions and geometric properties of porous media. The geometric properties include the porosity, specific surface, and "range" of correlation.

The zero lag value of the noncentered covariance is equal to porosity (Eqn. 6.3). This relation is the same as the areal fraction relation from stereology.

Specific surface is related to the slope of the one-dimensional NCC at the

origin,

$$S_V = -4NCC'(0) \; . \tag{6.10}$$

Debye *et al.* (1957) were apparently the first to derive Eqn. (6.10). Their equation contains an extra porosity dependent factor which appears to be inconsistent with their definitions of surface and volume, but probably results from the definition of their correlation function which is not explicitly given. The expression of specific surface in terms of the autocovariance function is strongly based on stereological concepts. Indeed, Debye *et al.* (1957) cite the stereological determination of specific surface developed by Chalkley *et al.* (1949). Watson (1975) derives Eqn. (6.10) from a set theory (i.e., mathematical morphology) approach.

For a deterministic compact set, the "range" of the covariance is the shift (lag) beyond which the covariance is identically equal to zero (Serra, 1982, p. 273). A sandstone image is the local representation of a nondeterministic set and the covariance (actually *NCC*) may never equal zero. Therefore, a different concept of range is required. The value of the *NCC* at large lags approaches asymptotically the square of the porosity. The "range" is taken as the lag at which the *NCC* becomes sufficiently close to the asymptotic value. This range is presumably related to the extent of order in the porous media. The range is closely related to what has been variously referred to as a "correlation length" or a "characteristic length" (Prager, 1961). Estimation of the range is considered in section 6.4.3.1.

In general, the SCF has the physical interpretation as the probability of a point at $x + h$ belonging to the pore phase when the point x belongs to the pore phase. Serra (1982, p. 272) states that the behavior of the covariance near zero lag reflects the nature of the pores and that the behavior at larger lags reflects the spatial arrangement of the pores. Clearly this statement is true for the porosity and specific surface which are determined from the near

zero lag behavior. Further, our results indicate that the range reflects the size of the pores. Thus, the spatial arrangement of the pores should be important only at lags greater than the range.

Other measures of spatial correlation, discussed above, have similar geometric interpretations because of the relations between the various measures. However, care must be taken to insure correct calculations and to preserve the geometric information.

6.3 Spatial Correlation by Fourier Methods

The use of Fourier methods to compute two-point spatial correlation functions of digital images is well-known in digital image processing (e.g., Castleman, 1979, p. 186). Here, the term autocovariance, $ACOV$, is used to refer to the noncentered covariance, NCC, computed by Fourier methods. Several aspects of the Fourier methods are of particular significance when these methods are applied to images of porous media with the goal of a quantitative interpretation. Specifically, the underlying assumption of a grossly periodic structure must be taken into account and the results must be normalized to allow accurate geometric interpretation. In this section, the Fourier computational methods and results are presented.

6.3.1 Transient Response versus Circular Response

A fundamental assumption of Fourier methods is that the function being represented is periodic with the period determined by the sampling frame (i.e., image size). This is usually an unreasonable constraint to force onto a digital image (Andrews, 1974; Castleman, 1979, Ch. 10; Gillott, 1980; Vollath, 1981). The consequence of such a constraint is the generation of artificially high amplitude, high spatial frequency components which attempt to recon-

struct the "step" between the left and right image borders and the top and bottom borders.

Various windows can be applied to the image prior to applying the Fourier transform in order to improve the match between the left-right and top-bottom. These windows, however, change the content of the image.

The autocovariance function obtained by simple Fourier methods is termed a "circular" autocovariance, where the image is assumed to "wrap" around to the starting values. It is unreasonable to force this periodicity onto the rock structure. Therefore, it is preferable to compute the "transient" autocovariance by padding the image with zeros. The original image then occupies the upper left quadrant of a padded image.

Circularity can also occur in computation by binary methods if the algorithm is allowed to "wrap" around to the beginning of the image when the edge is reached.

6.3.2 Normalizing for a Finite Computation Window

When the transient autocovariance is computed, normalization is required because the overlap of the non-zero (true) image area decreases as the shift increases. The normalizing factor is simply the fraction of overlap at each lag (shift). If this normalization is not applied, then the *ACOV* will appear to decrease at a rate faster than that due to the structure.

6.3.3 Computation of the Fourier *ACOV*

Our *ACOV* computation by Fourier methods is restricted to a 128×128 image size due to hardware limitations. The procedure begins with the selection of an intensity threshold using the method described in Chapter 3. This threshold was used with an intensity transform program (IMGTON) to produce a digital

image (full byte representation) with intensity 1 for pores and 0 for grains. The program **IMGFFA** performs the following transforms and normalizations. A 128×128 area of the image was copied into the real component of a 256×256 complex array with zero imaginary components, and zero real components outside the 128×128 upper left quadrant. A discrete Fourier transform was applied (Fraser, 1979), the power spectrum was computed from the resulting Fourier coefficients, and an inverse discrete Fourier transform applied. This result was normalized for the 256×256 area by the standard convention for discrete fast Fourier transforms. The DC component (zero frequency) of the power spectrum is saved prior to the inverse FFT for computation of the range. Normalizing for the transient response consisted of dividing the values by the number of pixels which overlapped at each lag. Results were printed to allow computation of slope at zero lag and range. Further, the results were plotted with a three-dimensional hidden line plotting program (**FFTPLT**).

Several tests were applied to check the programs. A constant (all pore) image was transformed and produced the expected constant autocovariance function. At the maximum shift (127×127), the point of greatest disagreement, the function was within 0.1% of the original constant. For binary images of sandstones, the zero lag values agree exactly with porosities determined from areal fractions. This agreement is expected because of the identity between the zero lag value and the area fraction. Further, it is easy to recognize that the surface area determinations from the slope of the $ACOV$ at zero lag should equal the surface area determined from line-sampled intercepts. Theoretically, the surface areas must be identical. However, because of statistical variation due to the criterion used for line-sampled intercepts, the values may not agree exactly. The two values are compared in Chapter 7.

An isotropic one-dimensional $ACOV$ function is obtained by averaging the two-dimensional $ACOV$ (i.e., $ACOV(m,n)$), at fixed radii. Berryman (1985b)

gives the following formula for such an average

$$ACOV(k) = \frac{1}{2k+1}\sum_{l=0}^{2k}\overline{ACOV}(k, \pi l/4k) \text{ , for } 0 \leq k \leq k_{max} \qquad (6.11)$$

where

$$\overline{ACOV}(k,\theta) = ACOV(k\cos\theta, k\sin\theta) \text{ ,} \qquad (6.12)$$

and the right side of Eqn. (6.12) is the bilinear interpolation from $ACOV(m,n)$ when $k\cos\theta$ and $k\sin\theta$ are not both integers.

6.3.4 Geometric Properties from the Fourier *ACOV*

The *ACOV*, properly computed by Fourier methods, will contain basic geometric information about the pore structure. The full intensity digital image must be dichotomized, the transient response must be computed, and the result must be normalized. If these steps are not taken, then the resulting *ACOV* will not accurately reflect the geometric information.

The slope of the *ACOV* function at the origin is computed from the zero lag value and values at one pixel lag in the X and Y lag directions. The "nugget effect" and noise effects described by Serra (1982, Ch. 9) are not present in our *ACOV* functions. The slope is used in Eqn. (6.10) to estimate S_{Vp}.

The range is a loosely defined parameter. Serra (1982, p. 283) gives formulae for estimating the range in 1, 2, and 3 dimensions. Assuming an isotropic covariance, the relation for one dimension is

$$a_1 = \frac{2d}{p_p - {p_p}^2}\sum_{k=1}^{k_{max}}(ACOV(k) - {p_p}^2) \text{ ,} \qquad (6.13)$$

where d is the pixel size and k_{max} is the maximum lag considered.

Figure 6.1 illustrates the simple geometric construction upon which Eqn. (6.13) is based. The range is equal to the base of a triangle with height $p_p - {p_p}^2$ and area equal to the area between the ${p_p}^2$ constant value and the

covariance function. For lags when the covariance is less than $p_p{}^2$, area is subtracted. This definition performs poorly when the covariance is less than $p_p{}^2$ at low to moderate lags (Figure 6.1b); a situation which occurs when the porosity is nonuniformly distributed spatially. Depending on the behavior of the $ACOV$ (e.g., strong periodicity), the range may depend on the distance over which the area is integrated. Further, the result depends on $p_p{}^2$ which is not always the best estimate of the asymptotic level of the $ACOV$ at large lags. These limitations apply mainly to single image covariance functions. If the covariance is averaged over X and Y orientations and averaged over several images, the asymptotic behavior is more uniform. Still, the triangle approximation underestimates the range because the covariance behaves more like an exponential function (Figure 6.1a).

Range can also be computed using the zero frequency (DC) component of the power spectrum, $g(0)$, and the autocovariance at zero lag, $ACOV(0)$ (Serra, 1982, p. 278),

$$a_1 = g(0)/ACOV(0) \; . \tag{6.14}$$

Note that this equation is also based on the simple geometric construction described above and it suffers the same limitations. However, the simplicity of Eqn. (6.14) makes it preferable to the integration of the $ACOV$. The power spectrum is readily available during the calculation of the $ACOV$. Also, Eqn. (6.14) intrinsically performs an orientation averaging if two-dimensional transforms are used. Still, these methods do not yield reasonable range estimates for our images. A better estimator is given in section 6.4.3.1.

6.3.5 Results of Fourier Computed $ACOV$

Results of autocovariance functions computed by Fourier methods are given only as selected plots of curves. Specific surface and range are computed from

binary covariance functions and are presented later.

Figure 6.2a is a three-dimensional hidden line plot of the autocovariance function of image #1048 (Figure 5.1) from sample 2710. In some cases, these plots are difficult to visualize and may be perceived differently by different observers. For all of the autocovariance functions, the plot has a similar configuration as follows. The perceived image should be that of a solid block with topography on the top surface which represents the autocovariance function. The block has background panels with straight lines of constant autocovariance to allow quantitative interpretation of the $ACOV$ function. The zero shift (zero lag) point is the back corner where the background panels meet near the center of the figure. The value at zero lag is the maximum value taken by the $ACOV$ function. Function values decrease in all directions away from the zero lag peak. At larger lags, the function forms an undulating surface.

The $ACOV$ function has mirror symmetry with respect to the X and Y shift axes. Therefore, it is only necessary to show a half-plane of the function. Figure 6.2b is the negative X-lag quadrant opposite the positive X quadrant in Figure 6.2a. Note that the behavior along the axes are identical for the two figures. These figures show values of the $ACOV$ for lags less than half the width of the 128×128 region. Values at larger lags are unreliable because of the decrease in the area of image overlap.

The $ACOV$ functions in Figures 6.2a and 6.2b reflect the local structure in the image. To obtain $ACOV$ functions which are representative of the rock, we must average the functions from the remaining quadrants of this image and from more images. The average character is the essence of describing the rock as a stochastic medium via the covariance function. Figure 6.3a is an average of the $ACOV$ at positive lags from all quadrants of image #1048. Figure 6.3b is an average of the $ACOV$ at negative lags. Figure 6.4 is an average of the positive and negative lags from all quadrants. Averaging the positive and

negative lags from a single image yields a smoother $ACOV$ in which the local structure of the image is not as prominent. This last average is valid only if the material is considered to be isotropic.

Figure 6.5 shows the one-dimensional $ACOV$ obtained by applying Eqn. (6.11) to the data of Figure 6.4. Also plotted on Figure 6.5 is the average of the X and Y covariances computed by binary methods. These two curves agree very well up to lags of 125 μm. The porosities (i.e., zero lag value) agree exactly and also agree with the areal fraction measure. The S_{Vp} (0.220 μm^{-1}) values agree to within 1% and also agree with the average S_{Vp} (0.222 μm^{-1}) found from linear intercepts (Chapter 4). The agreement between the S_{Vp} values is not surprising since they are based on the same data points (i.e., $ACOV(0,0)$, $ACOV(0,1)$, and $ACOV(1,0)$). The isotropic average also uses one additional point, $ACOV(1,1)$.

The range values (125 μm) of the two functions also agree. At lags greater than the range, the orientation averaged $ACOV$ shows a correlation at 190 μm. This distance agrees well with the average spacing of the larger pore features in the image (Figure 5.1).

Figure 6.6 is an example of an incorrectly computed $ACOV$ function. For this figure, the circular covariance was computed for the same area as used in Figure 6.2a. The behavior of the two functions is very similar for near zero lags but becomes quite different at larger lags. Of course, the zero lag values agree exactly. The S_{Vp} estimates from isotropic averages are within 2%.

6.3.6 Discussion of Fourier Computed $ACOV$

We have computed $ACOV$ functions by Fourier methods for three reasons. First, to demonstrate that certain computational aspects must be followed for accurate results. Second, to show that the porosity and specific surface estimated from the $ACOV$ agree with stereologically determined values. Third,

to show that upon averaging, the $ACOV$ looses the local details of the image and begins to represent the average character of the rock.

It is clear, without an example, that the results of an $ACOV$ computed from a full intensity (8 bit) image are meaningless from a geometric viewpoint, because the image is not a realization of the indicator function. The expectation of the intensity at any pixel is not equal to the porosity.

Figure 6.6 demonstrated the inaccurate results which occur if a circular $ACOV$ is computed. The circular $ACOV$ forces a periodicity onto the image structure. Consequently, the behavior, particularly at larger lags, will not represent the pore structure.

Because the X and Y average binary covariance is a very good approximation to the orientation averaged (isotropic) one-dimensional covariance $ACOV$, we have used the binary method for all images. An additional influence was our computer hardware limitations, and the longer time required for the Fourier computation. With binary methods, we are able to use the entire image area which yields more statistically representative results albeit only for X- and Y-lag axes.

6.4 Spatial Correlation by Binary Methods

In this section, the non-centered covariance, NCC, is computed for digital SEM images of sandstones using binary methods. The binary methods are preferable to Fourier methods for our purposes. Specifically, we compute the NCC only for pure X or Y lags. The binary algorithm is fast because it uses the binary operations of the computer. It is also easily normalized and it avoids circularity problems. The equivalent behavior of the X and Y averaged NCC and the isotropically averaged $ACOV$ support our approach.

6.4.1 Binary Algorithm

Covariance of the binary image is computed easily using a discrete version of Eqn. (6.2). Berryman (1985b) gives an estimator of the form

$$NCC(m,n) = \frac{1}{i_{\max} j_{\max}} \sum_{i=1}^{i_{\max}} \sum_{j=1}^{j_{\max}} f_{ij} f_{i+m,j+n} \,, \tag{6.15}$$

where f_{ij} is the indicator function value at pixel coordinates (i,j), $0 \leq m,n < N$, $i_{\max} = N - m$, and $j_{\max} = N - n$. Berryman (1985b) does not consider negative lags. If the full covariance function is of interest, then the negative lags can be computed via

$$NCC(-m,n) = \frac{1}{i_{\max} j_{\max}} \sum_{i=m+1}^{N} \sum_{j=1}^{j_{\max}} f_{ij} f_{i-m,j+n} \,. \tag{6.16}$$

If the isotropic function is of interest, the negative lags should be included in the averaging. Both positive and negative lag values are available directly when using Fourier methods.

In this study, only one-dimensional correlation functions have been computed for binary images. These one-dimensional functions correspond to the cases $NCC(m,0)$ and $NCC(0,n)$. The range of m and n is restricted to $0 \leq m,n < N/2$. Provided that the magnification is sufficiently low, the covariance typically approaches an asymptotic value before these maximum lags. Averaging over several images further smooths the *NCC*.

Note the normalizing factor in Eqn. (6.15). This factor is identical in function to the normalization described above for the $ACOV$ computed by Fourier methods. Note also that Eqn. (6.15) yields a transient response (i.e., no wrapping).

6.4.2 Computation of the Binary *NCC*

A computer program (**COVARX**) was written to compute *NCC* in the X direction for binary images. The computation is performed by shifting each line

of the binary image, AND'ing the line with an unshifted copy, and summing the number of pore pixels which overlap. This is a form of parallel computation (Fabbri, 1984, App. C) which has been used in this study whenever possible (e.g., for erosions and other set operations). To compute the *NCC* as a function of n (i.e., the Y direction), the binary image is rotated 90 degrees (with **IMGROT**) and **COVARX** is used. Another program (**COV2DB**) was developed to compute the two-dimensional *NCC* by binary methods. It was used solely to verify the results of the two-dimensional *ACOV* program. Despite the use of efficient coding methods and assembly language subroutines, **COV2DB** is effectively slower than **IMGFFA** for equal image areas. **COV2DB** must be run twice to compute both positive and negative lags, whereas both are available from one run of **IMGFFA**.

The binary computational method used here is equivalent to erosion with a two-point linear structuring element (Watson, 1975; Serra, 1982, p. 281).

6.4.3 Geometric Properties from the Binary *NCC*

Porosity is estimated directly from the zero lag value of the *NCC* and S_{Vp} is computed from Eqn. (6.10). The slope of the *NCC* at zero lag is obtained by dividing the difference between the one-pixel lag and zero lag values by the pixel size. This gives a minimum absolute value for the slope at zero lag and thus a minimum estimate of specific surface. It is not justifiable to fit a curve to the *NCC* function to estimate the slope at zero lag. This practice would imply knowledge of the form of the *NCC* function. It also implies the extraction of more information than is contained in the binary image.

6.4.3.1 Estimation of the Range

The range is defined as the length of correlation in the material. Therefore, the range should indicate at what lag the *NCC* function becomes close to and stays close to an asymptotic value. The estimator given by Serra (1982), Eqn. (6.13) in this paper, does not accurately indicate this behavior for sandstone images. A better indicator is one which depends on the local behavior of the *NCC* function near the asymptotic value. We formulated a simple estimator. Both the asymptotic value and the "closeness" to this value must be determined. Another consideration is the robustness of the range estimator when only a few images or a single image is studied as opposed to the average behavior of many images.

When few images are averaged, $p_p{}^2$ is not always a good estimator of the asymptotic value. A more reliable estimate, termed $p_p{}^{2\star}$, is simply the mean value of the *NCC* for all lags after the first local minimum. This estimate is reliable when the *NCC* is oscillatory at large lags and when it is well-behaved (i.e., tends to $p_p{}^2$).

A good *ad hoc* estimator of range, $a^\star$, was found to be the greater of the two values: 1) the lag corresponding to the first local minimum of the *NCC*, and 2) the lag at which the *NCC* first crosses the $p_p{}^{2\star}$ line. Almost always, the local minimum is selected. In practice, we use a 3-point local slope calculation and threshold slope value ($-0.0004\ \mu\text{m}^{-1}$) to indicate the local minimum. The estimator yields similar ranges for individual images from the same rock. Further, these estimates usually agree with the estimate found by averaging the *NCC* from many images. Rarely, the range estimator will fail, in which case the range is selected by inspection.

Perhaps a better estimate of range could be found by fitting an exponential function to the *NCC* and using a strict criteria of closeness with the asymptotic value. However, given the absence of a rigorous geometric interpretation or

application for the range parameter, it makes little sense to introduce such complexity.

6.4.4 Results from the Binary *NCC*

The X and Y averaged *NCC* functions for our 14 samples are shown in Figures 6.7a through 6.7n. All of the higher magnification images for each rock were used in the averages. The zero lag values, S_{V_p} estimates, asymptote estimates, and ranges are given in Table 6.1.

For the rocks with 9 images, the average *NCC* functions are smooth and do not indicate periodic structure. Some rocks with fewer images do show periodic structure in the *NCC* at larger lags. This structure is due to the use of only a few images and it would be smoothed by the addition of more images.

6.4.5 Discussion of the Binary *NCC*

We expect the porosity and specific surface determined from the X and Y averaged *NCC* function to be nearly identical to those determined by stereological methods because of the common theoretical foundation. Any differences between the porosities from the *NCC* and those given in Table 4.1 are due to the exclusive use of higher magnification images for the covariance computation. Specific surface estimates from the covariance functions agree very well with specific surface from linear intercepts (see Table 4.3 and section 7.2.2). Any differences between the two are due to the chord sampling criteria.

The range is a parameter which is unique to the covariance. Debye *et al.* (1957) have suggested that the range is a measure of "grain" size (pore size in our application). Because the representation on the image is a biased view of the sample, all we can say is that the range reflects the feature dimensions.

In general, the range correlates with the dimensions of the larger features in the images. Values of the range are compared with other characteristic length indicators (e.g., diameter of the mean pore volume-equivalent sphere) in Chapter 7.

6.5 Higher Order Spatial Correlation Functions

Spatial correlation functions of order three and higher play a significant role in theories of stochastic media. These higher order functions are necessary to obtain accurate representations of the media. A good discussion of higher order correlation functions is given in Torquato and Stell (1982). Berryman (1985b) has developed an efficient method for computing and storing the three-point correlation function of a digital image. We have not computed the three-point correlation functions in this study.

6.6 Discussion of Spatial Correlation Results

Contrary to the claims of Preston and Davis (1976), the *NCC* does not contain sufficient information to "permit realistic modeling of all physical properties that depend upon pore-grain geometry." Contrary to the conclusions of Lin (1982a), the *NCC does* provide specific textural information. The *NCC* contains well-defined geometric information, including ϕ and S_V. However, this information can be obtained more efficiently by other methods.

The specific surface computed by Lin (1982a) from the *NCC* did not agree with her stereologically determined specific surface. She concluded that the pore structure "may not be a realization of a Poisson process" and thus the theory is not appropriate. The theory requires only that the structure be

random, not that it follow a Poisson stochastic law. Lin (1982a) must have made an error when computing the *NCC*. Lin (1982a) also suggests that the power spectrum may be a better tool to characterize rock images. However, both the *NCC* and the power spectrum contain equivalent information and the information is more readily accessible from the *NCC* (Serra, 1982, p. 279).

Indeed, many investigators cite Jenkins and Watts (1968) and claim that the autocorrelation function may be difficult to interpret physically but that the power spectrum is more easily interpreted. For the case of rock images, these claims have not been substantiated. Almost certainly, the power spectrum approach is not a better means to study the structure. For example, to compute the porosity via the power spectrum requires an integration over the entire spectral range. The power spectrum does not readily present geometric information.

It is not reasonable to compute the *NCC* if only ϕ and S_V are desired. These two parameters can be obtained more efficiently by stereological methods (i.e., intercept sampling) or by feature analysis. The range is the only simple piece of information which is unique to the *NCC* function and the utility of this parameter is not yet known. To justify the computation of the *NCC*, the entire function should be used. For example, the *NCC* can be used in a stochastic model of the structure (Quiblier, 1984) or in a random media model of physical properties (Berryman, 1983, 1985a).

The image or images used to compute the *NCC* must be statistically representative of the pore structure. If a single image is used, the covariance may be dominated by local structure in the image. Further, if the magnification is high and only a few features constitute the image, then the *NCC* for that image is not likely to be representative of the rock structure. If high magnification images are used, then many images must be studied to produce significant numbers. These images should be selected by a nonsubjective process (e.g.,

images taken at the intersections of a pre-defined grid). If a subjective process is used (e.g., visual selection), the results will undoubtedly contain an operator bias, particularly if every image is required to contain a pore feature, perhaps with a minimum size. Figure 6.2a illustrates the local structure effect from a small image area with only a few pores. Note the difference between Figure 6.2a and Figure 6.3a which shows the $ACOV$ function averaged over a larger area.

Table 6.1 gave values of S_V and S_{V_p} in X and Y directions. The discussion of anisotropy in specific surface, in Chapter 4, applies equivalently to the values of S_V obtained here.

Chapter 7 contains a comparison of the range of the NCC with other measures of characteristic length in the pore structure. Spatial correlation in stochastic models of pore structure is also discussed in Chapter 7.

Figure Captions

Figure 6.1. Schematic illustration of range estimator (a_1) given by Serra (1982, Ch. 9). The range is always underestimated by a_1. The range estimator used in this study is shown by a^*. (*a*) Schematic of a multi-image average covariance function. (*b*) Schematic of a single image covariance function. Slashed areas are added to the area sum and the stippled area is subtracted.

Figure 6.2. $ACOV$ function for the upper left quadrant of image #1048 (Figure 5.1) of sample 2710. (*a*) Positive X-lag quadrant of $ACOV$. (*b*)

Negative X-lag quadrant of *ACOV*.

Figure 6.3. Average *ACOV* function for all 4 quadrants of image #1048 of sample 2710. (*a*) Positive X-lag quadrant of *ACOV*. (*b*) Negative X-lag quadrant of *ACOV*.

Figure 6.4. Average of positive and negative lag values of *ACOV* function in Figure 6.3. This average assumes an isotropic covariance function.

Figure 6.5. Orientation averaged, one-dimensional *ACOV* function from Figure 6.4. Also shown is the average of the X and Y *NCC* functions computed by binary methods.

Figure 6.6. Example of an *incorrectly* computed *ACOV* function. This is a circular autocovariance. The image was not padded with zeros. Contrast this function with Figure 6.2a. Both were computed from the same image area.

Figure 6.7. *NCC* results for sandstones.

(*a*) 2124.	(*e*) 2521.	(*i*) 2700.	(*m*) 2842.
(*b*) 2509.	(*f*) 2523.	(*j*) 2704.	(*n*) 2843.
(*c*) 2513.	(*g*) 2686.	(*k*) 2710.	
(*d*) 2519.	(*h*) 2687.	(*l*) 2841.	

Table 6.1

NCC Parameters

Sample Number	Axis	ϕ (p_p) (%)	S_V (μm^{-1})	S_{Vp} (μm^{-1})	${p_p}^2$	${p_p}^{2*}$	a^* (μm)
2124	X	20.44	0.0564	0.276	0.0418	0.0429	75
	Y	20.44	0.0623	0.305	0.0418	0.0420	69
	Avg	20.44	0.0594	0.290	0.0418	0.0424	75
2509	X	21.45	0.0334	0.156	0.0460	0.0463	111
	Y	21.45	0.0368	0.172	0.0460	0.0455	80
	Avg	21.45	0.0351	0.164	0.0460	0.0459	104
2513	X	21.08	0.0500	0.237	0.0444	0.0423	83
	Y	21.08	0.0538	0.255	0.0444	0.0445	70
	Avg	21.08	0.0519	0.246	0.0444	0.0434	80
2519	X	17.59	0.0264	0.150	0.0309	0.0368	122
	Y	17.59	0.0279	0.159	0.0309	0.0327	152
	Avg	17.59	0.0271	0.154	0.0309	0.0347	134
2521	X	24.45	0.0346	0.142	0.0598	0.0594	152
	Y	24.45	0.0360	0.147	0.0598	0.0600	116
	Avg	24.45	0.0353	0.144	0.0598	0.0597	122
2523	X	18.39	0.0629	0.342	0.0338	0.0335	103†
	Y	18.39	0.0635	0.345	0.0338	0.0335	122†
	Avg	18.39	0.0632	0.344	0.0338	0.0335	119†
2686	X	26.44	0.0445	0.168	0.0699	0.0661	140
	Y	26.44	0.0497	0.188	0.0699	0.0681	126
	Avg	26.44	0.0471	0.178	0.0699	0.0673	140
2687	X	18.57	0.0610	0.328	0.0345	0.0521	59
	Y	18.57	0.0636	0.343	0.0345	0.0449	59
	Avg	18.57	0.0623	0.336	0.0345	0.0486	59
2700	X	23.55	0.0608	0.258	0.0554	0.0566	119
	Y	23.55	0.0622	0.264	0.0554	0.0560	100
	Avg	23.55	0.0615	0.261	0.0554	0.0562	112

Table 6.1 (cont)

NCC Parameters

Sample Number	Axis	ϕ (p_p) (%)	S_V (μm^{-1})	S_{Vp} (μm^{-1})	${p_p}^2$	${p_p}^{2*}$	a^* (μm)
2704	X	19.28	0.0494	0.256	0.0372	0.0389	131
	Y	19.28	0.0518	0.269	0.0372	0.0395	97
	Avg	19.28	0.0506	0.262	0.0372	0.0392	103
2710	X	28.87	0.0600	0.208	0.0834	0.0878	153
	Y	28.87	0.0627	0.217	0.0834	0.0818	134
	Avg	28.87	0.0613	0.213	0.0834	0.0850	141
2841	X	32.68	0.0469	0.144	0.1068	0.1130	160
	Y	32.68	0.0556	0.170	0.1068	0.1062	176
	Avg	32.68	0.0512	0.157	0.1068	0.1094	164
2842	X	14.36	0.0321	0.224	0.0206	0.0203	88
	Y	14.36	0.0335	0.233	0.0206	0.0216	78
	Avg	14.36	0.0328	0.228	0.0206	0.0210	84
2843	X	26.58	0.0565	0.212	0.0706	0.0713	142
	Y	26.58	0.0628	0.236	0.0706	0.0729	96
	Avg	26.58	0.0597	0.224	0.0706	0.0721	124

NOTES: All values are from high magnification images only. For each rock, the high magnification images are all at the same magnification, typically 100×. Avg is from the combined X and Y *NCC* functions.

† The range estimator performed poorly for this rock. Inspection gave a visual estimate of 70μm.

Figure 6.1a Schematic Covariance

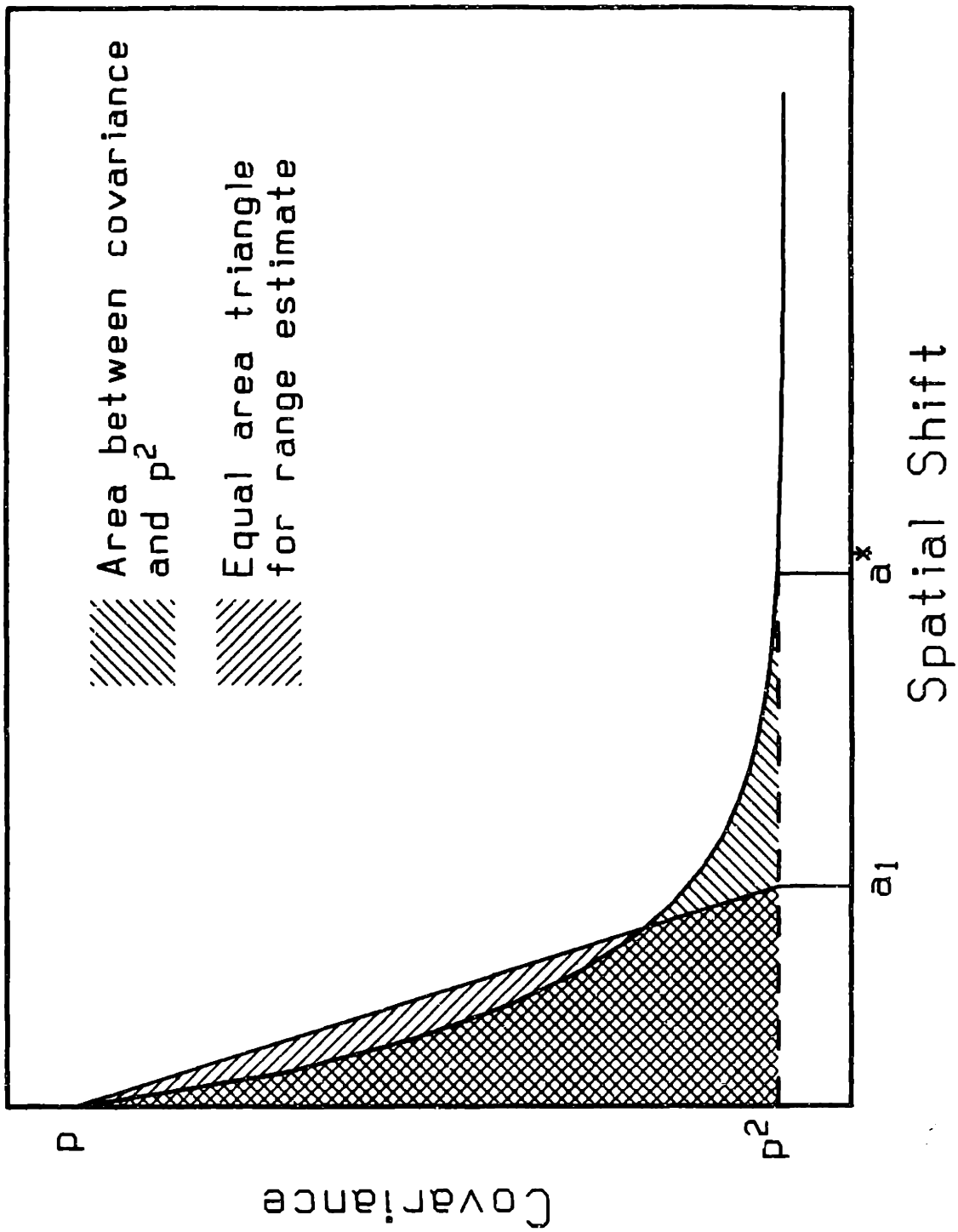

Figure 6.1b Schematic Covariance

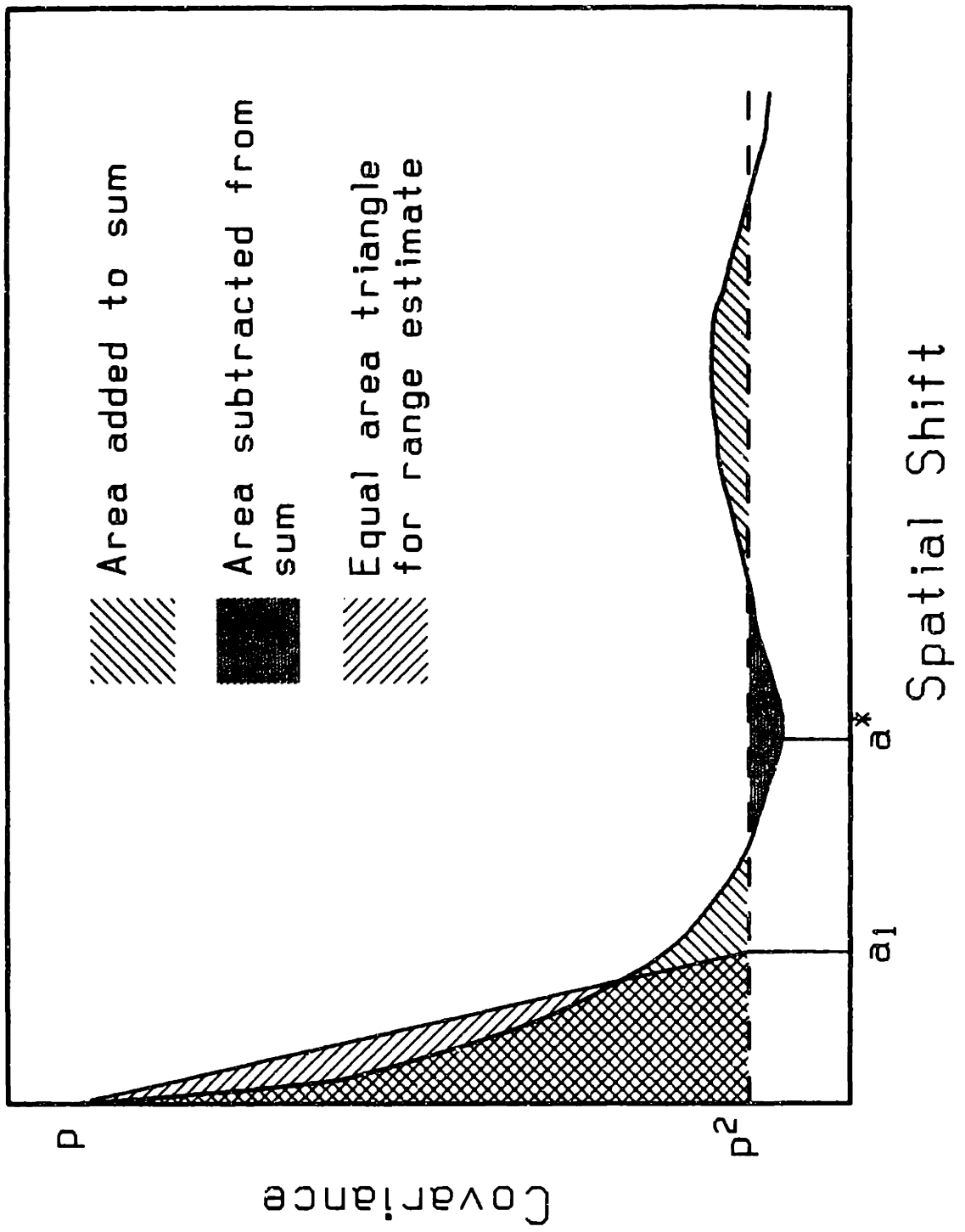

Figure 6.2a

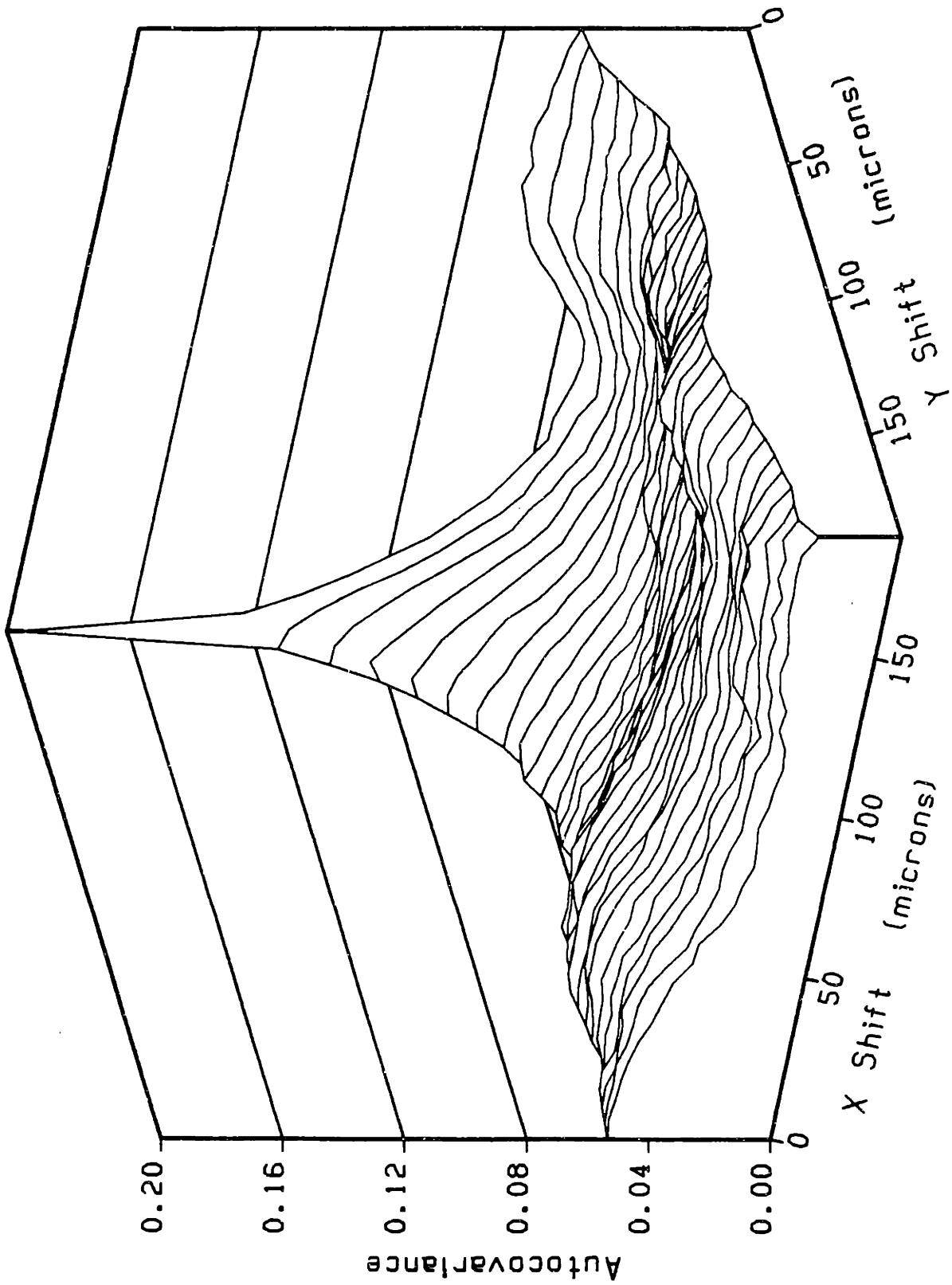
Autocovariance
0.20
0.16
0.12
0.08
0.04
0.00
X Shift (microns)
0
50
100
150
Y Shift (microns)
0
50
100
150

Figure 6.2b

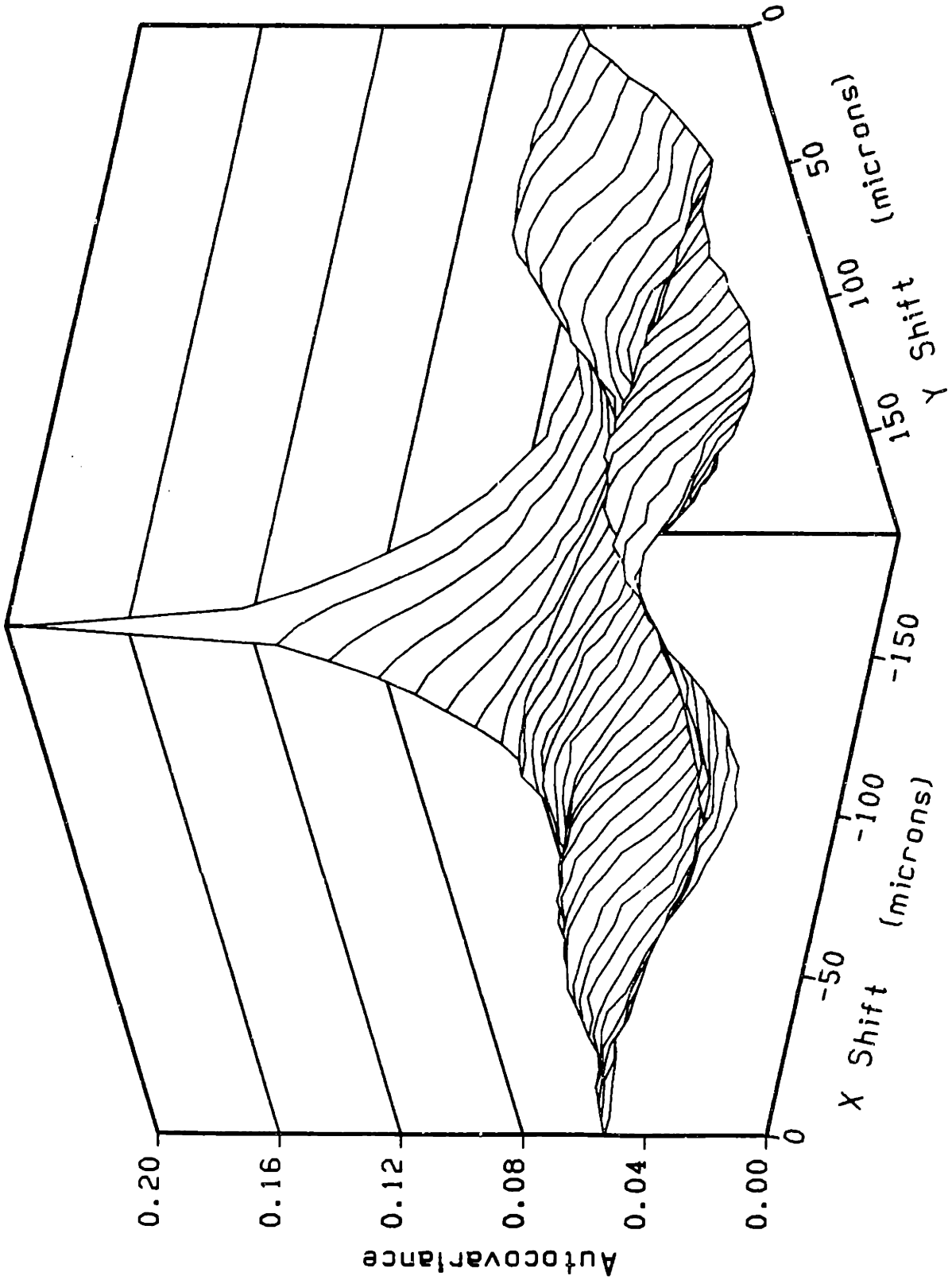
Autocovariance
0.20
0.16
0.12
0.08
0.04
0.00
X Shift (microns)
0
-50
-100
-150
Y Shift (microns)
0
50
100
150

Figure 6.3a

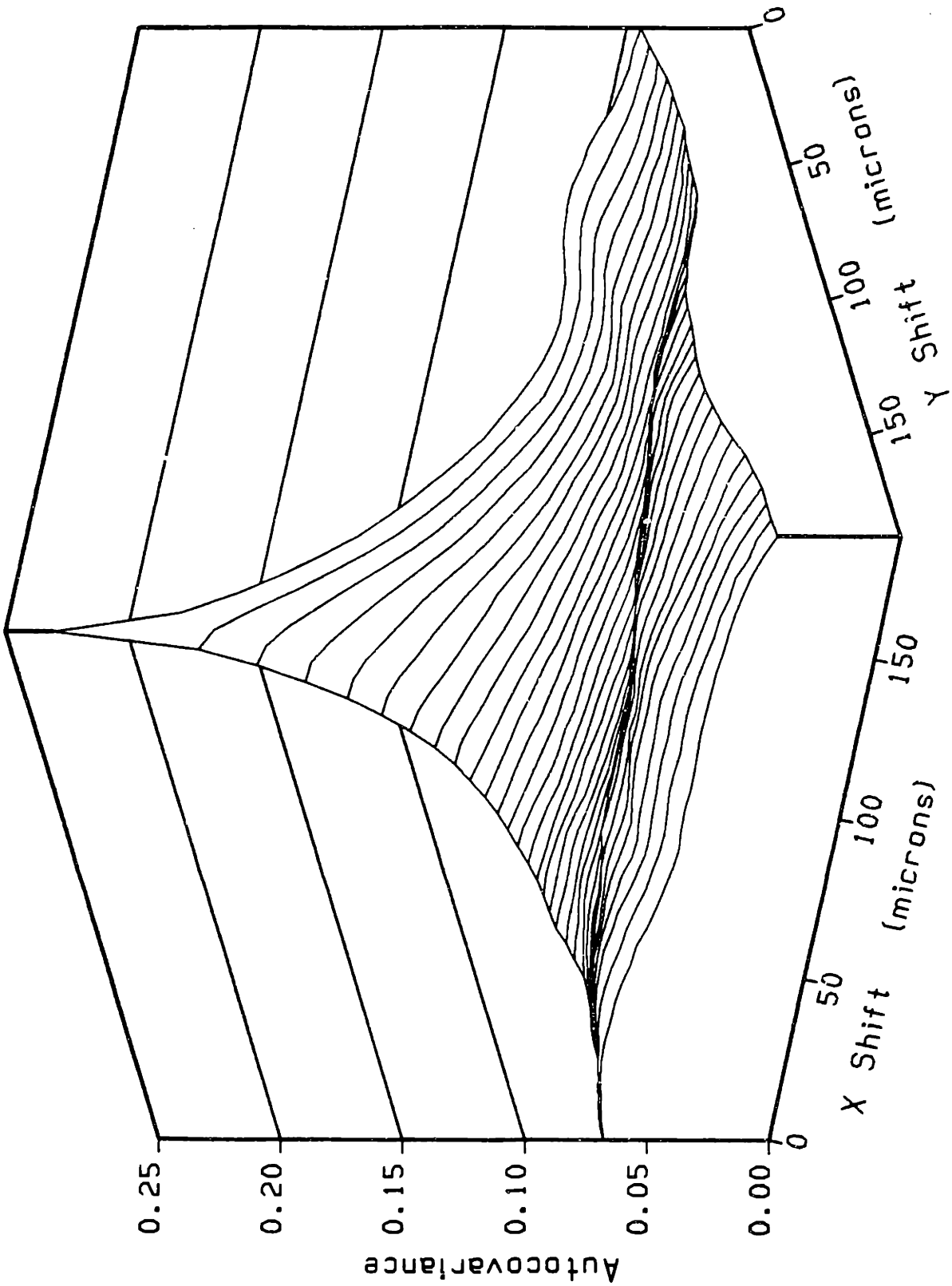
Autocovariance
0.25
0.20
0.15
0.10
0.05
0.00
X Shift (microns)
0
50
100
150
Y Shift (microns)
0
50
100
150

Figure 6.3b

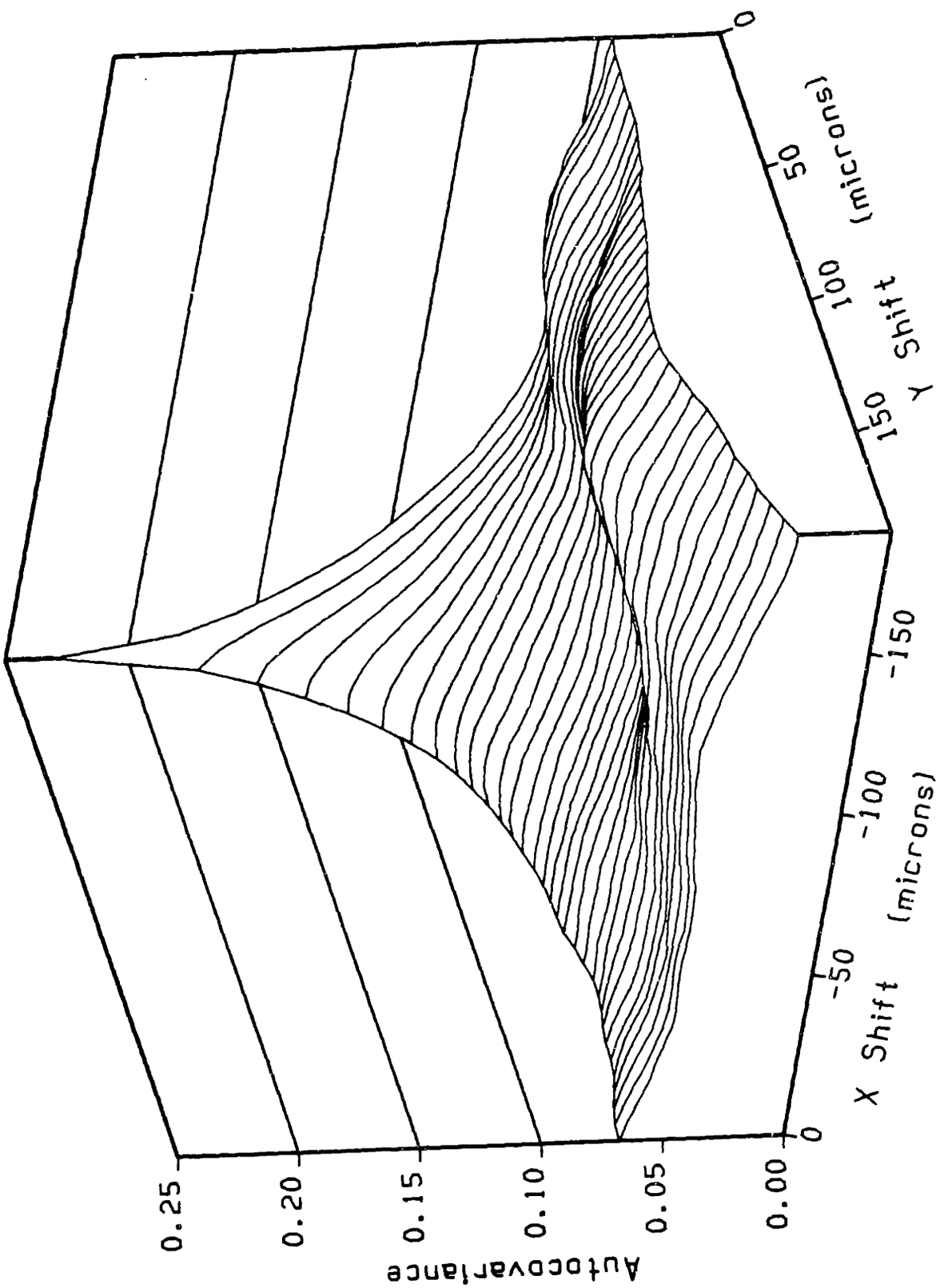
Autocovariance
0.25
0.20
0.15
0.10
0.05
0.00
X Shift (microns)
0
-50
-100
-150
Y Shift (microns)
0
50
100
150

Figure 6.4

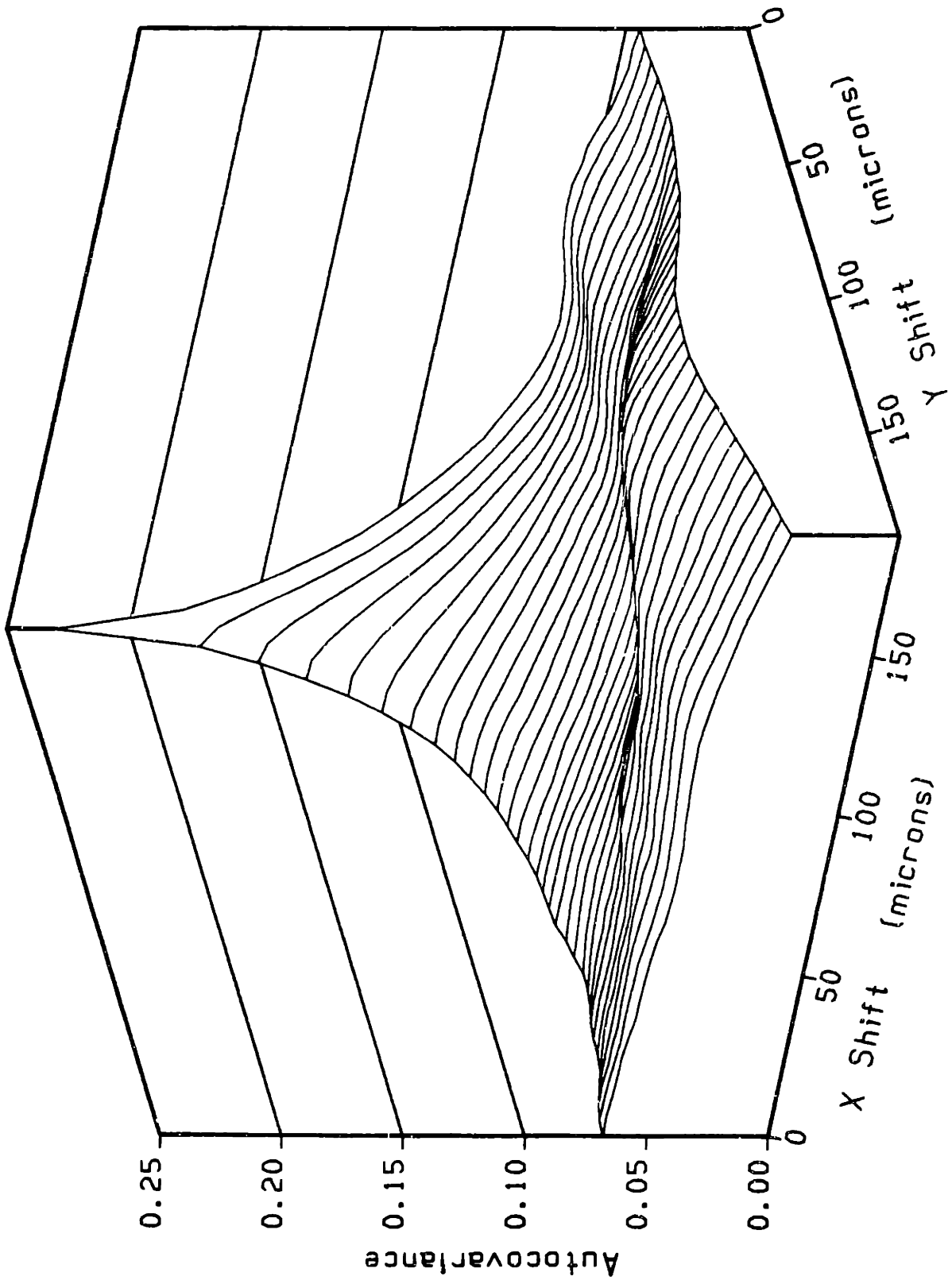
Autocovariance
0.25
0.20
0.15
0.10
0.05
0.00
X Shift (microns)
0
50
100
150
Y Shift (microns)
0
50
100
150

Figure 6.5 Isotropic Covariance

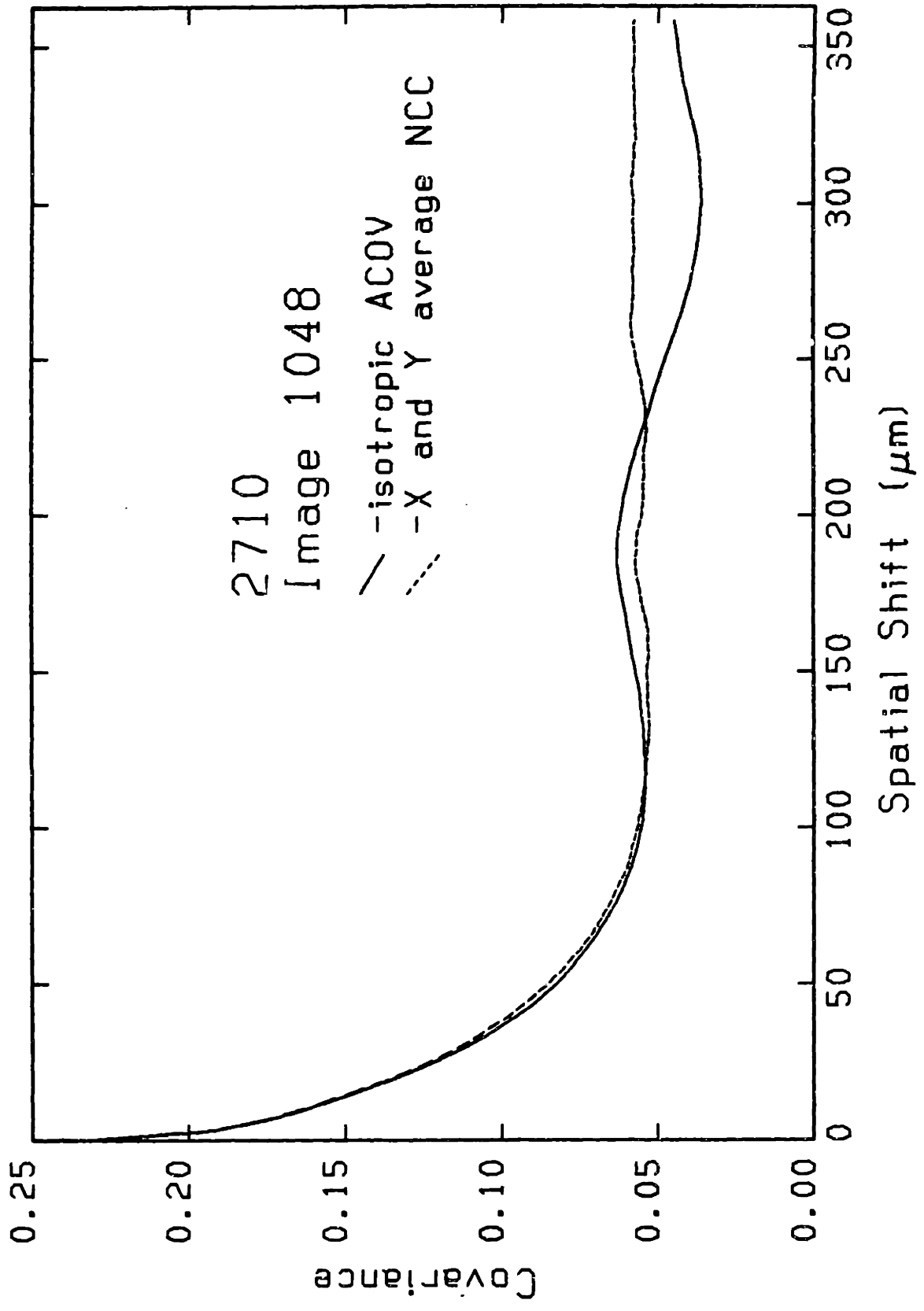

Figure 6.6

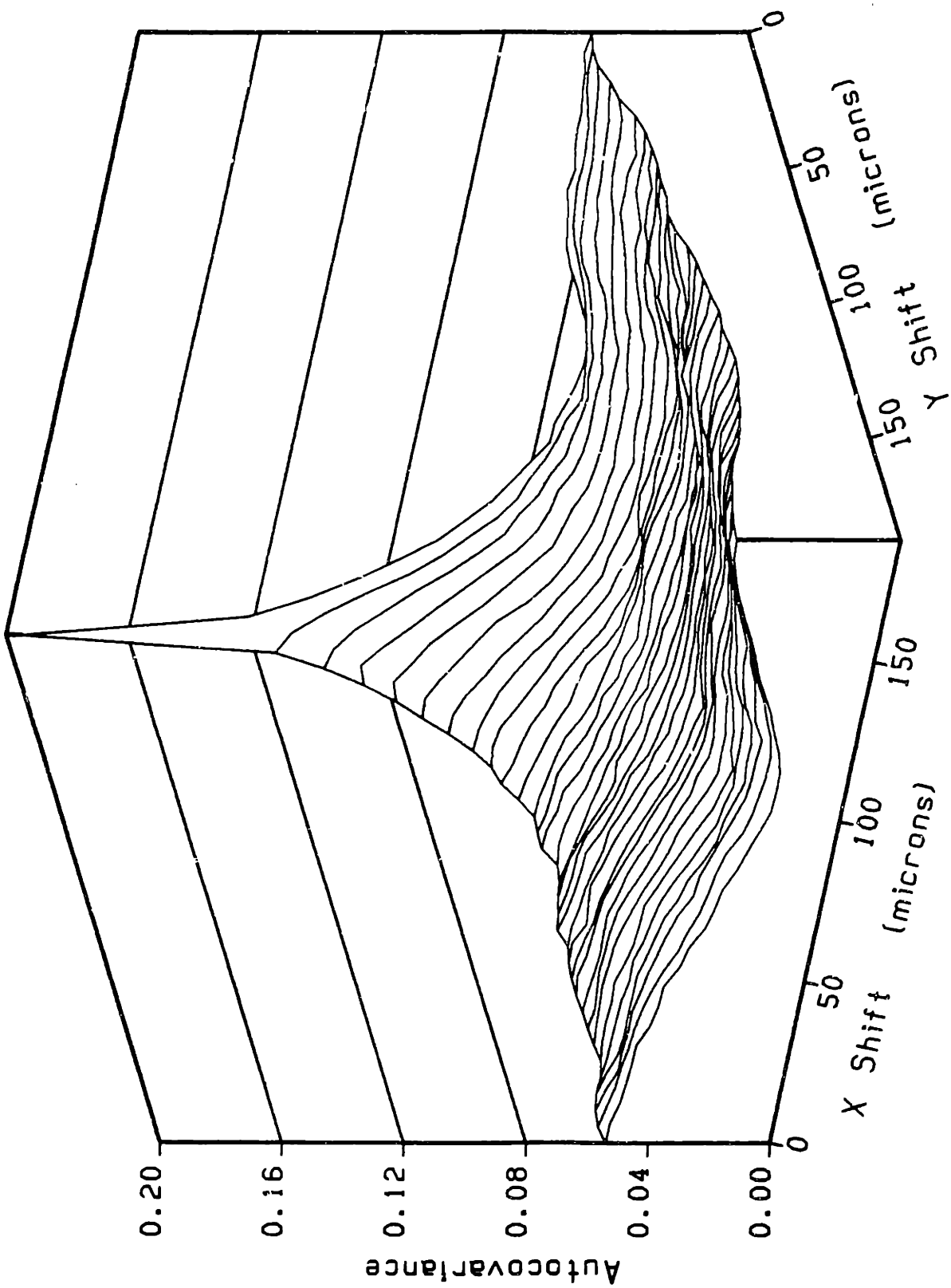
Autocovariance
0.20
0.16
0.12
0.08
0.04
0.00
X Shift (microns)
0
50
100
150
Y Shift (microns)
0
50
100
150

Figure 6.7a Covariance (2124)

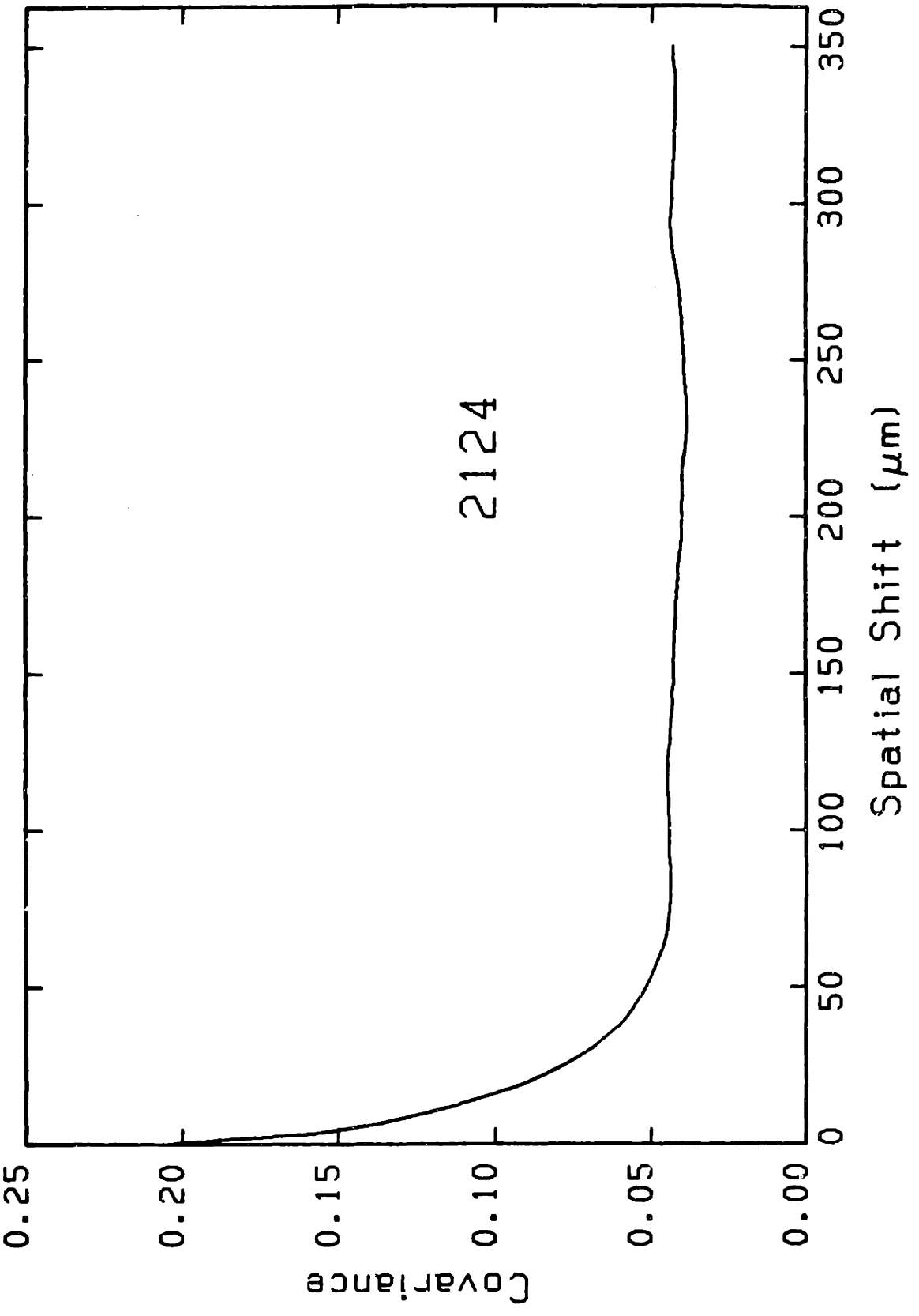

Figure 6.7b Covariance (2509)

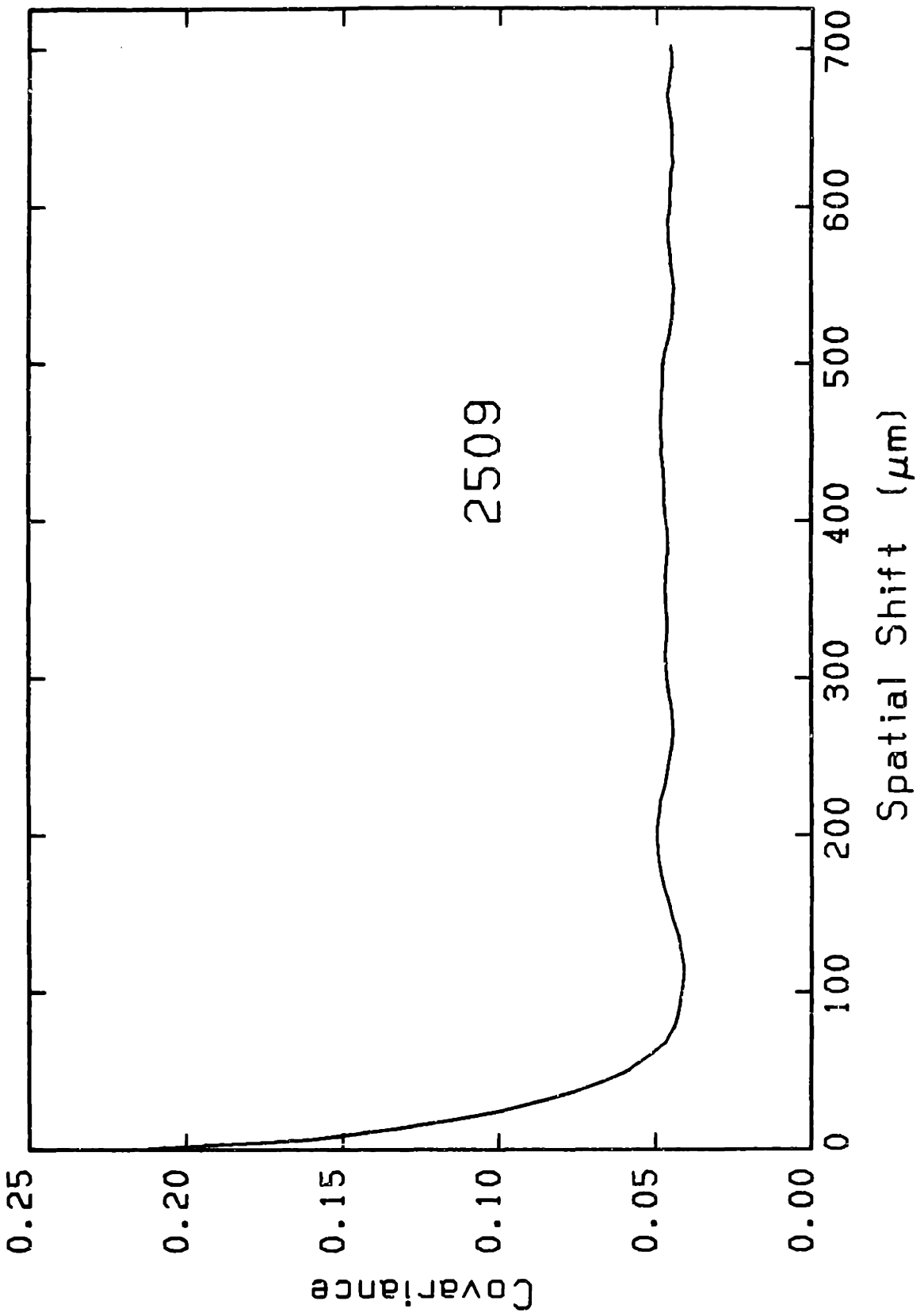

Figure 6.7c Covariance (2513)

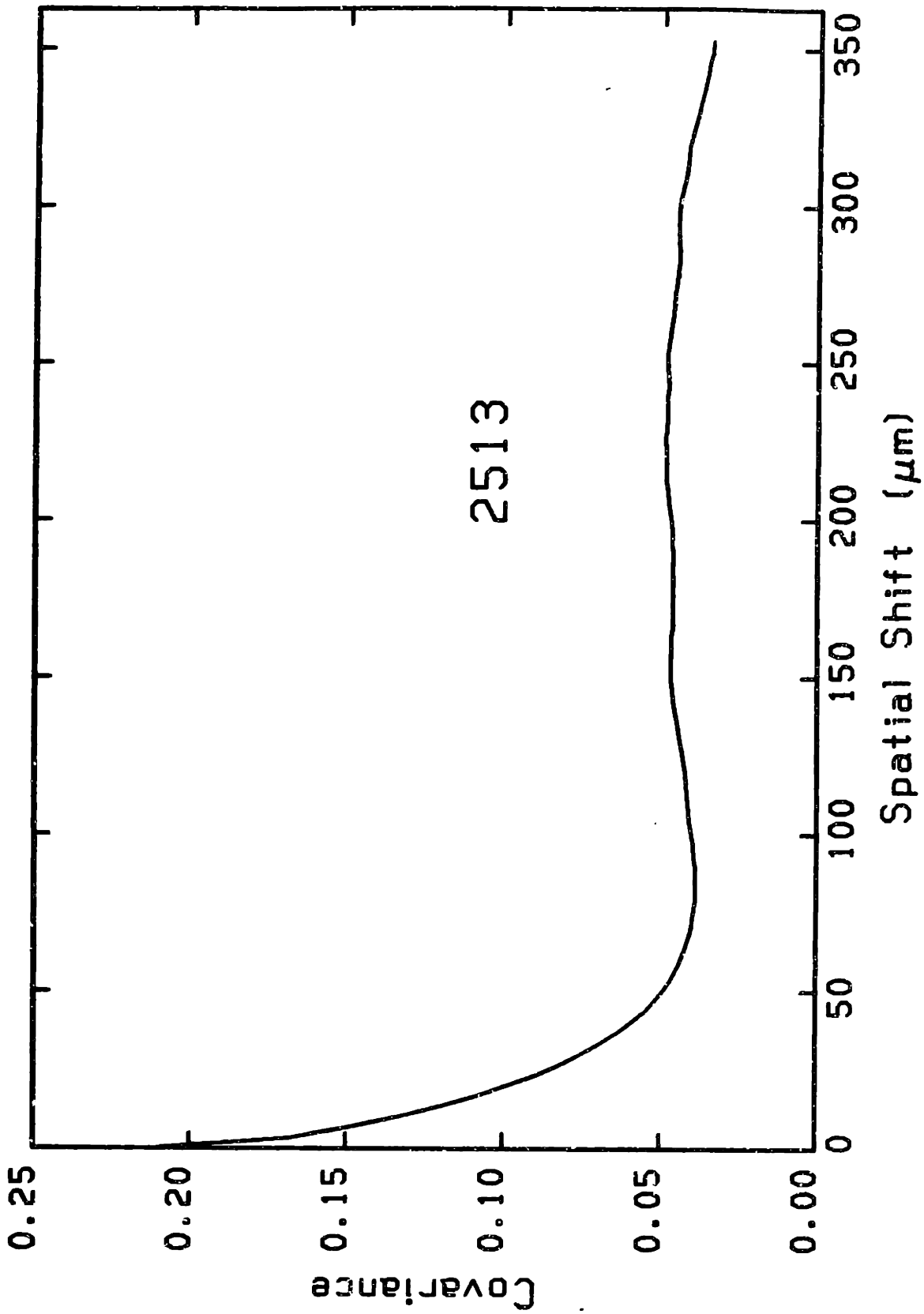

Figure 6.7d Covariance (2519)

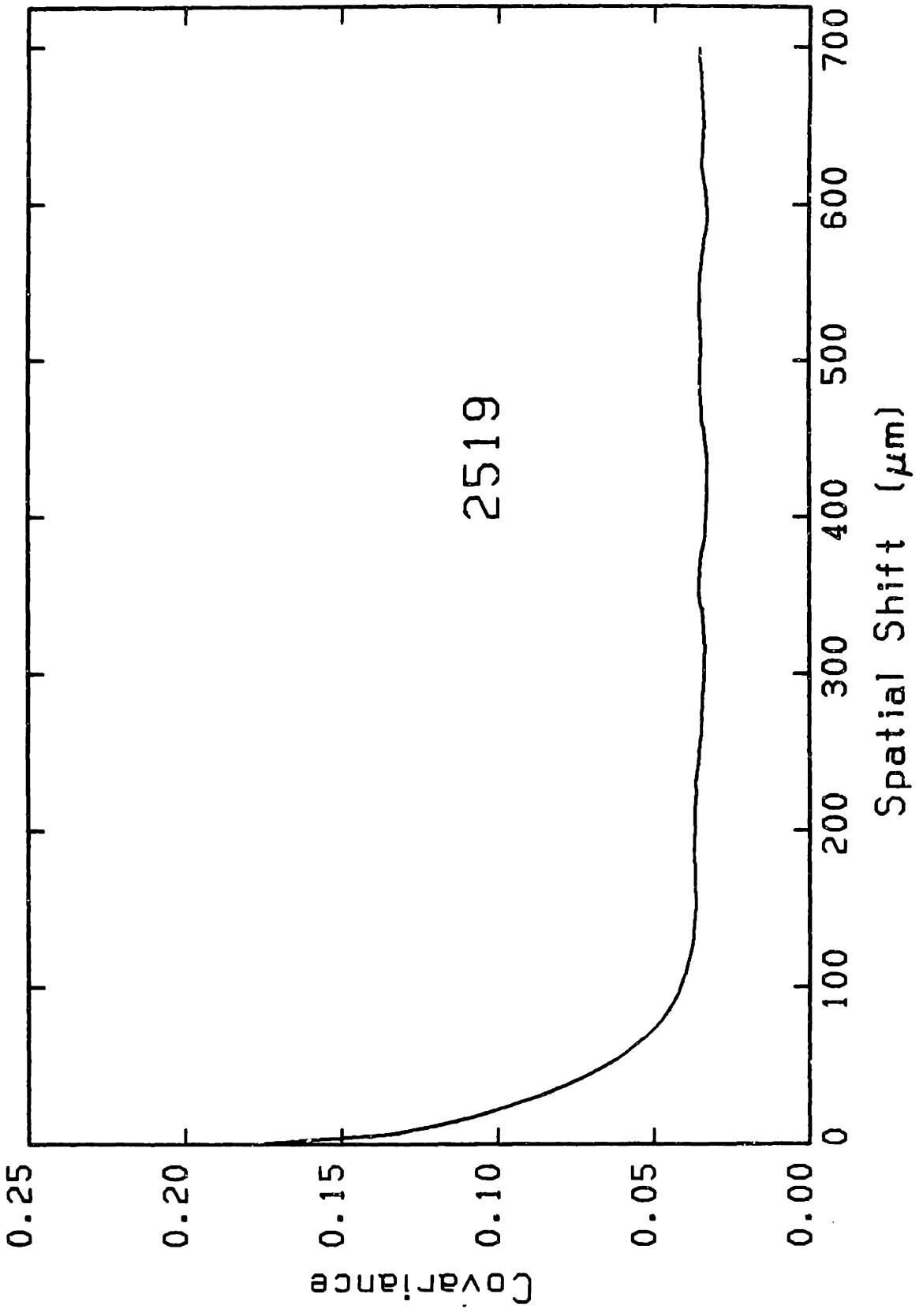

Figure 6.7e Covariance (2521)

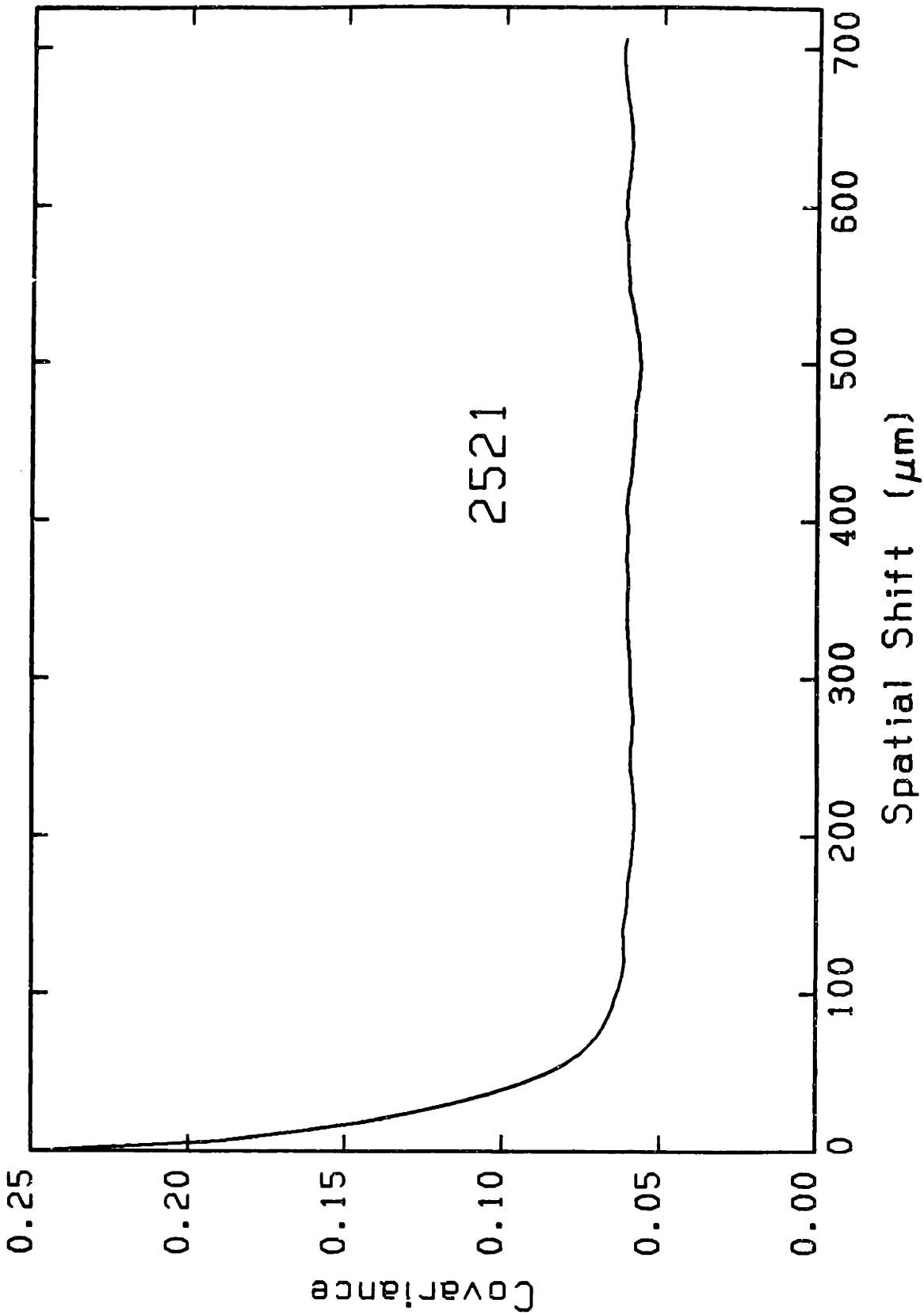

Figure 6.7f Covariance (2523)

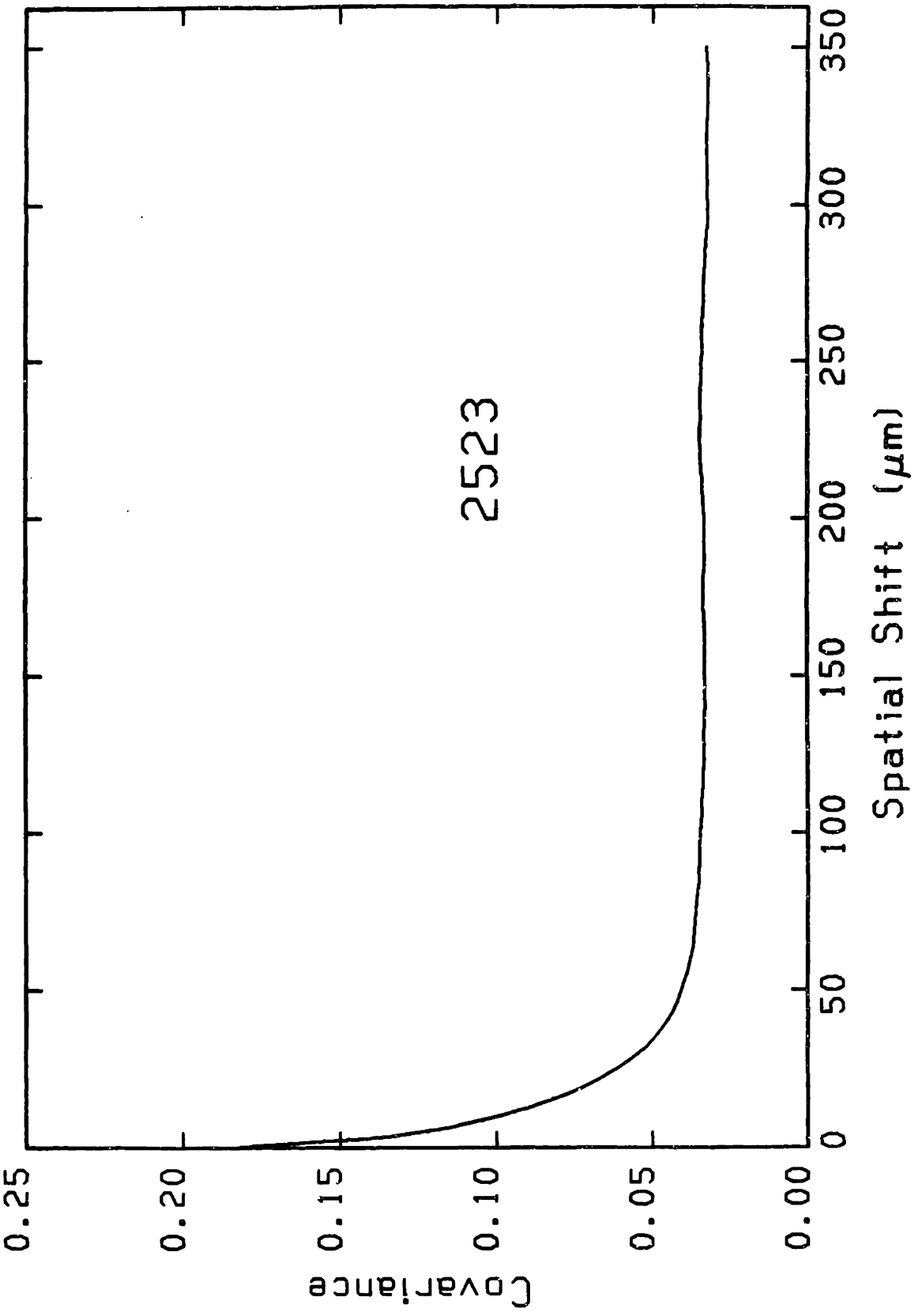

Figure 6.7g Covariance (2686)

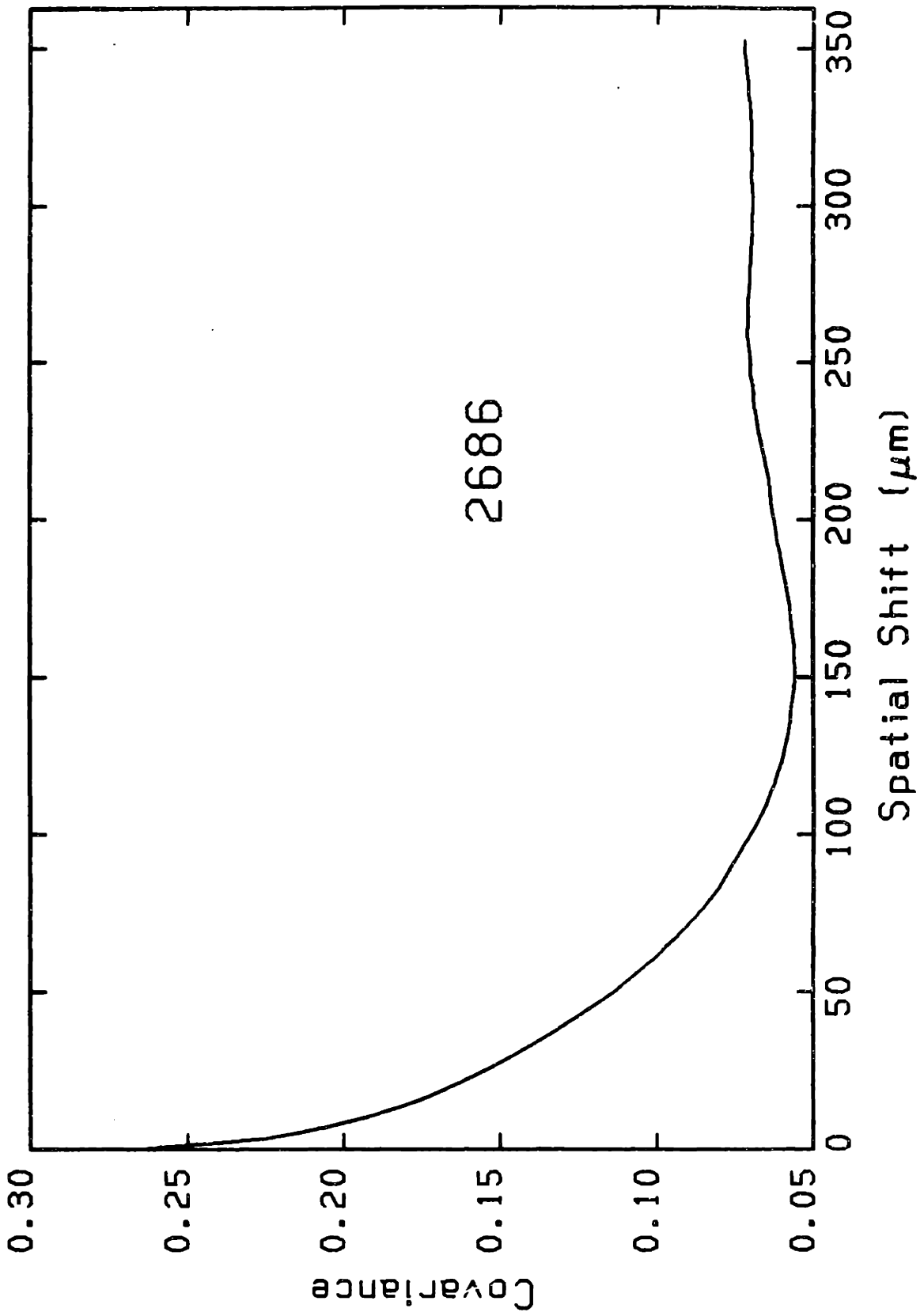

Figure 6.7h Covariance (2687)

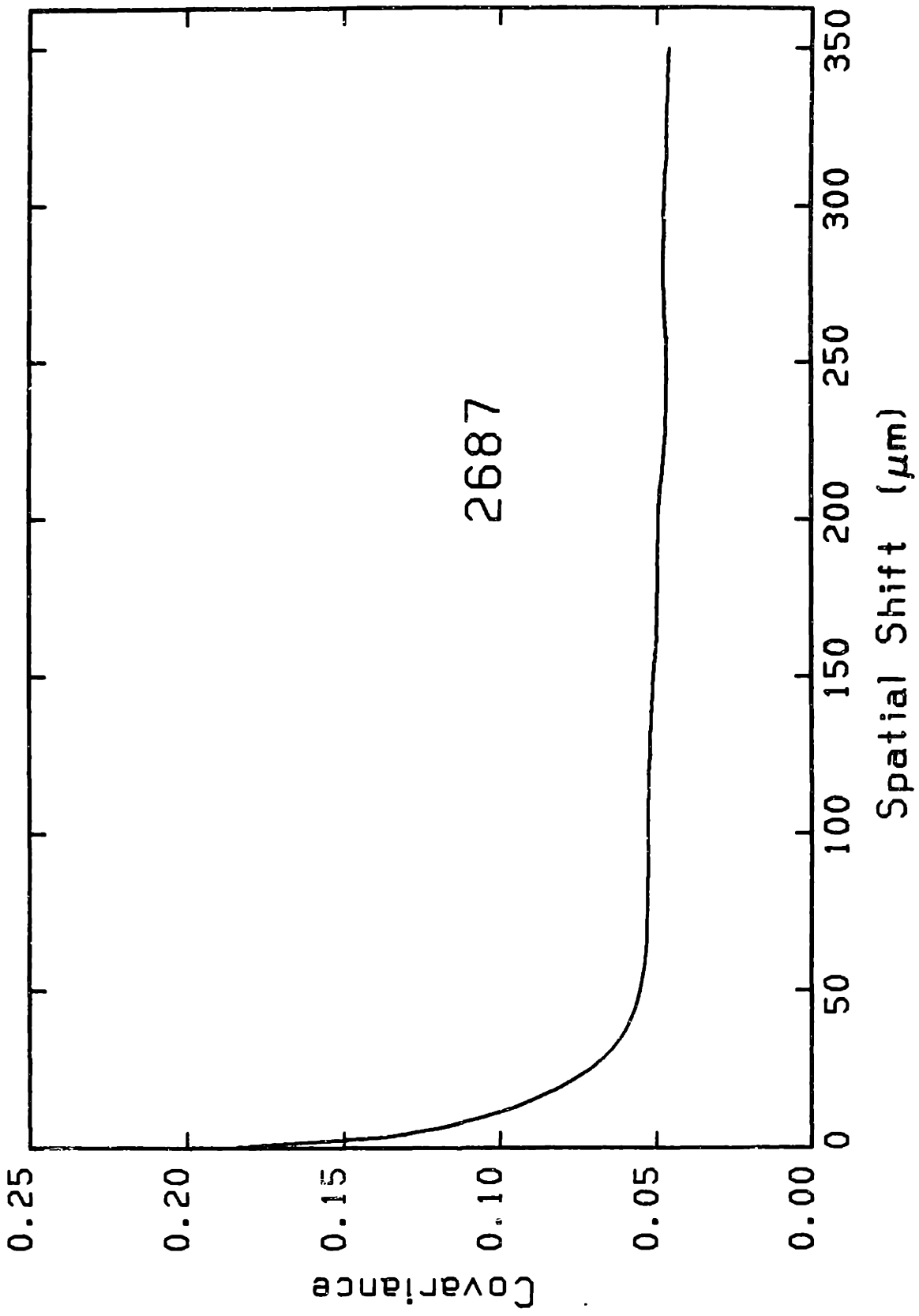

Figure 6.71 Covariance (2700)

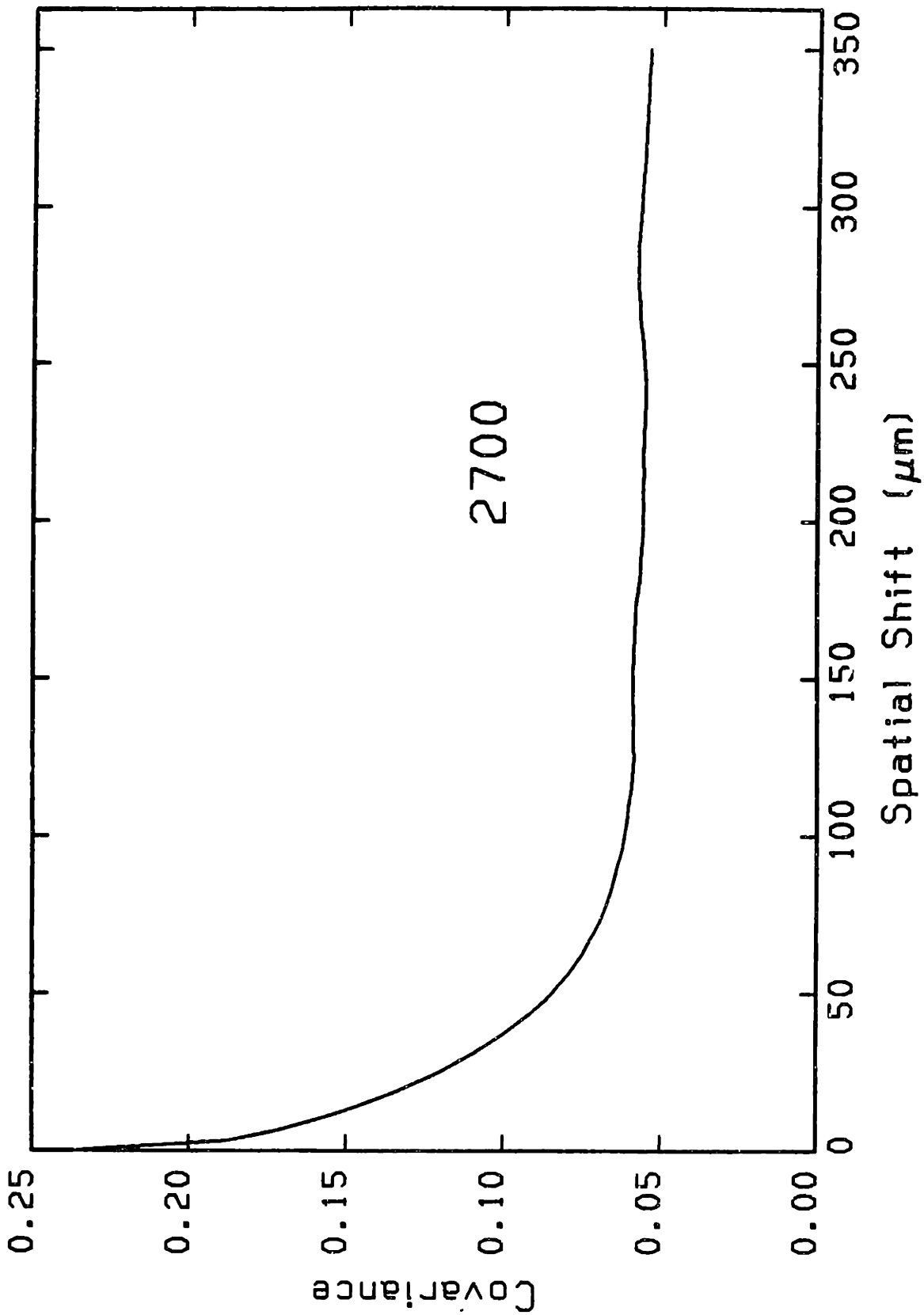

Figure 6.7j Covariance (2704)

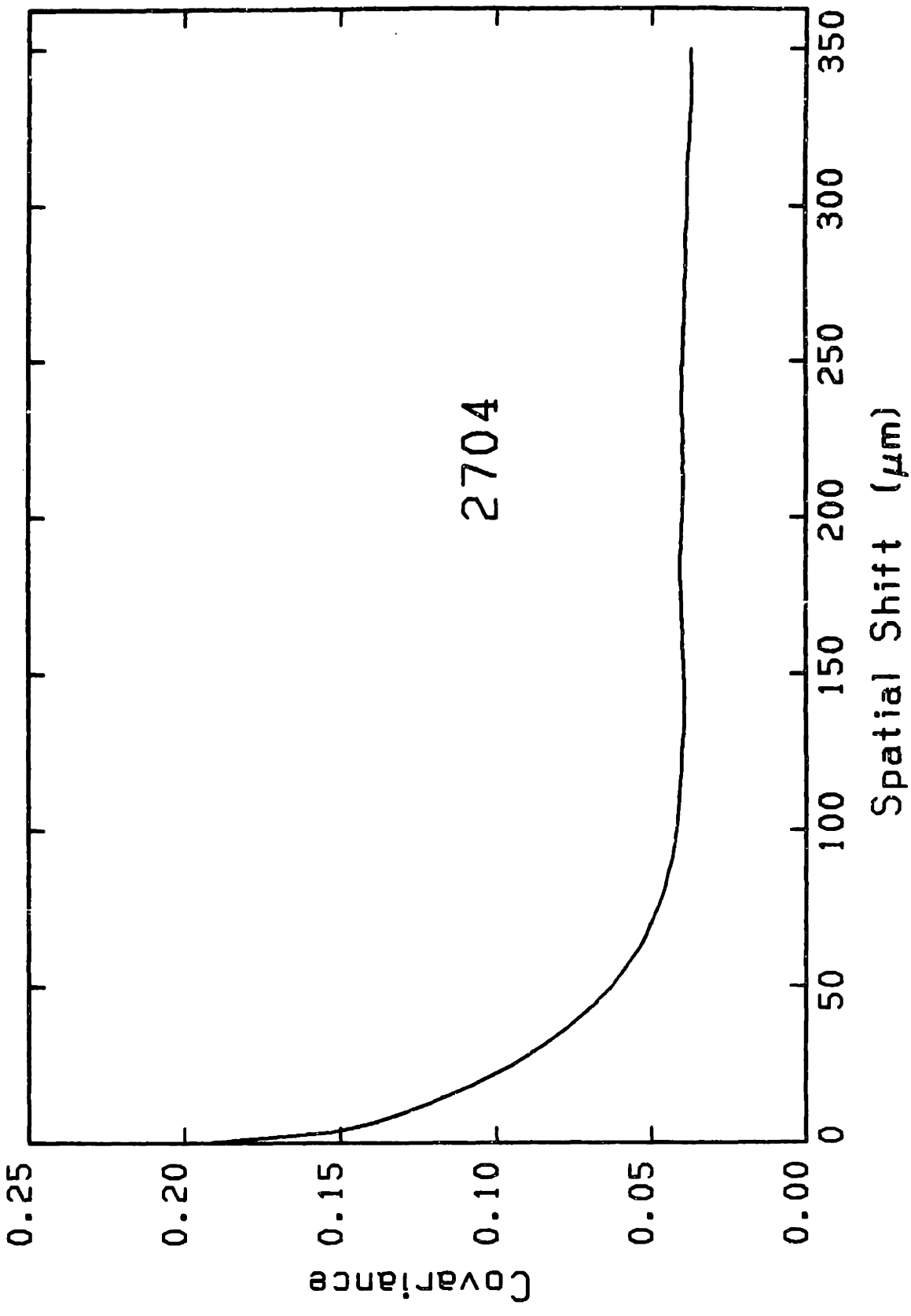

Figure 6.7k Covariance (2710)

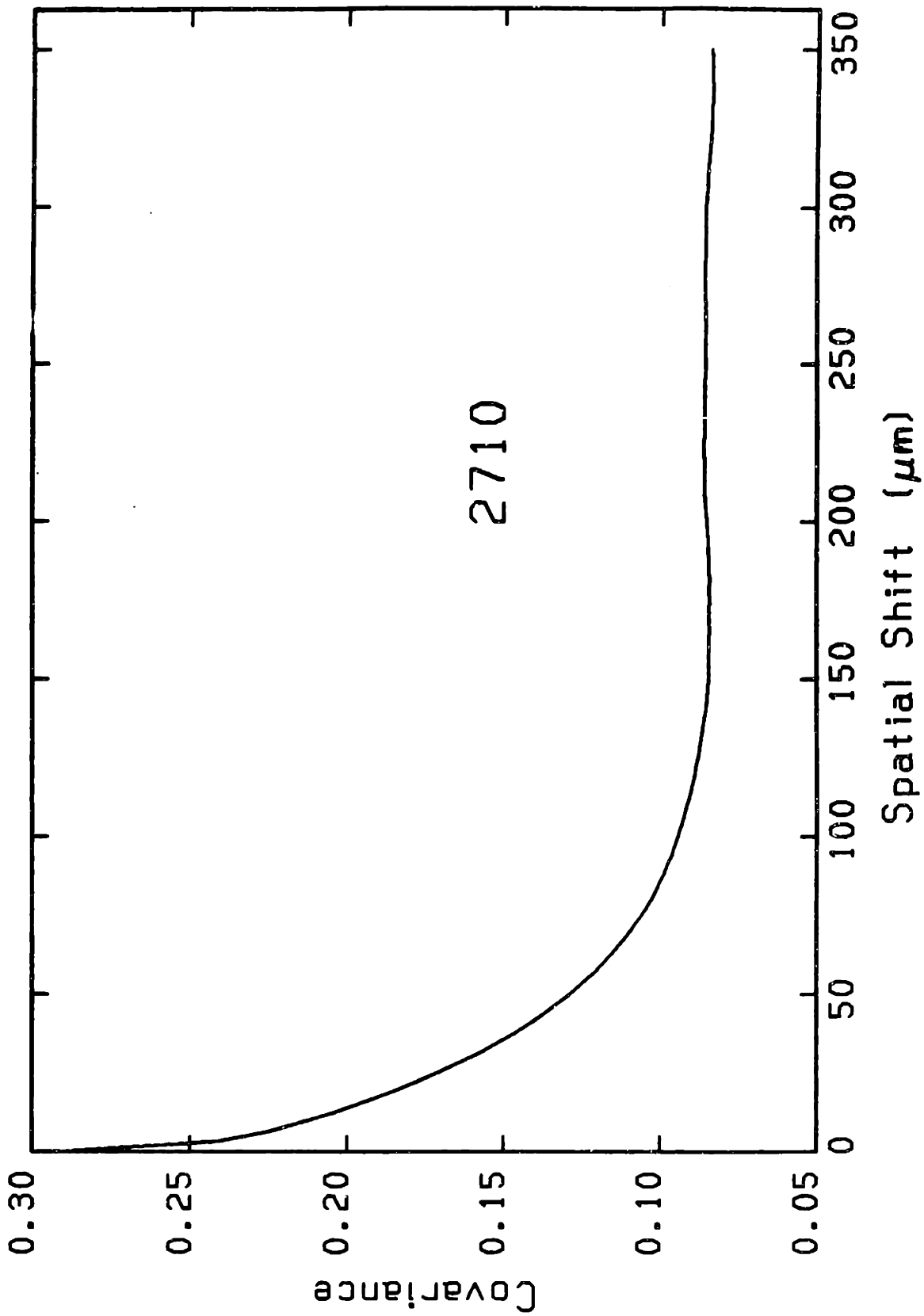

Figure 6.71 Covariance (2841)

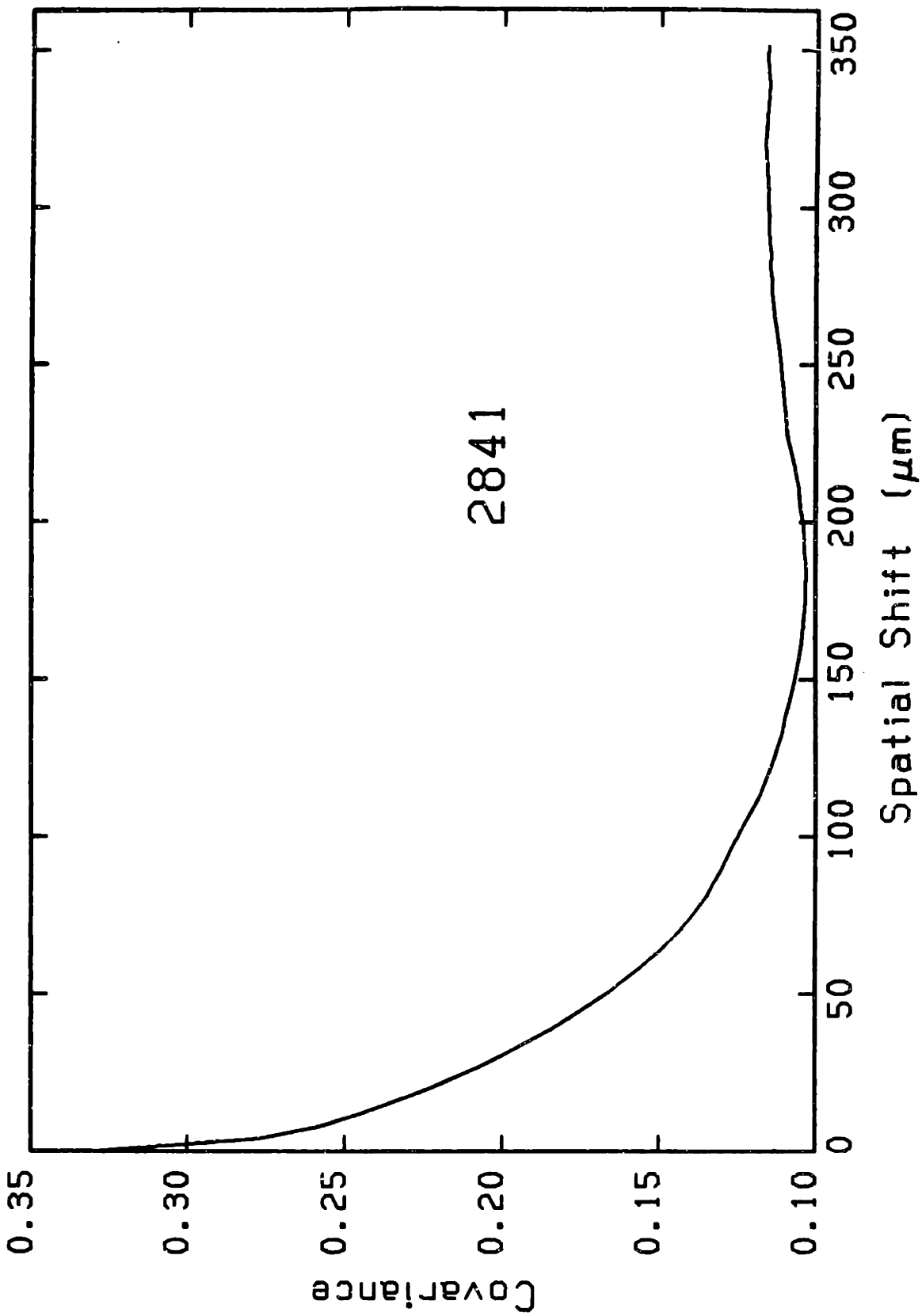

Figure 6.7m Covariance (2842)

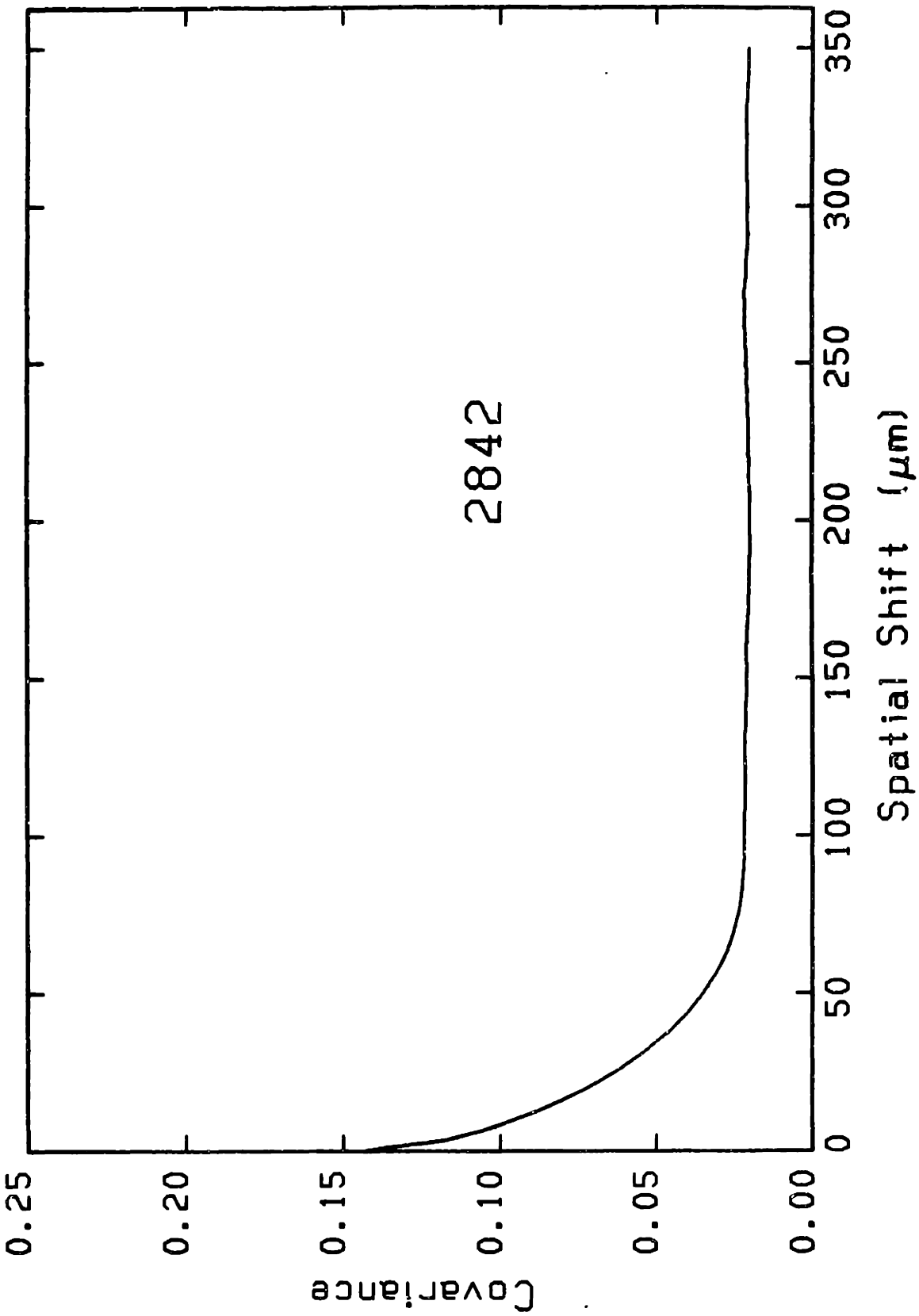

Figure 6.7n Covariance (2843)

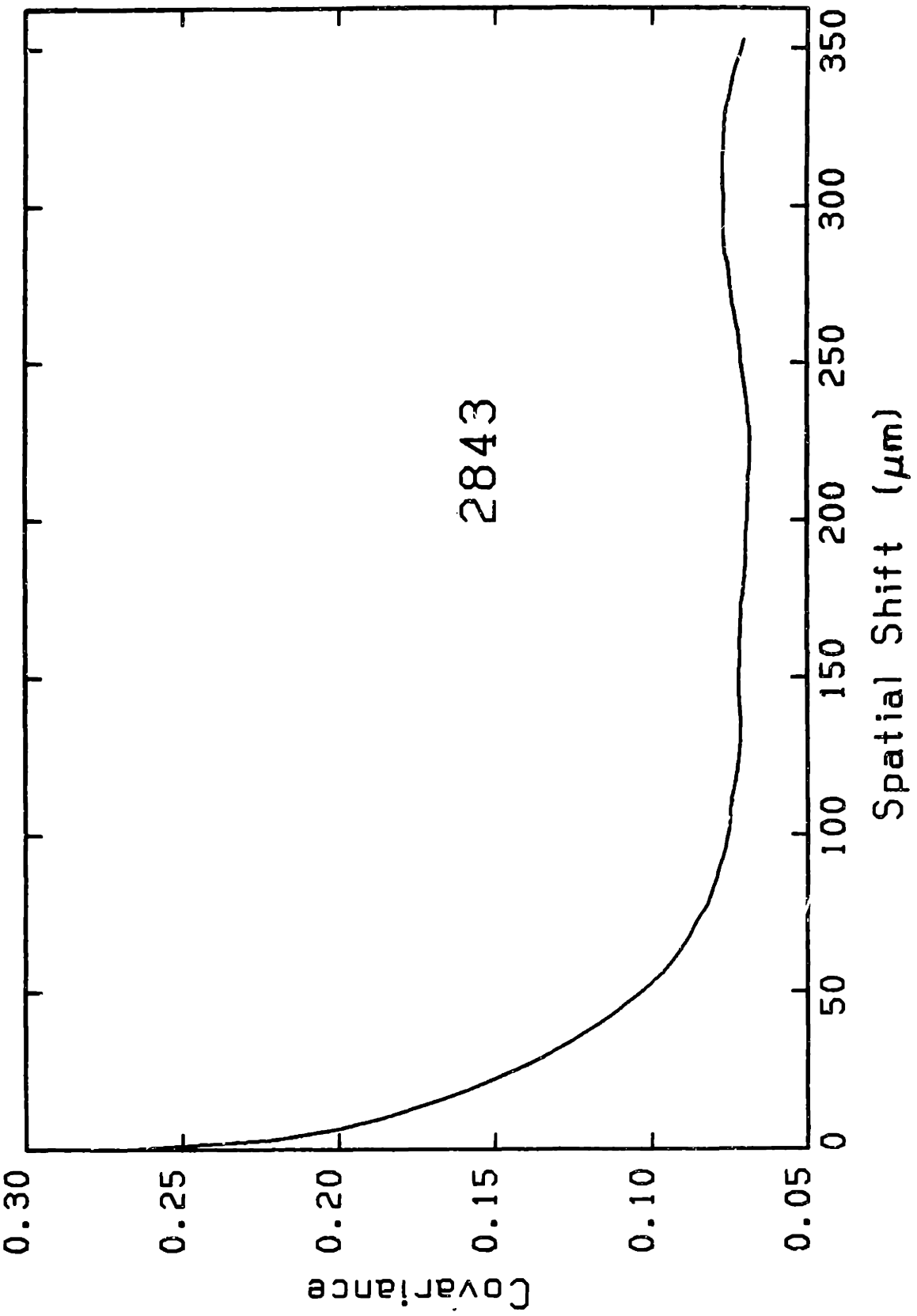

Chapter 7

Application of Pore Structure Parameters

7.1 Introduction

Pore structure parameters are used to describe the geometric nature of the pore structure and to understand the physical response of the structure. In this chapter, these two uses are explored. The pore structure parameters, obtained by different methods of direct analysis, are compared. Also, the relations between physical properties and pore structure parameters obtained by direct methods are investigated using existing models for physical properties.

The use of pore structure parameters to predict the physical response of sandstones is an ultimate goal of pore structure analysis by direct methods. Archie (1950) and many subsequent investigators have recognized the importance of pore structure and the value of the ability to estimate reliably physical properties from small chips of a rock (e.g., well cuttings). The models for physical properties are divided into 3 categories for convenience of discussion; namely:

Empirical models — are based on observations of data only; no physics is

incorporated, relations are found from mathematical curve fitting.

Phenomenological models — involve a gross simplification of structure; physics is introduced to describe the behavior of this structure, parameters of the simplified structure are found from inverting observed data, e.g., the equivalent conduit Kozeny–Carman model of permeability.

Mechanistic models — use a more realistic representation of the structure of the material, the behavior of elements which comprise the structure includes the physics of element interaction (e.g., self-consistent media).

Mechanistic and phenomenological models are preferable to empirical models because the dependence of the response on pore structure parameters (the physics) is better understood for the former. Thus, results are more readily extended to other cases. However, mechanistic models are not well-developed for most physical properties, so the empirical and phenomenological approaches are more common.

This chapter continues with a brief review of the correlations between stereological parameters and physical properties from metallurgy. Next, pore structure parameters of sandstones obtained by different direct analysis methods are compared. Stochastic models of pore structure, which constitute a major application for direct analysis parameters, are reviewed. Lastly, the relations between physical properties and pore structure of sandstones are investigated. Specific surface, measured by image analysis, is used in the Kozeny–Carman model to predict permeability of the sandstones in this study.

7.1.1 Microstructure and Physical Properties in Metallurgy

The field of quantitative metallography, the application of quantitative stereology to metallographic samples, is more developed than quantitative analysis of pore structure in sandstones. Thus, some insight into microstructure-physical property correlations may be gained by examining the correlations which metallurgists have found. Examples of correlations from metallography may indicate ways in which such correlations can be applied to sandstones. Rhines (1980) summarized several well-established correlations for metals and this review is based largely on his summary. More significant than the specific relations themselves are the general concepts which underly these relations. The general concepts are:

1. Microstructural measures which are additive correlate directly with physical properties which are additive. The simplest example of this correlation is that the density of a composite is a volume fraction weighted sum of the densities of its constituents.

2. Physical processes which occur inhomogeneously throughout a sample, as a function of local geometry, often depend on ratios of bulk (or additive) parameters. Presumably, the ratios indicate the variability of the parameters. For example, in steady-state grain growth, the average grain volume is proportional to the duration of heating (Rhines, 1980). The average grain volume is the reciprocal of the number of grains per unit volume (i.e., the ratio). The correlation thus reflects a constant form for the grain size distribution (i.e., the variability) as a function of heating time.

3. The microstructure of materials exists with an infinite variety of shapes. This natural irregularity should be provided for in the correlations, not suppressed. Essentially, this concept states that an explicit specification of shape should be avoided.

4. Because of the above reason, bulk parameters, which are additive geometric properties and which are unaffected by shape, size, and irregularity, are important in correlations. These bulk parameters are the stereological parameters described in Chapter 4, such as volume fraction (porosity), specific surface, and mean pore volume.

The metallurgical correlations are predominantly empirical. An underlying theme is the advantage obtained by avoiding shape dependent parameters.

Ondracek and Pejsa (1976) discuss the use of stereological parameters for predicting the physical properties of two-phase hard metals. They show that spherical inclusion models predict Young's modulus, electrical resistivity, and linear thermal expansion in the metals using stereological data. The only data required for the spherical models is volume fraction. They discuss more general ellipsoidal models which also require orientation and aspect ratio estimates.

Metallurgists are also concerned with evolution of microstructure, such as grain growth, evolution of specific structures, and change in the topology of the structure. These are not our current concerns when studying pore structure in sandstones. The approach used to study sedimentary rocks will be somewhat different because emphasis is placed on different physical properties. Nonetheless, the bulk stereological properties appear to form a good foundation for correlation studies.

We have omitted Rhines' (1980) discussion of topological parameters because they are used primarily to describe the *change* of a system due to, for example, sintering. The structure in sandstones is considered constant for the

present study (i.e., diagenesis is not considered). Topology certainly has a place in an exhaustive description of a continuous phase material, but it has not yet demonstrated the importance of other basic measures of the structure.

7.2 Comparisons Between Structural Parameters

In Chapters 4 through 6, quantitative measures of the pore structure in sandstones were obtained by several methods. Some parameters were measured by more than one method. In this section, parameters obtained by different methods are compared. Also, those parameters which might be simply related are compared.

7.2.1 Porosity

Porosity was measured by areal fraction analysis, by feature analysis, and from the zero lag spatial correlation. Each method measures the same area of the pore space expressed in the image and thus yields identical measures of porosity for the same images. In Chapter 4 it was shown that the image measured porosity agreed very well with the bulk porosity if sufficient random sampling was performed. As discussed in Chapter 4, it is important to use non-subjective selection of the images *and* dichotomization thresholds to obtain un-biased measurements.

7.2.2 Specific Surface Area

The specific surface area, S_V, of the pore-grain interface was measured using lineal analysis (i.e., linear intercepts), feature analysis, and spatial correlation.

Three different values are obtained by the three different methods. One additional method of estimating specific surface is given before comparing the different values.

7.2.2.1 Specific Surface Estimate from Grain Size Distribution

The surface area of the grains can be estimated from the grain size distribution. The grain size distribution was obtained by sieving a disaggregated piece of the sample. Disaggregation is accomplished by microshattering, which has been described by Caruso *et al.* (1985). Carbonate content was determined by dissolution in HCl prior to sieving. Standard techniques (Folk, 1974) were used for sieving.

A simple grain shape must be assumed to compute the surface area per unit weight of material and the shape chosen will affect the estimate. Here, oblate and prolate ellipsoids have been considered for the grain shape. For oblate ellipsoids, the sphere (aspect ratio of 1) will give a minimum surface area estimate. As the ellipsoid aspect ratio is decreased, the surface area per unit weight will increase. For prolate ellipsoids, the degenerate spherical shape gives a *maximum* surface area per unit weight. The surface area-to-volume ratio increases with increasing elongation of the prolate ellipsoid. However, larger volume grains will pass through smaller sieves as the elongation increases. Thus, it takes fewer grains to account for the weight fraction in a given class. The combined effect is to decrease the surface area per unit volume in the given size class. Therefore, the surface area per unit weight decreases with increasing elongation of the prolate ellipsoid.

Computation of Surface Area—Surface area is computed by partitioning the weight fraction of each size class over the class interval and integrating the surface area contributions from each class. For a general shape, surface area

per unit weight, S_W, can be expressed as a function of the grain shape as

$$S_W(q) = \int_{z_{min}}^{z_{max}} dS_W(q,z) = \int_{z_{min}}^{z_{max}} s(q,z) \frac{dW(z)}{\rho_g v(q,z)} , \qquad (7.1)$$

where $dW(z)$ is the weight fraction of size z. The surface area of each simple shape, $s(q,z)$, and the volume of each shape, $V(q,z)$, are functions of shape, q, and size, z. For oblate ellipsoids, z is the length of the major axis D_1, and q is the aspect ratio. This size of oblate ellipsoid can pass through the sieve which is equal to D_1. For prolate ellipsoids, z is D_1/q, where q is again the aspect ratio. The prolate ellipsoid with major axis D_1 can pass through the sieve of size z.

The phi intervals are divided as follows. Consider, for example, the 1.5 phi class. These grains pass through a 1.0 phi sieve (500 μm) and do not pass through the 1.5 phi sieve (350 μm). The 1.5 phi class is divided into 10 μm intervals for the range 350 to 500 μm. The weight fraction is assumed to be divided uniformly for the 15 intervals. The integrand in Eqn. (7.1) is computed for each of the 15 discrete intervals. This table of values is integrated using Simpson's rule to give the surface area contribution of the 1.5 phi class. The surface areas of the other classes are computed similarly although different interval sizes are used. Grains in the 1.0 phi class are all assumed to have diameters of 500 μm. The minimum size of the <4.5 phi (<44 μm) class was arbitrarily chosen as 2 μm. Specific surface was also computed with the <4.5 phi class omitted.

Surface area per unit gram of grains, S_W, is related simply to specific surface area, S_V, and to surface area per unit pore volume, S_{V_p},

$$S_{V_p} = \frac{S_V}{\phi} = \frac{S_W(1-\phi)}{\phi \rho_g} , \qquad (7.2)$$

where ρ_g is the measured grain density.

7.2.2.2 Results of Specific Surface from Grain Size Distributions

Without additional information on grain shape and because the S_{Vp} estimate for the sphere lies between the values obtained for oblate and prolate shapes, we have used the spherical shape for computing S_{Vp}.

Table 7.1 lists the S_{Vp} estimates from the grain size distributions. As expected, the estimates which omit the < 4.5 phi class are smaller than those which include the class. For those rocks with small weight percentages in the class, the difference is slight (e.g., samples 2509 and 2521). Sample 2687 shows a 50% decrease in S_{Vp} upon omission of the < 4.5 phi class because 18% of the grains, by weight, are in the class.

7.2.2.3 Comparison of Specific Surface Estimates

Figure 7.1 is a plot of S_{Vp} measured by feature analysis and by spatial correlation (*NCC*) methods versus S_{Vp} from lineal analysis. Feature analysis values are from SMS images. Agreement between lineal and *NCC* values is excellent. On average, the *NCC* values are about 2% smaller than the lineal values, which is due to the chord sampling criteria. The point of greatest disagreement is sample 2687. For this sample, S_{Vp} would be better estimated, from lineal data, by using the S_V value and the areal ϕ, for reasons discussed in Chapter 4. Such an estimate agrees exactly with the *NCC* estimate, which included image #1106. This image was not included in the lineal analysis.

Feature analysis estimates of S_{Vp} (Eqn. (2.5)) from SMS images are consistently higher than lineal and *NCC* estimates. If the 1-pixel features are omitted, the bias is less, but the estimates are still higher. If the features smaller than 5 pixels are omitted, the estimates from feature analysis agree well with the lineal and *NCC* estimates; some values are larger, some are smaller. The larger values from feature analysis are due in part to the increase

in S_{Vp} caused by segmentation. However, S_{Vp} values from feature analysis of unsegmented images are also about 10% larger than lineal estimates. Recall that the S_{Vp} estimates from SMS images, with the 1-pixel features omitted, agree with the feature analysis values of unsegmented images. We suggest that feature analysis overestimates the S_{Vp} values. Further, the overestimate is due to an overestimate of feature perimeter. Even with the inward angle correction (see Chapter 5), the perimeters are too long.

The overestimate can be reduced by using 8-fold connectivity instead of the 4-fold connectivity criterion which was used for all feature analysis. Using an 8-fold connectivity criterion gives S_{Vp} values which are as much as 10% smaller than 4-fold values. Thus, using 8-fold connectivity, the feature analysis values from unsegmented images would be very close to the lineal values. However, note that the lineal analysis effectively "sees" 4-fold connected feature boundaries. The 8-fold connectivity effect should be interpreted as a compensation for the excessive perimeter length, but it does not necessarily indicate a more accurate measurement.

The overestimate is not due to the fact that boundary touching features were allowed. The S_{Vp} computed using the intercept data from feature analysis of unsegmented images is typically a few percent *smaller* than the lineal values.

The agreement between S_{Vp} from the isotropic averaged $ACOV$ and from the X and Y averaged NCC (see Chapter 6) suggests that measurements in two orthogonal directions are adequate to obtain an orientation averaged S_{Vp} on the plane. The measurement of S_{Vp} on orthogonal planes remains to be investigated, but is beyond the scope of this study.

The estimates of S_{Vp} from the grain size distribution do not correlate with S_{Vp} measured by direct analysis. The values from the grain size distribution are all much larger than the image derived values. This is consistent with our expectations. Some percentage of the grain surface area will be consumed as

grain-to-grain contacts. The difference between image values and grain size values may indicate the amount of surface area in grain-to-grain contacts. This grain contact area may be related to elastic properties of the intact sandstones.

7.2.3 Size Measures

Numerous measures of "size" have been used in this study. These include measures of size in the three-dimensional sense of the pore size distribution from linear intercepts and the mean pore volume. Measures of feature size were found by feature analysis and by spatial correlation. In this section, the various measures of size are compared. Emphasis is placed on mean measures of size and on maximum sizes.

One of the most universal measures of size is the mean pore volume computed in Chapter 4. The mean pore volume satisfies stereological relations with a minimum of restrictive assumptions. To allow comparison of the mean pore volume with the more common linear measures of size, it can be converted to the diameter of an equivalent-volume sphere, $D_{\overline{V}_p}$ (Table 4.6). It is unfortunate, but necessary, to impose a shape restriction for this purpose.

Figure 7.2 is a plot of the range of the *NCC* versus $D_{\overline{V}_p}$. There is very good agreement between the values. Sample 2523 is an exception, due to an overestimate by the range estimator. A visual range estimate of 70 μm is in close agreement with $D_{\overline{V}_p}$. The coefficients for a linear least squares fit to the data, using the visual range estimate for sample 2523, are given in the figure caption.

Figure 7.3 is a plot of the maximum diameter from feature granulometry, λ_{max}, versus $D_{\overline{V}_p}$. There is good agreement between the values. The greater disagreements occur for larger $D_{\overline{V}_p}$ and are from the rocks with only 2 images each. Considering the good agreement between the range and $D_{\overline{V}_p}$, the maximum granulometry diameter is believed to be an underestimate for those

rocks. Additional images would yield more representative values and perhaps give better agreement. Alternatively, both the range and D_{V_p} are from linear measurements, whereas the feature granulometry is a two-dimensional (isotropic) sizing. With anisometric features, the maximum isotropic size will be smaller than the maximum lineal measure. However, the dynamic feature parameters do not indicate that the rocks with low λ_{max} (samples 2686, 2841, and 2843) have larger than average feature anisometry.

The mean pore intercept length was shown in Chapter 4 to have little relation to D_{V_p}. Likewise, the mean pore intercept lengths are all much shorter than the other measures of average size.

Compare the feature granulometry curve to the area-weighted equivalent-area circle diameter from feature analysis (i.e., Figures 5.16 and 5.21k). The feature granulometry values are smaller because they represent an isometric sizing. Perhaps the difference between the two values contains information on the feature anisometry.

The maximum diameters used in the size-shape inversion of Chapter 4 are much larger than the maximum granulometry diameters. Again, this is due to the isotropic sizing property of the feature granulometry. Intercept lengths equal to or greater than the maximum size-shape diameters were measured for most rocks. This set of data confirms that such lengths actually exist for the pore space. Indeed, the approximate maximum Feret diameters from feature analysis (see Chapter 5) can be even longer than the maximum intercept length for anisometric features which are not aligned with one of the image axes.

The feature granulometry, as an isotropic two-dimensional sizing, will probably be applicable where the physical property under investigation depends on the distance from a point in the pore space to the *nearest* pore-grain interface (e.g., NMR). For physical properties which are not strongly dependent on the nearest pore-grain interface, the sizes afforded by feature analysis, lineal

analysis, or spatial covariance may be more appropriate.

Mercury intrusion porosimetry curves have been measured on some of our samples. In general, there is no agreement between any of the size measures from direct analysis and the pore sizes suggested by mercury porosimetry. The mercury entry diameters (diameter corresponding to first intrusion) are less than 10 μm for all samples. Mercury porosimetry expresses a distribution of pore accessibility diameters which have little relation to the true pore sizes in the rock (for discussion, see Dullien, 1979, Ch. 3).

7.2.4 Shape Measures

The measures of pore shape, studied here, appear to be less discriminative than measures of pore size. However, the measures of shape are internally consistent.

The size-shape inversion of Chapter 4 showed that all samples were best approximated by oblate ellipsoids with aspect ratios near 0.3. Other valid three-dimensional estimates of shape are given by the Fischmeister shape factor, F, and by the mean object aspect ratio estimator, q^*, of Cruz Orive (1976).

The Fischmeister shape factor, measured on SMS images, is less than one and, therefore, cannot be produced by ellipsoidal objects. This low value of F is due to the single-pixel features which contribute large percentages of perimeter relative to area (i.e., surface area relative to porosity). With the single-pixel features omitted, F (for rocks with values greater than 1.0) is representative of ellipsoids with aspect ratios of about 0.45 (see q_F values in Table 5.5). Omission of the features smaller than 5 pixels yields aspect ratios around 0.30.

The aspect ratio in the size–shape inversion is adjusted to help match the measured S_{Vp}. However, given the wide range in S_{Vp} and the similarity of the

aspect ratios, we conclude that the S_{Vp} is largely determined by the pore size distribution. If we were to omit the single-pixel chords from the lineal estimate of S_{Vp}, the values would be smaller. Smaller values would favor a more equant aspect ratio in the inversion. Thus, the relation is consistent with the object aspect ratios predicted by F when the single-pixel features are omitted.

Ruzyla (1984) cross-plotted specific surface versus F for 11 carbonate samples (reproduced in Figure 7.4). Oblate ellipsoids of constant semi-major axis and variable aspect ratio plot as straight lines on such a figure, except for the behavior very near the aspect ratio of one. The slope of the line is determined by the semi-major axis length. Ruzyla (1984) suggested that the data from his samples do not agree with any simple geometric shapes (e.g., spheres, ellipsoids, rods). However, we observe that the oblate ellipsoids represent the data very well. The lines, representing the ellipsoids, which pass through or near his data points, come from ellipsoids with semi-major axes which agree very well with the mean maximum Feret diameters measured for his samples (and given in Figure 7.4). The position along the F axis represents the aspect ratio of the ellipsoids and correspondingly, the aspect ratio of the pores. This is additional evidence that the oblate ellipsoid approximation is a good representation of the pore space. The reason for the correlation between mean maximum Feret diameter and the semi-major axis has not been investigated.

The mean object aspect ratio estimates from feature semiaxes, q^* (see Chapter 4, Eqn. (4.36) and Chapter 5) agree with the size–shape inversion aspect ratios and with the aspect ratios estimated from F. The q^* values from SMS images (see Table 5.8) are all about 0.75 which is significantly larger than the size–shape inversion values. The near-equant aspect ratio is primarily due to the equant single-pixel features. When these features are omitted, q^* is reduced to about 0.44 for all rocks. Although they are still larger than the aspect ratios from the inversion, the consistency of the values supports the

shape similarity suggested by the inversion.

The aspect ratio from Fischmeister's shape factor agrees very well with q^*. Although F values less than one are not possible with true oblate ellipsoids, the measured values of about 0.95 for SMS images are closely represented by the sphere ($F = 1$). Thus, they are in close agreement with the q^* for the SMS images. The F values with single-pixel features omitted also agree with q^*. Omission of larger features causes q^* to increase, whereas aspect ratios from F continue to decrease. F is computed without any shape assumptions, whereas q^* is computed assuming the model shape of oblate ellipsoids. It is supportive of the ellipsoid model to find that F, when interpreted in the sense of oblate ellipsoids, agrees with q^*.

The two-dimensional shape descriptors in Chapter 5 do not show much variation from rock to rock. This is somewhat expected from the values of the three-dimensional shape estimates. Also, as discussed in Chapter 5, the similar values may be reflecting the overall similarity of the pore shapes in these rocks.

The object aspect ratios predicted from feature analysis data are larger (more equant) than those from the size–shape inversion. This may be due in part to the segmentation which is applied to the features prior to analysis. Segmentation is used to produce features which are describable with the available parameters. However, segmentation tends to produce features which are more nearly convex and more nearly isometric. Thus, the estimated aspect ratios are closer to one. Chord sampling also effects some degree of segmentation, but not to the same extent as the SMS operations.

7.3 Stochastic Models of Pore Structure

Stochastic modeling of pore structure is one approach for simulating the very complex structure found in natural sandstones. Stochastic models can express the complex structural relations with relatively few parameters. These parameters are found using the data measured by image analysis, so the modeling constitutes a major application for such data. Here, we examine stochastic models. Emphasis is placed on (1) what data are required from real rocks as input to the models, (2) how the models are verified, and (3) what additional structural parameters are predicted by the models. Verification is essentially a check on the implementation of the model simulation. Prediction applies to estimated parameters which are *not* used as input to the model.

Fara and Scheidegger (1961) first proposed that porous media be interpreted as a realization of a stochastic process. They suggested several measures which characterize the process, but did not propose a specific underlying stochastic process. Matheron (1967, 1975) developed the theoretical concepts much further, particularly with regard to the Boolean model of porous media. Preston and Davis (1976) consider sedimentary rocks as realizations of a stochastic process and give specific examples of the simplest such process, the Poisson model. Deffeyes *et al.* (1982) recently reviewed the application of stochastic geometry to the description of sediments and rocks. They discussed, briefly, aspects of the Boolean model as a stochastic model for sediments, but present no simulations or data.

Şen (1984) applied "autorun analysis" to describe and "model" porous media, but as discussed in Chapter 6, the autorun coefficients are simply an alternative representation of the autocovariance function. As such, they serve as a measure or characterization of the media, but do not serve as a model per se. To serve as a model, some stochastic process must be assumed. Şen (1984)

has assumed the first-order Markov process for his simulations. Contrary to Şen's assertions, he presents no evidence that the autorun coefficients are easier to interpret physically than more conventional autocorrelation functions. Additionally, his equation for specific surface is missing a factor of 2 because he failed to use orientation averaging (i.e., stereological formulae).

Lin and Harbaugh (1984) show how the parameters (transition matrix) for a first-order Markov model can be measured from a binary sandstone image and used to simulate the two-dimensional features. Visual similarity and statistical similarity were used to judge the quality of the simulation. The statistical comparison was made between the transition matrix of the original sandstone and transition matrix of the simulation. These matrices were comparable, as well they should be if the simulation is executed accurately.

Recently, Quiblier (1984) extended the clumping model of Joshi (1974) to three dimensions. This model is a "local order" model which is similar to a higher-order Markov model. This Joshi–Quiblier model shows promise as an investigative tool and will be discussed further.

Below, two classes of stochastic models, Poisson models and Markov models, are discussed. These models give insight into the use and descriptive potential of stochastic models. A few words are said about the Boolean model which has received considerable theoretical development, but perhaps because of inherent complexity, has seen little practical application (in the literature at least).

7.3.1 Poisson Model

The simplest stochastic model is one in which the state of a point (i.e., pore or grain) is determined only by the probability of each possible state. In this model, the Poisson point model, there is no spatial dependency. Preston and Davis (1976) have used the Poisson model to simulate porous media. They

based their modeling on the theoretical work of Roach (1968). The only data input to the Poisson model are the porosity of the material and the resolution of the simulation, Δx. Other pore structure parameters of the simulated material can depend *only* on these two parameters.

7.3.1.1 Line-sampled Intercept Length Distribution

The occurrence of adjacent pore or grain pixels is easily computed for the Poisson model. The number of pore intercepts, N_{Ip}, of length $n\Delta x$, in a sequence of M pixels is given by Roach (1968) as

$$N_{Ip}(n) = M p_p{}^n (1 - p_p)^2 \,, \tag{7.3}$$

where p_p is the probability of a pore pixel (i.e., porosity). Equation (7.3) simply represents the product of the individual probabilities of the occurrence of one grain pixel, n pore pixels, and another grain pixel. A similar relation is found for grain intercepts by interchanging the exponents on the right hand side of Eqn. (7.3). It is straightforward to simulate a Poisson process and determine the line-sampled intercept length distribution of the simulation (Roach, 1968; Preston and Davis, 1976). The intercept length distribution from such a simulation agrees with theoretical results as expected.

The two-dimensional simulation of a Poisson medium is seen to resemble a uniform fine-grained sandstone (Preston and Davis, 1976). We note that the simulation produced by this simple Poisson process will *always* produce what appears to be a uniform-grained sandstone. Additionally, the simulation will appear fine-grained when a high resolution is used in the simulation. This observation is true because the Poisson model has no ability to coalesce individual points (pixels) into fewer, but larger, features. Clumping or Markovian properties must be added to the model to produce larger, but fewer, features. By larger, we mean greater area in two dimensions, but do not require any

specific shape.

7.3.1.2 Tortuosity from Poisson Model

Preston and Davis (1976) showed that tortuosity, τ, could be estimated from the Poisson simulation. Predictably, a relation between tortuosity and porosity was found because porosity was the only model parameter employed. They did not address the effect of model resolution which could have been employed by using different numbers of nodes in their two-dimensional network. Preston and Davis (1976) found the following relation from simulation studies

$$\tau = \left(\frac{L_e}{L}\right)^2 = \frac{0.973}{{p_p}^{0.293}}\,, \tag{7.4}$$

where L_e is the effective path length for flow through a material and L is the macroscopic linear distance of flow. This result from simulation agrees well with the experimentally determined relationship of

$$\tau = \frac{1}{{p_p}^{0.30}}\,, \tag{7.5}$$

found by Archie (1942) for unconsolidated sands (Preston and Davis, 1976).

7.3.1.3 Specific Surface of the Poisson Model

Using the intercept length distribution for line-sampled pore intercepts, we can compute the specific surface predicted by the Poisson model. The standard stereological formula for specific surface is

$$S_V = 4N_L\,, \tag{7.6}$$

where N_L is the number of intercepts per unit length of test line. Summing over all lengths, the number of pore intercepts, N_{Ip}, in a sequence of M pixels is given by

$$N_{Ip} = \sum_{i=1}^{M} M{p_p}^i(1-p_p)^2\,. \tag{7.7}$$

Expanding Eqn. (7.7) yields

$$N_{Ip} = M(1 - p_p)^2(p_p + {p_p}^2 + {p_p}^3 + \ldots + {p_p}^M) \,. \tag{7.8}$$

For large M, the identity

$$(1 - x)^{-1} = 1 + x + x^2 + x^3 + \ldots \text{ for } x^2 < 1 \tag{7.9}$$

can be used to obtain

$$N_{Ip} = M(p_p - {p_p}^2) \,. \tag{7.10}$$

Combining Eqns. (7.10) and (7.6) and dividing by the length of the test line, $M\Delta x$, yields

$$S_V = \frac{4(p_p - {p_p}^2)}{\Delta x} \,. \tag{7.11}$$

As expected, the predicted S_V depends upon the porosity and the resolution of the simulation. This relation reinforces the ability of the simple Poisson model to simulate only a single type of uniform-grained sandstone.

The behavior of S_V for the Poisson model offers several interesting points. The inverse dependence on pixel size indicates that S_V is unbounded as the resolution increases. Figures 7.5a and 7.5b are plots of Eqn. (7.11) for typical pixel sizes as functions of porosity. Note that S_V is a maximum for 50% porosity (the equation is a parabola). This is the porosity at which there is a maximum probability that the next pixel will be in the opposite state. The S_V of the Poisson model gives an upper bound on the S_V at a given porosity and pixel size (resolution). If a material has any degree of positive local correlation, the S_V will be less than that for the Poisson material.

7.3.2 Markov Models—Clumping

The next degree of sophistication which can be added to the stochastic model is some form of clumping or Markovian behavior. Clumping provides the local

order which will occur if the resolution of the simulation is sufficiently high (i.e., small pixels). An additional model parameter is, logically, the degree of clumping. This degree of clumping is directly related to the specific surface of the porous material. Thus, the specific surface of the simulation should match that of the material which provides the model parameters. Both the specific surface and the clumping parameters are means of specifying the transition probability from the state at one pixel to the state at an adjacent pixel. The clumping parameter gives the simulation a short memory and results in a first-order Markov process.

Lin and Harbaugh (1984) present a lucid discussion of Markov models and their application to geology. In particular, they use a Markov model to simulate a two-dimensional slice through a sandstone. They measured transition probabilities from a sketch of a thin section and produced two simulations which appear, visually, similar to the original sketch. The transition probabilities of the simulations also agree with the input data.

The simulation process will not be discussed here, but we will show how the parameters which enter the simulation are directly related to the porosity and specific surface of the material.

7.3.2.1 Geometric Interpretation of Transition Probabilities

The pixels of the two-dimensional section are in one of two states; either the pore (P) state or the grain (G) state. The transition probability matrix gives the probability of an adjacent pixel being in state P (or G) if the current pixel is in state P (or G) and is represented by (Lin and Harbaugh, 1984, Ch. 4)

$$\mathbf{Pr} = \begin{pmatrix} Pr(P|P) & Pr(G|P) \\ Pr(P|G) & Pr(G|G) \end{pmatrix} . \tag{7.12}$$

The "marginal probabilities" are also required for the model and are simply the volume (areal) fractions of each phase.

The transition probabilities can be obtained from the line-sampled intercept distribution, $n_1(l_i)$ (see Chapter 4). For intercept lengths given in integer multiples of the pixel size, the transition frequencies are given by

$$N(P|P) = \sum_{i=1}^{M} n_{1p}(l_i) l_{i-1} , \tag{7.13}$$

$$N(G|P) = \sum_{i=1}^{M} n_{1p}(l_i) , \tag{7.14}$$

$$N(P|G) = \sum_{i=1}^{M} n_{1g}(l_i) , \tag{7.15}$$

$$N(G|G) = \sum_{i=1}^{M} n_{1g}(l_i) l_{i-1} , \tag{7.16}$$

where

$$l_i = i , \tag{7.17}$$

and M is the maximum length intercept. The subscripts on $n_1(l_i)$ indicate pore (P) intercept distribution or grain (G) intercept distribution and the (1) indicates line-sampled intercepts. Now, consider the sampling line to be one continuous line of length M pixels. The number of pore intercepts will be approximately equal to the number of grain intercepts. The difference can be one at most, and is negligible for a sufficiently long test line. Let N_I be the number of intercepts, N_P be the number of pore pixels, and N_G be the number of grain pixels. With these values, Eqns. (7.13) through (7.16) can be written as

$$N(P|P) = N_P - N_I , \tag{7.18}$$

$$N(G|P) = N_I , \tag{7.19}$$

$$N(P|G) = N_I , \tag{7.20}$$

$$N(G|G) = N_G - N_I . \tag{7.21}$$

Dividing by the length of the test line and putting the result in matrix form

yield

$$\mathbf{N} = \begin{pmatrix} p_p - N_I/N_T & N_I/N_T \\ N_I/N_T & (1-p_p) - N_I/N_T \end{pmatrix}, \tag{7.22}$$

where $p_p = N_P/N_T$ is the marginal probability of pore pixels.

Combining the standard stereological formula for specific surface from intercept counts, Eqn. (7.6), with Eqn. (7.22) gives

$$\mathbf{N} = \begin{pmatrix} p_p - S_V\Delta x/4 & S_V\Delta x/4 \\ S_V\Delta x/4 & (1-p_p) - S_V\Delta x/4 \end{pmatrix}. \tag{7.23}$$

Equation (7.23) is converted to a transition probability matrix by normalizing, so that the elements in each row sum to one. The normalization factors here are p_p for the first row and $1-p_p$ for the second row. The transition probability matrix is then

$$\mathbf{Pr} = \begin{pmatrix} 1 - S_V\Delta x/4p_p & S_V\Delta x/4p_p \\ S_V\Delta x/4(1-p_p) & 1 - S_V\Delta x/4(1-p_p) \end{pmatrix}. \tag{7.24}$$

Lin and Harbaugh (1984, p. 10) use Switzer's method to simulate the Markov process in two dimensions. The marginal probabilities and the parameter λ_M are used for the simulation, with λ_M given by

$$\lambda_M = -\frac{1}{2L}\ln\left(\frac{Pr(P|P) - Pr(P)}{1 - Pr(P)}\right), \tag{7.25}$$

where L is the spacing between two points in the simulation. Substituting the appropriate parameters into Eqn. (7.25) gives

$$\lambda_M = -\frac{1}{2L}\ln\left(1 - \frac{S_V\Delta x}{4p_p(1-p_p)}\right). \tag{7.26}$$

Equation (7.26) can also be found by using the probabilities for the grain (G) phase in Eqn. (7.25).

We have shown here that the parameters of the Markov model, the transition probabilities and the marginal probabilities, are completely specified by the porosity and the specific surface of the material.

As a special case, consider the Poisson process which has the transition probability matrix

$$\mathbf{Pr} = \begin{pmatrix} p_p & 1-p_p \\ p_p & 1-p_p \end{pmatrix} . \tag{7.27}$$

Equating elements $Pr(P|G)$ or $Pr(G|P)$ from equations (7.27) and (7.24) and solving for S_V gives Eqn. (7.11).

We note that Lin and Harbaugh (1984, p. 14) apply a correction to the sum of each row of the transition frequency matrix to yield correct marginal frequencies. By assuming one continuous sampling line, this correction becomes small and, in practice, with many long lines it appears negligible. In the example given by Lin and Harbaugh (1984, p. 23), the difference between the marginal frequencies of the simulations and the marginal frequencies of the input data is much greater than the value of the correction.

The simulation presented by Lin and Harbaugh (1984) produces an isotropic material. They indicate that anisotropic media can also be simulated (Lin and Harbaugh, 1984, p. 36). The dependence of the simulation on pixel size is interesting. The pixel size Δx used to determine S_V appears to be the correct value to use for the spacing L in the simulation. Lin and Harbaugh (1984) do not discuss the effects of L on the simulation, but since L influences the specific surface of the simulated material, it must be selected with care.

7.3.2.2 Joshi–Quiblier Clumping Model

Quiblier (1984) has recently presented the three-dimensional extension of a stochastic model by Joshi (1974). The model shows significant potential for understanding porous media because of the relatively simple form and the

limited number of model parameters. The model is able to simulate a porous medium which is geometrically realistic and fully determined (i.e., the coordinates of a point in the simulated material fully describe whether the point is matrix or pore). Input to the model is a probability density distribution and an autocorrelation function. Both of these can be measured on digital images of sandstones.

We will describe briefly the simulation process and then discuss the model attributes. The simulation begins by assigning random numbers, drawn from a Gaussian population with mean 0 and variance 1, to the nodes of a three-dimensional grid (i.e., the volume elements of the simulation). This set of random numbers, X, is combined in small neighborhoods to produce a correlated set of numbers. The combination is a "linear filter" using coefficients which give the correlated set, Y, a specified autocorrelation function. Any desired correlation function can be created in set Y, such as the correlation function measured from a digital image of a sandstone. A further "nonlinear filter" is applied to the set Y to obtain the required probability density function (i.e., the image intensity histogram). The coefficients for the filters are computed prior to simulation and form the core of the simulation process. For more details, refer to the original paper (Quiblier, 1984).

Quiblier (1984) demonstrates that the simulated medium *looks* like the starting material and that the autocorrelation function and the probability density function from the simulation are similar to the input functions. In his opinion, the material is geometrically realistic because these criteria are satisfied. We note that the simulation will have the same porosity and specific surface as the medium from which the autocorrelation function was taken.

The way in which clumping is included in this model is difficult to ascertain. Basically, the full autocorrelation function is used to describe the clumping. In this sense, the model can be considered more advanced than a first-order

Markov model. For convenience, I consider it a higher-order Markov model.

An important parameter of the model is the size of the neighborhood over which the linear filtering is performed. Quiblier gives the size as the distance at which the autocorrelation function vanishes. This distance is equivalent to the range of the autocovariance function discussed in Chapter 6. The range is the distance at which the autocovariance function is sufficiently close to the asymptotic value. It is apparent then that the range is an important parameter in the Joshi–Quiblier model.

Quiblier (1984) prefers to use the full intensity probability density function (viz., the intensity histograms of Chapter 3) in the simulation process, saying that it allows many realizations by selecting different thresholds after the simulation process. The binary probability density (i.e., porosity only) approach is probably better because it describes the geometric structure directly. To preserve the structural interpretation of the autocorrelation function, the image on which this function is measured *must* be binary (see Chapter 6). Further, the intensity variation in an image does not have significance for describing the geometric structure, other than identifying boundaries of phases. This is particularly true if optical and photographic processes are involved. There may be computational reasons why a full-intensity simulation is preferable. For example, realizations with the same autocorrelation function and different porosities may be generated with less effort. If so, then a simple ramp function may prove more useful than a "realistic" intensity histogram. The ramp offers the highest sensitivity of porosity to threshold intensity over the widest intensity range.

Quiblier (1984) gives, as an application of the stochastic model, the computation of topology of a simulation. This raises the hope of predicting tortuosity and topology from data contained in the autocovariance. However, a material composed of isolated pores in a continuous matrix can have the same auto-

correlation function as a material with a connected pore phase. Because of this non-uniqueness in the autocorrelation function we have some reservations about the predictive ability of the model. We do not know, for example, if different realizations using the same autocorrelation function all have similar topologies or if the topology varies widely. Only more simulations and studies will tell, and they appear warranted. Some insight is provided by variational bounds on permeability, which are discussed in section 7.4.5.

One additional simulation by Quiblier (1984) is noteworthy. In order to produce a medium which has a bimodal size distribution, it was necessary to superimpose the simulations from two different autocovariance functions. This suggests that a single autocovariance function cannot represent a bimodal size distribution.

7.3.3 The Boolean Model

The Boolean model for porous media was developed by Matheron (1967, 1975). This model has seen relatively little application, perhaps because of the inherent mathematical complexity. The mathematics is not particularly difficult, however, most descriptions of the model are steeped in the discussion of theorems and provide little geometric insight. In the following, we avoid equations and discuss the practical applicability of the Boolean model and what new information it provides.

The discussion presented here is distilled primarily from Deffeyes *et al.* (1982) and Serra (1982, Ch. 13). A realization of the Boolean model is accomplished by selecting "grains" from a grain population and placing these grains at randomly positioned points in a volume (or on a plane in 2-D). The grains are typically spheres (or discs in 2-D), and the point locations are given by the Poisson process. The "grains" may actually be pores in the study of a porous material.

One equation must be given because it forms the core of the Boolean model. This equation is termed the "fundamental formula" because it relates the character of the realization to the character of the primary grains. Serra (1982, p. 486) gives the geometric representation of the fundamental formula as

$$Q(B) = Pr(B \subset X^c) = \exp(-\rho E[mes(\acute{X} \oplus B)]) \; . \tag{7.28}$$

Equation (7.28) indicates that the nature of the aggregate is determined by the Lebesgue measure, *mes* (area in 2-D), of the dilation of the primary grains, $\acute{X}$, with a structuring element, B. The density of the Poisson process is ρ. ***Thus, for any structuring element, B, the nature of the aggregate is known if the nature of the components is known.*** The common structuring elements give porosity (B = a point), covariance (B = a pair of points), and specific surface (B = a small ball in 3-D). See Watson (1975) or Serra (1982) for other structuring elements. With additional restrictions on the primary grains, such as convexity, intercept length distributions and connectivity information are available (Serra, 1982, p. 489).

Use of the Boolean model involves two stages. First, the material to be modeled is tested to determine if the Boolean model is appropriate. Second, if appropriate, the Boolean parameters for the model are determined from measurements made on the material. Equation (7.28) predicts how a parameter, measurable via a structuring element, will behave for the Boolean medium and is used for both of these stages. The two applications discussed by Serra (1982, Ch. 13) use the point-sampled intercept length distribution and the autocovariance to perform the test and to determine the model parameters. Both of these structural measures have been measured in this study and can be used to investigate the Boolean model applied to sandstones.

7.3.3.1 Limitations of the Boolean Model

The Boolean model has restrictions, as do all models, which limit its usefulness. If the primary grains are not convex or completely known *a priori*, then the Boolean model cannot be used (Serra, 1982, p. 495). Scheidegger (1974) states, without specific criticism, that the set-theoretical probabilistic model of Matheron (1967) (i.e., the Boolean model) does not lead to easily applicable results. Deffeyes *et al.* (1982) present the fundamental formula but don't discuss the model further. They appear to have reservations about the use of analytic models. Instead, they suggest the use of computer simulations with *ad hoc* models, but they do not specify the objective of such modeling.

7.3.3.2 Discussion of the Boolean model

The Boolean model appears to be very powerful, but until it is cast into a more practical description, it will remain unaccessible to those who otherwise might apply it. If a material does indeed satisfy the Boolean model, then with a few measured parameters, the Boolean model parameters can be determined. These parameters can be used with the fundamental formula to predict any geometric property which can be expressed as a structuring element.

Data have been collected in this study which allow further study of the Boolean model. Application of the Boolean model requires a better understanding of the nature of the "grain" distribution, and this can be provided by the results of feature analysis. The size–shape inversion results suggest the use of a collection of oblate ellipsoid "grains" representing the pore space. These grains can be positioned randomly in space with random orientations. Structural parameters measured on slices through the simulated material can be compared to the parameters from rock images. Interpenetration of grains is allowed in the Boolean model.

As with any model, the Boolean model offers a means of describing a complex structure with relatively few parameters. Also, there is potential for discovering geometric information which was not known to be contained in some pore structure parameter. This potential for prediction is discussed further in the following section.

7.3.4 Verification and Prediction of Stochastic Models

Two important criteria by which stochastic models can be judged are how well the model satisfies known structural parameters (verification) and how good is the predictive ability of the model. Some structural parameters constitute the input parameters of the model and matching these is not a measure of the predictive ability of the model. Rather, this match verifies whether the theory was developed in a consistent manner and the simulation was performed correctly.

For an example of verification and predictive ability, consider the Poisson model. A simulation of the Poisson model can be *verified* by checking that the porosity of the model matches the porosity parameter which was used as input. The Poisson model *predicts* the surface area of the material (see above). However, this prediction will not be good for most realistic materials, thus, the predictive ability is poor.

7.3.4.1 Verification

Principal criteria used previously to verify models are (1) visual appearance and (2) match with input data. Visual verification is popular, but is not a good discriminant. The reason we use direct analysis and simulations is because the structure is too complex to interpret visually.

As stated above, the match of parameters from the simulation with input

parameters to the model does not show the "power" of the model, but rather, shows a consistent development and accurate implementation of the simulation. Verification is required to instill faith in the model simulation, but the predictive abilities of the model are the true measures of the usefulness of the model.

7.3.4.2 Prediction

Prediction is defined as the estimation, from a model simulation, of a structural parameter which was not explicitly contained in the input parameters. Predictions can be verified by comparison of estimated parameters with measured parameters or perhaps from correlations with behaviors of physical properties. For example, does the tortuosity predicted by the model aid in the estimation of permeability which correlates with measured permeability? Prediction is a tool which may disclose information that was not previously known to be contained within certain pore structure parameters.

Evaluating the prediction of topology may be one application where serial-section analysis (see Chapter 2) is justified. If it can be shown that estimated topological parameters are accurate by comparison with measured topological parameters, then faith can be placed in the topological estimates. It is more prudent, however, to understand fully the model through many simulations and thorough examination prior to performing the tedious serial-section analysis.

The more structural parameters a model satisfies, the more realistic the model becomes. Similarly, as more geometrical information is put into a model, the more realistic the simulation should be. More structural information may leave fewer parameters to predict, but those which are predicted should be more accurate.

7.3.5 Discussion of Stochastic Models of Pore Structure

Stochastic models are important because of their potential to allow the concise expression of complex structures and to improve our understanding of pore structure parameters. These models may also be able to direct the parameter measurements by indicating which structural parameters are most significant.

7.3.5.1 Expression of Complex Structure

One potential use of a stochastic model is to reduce the number of parameters required to describe a material. If the model faithfully reproduces the pore structure parameters of interest (e.g., porosity, specific surface, connectivity), then all of the essential information about the material is contained in the model parameters. Even if the use of a model does not result in a reduction of the number of parameters required for description, it may provide a more formalized framework with which to describe the material. For example, Lin and Harbaugh (1984, p. 103) state that Markov models are capable of expressing relationships, such as spatial correlations, which might be very difficult to represent otherwise.

7.3.5.2 New Information from Prediction

Do stochastic models yield new information about the material being modeled? Previous results are inconclusive but promising. The models *do* yield estimates of parameters, such as the tortuosity from the Poisson model or the topology from the Joshi–Quiblier model. The uncertainty remains as to whether the estimates accurately represent properties of the material. For the Poisson model, the predicted tortuosity apparently represents tortuosity for one type of material: unconsolidated sands (Preston and Davis, 1976). We do not know if the topology predicted by the Joshi–Quiblier model accurately reflects the

topology of real materials. Şen (1984) states that stochastic models do not yield new information, but he does not give reasons for his opinion.

Many pore structure parameters, which may be useful to judge the predictive ability of models, have been measured in this study. Specifically, these are mean pore volume (Chapter 4), line-sampled intercept distributions (Chapter 4), primary and secondary feature parameters (Chapter 5), and autocovariance (Chapter 6). Of course, for any of these used as a model parameter, the comparison will be one of verification, not prediction.

A model simulation is expected to satisfy all of the geometric information contained in the model parameters. However, the input data must be valid. Consider the example given in Chapter 6, where the autocovariance was computed for an insufficient image area. The resulting autocovariance was *not* representative of the overall material structure. Consequently, for example, it would not be suitable for the Joshi–Quiblier model.

7.3.5.3 Complexity of Models

The models considered here have been homogeneous and isotropic. The complexity of heterogeneity and anisotropy can be added to most of the models, but there is much to learn about the simpler formulations first. The Joshi–Quiblier model can be extended to be both inhomogeneous and anisotropic by using an initial random process which is inhomogeneous and a clumping function (autocovariance) which is both inhomogeneous and anisotropic.

7.4 Physical Properties and Pore Structure

Understanding the physics of the dependence of physical properties on pore structure is an ultimate goal of direct analysis of pore structure. A more immediate goal is the correlation and prediction of physical properties with

pore structure parameters.

This section begins with a review of some previous correlations between pore structure parameters obtained by direct analysis and physical properties. The relationships are vague. Models of physical properties were also examined to indicate which pore structure parameters appear to be important for controlling behaviors and, therefore, should be measured to allow prediction of behavior. These examinations were not very fruitful. Several models use parameters which are a direct function of the pore structure, but are not well-defined, measurable pore structure parameters. The equivalent-conduit, Kozeny–Carman model of permeability is based on measurable parameters. We examine this model in detail. Porosity and specific surface data from image analysis are used with measured formation factors to estimate permeability.

7.4.1 Review of Semi-Quantitative Studies

In this section, we review previous studies which have used direct analyses of pore structure to examine the relations between physical properties and pore structure in rocks. In these studies, qualitative or semi-quantitative measures of pore structure were found by direct examination of the rock.

Archie (1952) presented a classification scheme for carbonate rocks "to portray as much as possible the essential pore characteristics." Qualitative evaluation of the "texture of the matrix" and the "visible pore structure" was used to group the rocks for estimation of physical properties. Only the areal abundance of the visible pores (greater than 0.01 mm) is recorded as a quantitative estimate.

Winsauer *et al.* (1952) proposed a measure of packing in indurated sandstones and correlated this measure with formation factor. Their "packing index" has a simple geometric interpretation. It is the ratio of the surface area of

grain-to-grain contacts to the surface area of grain-to-non-grain contacts per unit volume. This packing index should be dependent on grain size and the abundance of matrix, along with the packing. Winsauer *et al.* (1952) found that high packing indices correlate with high formation factors. However, from their data we observe that packing indices were also strongly correlated with porosity. The formation factor correlation may result primarily from the porosity variation associated with the packing index variation.

Kahn(1956, 1959) renamed the "packing index" of Winsauer *et al.* (1952) and proposed an additional measure of packing in sandstones. These measures have subsequently been used by others (e.g., Morrow, 1971) to correlate "packing" with physical properties. The packing index was renamed the "packing proximity" and was thought to represent a "unit property of packing." The geometric significance of the packing proximity was described above. The second measure also has a simple geometric interpretation. The aggregate property of packing was termed "packing density," and is simply a measure of the volume fraction of framework grains (i.e., excluding matrix and cement) in the rock. Thus, this "packing density" will be related to the packing to the extent that bulk grain volume is related to the packing. The packing density is more a measure of volume abundance than a measure of geometric arrangement.

Stout (1964) proposed that the quality of a carbonate reservoir rock can be estimated from petrographic analysis. The petrographic features of interest appear to be (1) secondary mineralization, (2) dolomitization, and (3) size distribution of pores and throats. However, no procedures were suggested for estimating any of these features. Mercury porosimetry curves were used to interpret whether the pore size distributions were wide or narrow. Then it was claimed that extensive porosimetry measurements are not necessary. Instead, the petrographic features convey the necessary information.

Morgan and Gordon (1970) proposed that pore geometry affects relative permeability and that a binocular microscope can be used to detect the important features. Their optical assessment is purely qualitative. The pore geometry parameters of interest are pore size and surface area. Surface area is affected by most "textural" properties, such as grain size, mineralogy (e.g., clay), and packing, together with the diagenetic processes of cementation, replacement, and solution. Morgan and Gordon (1970) appear to have been unaware that surface area can be measured by stereological methods. No specific scheme was suggested for classifying the pore size-surface area groups by optical examination.

Delfiner (1972) cited the study by Delfiner (1971) in which mercury porosimetry curves were compared directly with granulometry curves from images (see Chapter 5). General "agreement" was claimed by Delfiner (1972), but no data were given.

Dhawan (1972) (see also Dullien and Dhawan, 1974) compared the image derived "structural difficulty index" to secondary recovery efficiency. The structural difficulty index is, in essence, a volume-weighted function of the estimated pore-to-throat size ratio. The pore size distributions determined by quantitative stereology were not otherwise interpreted.

Wardlaw (1976) measured maximum diameters of pore and grain features on random traverses of pore casts of carbonate rocks. The averages of these values were used as estimates of "pore diameter" and "grain diameter." Throat size was estimated from the pressure at which 50% of the pore volume was saturated in a mercury capillary-pressure experiment. A sheet-like pore model was used to convert pressure to aperture width. He also measured sheet-pore thickness from SEM micrographs of pore casts. Estimated sheet thickness was in good agreement with measured thickness. Pore diameter was found to be independent of porosity. However, using estimated

throat sizes, small pore-to-throat size ratios correlated positively with high porosity. Mercury ejection efficiency was found to correlate negatively with pore-to-throat size ratio. However, the positive correlation between porosity and mercury ejection efficiency is equally good, thus, it is not definite that the pore-to-throat size is the controlling factor.

Wardlaw and Cassan (1978) presented a classification scheme whereby recovery efficiency could be predicted from qualitative visual observations of thin sections and pore casts. Porosity was the single most important property. Pore-to-throat size ratios, coordination number, and heterogeneity were the other important characteristics. The classification scheme provides a slight improvement over a simple porosity-recovery efficiency relation, particularly at low recovery efficiencies. The scheme is primarily qualitative, however, pore-to-throat size ratios can be estimated by the methods described by Wardlaw (1976).

Wardlaw and Cassan (1979) offered one of the first quantitative assessments of pore geometry and correlation with oil recovery efficiency. They measured maximum Feret diameters of grain features touched by randomly-oriented traverses on thin sections. Only framework grains were measured, and these values were averaged to estimate "mean particle size." Mean pore size was estimated from the diameters of maximum inscribed circles on pore features seen in a section plane through a pore cast. One hundred circles were measured on randomly-oriented traverses. These data from pore casts could be obtained from standard sections because information below the plane of the section is neglected. They also made qualitative observations of the pore structure, primarily by indicating the effects of diagenesis (i.e., cementation and dissolution) on pore-to-throat size ratios. Cementation is thought to reduce the pore-throat ratio and dissolution may increase or decrease the ratio. They also state that the common form of throats in sandstones is as sheet-like

spaces. Both of the pore structure parameters measured (i.e., grain size, pore size) were found to correlate significantly with mercury recovery efficiency and oil recovery efficiency. They concluded that mercury recovery efficiency could be used to estimate oil recovery efficiency with certain restrictions. They did not address specifically how the pore structure or petrographic information can be used to estimate recovery efficiency.

Lucia (1983) presented a semi-quantitative description scheme for carbonate rocks and related the parameters to physical properties. Particle size is estimated using a comparator or ocular micrometer. Total porosity is measured by bulk methods on a core or estimated from well logs. Separate (i.e., isolated) vug porosity is estimated visually. A vug is "pore space larger than or within the particles of rock and commonly present as leached particles, fractures, and large irregular cavities." The presence of touching vugs, "interconnected large cavities, channels, and fractures," is noted if evident. These parameters are used with empirical correlations to estimate permeability, the exponent m in the Archie formula, and the entry pressure for mercury injection. Lucia's work indicates the importance of accounting for the larger pore spaces in a rock to allow a better interpretation of the smaller pore spaces which are more difficult to characterize. The particle size in this classification scheme is important because "the average size of the interparticle pore space is controlled by this particle size." Direct measurement of the interparticle pore space may be equivalent to and preferable to estimation of grain size because the pore space is of primary interest.

Sneider *et al.* (1983) developed an extensive classification scheme similar to that of Lucia (1983). They estimate grain sizes and sorting with comparators, and the abundance of "visible pores" at 20× magnification. Combining these estimated parameters with air permeability, other petrophysical data, geologic evaluation, well logs, and flow tests, potential pay zones are identified. There

are no direct relations established between pore geometry and physical properties, rather, a wide range of data is used to evaluate reservoir "potential." However, there is emphasis on the abundance of "visible" pores, indicating again the importance of describing the larger pores of the rock.

Thomeer (1983) presents a relation between air permeability and three parameters which describe the pore structure. The pore structure parameters are the size distribution of pore throats, the diameter of the largest throat, and the total porosity. In an earlier study (Thomeer, 1960), methods are given to estimate these parameters from capillary-pressure curves. Further, a relation was established between the capillary-pressure curve and air permeability. It is not stated how pore throat size distribution or the "largest pore throat" was found from the "detailed petrographic description."

In summary, it is evident from previous studies that semi-quantitative petrographic examination can be used to estimate physical properties such as permeability and recovery efficiency. It is not clear what specific geometric (or topological?) characteristics of the pore space are controlling the properties. Many previous studies center on a complementary space concept. Because it is difficult to characterize the pore space, the grain space ("texture") is characterized and used to infer the character of the pore space. This approach is rational because the pore space is a consequence of the solid constituents and their arrangement. Note that the correlations have all been empirical.

Our study has focused on characterizing directly the pore space. Our desire is to relate pore space parameters to physical properties. We believe that this approach is better than that of inferring pore structure from grain structure. However, it is not clear, at this point, which applications are best served by either approach.

Note that pore size and abundance are common themes and that they are measurable by quantitative stereology. Throat sizes can be estimated by

mercury porosimetry and other methods. Also, after the pore space of the larger pores is quantified, the remaining pore space of the smaller pores and throats may be characterized better and more easily.

7.4.2 Introduction to Permeability Models

The prediction of permeability from pore structure measurements is an important application of direct analysis methods. The goal of this approach is a reliable determination of permeability from a relatively easy measurement. Of equal importance is the determination of permeability when only a small fragment of the rock is available, as from well cuttings. This last problem has also been addressed by the prediction of permeability from mercury capillary pressure curves of small samples (e.g., Swanson, 1981). In this and the following sections, the prediction of permeability from pore structure parameters is investigated.

Three principal approaches have been used by others to relate permeability to pore structure parameters which were measured from images. The first approach is to model the rock as a simplified structure, such as a single tube, and use pore structure parameters (i.e., specific surface) to describe the tubes. This equivalent conduit approach is discussed and applied below.

The second approach is to relate pore structure parameters to measured permeability through empirical correlations (section 7.4.4). In this second approach, many pore parameters are regressed with the measured permeabilities to find some relation. A disadvantage of the empirical approach is that an understanding of the physics of why these particular pore parameters control the fluid flow is not advanced. There is no assurance that the relation will work for a slightly different rock type or account for anomalous behaviors.

The third approach is a stochastic model which uses spatial correlation functions (section 7.4.5). The physics of the stochastic model is based on

the minimization of energy dissipation due to an incompressible fluid flowing through the medium. The stochastic nature of the medium is described by the spatial correlation functions.

7.4.3 Equivalent Conduit Models of Fluid Permeability

Equivalent conduit models of permeability assume that the flow through the rock can be described by the flow through a conduit or a bundle of conduits. We consider only the simplest model with one equivalent conduit. Dullien (1979, Ch. 4) discusses more complicated models.

7.4.3.1 Classical Kozeny–Carman Model

The classical Kozeny–Carman (K–C) model has been studied extensively by Wyllie and colleagues (Rose and Bruce, 1949; Wyllie and Rose, 1950ab; Wyllie and Spangler, 1952; Wyllie and Gregory, 1955; Wyllie and Gardner, 1958ab). In this equivalent conduit conceptual model, the tubes of flow and, hence, the mean flow streamlines, are parallel to the macroscopic flow direction through the sample (Figure 7.6a). Permeability in the classical K–C model is given by

$$k = \frac{\phi^3}{k_0 (L_e/L)^2 S_V{}^2} , \tag{7.29}$$

where ϕ is the porosity, k_0 is a shape factor, and S_V is the specific surface. L_e is the "effective fluid path length" and L is the macroscopic flow length.

Wyllie–Rose Tortuosity—In the classical Kozeny–Carman model, the formation resistivity factor, F_R, is related to porosity and tortuosity, $(L_e/L)^2$, by (Wyllie and Rose, 1950ab)

$$F_R = \frac{(L_e/L)}{\phi} . \tag{7.30}$$

The tortuosity in this model is said to represent principally "variation in the area available for flow of fluids in the individual pores and at the connections

between pores" (Wyllie and Gardner, 1958a). The L_e in this conceptual model is a purely mathematical quantity, but can also be thought of as the effective streamline length (not effective conduit length). Equation (7.30) is referred to as the Wyllie–Rose tortuosity; it is combined with Eqn. (7.29) to eliminate the tortuosity term and give

$$k = \frac{\phi}{k_0(F_R S_V)^2} . \tag{7.31}$$

Equation (7.31) is based on the assumption of equivalent tortuous paths for the electrical current and the fluid. This assumption was used with prudence by early workers (Wyllie and Rose, 1950b; Wyllie and Spangler, 1952; Wyllie and Gregory, 1955; Wyllie and Gardner, 1958a). They believed that the tortuosities may not be identical, but they believed them to be very close numerically. Still, their awareness of the fundamental difference between viscous resistivity (i.e., dependence on r^4) and electrical resistivity (i.e., dependence on r^2) lent caution to their approach.

7.4.3.2 Geometric Equivalent Conduit

The geometric equivalent conduit (GEC) model gives the same relation for k (Eqn. 7.29) as did the classical K–C model, but uses a different relation for F_R (Eqn. (7.32)). The essential point to recognize is that the *geometric equivalent conduit is conceptually different from the classical K–C model.* In the GEC model, the equivalent conduits are arranged in a sinuous manner and they have a constant cross-sectional area, A_l (Figure 7.6b). In some respects, the GEC appears to be preferable because of the geometric interpretation. However, there is evidence that the classical K–C model gives better results.

Cornell–Katz Tortuosity—Winsauer *et al.* (1952) were the first to use a geometrical interpretation to arrive at the GEC relation for formation factor

and tortuosity

$$F_R = \frac{(L_e/L)^2}{\phi} . \tag{7.32}$$

The primary reason for their choice of formulation was to satisfy the pore volume predicted by their conceptual model. Subsequently, Cornell and Katz (1953) obtained the same relation by the *a priori* unproven relation

$$A_l = \frac{A_x}{(L_e/L)} , \tag{7.33}$$

$$A_x = \phi A , \tag{7.34}$$

where A_l is the cross-sectional area normal to the flow streamlines, A is the total cross-sectional area of the sample, L is the unit length of the sample, and L_e is the length of the sinuous conduit (see Figure 7.6b). Following Wyllie and Gregory (1955) and Wyllie and Gardner (1958ab), we refer to the tortuosity in Eqn. (7.32) as the Cornell–Katz tortuosity.

Combining Eqns. (7.29) and (7.32) to eliminate the tortuosity term yields

$$k = \frac{\phi^2}{k_0 F_R S_V^2} . \tag{7.35}$$

In the GEC model, the *a priori* assumption that the area available for flow is given by Eqn. (7.33) was unjustified. Previously, the only justifiable approach has been to arrive at Eqn. (7.33) by *a posteriori* requiring that the porosity of the sample be given by the product of the available cross-sectional area (A_l) and the ratio (L_e/L). This geometric argument was presented by Winsauer *et al.* (1952) and the resulting Cornell–Katz tortuosity was tested against experimental data.

A stereological relation exists which provides the necessary *a priori* justification for Eqn. (7.33). For tortuous tubules of constant cross-sectional area, the equation relates the average cross-sectional area to the volume fraction and tubule length (Baddeley and Averback, 1983). Further, the relation requires

an assemblage of non-kinked, non-penetrating tubules, each with a constant radius. This relation,

$$\pi\langle r^2\rangle_{\text{avg}} = V_V/L_V \ , \tag{7.36}$$

states that an unbiased estimate of average tubule area is given by the ratio of the volume fraction occupied by tubules to the length of tubule per unit volume of the sample. This equation substantiates, for the first time, the *a priori* use of Eqn. (7.33) when deriving the Cornell–Katz tortuosity. To convert Eqn. (7.36) to its familiar form, note that

$$V_V = A_x/L^2 \ , \tag{7.37}$$

$$L_V = L_c/L^3 \ , \tag{7.38}$$

where L is the characteristic length of the volume under consideration (i.e., $A = L^2$). Substituting Eqns. (7.37) and (7.38) into Eqn. (7.36) gives Eqn. (7.33).

Both Paterson (1983) and Walsh and Brace (1984) have recently presented "corrections of errors" in the Kozeny–Carman model as used by Wyllie and colleagues. These so-called corrections follow from the GEC conceptual model which is *different* from the classical K–C model. They both arrive at the Cornell–Katz tortuosity which is the accepted form in the GEC model.

7.4.3.3 Which Equivalent Conduit Model is Better?

Given the above described conceptual differences and the resulting model equations, which is the better model? Wyllie and Gardner (1958a) stress that the better model can only be determined by comparison of the models with experimental data.

Both approaches use crude geometrical assumptions about the flow through the rock. However, the GEC model appears more nearly correct geometrically because all parameters are well-defined geometric dimensions. The increased

streamline length in the Wyllie–Rose tortuosity is primarily due to cross-sectional area variations and is difficult to visualize in a "straight" conduit with a single average hydraulic radius. It is not clear that the additional geometric consistency of the GEC model is an advantage.

The tortuosity in the classical K–C model represents increased length of streamlines through variations in the cross-sectional area of the flow conduit, whereas the tortuosity in the GEC model represents a sinuous conduit which is physically longer than the macroscopic sample length. Thus, the GEC model appears to be more faithful to the Poiseuille relation of flow through a tube. However, because of canceling terms, the classical K-C model and the GEC model both yield the same expression for permeability. In the relation for F_R, faithfulness to the Poiseuille relation is not required, yet here is where the difference in the models becomes apparent.

Madden (1986, personal communication) suggested that the GEC model is more appropriate for equating the electrical and fluid tortuosities. With a constant tube radius, the tortuosity is due to the effective tube length only. Thus, provided the fluid and electrical current follow the same path, the tortuosities should be the same. In the classical K–C model, tortuosity is also a result of tube radius variation. Thus, even though the fluid and current follow the same path, the tortuosities will be different due to the different dependence on radius of fluid and current flow.

There is no geometrical conflict with the classical K–C model as has been asserted by Paterson (1983). The conceptual model is one of straight tubes parallel to the macroscopic flow direction. Thus, L is the correct length to multiply by the average cross-sectional area (A_z) to get the volume of pore space in the unit cube (Figure 7.6a). We disagree with Paterson (1983) and conclude that the Wyllie-Rose tortuosity is indeed a viable relation.

Experimental Verification—Wyllie and Gregory (1955) compared the Wyllie–

Rose tortuosity with the Cornell–Katz tortuosity in an attempt to determine the better relation. They found that the Wyllie–Rose tortuosity produced more consistent shape factors, k_0, which were between 2 and 3 (the theoretical range). The Cornell–Katz tortuosity gave k_0 values which were somewhat more variable with values as high as 7. Wyllie and Gregory (1955) present additional evidence which suggests that the Wyllie–Rose tortuosity is the preferable relation.

Using the data given in Table 1 of Paterson (1983), we have computed the permeability predicted by the classical K–C model (Eqn. (7.31)). The data used by Paterson (1983) are reproduced in Table 7.2a. Both Paterson (1983) and Brace (1977) mistook S_{Vg} for S_V in the original paper by Wyllie and Spangler (1952). Hydraulic radius, m, is related to S_V via

$$m = \frac{\phi}{S_V} = \frac{\phi}{S_{Vg}(1-\phi)} \,. \tag{7.39}$$

Correct m values are given in Table 7.2a. We include 4 additional rocks from Wyllie and Spangler (1952) which were omitted by Paterson (1983).

For *all* of the samples, the classical K–C model gives better agreement with the measured permeabilities than does the GEC model. Figure 7.7 is a plot of the calculated values from each model versus the measured permeabilities. The classical K–C model gives excellent agreement over 10 orders of magnitude in permeability. Samples include synthetic materials, sandstones, and crystalline rocks. The sample with greatest disagreement, Sherman granite, is believed to have an overestimated m (Paterson, 1983).

7.4.3.4 Previous Image Analysis Studies

The equivalent conduit models have been used by several investigators to relate image derived specific surface estimates to measured permeability (Wyllie and Spangler, 1952; Rink and Schopper, 1978; Ruzyla, 1984; Berryman and Blair,

1986).

Wyllie and Spangler (1952) measured S_V on thin sections with a manual lineal method. They did not compute estimated permeability directly from their data, and were more interested in the ability to predict S_V from the Kozeny–Carman model. We presented the estimated permeabilities in Table 7.2b and discussed the excellent agreement above.

Perez-Rosales (1969) suggested using S_V and ϕ, measured by stereological methods, with a Kozeny–Carman model to predict permeabilities. He presented Eqn. (7.29) and assumed a constant, unstated value for the quantity $k_o(L_e/L)^2$, but did not present any data or results.

Rink and Schopper (1978) also applied a form of the Kozeny–Carman model to image derived feature parameters. It is difficult to comprehend their approach. Basically, they used several *ad hoc* averaging schemes to convert feature parameters, measured on images, into various approximations of the hydraulic radius. Like Perez-Rosales (1969), they assume a constant value for $k_o(L_e/L)^2$ instead of using F_R to eliminate the tortuosity. Their *ad hoc* averaging schemes used many assumptions which are not required if the appropriate parameters are measured on the images. Predicted permeabilities were at least an order of magnitude larger than measured permeabilities. When they used a network model (a variant of the GEC model), with tortuosity accounted for by the formation factor, agreement between predicted and measured permeability was within factors of 1 to 6 for the four samples. Noteworthy was the better agreement found when using "S_V" from clear cut images (see Chapter 5). The S_V from clear cut images is smaller than that from original images. This reduction in S_V may have partially compensated for the overestimate of S_V by feature analysis (see section 7.2.2.3).

Ruzyla (1984) presents the Kozeny–Carman relation with an assumed Kozeny constant ($k_0(L_e/L)^2 = 5$), but he did not estimate permeabilities.

Rather, he plotted specific surface versus porosity to show clusters of samples with similar permeabilities. Because, as he states, tortuosity has not been accounted for, anomalous behavior is anticipated.

Berryman and Blair (1986) use the GEC model as derived by Walsh and Brace (1984). They measured specific surface by spatial correlation methods (e.g., Chapter 6). They found very good agreement between measured and calculated permeabilities using S_V from higher magnification (500×) images. Using their 100× data in the classical K–C model, we obtain excellent agreement. The difference is consistent with the tendency of the GEC model to overestimate k (e.g., Figure 7.7). The GEC model requires a larger S_V to reduce the estimate. There are too many uncertainties in the imaging approach of Berryman and Blair (1986) (e.g., low BSE S/N ratio, raster scan digitization of SEM photomicrographs, and subjective threshold selection) to address the resolution requirements further.

7.4.3.5 Averaging Schemes for Specific Surface

Several averaging schemes are available for combining the specific surface measurements made in this study for the purpose of predicting permeability. The simplest approach is to use the single value of specific surface, determined by stereological methods, in the single conduit equations discussed above. Alternatively, the distribution of specific surface as a function of volume fraction, determined by the size–shape inversion of Chapter 4, could be combined by parallel, serial, or network averaging. Such a network approach is referred to as the "generalized Kozeny–Carman model" (e.g., Wyllie and Gardner, 1958a) and is beyond the scope of the present study. A third approach is to use *ad hoc* averaging of the hydraulic radius determined for individual features by feature analysis methods (Chapter 5), such as the approach of Rink and Schopper (1978). While the first two approaches are justifiable in terms of the

specific surface measured by image analysis, the last approach has no rigorous stereological formulation.

7.4.3.6 Results of the Classical Kozeny–Carman Model

Porosity and specific surface measured by image analysis have been combined with measured formation factors to predict permeability using the classical Kozeny–Carman model (Eqn. (7.31)). The values are tabulated in Table 7.3. A value of 2.5 was used for k_o. Predicted permeabilities are plotted versus measured permeabilities in Figure 7.8.

In general, the agreement is very good. The predicted permeabilities for 6 of the 11 samples are within the range of the measured brine permeabilities on 3 orthogonal cores. Two of the samples are within a factor of one and the remaining three are within a factor of two.

The larger misfits can be attributed to several sources. F_R was not measured on sample 2686; it was taken from the literature. Also, the k_{meas} of sample 2686 was estimated from mercury porosimetry because the brine permeability was not measured. Thus, the misfit of sample 2686 is not meaningful. Sample 2687 contains 18% clay localized in bands, which would give a smaller F_R than that from the pore geometry alone, yielding an overestimate of k_{calc}. Also, the banded nature of the clay reduces permeability and generally violates an implicit assumption of homogeneity in the model. The accuracy of the permeability measurements may partially explain the disagreement of sample 2519. A steady state flow apparatus, which has large uncertainty at low permeabilities, was used. For sample 2519, fluid permeability of 24 md was estimated from mercury porosimetry data. The predicted permeability is in close agreement with this value. Overall, the differences between the measured and predicted permeabilities are readily explained by anomalous samples or anomalous measurements.

7.4.3.7 Discussion of the Classical Kozeny–Carman Model

Given the simplicity of the classical Kozeny–Carman model, it works surprisingly well. Pore casts of sandstones (Figure 1.2b; Pittman, 1984) clearly show that the flow path has a variable radius. The classical Kozeny–Carman model apparently treats this cross-sectional area variation better than the GEC model. However, even for crystalline rocks in which the cross-sectional area is presumably more nearly uniform, the classical K–C model is best (Figure 7.7).

It has been recognized by most investigators that the S_V measured by image analysis is subject to limitations in resolution. The S_V values are smaller than those estimated from mercury porosimetry or from gas adsorption. Apparently, the limitation in resolution is advantageous for the classical K–C model. However, note that some of the S_V values (i.e., m) in Table 7.2 are from capillary displacement (i.e., Wyllie and Rose (1950b)). The influence of resolution deserves additional study. We believe that a primary reason why the S_V from image analysis works in the K–C model is because it depends strongly on the size distribution of the pores. The ellipsoidal model presented in Chapter 4 supports this reasoning.

In conclusion, the available data support the classical Kozeny–Carman model as the better model.

7.4.4 Empirical Relations Between Pore Structure and Permeability

An empirical relation between pore structure parameters and measured permeability is an alternative to the phenomenological Kozeny–Carman approach of predicting permeability. In the empirical approach, many pore parameters are regressed with the measured permeabilities to find some relation. A dis-

advantage of this approach is that the understanding of the physics of why these particular pore parameters control the fluid flow is not advanced. The empirical relations *can* provide a consistent relation between pore structure parameters and permeability for the rocks used to determine the empirical relations. However, there is no assurance that the relation will work for a slightly different rock type or account for anomalous behaviors. In particular, it is not clear that the empirical relation will place similar levels of significance on the same pore structure parameters for different rocks. Rose (1986) has said, "Indeed, the uncertainties about the meaning of (empirical) values for permeability are all the more troubling when it is remembered that empirical correlations that are not rooted in a plausible physical model inherently are arbitrary and untrustworthy."

Empirical correlations between permeability and pore structure have not been studied as well as the model approaches. Semi-quantitative empirical relations were discussed in section 7.4.1. Ehrlich (1983, 1984) and Ehrlich *et al.* (1984) have used the empirical approach to predict permeabilities from feature parameters measured on digital transmitted light images. They used a general correlation approach to show that a few parameters can be put into an equation which adequately estimates permeability. In their example, a relation was established between permeability and (1) what appears to be the number fraction of pore throats with sizes 380 to 400 μm and (2) the number of pores with 22-fold coordination. Methods used to measure the throat sizes and coordination numbers were not given in the paper. A second relation was given between the log permeability and (1) the "ratio of mean smooth pore area to mean rough pore area" and (2) the volume percentage of a specific class of "small isolated moldic pores." Ehrlich *et al.* (1984) state that for other rocks, a subset of 96 pore structure parameters yields similar relations which "estimate" permeability. Presumably, the subset of parameters is different for

each reservoir rock. Thus, the information gained from one rock will be of little value for understanding the behavior of other rocks.

The two different forms for the empirical relation (linear and logarithmic) and the regression analysis yielded *different* significant pore structure parameters for the two relations. The difference emphasizes that there is no physics involved, merely the best approximation of data with a mathematical curve composed of many fundamental functions.

7.4.5 Variational Methods and Fluid Permeability

Variational methods can be used to estimate upper bounds on fluid permeability in a stochastic medium. The hope, as yet unrealized, is that the upper bound will be a good estimate of permeability. The medium is described by two-point (i.e., autocovariance) and higher-order spatial correlation functions, thus giving the stochastic description. The bound on permeability is found by minimizing the rate of energy dissipation by an incompressible fluid "creeping" through the medium. This minimization problem is a boundary value problem subject to conditions on the stress field at the pore-solid boundary. The details of the problem formulation and solution by variational methods is beyond the scope of this investigation. The variational approach does, however, offer an application for autocovariance functions obtained from digital SEM images of sandstones (Chapter 6). Further, the method offers insight into stochastic models of pore structure and the information contained in the covariance.

Berryman (1983,1985ab) has recently made significant advances in the calculations of upper bounds on permeability by variational methods. The salient results of earlier work and Berryman's work will be presented below. The upper bound given by Weissberg and Prager (1962) is computed from autocovariance functions of digital SEM images of sandstones. The limitations of

variational bounds and the origin of these limitations are discussed.

7.4.5.1 Previous Studies of Variational Bounds on Permeability

Prager (1961) derived a method for computing the upper bound on permeability from two- and three-point correlation functions of a porous medium. The mathematics are advanced, but the physical concepts are straightforward. The upper bound on permeability is found by minimizing the energy dissipation due to an incompressible fluid flowing through a porous medium. Energy dissipation is described by a "trial stress distribution," the two-point, and the three-point correlation functions of the medium. A guess is made as to the general form of the trial function. Next, a specific form is found which minimizes the energy loss. This is termed a "variational approach," and amounts to finding the specific form of the trial function which minimizes a complicated function of the trial function.

Prager (1961) used a simple trial function and other simplifications to obtain an upper bound which depends only on the two-point spatial correlation function. Weissberg and Prager (1962) used an approximation of the three-point correlation function to obtain a better (i.e., lower) upper bound which also depended only on the two-point correlation function. The Weissberg and Prager (1962) upper bound k_{W-P} is given by

$$k_{W-P} < \frac{0.9\Phi}{(1-\phi)^2}\,, \tag{7.40}$$

where

$$\begin{aligned}\Phi \;=\; & \frac{9}{8\phi}\left[\int_0^\infty \frac{S(x)}{x^2}\left(\int_0^x y^2 S(y)\mathrm{d}y\right)\mathrm{d}x - \right. \\ & \left. \frac{4}{9}\int_0^\infty \frac{S(x)}{x^3}\left(\int_0^x y^3 S(y)\mathrm{d}y\right)\mathrm{d}x\right] + \\ & \frac{19}{24}\phi\int_0^\infty x S(x)\mathrm{d}x\,,\end{aligned} \tag{7.41}$$

with

$$S(x) = NCC(x) - \phi^2 \, . \tag{7.42}$$

Doi (1976) developed an alternative variational approach which uses void-void, void-surface, and surface-surface correlation functions for the description of the porous medium (i.e., only two-point correlation functions).

Berryman (1983) compared Prager's (1961) and Doi's (1976) bounds for flow through a random aggregate of hard (impenetrable) spheres. He found that Doi's bound was better, however, he also concluded that the two-point bounds alone were not adequate for a porosity of less than 50% (i.e., all rocks of interest) and that the three-point correlation is required.

Berryman (1985a) compared various bounds for flow through interpenetrable spheres. The interpenetrable sphere model is one form of the Boolean stochastic model developed by Matheron (see section 7.3.3). The generalized relation for the n-point correlation function of interpenetrable spheres, given by Torquatto and Stell (1983b), is a specific form of the fundamental relation (Eqn. (7.28)) for the Boolean model. In the porosity range of our interest, Berryman found Prager's (1961) three-point bound to be two or more orders of magnitude larger than an "empirical Kozeny–Carman" relation. Berryman (1985a) introduced a new trial stress distribution function, termed the "Gaussian trial function," which gives much better agreement with his Kozeny–Carman relation. This is a significant advance for the variational method of permeability estimation. Still, the upper bound is more than an order of magnitude greater than the Kozeny–Carman relation for porosities less than 20%. There is a possibility of improving the bound by a method, also presented by Berryman (1985a), which uses the three-point correlation function in addition to the two-point function. We can gain insight by looking at Berryman's results and alternative forms of the Kozeny–Carman relation.

7.4.5.2 Kozeny–Carman Relations for Interpenetrable Spheres

Berryman (1983, 1985a) compares his bounds from the Gaussian trial function with an "empirical correlation due to Kozeny and Carman" of unstated origin,

$$k_{\text{BK-C}} \simeq \frac{1}{45}\frac{\phi^3 R^2}{(1-\phi)^2} \,. \tag{7.43}$$

A similar relation can be obtained from the classical Kozeny–Carman model (Eqn. 7.31) using a specific surface relation for interpenetrable spheres and Archie's formation factor relation. The two-point correlation function for interpenetrable spheres is given by (Berryman, 1985b)

$$S_2(x) = \exp(-\rho V_2(x)) \,, \tag{7.44}$$

with $V_2(x)$ given by

$$V_2(x) = \begin{cases} (4\pi R^3/3)\,(1 + (3x/4R) - (x^3/16R^3)) & \text{for } x/R \leq 2 \\ (8\pi R^3/3) & \text{for } x/R \geq 2 \,, \end{cases}$$

where ρ is the number of spheres per unit volume, R is the radius of the spheres, and ϕ is the resulting porosity. These last three parameters are related through

$$\phi = \exp\left(\frac{-\rho 4\pi R^3}{3}\right) \,. \tag{7.45}$$

The specific surface is given by

$$S_V = -4S_2'(0) \,. \tag{7.46}$$

Taking the derivative of Eqn. (7.44) and combining with Eqn. (7.46) yield

$$S_V = 4\pi R^2 \rho \phi \,. \tag{7.47}$$

Archie's relation is given by

$$F_R = \phi^{-2} \,. \tag{7.48}$$

Combining Eqns. (7.31), (7.47), and (7.48) yields a "tortuous" Kozeny–Carman relation for interpenetrable spheres,

$$k_{\text{TK-C}} = \frac{\phi^2 R^2}{9k_0(\ln\phi)^2} \,. \tag{7.49}$$

As a simpler alternative, we can use the classical Kozeny–Carman relation (Eqn. (7.29)) with a constant value for the "Kozeny constant", $\acute{k}$, given by

$$\acute{k} = k_0(L_e/L)^2 = 5 \,. \tag{7.50}$$

Combining Eqns. (7.29), (7.47), and (7.50) yields a "simple" Kozeny–Carman relation

$$k_{\text{SK-C}} = \frac{R^2}{9\acute{k}(\ln\phi)^2} \,. \tag{7.51}$$

Archie's relation has not been used in Eqn. (7.51). Using Archie's relation (i.e., accounting for variation in tortuosity) is probably a more realistic approach for interpenetrable spheres because the model resembles a consolidated medium more than a packed powder at the porosities of interest.

Figure 7.9 is a plot of Berryman's Kozeny–Carman relation (Eqn. (7.43)), the simple Kozeny–Carman relation (Eqn. (7.51)), and the tortuous Kozeny–Carman relation (Eqn. (7.49)) for the interpenetrable sphere medium. Also shown are the upper bounds estimated by the Weissburg-Prager bound and Berryman's Gaussian trial function. All values have been normalized by R^2. Berryman's K–C relation and the tortuous K–C relation are very similar in behavior, differing by a factor of 2 at 50% porosity and about a factor of 4 at 5% porosity. In the practical porosity range of less than 40%, these two relations differ greatly from the simple Kozeny–Carman relation (e.g., a factor of 200 at 5% porosity). Note that the behavior of the simple K–C relation is very similar to both variational bound estimates, indicating that the variational bound does *not* reflect the tortuosity variation of the material.

7.4.5.3 Upper Bounds on Permeability from Image Data

Equation (7.40) was used to compute upper bounds on permeability from the autocovariance measured on digital images of sandstones. Results are not presented because the estimates were so poor. For some rocks, the estimates were negative. For others, upper bounds were hundreds of darcies. The only practical use for these values may be to detect samples in which permeability was dominated by fractures in cores, or to detect errors in permeability measurements. Such anomalies are readily detected by simpler means.

7.4.5.4 Discussion of the Variational Method

The variational method is closely tied to stochastic models of pore structure. The Joshi–Quiblier model (section 7.3.2.2) is determined solely by the autocovariance of the medium. Because of the dismal performance of the variational bounds, the predictions of tortuosity and topology from the stochastic model will probably be meaningless.

The advances by Berryman (1985ab) are inspiring. But we question whether the three-point correlation functions will provide the additional discriminative information which is required to improve the estimates of upper bounds. The fundamental assumption of the variational method is that all of the geometric and connectivity information necessary to determine the permeability of the medium is contained in the two-point and three-point correlation functions. It is well-known that the two-point correlation function, the autocovariance, is non-unique. Two different structures, one with connected pores and one with isolated pores, can have *identical* autocovariance functions. The three-point correlation function is strongly bound by values of the two-point correlation function; Berryman (1985a) gives several of these bounds. Because the two-point functions are similar for very different pore structures (see Chapter 6),

there is no reason to expect that the three-point functions will be significantly dissimilar. Thus, the three-point functions are not expected to provide much additional discrimination.

The permeability behavior found from the variational models may tell us more about what can be expected from the stochastic models of pore structure. However, the classical Kozeny–Carman model performs much better and is preferred for practical applications.

7.4.6 Electrical Properties and Pore Structure

Only one previous study was found which relates directly observed pore structure in sandstones to electrical properties. Winsauer *et al.* (1952) showed an empirical non-linear positive correlation between "packing index" and formation factor. Recall that the packing index is the ratio of grain-grain surface area to grain-non-grain surface area.

Recent studies by Lysne (1983) and Korringa (1984) may be useful for comparing model predicted geometric structure with pore structure from direct analysis. Lysne (1983) developed a model for the high-frequency electrical response of wet rocks which yields distributions of pore shapes. The distribution is the volume fraction in aspect ratio classes. Prolate ellipsoids were used as the fundamental shape and the model was applied to 3 sandstones. For the rocks in our study, oblate ellipsoids yield a better approximation of the pore space. Lysne *et al.*, (1981) measured pore orientation on digitized photomicrographs and concluded that the pores were randomly oriented. In a more thorough examination of the samples, Duda and Pitman (1982b) concluded that the pores were more tabular than tubular, on the basis of F values. Although, Duda and Pitman (1982b) made several errors in computing F (see Chapter 2), the corrected results also support the oblate shape. The aspect ratio distributions, for prolate ellipsoids, calculated by Lysne (1983) are con-

sistent with our direct analysis results. For each sample, more than 80% of the pore volume was contained in pores with aspect ratios larger than 0.1. Pore size is not a factor in the model. Presumably, oblate ellipsoids could be used in the model. It would be interesting to compare the model results, from oblate ellipsoids, with the results of direct analysis.

Korringa (1984) showed that certain assumptions used by Lysne (1983) were not necessary and gave a formulation which contains "purely geometrical" parameters. In themselves, these geometrical parameters do not have a geometric interpretation. Presumably, they can be associated with simple shapes (e.g., spheroids) as was done by Lysne (1983). Inversion of experimental data for pore shape may then be compared with pore structure parameters obtained by stereological inversions.

7.4.7 Elastic Properties and Pore Structure

The influence of pore structure on the elastic response of rocks has long been recognized. Because of the highly compliant nature of low-aspect ratio cracks, their influence has been most thoroughly studied (see Simmons *et al.*, 1975, for a brief review). These studies have largely been indirect or theoretical. A few studies (Simmons *et al.*, 1975; Hadley, 1976) have used direct analysis of cracks and correlation with elastic properties.

Apparently, only Wilkens *et al.* (1986) have correlated direct pore analysis of sandstones to compressional wave velocity. Their study was limited to the estimation of the volume fractions of subjective "pore classes" and did not include dimensional measurements. Tatham (1982) gives a lucid review of the influence of pore geometry on the V_P/V_S ratio of rocks. He discusses the well-established links between lithology and elastic wave velocities. Because of the importance of pore shape, he suggests that direct observations of pore and crack geometry should be given high priority. He considers pores with

aspect ratios between 1 and 0.1 to be most significant in sandstones.

7.4.7.1 Crack Models

Aspect ratio modeling (Toksöz *et al.*, 1976; Cheng and Toksöz, 1979) is one method for describing the pressure dependence of velocity in a rock. The aspect ratio is the ratio of the minor to the major axis of an oblate spheroid. In order to account for the typical increases in velocity with increasing pressure, very small volume fractions of low aspect ratio cracks are required. Cheng and Toksöz (1979) inverted measured velocities to obtain the aspect ratio distributions for Navajo sandstone, Berea sandstone, and Boise sandstone, as well as other rocks. For each sandstone, more than 90% of the porosity was assigned to equant pores. This volume fraction is the difference between the measured bulk volume and the pore volumes assigned to other aspect ratio classes. The volume of equant pores is essentially inseparable from the matrix elastic moduli and, therefore, is unresolved. More than 99% of the porosity is assigned to the two classes 0.1 and 1.0 aspect ratios.

It is unlikely that direct analysis will be able to characterize the low aspect ratio pores (less than 1% of the porosity, $< 0.2\%$ bulk volume) in a manner which allows comparison with aspect ratio inversions. Direct analysis is well-suited for characterizing the remaining 99% of the porosity, which is poorly resolved by the aspect ratio model. We note that aspect ratio modeling provides no information on pore size.

The specific surface represented by the low aspect ratio cracks is reasonable. In sandstones, these cracks presumably occur at intergranular contacts (Tatham, 1982). For Berea sandstone, the cracks with aspect ratios between 10^{-2} and 3×10^{-3} represent S_V of 0.14 μm^{-1} (assuming semi-major axes of 10 μm). This is roughly one-quarter of the specific surface estimated from the grain size distribution. Stereological measurement of grain-grain contact

surface area may be a good approach for studying the low aspect ratio cracks.

An alternative to the emphasis on *change* in velocity with pressure, is the modeling of a set of samples at a single pressure (Wilkens *et al.*, 1986). This modeling uses identical theory, but for a different purpose. Wilkens *et al.* (1986) used point counting to estimate the relative fractions of intergranular pores, connective pores, and micro-pores in 20 sandstones. Aspect ratios were assigned to each of these classes, and forward modeling was used to predict dry acoustic velocities. Different aspect ratios were tried until the "best agreement" with measured velocities was found. Because forward modeling, rather than an inversion was used, there may be other combinations of aspect ratios which fit equally well. The intergranular pores and micro-pores represent most of the pore volume. The best aspect ratios for these classes were 0.15 and 0.125, respectively. However, the fit with aspect ratios of 0.25 for both classes was very good also. These values agree with the aspect ratios found from direct analysis. The best aspect ratio for the connective pores was 0.05. This value is larger than those needed to describe the pressure dependence.

In summary, it is difficult to compare stereological results with aspect ratio modeling of pressure dependence because the two methods are most accurate in different aspect ratio regimes. When aspect ratio modeling is used at a single pressure, there is general agreement with stereological results.

7.4.8 NMR and Pore Structure

Nuclear magnetic resonance techniques (NMR) can be used to study the pore structure in porous media. Based on the theoretical work of Korringa *et al.* (1962), Seevers (1966) developed a method to measure the specific surface of a porous media (i.e., sandstones). Timur (1969ab) extended Seevers' model and used NMR results to estimate moveable fluid and permeability of sandstones. The interpretational model divides the pore spaces into three classes

based on their specific surfaces. We are interested in this model because a similar division of specific surface by volume fraction is found through the size–shape inversion of point-sampled intercepts (Chapter 4). Comparisons between these two distributions of specific surface may serve as verification of the two approaches.

We do not have NMR data for our samples, nor do we make quantitative comparisons here. Our intention is to show the potential application of the image derived information. Such an application improves our understanding of the pore structure.

7.4.8.1 Specific Surface from Relaxation Times

The theory relating the NMR signal to specific surface is described by Seevers (1966) and Timur (1969ab). We present only a glimpse of their work here. The spin-lattice relaxation data are broken down into three components with relaxation times T_{1A}, T_{1B}, and T_{1C}. Each relaxation time is directly related to the specific surface of the corresponding component (i.e., fraction of pore volume). This relation is given by

$$S_V = \frac{\phi}{h_s r_s}\left[\frac{1}{T_1} - \frac{1}{T_b}\right] , \tag{7.52}$$

where h_s is the thickness of the fluid (boundary) layer influenced by the grain surface, T_b is the bulk relaxation time for the liquid (away from the surface), T_{1s} is the relaxation time in the boundary layer, τ is the residence time in the boundary layer, and $r_s = (T_{1s} + \tau)^{-1}$. Seevers (1966) and Timur (1969ab) do not actually compute values for specific surface. Rather, they combine the relation for specific surface with other models (e.g., Kozeny equation, empirical relations) to yield predictions of physical properties (e.g., permeability, free fluid). The calculation of specific surface requires an estimate of the parameters h, r_s, and the measurement of T_b. The estimate of the first two, combined

with the Kozeny constant, $\acute{k}$, from the Kozeny–Carman relation, are found empirically for rocks from each reservoir (Seevers, 1966; Timur, 1969ab).

Cowgill *et al.* (1982) apparently computed S_V from the T_1 components. Using a Kozeny–Carman relation, presumably with an assumed tortuosity, they then computed the permeability associated with each S_V. They used parallel, serial, and network averaging of these permeabilities to estimate permeability of the bulk rock. Estimated permeability was close to measured permeabilities for the network model with a coordination number of 3. They may have actually used the relation between relaxation times and permeability given by Seevers (1966) and bypassed the calculation of specific surface because they do not give S_V results.

Loren and Robinson (1970) also developed a model which relates the NMR response to the pore size distribution in rocks. They derived relations explicitly for comparing NMR measurements with pore size determined by mercury porosimetry. The model may also be suited for comparing NMR results with the stereologically determined pore size distribution.

In summary, the simple model developed by Seevers (1966) appears to be well-suited for comparison with direct pore structure analysis because the parameters of the NMR model have a direct geometrical interpretation. The specific surface distribution determined by NMR methods may serve to verify the volume distribution of size–shape found through stereological methods, or may serve as an additional *a priori* constraint.

7.5 Discussion and Summary

From comparisons of various measures of pore geometry, we conclude that several methods characterize size well, but shape is not as well-characterized. Alternatively, all sandstones may have similar average pore shapes.

Stochastic models offer concise ways to express complex structural information. They may also be able to predict structural information, or indicate information which was not known to be contained in structural parameters.

Empirical correlations currently dominate the (semi-quantitative) relations between pore structure and physical properties. We have avoided direct empirical relations between image measures and physical properties when there is an unknown transform between the image measures and the geometric structure. Understanding the relations between geometric parameters and physical behavior is sufficiently difficult. Use of arbitrary, non-stereological feature parameters obscures the geometric significance.

The classical Kozeny–Carman model is superior to the geometric equivalent conduit model for permeability in rocks. The success of S_V in describing the flow properties is believed to be due to it reflecting primarily the sizes of the pores.

Variational methods for estimating upper bounds on permeability are not useful in a practical sense. However, they may offer further insight on stochastic modeling of pore structure. For example, variational bounds indicate that stochastic models of pore structure lack tortuosity information.

Models for physical properties were discussed here because it is desirable to find or develop models which have direct geometric interpretations. A geometrical interpretation allows comparisons with pore structure measured by direct analysis. Models constructed for the sole purpose of describing a physical *behavior* are not likely to correspond geometrically with the structure of the material. Models for physical properties exist which use realistic geometrically defined parameters. These models should be exploited in conjunction with direct analysis of pore structure. The bulk stereological parameters, which are free from assumptions on shape, should be used wherever possible in the formulation of new models of physical properties.

In general, we believe that a promising approach to improve our understanding of pore structure is the application of physical property models. First, using physics as a foundation, develop a model with direct geometric interpretations. Next, select or develop the image analysis methods necessary to measure the geometry. Lord and Wilson (1984) have said that "All description is *purpose-oriented*, and the choice of descriptive method must, in practical situations, be guided by the problem context." Let the physical model define the context. Of course, there is still much to learn about the *basic* geometric structure in the rocks, but this too should be well-focused.

Figure Captions

Figure 7.1. Comparisons of S_{Vp} obtained by different methods. The abscissa values are S_{Vp} from the lineal analysis. Ordinate values are from feature analysis of SMS images and from *NCC* spatial correlation. The straight line is for a one-to-one correspondence.

Figure 7.2. Diameter of the mean-pore-volume-equivalent sphere versus the *NCC* range estimate a^*. The straight line is for a one-to-one correspondence. The range estimate a^* for sample 2523 was high. Visual examination gives an estimate of 70μm. The least squares fit line, omitting sample 2523, is given by

$$a^* = 0.95 D_{V_p} + 6.4\mu\text{m} \quad R = 0.96$$

Figure 7.3. Diameter of the mean-pore-volume-equivalent sphere versus the maximum granulometry diameter. Only two images were used for each

of the three samples (2686, 2841, and 2843) which depart the most from the one-to-one correspondence.

Figure 7.4. Fischmeister shape factor versus S_{Vp}. The lines represent oblate ellipsoids of constant semi-major axis length, $D_1/2$, and varying aspect ratios. The data points are from Ruzyla (1984) and the number next to each data point is the mean maximum Feret diameter, in microns, of the pore features.

Figure 7.5. Specific surface of the Poisson model as a function of porosity for different resolutions (pixel sizes). (*a*) 5, 10, 20, and 50 μm resolutions. (*b*) 0.5, 1, and 5 μm resolutions.

Figure 7.6. Schematic diagrams of: (*a*) the classical Kozeny–Carman (C K-C) model and (*b*) the geometric equivalent conduit (GEC) model.

Figure 7.7. Comparison of the classical Kozeny–Carman model and the GEC model using data from the literature. The straight line represents a one-to-one correspondence.

Figure 7.8. Comparison of predicted permeability from the classical Kozeny–Carman model and measured permeability.

Figure 7.9. Permeability models for the penetrable sphere medium. Note the similar behavior of the Weissberg–Prager variational bound, the Berryman Gaussian bound, and the simple (non-tortuous) Kozeny–Carman relation. $k_0 = 2.5$ for all but the simple K–C relation.

Table 7.1

Specific Surface from Grain Size Distribution

Sample Number	S_W (cm^2/g)		ρ_g (g/cm^3)	S_{Vp} (μm^{-1})	
	< 4.5 phi			< 4.5 phi	
	Inc.	Omit		Inc.	Omit
2124	698.5	560.0	2.60	0.709	0.568
2509	607.3	594.6	2.61	0.582	0.570
2513	659.6	597.9	2.59	0.613	0.555
2519	268.5	256.4	2.61	0.509	0.486
2521	565.0	529.1	2.56	0.468	0.438
2523	561.3	492.6	2.62	0.652	0.572
2686†					
2687	1113.7	496.1	2.65	1.292	0.575
2700	705.6	555.8	2.63	0.601	0.473
2704	664.8	581.8	2.60	0.723	0.632
2710	648.7	591.1	2.56	0.408	0.372
2841†					
2842†					
2843†					

NOTES: Porosity used in Eqn. (7.2) was taken from Table 4.1. Inc. values include the < 4.5 phi class. Omit values do not include the < 4.5 phi class.

† Grain size distribution was not measured.

Table 7.2a

Data for Classical K–C and GEC Permeability Comparison

Material	ϕ^*	F_R	m (μm)	k_{meas} (md)	Ref†
Sintered Pyrex 1	0.37	4.4	0.4	8	[1]
Sintered Pyrex 2	0.29	6.2	10	3950	[1]
Sintered alundum	0.24	11.5	1.9	64	[1]
Berea ss.	0.23	11.7	7	890	[1]
Nicholls Buff ss.	0.20	11.7	3.6	230	[1]
Oligocene ss.	0.22	13.1	5.5	340	[2]
F151 Penn. ss.	0.16	20.1	5.0	122	[2]
F154 Penn. ss.	0.18	14.0	5.0	267	[2]‡
F220 Penn. ss.	0.20	13.9	6.4	336	[2]‡
F250 Penn. ss.	0.21	13.0	6.1	516	[2]
F252 Penn. ss.	0.18	16.9	6.3	296	[2]‡
F228 Penn. ss.	0.20	17.5	6.3	278	[2]‡
Sherman granite	0.03	880	6	0.1	[3]
Westerly granite					
–(5 MPa)		1030		350×10^{-6}	[3]
–(50 MPa)	0.01	3100	0.1	64×10^{-6}	[3]
–(400 MPa)		16300		4×10^{-6}	[3]

NOTES: After Paterson (1983). Permeability was converted to millidarcies (md). Errors in Paterson's R values (m here) from [2] were corrected.

* Porosity measured at 0.1 MPa.

† References for data.

[1] Wyllie and Rose (1950a,b).

[2] Wyllie and Spangler (1952).

[3] Brace *et al.* (1968) and Brace (1977).

‡ Additional samples from [2], omitted by Paterson (1983).

Table 7.2b

Data for Classical K–C and GEC Permeability Comparison

Material	k_{meas} (md)	k_{GEC} (md)	$\frac{k_{GEC}}{k_{meas}}$	k_{CK-C} (md)	$\frac{k_{CK-C}}{k_{meas}}$
Sintered Pyrex 1	8	15	1.8	9	1.1
Sintered Pyrex 2	3950	6540	1.7	3640	0.9
Sintered alundum	64	127	2.0	46	0.7
Berea ss.	890	1700	1.9	631	0.7
Nicholls Buff ss.	230	420	1.8	168	0.7
Oligocene ss.	340	935	2.7	328	1.0
F151 Penn. ss.	122	513	4.2	157	1.3
F154 Penn. ss.	267	737	2.8	291	1.1
F220 Penn. ss.	336	1210	3.6	446	1.3
F250 Penn. ss.	516	1170	2.3	439	0.8
F252 Penn. ss.	296	943	3.2	302	1.0
F228 Penn. ss.	278	925	3.3	263	0.9
Sherman granite	0.1	16	160	6.3	6.2
Westerly granite					
–(5 MPa)	350×10^{-6}	3900×10^{-6}	11	382×10^{-6}	1.1
–(50 MPa)	64×10^{-6}	1310×10^{-6}	20	42×10^{-6}	0.7
–(400 MPa)	4×10^{-6}	250×10^{-6}	61	1.5×10^{-6}	0.4

NOTES: After Paterson (1983). k_{GEC} values were recomputed using correct $\overline{m}$ from [2]. $k_0 = 2.5$ for all calculations.

Table 7.3

Predicted Permeability from the Classical Kozeny–Carman Model

Sample Number	F_R	S_V (μm^{-1})	ϕ_i (%)	$\overline{k_{meas}}$ (md)	k_{calc} (md)
2124	20.5	0.059	20.5	40	57
2509	16.7	0.035	21.4	326	254
2513	12.1	0.052	21.8	286	216
2519	62.2	0.027	12.1	4.5	17
2521	12.6	0.035	23.6	616	493
2523	21.1	0.063	18.4	22	42
2686	11.8§	0.047	26.8	1300†	353
2687	14.9	0.062	18.6	16	88
2700	12.2	0.061	23.6	295	172
2704	14.5	0.051	19.3	303	143
2710	8.3	0.060	28.9	1454	472
2841‡					
2842‡					
2843‡					

NOTES: ϕ_i was taken from Table 4.1. S_V was taken from Table 4.2. $k_0 = 2.5$ for all calculations.

§ From Koplik *et al.* (1984).

† Permeability estimated from mercury porosimetry data.

‡ No F_R data available.

Figure 7.1 S_{Vp} Comparisons

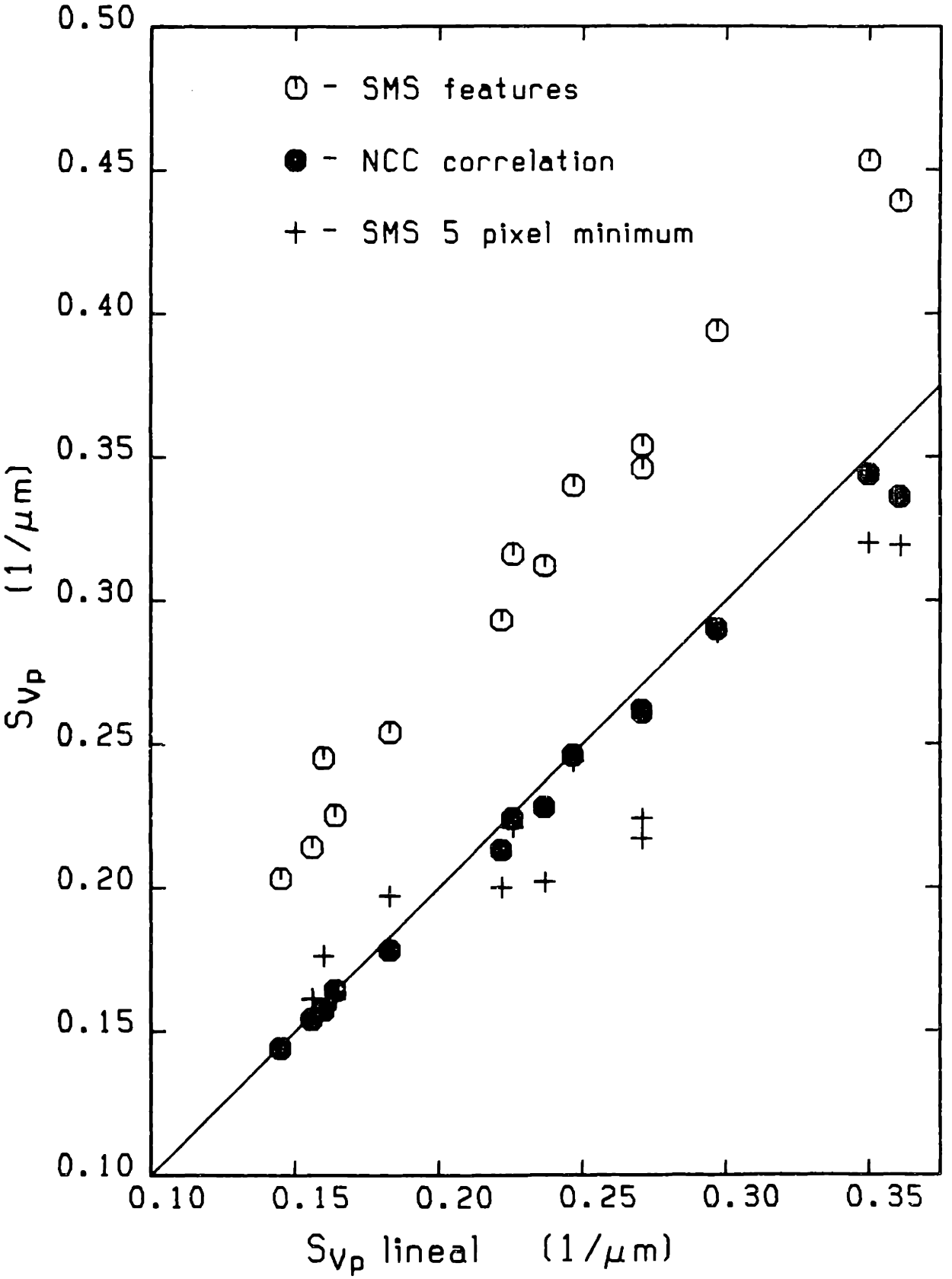

Figure 7.2 $D_{\overline{V_p}}$ versus NCC range estimate a^*

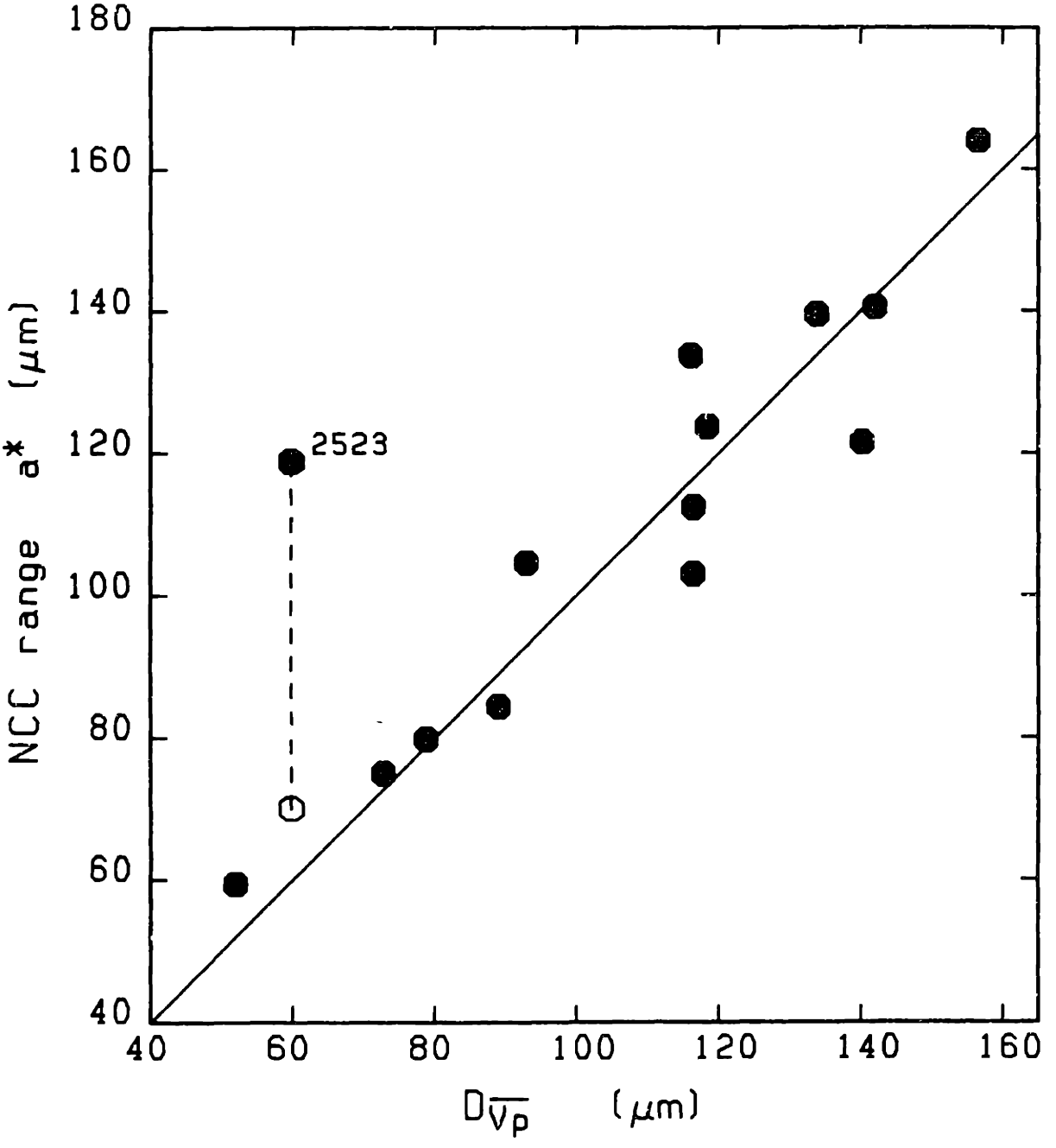

Figure 7.3 $D\overline{v_p}$ versus λ_{max}

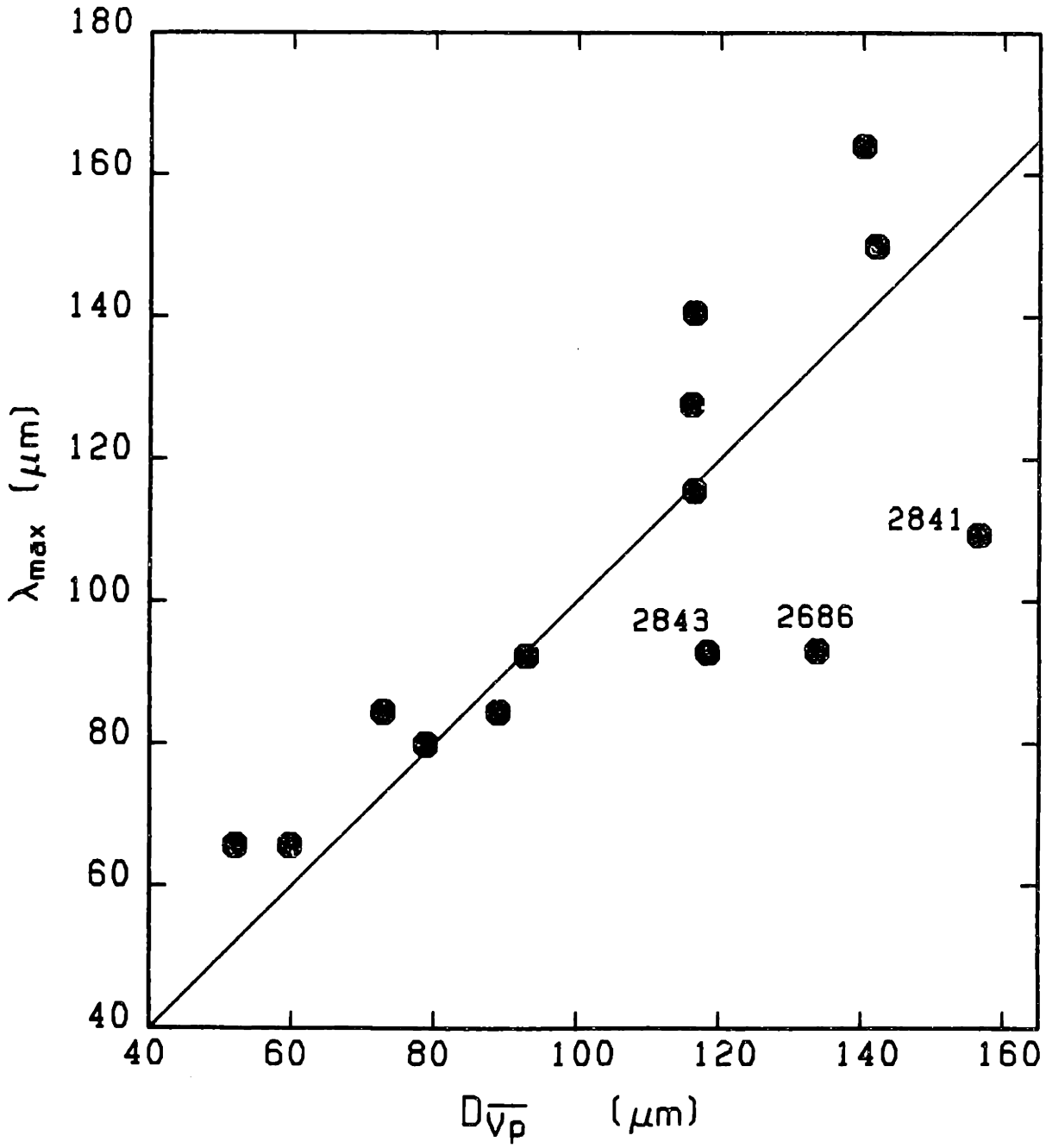

Figure 7.4 Fischmeister Shape Factor versus S_{Vp}

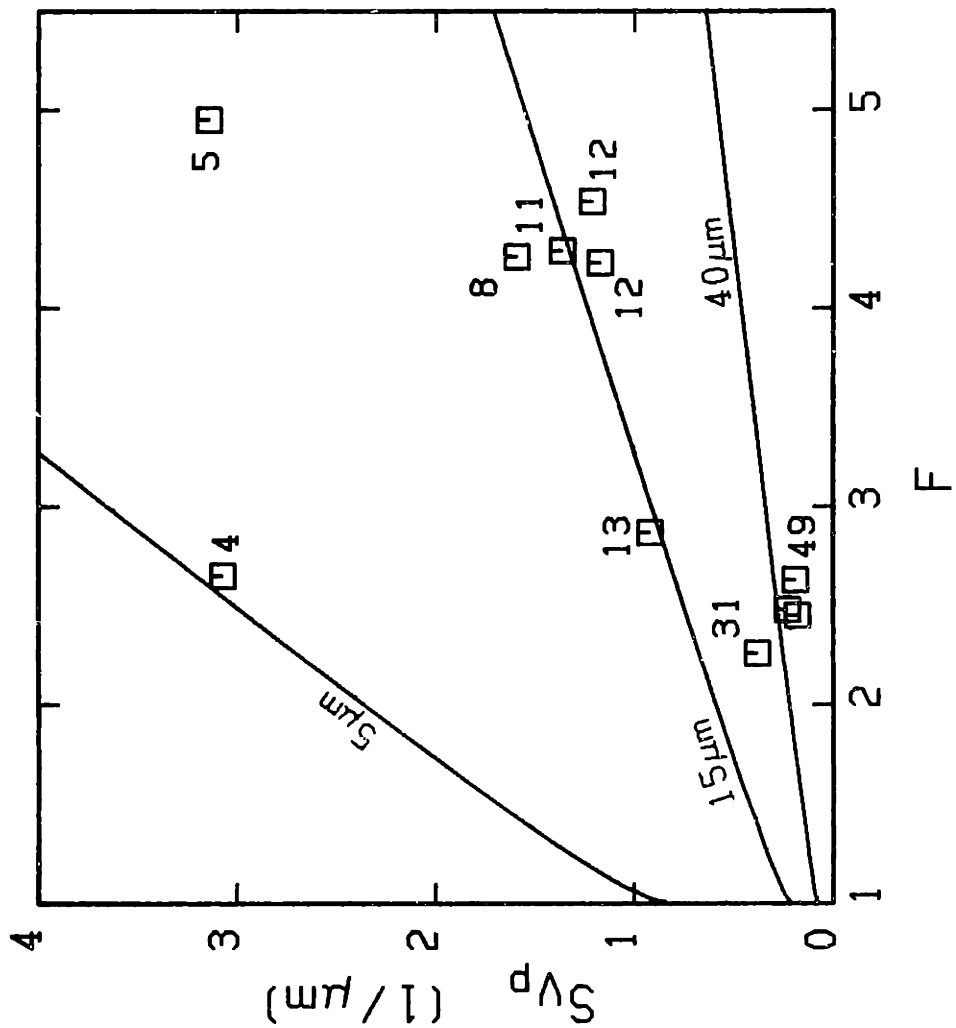

Figure 7.5 Specific Surfac of Poisson Model

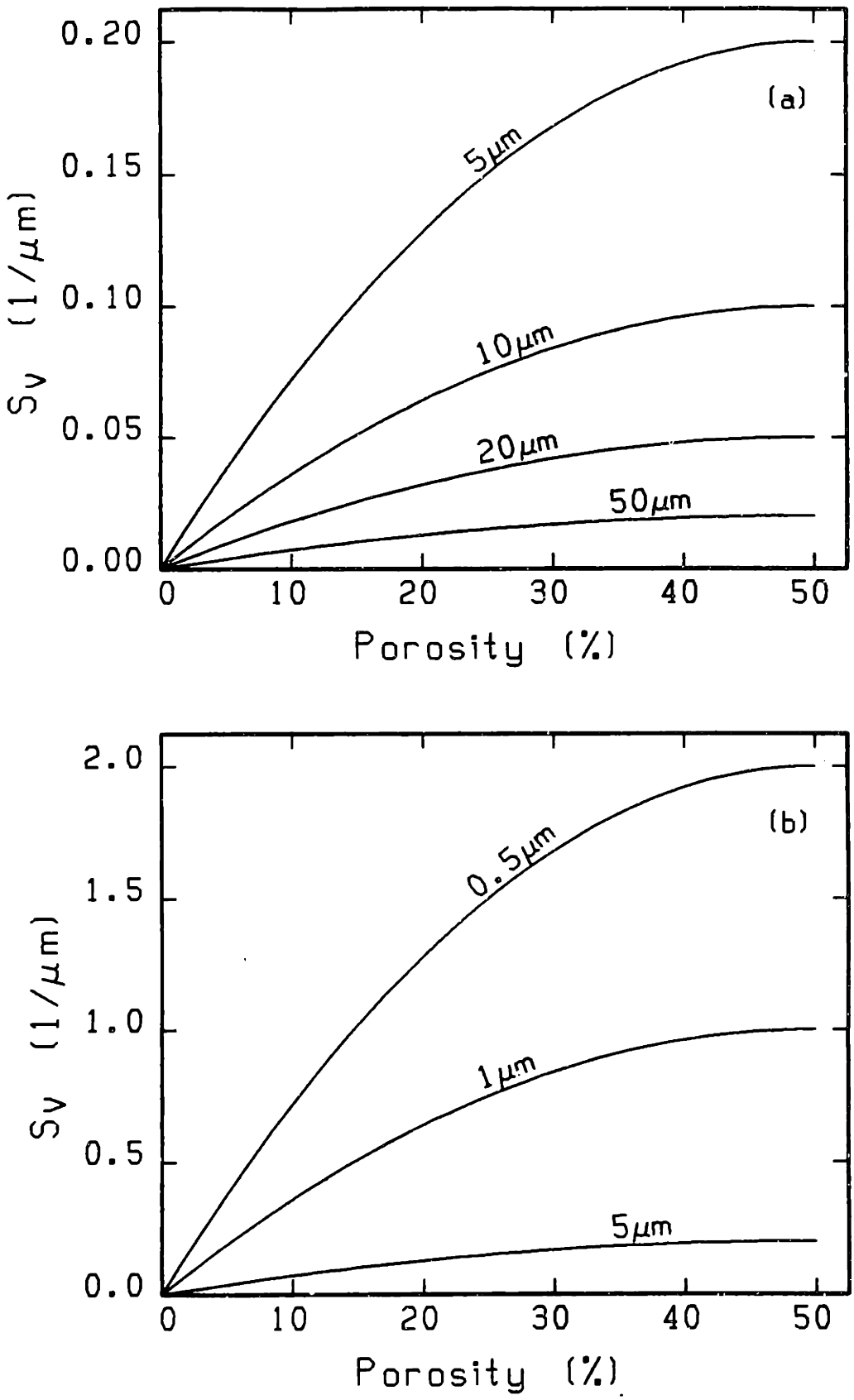

Figure 7.6 Equivalent Conduit Schematics

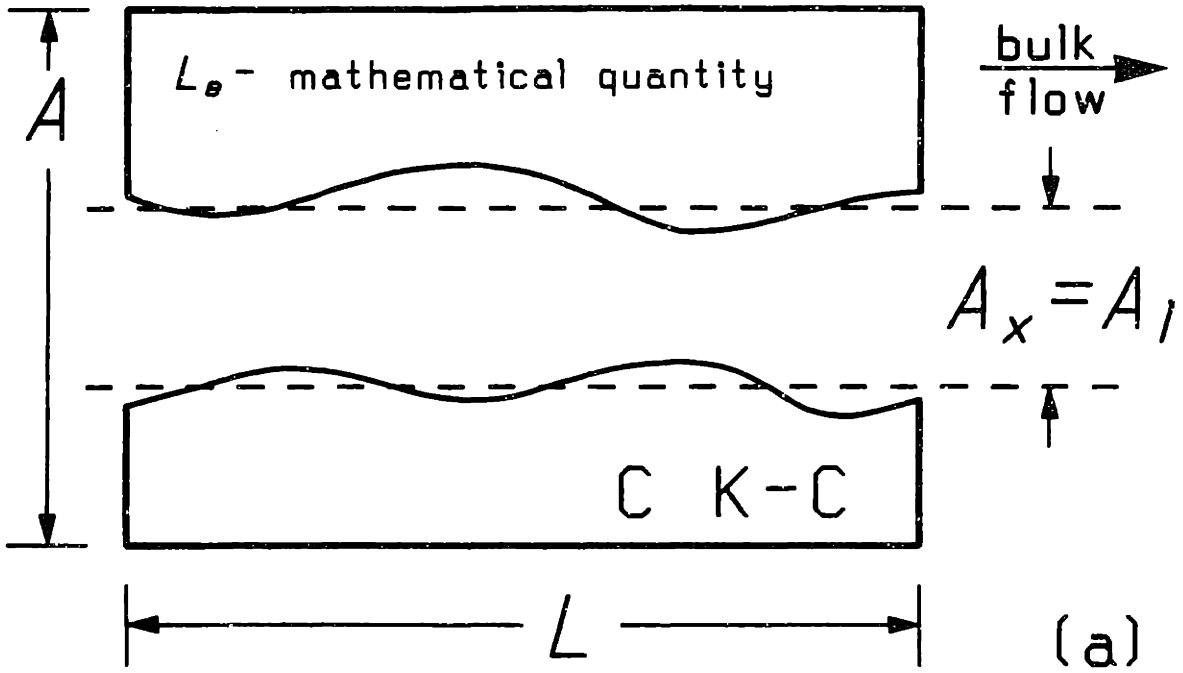

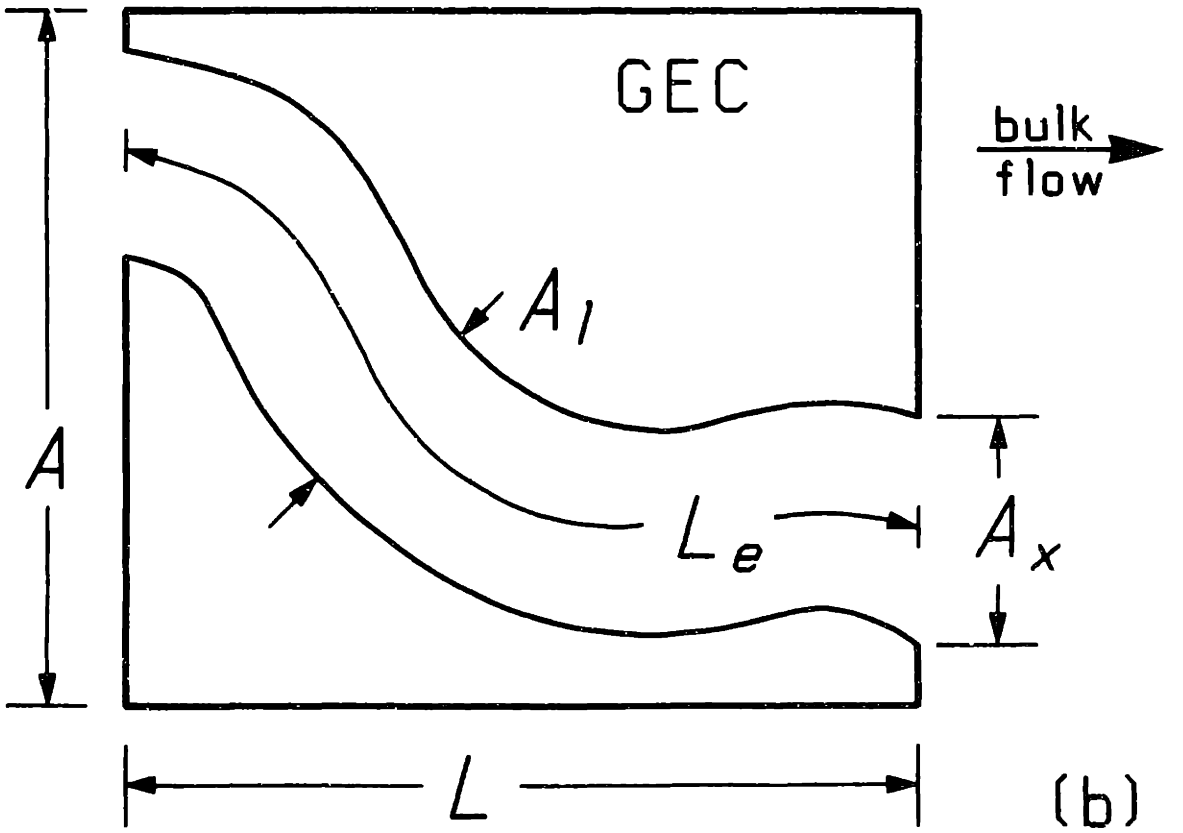

Figure 7.7 Comparison of Equivalent Conduit Models

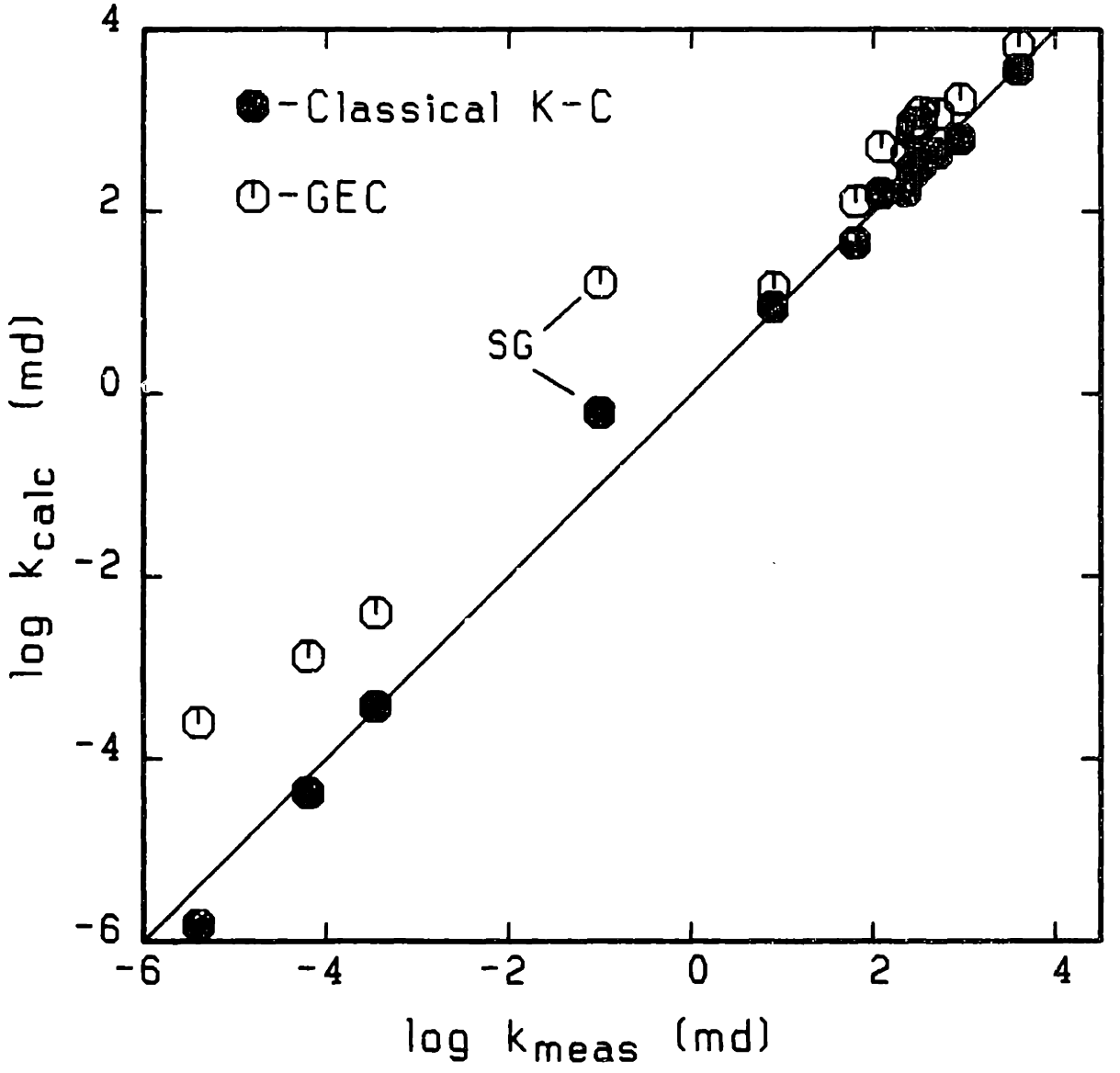

Figure 7.8 Predicted permeability using the classical Kozeny-Carman model versus measured permeability

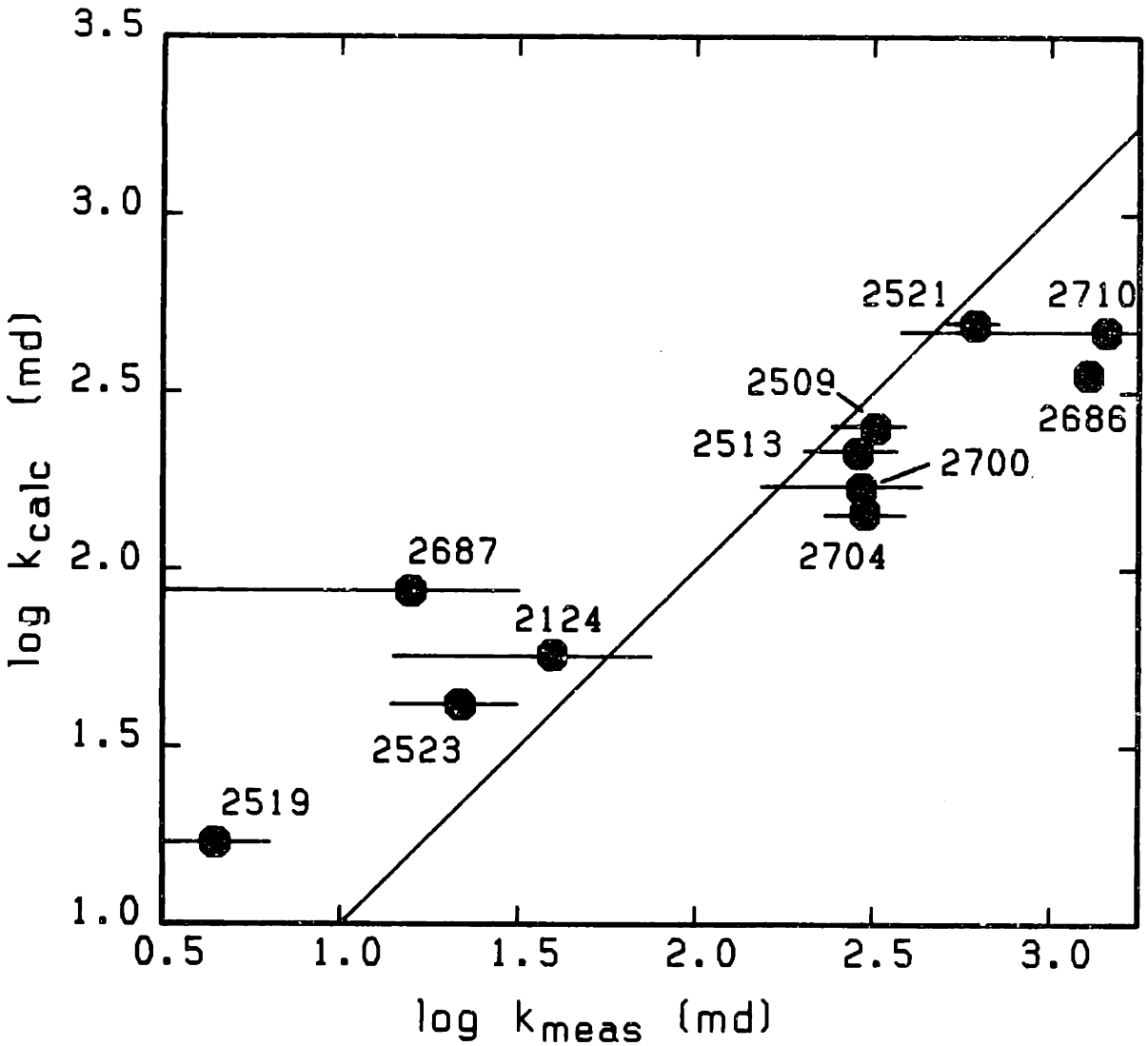

Figure 7.9 Penetrable Sphere Permeability Models

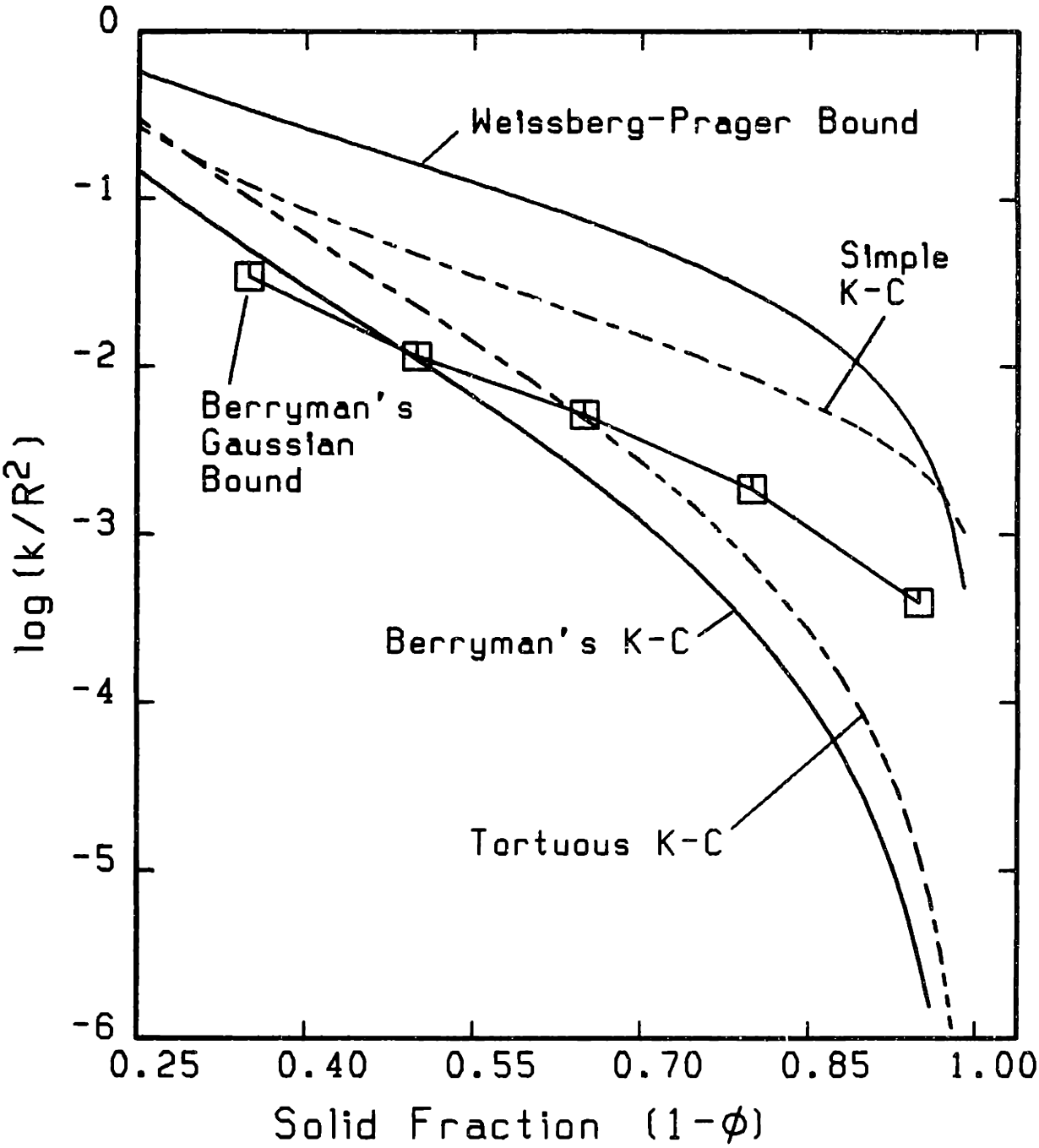

Chapter 8

Summary and Conclusions

In this study, the pore structure of sandstones has been quantified from digital backscattered electron SEM images of polished epoxy impregnated sections. Methods of quantitative stereology, feature analysis, and spatial correlation have been applied. These methods yield unique pieces of information, but they are tied together with stereological concepts. The stereological concepts are essential because they relate measurements made on a plane to three-dimensional *geometric* parameters.

Our review of previous studies showed that many promising methods exist for characterizing sandstone pore structure. Lack of data and absence of systematic data analysis are the primary shortcomings in the current literature. Although many tools for describing structure currently exist, they have been used very little.

Stereological parameters such as porosity (ϕ), specific surface (S_V), and the Fischmeister shape factor (F) have been established previously as useful parameters for describing pore structure. Other parameters with strong significance for describing pore structure have not yet been identified and their nature will depend on the structural information required for specific applications.

Imaging conditions must be controlled carefully to obtain high quality digital SEM images for quantitative analysis. The signal current and dwell time required to obtain true 8-bit resolution in digital images must be established and used. Probe size should be matched to the physical pixel size to represent best the content of the physical pixel area. Specimens should not be tilted with respect to the electron beam to prevent distortion and to reduce contrast due to specimen topography.

The record CRT was the primary source of geometric distortion at the operating conditions used in this study. Direct digitization of the BSE detector signal eliminates this source of distortion and allows recording of the true 8-bit signal. The addition of a lead shield to the Robinson backscattered electron detector provides a more symmetric detector area and further reduces contrast due to specimen topography.

A threshold selection method for dichotomization of full intensity images was developed. The method uses the midpoint between the locations of the primary pore and grain peaks in the intensity histogram. Peak locations and other parameters were determined by iterative least squares fitting of Gaussian curves. The resulting threshold is non-subjective and yields consistent porosity estimates which agree with bulk measurements of porosity. Any disagreement is attributable to insufficient sampling for the scale of heterogeneity in the sample or to subjective bias in the selection of micrograph areas.

Stereological parameters provide fundamental geometric information about the pore structure. The bulk properties of porosity, specific surface, and mean pore volume (interpreted as the "star") require no assumptions about the size and shape of the pore space. The size–shape volume distribution requires assumptions about the nature of the pore space. In turn, the volume distribution satisfies the fundamental bulk properties and yields additional information.

Provided that no subjective bias was introduced, the image measured

porosity was found to be in very good agreement with bulk measurements. Inhomogeneity at the scale of sampling of the digital images could be detected from the experimental and theoretical statistics derived from the images.

If a sufficiently large sample is available, it may be preferable to measure porosity by bulk methods. In this way, a better average may be obtained. Image derived parameters, such as S_{Vp}, can then be related to the bulk porosity. However, if only small samples (e.g., cuttings) are available, the application of stereological methods can yield accurate values.

Specific surface measured by lineal analysis does not indicate strong anisotropy of pore structure in our samples. The observed directional bias in S_V, due probably to imaging artifacts, is smaller than the standard deviations in S_V, but it precludes detection of slight anisotropy.

The mean pore volume, $\overline{V}_p$, computed from point-sampled intercepts, appears to be a good single-size parameter for the pore space. The interpretation of the mean pore volume as the "star", the mean volume seen from each point in the pore space, is free of restrictive assumptions about the pore shape. Mean intercept length computed from line-sampled intercepts greatly underestimates the "average size" of the pores.

Size–shape volume distributions were obtained by inverting point-sampled intercept distributions by least squares methods. Oblate ellipsoids are the best fitting spheroidal shapes and the volume distributions are nearly uniform for the samples studied. Best fitting aspect ratios are between 0.27 and 0.36. The character of the distributions at large sizes corresponds with qualitative petrographic descriptions of the pore space. In addition to providing the best numerical fits, the distributions also satisfy the bulk stereological properties of ϕ, S_V, and $\overline{V}_p$. The distribution is important because it shows how, for example, the surface area is partitioned among the various pore sizes. Otherwise, the bulk specific surface could be satisfied with a single pore size or various

other size distributions. Because of the wide range in S_V in our samples and the restricted range of best fitting ellipsoid aspect ratios, we conclude that S_V is primarily controlled by the size distribution of the pores.

The features in the binary image contain all of the geometric information that is available on a single plane through the material. Thus, the better these features are characterized, the more information we have about the pore structure. Because the pore features in sandstones are very complex, our approach has been to simplify the features by segmentation and then to characterize the simpler features.

Subtractive mask segmentation, SMS, was developed to simplify the complex pore features. SMS performs better than the "cutting" segmentation of Rink (1976a) because SMS preserves all of the porosity, preserves greater detail of the features, and does not fragment the intermediate size features.

Bulk stereological parameters from individual feature analysis include porosity, specific surface, and the Fischmeister shape factor. The porosity is identical to that from other areal analysis methods. The S_V calculated from feature perimeter and area is larger than that obtained from lineal analysis. This bias is probably due to the overestimation of feature perimeter on the discrete grid.

Dynamic feature parameters represent the SMS segmented features very well. The dynamic feature parameters give location, orientation, and anisometry information. Aspect ratios of the dynamic-equivalent ellipses were used to estimate the aspect ratios of the underlying oblate ellipsoids. The estimated ellipsoid aspect ratios agree with those used in the size–shape inversion.

The operation of opening was applied to binary images to yield feature granulometry curves. These granulometry curves basically represent the area-weighted distribution of isometric feature size. As such, they do not represent the largest dimensions of the pore structure. Interpretation of the granulometry curves is currently restricted to *classifiers* of pore structure and factor

analysis. Neither of these is well-developed in terms of a structural interpretation.

The non-centered covariance, *NCC*, has been computed by Fourier and binary methods. Both methods give identical results provided that appropriate procedures are followed for their computation. Specifically, the image must be binary and the transient response must be computed. The porosity estimate from the zero-lag value is identical to the area fraction estimates. Provided that sufficient image area is examined, the behavior of the average of the X and Y orientation one-dimensional *NCC* closely approximates the orientation averaged two-dimensional *NCC*. S_V from the slope of the *NCC* at zero-lag is the same as that from lineal analysis. Slight differences are attributable to intercept sampling criteria. The range of correlation is related to the diameter of the mean pore volume-equivalent sphere. Thereby, it reflects a mean dimension of the pores.

Our study of pore structure was motivated by the desire to relate the physical response of the material to the character of the pore structure. Stochastic models can be used to express the complex pore structure with relatively few parameters. Such models may also be able to reveal (predict) information which is not otherwise known to be contained in pore structure parameters.

We have investigated the character of two simple stochastic models. All properties predicted by the Poisson model can depend only on porosity and the resolution of the simulation. The first-order Markov model was shown to be completely specified by the porosity and S_V of the material (and the resolution of the simulation). Higher order models, such as the Joshi-Quiblier and Boolean models, contain more information about the structure and can express more of the character of the material.

The classical Kozeny–Carman equivalent conduit model for fluid permeability as used by Wyllie and collegues (Rose and Bruce, 1949; Wyllie and

Rose, 1950ab; Wyllie and Spangler, 1952; Wyllie and Gregory, 1955; Wyllie and Gardner, 1958ab) has been shown to be better than the geometric equivalent conduit model used by Winsauer *et al.* (1952), Cornell and Katz (1953), and more recently by Paterson (1983) and Walsh and Brace (1984). The image measured S_V and porosity were used together with the measured formation factors of 11 sandstones to predict permeability using the classical Kozeny–Carman model. The predicted permeabilities for 6 samples are within the range of brine permeabilities measured on 3 orthogonal cores from each sample. Other samples are within a factor of 2.

Although we have identified many significant relations and attributes of pore structure in sandstone, the potential of image analysis methods has just begun to be realized. For example, the data from feature analysis are voluminous, yet primarily the bulk stereological parameters are used. Currently, not even the distribution of feature areas (from individual analysis or granulometry) has been used in a geometric interpretation. Use of other feature parameters appears to rest on the development of models of pore structure and models of physical properties which incorporate such parameters.

References

Abdou, I.E. and W.K. Pratt, 1979, Quantitative design and evaluation of enhancement/thresholding edge detectors, *Proc. IEEE, 67*, pp. 753–763.

Agrawala, A.K. and A.V. Kulkarni, 1977, A sequential approach to the extraction of shape features, *Comp. Graphics and Image Proc., 6*, pp. 538–557.

Aigeltinger, E.H. and R.T. Dehoff, 1975, Quantitative determination of topological and metric properties during sintering of copper, *Metallurgical Trans. A, 6A*, pp. 1853–1862.

Aki, K. and P.G. Richards, 1980, *Quantitative Seismology—Theory and Methods, Volume II*, W. H. Freeman and Co., San Francisco, p. 932.

Alt, F.L., 1962, Digital pattern recognition by moments, *J. Assoc. Comp. Mach., 11*, pp. 240–258.

Anderssen, R.S. and A.J. Jakeman, 1975a, Abel type integral equations in stereology. II. Computational methods of solution and the random spheres approximation, *J. Microscopy, 105*, p. 135.

Anderssen, R.S. and A.J. Jakeman, 1975b, Product integration for functionals of particle size distributions, *Util. Math., 8*, p. 111.

Anderssen, R.S. and A.J. Jakeman, 1976, Computational methods in stereology, in *National Bureau of Standards Special Publ. 431*, E.E. Underwood, R. de Wit, and G.A. Moore (eds.), Proc. Fourth Int. Congress for Stereology, pp. 13–18.

Andrews, H.C., 1974, Digital Fourier transforms as means for scanner evaluation, *Applied Optics, 13*, pp. 146–149.

Anstey, R.L. and D.A. Delmet, 1973, Fourier analysis of zooecial shapes in fossil tubular bryozoans, *Geol. Soc. of Amer. Bull., 84*, pp. 1753–1764.

Archie, G.E., 1942, The electrical resistivity log as an aid in determining some reservoir characteristics, *Trans. AIME, 146*, p. 54.

Archie, G.E., 1950, Introduction to petrophysics of reservoir rocks, *Amer. Assoc. Pet. Geol. Bull., 34*, pp. 943–961.

Archie, G.E., 1952, Classification of carbonate reservoir rocks and petrophysical considerations, *Amer. Assoc. Pet. Geol. Bull., 36*, pp. 278–298.

Baddeley, A. and P. Averback, 1983, Stereology of tubular structures, *J. Microscopy, 131*, pp. 323–340.

Barrett, L.K. and C.S. Yust, 1970, Some fundamental ideas in topology and their application to problems in metallography, *Metallography, 3*, pp. 1–33.

Barrett, P.J., 1980, The shape of rock particles, a critical review, *Sedimentology, 27*, pp. 291–303.

Batra, V.K., 1973, *An experimental investigation of the structure of porous media and its relation to oil recovery*, Ph.D. thesis, University of Waterloo, Waterloo, Ontario, p. 253.

Beddow, J.K., 1984, Recent applications of morphological analysis, in *Particle Characterization in Technology, Volume 2, Morphological Analysis*, J.K. Beddow (ed.), CRC Press Inc., Boca Raton, Florida.

Berryman, J.G., 1983, Computing variational bounds for flow through random aggregates of spheres, *J. Comp. Phys., 52*, pp. 142–162.

Berryman, J.G., 1985a, Measurement of spatial correlation functions using image processing techniques, *J. Appl. Phys., 57*, pp. 2374–2383.

Berryman, J.G., 1985b, Bounds on fluid permeability for viscous flow through porous media, *J. Chem. Phys., 82*, pp. 1459–1468.

Berryman, J.G. and S.C. Blair, 1986, Use of digital image analysis to estimate fluid permeability of porous materials: I. Application of two-point correlation functions, submitted to *J. Appl. Phys.*.

Bisdom, E.B.A., H.A. van Adrichem Boogaert, G. Heintzberger, D. Schoonderbeek and F. Thiel, 1983a, Porosity measurements and form analysis of mineral grains in thin sections from oil-gas reservoir rocks using Quantimet 720 and BESI, *Geoderma, 30*, pp. 323–337.

Bisdom, E.B.A. and D. Schoonderbeek, 1983, The characterization of the shape of mineral grains in thin sections of soils by Quantimet and BESI, *Geoderma, 30*, pp. 303–322.

Bisdom, E.B.A., F. Thiel, B. Volbert and J. Jackman, 1983b, Variations in backscattered electron (BSE) images with a scanning electron microscope (SEM) as applied to mineral grains and excrements in a podzol, to precipitates on a water-tube filter and to bauxite. *Geoderma, 30*, pp. 93–116.

Blatt, H., G. Middleton and R. Murray, 1972, *Origin of Sedimentary Rocks*, Prentice–Hall, New Jersey, p. 634.

Blum, H., 1973, Biological Shape and Visual Science (Part I), *J. Theor. Biol.*, *38*, pp. 205–287.

Bockstiegel, G., 1972a, The correction of edge errors in determination of size distributions with linear scanning instruments—Answers to A. P. Welboren's and O. Meijer's comments, *Prakt. Metallographie*, *9*, pp. 291–292.

Bockstiegel, G., 1972b, A new formula permitting straight-forward correction of edge errors in size distribution measurements with linear scanning instruments, *Prakt. Metallographie*, *9*, pp. 329–341.

Boon, J.D., III, D.A. Evans and H.F. Hennigar, 1982, Spectral information from Fourier analysis of digitized quartz grain profiles, *Mathematical Geology*, *14*, pp. 589–605.

Bowie, J.E. and I.T. Young, 1977a, An analysis technique for biological shape—II, *Acta Cytologica*, *21*, pp. 455–464.

Bowie, J.E. and I.T. Young, 1977b, An analysis technique for biological shape—III, *Acta Cytologica*, *21*, pp. 739–746.

Boyde, A., 1970, Practical problems and methods in the 3-D analysis of SEM images, *Scanning Electron Microscopy/1970*, pp. 105–112.

Boyde, A., 1974, Photogrammetry of stereo pair SEM images using separate measurements from the two images, *Scanning Electron Microscopy/1974/II*, pp. 101–108.

Boyde, A., P.G.T. Howell and S.J. Jones, 1974, Measurement of lacunar volume in bone using a stereological grid counting method evolved for the scanning electron microscope, *J. Microscopy*, *101*, pp. 261–266.

Brace, W.F., 1977, Permeability from resistivity and pore shape, *J. Geophys. Res.*, *82*, pp. 3343–3349.

Brace, W.F., J.B. Walsh and W.T. Frangos, 1968, Permeability of granite under high pressure, *J. Geophys. Res.*, *73*, pp. 2225–2236.

Bradbury, S., 1983, Commercial Image analysers and the characterization of microscopical images, *J. Microscopy*, *131*, pp. 203–210.

Brower, K.R. and N.R. Morrow, 1985, Fluid flow in cracks as related to low-permeability gas sands, *Soc. Pet. Eng. J.*, *25*, pp. 191–201.

Brown, L.M., 1978, Calibration of a commercial electron microscope with a grating replica to an accuracy of better than 1%, *J. Microscopy*, *113*, pp. 149–160.

Bullock, P. and C.P. Murphy, 1980, Towards the quantification of soil structure, *J. Microscopy, 120*, pp. 317–328.

Cahn, J.W., 1972, The generation and characterization of shape, in *Suppl. Adv. Appl. Prob.*, W.L. Nicholson (ed.), pp. 221–242.

Cahn, J.W. and R.L. Fullman, 1956, On the use of lineal analysis for obtaining particle size distribution functions in opaque samples, *Trans. AIME, 41*, pp. 610–612.

Canny, J.F., 1983, *Finding Edges and Lines in Images*, Technical Report No. 720, AI–TR–720, MIT Artificial Intelligence Lab., p. 145.

Caruso, L., G. Simmons and R. Wilkens, 1985, Physical properties of a set of sandstones—Part I. The samples, *Int. J. Rock Mech. Min. Sci., 22*, pp. 381–391.

Caruso, L.J. and G. Simmons, 1981, Geological applications of backscattered electron imaging, presented at the symposium on *Electron Microscopy in Geology*, held at Arizona State Univ. 6-11 May, 1981, p. 17.

Castleman, K.R., 1979, *Digital Image Processing*, Prentice-Hall, Inc., New Jersey, p. 429.

Chalkley, H.W., J. Cornfield and H. Park, 1949, A method for estimating volume-surface ratios, *Science, 110*, pp. 295–297.

Chang, K.S. and F.A.L. Dullien, 1976, Section diameter method for non-spherical objects, *J. Microscopy, 108*, pp. 61–68.

Chatzis, I. and F.A.L. Dullien, 1977, Modelling pore structure by 2-D and 3-D networks with application to sandstones, *J. Can. Pet. Tech., 16*, pp. 97–108.

Chayes, F., 1949, A simple point counter for thin section analysis, *Amer. Mineral., 34*, pp. 1–11.

Chayes, F., 1956, *Petrographic Modal Analysis*, John Wiley & Sons, Inc., New York, p. 113.

Cheng, C.H. and M.N. Toksõz, 1979, Inversion of seismic velocities for the pore aspect ratio spectrum of a rock, *J. Geophys. Res., 84*, pp. 7533–7543.

Choquette, P.W. and L.C. Pray, 1970, Geologic nomenclature and classification of porosity in sedimentary carbonates, *Amer. Assoc. Pet. Geol. Bull., 54*, pp. 207–250.

Chretien, J. and E.B.A. Bisdom, 1983, The development of soil porosity in experimental sandy soils with clay admixtures as examined by Quantimet 720 from BESI and by other techniques, *Geoderma, 30*, pp. 285–302.

Clark, M.W., 1981, Quantitative shape analysis: A review, *J. Int. Assoc. Math. Geol., 13*, pp. 303–320.

Cornell, D. and D.L. Katz, 1953, Flow of gases through consolidated porous media, *Ind. Eng. Chem., 45*, pp. 2145–2152.

Cole, M. and C.P. Bond, 1972, Recent advances in automatic image analysis using a television system, *J. Microscopy, 96*, pp. 89.

Cowgill, D.F., J.K. Pitman and D.O. Seevers, 1982, NMR and flow estimation, in *Western Tight Gas Sands Advanced Logging Workshop Proceedings*, CONF-8103113, DE82 014589, J.B. Jennings and H.B. Carroll, Jr. (eds.), pp. 26–46.

Coyner, K.B., 1984, *Effects of stress, pore pressure, and pore fluids on bulk strain, velocity, and permeability in rocks*, Ph.D. thesis, M.I.T., Cambridge, Mass.

Cruz Orive, L.M., 1976, Particle size–shape distributions: The general spheroid problem I. Mathematical Model, *J. Microscopy, 107*, pp. 235–253.

Cruz Orive, L.M., 1978, Particle size–shape distributions: The general spheroid problem II. Stochastic model and practical guide, *J. Microscopy, 112*, pp. 153–167.

Cruz-Orive, L.M., 1983, Distribution-free estimation of sphere size distributions from slabs showing overprojection and truncation, with a review of previous methods, *J. Microscopy, 131*, pp. 265–290.

Davis, J.C. and F.W. Preston, 1972, Optical processing: An alternative to digital computing, in *Geological Society of America, Special Paper #146*, pp. 49–68.

Debye, P., H.R. Anderson, Jr. and H. Brumberger, 1957, Scattering by an inhomogeneous solid, II. The correlation function and its application, *J. Appl. Phys., 28*, pp. 679–683.

Deer, W.A., R.A. Howie and J. Zussman, 1966, *An introduction to the rock-forming minerals*, Longman Group Ltd., London, p. 528.

Deffeyes, K.S., B.D. Ripley and G.S. Watson, 1982, Stochastic geometry in petroleum geology, *J. Int. Assoc. Math. Geol., 14*, pp. 419–432.

DeHoff, R.T., 1962, The determination of the size distribution of ellipsoidal particles from measurements made on random plane sections, *Trans. Met. Soc. AIME, 224*, pp. 474–477.

DeHoff, R.T., 1965, The estimation of particle-size distributions from simple counting measurements made on random plane sections, *Trans. Met. Soc. AIME, 233*, pp. 25–29.

DeHoff, R.T., 1977, The geometrical meaning of the integral mean curvature, *Microstructural Sci., 5*, pp. 331–348.

DeHoff, R.T., 1983, Quantitative serial sectioning analysis: Preview, *J. Microscopy, 131*, pp. 259–263.

DeHoff, R.T., E.H. Aigeltinger and K.R. Craig, 1972, Experimental determination of the topological properties of three-dimensional microstructures, *J. Microscopy, 95*, pp. 69–91.

DeHoff, R.T. and P. Bousquet, 1970, Estimation of the size distribution of triaxial ellipsoidal particles from the distribution of linear intercepts, *J. Microscopy, 92*, pp. 119–135.

DeHoff, R.T. and F.N. Rhines (eds.), 1968, *Quantitative Microscopy*, McGraw-Hill, New York, p. 422.

Delesse, A., 1848, Pour déterminer la composition des roches, *Annales des Mines, 13*, pp. 379–388.

Delfiner, P., 1971, *Etude morphologique des milieux poreux et automatisation des mesures en plaques minces*, Ph.D. thesis, University of Nancy.

Delfiner, P., 1972, A generalization of the concept of size, *J. Microscopy, 95*, pp. 203–216.

Deutsch, E.S., 1972, Thinning algorithms on rectangular, hexagonal, and triangular arrays, *Comm. of the Assoc. for Computing Machinery Inc., 15*, pp. 827–837.

Dhawan, G.K., 1972, *Photomicrographic investigation of the structure of sandstones and other porous media by the methods of quantitative stereology: with application to oil recovery*, Ph.D. thesis, University of Waterloo, Waterloo, Ontario, p. 342.

Dilks, A. and S.C. Graham, 1985, Quantitative mineralogical characterization of sandstones by back-scattered electron image analysis, *J. Sed. Pet., 55*, pp. 347–355.

Doe, P.H. and J.M. Haynes, 1979, Mechanistic aspects of capillary hysteresis in pore networks, in *Characterisation of porous solids*, S.J. Gregg, K.S.W. Sing and H.F. Stoeckli (eds.), The Society of Chemical Industry, London, pp. 253–265.

Doi, M., 1976, A new variational approach to the diffusion and the flow problem in porous media, *J. Phys. Soc. Japan*, *40*, pp. 567–572.

Duda, L.E. and J.K. Pitman, 1982a, Pore structure measurements in WTGS, in *Western Tight Gas Sands Advanced Logging Workshop Proceedings*, USDOE CONF-8103113, DE82 014589, J.B. Jennings and H.B. Carroll, Jr. (eds.), pp. 98–127.

Duda, L.E. and J.K. Pitman, 1982b, Pore structure analysis of sandstones using computer-processed photomicrographs, SAND-82-1083, Sandia National Labs Report, p. 43.

Duda, R.O. and P.E. Hart, 1973, *Pattern Classification and Scene Analysis*, John Wiley & Sons, New York, p. 482.

Dudley, R.M., P.C. Perkins, and E. Gine M., 1975, Statistical tests for preferred orientation, *J. Geology*, *83*, pp. 685–705.

Dullien, F.A.L., 1979, *Porous Media—Fluid Transport and Pore Structure*, Academic Press, New York, p. 396.

Dullien, F.A.L. and G.K. Dhawan, 1973, Photomicrographic size distribution determination of non-spherical objects, *Powder Technology*, *7*, pp. 305–313.

Dullien, F.A.L. and G.K. Dhawan, 1974, Characterization of pore structure by a combination of quantitative photomicrography and mercury porosimetry, *J. Colloid and Interface Sci.*, *47*, pp. 337–349.

Dullien, F.A.L. and G.K. Dhawan, 1975, Bivariate pore-size distribution of some sandstones, *J. Colloid and Interface Sci.*, *52*, pp. 129–135.

Ehrlich, R., 1983, Direct estimation of flow properties from petrographic thin-section image analysis (abs), presented at the Second International Congress on Applied Mineralogy in the Minerals Industry, San Francisco, 22–25 February.

Ehrlich, R., 1984, A strong transfer function links thin section data to reservoir physics (abs), presented at 59th Annual Technical Conference of Society of Petroleum Engineers of AIME.

Ehrlich, R., S.K. Kennedy, S.J. Crabtree and R.L. Cannon, 1984, Petrographic image analysis, I. Analysis of reservoir pore complexes, *J. Sed. Pet.*, *54*, pp. 1365–1378.

Ehrlich, R. and B. Weinberg, 1970, An exact method for characterization of grain shape, *J. Sed. Pet.*, *40*, pp. 205–212.

Evans, D.G., P.N. Schweitzer and M.S. Hanna, 1985, Parametric cubic splines and geologic shape descriptions, *J. Int. Assoc. Math. Geol.*, *17*, pp. 611–624.

Exner, H.E., 1972, Methods for edge error correction in lineal analysis, *Prakt. Metallographie*, *9*, pp. 383–392.

Fabbri, A.G., 1980, GIAPP: Geological image-analysis program package for estimating geometrical probabilities, *Computers & Geosciences*, *6*, pp. 153–161.

Fabbri, A.G., 1984, *Image Processing of Geologic Data*, Van Nostrand-Reinhold, New York, p. 244.

Fara, H.D. and A.E. Scheidegger, 1961, Statistical geometry of porous media, *J. Geophys. Res.*, *66*, pp. 3279–3284.

Fischmeister, H.F., 1974a, Shape factors in quantitative microscopy, *Z. Metallkunde*, *65*, pp. 558–562.

Fischmeister, H.F., 1974b, Determination of pore structure by stereological measurements, in *Pore Structure and Properties of Materials*, S. Modry and M. Svata (eds.), Proc. RILEM-IUPAC Int. Symp., Prague, 1973, Final Report, Part 2, Vol. IV, pp. C437–C476.

Fischmeister, H.F., 1974c, Conclusions of general reporter, in *Pore Structure and Properties of Materials*, S. Modry and M. Svata (eds.), Proc. RILEM-IUPAC Int. Symp., Prague, 1973, Final Report, Part 2, Vol. IV, pp. C545–C550.

Fisher, C.F., 1971, The new Quantimet 720, *Microscope*, *19*, pp. 1–20.

Folk, R.L., 1974, *Petrology of sedimentary rocks*, Hemphill Publishing Co., Austin, Texas, p. 182.

Fraser, D., 1979, Optimized mass storage FFT program, in *Programs for Digital Signal Processing*, edited by the Digital Signal Processing Committee, IEEE Acoustics, Speech, and Signal Processing Society, IEEE Press, New York, Section 1.5, pp. 1–40.

Freeman, H., 1961, On the encoding of arbitrary geometric configurations, *IRE Trans. on Elec. Comp., EC–10*, pp. 260–268.

Gardner, K.L., 1980, Impregnation technique using colored epoxy to define porosity in petrographic thin sections, *Can. J. Earth Sci., 17*, pp. 1104–1107.

Ghosh, S.K., 1979, *Analytical photogrammetry*, Pergamon Press, New York, p. 203.

Gillott, J.E., 1980, Use of the scanning electron microscope and Fourier methods in characterization of microfabric and texture of sediments, *J. Microscopy, 120*, pp. 261–277.

Golden, J.F. and W. Hunn, 1980, Microstructural analysis by new image analysis techniques, *Microstructural Sci., 8*, pp. 305–309.

Goldstein, J.I., D.E. Newbury, P. Echlin, D.C. Joy, C. Fiori, and E. Lifshin, 1981, *Scanning Electron Microscopy and X-Ray Microanalysis*, Plenum Press, New York, p. 673

Grant, G. and A.F. Reid, 1981, An efficient algorithm for boundary tracing and feature extraction, *Comp. Graphics and Image Proc., 17*, pp. 225–237.

Gray, S.B., 1971, Local properties of binary images in two dimensions, *IEEE Transactions on Computers, C–20*, pp. 551–561.

Griffiths, J.C., 1952, Grain-size distribution and reservoir-rock characteristics, *Amer. Assoc. Pet. Geol. Bull., 36*, pp. 205–229.

Gundersen, H.J.G. and E.B. Jensen, 1983, Particle sizes and their distributions estimated from line- and point-sampled intercepts. Including graphical unfolding, *J. Microscopy, 131*, pp. 291–310.

Gundersen, H.J.G. and E.B. Jensen, 1985, Stereological estimation of the volume-weighted mean volume of arbitrary particles observed on random sections, *J. Microscopy, 138*, pp. 127–142.

Haas, A., G. Matheron and J. Serra, 1967a, Morphologie mathematique et granulometriies en place, Part I, *Annales Des Mines, 736–XI*, pp. 39–57.

Haas, A., G. Matheron and J. Serra, 1967b, Morphologie mathematique et granulometriies en place, Part II, *Annales Des Mines, 768–XII*, pp. 12–26.

Hadley, K., 1976, Comparison of calculated and observed crack densities and seismic velocities in Westerly granite, *J. Geophys. Res.*, *81*, pp. 3484–3494.

Hall, M.G. and G.E. Lloyd, 1981, The SEM examination of geologic samples with a semi-conductor back-scattered electron detector, *Amer. Mineral.*, *66*, pp. 362–368.

Haralick, R.M., 1979, Statistical and structural approaches to texture, *Proc. IEEE*, *67*, pp. 786–804.

Haralick, R.M. and K. Shanmugam, 1973, Computer classification of reservoir sandstones, *IEEE Trans. Geosci. Electron.*, *GE-11*, pp. 171–177.

Hearle, J.W.S., B. Lomas and J.T. Sparrow, 1970, The selection of conditions for examination of specimens in a scanning electron microscope, *J. Microscopy*, *92*, pp. 205–216.

Hilliard, J.E., 1962, Specification and measurement of microstructural anisotropy, *Trans. AIME*, *224*, pp. 1201–1211.

Hilliard, J.E., 1968a, Estimation of microstructural properties in the presence of anisotropy, in *Ceramic Microstructures, Their Analysis, Significance, and Production*, R.M. Fulrath and J.A. Pask (eds.), John Wiley & Sons, Inc., New York, pp. 53–70.

Hilliard, J.E., 1968b, Direct determination of the moments of the size distribution of particles in an opaque sample, *Trans. AIME*, *242*, pp. 1373–1380.

Hilliard, J.E., 1972, Quantitative analysis of scanning electron micrographs, *J. Microscopy*, *95*, pp. 45–58.

Hilliard, J.E. and J.W. Cahn, 1961, An evaluation of procedures in quantitative metallography for volume-fraction analysis, *Trans. AIME*, *221*, pp. 344–352.

Hougardy, H.P., 1981, Present state and new development in quantitative metallography, *Microstructural Sci.*, *9*, pp. 111–122.

Howell, P.G.T., 1975, A practical method for the correction of distortions in SEM photogrammetry, *Scanning Electron Microscopy/1975/I*, pp. 199–206.

Hu, M.K., 1962, Visual pattern recognition by moment invariants, *IRE Trans. on Information Theory*, *IT-8*, pp. 179–187.

Huijbregts, C.J., 1975, Regionalized variables and quantitative analysis of spatial data, in *Display and Analysis of Spatial Data*, NATO Advanced

Study Institute, J.C. Davis and M.J. McCullagh (eds.), John Wiley & Sons, New York, pp. 39–53.

Jager, A., O. Boersma and E.B.A. Bisdom, 1983, The characterization of microporosity in a ploughpan by submicroscopic and Quantimet techniques, *Geoderma, 30*, pp. 277–283.

Jenkins, G.M. and D.G. Watts, 1968, *Spectral analysis and its applications*, Holden-Day, New York, p. 525.

Jensen, E.B. and H.J.G. Gundersen, 1985, The stereological estimation of moments of particle volume, *J. Appl. Prob., 22*, pp. 82–98.

Jones, A.V. and K.C.A. Smith, 1978, Image processing for scanning microscopists, *Scanning Electron Microscopy/1978/I*, pp. 13–26.

Jones, A.V. and B.M. Unitt, 1980, Computers in scanning microscopy, *Scanning Electron Microscopy/1980/I*, pp. 113–124.

Jones, A.V. and B.M. Unitt, 1982, An integrated approach to scanning microscope data acquisition, *J. Microscopy, 127*, pp. 61–68.

Joshi, M., 1974, Ph.D. thesis, University of Kansas.

Kahn, J.S., 1956, The analysis and distribution of the properties of packing in sand-sized sediments 1. On the measurement of packing in sandstones, *J. Geology, 64*, pp. 385–395.

Kahn, J.S., 1959, Anisotropic sedimentary parameters, *New York Acad. Sci., Trans., Ser. II, 21*, pp. 373–386.

Kanasewich, E.R., 1975, *Time sequence analysis in geophysics*, The University of Alberta Press, Alberta, Canada, p. 364.

Kanaya, K. and S. Okayama, 1972, *J. Physics D Appl. Phys., 5*, p. 43.

Katz, A.J. and A.H. Thompson, 1985, Fractal sandstone pores: Implications for conductivity and pore formation, *Physical Review Letters, 54*, pp. 1325–1328.

Kaye, B.H., 1984, Fractal description of fineparticle systems, in *Particle Characterization in Technology, Volume I—Applications and Microanalysis*, J.K. Beddow (ed.), CRC Press Inc., pp. 81–100.

Kellerhals, R., J. Shaw and V.K. Arora, 1975, On grain size from thin section, *J. Geology, 83*, pp. 79–96.

Kendall, M.G. and P.A.P. Moran, 1963, *Geometrical Probability*, Charles Griffin & Co., London, p. 125.

Kennedy, S.K. and W.H. Lin, 1986, FRACT—A FORTRAN subroutine to calculate the variables necessary to determine the fractal dimension of closed forms, *Computers & Geosciences*, *12*, pp. 705–712.

Kiss, L.T. and H.G. Brinkies, 1976, Scanning electron microscopy: the use of the backscattered electron image in materials investigations, *J. Aust. Inst. Metals*, *21*, pp. 178–182.

Klein, J.C. and J. Serra, 1972, The texture analyser, *J. Microscopy*, *95*, pp. 349–356.

Kolomenski, E.N. and J. Serra, 1976, La quantification en pétrologie, *Bull. Int. Assoc. Eng. Geol.*, *13*, p. 83–97.

Koplik, J., C. Lin and M. Vermette, 1984, Conductivity and permeability from microgeometry, *J. Appl. Phys.*, *56*, pp. 3127–3131.

Korringa, J., 1984, The influence of pore geometry on the dielectric dispersion of clean sandstone, *Geophysics*, *49*, pp. 1760–1762.

Korringa, J., D.O. Seevers and H.C. Torrey, 1962, Theory of spin pumping and relaxation in systems with a low concentration of electron spin resonance centers, *Physical Review*, *127*, pp. 1143–1150.

Krumbein, W.C., 1935, Thin-section mechanical analysis of indurated sediments, *J. Geol.*, *43*, pp. 482–496.

Kulpa, Z., 1977, Area and perimeter measurement of blobs in discrete binary pictures, *Comp. Graphics and Image Proc.*, *6*, pp. 434–451.

Lane, G.S., 1969, The application of stereographic techniques to the scanning electron microscope, *J. Sci. Instr., Ser. 2*, *2*, pp. 565.

Lin, C., 1982a, Microgeometry I: Autocorrelation and rock microstructure, *J. Int. Assoc. Math. Geol.*, *14*, pp. 343–360.

Lin, C., 1982b, Microgeometry II: Testing for homogeneity in Berea sandstone, *J. Int. Assoc. Math. Geol.*, *14*, pp. 361–370.

Lin, C., 1983, Shape and texture from serial contours, *J. Int. Assoc. Math. Geol.*, *15*, pp. 617–632.

Lin, C. and M.H. Cohen, 1982, Quantitative methods for microgeometric modeling, *J. Appl. Physics*, *53*, pp. 4152–4165.

Lin, C., G. Pirie and D.A. Trimmer, 1986, Low permeability rocks: Laboratory measurements and three-dimensional microstructural analysis, *J. Geophys. Res.*, *91*, pp. 2173–2181.

Lin, Cunshan and J.W. Harbaugh, 1984, *Graphic Display of Two- and Three-Dimensional Markov Computer Models in Geology*, Van Nostrand Reinhold Co. Inc., New York, p. 180.

Lohmann, G.P., 1983, Eigenshape analysis of microfossils: A general morphometric procedure for describing changes in shape, *J. Int. Assoc. Math. Geol.*, *15*, pp. 659–672.

Lord, E.A. and C.B. Wilson, 1984, *The Mathematical Description of Shape and Form*, E. H. Ltd., John Wiley & Sons, New York, p. 260.

Loren, J.D. and J.D. Robinson, 1970, Relations between pore size fluid and matrix properties, and NML measurements, *Trans. Soc. Pet. Eng.*, *249*, pp. 268–278.

Lucia, F.J., 1983, Petrophysical parameters estimated from visual descriptions of carbonate rocks: A field classification of carbonate pore space, *J. Pet. Tech.*, *35*, pp. 629–637.

Lysne, P.C., 1983, A model for the high-frequency electrical response of wet rocks, *Geophysics*, *48*, pp. 775–786.

Lysne, P.C., J.S. Yu, C.N. Vittitoe, L.E. Duda and P.C. Reardon, 1981, Dielectric log interpretation: Probe responses and dielectric properties of rocks, *Trans. SPWLA*, *22*, p. 17.

Mandelbrot, B.B., 1977, *Fractals: Form, Chance, Dimension*, W. H. Freeman and Co., San Francisco.

Mandelbrot, B.B., 1982, *The Fractal Geometry of Nature*, W. H. Freeman and Co., San Francisco.

Mardia, K.V., 1972, *Statistics of Directional Data*, Academic Press, New York, p. 357.

Matheron, G., 1967, *Elements pour une theorie des milieux poreux*, Masson, Paris.

Matheron, G., 1975, *Random Sets and Integral Geometry*, John Wiley & Sons, New York.

Maune, D.F., 1975, SEM photogrammetric calibration, *Scanning Electron Microscopy/1975/I*, pp. 207–215.

Meakin, J.D. and L.M. Fallon, 1973, Low magnification scanning electron microscopy, in *Scanning Electron Microscopy/1973/I*, pp. 145–150.

Medalia, A.I., 1967, Morphology of aggregates—I. Calculation of shape and bulkiness factors; Application to computer-simulated random flocs, *J. Colloid and Interface Sci.*, *24*, pp. 393–404.

Medalia, A.I., 1970, Dynamic shape factors of particles, *Powder Technology*, *4*, pp. 117–138.

Medalia, A.I. and F.A. Heckman, 1969, Morphology of aggregates—II. Size and shape factors of carbon black aggregates from electron microscopy, *Carbon*, *7*, pp. 567–582.

Menke, W., 1984, *Geophysical Data Analysis: Discrete Inverse Theory*, Academic Press, Inc., New York, p. 260.

Mersereau, R.M., 1979, The processing of hexagonally sampled two-dimensional signals, *Proc. IEEE*, *67*, pp. 930–949.

Minoura, N. and C.D. Conley, 1971, Technique for impregnating porous rock samples with low-viscosity epoxy resin, *J. Sed. Pet.*, *41*, pp. 858–861.

Moore, G.A., 1968, Application of computers to quantitative analysis of microstructures, in *Ceramic Microstructures, Their Analysis, Significance and Production*, R.M. Fulrath and J.A. Pask (eds.), John Wiley & Sons, New York, pp. 71–120.

Moore, G.A., 1964, Direct quantitative analysis of photomicrographs by a digital computer, *Photographic Science and Engineering*, *8*, pp. 152–161.

Moore, G.A., 1970, Is quantitative metallography quantitative?, in *Applications of Modern Metallographic Techniques*, ASTM STP 480, American Society for Testing and Materials, pp. 3–48.

Moore, G.A., 1972, Gestalt properties of aggregate materials, *Prakt. Metallographie*, *9*, pp. 76–97.

Moore, G.A. and L.L. Wyman, 1963, Quantitative metallography with a digital computer: Application to a Nb-Sn superconducting wire, *J. Res. NBS*, *67A*, pp. 127–147.

Moore, G.A., L.L. Wyman and H.M. Joseph, 1968, Comments on the possibilities of performing quantitative metallographic analyses with a digital computer, in *Quantitative Microscopy*, R.T. DeHoff and F.N. Rhines (eds.), McGraw-Hill Book Co., New York, pp. 380–403.

Morgan, J.T. and D.T. Gordon, 1970, Influence of pore geometry on water-oil relative permeability, *J. Pet. Tech.*, *22*, pp. 1199-1208.

Morrow, N.R., 1971, Small-scale packing heterogeneities in porous sedimentary rocks, *Amer. Assoc. Pet. Geol. Bull.*, *55*, pp. 514-522.

Murata, K., 1973, Monte Carlo calculations on electron scattering and secondary electron production in the SEM, *Scanning Electron Microscopy/-1973/II*, pp. 267–276.

Newbury, D.E. and D.C. Joy, 1973, Characteristics of SEM signals and techniques for signal processing, *Scanning Electron Microscopy/1973/I*, pp. 151–158.

Nicholson, W.L., 1978, Application of statistical methods in quantitative microscopy, *J. Microscopy*, *113*, pp. 223–239.

Nicholson, W.L. and K.R. Merckx, 1967, *Unfolding Particle Size Distributions*, BNWL-210, Battelle-Northwest, Pacific Northwest Laboratory, Richland, Washington, p. 60.

Nicholson, W.L. and K.R. Merckx, 1969, Unfolding particle size distributions, *Technometrics*, *11*, pp. 707–723.

Ondracek, G. and R. Pejsa, 1976, Stereological microstructure analysis as a tool for quantitative quality control and property determination, *J. Microscopy*, *107*, pp. 335–341.

Panozzo, R.H., 1983, Two-dimensional analysis of shape-fabric using projections of digitized lines in a plane, *Tectonophysics*, *95*, pp. 279–294.

Paterson, M.S., 1983, The equivalent channel model for permeability and resistivity in fluid-saturated rock—A re-appraisal, *Mech. Mater.*, *2*, pp. 345–352.

Patterson, B.R. and F.N. Rhines, 1979, Serial section estimation of number per unit volume, *Microstructural Sci.*, *7*, pp. 457–462.

Pavlidis, T., 1978, A review of algorithms for shape analysis, *Comp. Graphics and Image Proc.*, *7*, pp. 243–258.

Perez-Rosales, C., 1967, A simplified method for determining specific surface, *J. Pet. Tech.*, *19*, pp. 1081–1084.

Perez-Rosales, C., 1969, Simultaneous determination of basic geometrical characteristics of porous media, *Soc. Pet. Eng. J.*, *9*, pp. 413–416.

Perez-Rosales, C. and J.J. Martinez, 1971, Structural characteristics of granular porous media, *Soc. Pet. Eng. J.*, *11*, pp. 363–366.

Pfefferkorn, G.E., A. Boyde and R. Blaschke, 1978, How to get the best from your SEM, *Scanning Electron Microscopy/1978/I*, pp. 1–12.

Picklesimer, M.L., 1968, Theory and practice of the selection of the plane of examination, in *Quantitative Microscopy*, R.T. DeHoff and F.N. Rhines (eds.), McGraw-Hill, New York, pp. 326–325.

Pinault, J.L., J.M. Prevosteau and D.G. Williams, 1972, Perspectives of application of quantitive television microscopy to earth sciences, *J. Microscopy*, *95*, pp. 357–365.

Pincus, H.J., 1966, Optical processing of vectorial rock fabric data, in *Proc. First Int. Cong. on Rock Mechanics*, Lisbon, *1*, pp. 173–177.

Pincus, H.J., 1969a, Sensitivity of optical data processing to changes in rock fabric. Part I—Geometric patterns, *Int. J. Rock Mech. Min. Sci.*, *6*, pp. 259–268.

Pincus, H.J., 1969b, Sensitivity of optical data processing to changes in rock fabric. Part II—Standardized grain patterns, *Int. J. Rock Mech. Min. Sci.*, *6*, pp. 269–272.

Pincus, H.J., 1969c, Sensitivity of optical data processing to changes in rock fabric. Part III—Rock fabrics, *Int. J. Rock Mech. Min. Sci.*, *6*, pp. 273–276.

Pincus, H.J. and S.A. Ali, 1968, Optical data processing of multispectral photographs of sedimentary structures, *J. Sed. Pet.*, *38*, pp. 457–461.

Pittman, E.D., 1979a, Recent advances in sandstone diagenesis, *Ann. Rev. Earth Planet. Sci.*, *7*, pp. 39–62.

Pittman, E.D., 1979b, Porosity, diagenesis, and productive capability of sandstone reservoirs, in *Aspects of Diagenesis, SEPM Spec. Pub. No. 26*, P.A. Scholle and P.R. Schluger (eds.), pp. 159–173.

Pittman, E.D., 1984, An overview of the pore geometries in reservoir rocks, in *Physics and Chemistry of Porous Media*, AIP Conference Proceedings no. 107, D.L. Johnson and P.N. Sen (eds.), pp. 1–19.

Pittman, E.D. and R.W. Duschatko, 1970, Use of pore casts and scanning electron microscope to study pore geometry, *J. Sed. Pet.*, *40*, pp. 1153–1157.

Prager, S., 1961, Viscous flow through porous media, *Physics of Fluids*, *4*, pp. 1477–1482.

Pratt, W.K., 1978, *Digital Image Processing*, John Wiley & Sons, New York, p. 750.

Preston, F.W. and J.C. Davis, 1972, Application of optical processors to geological images, in *Machine Perception of Patterns and Pictures*, P.A. Walker (ed.), London, pp. 223–232.

Preston, F.W. and J.C. Davis, 1976, Sedimentary porous materials as a realization of a stochastic process, in *Random Processes in Geology*, D.F. Merriam (ed.), Springer-Verlag, New York, pp. 63– 86.

Preston, F.W. and D.W. Green, 1969, Numerical characterization of reservoir pore rock structure, Second Ann. Rept., Amer. Pet. Inst., proj. 103, p. 84.

Preston, F.W., D.W. Green and J.C. Davis, 1970, Numerical characterization of reservoir pore rock structure, Final Ann. Rept., Amer. Pet. Inst., proj. 103, p. 98.

Pye, K., 1984, Rapid estimation of porosity and mineral abundances in backscattered electron images using a simple SEM image analyzer, *Geol. Mag.*, *121*, pp. 81–84.

Pye, K. and D.H. Krinsley, 1984, Petrographic examination of sedimentary rocks in the SEM using backscattered electron detectors, *J. Sed. Pet.*, *54*, pp. 877–888.

Quiblier, J.A., 1984, A new three-dimensional modeling technique for studying porous media, *J. Colloid and Interface Sci.*, *98*, pp. 84–102.

Rhines, F.N., 1980, Use of the global and topological parameters in microstructure–property correlation, *Microstructural Sci.*, *8*, pp. 123–139.

Rhines, F.N., R.T. DeHoff and J. Kronsbein, 1969, A topological study of the sintering process, AEC Contract AT-(40-1)-2581, TID-25376, Final report.

Rigaut, J.P., 1984, An empirical formulation relating boundary lengths to resolution in specimens showing 'non-ideally fractal' dimensions, *J. Microscopy*, *133*, pp. 41–54.

Rink, M., 1970, *Automatische morphometrische Bildanalyse mit Hilfe eines elektronischen Digitalrechners*, Diss. Techn. Univ. Clausthal, BRD.

Rink, M., 1973, Porengeometrische Untersuchungen an Sedimentgesteinen mit einem Bildanalyseverfahren fur Digitalrechner, *Z. Geophysik*, *39*, pp. 989–1005.

Rink, M., 1974, An image analysis procedure for digital computers and its application to investigations on pore structures, in *Pore Structure and*

Properties of Materials, S. Modry and M. Svata (eds.), Proc. RILEM-IUPAC Int. Symp., Prague, 1973, Final Report, Part 2, Vol. IV, pp. C497–C506.

Rink, M., 1976a, A computerized quantitative image analysis procedure for investigating features and an adapted image process, *J. Microscopy, 107*, pp. 267–286.

Rink, M., 1976b, A new, fast and storage-saving image analysis procedure for investigating individuals by a digital computer, in *National Bureau of Standards Special Publ. 431*, E.E. Underwood, R. de Wit, and G.A. Moore (eds.), Proc. Fourth Int. Congress for Stereology, pp. 117–120.

Rink, M., 1976c, A computerized image process for isolating individuals in an originally netted pattern, in *National Bureau of Standards Special Publ. 431*, E.E. Underwood, R. de Wit, and G.A. Moore (eds.), Proc. Fourth Int. Congress for Stereology, pp. 155–158.

Rink, M. and J.R. Schopper, 1976, Pore structure and physical properties of porous sedimentary rocks, *Pageoph, 114*, pp. 273–284.

Rink, M. and J.R. Schopper, 1978, On the application of image analysis to formation evaluation, *The Log Analyst, 19*, pp. 12–22.

Roach, S.A., 1968, *The theory of random clumping*, Methuen & Co. Ltd., London, p. 94.

Robinson, B.W. and E.H. Nickel, 1979, A useful new technique for mineralogy: the backscattered-electron / low vacuum mode of SEM operation, *Amer. Mineral., 64*, pp. 1322–1328.

Robinson, V.N.E., 1975, Backscattered electron imaging, *Scanning Electron Microscopy/1975/I*, pp. 51–60.

Roethlisberger, H., 1955, An adequate method of grain-size determination in sections, *J. Geology, 63*, pp. 579–584.

Rose, W., 1986, A rational scheme for calculating sidewall core permeability, *The Log Analyst, 27*, pp. 21–24.

Rose, W. and W.A. Bruce, 1949, Evaluation of capillary character in petroleum reservoir rock, *Trans. Am. Inst. Min. Metall. Pet. Eng., 186*, pp. 127–142.

Rose, W.D. and M.R.J. Wyllie, 1950, Specific surface area and porosities from photomicrographs, *Amer. Assoc. Pet. Geol. Bull., 34*, pp. 1748–1749.

Ruzyla, K., 1984, Characterization of pore space by quantitative image analysis, SPE Paper #13133, presented at the 59th Annual Technical Conference and Exhibition in Houston TX, 16–19 September 1984.

Scheidegger, A.E., 1974, Models and geometry of pore structure, in *Pore Structure and Properties of Materials*, S. Modry and M. Svata (eds.), Proc. RILEM-IUPAC Int. Symp., Prague, 1973, Final Report, Part 1, Vol. III, pp. A1–A12.

Scheil, E. and H. Wurst, 1936, Statistische Gefügeuntersuchungen II. Messung der räumlichen Kristallgrösse, *Z. Metallk.*, *28*, pp. 340.

Schmidt, V. and D.A. McDonald, 1979, Texture and recognition of secondary porosity in sandstones, in *Aspects of Diagenesis*, P.A. Scholle and P.R. Schluger (eds.), SEPM Special Publication No. 26, pp. 209–225.

Schmidt, V., D.A. McDonald and R.L. Platt, 1977, Pore geometry and reservoir aspects of secondary porosity in sandstones, *Bull. Can. Pet. Geol.*, *25*, pp. 271–290.

Schoonderbeek, D., F. Thiel and E.B.A. Bisdom, 1983, Quantimet 720 analysis of porosities in backscattered electron scanning images made with different photo-techniques, *Geoderma*, *30*, pp. 271–275.

Schrank, J.A. and E. Hunt, 1980, Improved reservoir evaluation with the SEM, in *Scanning Electron Microscopy/1980/I*, pp. 573–578.

Schreiber, W.F., 1981, Aspects of Image Processing, preliminary draft copy, course notes, MIT.

Schwarcz, H.P. and K.C. Shane, 1969, Measurement of particle shape by Fourier analysis, *Sedimentology*, *13*, pp. 213–231.

Schwarz, H. and H.E. Exner, 1983, The characterization of the arrangement of feature centroids in planes and volumes, *J. Microscopy*, *129*, pp. 155–169.

Seevers, D.O., 1966, A nuclear magnetic method for determining the permeability of sandstones, *Trans. SPWLA*, *7*, p. 14.

Şen, Z., 1984, Autorun analysis of sedimentary porous materials, *J. Int. Assoc. Math. Geol.*, *16*, pp. 449–463.

Sergeyev, Y.M., B. Grabowska-Olszewska, V.I. Osipov, V.N. Sokolov and Y.N. Kolomenski, 1980, The classification of microstructures of clay soils, *J. Microscopy*, *120*, pp. 237–260.

Serra, J., 1972, Stereology and structuring elements, *J. Microscopy*, *95*, pp. 93–103.

Serra, J., 1980, Principles, criteria and algorithms in mathematical morphology, in *Issues in digital image processing*, R.M. Haralick and J.C. Simon (eds.), Proc. NATO Adv. Study Inst. on Digital Image Proc. and Anal., Bonas, France, 1978, pp. 73–105.

Serra, J., 1982, *Image Analysis and Mathematical Morphology*, Academic Press, New York, p. 610.

Simmons, G., T. Todd and W.S. Baldridge, 1975, Toward a quantitative relationship between elastic properties and cracks in low porosity rocks, *Amer. J. Sci.*, *275*, pp. 318–345.

Simmons, G., R. Wilkens, L. Caruso, T. Wissler, and F. Miller, 1982, *Physical Properties and Microstructures of a Set of Sandstones*, Annual Report to the Schlumberger-Doll Research Center.

Simmons, G., R. Wilkens, L. Caruso, T. Wissler, and F. Miller, 1983, *Physical Properties and Microstructures of a Set of Sandstones*, Annual Report to the Schlumberger-Doll Research Center.

Sneider, R.M., H.R. King, H.E. Hawkes and T.B. Davis, 1983, Methods for detection and characterization of reservoir rock, Deep Basin Gas Area, Western Canada, *J. Pet. Tech.*, *35*, pp. 1725–1734.

Stout, J.L., 1964, Pore geometry as related to carbonate stratigraphic traps, *Amer. Assoc. Pet. Geol. Bull.*, *48*, pp. 329–337.

Straley, C. and M.M. Minnis, 1983, Epoxy rock replicas for microtoming, *J. Sed. Pet.*, *53*, pp. 667–670.

Stroeven, P., 1976, Application of various stereological methods to the study of the grain and crack structure of concrete, *J. Microscopy*, *107*, pp. 313–321.

Swanson, B.F., 1979, Visualizing pores and nonwetting phase in porous rock, *J. Pet. Tech.*, *31*, pp. 10–18.

Swanson, B.F., 1981, A simple correlation between permeabilities and mercury capillary pressure, *J. Pet. Tech.*, *33*, pp. 2498–2504.

Tallis, G.M., 1970, Estimating the distribution of spherical and elliptical bodies in conglomerates from plane sections, *Biometrics*, *26*, pp. 87–103.

Tatham, R.H., 1982, V_P/V_S and lithology, *Geophysics*, *47*, pp. 336–344.

Terrell, A.C., 1974, Recent advances in automatic image analysis, in *Pore Structure and Properties of Materials*, S. Modry and M. Svata (eds.), Proc. RILEM-IUPAC Int. Symp., Prague, 1973, Final Report, Part 2, Vol. IV, pp. C507–C516.

Thomeer, J.H., 1960, Introduction of a pore geometrical factor defined by the capillary pressure curve, *J. Pet. Tech.*, *12*, pp. 73–77.

Thomeer, J.H., 1983, Air permeability as a function of three pore-network parameters, *J. Pet. Tech.*, *35*, pp. 809–814.

Timur, A., 1969a, Producible porosity and permeability of sandstones investigated through nuclear magnetic resonance principles, *The Log Analyst*, *10*, pp. 3–11.

Timur, A., 1969b, Pulsed nuclear magnetic resonance studies of porosity, movable fluid, and permeability of sandstones, *Trans. Soc. Pet. Eng.*, *246*, pp. 775–786.

Timur, A., W.B. Hempkins and R.W. Weinbrandt, 1971, Scanning electron microscope study of pore systems in rocks, *J. Geophys. Res.*, *76*, pp. 4932–4948.

Toksöz, M.N., C.H. Cheng and A. Timur, 1976, Velocities of seismic waves in porous rocks, *Geophysics*, *41*, pp. 621–645.

Torquato, S. and G. Stell, 1982, Microstructure of two-phase random media. I. The n-point probability functions, *J. Chem. Phys.*, *77*, pp. 2071–2077.

Torquato, S. and G. Stell, 1983a, Microstructure of two-phase random media. II. The Mayer–Montroll and Kirkwood–Salsburg hierarchies, *J. Chem. Phys.*, *78*, pp. 3262–3272.

Torquato, S. and G. Stell, 1983b, Microstructure of two-phase media. III. The n-point matrix probability functions for fully penetrable spheres, *J. Chem. Phys.*, *79*, pp. 1505–1510.

Tovey, N.K., 1980, A digital computer technique for orientation analysis of micrographs of soil fabric, *J. Microscopy*, *120*, pp. 303–315.

Underwood, E.E., 1968, Surface area and length in volume, in *Quantitative Microscopy*, R.T. DeHoff and F.N. Rhines (eds.), McGraw-Hill, New York, pp. 77–127.

Underwood, E.E., 1970, *Quantitative Stereology*, Addison-Wesley Publishing Co., Reading, MA, p. 274.

Underwood, E.E., 1975, Quantitative shape indices by stereological methods, in *Quantitative analysis of microstructures in medicine, biology and materials development*, H.E. Exner (ed.), Practical Metallography Special Issue 5, Proc. Quant. Anal. of Microstructures, Leoben, Austria, 1974, pp. 223–241.

Underwood, E.E., A.R. Colcord and R.C. Waugh, 1968, Quantitative relationships for random microstructures, in *Ceramic Microstructures, Their Analysis, Significance, and Production*, R.M. Fulrath and J.A. Pask (eds.), John Wiley & Sons, Inc., New York, pp. 25–52.

Vollath, D., 1981, The application of a normalized correlation function in image analysis, *J. Microscopy, 122*, pp. 35–48.

Walker, B.M., 1978, Chalk pore geometry using resin pore casts, in *SEM in the Study of Sediments, Geo Abstracts*, W.B. Whalley (ed.), Norwich, England, pp. 17–27.

Walsh, J.B. and W.F. Brace, 1984, The effect of pressure on porosity and the transport properties of rock, *J. Geophys. Res., 89*, pp. 9425–9431.

Wardlaw, N.C., 1976, Pore geometry of carbonate rocks as revealed by pore casts and capillary pressure, *Amer. Assoc. Pet. Geol. Bull., 60*, pp. 245–257.

Wardlaw, N.C. and J.P. Cassan, 1978, Estimation of recovery efficiency by visual observation of pore systems in reservoir rocks, *Bull. Can. Pet. Geol., 26*, pp. 572–585.

Wardlaw, N.C. and J.P. Cassan, 1979, Oil recovery efficiency and the rock-pore properties of some sandstone reservoirs, *Bull. Can. Pet. Geol., 27*, pp. 117–138.

Wardlaw, N.C. and R.P. Taylor, 1976, Mercury capillary pressure curves and the interpretation of pore structure and capillary behaviour in reservoir rocks, *Bull. Can. Pet. Geol., 24*, pp. 225–262.

Watson, G.S., 1966, The statistics of orientation data, *J. Geology, 74*, pp. 786–797.

Watson, G.S., 1970a, Orientation statistics in the earth sciences, *Bull. Geol. Instn. Univ. Upsala N. S., 2*, pp. 73–89.

Watson, G.S., 1970b, The statistical treatment of orientation data, in *Geostatistics*, Proc. of a Colloquium on Geostatistics at The University of Kansas, Lawrence on 7–9 June 1970, D.F. Merriam (ed.), Plenum Press, New York, pp. 1–9.

Watson, G.S., 1971, Estimating functionals of particle size distributions, *Biometrika, 58*, pp. 483–490.

Watson, G.S., 1975, Texture analysis, in *Geological Society of America, Memoir 142*, E.H.T. Whitten (ed.), pp. 367–391.

Weibel, E.R., 1974, Selection of the best method in stereology, *J. Microscopy, 100*, pp. 261–269.

Weinbrandt, R.M. and I. Fatt, 1969, A scanning electron microscope study of the pore structure of sandstone, *J. Pet. Tech., 21*, pp. 543–548.

Weissberg, H.L. and S. Prager, 1962, Viscous flow through porous media. II. Approximate three-point correlation function, *Phys. Fluids, 5*, pp. 1390–1392.

Wells, O.C., 1977, Backscattered electron image (BSI) in the scanning electron microscope (SEM), *Scanning Electron Microscopy/1977*, Vol. I, pp. 747–771.

Weszka, J.S., 1978, A survey of threshold selection techniques, *Comp. Graphics and Image Proc., 7*, pp. 259–265.

White, S.H., H.F. Shaw and J.M. Huggett, 1984, The use of back-scattered electron imaging for the petrographic study of sandstones and shales, *J. Sed. Pet., 54*, pp. 487–494.

Wicksell, S.D., 1926, The corpuscle problem II: Case of ellipsoidal corpuscles, *Biometrika, 18*, pp. 151–172.

Wilkens, R.H., G. Simmons, T.M. Wissler and L. Caruso, 1986, The physical properties of a set of sandstones—Part III. The effects of fine-grained pore-filling material on compressional wave velocity, *Int. J. Rock Mech. Min. Sci., 23*, pp. 313–325.

Winsauer, W.O., J.r. H. M. Shearin, P.H. Masson and M. Williams, 1952, Resistivity of brine-saturated sands in relation to pore geometry, *Amer. Assoc. Pet. Geol. Bull., 96*, pp. 253–277.

Wissler, T.M. and G. Simmons, 1985, The physical properties of a set of sandstones—Part II. Permanent and elastic strains in sandstones during hydrostatic compression to 200 MPa, *Int. J. Rock Mech. Min. Sci., 22*, pp. 393–406.

Wright, K. and B. Karlsson, 1983, Fractal analysis and stereological evaluation of microstructures, *J. Microscopy, 129*, pp. 185–200.

Wyllie, M.R.J. and G.H.F. Gardner, 1958a, The generalized Kozeny–Carman equation, its application to problems of multiphase flow in porous media; part 1—Review of existing theories, *World Oil, March*, pp. 121–126.

Wyllie, M.R.J. and G.H.F. Gardner, 1958b, The generalized Kozeny–Carman equation, its application to problems of multiphase flow in porous media; part 2—A novel approach to problems of fluid flow, *World Oil, April*, pp. 210–228.

Wyllie, M.R.J. and A.R. Gregory, 1955, Fluid flow through unconsolidated porous aggregates, *Ind. Eng. Chem.*, *47*, pp. 1379–1388.

Wyllie, M.R.J. and W.D. Rose, 1950a, Application of the Kozeny equation to consolidated porous media, *Nature*, *165*, p. 972.

Wyllie, M.R.J. and W.D. Rose, 1950b, Some theoretical considerations related to the quantitative evaluation of the physical characteristics of reservoir rock from electrical log data, *Trans. AIME*, *189*, pp. 105–118.

Wyllie, M.R.J. and M.B. Spangler, 1952, Application of electrical resistivity measurements to problem of fluid flow in porous media, *Amer. Assoc. Pet. Geol. Bull.*, *36*, pp. 359–403.

Yanguas, J.E. and J.J. Dravis, 1985, Blue flourescent dye technique for recognition of microporosity in sedimentary rocks, *J. Sed. Pet.*, *55*, pp. 600–602.

Yanuka, M., F.A.L. Dullien and D.E. Elrick, 1984, Serial sectioning and digitization of porous media for two- and three-dimensional analysis and reconstruction, *J. Microscopy*, *135*, pp. 159–168.

Yew, N.C. and D.E. Pease, 1974, Signal storage and enhancement techniques for the SEM, *Scanning Electron Microscopy/1974/I*, pp. 191–198.

Young, I.T., R.L. Peverini, P.W. Verbeek and P.J. van Otterloo, 1981, A new implementation of the binary and Minkowski operators, *Comp. Graphics and Image Proc.*, *17*, pp. 189–210.

Young, I.T., J.E. Walker and J.E. Bowie, 1974, An analysis technique for biological shape. I, *Information and Control*, *25*, pp. 357–370.

Appendix A

SEM–Digital Imaging and Analysis Hardware

In this appendix, the hardware used for digital imaging and image analysis is described. The hardware consists entirely of commercially available products. The SEM–digital imaging system is shown schematically in Figure A.1. Basically, a digital beam control (digital scan generator) has been added to a conventional SEM to direct the beam in a discrete raster pattern. The digital beam control also contains an analog-to-digital converter which samples (digitizes) a detector signal. The digitized detector signal is stored in a memory buffer then written to a diskette. The program written to control image acquisition (**IAP**—Image Acquisition Program) is described briefly in Appendix D. Images are transferred from diskette to a minicomputer via a serial communications interface.

All image analysis is performed on the minicomputer system shown schematically in Figure A.2. Note the absence of any specialized image display or analysis hardware in this system. A Tektronix-compatible graphics display terminal and a Versatec electrostatic printer-plotter are the only "image" oriented devices. Because binary (two phase) images are the subject of most analysis, the Versatec is an adequate display device.

The components in Figures A.1 and A.2 are listed in Tables A.1 and A.2, respectively.

A.1 Beam Blanking

The topic of beam blanking in the SEM merits discussion. Except in some specialized SEMs which are used for micro-manufacturing, the electron beam continuously hits the specimen even though the CRT display may be blanked. The specialized SEMs contain additional coils which direct the beam off axis. When the scan is controlled digitally, unlike under analog scan control, the electron beam can be stopped at a specified location. If the CRT is blanked, the operator may not be aware that the beam is stationary and specimen damage can occur. For example, the CRT may be blanked to allow an operator to open a camera shutter. A special effort has been made so that the **IAP** program does not stop the beam for any time period longer than the specified acquisition dwell times.

Table A.1

SEM-Digital Imaging Hardware Components

Code†	Component/Manufacturer/Model
A	Dual screen SEM w/large specimen chamber. International Scientific Instruments (ISI), DS-130.
B	SEM Detectors. Robinson Backscattered Electron Detector, large solid angle scintillator-photomultiplier style detector. ETP SEMRA Pty. Ltd., RBSE-130. Secondary Electron Detector, biased scintillator style detector. ISI, SE-2-130. Cathode Luminescence Detector. ISI, CL-2-130.
C	EDS X-Ray Si(Li) Detector. Tracor Northern Inc. TX-30/148-676-R,H,TH,(TP).
D	Quantitative X-Ray Analyzer System with graphics monitor. Tracor Northern Inc., TN-2000-2K.
E	Central Processing Unit with 48 Kbytes memory. Digital Equipment Corp., LSI-11/2 CPU.
F	Dual Diskette Subsystem. Data Systems Design, Inc. obtained through Tracor Northern Inc., TA-2061 (DSD 440-DOC-PRE).
G	Digital Beam Control System with 4096X4096 positioning resolution and 8 bit analog-to-digital converter for detector signals (B). Tracor Northern Inc.,TN-1310-20.
H	Hardcopy I/O Terminal. Digital Equipment Corp., LA-34.
I	Communication Interface, serial RS-232, 9600 baud, link to PDP 11/34 minicomputer system. Tracor Northern Inc., TN-2050.

† Codes correspond to Figure A.1.

Table A.2

Image Analysis Minicomputer Hardware Components

Code†	Component/Manufacturer/Model
A	PDP 11/34a CPU with Floating Point Processor and 224 Kbytes memory. Digital Equipment Corporation.
B	Removable Hard Disk Drives, 2.4 Mbytes each. Digital Equipment Corporation, RK05j.
C	Graphics Terminal, emulates Tektronix 4014. Digital Equipment Corporation, VT240.
D	Hardcopy I/O Terminal. Digital Equipment Corp., LA-36.
E	Serial Communication Link to SEM, RS-232, 9600 baud. Digital Equipment Corporation, DL-11W.
F	Electrostatic Printer - Plotter, 11 inch width. Versatec Inc., Model 1200A.
G	Magnetic Tape Transport, 9 track, 1600 bpi. Kennedy Co., Model 9100.

† Codes correspond to Figure A.2.

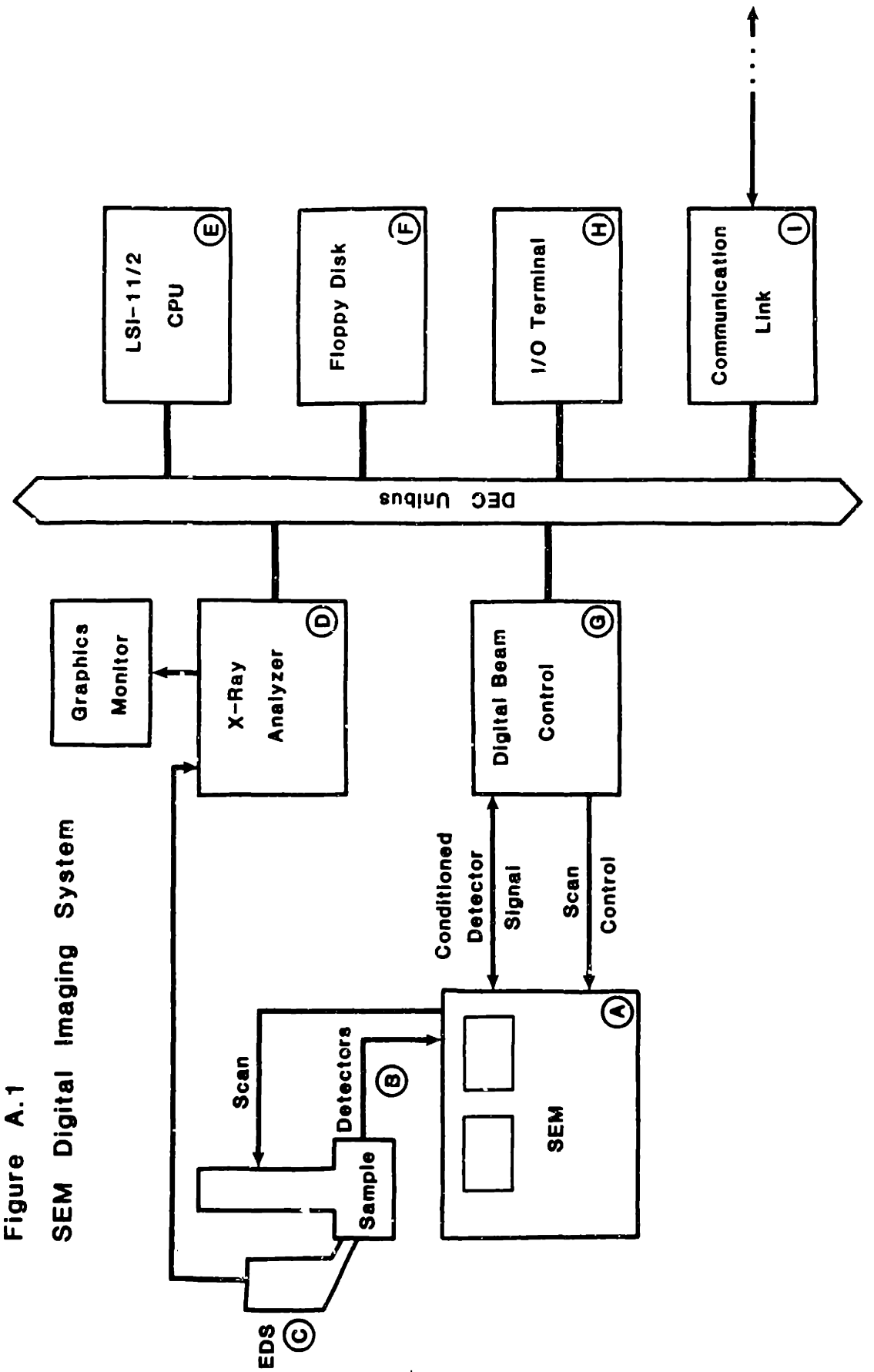

Figure A.1
SEM Digital Imaging System

Figure A.2

Minicomputer Hardware Components

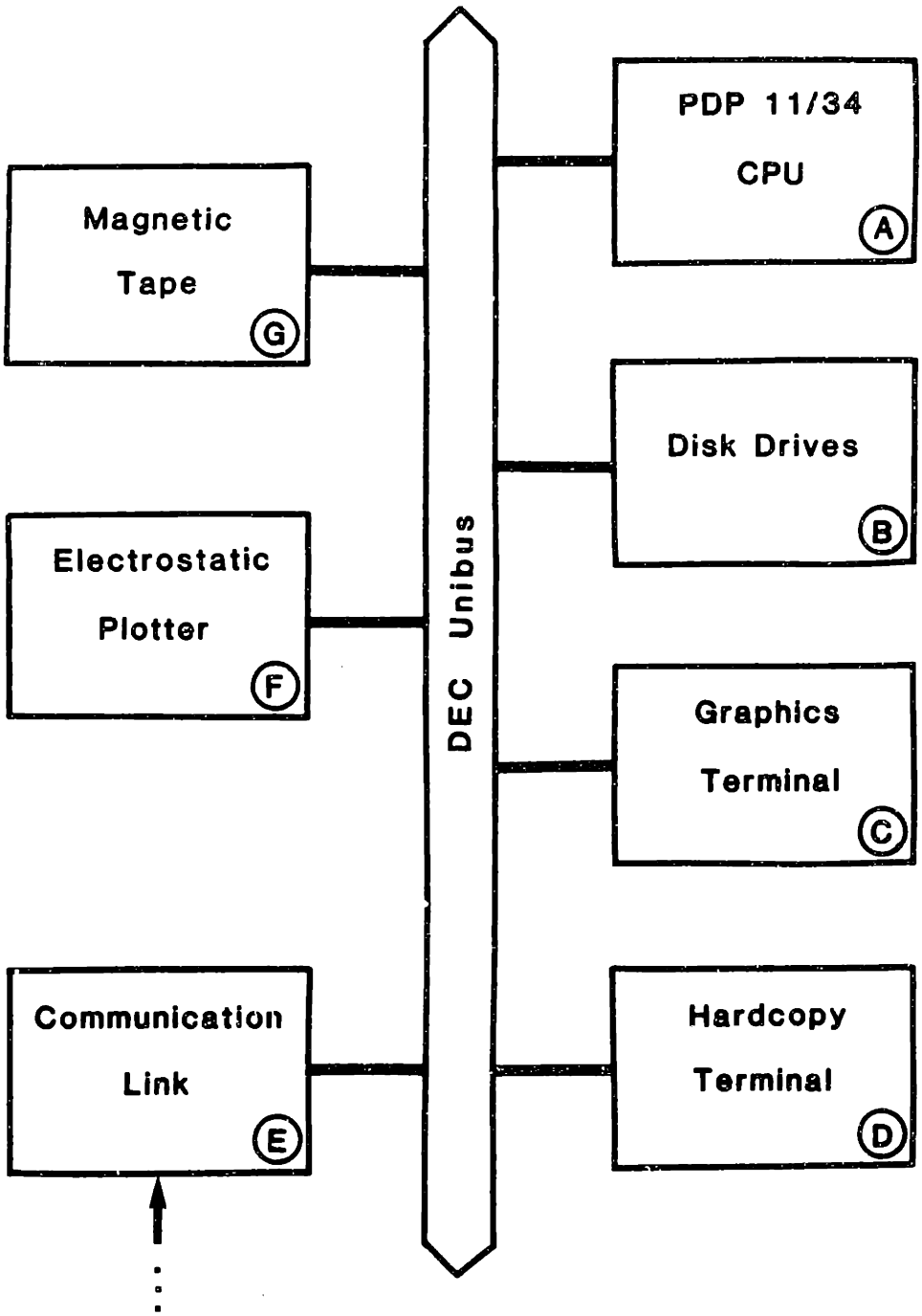

Appendix B

SEM Sample Preparation

In this study, polished thin sections and polished stubs were used for analysis. Generally, any epoxy-impregnated, uncovered, flat, polished section can be used for quantitative analysis. However, epoxy-impregnated stubs are preferred for two reasons. First, the vacuum-pressure impregnation, prior to sectioning and polishing, helps to preserve the microstructure and fills the pores with epoxy. Thin sections and crack sections are usually just surface impregnated, which does not fill the pores as well as does vacuum-pressure impregnation. Second, the polished stubs require polishing of only one surface and can be prepared easily in-house. Uniform thickness is not important. The procedure for preparing polished stubs is described below.

One inch (25 mm) diameter cylinders, with a nominal length of 1 inch (25 mm), are cored from an oriented laboratory sample. A 10 mm thick wafer is cut from the center of the core using a low speed cutoff saw with water as a coolant. It is important to preserve coordinate directions on the wafer. The wafer is washed thoroughly in running water then placed in a vacuum oven at 40°C and 0.1 torr for 24 hours.

Impregnation With Epoxy — A conventional Spurr low-viscosity embedding medium is used for impregnation (Ladd Research Industries, Inc. Burlington, VT, 05401, Catalog # 21670). The weight ratios recommended by Ladd (Table B.1) produce an epoxy which cures to a hardness suitable for polishing. The wafer is immersed in epoxy and evacuated at room temperature for one hour. The wafer and cup are transferred to a pressure vessel and pressurized to 2000 psi (12MPa) at room temperature for 4 hours. Lastly, the wafer and cup are placed in an oven at atmospheric pressure and 70°C for 8 hours.

Polishing — The impregnated wafer is cut in half, normal to the core axis. The exposed cut is hand polished with 180 grit silicon carbide paper until all saw marks are removed. A Beuhler Minimet Polisher is used for subsequent polishing. First, 240, 320, 400, and 600 grit papers are used in sequence. Next, polishing compounds of 6 μm, 1 μm, and 0.3 μm are used with nylon polishing cloth. The final polish is obtained with 0.05 μm compound on a textured polishing cloth.

Carbon Coating — All samples are coated with carbon prior to examination. A Polaron E6100 Vacuum Coater (Polaron Instruments Inc., Hatfield, PA. 19440) is used with an evaporative carbon source. The sample is rotated during coating or recoated at different orientations to produce an even coating and to lessen directional imaging artifacts (e.g., charge buildup at thinly coated edges).

Comments — Plucking of grains has not been observed in the stubs prepared according to the above procedure. However, bubbles have occasionally been found within the epoxy in the pores. A potential improvement in the impregnation procedure would be to cure the epoxy at 70°C *while* under pressure.

It is good practice to mark the polished surface of the sample, in the direction of one of the horizontal axes, to facilitate orientation of the sample in the SEM.

Table B.1

Weight Ratios for Spurr Epoxy

Vinylcyclohexene dioxide (VCD)	10.0g
Diglycidyl ether of polypropylene glycol (DER 736)	6.0g
Nonenyl succinic anhydride (NSA)	26.0g
Dimethylaminoethanol (DMAE)	0.4g

Appendix C

Sample Descriptions, Physical Properties, and Binary Images

The samples used in this study are described in this appendix. Basic physical properties of the samples are also given. The values of physical properties are averages of 3 values which were measured on 3 orthogonal cores of each sample. Additional descriptions and physical properties can be found in Simmons *et al.* (1982, 1983), Caruso *et al.* (1985), Wissler and Simmons (1985), and Wilkens *et al.* (1986).

Table C.1 lists petrographic information. The sample numbers in Table C.1 are used to key all additional information. Table C.2 lists bulk porosity, bulk density, formation factor, and brine permeability.

Figures C.1a through C.1n are typical binary images of the samples.

Figure Captions

Figure C.1. Typical binary images of the samples.

(*a*) 2124.	(*e*) 2521.	(*i*) 2700.	(*m*) 2842.
(*b*) 2509.	(*f*) 2523.	(*j*) 2704.	(*n*) 2843.
(*c*) 2513.	(*g*) 2686.	(*k*) 2710.	
(*d*) 2519.	(*h*) 2687.	(*l*) 2841.	

Table C.1

Sample Descriptions

Sample Number	Formation Name	Rock Type	Comments (% in volume)
2124	Berea ss	Quartz arenite	1% clay 4% dolomite
2509	Tensleep fm	Quartz arenite	1% clay
2513	Frontier fm	Quartz arenite	3-5% detrital clay
2519	Flathead fm	Quartz arenite	1-2% detrital clay
2521	Tensleep fm	Quartz arenite	1-2% detrital clay
2523	Darwin fm	Quartz arenite	7% calcite 1-2% detrital clay
2686†	Massilon ss	Quartz arenite	5% clay
2687	Dakota fm	Argillaceous	18% clay filling pores in bands
2700	Morrison fm	Quartz arenite	6% clay
2704	Morrison fm	Subarkose	7% clay
2710	Morrison fm	Subarkose	3% clay
2841‡	Boise ss	Arkosic wacke	23% clay
2842‡	Navajo ss	Quartz arenite	Secondary quartz cement
2843‡	Kayenta ss	Arkose	20% calcite

† Sample and description furnished by K. Winkler, Schlumberger-Doll Research.

‡ Sample furnished by K. Coyner. Description from Coyner (1984).

Table C.2

Sample Physical Properties

Sample Number	ϕ_b (%)	ρ (g/cc)	F_R	k_{meas} (millidarcy)
2124	17.8	2.14	20.5	40
2509	18.1	2.13	16.7	326
2513	21.7	2.03	12.1	286
2519	10.6	2.33	62.2	4.5
2521	24.1	1.95	12.6	616
2523	16.8	2.18	21.1	22
2686	26.0	2.05	11.8†	1300‡
2687	24.1	2.01	14.9	16§
2700	23.4	2.01	12.2	295
2704	23.8	1.98	14.5	303
2710	30.5	1.78	8.3	1450§
2841	26.7	1.99	ND	1410‡
2842	13.8	2.32	ND	64‡
2843	23.1	2.02	ND	683‡

*NOTES:*ND indicates no data.

† Formation factor from Koplik *et al.* (1984).

‡ Estimated permeability from mercury porosimetry data, courtesy of Dave Hurd, Shell Development Co.

§ Strongly anisotropic behavior.

100 μm

Figure C.1a

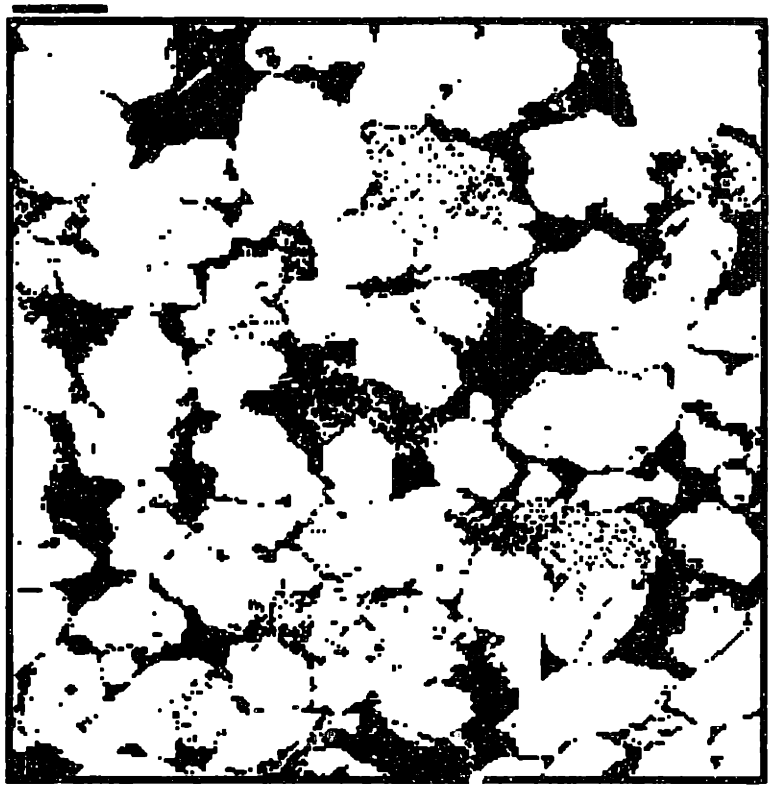

500 μm

Figure C.1b

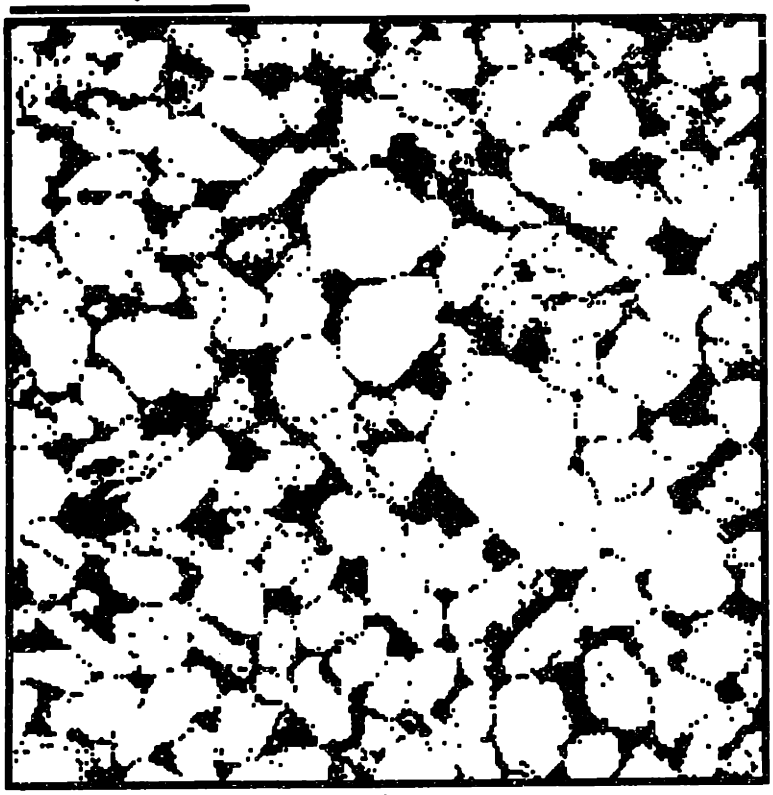

100 μm

Figure C.1c

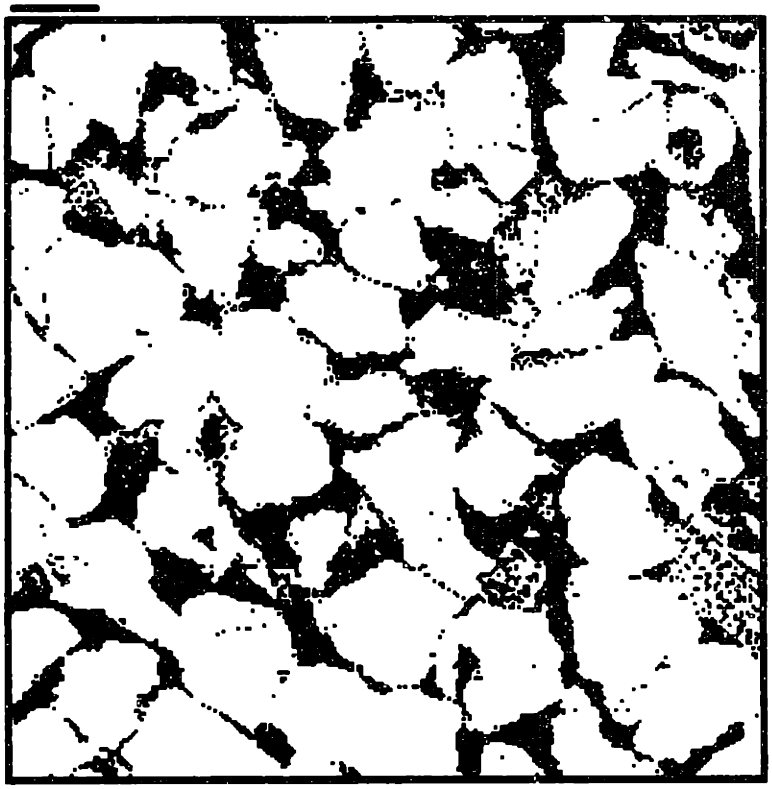

500 μm

Figure C.1d

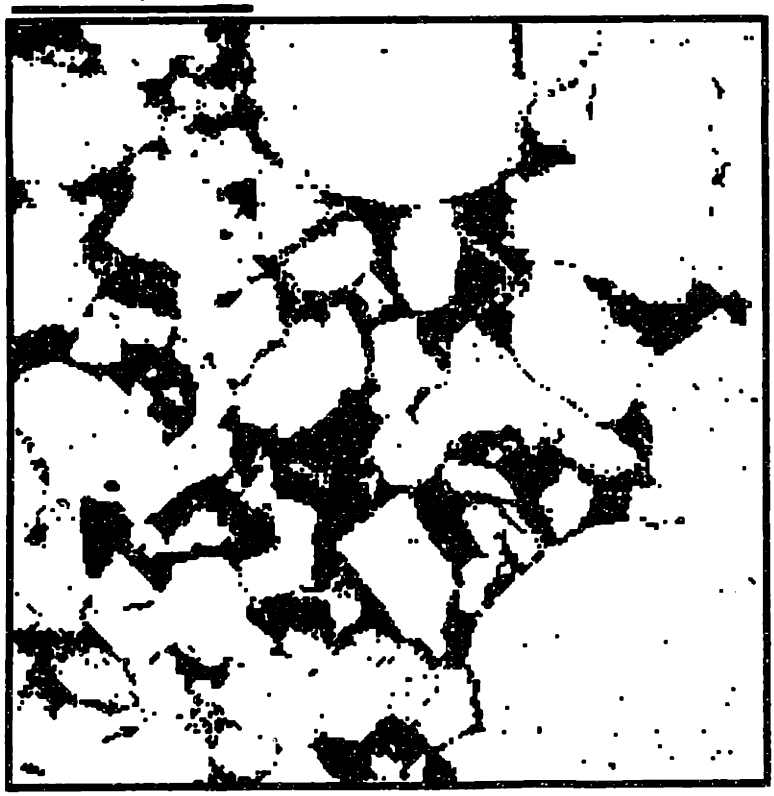

500 μm

Figure C.1e

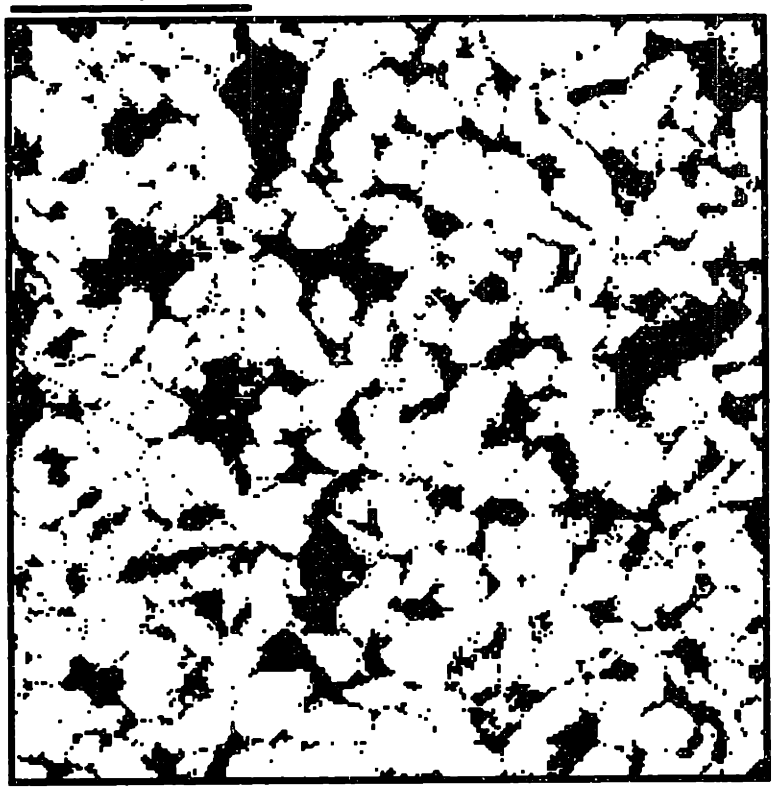

100 μm

Figure C.1f

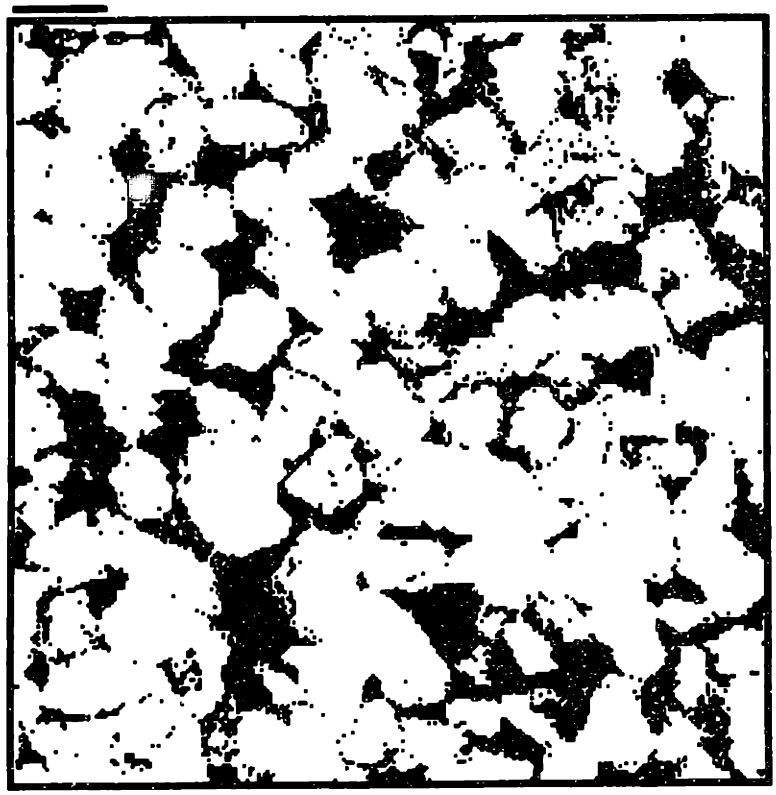

100 μm

Figure C.1g

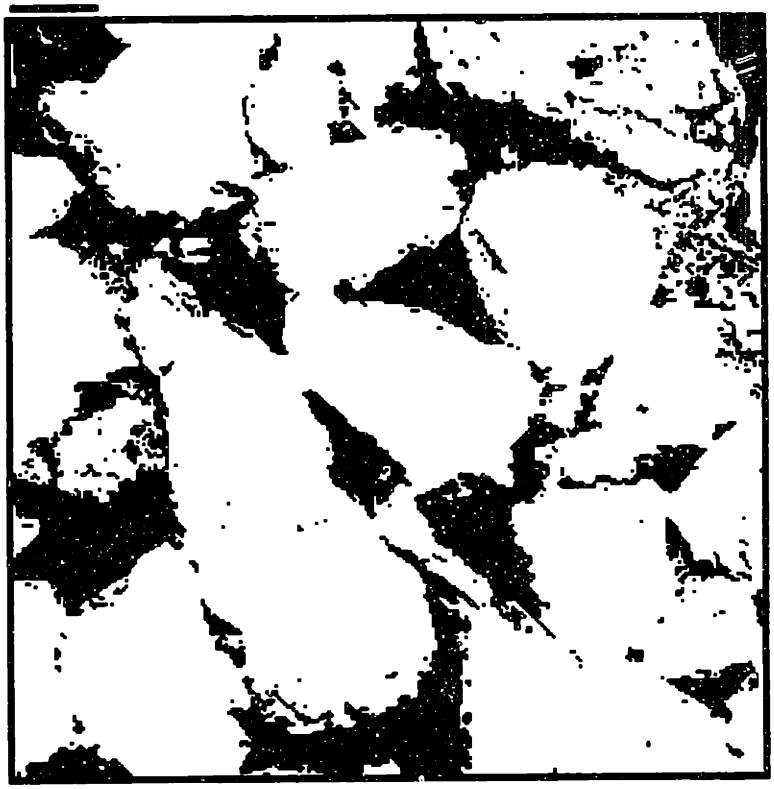

100 μm

Figure C.1h

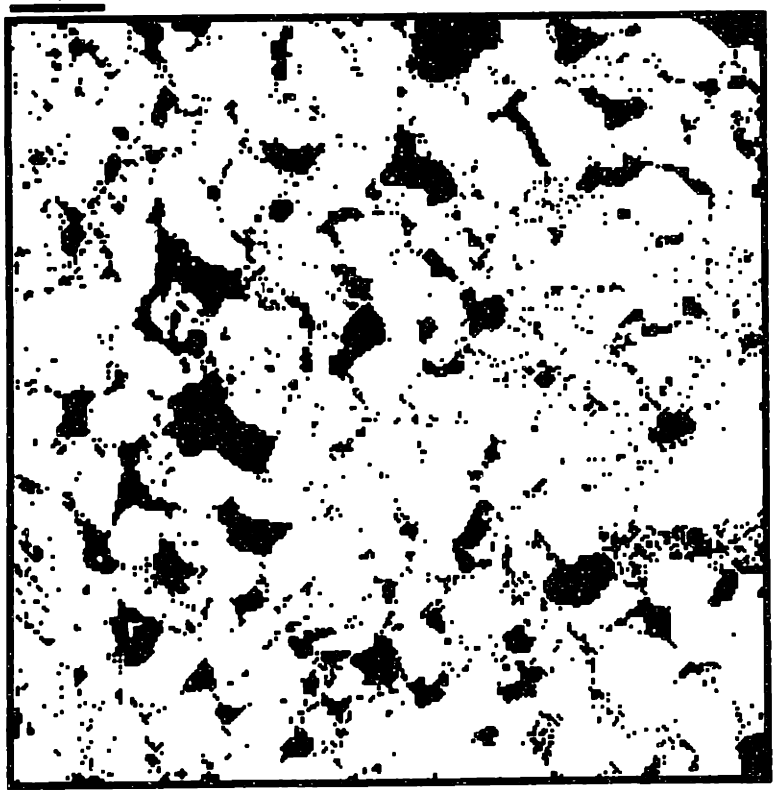

100 μm

Figure C.1i

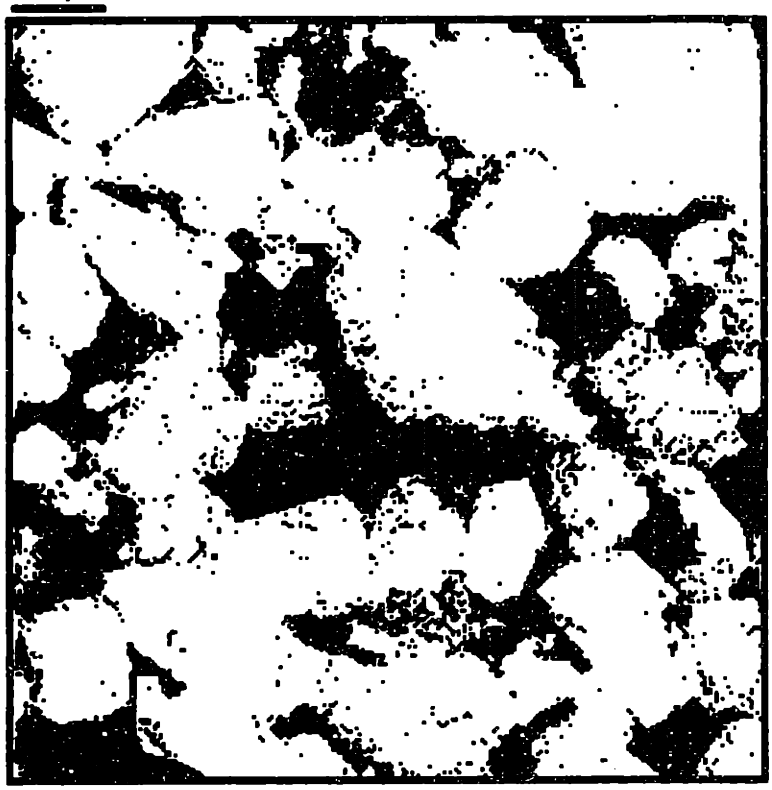

100 μm

Figure C.1j

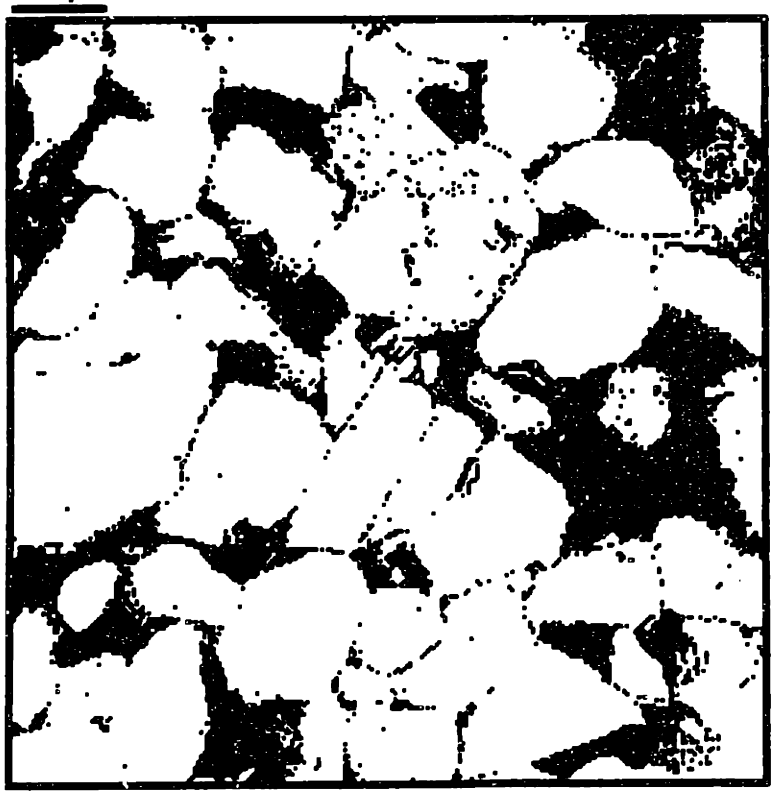

100 μm

Figure C.1k

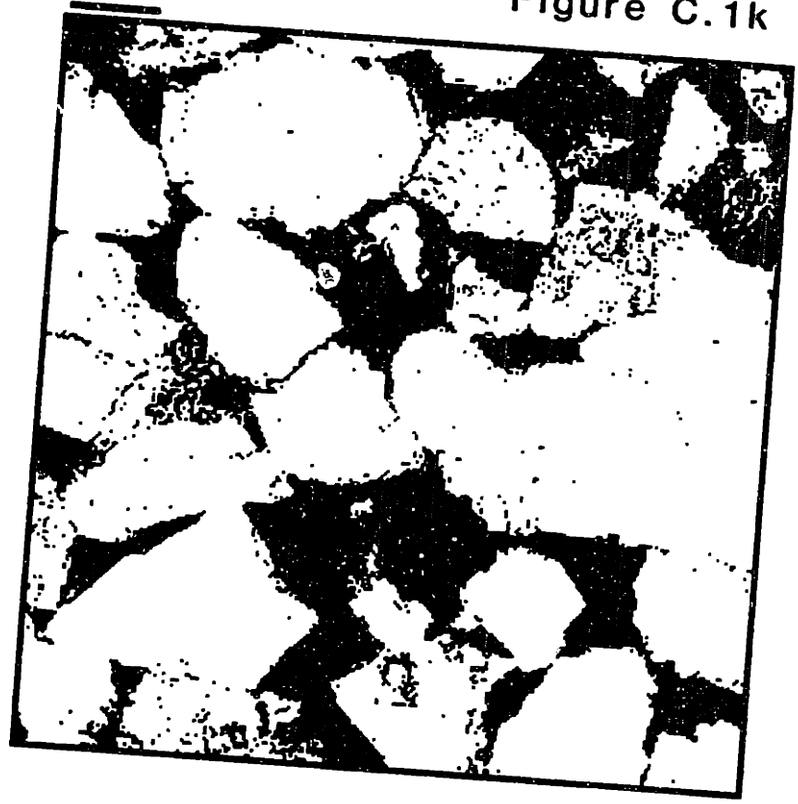

100 μm

Figure C.1l

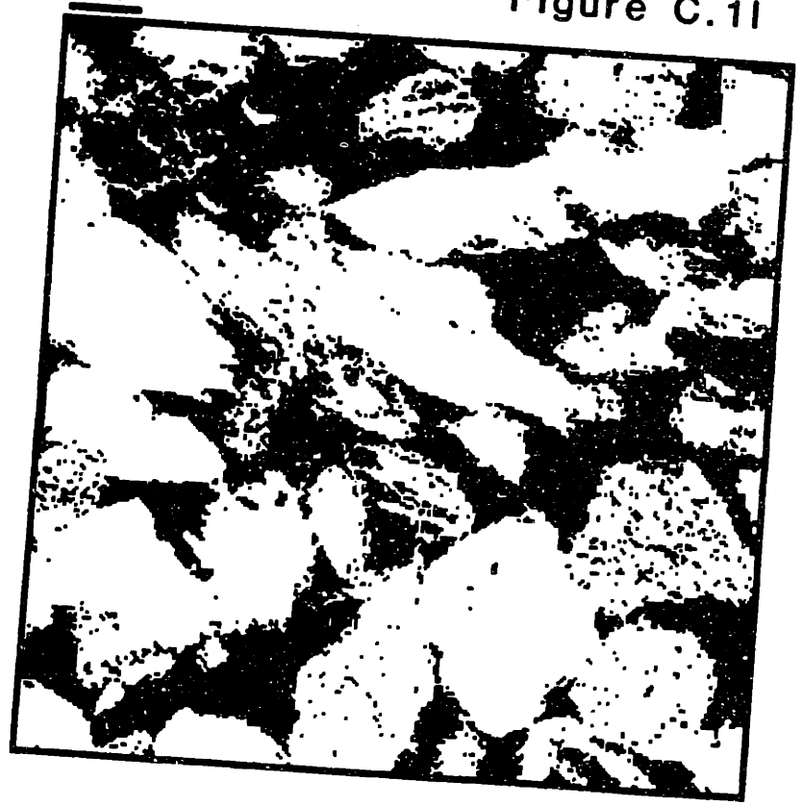

100 μm

Figure C.1m

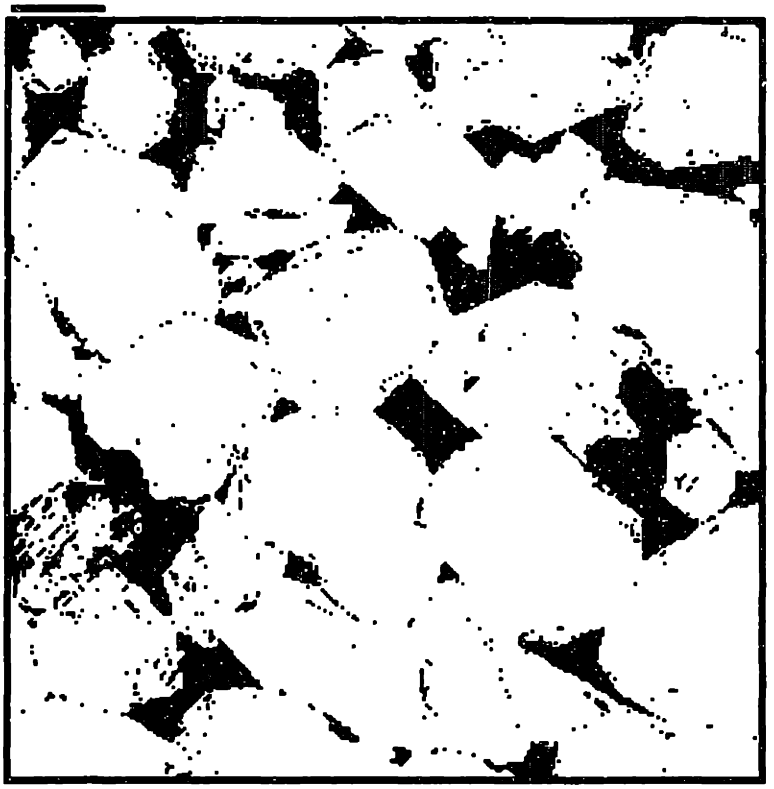

100 μm

Figure C.1n

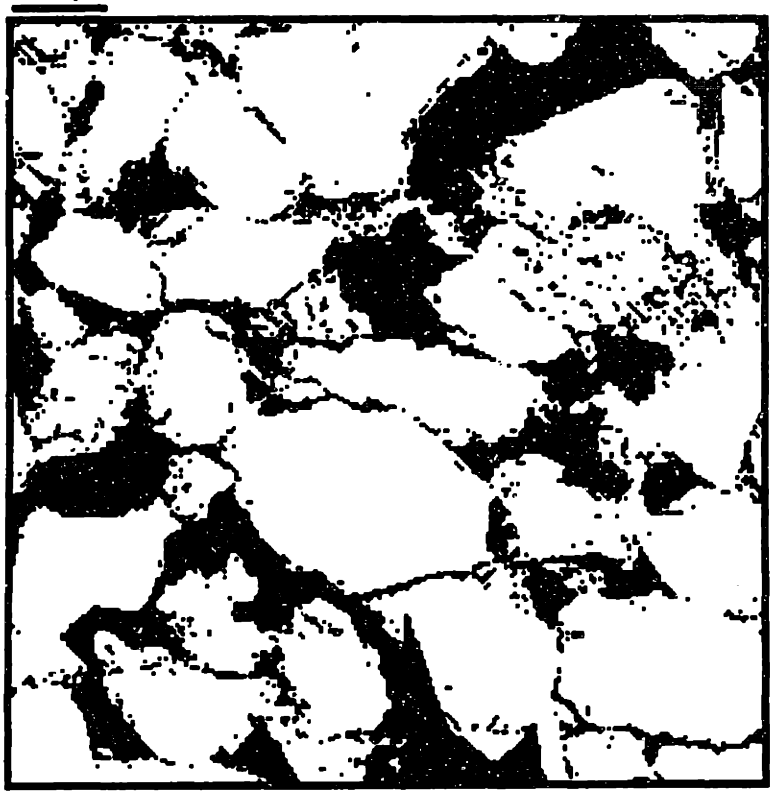

Appendix D

Digital Image Analysis Software

D.1 Introduction

This appendix contains documentation about the software developed in this study. All software was developed from scratch, with the exception of a grey scale display algorithm, matrix inversion routines, and Fourier analysis subroutines. System-dependent considerations were used during software development and may not apply for different hardware configurations. In particular, due to memory and speed limitations, programs usually performed a single function as opposed to creating a processing environment (e.g., GIAPP (Fabbri, 1980, 1984)). Also, the programs were not written for general purpose image analysis, but rather, they are specifically intended for analysis of digital SEM images. Image acquisition hardware and processing hardware are described in Appendix A.

The main bodies of programs were written in FORTRAN IV. However, all subroutines which operate on binary images were written in MACRO (DEC, PDP-11 Assembly Language). Assembly language was used primarily to increase execution speed, but also because of the ease with which bits (i.e., binary pixels) can be manipulated. Following is a description of the image file structure and brief descriptions of the programs. These descriptions are intended to show the principal operations used in the study of pore structure.

D.2 Image File Structure

The image file consists of an image header followed by the pixel values. The image header contains all of the parameters used during image acquisition (e.g., sample information, SEM settings, dwell time) and it contains a terse history of the image processing which produced the current image. The contents of the image header are given in Table D.1.

The pixel values can be one of two forms: (1) full byte intensity or (2) packed one-bit binary values. The image collected with the SEM is in the full byte format. This full byte image is evaluated for threshold selection (Chapter 3). The threshold is applied to the full intensity image to produce a packed image where each pixel is represented by a single bit (on or off). Eight pixels are represented by each byte in the packed image. Image analysis is done almost exclusively on these packed binary images. The full intensity image is used only for Fourier autocovariance calculation (after dichotomization to full intensity 1 or 0 values), and grey scale display on the electrostatic plotter. Note that the packed binary image reflects an eight-fold reduction in image size.

D.3 Image Analysis Programs

Below, the programs developed for image analysis are listed in alphabetical order with a brief description of their function. All of the programs allow specification of a mask within which the function is performed. If appropriate, the programs allow complementation of binary images prior to analysis.

A2DCOV Averages the two-dimensional covariance functions from several images.

AVGCOV Averages the one-dimensional covariance functions from several images.

BDYSTA Computes the parameters and statistics of boundary contours which were mapped by **MAPCNT**. The parameters include feature area, perimeter, bending energy, hydraulic radius, and perimeter-to-area ratios. The statistics include mean values, standard deviations, minimum values, and maximum values.

BINDSP Displays a packed binary image on the Versatec electrostatic plotter. The image can be complemented and replicated (magnified) prior to display.

CHORDX Measures the line-sampled intercept length distribution in a binary image. Several boundary conditions, including exclusion regions and omission of boundary touching chords, can be specified (see Chapter 4).

CNTSET Counts the number of set bits (i.e., pore pixels) in a binary image.

COMIMG Complements (i.e., changes set bits to clear and vice versa) a binary image.

COV2DB Computes the two-dimensional covariance (*NCC*) for a binary image.

COVARX Computes the one-dimensional X-direction (i.e., line-scan direction) covariance (*NCC*) of a binary image.

CRDSTA Computes stereological parameters and statistics of a line-sampled chord distribution. Stereological parameters include lineal fraction, mean intercept length, and specific surface. Statistics include the mean and standard deviation of the chord length and geometric mean length.

CVTCRD Converts a line-sampled chord distribution into a point-sampled chord distribution for use with **PLSELP** and **SIZELP**.

DICHOT Dichotomizes a full intensity image to produce a packed binary image.

DTP The data transfer program is a FLEXTRAN program which runs on the Tracor Northern TN-2000 system. **DTP** works in conjunction with **TN2PDP** to transfer images from the TN-2000 system to the PDP 11/34a system. EDX spectra may also be transferred.

EARATO Estimates the aspect ratio of oblate ellipsoids given the distribution of ellipse aspect ratios of features in an image. The estimator is from Cruz Orive (1976, 1978).

ELPIMG Makes a synthetic ellipse image. Uses output from **FTRSTA** in the form of location, semi-axes lengths, and orientation of the dynamic ellipse approximations.

FFTPLT Plots the autocovariance output of **IMGFFA** or **COV2DB** in a three-dimensional hidden line plot.

FTREXT Performs the line-by-line feature parameter extraction from a binary image (see Chapter 5). All primary feature parameters (Table 5.1) are stored during counting. Results are written to a file which is input for **FTRSTA**.

FTRSTA Computes secondary feature parameters (Tables 5.2 and 5.3) and statistics for primary and secondary parameters from the output of **FTREXT**. Statistics include the mean, standard deviation, and minimum and maximum values of all primary and secondary feature parameters (see Chapter 5).

GRANUL Applies the opening operation to a binary image with a user-specified pair of structuring elements. Granulometry of the features is computed and stored (see Chapter 5). Either a rigorous local mask or the "infinite image" mask (used for SMS segmentation) can be specified. The opened images can be stored.

GRNAVG Averages the granulometry functions from several images.

GRNHST Computes an areal fraction histogram of feature diameters from the granulometry output of **GRANUL**.

HISFIT Fits Gaussian curves to an image histogram (see Chapter 3). The number of curves and the intensity region for fitting are user-specified. The inversion is a linearized iterative least squares. Results are used to select a dichotomization threshold.

HISINF Finds the point of inflection on the cumulative intensity distribution between the pore pixel intensities and the grain pixel intensities. A least squares cubic spline is fit to the distribution and the point of inflection is found from the analytic derivative.

IAP The image acquisition program is a FLEXTRAN program which runs on the Tracor Northern TN-2000 system. **IAP** controls the digital scan of the TN-1310 for image acquisition and stores the digitized values on

diskette. Features include histogram displays, digital line scans, and complete documentation of SEM acquisition parameters.

IMGBIN Produces grey scale or binary packed images from a full intensity image. The binary packed images can be used for further processing (same as **DICHOT**). The grey scale or binary images are displayed with **BINDSP**.

IMGCMB Performs a logical combination of two binary images. The combination is either BIS, XOR or BIC. BIS sets the bits in one image that are set in the other. XOR is the exclusive OR of the two images. BIC clears the bits in one image that are set in the other. The input and output images can be complemented and subregions of the input images can be selected. **IMGCMB** is used to produce boundary images, cut images, and SMS segmentations (see Chapter 5).

IMGDMP Dumps the pixel values of a full intensity image.

IMGERO Erodes a binary image with a user-specified 3×3 structuring element. The image can be complemented before, between, and after erosions. Dilations are accomplished by appropriate selection of complementation.

IMGFFA Computes the autocovariance of a dichotomized full intensity image (i.e., full byte values of 1 or 0) by Fourier methods. The covariance is transient and is normalized for image overlap (see Chapter 6). The power spectrum is also computed and can be stored.

IMGHDR Displays and allows modification of image headers.

IMGHIS Tabulates the intensity histogram of a full intensity image.

IMGRAS Produces a raster tape of a binary image which can be displayed with the Versatec program RASR (see Versatec documentation). **IMGRAS** is used to produce high quality hardcopies of images.

IMGROT Rotates a binary image counterclockwise by a multiple of 90 degrees. **IMGROT** is used to rotate the image so that **COVARX** or **CHORDX** can be applied to the Y direction.

IMGTON Transforms full intensity images according to a user-specified intensity transform. The default transform converts the image from unsigned

byte integers (used by the acquisition computer) to signed byte integers (used by the processing computer). The user can specify an arbitrary transform based on linear interpolation between breakpoints. This last mode is used to dichotomize a full intensity image for use with **IMGFFA**.

ISOCOV Performs orientation averaging of two-dimensional covariance functions to yield a one-dimensional isotropic covariance.

LINFFA Extracts a horizontal (X lags) or vertical (Y lag) line from the 2-D autocovariance computed by **IMGFFA**. The line can be plotted with **PLTDIA**.

MAPCNT Maps the boundary contours of features. The boundary image is described in Chapter 5. The map is a sequence of Freeman (1961) codes. Boundary maps are stored for later input to **BDYSTA**.

PLSELP Inverts a point-sampled chord length distribution for the volume fraction size–shape distribution of ellipsoids. The inversion uses a positivity constrained least squares algorithm (see Chapter 4). Size–shape classes and a subsection of the chord length distribution are user-selected.

PLTDIA Plots the results from most image analysis programs. Several standard functions (e.g., histograms, chord length distributions, size distributions, covariance) and a general data option are available.

PNTCNT Performs a point count of a binary image using a user-specified sampling grid. Note that point-counting is different from the areal analysis of **CNTSET**.

PTCRDX Measures the true point-sampled intercept length distribution on a binary image. The sampling grid is user-specified.

RNGCOV Estimates the range of the one-dimensional covariance. Estimates the asymptotic value, asymptote crossings, and computes the Weissberg–Prager (1962) permeability bound.

SIZELP Inverts a point-sampled intercept length distribution for the volume fraction size–shape distribution of ellipsoids. The inversion uses a damped least squares algorithm. Resolution and covariance matrices can be computed. Size–shape classes and a subsection of the intercept length distribution are user-selected.

SUMCRD Combines the line-sampled or point-sampled intercept length distributions from two or more images.

SYNCRD Computes a synthetic point-sampled intercept length distribution based on user-specified size–shape classes and volume fractions.

TN2PDP This program is used in conjunction with **DTP** to transfer images from the TN-2000 system to the PDP 11/34a system.

Table D.1

Image Header Contents

Group	Name	Range	Length (bytes)	FLEXT. add.	FORTRAN address
SAMPLE	LABEL	79 char	80	BP(0)	AHEDER(1)
	MITNO	0–9999	2	IP(40)	IHEDER(41)
	AXIS	2 char	4	BP(82)	AHEDER(83)
	DATE	DD-MMM-YY	10	BP(86)	AHEDER(87)
				5 bytes unused	
STAGE	X	0–999	2	IP(50)	IHEDER(51)
	Y	0–999	2	IP(51)	IHEDER(52)
	Z	0–50	2	IP(52)	IHEDER(53)
	TILT	-10–80	2	IP(53)	IHEDER(54)
	ROTAT	0–99	2	IP(54)	IHEDER(55)
	XSHIFT	0–999	2	IP(55)	IHEDER(56)
	YSHIFT	0–999	2	IP(56)	IHEDER(56)
	SCANROT	0–360	2	IP(57)	IHEDER(57)
				4 bytes unused	
BEAM	FUNCTION	3 char	4	BP(120)	AHEDER(121)
	SPOTSIZE	1 char	2	BP(124)	AHEDER(125)
	WORKDIST	10–30	2	IP(63)	IHEDER(64)
	EMISSION	0–100	2	IP(64)	IHEDER(65)
	ACCVOLTS	1–40	2	IP(65)	IHEDER(66)
				1 byte unused	

Table D.1 (cont.)

Image Header Contents

Group	Name	Range	Length (bytes)	FLEXT. add.	FORTRAN address
CONSOLE	MAG	5.0–3.E4	6	PM(22)	HEADER(34)
	DETECTOR	3 char	4	BP(140)	AHEDER(141)
	HIGHTEN	3 char	4	BP(144)	AHEDER(145)
	GAMMA	0–4360	2	IP(74)	IHEDER(75)
	CONTRAST	0–360	2	IP(75)	IHEDER(76)
	BRIGHT	0–360	2	IP(76)	IHEDER(77)
				4 bytes unused	
	DISK#	0–9999	2	IP(79)	IHEDER(80)
GRID	GRIDTYPE	0–3	2	IP(80)	IHEDER(81)
	NPTS	128,256,512	2	IP(81)	IHEDER(82)
	DWELL	1–4095	2	IP(82)	IHEDER(83)
				16 bytes unused	
PHOTO	PHOTOLAB	40 char	42	BP(182)	AHEDER(183)
POSITION	SHIFTX	0–999	2	IP(112)	IHEDER(113)
	SHIFTY	0–999	2	IP(113)	IHEDER(114)
IMAGE	LOTHRESH	0–255	1	BP(228)	AHEDER(229)
	HITHRESH	0–255	1	BP(229)	AHEDER(230)
				4 bytes unused	
ACQUIRE	IMAGEID#	1000–9999	2	IP(115)	IHEDER(116)
PROCESS	NPIXEL	1–1024	2	IP(116)	IHEDER(117)
CALIBRATE	DELTA	0.–100.	6	PM(39)	HEADER(60)

Table D.1 (cont.)

Image Header Contents

Group	Name	Range	Length (bytes)	FLEXT. add.	FORTRAN address
PROCESS	SETBIT	0.–1.E9	4		HEADER(61)
	NEROSN	0–9999	2		IHEDER(123)
				2 bytes unused	
	TSTLEN	0.–1.E9	4		HEADER(63)
	SVRBLK	0.–1.E9	4		HEADER(64)
PROCESS	LENHIS	0–254	2		IHEDER(129)
	HISTORY	254 char	254		AHEDER(259)

NOTES: 1. Two differences exist between addressing variables in FLEXTRAN and FORTRAN. FLEXTRAN uses zero for the first index of an array, whereas FORTRAN uses one. FLEXTRAN uses a 6 byte floating point format, whereas FORTRAN uses a 4 byte format. The first program (**IMGTON**) run on the image after transfer to the PDP11/34a based system converts the byte integer format from the unsigned values used on the TN2000 to the 2's complement representation used on the PDP. **IMGTON** also converts the 6 byte floating point numbers to 4 byte floating point numbers.

2. IP is an integer array used to access integer variables in FLEXTRAN program. BP is a byte array used to access character variables and single byte integers in FLEXTRAN program. PM is a floating point array used in FLEXTRAN programs to access floating point numbers. IP, BP, and PM are overlaid.

3. HEADER is a floating point (REAL*4) array used in FORTRAN programs to access floating point variables. IHEDER is an integer (I*2) array used in FORTRAN programs to access integer variables. AHEDER is a byte array (BYTE) used in FORTRAN programs to access character variables and single byte integers. HEADER, IHEDER, and AHEDER are overlaid.